PD F
FCT PhD
PROGRAMMES

QUALIFICAR É CRESCER.

QUADRO
DE REFERÊNCIA
ESTRATÉGICO
NACIONAL
PORTUGAL 2007.2013

UNIÃO EUROPEIA
Fundo Social Europeu

Multifunctional Silk Fibroin-Based Constructs for Tissue Engineering and Regenerative Medicine Applications

Viviana Pinto Ribeiro

UMinho | 2018

Universidade do Minho
Escola de Engenharia

Viviana Pinto Ribeiro

Multifunctional Silk Fibroin-Based Constructs for Tissue Engineering and Regenerative Medicine Applications

Março de 2018

Universidade do Minho
Escola de Engenharia

Viviana Pinto Ribeiro

Multifunctional Silk Fibroin-Based Constructs for Tissue Engineering and Regenerative Medicine Applications

Tese de Doutoramento
Programa Doutoral em Engenharia de Tecidos Medicina Regenerativa e Células Estaminais

Trabalho efetuado sob a orientação de
Professor Rui Luís Gonçalves dos Reis
Doutor Joaquim Miguel Antunes de Oliveira
Doutora Ana Leite de Almeida Monteiro de Oliveira

Março de 2018

STATEMENT OF INTEGRITY

I hereby declare having conducted my thesis with integrity. I confirm that I have not used plagiarism or any form of falsification of results in the process of elaboration of the thesis. I further declare that I have fully acknowledged the Code of Ethical Conduct of the University of Minho.

University of Minho, 22 de Março de 2018

Full name: Viviana Pinto Ribeiro

Signature: Viviana Pinto Ribeiro

In Memory of my Lovely Father

ACKNOWLEDGMENTS

This preparation of this thesis would not be possible without the important contribution of several people. To them, I am and will always be grateful.

I would like to take this opportunity to express my gratitude to my formal PhD supervisor, Prof. Rui Reis. He not only gave me the opportunity to joint his privileged research group, in the beginning not even as PhD student, but he also supported my work and progress. I would like to specially acknowledge his support and trust on me, for his huge assistance in the PhD scholarship application, and also for allow me to work with such good co-supervisors. He also gave me the opportunity to join a privileged investigation group in Madrid, which allowed me to grow at professional and personal level. In these years, he always inspires me, supported my new ideas and provide me the opportunity to attend important scientific conferences. I believe that he is one of the most intelligent people that I had the privilege to deal, a great leader of his group, and most important a good example to follow.

I would like to express my gratitude to Prof. Julio San Roman, at the CSIC, in Madrid for receiving me in his lab and making me part of his group. It was a great experience due to the insights to my work, and also for the amazing integration in the lab, making me part of it.

No words can express my gratitude to Dr. Joaquim Miguel Oliveira. Since the beginning, he accepted me as his student even though It was not his choice. He trusted me with responsibilities and challenges that made be a better researcher and person, with goals that not even me knew that I could achieve. With him I had the opportunity to work in different projects and works with my colleagues, which gave a valuable input in my scientific career. More importantly, thank you Miguel for all the words of encouragement that always made me see the “glass half full”, even when it was “half empty”.

To Dr. Ana Leite Oliveira I have a special acknowledgment, because I truly believe that she had a major contribution in what I have become during the past 4 years. She was the person that trusted me, even when I was afraid of not being up to the group expectations. I had a great pleasure to work, learn and most importantly to grow with her, at professional and personal level. For all of these and much more, thank you Ana.

I would like to acknowledge to the co-authors in this thesis and to my colleagues currently working with the materials that I developed in the scope of this thesis.

I would like to express my gratitude to my colleagues that indirectly contributed to this thesis, namely, those that gave me training in the labs and equipment’s. To the management team and to support and

administration staff, for trying to help in all my requests. I want to also acknowledge the technical support given by Elsa Ribeiro.

I am very grateful to my colleagues and friends in 3B's research group. We share good and less good moments, frustrations and achievements, and during these times I have found really special people. I would like to thank Alain, Albino, Ana Martins, Cristiana e Mariana, Ivo, Joana Silva-Correia, João Costa, Lucília, Pedro Babo, Raquel Maia, Raphael, Sandra Pina, and of course to Ana Gi, Rita e Sara.

Thanks to Le-ping Yan, for the aid advices and all the help at the beginning of my PhD.

I would like to thank my friends and family for all the emotional support during this journey. I have a special thanks to my mother for all the advices that made me accept this challenge, and unconditional love at the most difficult times.

It is hard to put in words the gratefulness to someone so special as my husband Vitor. Without him none of this would be possible. His love and support were crucial for giving me the strength to accept and continue my work in the most difficult times. He was always by my side and without any complain. Thank you for being there!

Finally, I acknowledge to FCT/MCTES (Fundação para a Ciência e a Tecnologia/Ministério da Ciência, Tecnologia, e Ensino Superior) and Fundo Social Europeu através do Programa Operacional do Capital Humano (FSE/POCH), PD/59/2013, for my scholarship PD/BD/113806/2015, and for giving me the financial support to develop this thesis.

ABSTRACT

Osteochondral (OC) defects are a common problem in orthopedics, affecting simultaneously the articular cartilage and underlying subchondral bone tissue. In order to repair an OC defect, the needs of cartilage, bone and bone-cartilage interface must be considered. OC tissue engineering (TE) strategies may include the use of biomaterials processed into porous scaffolds, fiber materials or hydrogels. Bilayered scaffolds, developed by combining these structures into layered and graded forms, have been receiving much attention (Chapter 1). While the ideal TE strategy has not yet been achieved, great efforts have been made in terms of pre-clinical and clinical applications of engineered biomaterials for OC regeneration, some of them overviewed in this thesis (Chapter 2).

As a natural-based polymer silk fibroin (SF) has a particular interest as scaffolding material. The most recently developed biomimetic strategies and processing routes of SF-based materials aiming bone, cartilage and OC tissues regeneration, were summarized and discussed in this thesis (Chapter 3). The high processability of this protein, also motivated the use of silk in the herein developed work.

Textile-based SF scaffolds were produced by a weft-knitting technology and surface modified to be modulated according to the target TE application (Chapter 5). The same textile-based technology was used to process novel weft-knitted SF spacer scaffolds for bone TE applications (Chapter 6). A monofilament of polyethylene terephthalate (PET) was used to increase the scaffolds three-dimensionality (3D), inducing structural similarities adequate for flat bone regeneration. A horseradish peroxidase (HRP)-mediated crosslinking system was used in combination with salt-leaching and freeze-drying methodologies for preparing porous SF scaffolds for cartilage TE applications (Chapter 7). Considering the stratified and hierarchical characteristics of OC tissue, bilayered scaffolds composed of a HRP-crosslinked SF layer and a composite layer combining HRP-crosslinked SF and ionic-doped (zinc and strontium) β-tricalcium phosphate (β-TCP), were proposed for OC regeneration (Chapter 8). The use of HRP-crosslinked SF hydrogels with spatial tunable properties and cell-encapsulation ability, was also proposed in this thesis as a novel strategy for the fundamental study of hydrogel-based 3D models in cancer research (Chapter 9).

In summary, the presented results indicated the versatility of the proposed biomimetic strategies for improving the performance of SF as biomaterial for bone, cartilage and OC tissue engineering, or for using in 3D culture technologies to build better *in vitro* 3D tumor models for cancer research.

RESUMO

Defeitos osteocondrais são dos maiores problemas em cirurgia ortopédica, afetando em simultâneo a cartilagem articular e o tecido ósseo subcondral adjacente. A reparação destes defeitos, envolve ações no osso, cartilagem e na interface que os une, sendo que diferentes abordagens em engenharia de tecidos e uso de biomateriais foram já propostas nesse sentido. Biomateriais porosos, à base de fibras, hidrogéis e estruturas em bicamada, foram já explorados para engenharia do tecido osteocondral (Capítulo 1), e apesar de não ser reconhecida a estratégia ideal para a reparação deste tecido, avanços significativos têm sido demonstrados em estudos pré-clínicos e clínicos (Capítulo 2).

A fibroína da seda (*Silk Fibroin* - SF) tem sido proposta em algumas estratégias envolvendo biomateriais para aplicações no osso, cartilagem ou tecido osteocondral, algumas descritas nesta tese (Capítulo 3). A elevada processabilidade da SF suscitou o interesse da sua aplicação neste trabalho.

Através da tecnologia têxtil *weft-knitting*, foi possível produzir novas estruturas à base de SF capazes de serem modificadas superficialmente de acordo com a aplicação desejada (Capítulo 5). Estruturas de SF *weft-knitted* foram também utilizadas em combinação com um monofilamento de politereftalato de etileno (PET), para produzir biomateriais porosos com superior tridimensionalidade e semelhanças estruturais ao osso achatado (Capítulo 6). Um sistema de reticulação enzimática com base na enzima peroxidase (*Horseradish peroxidase* - HRP) foi proposto para reticulação da SF, e em combinação com metodologias de *salt-leaching* e *freeze-drying* formar estruturas porosas para aplicações na cartilagem (Capítulo 7). Tendo em conta as propriedades estratificadas e hierárquicas do tecido osteocondral, estruturas em bicamada foram também desenvolvidas, envolvendo uma camada condral porosa de SF reticulada enzimaticamente e uma camada subcondral em que as mesmas estruturas foram incorporadas com partículas de β-tricálcio fosfato (β-TCP) dopadas com iões zinco e estrôncio (Capítulo 8). Hidrogéis de SF reticulados pela HRP foram também desenvolvidos com propriedades estruturais ajustáveis e capacidade de encapsulamento celular, propostos nesta tese para o estudo fundamental de modelos 3D com base em hidrogéis, na investigação do cancro (Capítulo 9).

Em suma, os resultados obtidos demonstram a versatilidade das estratégias biomiméticas propostas, de modo a melhorar as propriedades dos biomateriais de SF para aplicações na engenharia do tecido ósseo, cartilagem e osteocondral, ou para aplicações na investigação do cancro como tecnologias 3D que mimetizem o microambiente tumoral *in vitro*.

TABLE OF CONTENTS

ACKNOWLEDGMENTS vii
ABSTRACT ix
RESUMO xi
TABLE OF CONTENTS xiii
LIST OF ABBREVIATIONS xix
LIST OF FIGURES xxiii
LIST OF TABLES xxix
LIST OF EQUATIONS xxxi
SHORT CORRICULUM VITAE xxxiii
LIST OF PUBLICATIONS xxxv
INTRODUCTION TO THE THESIS FORMAT xli

SECTION I GENERAL INTRODUCTION 1

Chapter 1 Fundamentals on osteochondral tissue engineering 3

1.1. Abstract 5
1.2. Introduction 6
1.3. Osteochondral tissue: Structure and properties 7
  1.3.1. Articular cartilage 7
  1.3.2. Subchondral bone 9
1.4. Strategies for osteochondral tissue engineering 11
  1.4.1. Bilayered scaffolds 11
  1.4.2. Fibrous scaffolds 14
  1.4.3. Hydrogel scaffolds 16
1.5. Concluding remarks 17
1.6. References 18

Chapter 2 Pre-clinical and clinical management of osteochondral lesions 25

2.1. Abstract 27
2.2. Introduction 28
2.3. Pre-clinical studies for osteochondral regeneration 30
2.4. Clinical trials for osteochondral regeneration 33
2.5. Marketed products for osteochondral regeneration 36
2.6. Conclusions 37
2.7. References 38

Chapter 3 Silk fibroin-based hydrogel and scaffolds for osteochondral repair and regeneration 43

3.1. Abstract 45
3.2. Introduction 46
3.3. Characteristics of silk fibroin 48
3.4. Silk fibroin-based hydrogels 49
3.5. Silk fibroin-based scaffolds 54
3.6. Concluding remarks and research efforts 61

3.7. References ... 62

SECTION II EXPERIMENTAL SECTION ... 69

Chapter 4 Materials and Methods ... 71

4.1. Materials ... 73
4.1.1. Silk fibroin (SF) ... 73
4.1.2. Polyethylene terephthalate (PET) ... 74
4.1.3. β-tricalcium phosphate (β-TCP) ... 75
4.2. Reagents ... 76
4.3. Scaffolds and hydrogels preparation ... 76
4.3.1. Methodologies for scaffolds and hydrogels processing: Overview ... 76
4.3.2. Production of textile-based scaffolds ... 80
4.3.3. Production of SF membranes ... 83
4.3.4. Production of SF hydrogels ... 83
4.3.5. Salt-leached enzymatically crosslinked SF scaffolds ... 85
4.3.6. Salt-leached enzymatically crosslinked bilayered SF/SF-β-TCP scaffolds ... 86
4.4. Physicochemical characterization ... 88
4.4.1. Morphology and microstructure evaluation ... 88
4.4.2. Chemical analysis ... 91
4.4.3. Surface characterization ... 93
4.4.4. Mechanical properties ... 95
4.4.5. Swelling ratio ... 98
4.4.6. Degradation profile ... 99
4.4.7. *In vitro* mineralization ... 100
4.5. *In vitro* biological characterization ... 101
4.5.1. Cell sources ... 101
4.5.2. Cryopreservation ... 103
4.5.3. Cell seeding procedures ... 103
4.5.4. Metabolic activity and cell viability examination ... 107
4.5.5. Cell attachment, morphology and arrangement on the scaffolds and hydrogels ... 110
4.5.6. Biochemical characterization ... 112
4.5.7. Gene expression profiles ... 115
4.5.8. Histological analysis ... 118
4.5.9. Immunocytochemistry ... 120
4.5.10. Immunohistochemistry ... 121
4.5.11. Biomechanical analysis ... 122
4.6. *In vivo* studies ... 123
4.6.1. Chich choriallantoic membrane (CAM) assay ... 123
4.6.2. Subcutaneous implantation ... 124
4.6.3. Explants characterization ... 125
4.7. Statistical analysis ... 126
4.8. References ... 127

SECTION III EXPERIMENTAL STUDIES ... 135

Chapter 5 Influence of different surface modifcation treatments on silk biotextiles for tissue engineering applications ... 137

5.1. Abstract 139
5.2. Introduction 140
5.3. Materials and Methods 141
  5.3.1. Production of the textile constructs and membranes 141
  5.3.2. Surface treatments 142
  5.3.3. Mechanical properties 143
  5.3.4. Scanning electron microscopy 143
  5.3.5. Atomic force microscopy 144
  5.3.6. Contact angle and surface energy 144
  5.3.7. X-ray photoelectron spectroscopy 145
  5.3.8. Cell culture 145
  5.3.9. DNA quantification assay 146
  5.3.10. Statistical analysis 146
5.4. Results and Discussion 146
  5.4.1. Mechanical properties 146
  5.4.2. Surface morphology and topography 148
  5.4.3. Surface wettability and composition 151
  5.4.4. Cell morphology 153
  5.4.5. Cell adhesion 156
5.5. Conclusions 157
5.6. Supplementary information 158
5.7. References 159

Chapter 6 Silk-based anisotropical 3D biotextiles for bone regeneration 165

6.1. Abstract 167
6.2. Introduction 168
6.3. Materials and Methods 170
  6.3.1. Materials 170
  6.3.2. Production of the textile-based scaffolds 170
  6.3.3. Morphological characterization 171
  6.3.4. Mechanical properties 171
  6.3.5. *In vitro* cell studies 172
  6.3.6. *In vivo* angiogenesis evaluation 176
  6.3.7. Subcutaneous implantation 178
  6.3.8. Statistical analysis 178
6.4. Results 179
  6.4.1. Morphological characterization 179
  6.4.2. Mechanical properties 181
  6.4.3. *In vitro* assessment of the textile-based scaffolds 182
  6.4.4. Angiogenic potential of the textile-based scaffolds 187
  6.4.5. Subcutaneous implantation of the textile-based scaffolds 188
6.5. Discussion 189
6.6. Conclusions 193
6.7. Supplementary information 194
6.8. References 195

Chapter 7 Combinatory approach for developing silk fibroin scaffolds for cartilage regeneration 199

7.1. Abstract 201
7.2. Introduction 202
7.3. Materials and Methods 204
7.3.1. Materials and reagents 204
7.3.2. Preparation of aqueous silk fibroin solution 204
7.3.3. Preparation of salt-leached enzymatically crosslinked silk fibroin scaffolds 205
7.3.4. Physicochemical characterization 205
7.3.5. Swelling ratio and degradation profile 206
7.3.6. *In vitro* cell studies 207
7.3.7. Subcutaneous implantation 213
7.3.8. Statistical analysis 213
7.4. Results 214
7.4.1. Morphology and microstructure characterization 214
7.4.2. Chemical structure and protein conformation 216
7.4.3. Mechanical properties, swelling ratio and degradation profile 216
7.4.4. *In vitro* characterization of the HRP-crosslinked SF scaffolds 217
7.4.5. Subcutaneous implantation of the HRP-crosslinked SF scaffolds 222
7.5. Discussion 223
7.6. Conclusions 229
7.7. Supplementary information 230
7.8. References 230

Chapter 8 Silk fibroin-based monolithic and hierarchical scaffolds for osteochondral regeneration 235

8.1. Abstract 237
8.2. Introduction 238
8.3. Materials and Methods 240
8.3.1. Materials and reagents 240
8.3.2. Preparation of the bilayered scaffolds 241
8.3.3. Physicochemical characterization 241
8.3.4. Degradation profile 243
8.3.5. *In vitro* bioactivity assay 243
8.3.6. *In vitro* cell studies 244
8.3.7. Statistical analysis 248
8.4. Results 249
8.4.1. Microstructure, elemental composition and TCP distribution into the bilayered scaffolds 249
8.4.2. Crystalline structure and mechanical properties of the scaffolds 251
8.4.3. Degradation properties and bioactivity evaluation of the scaffolds 253
8.4.4. *In vitro* characterization of the bilayered scaffolds 254
8.5. Discussion 260
8.6. Conclusions 266
8.7. Supplementary information 267
8.8. References 268

SECTION IV EXPERIMENTAL STUDIES 273

Chapter 9 Rapidly responsive silk fibroin hydorgels as an artificial matrix for the programmed tumor cells death 275

- 9.1. Abstract 277
- 9.2. Introduction 278
- 9.3. Materials and Methods 280
  - 9.3.1. Materials 280
  - 9.3.2. Preparation of silk fibroin aqueous solution and hydrogels 280
  - 9.3.3. Structural analysis of the SF hydrogels 281
  - 9.3.4. Physicochemical characterization of the SF hydrogels 281
  - 9.3.5. Cell culture and encapsulation in the SF hydrogels 283
  - 9.3.6. Cell viability and proliferation in the SF hydrogels 283
  - 9.3.7. Statistical analysis 286
- 9.4. Results 286
  - 9.4.1. Structural and multi-scale conformational transitions of the SF hydrogels 286
  - 9.4.2. Viscoelastic properties and hydrogelation kinetics of the SF hydrogels 289
  - 9.4.3. Assessment of the programmed cell death in U251 cell-laden SF hydrogels and live conformational changes 292
- 9.5. Discussion 294
- 9.6. Conclusions 297
- 9.7. Supplementary information 298
- 9.8. References 300

SECTION V GENERAL CONCLUSIONS 305

Chapter 10 General conclusions and final remarks 307

- 10.1. General conclusions 309
  - 10.1.1. Surface modification treatments on SF biotextiles for tissue engineering applications..310
  - 10.1.2. SF-based 3D biotextiles for bone regeneration 311
  - 10.1.3. Enzymatically crosslinked SF scaffolds with potential for cartilage tissue engineerin .. 312
  - 10.1.4. Enzymatically crosslinked bilayered SF/SF-β-TCP scaffolds with potential for osteochondral tissue engineering 313
  - 10.1.5. Enzymatically crosslinked SF hydrogels as 3D matrices for cell encapsulation studies..313
- 10.2. Final remarks 314

LIST OF ABBREVIATIONS

2D – Two-dimensional
3D – Three-dimensional

A

Å - ångström
AAC – Acrylic acid
ACI – Autologous Condrocyte Implantation
AFM – Atomic Force Microscopy
AFM-IR - Atomic Force Microscopy combined to Infrared nano-spectroscopy
ALP – Alkaline phosphatase
α-MEM– Alpha-Minimum Essential Medium
ANOVA – One-way analysis of variance
APPACDM – The Portuguese Association of Parents and Friends of Mentally Disabled Citizens
ASCs – Adipose tissue derived stromal cells
ATP - Adenosine Triphospate
ATR – Attenuated Total Reflectance

B

BdTCP – Bilayered HSF/HSF-dTCP scaffolds
bFGF – Basic Fibroblast Growth Factor
BMP - Bone Morphogenetic Protein
BMSCs - Bone marrow mesenchymal stromal cells
BSA - Bovine Serum Albumin
β-sheet – Beta-sheet
β-TCP – Beta-tricalcium phosphate
BTCP – Bilayered HSF/HSF-TCP scaffolds

C

Ca^{2+} - Calcium
CAE - Constant Analyzer Energy
Calcein-AM - Calcein-Acetoxymethyl
CAM - Chick Chorioallantoic Membrane
CaP - Calcium phosphate
CH - Close from the head
CH_2I_2 - Diiodomethane
CO_2 – Carbon dioxide
COL1A1 - Collagen type I, alpha 1
COL2A1 - Collagen type II, alpha 1
Cl^- - Chloride
Col I - Collagen type I
Col II - Collagen type II
CS-PCL - Chitosan-polycaprolactone

D

dTCP – Ionic-doped β-TCP
DAPI – 4',6-diamidino-2-phenylindole
DGAV – Direcção Geral de Alimentação e Veterinária
DMEM – Dulbecco's modified eagle medium
DMA - Dynamic mechanical analysis
DNA - Deoxyribonucleic acid
dsDNA - Double-stranded DNA

E

E - Elastic modulus
E' – Storage modulus
Ev – Eletronvolt
ECM – Extracellular matrix
EDS - Energy Dispersive Spectrometer
EDTA - Ethylenediaminetetraacetic acid
EMEA - European Medicines Agency

F

FACS – Fluorescence-activated cell sorting
FBS – Fetal Bovine Serum
FDA - Food and Drug Administration
FEP - Fluorinated Ethylene Propylene
FGF – Fibroblast Growth Factor
FH – Far from the head
FITC – Fluorescein isothiocyanate
FTIR - Fourier Transform Infrared

G

G′ – Storage modulus
G′′ – Loss modulus
GAG - Glycosaminoglycan
GFs – Growth factors

H

H - Heavy
H&E – Hematoxylin and Eosin

H_2O - Water
H_2O_2 – Hydrogen peroxide
HAp - Hydroxyapatite
hACs – Human articular chondrocytes
hASCs – Human adipose stem cells
hBMSCs - Human BMSCs
HCl - Hydrorochloric acid
HCO_3^{2+} - Bicarbonate
HFIP - Hexafluoroisopropanol
hOBs – Human osteoblasts
HPO_4^- - Hydrogen phosphate
HRP - Horseradish peroxidase
HSF - HRP-crosslinked silk fibroin
Hz – Hertz

I
IGF - Insulin-like Growth Factor
IL - Interleukin

K
K^+ - Potassium
KDa - Kilo daltons
kPa – Kilo pascal
kHz – Kilohertz

L
L - Light
L – Litter
LAGG - Low Acyl Gellan Gum
L929 – Mouse C3H/An connective tissue fibroblast like cell line
LiBr - Lithium bromide

M
M - Molar
mA - Milliampere
m_f - Dry weight
µg - Microgram
µg/mL - Microgram per milliliter
mg - Milligram
Mg^{2+} - Magnesium
MHz – Megahertz
m_i - Initial weight
Micro-CT – Micro-computed tomography
mL – Milliliter
mM – Millimolar
mm- Millimeter
µmol - Micromol
MMPs - Matrix metalloproteinases
MPa - Mega pascal
MSC – Mesenchymal stem cell
MT - Masson's trichrome
mths - Months
MWCO - Molecular weight cut off
m_W – Wet weight

N
Na^+ - Sodium
N/A – Not applicable, Not available
Na_2CO_3 - Sodium carbonate
NaCl - Sodium chloride
NaOH - Sodium hydroxide
n.d – Not defined
nm – Nanometer

O
°C - Degree Celsius
O_3 - Ozone
OC - Osteochondral
OCD - Osteochondral defect
OD - Optical density
OPT – Optical Projection Tomography

P
P0 - Passage 0
P3 – Passage 3
P4 - Passage 4
P5 - Passage 4
P6 - Passage 4
Pa - Pascal
PBS – Phosphate-buffered saline
PCL - Polycaprolactone
PDGF – Platelet-derived growth factor
PDLLA - Poly-DL-lactide
PDMS - Polydimethylsiloxane
PEG - Polyethylene Glycol
PET - Polyethylene terephthalate
PGA - Poly(glycolic acid)
PI – Propidium iodide
PLA - Poly(lactic aci)
PLGA - Poly(D,L lactide-glycolide)
PLLA - Poly-L-lactide
pNP - p-nitrophenol
pNPP - p-nitrophenyl phosphate disodium
PTHrP - Parathyroid hormone-related protein

PVA - Poly(vinyl alcohol)

R
RA - Radiofrequency
RBMSCs - Rabbit BMSCs
RNA - Ribonucleic acid
RPM – Rotations per minute
RT – Room temperature
Runx2 - Runt-related transcription factor2

S
SBF – Simulated Body Fluid
SD – Standard deviation
SEM – Scanning Electron Microscopy
SF – Silk Fibroin
SF/CS – SF/Chondroitin sulfate
SF-G – SF-Gelatin
Sn – Strontium
SO_4^{2-} - Sulfate
SPCL - Starch polycaprolactone
SPIM - Selective Plane Illumination Microscopy
SVF – Stromal Vascular Fraction

T
Tan δ - Loss factor
TCP – Undoped β-TCP
TCPs - Tissue culture polystyrene
TE – Tissue engineering
TEM – Transmission Electron Microscopy
TGF-β – Transforming growth factor-β
TIPS - Temperature gradient-guided thermal-induced phase separation
Tris-EDTA - Tris(hydroxymethyl)aminomet hane-EDTA
TUNEL - Terminal deoxynucleotidyl transferase dUTP nick end labeling

U
U251 - Human neuronal glioblastoma cell line
UV – Ultraviolet

V
V - Volt
v/v – Volume/Volume
VEGF – Vascular Endothelial Growth Factor
vol – Volume
VPA - Vinyl Phosphonic Acid
VSA - Vinyl Sulfonic Acid

X
XPS – X-ray Photoelectron Spectroscopy
XRD - X-Ray Diffraction

W
wt. – Weight
w/w – Weight/Weight
w/v – Weight/Volume

Y
yrs - Years

Z
Zn - Zinc

LIST OF FIGURES

Figure 1-1. Osteochondral tissue engineering strategy. ______ 6

Figure 1-2. Schematic diagram of a long bone cross section. ______ 9

Figure 1-3. Chitosan/HAp bilayered scaffold showing two different layers, respectively for cartilage (upper layer) and bone (bottom layer). ______ 12

Figure 1-4. Image of the articular cartilage ECM/HAp bilayered scaffold prototype (A) and respective scanning electron microstructures: (B) upper layer, (C and D) interface region, nanofibrous ECM orientation in the (E) upper layer of the scaffold wall at a high magnification, and in the (F) lower layer. ______ 13

Figure 1-5. (A) Schematic diagram of the bilayered composite scaffolds, and (B) scanning electron micrograph of the scaffolds cross-section. ______ 15

Figure 1-6. Macroscopic appearance of the LAGG/LAGG-HAp hydrogels. ______ 16

Figure 1-7. Image of agarose-SPCL bilayered scaffold. ______ 17

Figure 2-1. Illustrative image of a knee healthy joint and joint with osteoarthritis. ______ 29

Figure 2-2. Microscopy images of histological hematoxylin-eosin stained sections of gelatin/β-TCP scaffolds, with (Test group) or without (Control group) MSCs and growth factors, after implantation in horses for 4 months. ______ 33

Figure 2-3. Commercial bi-multilayered scaffolds for OC repair/regeneration: (a) TruFit®; (b) MaioRegen®; and (c) CRD technology ______ 37

Figure 3-1. Schematic illustration of the natural SF protein composition. ______ 49

Figure 3-2. Schematic illustration of the physicochemical processes used to prepare SF hydrogels. ______ 50

Figure 3-3. Macroscopic images of the horseradish peroxidase-mediated crosslinked SF hydrogels. ______ 51

Figure 3-4. Photographs of the sonication-induced SF hydrogels and rabbit maxillary sinus surgery. ______ 52

Figure 3-5. Histological analysis of the SF- and agarose-based hydrogels combined with silk microfibers. 54

Figure 3-6. (I) Microstructure of SF and SF/CS scaffolds observed by scanning electron microscopy. (II) Cytocompatibility of SF and SF/CS scaffolds with hACs. (III) Histological evaluation after 12 weeks post-implantation: (A) Hematoxylin and eosin (H&E) histological images. (B) Safranin-O staining of histological sections. ______ 57

Figure 3-7. (A) Macroscopic image of the bilayered scaffolds. (B) Images of the bilayered explants after implantation in rabbit OC defects. (C) Images of the bilayered explants after subcutaneous implantation in rabbit. ______ 58

Figure 3-8. Scanning electron micrographs of SF, SF/TCP and SF/ionic-doped TCP scaffolds. (A) Before and (B) after 15 days of mineralization. (C) Viability and proliferation of hASCs seeded in the scaffolds: Alamar blue assay of hASCs cultured for 14 days (left), and DNA quantification at different time points (right). 59

Figure 3-9. Macroscopic image of the OC scaffold showing the microstructure of bone and chondral layers. 61

Figure 4-1. Silk cocoons purification process. 74

Figure 4-2. Chemical structure of Polyethylene terephthalate. 75

Figure 4-3. Schematic illustration of the wales and courses components of the knitted fabrics. The principles of (a) weft- and (b) warp-knitting technologies. 77

Figure 4-4. (a) Macroscopic images of the 3D weft-knitted SF scaffolds. (b) Tricolab machine used for the fabrication of the jersey weft-knitted SF fabrics. 80

Figure 4-5. Macroscopic images of the (a, b) SF-PET scaffolds and (c, d) PET scaffolds. 82

Figure 4-6. Concentrated aqueous SF solution. 84

Figure 4-7. Macroscopic image of the HRP-crosslinked SF hydrogels. 85

Figure 4-8. Macroscopic image of the HRP-crosslinked SF scaffolds prepared by salt-leaching/freeze-drying technologies. 86

Figure 4-9. Macroscopic image of the bilayered scaffolds prepared by combining a HSF cartilage-like layer with a HSF/ZnSr-β-TCP or HSF/β-TCP bone-like layer. 87

Figure 4-10. Interfacial tension at the 3-phase contact line. 95

Figure 4-11. Illustrative image of the specimens immersed into the SBF solution. 100

Figure 5-1. Effect of the different surface modifications on (a) maximum strength (MPa), (b) E modulus (MPa), and (c) strain at maximum load (%) obtained for SF textile matrices in dry and hydrated state (PBS; 37°C), in the longitudinal direction. 147

Figure 5-2. Scanning electron micrographs of (a) side A and (b) side B of the SF knitted structure and magnifications of the fibers on the top side (c) before and (d–h) after the different surface treatments. 149

Figure 5-3. AFM images of the SF surfaces (a) before and (b–f) after the different surface treatments. 150

Figure 5-4. Average roughness (R_a) of the SF surfaces before and after the different surface treatment. 150

Figure 5-5. Water contact angles obtained for the untreated and treated SF surfaces. 151

Figure 5-6. Scanning electron micrographs showing the L929 cell morphology and adhesion at the surface of (a–c) 2D silk membranes, 3D silk textile scaffolds (d–f) untreated and after the different surface modifications: (g–i) NaOH; (j–l) UV/O$_3$; (m–o) plasma/AAc; (p–r) plasma/VPA; (s–u) plasma/VSA, for (a, d, g, j, m, p, and s) 1 hour, (b, e, h, k, n, q, and t) 5 hours, and (c, f, i, l, o, r, and u) 24 hours of culture. ______ 155

Figure 5-7. DNA amount corresponding to the number of L929 cells adhered on untreated and surface-treated 3D silk textile scaffolds after 1, 5 and 24 hours of culture. ______ 156

Supplementary Figure 5-1. C1s core level spectra of a) untreated and modified SF samples: b) NaOH, c) UV/O$_3$, d) plasma/AAc, e) plasma/VPA, f) plasma/VSA. ______ 158

Supplementary Figure 5-2. P2p (a) and S2p (b) high resolution spectra for SF treated by plasma/VPA and plasma/VSA, respectively. ______ 158

Figure 6-1. Illustrative images showing the wale and course components of the (a) weft and (e) warp knitting technologies, used for processing the SF and PET filaments in the scaffolds external layers, respectively. SEM micrographs of (b-d) SF-PET and (f-h) PET knitted spacer fabrics showing different levels of detail. ______ 179

Figure 6-2. (a) Compressive modulus and (b) representative stress–strain plot of the SF-PET and PET knitted spacer fabrics measured in the dry state. (c) Storage modulus (E') and loss factor (tan δ) of the SF-PET and PET knitted spacer fabrics determined in the hydrated state, after 3 days of immersion. ______ 182

Figure 6-3. Normalized ALP activity of hASCs cultured on SF-PET and PET knitted spacer fabrics, after 1, 7, 14, 21 and 28 days in osteogenic and basal culture medium. ______ 183

Figure 6-4. (a) Calcium quantification on the SF-PET and PET knitted spacer fabrics, cultured with hASCs in osteogenic and basal medium for 7, 14, 21 and 28 days. (b) Alizarin red staining performed directly into the textile constructs, after 7, 14, 21 and 28 days of culture in osteogenic and basal medium. ______ 184

Figure 6-5. SEM micrographs (inset) and EDS spectra with Ca/P ratios determined for the SF-PET and PET knitted spacer fabrics, after 14, 21 and 28 days of culture in osteogenic medium. ______ 185

Figure 6-6. Quantitative and qualitative expression of osteogenic-related markers by hASCs after 28 days of culture on the SF-PET and PET knitted spacer fabrics. ______ 186

Figure 6-7. Chorioallantoic membrane (CAM) assay, after 4 days of SF-PET, PET textiles and gelatin sponges implantation. ______ 187

Figure 6-8. Subcutaneous implantation of the SF-PET and PET knitted spacer fabrics in mice. ______ 188

Supplementary Figure 6-1. SEM micrographs of the SF-PET and PET knitted spacer fabrics, cultured with hASCs in osteogenic and basal medium for 7, 14, 21 and 28 days. ______ 194

Supplementary Figure 6-2. Representative image of the structure of a flat bone. ______ 194

Figure 7-1. Schematic illustration of the experimental setup proposed in this study. 214

Figure 7-2. SEM micrographs of the (a, b) surface and respective (c, d) cross-sections of the HRP-crosslinked SF scaffolds. Micro-CT analysis showing the (e) 2D cross-sectional image for porosity representation, (f, g) 3D reconstruction of top and side views, respectively, (h) mean pore size distribution, and (i) mean wall thickness distribution of the HRP-crosslinked SF scaffolds. 215

Figure 7-3. ATR-FTIR spectra of the HRP-crosslinked SF scaffolds. 216

Figure 7-4. (a) Box and whisker graph plot of the compressive modulus and (b) representative stress-strain plot of the HRP-crosslinked SF scaffolds measured in the dry and hydrated state. (c) Swelling ratio, and (d) enzymatic degradation profile of the HRP-crosslinked SF scaffolds for a period of 30 days (% weight). 217

Figure 7-5. (a) Box and whisker graph plot of the alamar blue metabolic activity and (b) live/dead staining of the hASCs cultured on the HRP-crosslinked SF scaffolds for 1, 7, 14, 21 and 28 days in chondrogenic and basal culture medium. 218

Figure 7-6. Box and whisker graph plot of the (a) DNA quantification, (b) GAGs content normalized against the amount of DNA, and (c) collagenous proteins quantification at the HRP-crosslinked SF scaffolds cultured with hASCs in chondrogenic and basal medium for 1, 7, 14, 21 and 28 days. 220

Figure 7-7. HRP-crosslinked SF scaffolds after 28 days of culturing with hASCs in chondrogenic and basal medium. (a) Box and whisker graph plot of the real-time PCR results of Col II, Sox-9 and ACAN. (b) Immunofluorescence analysis of the chondrogenic-related markers. (c) Histological analysis of the HRP-crosslinked SF constructs. (d) Storage modulus (*E'*) and loss factor (*tan δ*) of the HRP-crosslinked SF scaffolds and constructs determined in chondrogenic differentiation medium. 222

Figure 7-8. Subcutaneous implantation of the HRP-crosslinked SF scaffolds in mice. 223

Supplementary Figure 7-1. Human ASCs characterization by flow cytometry prior differentiation assays. 230

Figure 8-1. Schematic illustration of the experimental setup adopted in this study. 248

Figure 8-2. SEM micrographs and EDS elemental spectra with the ionic elements and Ca/P ratios determined at the different regions of the BdTCP and BTCP scaffolds. 249

Figure 8-3. Micro-CT analysis of the BdTCP and BTCP scaffolds. 251

Figure 8-4. Crystalline structure and mechanical characterization of the BdTCP and BTCP scaffolds. 252

Figure 8-5. Degradation profile and *in vitro* bioactivity evaluation of the BdTCP and BTCP scaffolds. 254

Figure 8-6. Metabolic activity of the hOBs and hACs co-cultured in the BdTCP and BTCP scaffolds for 1, 7 and 14 days as determined by Alamar blue. 255

Figure 8-7. SEM micrographs of the adhered hOBs and hACs co-cultured in the BdTCP and BTCP scaffolds, after 1, 7 and 14 days. 255

Figure 8-8. Quantification of *in vitro* osteogenesis and chondrogenesis. 257

Figure 8-9. Histological and immunofluorescence analysis of the hOBs and hACs co-cultured in the BdTCP scaffolds for 1, 7 and 14 days. 258

Figure 8-10. Histological and immunofluorescence analysis of the hOBs and hACs co-cultured in the BTCP scaffolds for 1, 7 and 14 days. 259

Figure 8-11. Histological and immunofluorescence analysis of the hACs monocultured in the HSF scaffolds and hOBs monocultured in the HSF-dTCP and HSF-TCP scaffolds for 1, 7 and 14 days. 260

Supplementary Figure 8-1. Representative negative controls for immunofluorescence analysis of the osteogenic-related marker OPN and chondrogenic-related marker ACAN in the (a) HSF, (b) HSF-dTCP and (c) HSF-TCP constructs. 267

Supplementary Figure 8-2. In vitro bioactivity evaluation of the BdTCP and BTCP scaffolds. 267

Figure 9-1. Structural evaluation of the SF hydrogels after incubation in PBS at 37°C for 1, 3, 7, 10 and 14 days. 287

Figure 9-2. Physicochemical characterization of the SF hydrogel after incubation in PBS at 37°C for 3, 7 and 14 days. 289

Figure 9-3. Rheological properties of the SF/HRP/H_2O_2 mixture before gelation, after SF hydrogels formation and incubation in PBS at 37°C for 1, 3, 7 and 14 days. 291

Figure 9-4. U251 cell-laden SF hydrogels cultured for 1, 7, 10 and 14 days. Cell viability and proliferation analyzed by (a) ATP assay and (b) DNA quantification, respectively. (c) Macroscopic images of the U251 cell-laden SF hydrogels. (d) Live/Dead staining and fluorescence TUNEL assay of the U251 cell-laden SF hydrogels. 293

Figure 9-5. U251 cell-laden SF hydrogels cultured for 1, 7, 10 and 14 days. (a) OPT projections, OPT reconstructions and SPIM reconstructions of the U251 cell-laden SF hydrogels. (b) Fluorescence TUNEL assay of the sections from the U251 cell-laden SF hydrogels for 1, 7, 10 and 14 days. (d) Schematic illustration of the morphological changes of U251 cells during apoptosis induced by the conformational transitions of the cell-laden SF hydrogels. 294

Supplementary Figure 9-1. Schematic illustration of redox-responsive enzymatically crosslinked SF hydrogels. 298

Supplementary Figure 9-2. Schematic illustration of *in situ* fast-formed enzymatically crosslinked SF hydrogels and *in vitro* response of U251 cell-laden SF hydrogels. 299

Supplementary Figure 9-3. Positive control for fluorescence TUNEL assay. ________________________ 299

LIST OF TABLES

Table 2-1. Recent pre-clinical studies for OC repair using different animal models. 30
Table 2-2. Overview of ongoing and complete clinical trials using strategies for OC regeneration. Information obtained from https://clinicaltrials.gov/. 34
Table 3-1. Osteochondral TE scaffolding design approaches. 48
Table 4-1. Primers list for the studied genes. 118
Table 4-2. Antibodies used for immunocytochemistry of *in vitro* samples. 121
Table 4-3. Antibodies used for immunohistochemistry of *in vitro* samples. 122
Table 5-1. Contact angle values (θ) measured for the untreated and treated surfaces and respective calculated surface energies (γ_s). 152
Table 5-2. Surface composition and atomic ratios of modified and nonmodified SF samples determined by XPS. 152
Table 6-1. Primers list for the studied genes. 176
Table 6-2. 3D reconstructions of the SF-PET and PET knitted spacer fabrics, mean porosity, pore size and trabeculae thickness, calculated from the micro-CT data. 181
Table 7-1. Primers list for the studied genes. 211
Table 7-2. Microstructure of the HRP-crosslinked SF scaffolds determined from the micro-CT data. 215
Table 8-1. Microstructure of the BdTCP and BTCP scaffolds analyzed by micro-CT. 250
Table 9-1. Damping factor of SF hydrogels after incubation in PBS at 37°C for 1, 3, 7, 10 and 14 days. 291

LIST OF EQUATIONS

Equation 4-1. Water uptake (%) = $[(m_w-m_i)/m_i] \times 100$ 98

Equation 4-2. Water uptake (%) = $[(m_i-m_f)/m_i] \times 100$ 99

SHORT CURRICULUM VITAE

Viviana Pinto Ribeiro was born in 1987 in Vila Real, Portugal. Nowadays, she works as a researcher in 3B's Research Group (Biomaterials, Biodegradable and Biomimetics), University of Minho, Portugal, under the supervision of Prof. Rui L. Reis, Dr. Joaquim M. Oliveira, and Dr. Ana L. Oliveira.

Her background includes a four-year graduation in Genetics and Biotechnology (2005-2009) at the University of Trás-os-Montes e Alto Douro, followed by a Master Degree in Clinic Biology and Laboratory (2009-2011) also by the University of Trás-os-Montes e Alto Douro. During the final year of her Master Degree she developed her Master Thesis on the general topic of "Bisphosphonates effects on angiogenesis/osteogenesis of bone tissue: *In vitro* evaluation using co-culture of osteoblasts and endothelial cells", in collaboration with the Faculdade de Medicina Dentária from the University of Porto. Her undergraduate thesis was awarded as Excellent (19 values).

In April of 2012, she was awarded with a research grant at 3B's Research Group under the scope of the Fundação para a Ciência e Tecnologia (FCT) project TISSUE2TISSUE, with supervision of Prof. Rui L. Reis and Dr. Ana L. Oliveira. In January of 2014, she continued her work at 3B's Research Group under the support of the FCT project PEst - 2013-2014, and European Commission (EC) founded project NOVOMAR, with supervision of Prof. Rui L. Reis and Dr. Joaquim M. Oliveira. During this period, she focused on studding different silk fibroin-based scaffolds for bone and cartilage tissue engineering applications.

In September of 2015, she was invited to pursue her PhD in 3B's Research Group, after being awarded a PhD scholarship under the financial support from FCT/Ministerio da Ciência, Tecnologia e Ensino Superior (MCTES) and FSE/POCH (Fundo Social Europeu from Programa Operacional do Capital Humano), PD/59/2013. Her PhD study has been carried under the supervision of Prof. Rui L. Reis, Dr. Joaquim M. Oliveira, and Dr. Ana L. Oliveira. During the four years PhD study in 3B's Research Group, she focused on the development of novel silk fibroin-based scaffolds and hydrogels with improved and multifunctional performance for tissue engineering and regenerative medicine applications.

Viviana Pinto Ribeiro has also been involved in the FCT projects HierarchiTech and EPIDisc. Moreover, she has been involved in the preparation of FCT project proposals and National Patents, related with her research work. She also participated in the organization of the scientific meetings Term Stem 2012-2017. Additionally, she collaborated with her colleagues in different works, gave training to junior researchers and helped her colleagues on the preparation of silk fibroin-based biomaterials. She also had the opportunity to establish an external collaboration with the Faculdade de Engenharia form the University of Porto, which resulted in a scientific publication in an International Journal with scientific arbitration.

As a result of her research work, she is author or co-author of 10 papers in international journals (7 published, 3 submitted), 3 book chapters and 2 issued patents, 1 conference proceeding, 5 abstracts published in international conference proceedings, 6 oral presentations, and 15 poster presentations. She attended several important international meetings in the field of tissue engineering and regenerative medicine.

LIST OF PUBLICATIONS

The research work performed during the PhD period resulted in the following publications.

International Journals with Referee:

Ribeiro VP, Pina S, Costa JB, Cengiz IF, García-Fernández L, Fernández-Gutierrez M, Oliveira AL, San-Román J, Oliveira JM, Reis RL. Silk fibroin-based monolithic and hierarchical scaffolds for osteochondral regeneration. 2018, Submitted.

Ribeiro VP, da Silva Morais A, Maia FR, Canadas R, Costa JB, Oliveira AL, Oliveira JM, Reis RL. Combinatory approach for developing silk fibroin scaffolds for cartilage regeneration. 2018, Submitted.

Ribeiro VP, Silva-Correia J, Gonçalves G, Pina S, Radhouani H, Montonen T, Hyttinen J, Roy A, Oliveira AL, Reis RL, Oliveira JM. Rapidly responsive silk fibroin hydrogels as an artificial matrix for the programmed tumor cells death. 2018, Accepted in PLOS ONE Journal.

Ribeiro VP, Silva-Correia J, Nascimento AI, da Silva Morais A, Marques AP, Ribeiro AS, Silva CJ, Bonifácio G, Sousa RA, Oliveira JM, Oliveira AL, Reis RL. Silk-based anisotropical 3D biotextiles for bone regeneration. Biomaterials. 2017, 123:92-106. doi: 10.1016/j.biomaterials.2017.01.027.

Ribeiro VP, Almeida LR, Martins AR, Pashkuleva I, Marques AP, Ribeiro AS, Silva CJ, Bonifácio G, Sousa RA, Oliveira AL, Reis RL. Modulating cell adhesion to polybutylene succinate biotextile constructs for tissue engineering applications. Journal of Tissue Engineering and Regenerative Medicine. 2016, 11(10):2853-2863. doi: 10.1002/term.2189.

Ribeiro VP, Castro F, Fereira A, Oliveira AL, Reis RL, Teixeira JA, Rocha F. Continuous-flow precipitation as a route to prepare highly controlled nanohydroxyapatite: *in vitro* mineralization and biological evaluation. Materials Research Express. 2016, 3(7). doi: 10.1088/2053-1591/3/7/075404.

Ribeiro VP, Almeida LR, Martins AR, Pashkuleva I, Marques AP, Ribeiro AS, Silva CJ, Bonifácio G, Sousa RA, Reis RL, Oliveira AL. Influence of different surface modification treatments on silk biotextiles for tissue engineering applications. Journal of Biomedical Materials Research Part B: Applied Materials. 2015, 104(3):496-507. doi: 10.1002/jbm.b.33400.

Ribeiro VP, Ribeiro AS, Silva CJ, Durães NF, Bonifácio G, Correlo VM, Marques AP, Sousa RA, Oliveira AL, Reis RL. Evaluation of novel 3D architectures based on knitting technologies for engineering biological tissues. Journal of Donghua University (English Edition). 2013, 5:421-426.

As Co-author

Yan LP, Silva-Correia J, **Ribeiro VP**, Miranda-Gonçalves V, Correia C, da Silva Morais A, Sousa RA, Reis RM, Oliveira AL, Oliveira JM, Reis RL. Tumor growth suppresion induced by biomimetic silk fibroin hydrogels. Scientific Reports. 2016, 6:31037. doi:10.1038/srep31037.

Costa JB, Silva-Correia J, **Ribeiro VP**, da Silva Morais A, Oliveira JM, Reis RL. Engineering patient-specific bioprinted constructs for treatment of degenerated intervertebral disc. Materials Today Communications. 2018, doi:10.1016/j.mtcomm.2018.01.011.

Monzón M, Liu C, Ajami S, Oliveira JM, Donate R, **Ribeiro VP**, Reis RL. Functionally graded additive manufacturing to achieve functionality specifications of osteochondral scaffolds. Bio-Design and Manufacturing. 2018, doi:10.1007/s42242-018-0003-4.

Patent:

As Co-author

Pina S, **Ribeiro VP**, Reis RL, Oliveira JM. Ionic-doped composition methods and uses thereof. National Patent, Nr. 110106 N, 2017.

Carvalho CR, Costa JB, **Ribeiro VP**, Silva-Correia J, Oliveira JM, Reis RL, Nerve guidance conduits derived from silk fibroin hydrogels: methods of production and uses thereof. National Patent, Nr. 109562 01.08.2016 N, 2018.

Book Chapters:

Ribeiro VP, Pina S., Oliveira JM, Reis RL. Silk fibroin-based hydrogels and scaffolds for osteochondral repair and regeneration, in Osteochondral Tissue Engineering - Nanotechnology, Scaffolding-Related Developments and Translation, Advances in Experimental Medicine and Biology, JM Oliveira, S Pina, RL Reis and JS Roman (Eds), Springer International Publishing AG, ISBN: 978-3-319-76710-9.

Ribeiro VP, Pina S., Oliveira JM, Reis RL. Fundamentals on osteochondral tissue engineering, in Regenerative Strategies for the Treatment of Knee Joint Disabilities, Studies in Mechanobiology, Tissue Engineering and Biomaterials, JM Oliveira and RL Reis (Eds), Springer International Publishing AG, ISSN-1868-2006, vol.21, doi: 10.1007/978-3-319-44785-8_7, 2016.

Ribeiro VP, Pina S., Oliveira JM, Reis RL. Pre-clinical and clinical management of osteochondral lesions, in Regenerative Strategies for the Treatment of Knee Joint Disabilities, Studies in Mechanobiology, Tissue Engineering and Biomaterials, JM Oliveira and RL Reis (Eds), Springer International Publishing AG, ISSN-1868-2006, vol.21, doi: 10.1007/978-3-319-44785-8_8, 2016.

Communications in international conferences:

Oral presentations

Ribeiro VP, da Silva Morais A, Maia FR, Oliveira AL, Oliveira JM, Reis RL. Combinatory approach for developing silk fibroin-based scaffolds seeded with human adipose-derived stem cells for a cartilage tissue engineering applications. European Cells and Materials, vol. 33 suppl. 2 (0324). TERMIS-EU, Davos, Switzerland, June 26-30, 2017.

Ribeiro VP, da Silva Morais A, Oliveira AL, Oliveira JM, Reis, RL. Enzymatically cross-linked silk fibroin scaffolds support human adipose-derived stem cells chondrogenesis for cartilage tissue engineering applications. CHEM2NATURE First School, Guimarães, Portugal, November 21-25, 2016.

Ribeiro VP, Silva-Correia J, da Silva Morais A, Correlo VM, Marques AP, Ribeiro AS, Silva CJ, Durães NF, Bonifácio G, Sousa RA, Oliveira JM, Oliveira AL, Reis RL. Finely tuned fiber-based porous structures for bone tissue engineering applications. Frontiers in Bioengineering and Biotechnology, doi: 10.3389/conf.FBIOE.2016.01.02658. 10th World Biomaterials Congress (WBC), Montréal, Canada, May 17-22, 2016.

Ribeiro VP, **Silva-Correia J**, Miranda-Gonçalves V, Yan LP, Oliveira AL, Reis RM, Reis RL, Oliveira JM. Novel enzymatically cross-linked silk fibroin hydrogel with potential applications as suppressor of angiogenesis and tumor progression. 27th European Conference on Biomaterials ESB, Kraków, Poland, August 30-September 3, 2015.

Ribeiro VP, da Silva Morais A, Correlo VM, Marques AP, Ribeiro AS, Silva CJ, Durães NF, Bonifácio G, Sousa RA, Oliveira JM, Reis RL, **Oliveira AL**. Complex 3D architectures based on knitting technologies for bone tissue engineering applications", MedTex 2015, International Conference on Medical Textiles and Healthcare Products, Lodz, Poland, May 13-15, 2015.

Ribeiro VP, Ribeiro AS, Silva CJ, Durães NF, Bonifácio G, Correlo VM, Marques AP, Sousa RA, **Oliveira AL**, Reis RL. Novel 3D architectures based on knitting technologies for engineering biological tissues. MedTex 2013, International Conference on Medical Textiles and Healthcare Products, Raleigh, North Carolina, USA, May 13-15, 2013.

Poster presentations

Ribeiro VP, Pina S, Costa JB, Cengiz IF, Garc'ia-Fernández L, Fernández-Gutierrez M, Oliveira AL, San-Román J, Oliveira JM, Reis RL. Novel bilayered silk fibroin-based scaffolds incorporating Sr- and Zn-ions for osteochondral tissue engineering. TERM STEM/FORECAST 2017, Porto, Portugal, November 13-15, 2017.

Ribeiro VP, da Silva Morais A, Maia FR, Oliveira AL, Oliveira JM, Reis RL. Combinatory approach for developing silk fibroin-based scaffolds to support human adipose-derived stem cells chondrogenic differentiation. 28th Conference of the European Society for Biomaterials (ESB), Athenes, Grece, September 4-8, 2017.

Ribeiro VP, da Silva Morais A, Maia FR, Oliveira AL, Oliveira JM, Reis RL. Enzymatically cross-linked silk fibroin scaffolds support human adipose-derived stem cells chondrogenesis. Society for Biomaterials (SFB), Minneapolis, Minnesota, USA, April 5-8, 2017.

Ribeiro VP, da Silva Morais A, Oliveira AL, Oliveira JM, Reis RL. Enzymatically cross-linked silk fibroin scaffolds support human adipose-derived stem cells chondrogenesis for cartilage tissue engineering applications. TERM STEM 2016, Guimarães, Portugal, October 27-28, 2016.

Ribeiro VP, Yan LP, Oliveira AL, Oliveira JM, Reis RL. Combinatory approach for developing silk fibroin-based scaffolds with hierarchical porosity and enhanced performance for cartilage tissue engineering applications. Frontiers in Bioengineering and Biotechnology, doi: 10.3389/conf.FBIOE.2016.01.01708. 10th World Biomaterials Congress (WBC), Montréal, Canada, May 17-22, 2016.

Ribeiro VP, da Silva Morais A, Correlo VM, Marques AP, Ribeiro AS, Silva CJ, Durães NF, Bonifácio G, Sousa RA, Oliveira JM, Reis RL, Oliveira AL. Textile-based silk scaffolds for bone tissue engineering applications. 27th European Conference on Biomaterials ESB, Kraków, Poland, August 30-September 3, 2015.

Ribeiro VP, Silva-Correia J, Miranda-Gonçalves V, Yan LP, Oliveira AL, Reis RM, Oliveira JM, Reis RL. Smart silk fibroin hydrogels and its potential application as suppressor of angiogenesis and tumor progression. TERM STEM 2014, Porto, Portugal, October 23-24, 2014.

Ribeiro VP, Ribeiro AS, Silva CJ, Durães NF, Bonifácio G, Marques AP, Sousa RA, Oliveira AL, Reis RL. Silk-based 3D biotextiles support human adipose-derived stem cells towards osteogenic differentiation. Journal of Tissue Engineering and Regenerative Medicine, 7(1): 6-52, doi: 10.1002/term.1822. TERM STEM 2013, Porto, Portugal, October 10-12, 2013.

Ribeiro VP, Ribeiro AS, Silva CJ, Durães NF, Bonifácio G, Correlo VM, Marques AP, Sousa RA, Oliveira AL, Reis RL. Complex 3D architectures using a textile technology for bone tissue engineering applications. TERMIS-EU, Istanbul, Turkey, June 17-20, 2013.

Ribeiro VP, Martins AR, Marques AP, Bonifácio G, Oliveira AL, Sousa RA, Reis RL. Suitability of silk-based 3D biotextiles seeded with human adipose-derived stem cells for a bone tissue engineering approach. Journal of Tissue Engineering and Regenerative Medicine, 6(2):8-39, doi: 10.1002/term.1608. TERM STEM 2012, Guimarães, Portugal, October 9-13, 2012.

INTRODUCTION TO THE THESIS FORMAT

This thesis is divided in five sections containing ten different chapters. The first section is composed of three published book chapters presenting the state-of-the art on ostechondral tissue engineering and silk fibroin-based strategies for osteochondral tissue applications. The second section describes the materials and methods used for the experimental works proposed in this thesis, and mentioned in the following sections three and four. Section three (four chapters) and four (one chapter) are based on a series of papers published or submitted for publication. These are presented in the format of manuscripts, including abstract, introduction, materials and methods, results, discussion, conclusions and references. The major conclusions of the thesis and future remarks are addressed in section five. The content of each section is briefly summarized below.

Section I (Chapter 1, 2, 3), presents an extensive overview on the development of silk fibroin-based materials and the several aspects that make this raw material suitable for the production of improved tissue engineered osteochondral materials. Chapter 1 starts by making a statement of the osteochondral tissue nature, composing tissues (articular cartilage and bone) and properties. Moreover, a review of the literature on the emerged strategies for scaffolds design and applications on osteochondral tissue, is also presented. Chapter 2, reviews the pre-clinical and clinical studies employing tissue engineering strategies for osteochondral regeneration in the last decade. Besides, the promising new trends and directions for osteochondral tissue engineering are proposed, covering nanotechnology and cell-based therapy integrating customized scaffolds. Chapter 3, is focused on recent research based on silk fibroin in the field of osteochondral tissue engineering and describes future prospects for further developments in therapeutic related applications. This chapter starts with a brief overview of silk fibroin in terms of structure and morphologies. The different silk-based platforms are discussed, followed by an account of their applications in osteochondral tissue regeneration.

Section II (Chapter 4), describes in detail materials, experimental procedures and protocols used in the research work of this thesis. Moreover, it provides the rationale for the selection of the silk fibroin processing approaches for scaffolds and hydrogels design. The physicochemical and biological characterization methodologies are also described.

Section III (Chapter 5, 6, 7, 8), presents different studies that explore the proposed silk fibroin material for producing tailored textile-based scaffolds and hydrogels-based porous structures. In Chapter 5, weft-knitted silk fibroin scaffolds were surface modified by chemical and physical treatments and evaluated for tissue engineering applications. In Chapter 6, a different concept is proposed by means of creating weft-knitted silk fibroin scaffolds spaced by a monofilament of polyethylene terephthalate to increase the scaffolds thee-dimensionality for specific bone tissue engineering applications. A warp-knitted spacer scaffold entirely made of polyethylene terephthalate was used for comparative purposes. Chapter 7, describes the feasibility of producing enzymatically crosslinked silk fibroin scaffolds for specific cartilage tissue engineering applications. A highly-concentrated silk fibroin solution was used in combination with a horseradish peroxidase and hydrogen peroxide complex, followed by structuring using salt-leaching and freeze-drying methodologies. The possibility of including bioresorbable ionic-doped β-tricalcium phosphate (zinc and strontium) particles to the produced enzymatically crosslinked silk fibroin scaffolds for producing novel bilayered structures for osteochondral regeneration applications, is described in Chapter 8. Bilayered scaffolds of pure β-tricalcium phosphate were used for comparative purposes.

Section IV (Chapter 9), describes a research work that although connected with the above-described Chapters 7 and 8, involving enzymatically crosslinked silk fibroin hydrogels, is a different study that potentiates the application of this system for different biomedical applications. In this study, silk fibroin hydrogels were prepared via the peroxidase mediated crosslinking procedure and envisioned as three-dimensional *in vitro* tumor models. These are fast-formed SF hydrogels, produced at physiological conditions and in an amorphous state, serving as injectable systems and cell-encapsulation platforms. The novelty of this work is that these SF hydrogels undergo a spontaneous conformation transition from random coil-to-β-sheet that affects cell viability, being proposed as a powerful tool for the investigation of the microenvironment on tumor-like cells death.

Section V (Chapter 10), contains the summarization and general conclusions regarding the overall work developed in the scope of this thesis, as well as, some final remarks concerning future directions and proposed works

SECTION I

GENERAL INTRODUCTION

CHAPTER 1

Fundamentals on Osteochondral Tissue Engineering

CHAPTER 1.

Fundamentals on osteochondral tissue engineering*

1.1. Abstract

The repair and regeneration of osteochondral (OC) defects has been increasing owing the high number of diseases, trauma and injuries. Although current clinical options are effective for the treatment of the OC lesions, new therapeutic options are necessary for the complete regeneration of the damaged articular cartilage which has a limited healing capacity. OC tissue engineering has been proposing advanced tools and technologies involving structured scaffolds, bioactive molecules, and cells for the repair and regeneration of the bone and cartilage tissues, as well as their interface. Multi-phased or stratified scaffolds with distinct bone and cartilage sections have been designed for OC repair. Diverse forms, as porous scaffolds, fibers, and hydrogels are the most commonly strategies used for OC tissue engineering. This chapter presents the current treatment and biomimetic strategies for OC tissue engineering. Structure and properties of the OC tissue are also briefly described.

*This chapter is based on the following publication:

Ribeiro VP, Pina S., Oliveira JM, Reis RL. Fundamentals on osteochondral tissue engineering, in Regenerative Strategies for the Treatment of Knee Joint Disabilities, Studies in Mechanobiology, Tissue Engineering and Biomaterials, JM Oliveira and RL Reis (Eds), Springer International Publishing AG, ISSN-1868-2006, vol.21, doi: 10.1007/978-3-319-44785-8_7, 2016.

1.2. Introduction

Osteochondral (OC) tissue engineering has the potential of producing grafts with tailor-made mechanical properties and topology of the graft essential for the repair/regeneration of OC defects. The purpose is to culture cells on the scaffolds over a period of time to be further implanted *in vivo* (Figure 1-1). OC defects are lesions of the articular cartilage and underlying subchondral bone often derived from trauma related injuries or osteoarthritis, causing joint pain and deformity, impaired function, limited range of motion and stiffness [1].

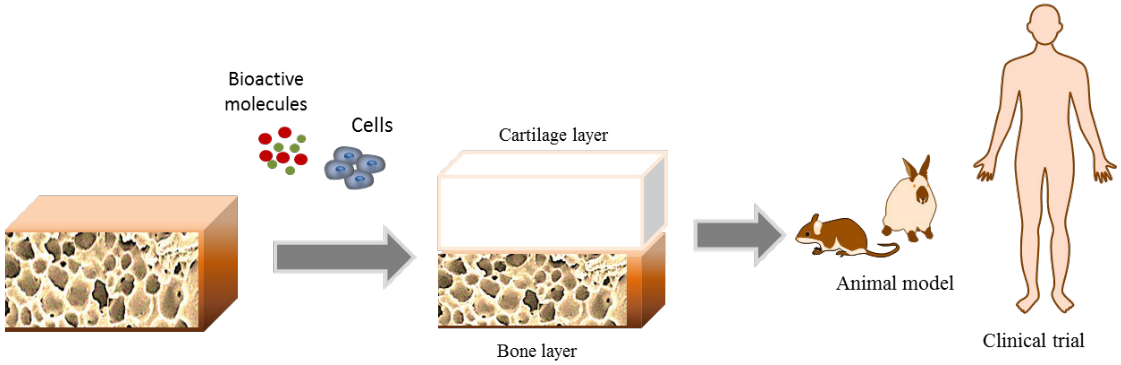

Figure 1-1. Osteochondral tissue engineering strategy.

Currently, OC treatment strategies include nonsurgical treatment with immobilization and use of non-steroidal anti-inflammatory drugs, and surgical treatment such as osteotomy, abrasion arthroplasty, microfracture, implantation of autografts, and autologous chondrocyte implantation [2-5]. These treatments are well established and effective for reducing pain improving the patient's quality of life. However, the articular cartilage has a limited regeneration capacity demanding new therapeutic options for complete healing of the OC lesions. Thus, specific structured biomimetic scaffolds have emerged as promising alternatives for the repair and regeneration of subchondral bone and cartilage considering their different architectures [6]. Cartilage can be distinguished into four distinct zones, defined by a particular composition and organization of cells and extracellular matrix (ECM) that significantly influence the mechanical properties of each area [7]. Bone is a dynamic and complex tissue composed of water and an ECM consisting of an organic matrix (collagen and non-collagenous proteins) and hydroxyapatite (HAp) crystals that provide stiffness and structural support to the body [8, 9]. It is a highly vascularised tissue with a remarkable intrinsic ability to remodel and spontaneously regenerate [10]. However, the true challenge lies in the complexity of the tissue interface, making it challenging for the design and fabrication of scaffolds [1, 9].

Different strategies have been proposed for OC repair and regeneration namely the development of different scaffold types: (i) single scaffolds for the bone and the cartilage parts combined at the time of implantation, (ii) single scaffold for the bone part, (iii) single homogeneous scaffold for both components, and (iv) single heterogeneous composite scaffolds [8, 11]. The latter, also known as bilayered scaffolds, have attracted singular attention and some of them have already been used in preclinical animal studies and clinical trials [12]. These types of scaffolds have unique composition and organization, structural strength and specific biological properties. They engineer cartilage using biopolymers (e.g., proteins, polysaccharides, glycosaminoglycans) and synthetic polymers, and bone engineering is carried out by combining polymers with bioactive/resorbable inorganic materials. Polymers have high strength and design flexibility and natural polymers also hold significant similarities with the ECM, chemical versatility, and good biological performance without toxicity or immunological reactions [13]. Conversely, bioresorbable materials, such as calcium phosphates (CaPs) (e.g., β-tricalcium phosphate, HAp) and bioactive glasses have favourable osteoconductivity, resorbability and biocompatibility [14, 15].

Usefulness of bilayered scaffolds, however, is limited by the lack of stability and scarce tissue integration. To overcome these limitations, adherent multi-phased or stratified scaffolds with distinct subchondral bone and cartilage compartments have been employed. This was based on the use of different biomaterials and entailed stratifications of mineral content, ECM components and porosity. These studies propose the incorporation of an interface band with homogeneous intermediate characteristics, a strategy that has brought forth promising results.

Herein, it is updated current treatments and strategies for OC repair and regeneration, with special focus on the scaffolds design. OC tissue structure and properties are briefly presented, in order to better understand the ideal constructs to be developed.

1.3. Osteochondral tissue: Structure and properties

Before designing scaffolds for OC tissue engineering, it is essential to consider the functional environment where the scaffolds will be implanted, as well as the anatomy of the surrounding tissues involved in the regenerative process. The natural OC tissue consists of two main tissues, articular cartilage and subchondral bone, connected by a stable interface. A description of each tissue is issued as follows.

1.3.1. Articular cartilage

Cartilage is a flexible and supportive tissue found in several areas of the human body. The three main types of cartilage are the fibrocartilage, elastic cartilage and hyaline cartilage. Hyaline cartilage is a dense connective tissue that provides smooth surfaces for joint motion, being found in the articular cartilage of all human body joints [1, 16, 17]. Biochemically, articular cartilage tissue is comprised of a solid phase of about 15-32% and a fluid phase of about 68-85%. Collagen, chondrocytes, proteoglycans and a few more minor proteins are the main constituents of the solid phase. The fluid phase is mainly composed of water [17-19]. Each component of cartilage holds a specific role to maintain its supportive nature. Unlike highly vascularised tissues like bone, articular cartilage is avascular and has a low cell density, which leads to a poor self-repair capacity [7]. In all areas of the tissue, collagen fibrils form a dense and highly interconnected matrix that host aggrecan, a highly-glycosylated molecule with net negative charge. It is bound in large amounts to glycosaminoglycans (GAGs) chains, including hyaluronic acid, chondroitin and keratin sulphates, to form proteoglycan aggregates responsible for raising the osmolarity of the tissue. The resulting swelling is countered by the resistance of the collagen matrix, generating a large internal pressure that gives to cartilage its unique mechanical properties [16, 20]. Type II collagen is the main containing of articular cartilage, however, types V, VI, IX and XI also play an important role in the intermolecular interactions and as modulators of type II collagen activity [19]. The entire articular cartilage contains the same basic components. However, their different proportions and arrangement in ECM composition allowed defining the cartilage tissue as a multi-layered structure composed of four distinct zones: superficial (tangential), middle (transitional), deep (radical) and calcified cartilage zones (Figure 1-2) [8, 17, 19]. The superficial zone constitutes the upper 10-20% of the articular cartilage and is composed of thin collagen fibrils parallel to the articular surface. Cell density is at its highest point, unlike aggrecan that is found at the lowest concentrations. The flattened chondrocytes found in this zone also secrete specialized proteins that maintain the upper region of the articular surface lubricated and prevents the wear and friction of the tissue [18, 21-23]. The next zone is the middle zone, which consists of the following 40-60% of the articular cartilage. It is composed by thicker collagen fibrils with a more random organization (less parallel) [24]. Chondrocytes are presented in a lower number with a round morphology, however, it is noted an abundance of proteoglycans. The properties presented by the middle zone lead to high compressive modulus that facilitates the recovery from impacts sustained by the articular surface [16, 18, 21, 25]. The remaining thickness of the articular cartilage is taken up by the deep zone and the calcified cartilage zone [21]. In the deep zone, both cells and collagen fibrils are perpendicularly orientated to the articular surface, with the chondrocytes grouped in vertical columns or clusters. Collagen fibrils diameter is maximal in this region, but the collagen content is also the lowest [24]. This zone also has a high compressive modulus and content of proteoglycans, but chondrocytes are presented in its lowest number and with a larger size [16, 18, 25]. In the bottom of the deep zone is a thin wavy line known as “tidemark”. This mark represents a calcification front by dividing the deep zone and the last small region, the calcified zone [26]. The calcified cartilage zone constitutes the interface between the flexible cartilage and the rigid subchondral bone [1]. This region contains hypertrophic circular chondrocytes surrounded by type X collagen that is believed to assist the mineralization process between the cartilage and the underlying bone [18, 27, 28]. Structurally, the collagen fibrils from the deep zone traverse through this area anchoring in the subchondral bone. The existence of interdigitations ("cement line") between the calcified cartilage and the underlying bone provides a tighter adherence at the interface, favouring the load bearing and force distribution [7, 29-31]. The wavy tidemark and vertical orientation of the collagen fibrils, combined with the interdigitations existing at the interface, may reduce the stress concentrated at this area and allow for a better integration within the bone tissue [9].

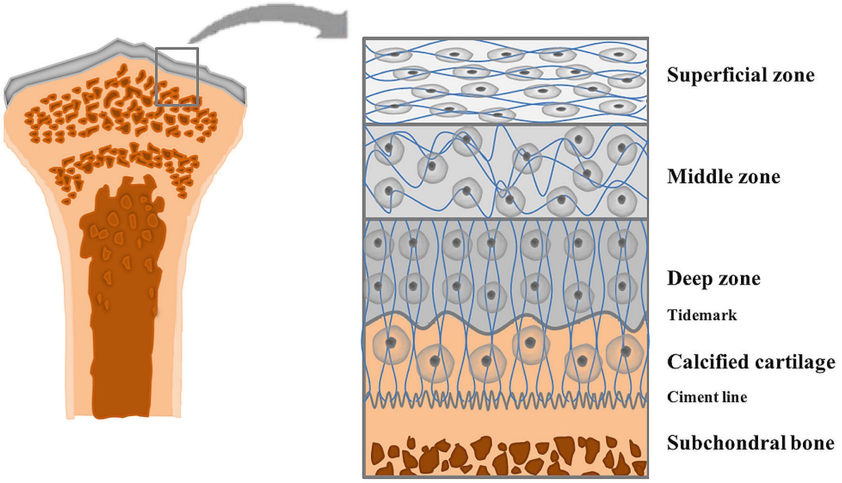

Figure 1-2. Schematic diagram of a long bone cross section. The normal articular cartilage is divided in superficial, middle, deep and calcified cartilage zones with a tidemark between the deep zone and the calcified region, followed by the underling subchondral bone with a cement line at the interface.

1.3.2. Subchondral bone

Bone is a dynamic and complex tissue with a high ability for self-repair and remodelling. The main roles of bone tissue are to provide mechanical support to the body and mineral homeostasis [32, 33]. Briefly, bone tissue can be arranged in two architectural forms: compact or cortical bone and trabecular or spongy bone. Compact bone is a dense structural tissue that comprises 80% of an adult human skeleton, with a low porosity of about 5-10% [32-34]. The components of compact bone are organized into repeated cylindrical units called osteons or haversian systems, composed of a central (haversian) canal surrounded by concentric lamellae rings of calcified extracellular matrix [35]. Trabecular bone presents a higher porosity of 50-90% and comprises about 20% of the total skeleton. It is arranged in a sponge-like form, characterized by plates or struts of various sizes called trabeculae. Another important function of trabecular bone is to host the bone marrow that contains high proportions of mesenchymal and hematopoietic stem cells [32-34]. The elaboration, maintenance and resorption of bone tissue results from the interaction of three cell types originating from the bone marrow reservoir: osteoblasts (bone formation), osteocytes (calcification of the matrix and calcium homeostasis) and osteoclasts (bone resorption) [36, 37]. The cooperation of these cells makes possible the constant production and degradation of bone tissue, but there is a need for a balance between bone formation and resorption that is controlled by signalling molecules and biochemical forces. Quantitatively, cells do not represent a high volume of the bone tissue, which is mainly composed of small crystals of an inorganic phase of HAp and some amorphous calcium phosphate compounds (65-70% of the matrix), and an organic phase composed of collagen, glycoproteins, proteoglycans, sialoproteins and bone "gla" proteins (25-30% of the total matrix) [38]. Bone tissue formation process (osteogenesis) is characterized by relatively high cell content with numerous osteoprogenitor cells and growth factors. Similarly, the bone healing process after a fracture event also mobilize a high number of cells and growth factors, however at this stage the inflammatory response is also initiated [39]. Subchondral bone comprises the latter region of the OC tissue, composed of two bone types: immediately below the calcified cartilage lies compact bone (subchondral bone plate) followed by trabecular bone (supporting trabecular bone) [31]. The subchondral bone plate consists of a solid mineralized mass of bone with low porosity and vascularity that separates the articular cartilage from the bone marrow. Depending upon the joint, the subchondral bone plate varies in thickness, ranging from 0.2-0.4 mm in humans. It is composed of an abundant matrix of collagen fibrils, mainly type I collagen, and minerals (e.g. calcium and phosphate), able to adapt its structure for acting on load bearing. This functional adaptation of the subchondral bone plate results in a preferential direction of the collagen fibrils at microstructural level [9, 17]. The trabeculae of the supporting trabecular bone are highly vascularised and present a predominant perpendicular orientation to the joint surface. These trabeculae are themselves crossed perpendicularly by finer trabeculae that continue from the lamellar sheets of the subchondral bone plate [31]. The two main functions of subchondral bone are to absorb and maintain joint shape. Although articular cartilage provides some compressive strength to the joint, it is the subchondral bone that sustains most of the strength since it has a larger area and a lower modulus of elasticity [40]. In fact, there is an increased stiffness gradient among the non-calcified cartilage, calcified cartilage, subchondral bone plate and supporting trabecular bone, which may be one of the causes of the cartilage damage caused by mechanical stresses [31]. While more research has been directed to the damages on articular cartilage resulting from certain OC defects [41-44], it is now recognized the integral role of subchondral bone in the pathogenesis of these defects [45]. The loss of articular cartilage associated with some OC defects, at some point leads to the exposure of the underlying subchondral bone to the surrounding forces, which is signalized by the occurrence of pain generated by the nerve endings existing at this tissue [46]. Therefore, changes in subchondral bone may act as an early marker for more complicated OC defects.

Summarizing, the natural joint is a complex composite that gradually changes the material combinations/properties, volume fractions and anisotropy along its structure. It can be modelled as a biphasic system composed of a permeable cartilage phase and an underlying porous but rigid subchondral bone region. Given the complexity of the biology and mechanisms of OC tissue, the challenges to engineer this tissue include developing a low friction surface that integrates well with the surrounding cartilage tissue and ensuring a proper implant integration maintaining the mechanical properties of the tissue.

1.4. Strategies for osteochondral tissue engineering

OC tissue engineering involve bioactive and biodegradable structures with controlled pore structure and mechanical stability, and capable of directing cell-matrix and cell–cell interactions, thus mimicking the natural ECM. Scaffolding materials such as porous structures (single and bilayered), hydrogels and fibrous networks are the prospective candidates for OC defects repair/regeneration which promote growth of both bone and cartilage layers in a single integrated scaffold. The following section presents a brief description of OC tissue engineering approaches focusing on bilayered, fibrous and hydrogel scaffolds, design and properties.

1.4.1. Bilayered scaffolds

Scaffolds are designed to act as temporary support structures to the surrounding bone tissue mimicking ECM, with advantageous characteristics, including: (i) porous structure that promotes cell-biomaterial interactions, cell adhesion, growth and migration, (ii) interconnected pores to facilitate transport of mass, nutrients, and regulatory factors to allow cell survival, proliferation, and differentiation, (iii) adequate mechanical properties as tensile strength and elasticity, (iv) controlled degradation, (v) synthesis of new bone formation with homogeneous distribution to avoid necrosis, and (vi) minimal degree of inflammation or toxicity *in vivo* [47]. Besides, scaffolds have desirable characteristics for cell transfer into a defect site and to restrict cell loss, instead of simple injection of cells to the defects.

Several conventional methods have been used to produce scaffolds with controlled pore size and porosity, such as foam replica, particulate-leaching/solvent casting, freeze-drying, phase separation, gas foaming, and rapid prototyping [48-52]. The challenge is the production of scaffolds ensuring a good compatibility between the phases while keeping the porous structure and the mechanical properties. It has been reported that a pore size larger than 300 µm and porosity of about 50-90% is acclaimed for an enhanced osteogenesis, while a pore size in the range 90-120 µm are recommended for chondrogenesis [53, 54]. Besides, it is important to achieve a homogeneous structure between the polymer matrix and the bioresorbable fillers.

Bilayered scaffolds have been constructed aiming OC tissue engineering applications, consisting of both osteogenic and chondrogenic regions, manufactured in a single integrated implant, thus simultaneously promoting regeneration of bone and cartilage with different properties and biological requirements [49, 55-57]. Oliveira *et al.* [49] developed an integrated macro-porous bilayered scaffold made of HAp and chitosan combining sintering and freeze-drying techniques, with two distinct layers, respectively for cartilage and bone (Figure 1-3). The bone layer was constituted of porous HAp and produced through foam replica method, while the cartilage layer was composed of chitosan poured on the top of the HAp scaffold, previously prepared, followed by freeze-drying technique. The scaffolds presented porosities of 59.3 ± 1.7% for HAp layer and 74.6 ± 1.2% for chitosan layer. The compression modulus for the HAp and chitosan was determined to be 153 ± 12 and 2.9 ± 0.4 MPa, respectively. Moreover, it was shown through *in vitro* cell studies that both layers provided an adequate support for cell attachment, proliferation and differentiation into osteoblasts and chondrocytes, respectively.

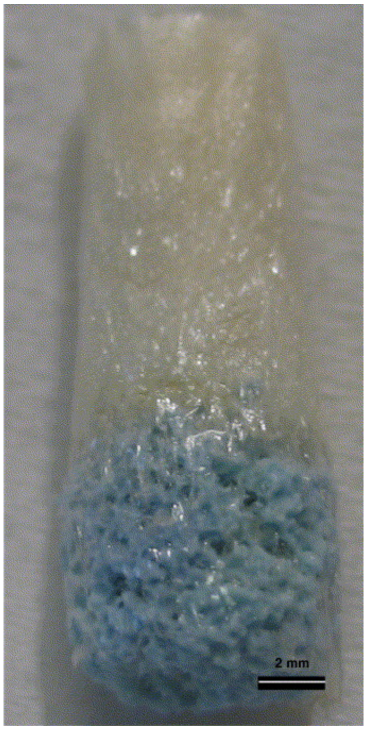

Figure 1-3. Chitosan/HAp bilayered scaffold showing two different layers, respectively for cartilage (upper layer) and bone (bottom layer). Reprinted with permission [49]. Copyright 2006, Elsevier.

More recently, Yao *et al*. [57] prepared a 45S5 Bioglass®/chitosan-polycaprolactone (CS-PCL) bilayered scaffold by a combination of foam replication and freeze-drying methods aiming OC tissue engineering applications. The bone layer was composed by a bioglass-based scaffold coated with CS-PCL blend, while a PCL-CS foam fabricated by freeze-drying was used in the cartilage layer. The scaffolds showed a porosity of 81% with favourable mechanical strength. *In vitro* studies indicated that the scaffolds supported the adhesion and growth of MG-63 cells with favourable proliferation behavior after 3 weeks of incubation. Wang *et al*. [56] fabricated a bilayered scaffold using articular cartilage extracellular matrix and HAp, which involved a porous oriented upper layer and a dense mineralized lower layer using the "liquid-phase cosynthesis" technique (Figure 1-4) [58]. Mean pore sizes of 21.2 ± 3.1 μm and 128.2 ± 20.3 μm, and porosity of 92.6 ± 6% and 44 ± 3%, respectively for the upper and lower layers were obtained. *In vitro* culture performed using rabbit chondrocytes seeded on the bilayered scaffolds showed that the chondrocytes were well-distributed in the non-mineralized component (upper layer) and do not penetrated into the mineralized component (lower layer).

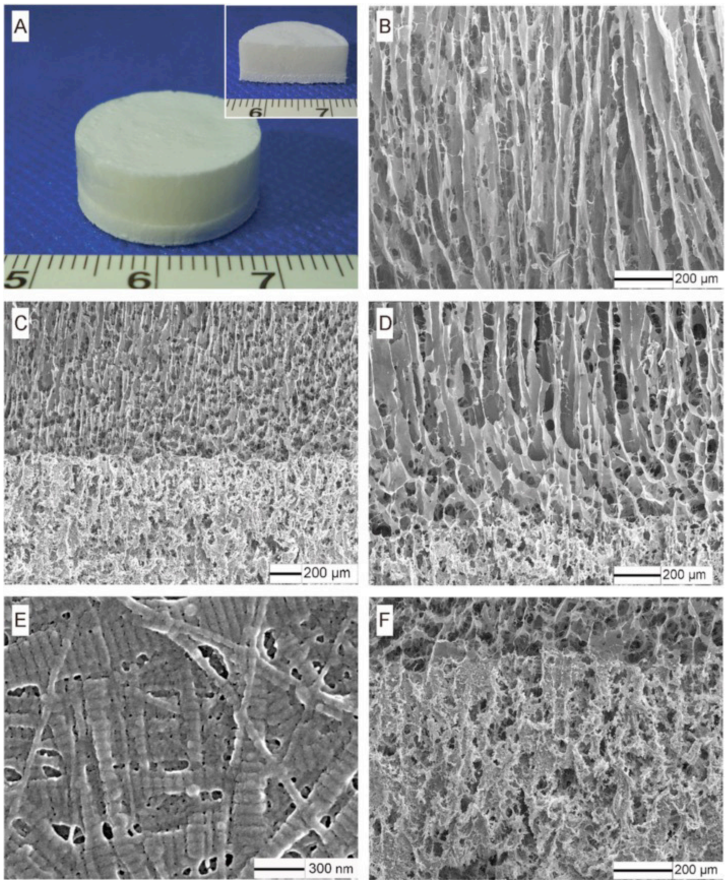

Figure 1-4. Image of the articular cartilage ECM/HAp bilayered scaffold prototype (A) and respective scanning electron microstructures: (B) upper layer, (C and D) interface region, nanofibrous ECM orientation in the (E) upper layer

of the scaffold wall at a high magnification, and in the (F) lower layer. Reprinted with permission [56]. Copyright 2014, BioMed Central.

Growth factors have been used for tissue engineering due to their beneficial effect in the cell growth and tissue formation. The construction of scaffolds using this strategy has been endeavoured. A biomimetic and multi-phasic scaffold design, spatially controlled and localized gene delivery system and multi-lineage differentiation of a single stem cell population were combined to design a bilayered gene-activated OC scaffold [59]. The scaffold consisted of plasmid transforming growth factor-β1 (TGF-β1)-activated chitosan-gelatin for the cartilage layer and plasmid bone morphogenetic protein-2 (BMP-2)-activated HAp/chitosan-gelatin for the subchondral bone layer. This scaffold could induce mesenchymal stem cells (MSCs) to differentiate into chondrocytes and osteoblasts, respectively for the cartilage and subchondral bone, using a rabbit knee OC defect model. Results showed cell proliferation, high expression of TGF-β1 protein and BMP-2 protein. In another study, a scaffold made of poly D,L-lactic-co-glycolic acid (PLGA) microspheres combined with TGF-β1 and BMP-2 was prepared for OC repair [60]. This scaffold consisted of PLGA microspheres and TGF-β1 for the chondrogenic layer and PLGA microspheres and BMP-2 with or without HAp for the osteogenic layer. *In vivo* results showed complete bone ingrowth, with an overlying cartilage layer with high glycosaminoglycan content, appropriate thickness, and integration with the surrounding cartilage and underlying bone, after implantation in rabbit knees.

Recently, Ding *et al*. [61] took a different approach by preparing an integrated trilayered scaffold composed of silk fibroin and HAp by combining paraffin-sphere leaching with a modified temperature gradient-guided thermal-induced phase separation (TIPS) technique for OC tissue engineering. The scaffold is constituted by three layers: longitudinally oriented microtubular structure for the cartilage layer, a porous structure for the bone layer and an intermediate layer with a dense structure. Live/dead tests indicated good biocompatibility of the scaffolds for supporting the growth, proliferation, and infiltration of adipose-derived stem cells, which could be induced to differentiate toward chondrocytes or osteoblasts in the presence of chondrogenic- or osteogenic-induced culture medium, respectively for the cartilage and bone layers. Besides, the intermediate layer could play an isolating role for preventing the mixture of the cells within the cartilage and bone layers.

1.4.2. Fibrous scaffolds

Fibrous scaffolds, particularly nanoscale fibrous, have been employed for the repair and regeneration of natural tissues, as they are capable of mimicking the network of ECM. These types of scaffolds have high porosities and homogeneous pore distribution, which facilitates cell adhesion, proliferation, and differentiation [62].

Fibrous scaffolds can be obtained through electrospinning, phase separation, and molecular self-assembly. Electrospinning is the most commonly used technique since it can produce fibers in the order of nanometers, with interconnected pore structure and higher mechanical strength [63].

Composite scaffolds using fibers have been used as a strategy for developing OC tissue repair [64]. Yunos *et al*. [64] developed a bilayered scaffold using a matrix of electrospun poly-DL-lactide (PDLLA) fibers combined with 45S5 Bioglass®-based foam for OC tissue replacement (Figure 1-5). PDLLA fibers were produced through electrospinning with diameters between ~100 nm and ~0.2 µm and good integration onto the scaffolds (Figure 1-5B). *In vitro* tests using chondrocyte cells showed increased cell attachment and proliferation on the scaffolds.

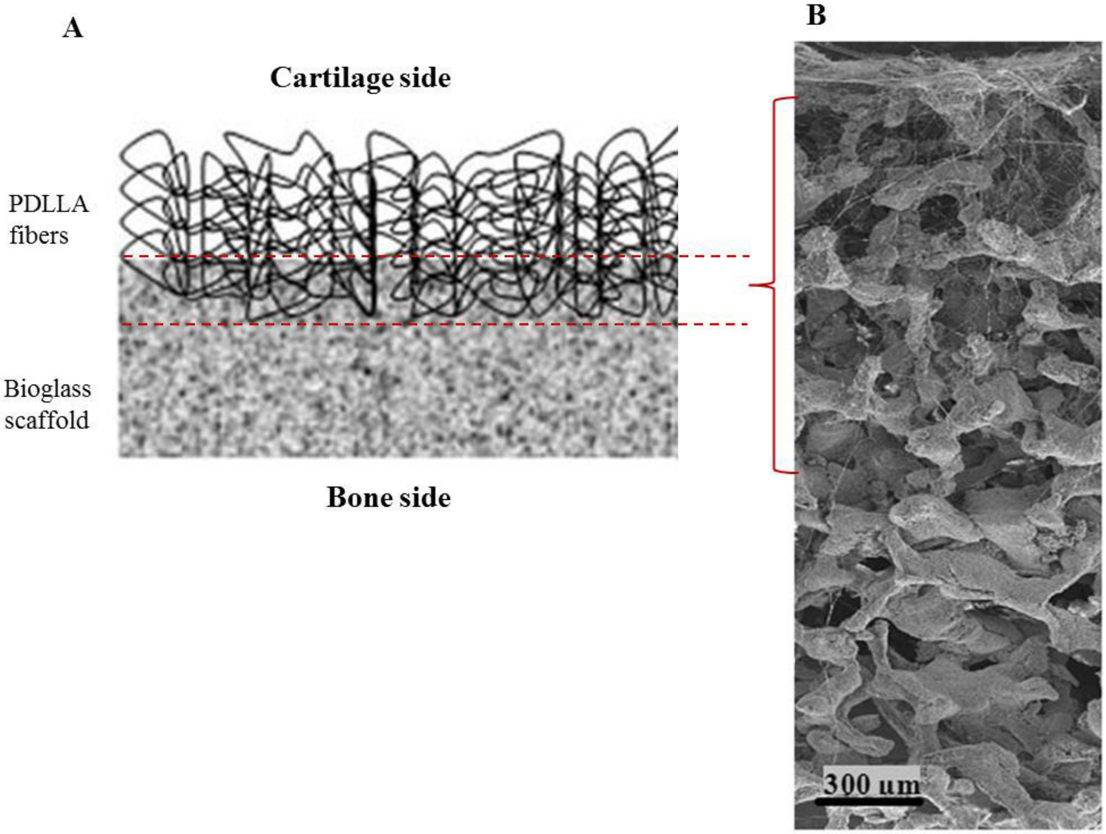

Figure 1-5. (A) Schematic diagram of the bilayered composite scaffolds, and (B) scanning electron micrograph of the scaffolds cross-section. Adapted with permission [64]. Copyright 2011, SAGE Publications.

By its turn, Zhang *et al*. [65] fabricated a bilayered collagen/micro-porous poly-L-lactide (PLLA) nanofibers scaffold for focal OC defect regeneration. It was shown that the scaffolds promoted osteogenic differentiation of bone marrow stem cells (BMSCs) *in vitro*, and improved bone tissue formation after implantation in a rabbit. Filová *et al*. [66] evaluated the effect of a hyaluronate/ collagen Type I /fibrin composite scaffold containing polyvinyl alcohol (PVA) nanofibers with liposomes and functionalized with basic fibroblast growth factor (bFGF) and insulin on the regeneration of OC defects. It was shown that the nanofibers improved the composite scaffolds mechanical properties and MSC viability *in vitro*. Besides, OC regeneration towards hyaline cartilage and/or fibrocartilage was enhanced after 12 weeks implantation in miniature pig.

1.4.3. Hydrogel scaffolds

Hydrogels comprise a three-dimensional network highly hydrated, hydrophilic crosslinked that mimic the natural ECM, including cartilage [67]. Hydrogels have been employed as scaffolding materials for tissue engineering owed their swollen network structure, diffusion of nutrients and by-products from cells metabolism, and biocompatibility. In addition, hydrogels are able to encapsulate cells, biomolecules and growth factors, for a controlled delivery after implantation. Techniques such as, solvent casting and particulate leaching, freeze-drying, phase separation, gas foaming, solvent evaporation, and blending with non-crosslinkable linear polymers have been used to produce the porosity in hydrogels [68].

Hydrogel biphasic scaffolds combining different materials have attracted great deal of attention for OC repair/regeneration. Pereira *et al*. [69] produced biphasic hydrogel scaffolds consisting of low acyl gellan gum (LAGG) and HAp for the bone layer and LAGG for the cartilage layer, with total cohesion of the whole structure (Figure 1-6). Rodrigues *et al*. [70] reported the development of a bilayered scaffold which combines a starch/polycaprolactone (SPCL) scaffold for osteogenesis and hydrogel of agarose for chondrogenesis and containing pre-differentiated amniotic fluid-derived stem cells (Figure 1-7).

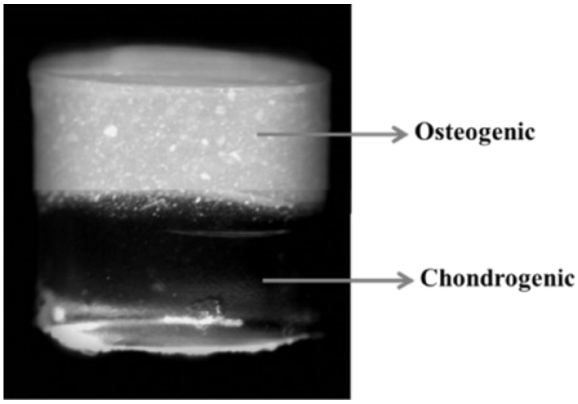

Figure 1-6. Macroscopic appearance of the LAGG/LAGG-HAp hydrogels. Reprinted with permission [69]. Copyright 2014, Trans Tech Publications.

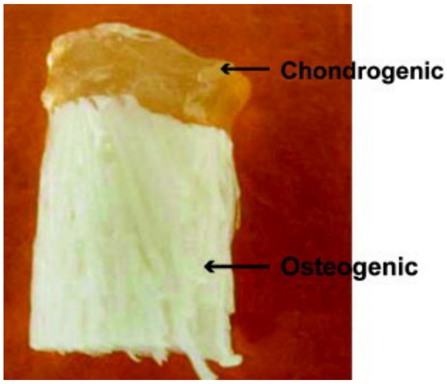

Figure 1-7. Image of agarose-SPCL bilayered scaffold. Reprinted with permission [70]. Copyright 2012, Elsevier.

Biodegradable composite hydrogels encapsulating growth factors have been also investigated. Bilayered OC constructs mimicking the hierarchical OC structure were produced using oligo polyethylene glycol fumarate hydrogel containing gelatin microparticles and stem cells, via a two-step crosslinking process [71, 72]. Results of live/dead assay showed that cell viability was maintained in osteogenic and chondrogenic layers and the incorporation of TGF-β3 significantly stimulated chondrogenic differentiation of the stem cells in the chondrogenic layer [71]. Besides, after 12 weeks of implantation in a rabbit full-thickness OC defect, it was observed a significant improvement in the cartilage morphology when comparing with a blank hydrogel [72].

1.5. Concluding remarks

Functional repair and regeneration of OC tissue remains a challenge, and none of the existing treatment procedures gives the reliable good outcome. OC tissue engineering has the potential to develop novel strategies for the repair and regeneration of OC lesions comprising subchondral bone, and cartilage, as well as the interface between them, which involve physicochemical and mechanical properties of materials, cell types and interaction between scaffolds and native tissues. These strategies are influenced by the complexity of the cartilage and underlying subchondral bone compositions, mechanical structure, and functional properties.

Stratified scaffolds with distinct bone and cartilage phases in a single structure have been proposing as one of the most optimal OC scaffolds, characterized by differential microporosity, chemical composition, and good mechanical properties, aiming ECM deposition and adequate cell differentiation and proliferation, and for the regeneration of new tissue. Current emerging trends for OC tissue engineering focused on the production of different scaffolding structures e.g., bilayered structures, fibrous, and hydrogels, using diverse natural and synthetic polymers, and inorganic materials, and resulting composites, using several fabrication methods. Inorganic materials are optimal candidates for the bone part due to their inherent biocompatibility, while the polymers are suitable for the cartilage part because they confer adequate mechanical strength and toughness to the structures.

Another important factor to be considered in OC tissue engineering is the combination of the scaffolds with specific cells for chondrogenic and osteogenic potential, and growth factors in order to regulate cell differentiation and also to improve the mechanical properties after implantation. Under this perspective, *in vivo* studies in animal models must be considered to evaluate integration, osteogenesis, and vascularization of the scaffolds, and long term stability to translate into the clinical.

1.6. References

[1] S.P. Nukavarapu, D.L. Dorcemus, Osteochondral tissue engineering: Current strategies and challenges, Biotechnol Adv 31(5) (2013) 706-721.

[2] L.Z. Xing, et al., Microfracture combined with osteochondral paste implantation was more effective than microfracture alone for full-thickness cartilage repair, Knee Surg Sport Tr A 21(8) (2013) 1770-1776.

[3] Y.S. Kim, et al., Clinical Comparison of the Osteochondral Autograft Transfer System and Subchondral Drilling in Osteochondral Defects of the First Metatarsal Head, Am J Sport Med 40(8) (2012) 1824-1833.

[4] L. de Girolamo, et al., Modified autologous matrix-induced chondrogenesis (AMIC) for the treatment of a large osteochondral defect in a varus knee: a case report, Knee Surg Sport Tr A 20(11) (2012) 2287-2290.

[5] M. Miska, et al., Reconstruction of a Large Osteochondral Lesion of the Distal Tibia with an Iliac Crest Graft and Autologous Matrix-induced Chondrogenesis (AMIC): A Case Report, J Foot Ankle Surg 51(5) (2012) 680-683.

[6] D. Puppi, et al., Polymeric materials for bone and cartilage repair, Prog Polym Sci 35(4) (2010) 403-440.

[7] B.A. Harley, et al., Design of a multiphase osteochondral scaffold III: Fabrication of layered scaffolds with continuous interfaces, J Biomed Mater Res A 92A(3) (2010) 1078-1093.

[8] P. Nooeaid, et al., Osteochondral tissue engineering: scaffolds, stem cells and applications, J Cell Mol Med 16(10) (2012) 2247-2270.

[9] P.J. Yang, J.S. Temenoff, Engineering orthopedic tissue interface, Tissue eng: Part B 15(2) (2009) 127-141.

[10] A.R. Shrivats, et al., Bone tissue engineering: state of the union, Drug Discov Today 19(6) (2014) 781-786.

[11] I. Martin, et al., Osteochondral tissue engineering, J Biomech 40(4) (2007) 750-765.

[12] L. Yan, et al., Silk Fibroin/Nano-CaP Bilayered scaffolds for Osteochondral Tissue Engineering, Key Eng Mater 587 (2014) 245.

[13] J. Mano, et al., Natural origin biodegradable systems in tissue engineering and regenerative medicine: present status and some moving trends, J R Soc Interface. 4 (2007) 999-1030.

[14] M. Bohner, Calcium orthophosphates in medicine: from ceramics to calcium phosphate cements, Injury-International Journal of the Care of the Injured 31 (2000) 37-47.

[15] S. Dorozhkin, Calcium Orthophosphates in Nature, Biology and Medicine Materials 2 (2009) 399-498.

[16] G. Verbruggen, et al., Biology of articular cartilage, Proceedings of the 5th Symposium of the International Cartilage Repair Society - Icrs (2004) 21-25.

[17] W. Swieszkowski, et al., Repair and regeneration of osteochondral defects in the articular joints, Biomol Eng 24(5) (2007) 489-495.

[18] A.R. Poole, et al., Composition and structure of articular cartilage - A template for tissue repair, Clin Orthop Relat R (391) (2001) S26-S33.

[19] Z.Y. García-Carvajal, et al., Cartilage Tissue Engineering: The Role of Extracellular Matrix (ECM) and Novel Strategies, 2013.

[20] K.A. Athanasiou, et al., Effects of aging and dietary restriction on the structural integrity of rat articular cartilage, Ann Biomed Eng 28(2) (2000) 143-149.

[21] A.D. Pearle, et al., Basic science of articular cartilage and osteoarthritis, Clin Sport Med 24(1) (2005) 1-+.

[22] A. Khalafi, et al., Increased accumulation of superficial zone protein (SZP) in articular cartilage in response to bone morphogenetic protein-7 and growth factors, J Orthop Res 25(3) (2007) 293-303.

[23] C.P. Neu, et al., Mechanotransduction of bovine articular cartilage superficial zone protein by transforming growth factor beta signaling, Arthritis Rheum-Us 56(11) (2007) 3706-3714.

[24] R.K. Korhonen, et al., Importance of collagen orientation and depth-dependent fixed charge densities of cartilage on mechanical behavior of chondrocytes, J Biomech Eng-T Asme 130(2) (2008).

[25] M. Huber, et al., Anatomy, biochemistry, and physiology of articular cartilage, Invest Radiol 35(10) (2000) 573-580.

[26] T.J. Lyons, et al., The tidemark of the chondro-osseous junction of the normal human knee joint, J Mol Histol 36(3) (2005) 207-215.

[27] D. Eyre, Collagen of articular cartilage, Arthritis Res Ther 4(1) (2002).

[28] A. Hyc, et al., The morphology and selected biological properties of articular cartilage, Ortopedia, traumatologia, rehabilitacja 3(2) (2001) 151-62.

[29] I. Zizak, et al., Characteristics of mineral particles in the human bone/cartilage interface, J Struct Biol 141(3) (2003) 208-217.

[30] H.H. Lu, et al., Tissue Engineering Strategies for the Regeneration of Orthopedic Interfaces, Ann Biomed Eng 38(6) (2010) 2142-2154.

[31] H. Madry, et al., The basic science of the subchondral bone, Knee Surg Sport Tr A 18(4) (2010) 419-433.

[32] A.R. Costa-Pinto, et al., Scaffolds Based Bone Tissue Engineering: The Role of Chitosan, Tissue Eng Part B-Re 17(5) (2011) 331-347.

[33] T. Cordonnier, et al., Biomimetic Materials for Bone Tissue Engineering - State of the Art and Future Trends, Adv Eng Mater 13(5) (2011) B135-B150.

[34] A.J. Salgado, et al., Bone tissue engineering: State of the art and future trends, Macromol Biosci 4(8) (2004) 743-765.

[35] D.W. Hutmacher, et al., State of the art and future directions of scaffold-based bone engineering from a biomaterials perspective, J Tissue Eng Regen Med 1(4) (2007) 245-60.

[36] P. Ducy, et al., The osteoblast: a sophisticated fibroblast under central surveillance, Science 289(5484) (2000) 1501-4.

[37] E.J. Mackie, Osteoblasts: novel roles in orchestration of skeletal architecture, The international journal of biochemistry & cell biology 35(9) (2003) 1301-5.

[38] D.W. Sommerfeldt, C.T. Rubin, Biology of bone and how it orchestrates the form and function of the skeleton, Eur Spine J 10 (2001) S86-S95.

[39] S. Sundelacruz, D.L. Kaplan, Stem cell- and scaffold-based tissue engineering approaches to osteochondral regenerative medicine, Semin Cell Dev Biol 20(6) (2009) 646-655.

[40] C.E. Kawcak, et al., The role of subchondral bone in joint disease: a review, Equine Vet J 33(2) (2001) 120-126.

[41] N. Mahmoudifar, P.M. Doran, Tissue engineering of human cartilage and osteochondral composites using recirculation bioreactors, Biomaterials 26(34) (2005) 7012-7024.

[42] R.L. Dahlin, et al., Articular chondrocytes and mesenchymal stem cells seeded on biodegradable scaffolds for the repair of cartilage in a rat osteochondral defect model, Biomaterials 35(26) (2014) 7460-9.

[43] E. Kon, et al., Acellular matrix–based cartilage regeneration techniques for osteochondral repair, Operative Techniques in Orthopaedics 24(1) (2014) 14-18.

[44] J.K. Sherwood, et al., A three-dimensional osteochondral composite scaffold for articular cartilage repair, Biomaterials 23(24) (2002) 4739-4751.

[45] D.B. Burr, Anatomy and physiology of the mineralized tissues: role in the pathogenesis of osteoarthrosis, Osteoarthritis and cartilage / OARS, Osteoarthritis Research Society 12 Suppl A (2004) S20-30.

[46] K. Moisio, et al., Denuded subchondral bone and knee pain in persons with knee osteoarthritis, Arthritis Rheum 60(12) (2009) 3703-10.

[47] L. Thorrez, et al., Growth, differentiation, transplantation and survival of human skeletal myofibers on biodegradable scaffolds, Biomaterials 29(1) (2008) 75-84.

[48] Q. Hou, et al., Porous polymeric structures for tissue engineering prepared by a coagulation, compression moulding and salt leaching technique, Biomaterials 24 (2003) 1937-47.

[49] J.M. Oliveira, et al., Novel hydroxyapatite/chitosan bilayered scaffold for osteochondral tissue-engineering applications: Scaffold design and its performance when seeded with goat bone marrow stromal cells, Biomater 27 (2006) 6123-6137.

[50] F. Dehghani, N. Annabi, Engineering porous scaffolds using gas-based techniques, Current Opinion in Biotechnology 22 (2011) 661-6.

[51] P. vandeWitte, et al., Phase separation processes in polymer solutions in relation to membrane formation, J Memb Sci 117 (1996) 1-31.

[52] T.B.F. Woodfield, et al., Rapid prototyping of anatomically shaped, tissue-engineered implants for restoring congruent articulating surfaces in small joints, Cell Proliferation 42(4) (2009) 485-497.

[53] V. Karageorgiou, D. Kaplan, Porosity of 3D biomaterial scaffolds and osteogenesis, Biomaterials 26 (2005) 5474-5491.

[54] K. Kim, et al., Stereolithographic bone scaffold design parameters: osteogenic differentiation and signal expression, Tissue Eng Part B Rev 16 (2010) 523-539.

[55] L.P. Yan, et al., Bioactive macro/micro porous silk fibroin/nano-sized calcium phosphate scaffolds with potential for bone-tissue-engineering applications, Nanomedicine (Lond) 8(3) (2013) 359-78.

[56] Y. Wang, et al., Fabrication and in vitro evaluation of an articular cartilage extracellular matrix-hydroxyapatite bilayered scaffold with low permeability for interface tissue engineering, Biomed Eng Online 13 (2014) 80.

[57] Q. Yao, et al., Bioglass((R)) /chitosan-polycaprolactone bilayered composite scaffolds intended for osteochondral tissue engineering, J Biomed Mater Res A 102(12) (2014) 4510-8.

[58] B. Harley, et al., Design of a multiphase osteochondral scaffold III: Fabrication of layered scaffolds with continuous interfaces, J Biomed Mater Res A 92 (2010) 1078-1093.

[59] J. Chen, et al., Simultaneous regeneration of articular cartilage and subchondral bone in vivo using MSCs induced by a spatially controlled gene delivery system in bilayered integrated scaffolds, Biomaterials 32(21) (2011) 4793-4805.

[60] N. Mohan, et al., Continuous gradients of material composition and growth factors for effective regeneration of the osteochondral interface, Tissue Eng Part A 17(21-22) (2011) 2845-55.

[61] X. Ding, et al., Integrated Trilayered Silk Fibroin Scaffold for Osteochondral Differentiation of Adipose-Derived Stem Cells, ACS Applied Materials & Interfaces 6(19) (2014) 16696-16705.

[62] R. Ng, et al., Three-dimensional fibrous scaffolds with microstructures and nanotextures for tissue engineering, RSC Advances 2 (2012) 10110-24.

[63] J. Hong, S. Madihally, Next generation of electrosprayed fibers for tissue regeneration, Tissue Eng, Part B: Rev 17 (2011) 125-142.

[64] D.M. Yunos, et al., Stratified scaffolds for osteochondral tissue engineering applications: electrospun PDLLA nanofibre coated Bioglass(R)-derived foams, Journal of biomaterials applications 27(5) (2013) 537-51.

[65] S. Zhang, et al., Bi-layer collagen/microporous electrospun nanofiber scaffold improves the osteochondral regeneration, Acta Biomaterialia 9(7) (2013) 7236-7247.

[66] E. Filová, et al., A cell-free nanofiber composite scaffold regenerated osteochondral defects in miniature pigs, International Journal of Pharmaceutics 447(1–2) (2013) 139-149.

[67] B.V. Slaughter, et al., Hydrogels in regenerative medicine, Adv Mater 21(32-33) (2009) 3307-29.

[68] N. Annabi, et al., Controlling the Porosity and Microarchitecture of Hydrogels for Tissue Engineering, Tissue Eng Part B Rev 16 (2010) 371-383.

[69] D. Pereira, et al., Gellan gum-based Hydrogel Bilayered Scaffolds for Osteochondral Tissue Engineering, Key Engineering Materials 587 (2014) 255-60.

[70] M.T. Rodrigues, et al., Bilayered constructs aimed at osteochondral strategies: The influence of medium supplements in the osteogenic and chondrogenic differentiation of amniotic fluid-derived stem cells, Acta Biomaterialia 8(7) (2012) 2795-2806.

[71] X. Guo, et al., The Effects of TGF-β3 and Preculture Period of Osteogenic Cells on the Chondrogenic Differentiation of Rabbit Marrow Mesenchymal Stem Cells Encapsulated in a Bilayered Hydrogel Composite, Acta biomaterialia 6(8) (2010) 2920-2931.

[72] K. Kim, et al., Osteochondral tissue regeneration using a bilayered composite hydrogel with modulating dual growth factor release kinetics in a rabbit model, Journal of Controlled Release 168(2) (2013) 166-178.

CHAPTER 2

Pre-clinical and Clinical Management of Osteochondral Lesions

CHAPTER 2.

Pre-clinical and clinical management of osteochondral lesions*

2.1. Abstract

The majority of osteochondral (OC) lesions occur after injury or trauma of both bone and the overlying cartilage, and symptoms are pain and disability, leading to the risk of inducing osteoarthritis. These lesions are currently repaired by non-surgical and surgical methods or by advanced tissue engineering strategies, which require a proof of efficacy and safety for regulatory approval for human application. Pre-clinical studies using animal models have been the support of OC repair and regeneration with successful clinical outcomes. Small animal models as mice and rabbits, and large animal models as sheep, goats and horses, have been most commonly used according with the outcome goals. Small animals are recommended as a proof of concept, while large animals are endorsed for truly translational research in order to get the regulatory approval for clinical use in humans. An up-to-date of the *in vivo* studies using different animal models and ongoing clinical trials for the repair and regeneration of OC lesions are presented. Commercialised products for OC repair are also indicated.

*This chapter is based on the following publication:

Ribeiro VP, Pina S., Oliveira JM, Reis RL. Pre-clinical and clinical management of osteochondral lesions, in Regenerative Strategies for the Treatment of Knee Joint Disabilities, Studies in Mechanobiology, Tissue Engineering and Biomaterials, JM Oliveira and RL Reis (Eds), Springer International Publishing AG, ISSN-1868-2006, vol.21, doi: 10.1007/978-3-319-44785-8_8, 2016.

2.2. Introduction

Osteochondral (OC) lesions may have numerous causes, varying from natural degradation to trauma related lesions that involve the degeneration of articular cartilage, subchondral bone and bone-cartilage interface. Articular cartilage and subchondral bone form the load-bearing system allowing joint motion, stability and uniform distribution of high acting loads [1]. Articular cartilage increases joint congruence and protects the subchondral bone from high stresses, reducing the friction movements within the joint and the normal contact pressure at the edge of bones [1, 2]. Considering the avascular nature of cartilage tissue, in case of injury its response does not follow the typical tissue remodeling cascade events. Cartilage lesions are therefore usually irreversible [3, 4]. Subchondral bone lesions are commonly associated with articular cartilage defects. In the past two decades, promising results have been achieved for the treatment of isolated articular cartilage defects [5-8]. However, deeper OC defects are related to an extension of the cartilage defect into the underlying subchondral bone. Other possible scenarios could be that the subchondral bone becomes less dense and unable to support cartilage in transmitting loads to the cancellous and cortical bone, resulting in the fracture of the articular cartilage [1]. In this sense, basic scientific and technical issues that continue to complicate the treatment of OC lesions must be considered for the development of new strategies.

Osteoarthritis (OA) is the major cause of natural OC defects (Figure 2-1). It is a common disease causing joint paint, deformity and functional disability and is expected that at least 40% of patients aged 65 years and older may suffer of OA in large joints [9, 10]. Since 2008, it was estimated that over 39 million people in Europe and over than 20 million Americans suffer of OA, expecting that this number will double in 2020 [11]. Nowadays, OA can be treated using non-surgical (pharmacologic and/or physical treatments) and surgical (joint replacement and osteotomy) therapies, depending on the severity of the damage [12-14]. These treatments are well established and demonstrated to be effective for reducing pain improving the patient's quality of life, but are not regenerative thus limiting the complete healing of the articular cartilage [1, 15, 16].

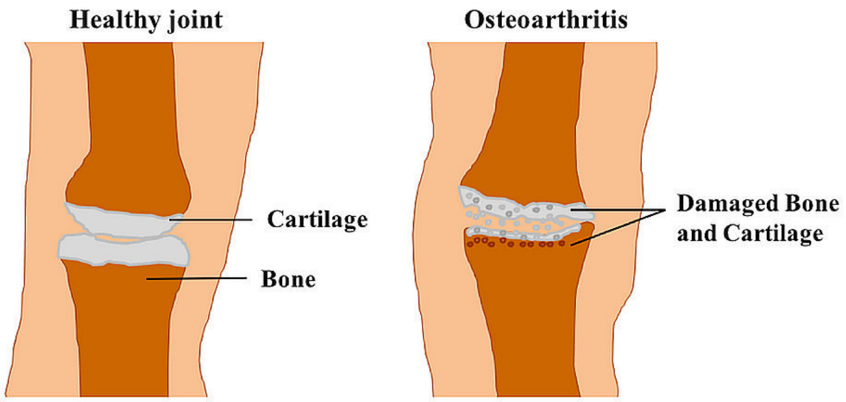

Figure 2-1. Illustrative image of a knee healthy joint and joint with osteoarthritis.

Surgeons and researchers have been testing different treatments for the repair and regeneration of OC defects. The most common methods are joint debridement, bone marrow stimulation technique (microfracture) and the use of OC allografts. OC autograft implantation (mosaicplasty) and cell-based therapy, as autologous chondrocytes implantation (ACI), are other possibilities [2, 17-21]. Joint debridement method eliminates debris from the joint space or surface and is applied only as a palliative treatment. In clinical treatment, it is usually associated with the microfracture technique that consists in penetrating the subchondral bone and releasing bone marrow progenitor cells into the defect [22, 23]. Mosaicplasty technique removes cylindrical plugs of the hyaline cartilage with subchondral bone from an unaffected area and implants the removed tissue into the chondral defect. Perpendicular edges of normal cartilage are previously prepared to create a "mosaic" pattern [24]. For OC defects, greater than 2.5 cm^2, OC allografts and cells with chondrogenic potential are usually the chosen treatments. ACI technique consist of isolate chondrocytes from a small cartilage piece in a low-weight-bearing area of the knee joint, and after 2-3 weeks of expansion *in vitro,* cells are implanted into the chondral defect [25]. Surgical approaches using OC allografts are often indicated as rescue treatments for post-traumatic lesions related to articular fractures in which there is a significant bone loss [24]. Although these treatments are effective, significant disadvantages exist, such as the lack of regenerative hyaline cartilage tissue, immune rejection and limited available tissues [26, 27]. Tissue engineering strategies emerged as promising alternatives to overcome such problems, mainly involving biodegradable scaffolds, tissue forming cells and growth factors. The initially proposed OC scaffolds were made out of a single phase structure, including different scaffolds for bone and cartilage layers or single homogeneous scaffolds for both components [28]. Recently, it was found that a successful tissue-engineered approach for the treatment of OC lesions involves the development of bilayered or stratified scaffolds, with distinct bone and cartilage parts, holding great biocompatibility, biodegradability, and biomechanical features able to establish an adequate environment for cell distribution, proliferation and differentiation [27, 29-32]. Different cell-based tissue engineering strategies have also been studied, in which OC scaffolds are combined with appropriate cells, progenitor cells (mesenchymal stem cells) or tissue specific cells (osteocytes and chondrocytes), and growth factors in order to generate and deposit new extracellular matrix (ECM) [33-36].

Several tissue-engineered structures have been developed for OC repair and regeneration and tested preclinically, but only some them, have been investigated through clinical trials. In this context, this chapter provides an up-to-date of pre-clinical animal models studies in OC tissue engineering approaches applying different scaffolding strategies. Ongoing and complete clinical trials with high relevance and the related marketed tissue-engineered products towards OC tissue regeneration are also presented.

2.3. Pre-Clinical studies for osteochondral regeneration

As above mentioned, OC defects can be conventionally treated by clinical/surgical methods or by advanced tissue engineering strategies [2, 28, 37-40]. As any tissue engineering approach, the development of OC constructs requires the evaluation of its performance on several pre-clinical studies prior to the evaluation in humans. There is a need to evaluate the structures response under physiologic conditions that better simulate human clinical pathologies. Recently reported animal pre-clinical studies for the treatment of OC lesions using different scaffolds strategies are summarized in Table 2-1.

Table 2-1. Recent pre-clinical studies for OC repair using different animal models.

Scaffold	**Animal model**	**Cells/growth factors incorporation**	**Results**	**Reference**
Alginate/PCL triphasic scaffolds	Rats	Chondrocytes, BMP-7	Limited bone formation after 12 weeks of implantation	[44]
Poly(ester-urethane)/HAp scaffolds	Rabbit	n.a.	Tissue repair after 12 weeks implantation	[45]
Platelet-rich fibrin glue/HAp biphasic scaffolds	Rabbit	MSCs	OC defects were resurfaced with more hyaline-like at 8 weeks post-implantation	[46]

PEG hydrogel/β-TCP biphasic scaffolds	Rabbit	n.a.	Tidemark formation at 52 weeks post-implantation. Formation of the repaired subchondral bone from 16 to 52 weeks in a "flow like" manner from surrounding bone to the defect center gradually.	[47]
PLLA nanofibers/collagen bilayered scaffolds	Rabbit	MSCs	Rapid induction of subchondral bone appearance, and better cartilage formation after 12 weeks implantation	[48]
Oligo(poly(ethylene glycol) fumarate)/gelatin composites	Rabbit	IGF-1 and TGF-β3	Significant improvement in cartilage morphology at 12weeks post-implantation	[49]
Collagen/HAp-silk bilayered scaffolds	Rabbit	Administration of parathyroid hormone-related protein (PTHrP)	Optimal time for administering PTHrP with the scaffold is 4–6 weeks post-injury for OC defect repair	[50]
HAp/chitosan-gelatin scaffolds	Rabbit	MSCs, TGF-β1, and BMP-2	Good restoration of OC defect and excellent integration with the native OC tissues after 12 weeks of implantation	[51]
Coralline aragonite and hyaluronic acid biphasic scaffolds	Goat	n.a.	Nearly completely biodegradation and replacement by newly OC formation tissue by 6 months after implantation	[52]
PLGA scaffolds	Sheep	Autologous chondrocytes	Significant improvement of the OC lesion after 20 weeks implantation	[53]
Allogenous bone/collagen biphasic scaffold	Sheep	Autologous chondrocytes	Full integration of the allogenous bone cand detection of conntinuous	[54]

			chondral layer after 6 months implantation	
Micro-porous β-TCP scaffolds	Sheep	Autologous chondrocytes	Degradation and subchondral bone formation after 52 weeks of implantation. Healthy and biomechanical stable cartilage were not reached after 1 year.	[55]
Collagen TypeI/HAp scaffolds	Pig	Autologous chondrocytes	Formation of a reparative tissue with high cellularity after 3 months of implantation	[42]
β-TCP/collagen Types I and III scaffolds	Mini-pig	BMP-2, 3, 4, 6, 7, and TGF-β1, 2, 3	Increasing new bone formation at 12 weeks post-implantation, and almost fully degradation after 52 weeks, and defect restoration	[56]
Gelatin-β-TCP bilayered sponge scaffolds	Horse	MSCs, chondrocytes, BMP-2, and platelet rich plasma	OC regeneration after 4 months of implantation	[43]

n.a.: not applicable.

PCL: Polycaprolactone; BMP: Bone morphogenetic protein; HAp: Hydroxyapatite; MSCs: Mesenchymal stem cells; TGF: Transforming growth factor; IGF: Insulin-like growth factor; BMSCs: Bone marrow-derived stem cells; PLLA: Poly-L-lactide; PLGA: Poly-L-glycolide; PEG: Poly(ethylene glycol); β-TCP: β-Tricalcium phosphate.

The success of a pre-clinical study is determined by an appropriate selection of the animal model, such as mice, rabbit, and sheep, chosen based on the final functional application of the tissue-engineered construct [41]. Small-animal models (e.g. mice and rabbit) are usually used as proof-of-concept, mainly because they can reproduce fast, which enable the study of the function of particular genes during a reasonable period of time, and they are quite inexpensive [42]. However, the absence of the joint biochemical and biomechanical environment in small animals can significantly prejudice the results, therefore considering large animals more appropriate for modelling human OC defects, thus used for final preclinical evaluation. Though, few published pre-clinical using large animal models for OC repair/regeneration are available. A typical image section stained with hematoxylin–eosin of gelatin/β-tricalcium phosphate (β-TCP) scaffolds after implantation in horses talus defect for 4 months is presented in Figure 2-2, combined with or without cells and growth factors, respectively, Test group and Control group [43]. It can be seen that histological scores were significantly superior in the test group that in the control group. Moreover, no remaining implant material, any chronic inflammations, and bone regeneration was observed.

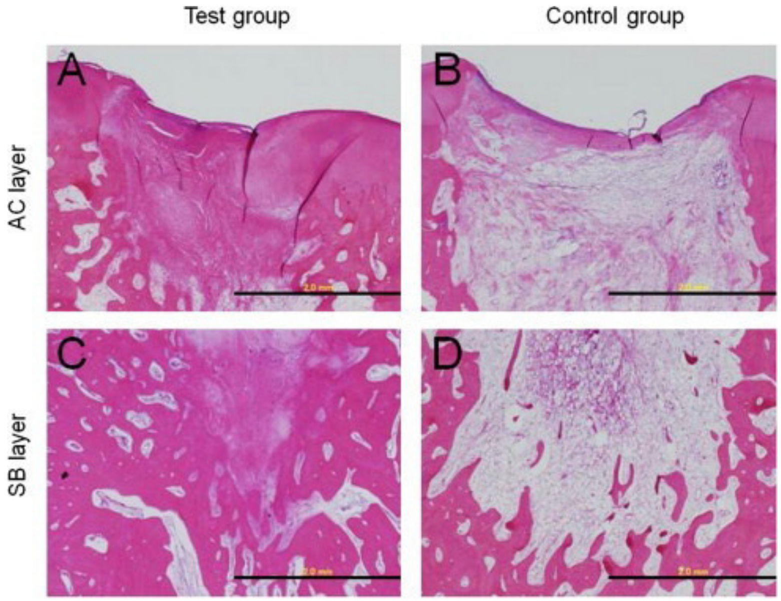

Figure 2-2. Microscopy images of histological hematoxylin-eosin stained sections of gelatin/β-TCP scaffolds, with (Test group) or without (Control group) MSCs and growth factors, after implantation in horses for 4 months. AC: articular cartilage; SB: subchondral bone. Scale bar: 2 mm. Reprinted with permission from [43]. Copyright 2013, Elsevier.

2.4. Clinical trials for osteochondral regeneration

Although most of the pre-clinical approaches are yet to be translated into clinical trials, the outcomes reveal several tissue engineered OC grafts promising for future clinical applications. For example, Kon *et al.* [57] performed a short-term clinical trial in thirteen human patients treated with nanostructured and multilayered scaffolds for OC defects of the knee joint. The clinical observation period provided promising preliminary results for the constructs attachment rate, stability and healing process, encouraging a clinical study with longer follow-up to confirm the high potential of the proposed OC scaffold. Williams *et al.* [58] developed a synthetic resorbable biphasic device made predominantly from polylactide-coglycolide (PLGA) copolymer, calcium sulphate and PGA, revealing favourable clinical results and a good safety profile. In fact, this clinically tested OC device has already been approved by the European Medicines Agency (EMEA) for the treatment of accurate focal articular cartilage or OC defects. Looking at the increasing progress in this area, US Food and Drug Administration (FDA) revealed that tissue engineered OC grafts would be expected to be seen in the market within the next 5-10 years. Considering all OC tissue engineering strategies for clinical application, ongoing and completed clinical trials (with no reported results yet) for OC repair and regeneration using scaffolds or cell therapies, or even scaffolds combined with cells pre-cultures *in vitro* are listed in Table 2-2.

Table 2-2. Overview of ongoing and complete clinical trials using strategies for OC regeneration. Information obtained from https://clinicaltrials.gov/.

NCT number	Denomination	Procedure	Patients age	Follow-up	Period time
NCT00891501	The Use of Autologous bone marrow MSCs in the Treatment of Articular Cartilage Defects	Bone marrow MSCs aspiration and implantation	15-55 yrs	n.d.	2006-2014
NCT00560664	Comparison of ACI Versus Mosaicoplasty	Autologous chondrocytes transplantation and mosaicoplasty	18-50 yrs	2 yrs	2007-2013
NCT00945399	Comparison of Microfracture Treatment and CARTIPATCH® Chondrocyte Graft Treatment in Femoral Condyle Lesions	ACI and microfracture	18-45 yrs	18 mths	2008-2011
NCT00793104	Evaluation of the CR Plug (Allograft) for the Treatment of a Cartilage Injury in the Knee	Placement of allograft CR Plug in primary injury site	≥ 18 yrs	2 yrs	2008-2012
NCT00821873	Evaluation of the CR Plug for Repair of Defects Created at the Harvest Site From an Autograft in the Knee	CR Plug implantation in the harvest site	18-55 yrs	2 yrs	2008-2012
NCT01409447	Repair of Articular OCD	Biphasic OC composite implantation	18-60 yrs	1 year	2009-2011
NCT00984594	Evaluation of a Composite Cancellous and Demineralized Bone Plug (CR-Plug) for Repair of Knee OCDs	Autograft implantation in the primary defect site; CR-Plug implantation in the harvest site	18-55 yrs	2 yrs	2009-2012

NCT01183637	Evaluation of an Acellular OC Graft for Cartilage Lesions	Microfacture	≥ 21 yrs	2 yrs	2010-2014
NCT01159899	Transplantation of BM Stem Cells Stimulated by Proteins Scaffold to Heal Defects Articular Cartilage of the Knee	Transplantation of BM stem cells activated in knee arthrosis	30-75 yrs	1year	2010-2014
NCT01209390	A Prospective, Post-marketing Registry on the Use of ChondroMimetic for the Repair of OCDs	Chondromimetic	18-65 Yrs	3 yrs	2010-2016
NCT01473199	BioPoly RS Knee Registry Study for Cartilage Defect Replacement	BioPoly RS partial resurfacing knee implantation	≥ 21 yrs	5 yrs	2011
NCT01290991	A Study to Evaluate the Safety of Augment™ Bone Graft	Augment Bone Graft	18-40 yrs	1 year	2011-2012
NCT01410136	Chondrofix OC Allograft Prospective Study	Allogeneic OC grafting	18-70 yrs	2 yrs	2011-2014
NCT01477008	Biphasic Cartilage Repair Implant	Marrow Stimulation	Up to 54 yrs	1 year	2011-2014
NCT01282034	Study for the Treatment of Knee Chondral and OC Lesions	Marrow stimulation - Drilling or Microfractures	18-60 yrs	2 yrs	2011-2015
NCT01471236	Evaluation of the Agili-C Biphasic Implant in the Knee Joint	Agili-C Biphasic implantation and mini-arthrotomy or arthroscopy	18-55 yrs	2 yrs	2011-2017
NCT01347892	DeNovo NT Ankle LDC Study	DeNovo NT Natural Tissue Grafting	≥ 18 yrs	5 yrs	2011-2019
NCT01747681	Results at 10 to 14 Years After Microfracture in the Knee	Microfracture	18-80 yrs	10 yrs	2012-2013

NCT01554878	Observational Study on the Treatment of Knee OC Lesions of Grade III-IV	Knee surgery	30-60 yrs	1 year	2012-2014
NCT01920373 (cancelled)	Platelet-Rich Plasma vs Corticosteroid Injection as Treatment for Degenerative Pathology of the Temporo-mandibular Joint	Corticosteroid and platelet rich plasma injection	n.d.	6 mths	2013
NCT01799876	Use of Cell Therapy to Enhance Arthroscopic Knee Cartilage Surgery	Autologous cell and standard microfracture arthroscopic surgery	18-68 yrs	1 year	2013-2015
NCT02005861	"One-step" BM Mononuclear Cell Transplantation in Talar OC Lesions	Bone marrow derived cells transplantation on collagen scaffold	15-50 yrs	2 yrs	2013-2016
NCT02011295	BM Aspirate Concentrate Supplementation for OC Lesions	Ankle arthroscopy with debridement and microfracture	18- 95 yrs	2 yrs	2013-2017

n.d.: not defined.

OC: osteochondral; MSCs: mesenchymal stem cells; ACI: autologous chondrocyte implantation; OCDs: osteochondral defects.

2.5. Marketed products for osteochondral regeneration

The commercialization process of the scaffolds for implantation involves multiple stages of R&D replications before reaching the final approval from the government. R&D stages ensure safety and efficacy of the implants, which involve the production of medical grade scaffolds followed by animal testing under regulatory approved conditions. Some of the products present in Table 2-2 have been proposed for commercialization. However, only a few scaffolds are reported in the literature for OC applications, including: (i) TruFit® (Smith & Nephew, USA) that is a bilayered 75:25 PLGA-PGA/calcium-sulfate copolymer porous and resorbable scaffold (Figure 2-3a) [59]; (ii) MaioRegen® (Finceramic, Italy) is a trilayered porous scaffold composed of collagen and Mg enriched Hap (Figure 2-3b) [60]; and (iii) Cartilage Repair Device (Kensey Nash Corp.) is a biphasic bioresorbable scaffold consisting of a unique bovine collagen Type I matrix and β-TCP, intended to be implanted at the site of a focal articular cartilage lesion or OC in the knee (Figure 2-3c) [61]. In addition, ChondroMimetic is a bilayered implant based on collagen and calcium phosphate for the treatment of small chondral and subchondral defects. The literature also describes Agili-C™, an aragonite-based cell-free implant that reproducibly regenerates hyaline cartilage and its underlying subchondral bone. Another available medical product to repair full-thickness OC lesions is Chondrofix® Allograft, the first OC allograft [62]. It is composed of donated human decellularized hyaline cartilage and cancellous bone, and possesses relevant mechanical properties that are comparable to unprocessed OC tissue.

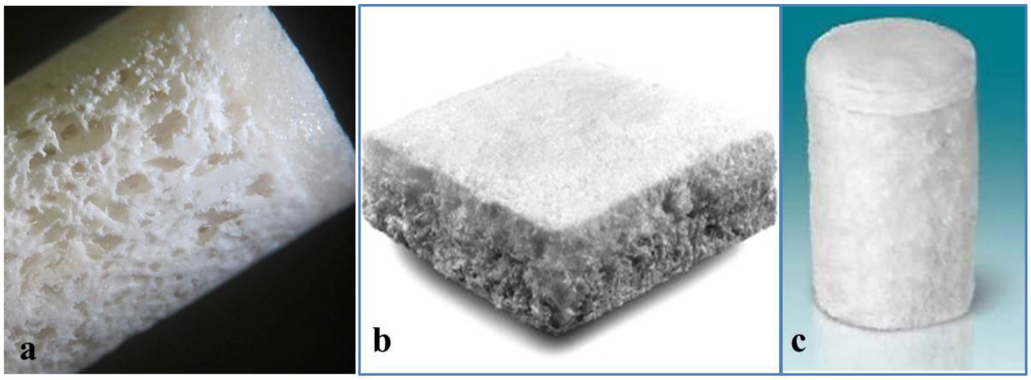

Figure 2-3. Commercial bi-multilayered scaffolds for OC repair/regeneration: (a) TruFit® (Reprinted with permission from [59]); (b) MaioRegen® (Reprinted with permission from [60]); and (c) CRD technology (Reprinted with permission from [61]).

2.6. Conclusions

Over the last few years, great progress has been made to validate tissue engineering strategies in pre-clinical studies and clinical trials on the regeneration of OC defects. Foremost strategies used in pre-clinical studies involve the development of bi/multilayered scaffolds, alone or incorporating stem cells and/or growth factors. The chondrogenic and osteogenic repair capacities of OC defects have been evaluated subcutaneously in mice and rabbit models, although large animal models (e.g., sheep or horse) closely resemble the human tissue compared to smaller animal models, being therefore crucial for a final *in vivo* testing prior to clinical application in controlled clinical trials. Animal studies are used to assess biological responses, degradation and durability time, and dose response of the implanted materials, as a proof-of-concept.

Concerning commercialized OC scaffolds, only a few were documented in the literature. The three-layered scaffold MaioRegen® showed promising results for OC treatment, forming graded structures with a cartilage-bone interface that reproduced the tidemark of the native OC tissue. Still, reported studies has shown a non-homogeneous repair of the tissues in the defective areas. The TruFit® bilayered scaffold showed good short-term results in most of the patients. However, in 2009 and in the following years different authors reported foreigen body reactions and lack of bone ingrowth, being removed from the market in 2013.

Despite the significant advances in OC scaffolding, further investigations relating to clinical surveys are demanded for consistent long-term efficacy, as many challenges remain to be determined.

2.7. References

[1] W. Swieszkowski, et al., Repair and regeneration of osteochondral defects in the articular joints, Biomol Eng 24(5) (2007) 489-495.

[2] S. Panseri, et al., Osteochondral tissue engineering approaches for articular cartilage and subchondral bone regeneration, Knee Surg Sport Tr A 20(6) (2012) 1182-1191.

[3] A.D. Pearle, et al., Basic science of articular cartilage and osteoarthritis, Clin Sport Med 24(1) (2005) 1–12.

[4] M. Liu, et al., Tissue Engineering Stratified Scaffolds for Articular Cartilage and Subchondral Bone Defects Repair, Orthopedics 36(11) (2013) 868-873.

[5] C.R. Chu, et al., Articular cartilage repair using allogeneic perichondrocyteseeded biodegradable porous polylactic acid (PLA): A tissue-engineering study, Journal of biomedical materials research 29(9) (1995) 1147-1154.

[6] J.K. Sherwood, et al., A three-dimensional osteochondral composite scaffold for articular cartilage repair, Biomaterials 23(24) (2002) 4739-4751.

[7] L.P. Yan, et al., Genipin-cross-linked collagen/chitosan biomimetic scaffolds for articular cartilage tissue engineering applications, Journal of Biomedical Materials Research Part A 95(2) (2010) 465-475.

[8] L.-P. Yan, et al., Macro/microporous silk fibroin scaffolds with potential for articular cartilage and meniscus tissue engineering applications, Acta biomaterialia 8(1) (2012) 289-301.

[9] K. Shimomura, et al., Osteochondral tissue engineering with biphasic scaffold: current strategies and techniques, Tissue Engineering Part B: Reviews 20(5) (2014) 468-476.

[10] R. Moyer, et al., Osteoarthritis Year in Review 2014: mechanics–basic and clinical studies in osteoarthritis, Osteoarthritis and Cartilage 22(12) (2014) 1989-2002.

[11] C. Csaki, et al., Mesenchymal stem cells as a potential pool for cartilage tissue engineering, Annals of Anatomy-Anatomischer Anzeiger 190(5) (2008) 395-412.

[12] W. Zhang, et al., OARSI recommendations for the management of hip and knee osteoarthritis, part I: critical appraisal of existing treatment guidelines and systematic review of current research evidence, Osteoarthritis and Cartilage 15(9) (2007) 981-1000.

[13] W. Zhang, et al., OARSI recommendations for the management of hip and knee osteoarthritis, Part II: OARSI evidence-based, expert consensus guidelines, Osteoarthritis and Cartilage 16(2) (2008) 137- 162.

[14] W. Zhang, et al., OARSI recommendations for the management of hip and knee osteoarthritis: part III: Changes in evidence following systematic cumulative update of research published through January 2009, Osteoarthritis and Cartilage 18(4) (2010) 476-499.

[15] S. Redman, et al., Current strategies for articular cartilage repair, Eur Cell Mater 9(23-32) (2005) 23-32.

[16] K. Shimomura, et al., The influence of skeletal maturity on allogenic synovial mesenchymal stem cell-based repair of cartilage in a large animal model, Biomaterials 31(31) (2010) 8004-8011.

[17] L. Xing, et al., Microfracture combined with osteochondral paste implantation was more effective than microfracture alone for full-thickness cartilage repair, Knee Surgery, Sports Traumatology, Arthroscopy 21(8) (2013) 1770-1776.

[18] Y.S. Kim, et al., Clinical comparison of the osteochondral autograft transfer system and subchondral drilling in osteochondral defects of the first metatarsal head, The American journal of sports medicine 40(8) (2012) 1824-1833.

[19] L. De Girolamo, et al., Modified autologous matrix-induced chondrogenesis (AMIC) for the treatment of a large osteochondral defect in a varus knee: a case report, Knee Surgery, Sports Traumatology, Arthroscopy 20(11) (2012) 2287-2290.

[20] M. Miska, et al., Reconstruction of a large osteochondral lesion of the distal tibia with an iliac crest graft and autologous matrix-induced chondrogenesis (AMIC): a case report, The Journal of Foot and Ankle Surgery 51(5) (2012) 680-683.

[21] B.B. Christensen, et al., A novel nano-structured porous polycaprolactone scaffold improves hyaline cartilage repair in a rabbit model compared to a collagen type I/III scaffold: in vitro and in vivo studies, Knee Surgery, Sports Traumatology, Arthroscopy 20(6) (2012) 1192-1204.

[22] R.W. Jackson, C. Dieterichs, The results of arthroscopic lavage and debridement of osteoarthritic knees based on the severity of degeneration, Arthroscopy: The Journal of Arthroscopic & Related Surgery 19(1) (2003) 13-20.

[23] F. Shannon, et al., Short-term benefit of arthroscopic washout in degenerative arthritis of the knee, International orthopaedics 25(4) (2001) 242-245.

[24] L. Hangody, et al., Arthroscopic autogenous osteochondral mosaicplasty for the treatment of femoral condylar articular defects A preliminary report, Knee Surgery, Sports Traumatology, Arthroscopy 5(4) (1997)

262-267.

[25] T. Minas, L. Peterson, Autologous chondrocyte transplantation, Operative Techniques in Sports Medicine 20(1) (2012) 72-86.

[26] A.M. Getgood, et al., Evaluation of early-stage osteochondral defect repair using a biphasic scaffold based on a collagen–glycosaminoglycan biopolymer in a caprine model, The Knee 19(4) (2012) 422-430.

[27] A. Siclari, et al., A cell-free scaffold-based cartilage repair provides improved function hyaline-like repair at one year, Clinical Orthopaedics and Related Research® 470(3) (2012) 910-919.

[28] I. Martin, et al., Osteochondral tissue engineering, J Biomech 40(4) (2007) 750-765.

[29] A. Sotoudeh, et al., Study on nano-structured hydroxyapatite/zirconia stabilized yttria on healing of articular cartilage defect in rabbit, Acta Cirurgica Brasileira 28(5) (2013) 340-345.

[30] J. Jiang, et al., Bioactive stratified polymer ceramic-hydrogel scaffold for integrative osteochondral repair, Annals of biomedical engineering 38(6) (2010) 2183-2196.

[31] H. Nejadnik, H.E. Daldrup-Link, Engineering stem cells for treatment of osteochondral defects, Skeletal radiology 41(1) (2012) 1-4.

[32] M. Keeney, A. Pandit, The osteochondral junction and its repair via bi-phasic tissue engineering scaffolds, Tissue Engineering Part B: Reviews 15(1) (2009) 55-73.

[33] X. Wang, et al., Growth factor gradients via microsphere delivery in biopolymer scaffolds for osteochondral tissue engineering, Journal of Controlled Release 134(2) (2009) 81-90.

[34] G.I. Im, J.H. Lee, Repair of osteochondral defects with adipose stem cells and a dual growth factor-releasing scaffold in rabbits, Journal of Biomedical Materials Research Part B: Applied Biomaterials 92(2) (2010) 552-560.

[35] N. Mohan, et al., Continuous gradients of material composition and growth factors for effective regeneration of the osteochondral interface, Tissue Engineering Part A 17(21-22) (2011) 2845-2855. [36] K. Schütz, et al., Cell-laden biphasic scaffolds with anisotropic structure for the regeneration of osteochondral tissue, Journal of tissue engineering and regenerative medicine (2014).

[37] B.A. Harley, et al., Design of a multiphase osteochondral scaffold III: Fabrication of layered scaffolds with continuous interfaces, J Biomed Mater Res A 92A(3) (2010) 1078-1093.

[38] W.L. Grayson, et al., Engineering custom-designed osteochondral tissue grafts, Trends Biotechnol 26(4) (2008) 181-189.

[39] S.P. Nukavarapu, D.L. Dorcemus, Osteochondral tissue engineering: Current strategies and challenges, Biotechnol Adv 31(5) (2013) 706-721.

[40] P. Nooeaid, et al., Osteochondral tissue engineering: scaffolds, stem cells and applications, J Cell Mol Med 16(10) (2012) 2247-2270.

[41] S.A. Goldstein, Tissue engineering - Functional assessment and clinical outcome, Ann Ny Acad Sci 961 (2002) 183-192.

[42] C. Sosio, et al., Osteochondral repair by a novel interconnecting collagen-hydroxyapatite substitute: a large-animal study, (1937-335X (Electronic)) (2015).

[43] J.-P. Seo, et al., Effects of bilayer gelatin/β-tricalcium phosphate sponges loaded with mesenchymal stem cells, chondrocytes, bone morphogenetic protein-2, and platelet rich plasma on osteochondral defects of the talus in horses, Research in Veterinary Science 95(3) (2013) 1210-1216. [44] J.E. Jeon, et al., Multiphasic construct studied in an ectopic osteochondral defect model, 2014. [45] I. Dresing, et al., Evaluation of a press-fit osteochondral poly(ester-urethane) scaffold in a rabbit defect model, J Mater Sci: Mater Med 25(7) (2014) 1691-1700.

[46] K.M. Jang, et al., Xenotransplantation of human mesenchymal stem cells for repair of osteochondral defects in rabbits using osteochondral biphasic composite constructs, Knee Surg Sport Tr A 22(6) (2014) 1434-1444.

[47] W.J. Zhang, et al., Cartilage Repair and Subchondral Bone Migration Using 3D Printing Osteochondral Composites: A One-Year-Period Study in Rabbit Trochlea, Biomed Research International (2014).

[48] S.F. Zhang, et al., Bi-layer collagen/microporous electrospun nanofiber scaffold improves the osteochondral regeneration, Acta Biomater 9(7) (2013) 7236-7247.

[49] K. Kim, et al., Osteochondral tissue regeneration using a bilayered composite hydrogel with modulating dual growth factor release kinetics in a rabbit model, J Control Release 168(2) (2013) 166- 178.

[50] W. Zhang, et al., The promotion of osteochondral repair by combined intra-articular injection of parathyroid hormone-related protein and implantation of a bi-layer collagen-silk scaffold, Biomaterials 34(25) (2013) 6046-6057.

[51] J.N. Chen, et al., Simultaneous regeneration of articular cartilage and subchondral bone in vivo using MSCs induced by a spatially controlled gene delivery system in bilayered integrated scaffolds, Biomaterials 32(21) (2011) 4793-4805.

[52] E. Kon, et al., Osteochondral regeneration using a novel aragonite-hyaluronate bi-phasic scaffold in a goat model, (1433-7347 (Electronic)) (2015).

[53] C. Fonseca, et al., An arthroscopic approach for the treatment of osteochondral focal defects with cell-free and cell-loaded PLGA scaffolds in sheep, Cytotechnology 66(2) (2014) 345-354.

[54] I. Schleicher, et al., Biphasic scaffolds for repair of deep osteochondral defects in a sheep model, Journal of Surgical Research 183(1) (2013) 184-192.

[55] A. Bernstein, et al., Microporous calcium phosphate ceramics as tissue engineering scaffolds for the repair of osteochondral defects: Histological results, Acta Biomaterialia 9(7) (2013) 7490-7505. [56] T. Gotterbarm, et al., Complete subchondral bone defect regeneration with a tricalcium phosphate collagen implant and osteoinductive growth factors: a randomized controlled study in Gottingen minipigs, (1552-4981 (Electronic)) (2014).

[57] E. Kon, et al., A novel nano-composite multi-layered biomaterial for treatment of osteochondral lesions: Technique note and an early stability pilot clinical trial, Injury 41(7) (2010) 693-701.

[58] R.J. Williams, S.C. Gamradt, Articular cartilage repair using a resorbable matrix scaffold, Instr Course Lect 57 (2008) 563-71.

[59] J.T.K. Melton, et al., TruFit CB® bone plug: chondral repair, scaffold design, surgical technique and early experiences, Expert Review of Medical Devices 7(3) (2010) 333-341.

[60] E. Kon, et al., A novel nano-composite multi-layered biomaterial for treatment of osteochondral lesions: Technique note and an early stability pilot clinical trial, Injury 41 (2010) 693–701.

[61] G. Ostrovsky, Bioresorbable, Acellular, Biphasic Scaffold Gets EU Approval for Knee Cartilage Repair. medGadget. Accessed 25 Nov 2014.

[62] A.H. Gomoll, Osteochondral Allograft Transplantation Using the Chondrofix Implant, Operative Techniques in Sports Medicine 21(2) (2013) 90-94.

CHAPTER 3

Silk Fibroin-Based Hydrogels and Scaffolds for Osteochondral Repair and Regeneration

CHAPTER 3.

Silk fibroin-based hydrogels and scaffolds for ostechondral repair and regeneration*

3.1. Abstract

Osteochondral lesions treatment and regeneration demands biomimetic strategies aiming physicochemical and biological properties of both bone and cartilage tissues, with long-term clinical outcomes. Hydrogels and scaffolds appeared as assertive approaches to guide the development and structure of the new osteochondral engineered tissue. Moreover, these structuresalone or in combination with cells and bioactive molecules, bring the mechanical support after *in vitro* and *in vivo* implantation. Moreover, multilayered structures designed with continuous interfaces, furnish appropriate features of the cartilage and subchondral regions, namely microstructure, composition, and mechanical properties. Owing the potential as scaffolding materials, natural and synthetic polymers, bioceramics, and composites have been employed. Particularly, significance is attributed to the natural-based biopolymer silk fibroin from the *Bombyx mori* silkworm, considering its unique mechanical and biological properties. The significant studies on silk fibroin-based structures, namely hydrogels and scaffolds, towards bone, cartilage, and osteochondral tissue repair and regeneration are overviewed herein. The developed biomimetic strategies, processing methodologies, and final properties of the structures are summarized and discussed in depth.

*This chapter is based on the following publication:

Ribeiro VP, Pina S., Oliveira JM, Reis RL. Silk fibroin-based hydrogels and scaffolds for osteochondral repair and regeneration, in Osteochondral Tissue Engineering - Nanotechnology, Scaffolding-Related Developments and Translation, Advances in Experimental Medicine and Biology, JM Oliveira, S Pina, RL Reis and JS Roman (Eds), Springer International Publishing AG, ISBN: 978-3-319-76710-9.

3.2. Introduction

Tissue engineering (TE) field has been evolved as a way to compensate the limited supply of donor tissue and organ transplants related to a high morbidity and mortality [1]. TE approaches involve different research areas simultaneously, including cell biology, materials science, and clinical evaluation, with the final purpose of creating a suitable microenvironment that mimics the tissue at the host site in a desired and faster regeneration [2]. Such microenvironment is typically composed by three-dimensional (3D) porous scaffolds, on which cells are stimulated to grow and organize to form an extracellular matrix (ECM) used to initiate the regenerative process [3]. These 3D constructs provide the chemical and mechanical support for *in vitro* ECM formation, being gradually degraded, resorbed or metabolized after *in vivo* implantation. Therefore, apart from an essential biocompatibility, the scaffolds must possess an equivalent degradation profile to the host tissue, while keeping the mechanical properties and structural integrity promoted by the forming ECM [4, 5].

Natural- and synthetic-based polymers, ceramic materials, and composites have been proposed for scaffolding strategies in TE approaches [6, 7]. Natural-based polymers have emerged as preferred sources for the development of scaffolds with better biocompatibility and lower risk of metabolized degradation products, while the synthetic polymers are more stable and easier to process and modify [8, 9]. For example, collagen, gelatin, and chitosan include some of the most investigated natural polymers in TE field. However, these scaffold materials may present poor mechanical properties associated to a rapid degradation profile. Structural proteins like elastin, fibrin, silk, and albumin have also been used as sutures, and more recently for scaffolds production, and as drug delivery agents [10, 11]. Among them, special interest has been attributed to silk protein produced by a wide range of arthropods and lepidopteran insects, including spiders, scorpions, mites, flies, and silkworms, which possess a large molecular weight of 200–350 kDa. It has been used for centuries in textiles production and as clinical sutures (good skin affinity). Their availability for large-scale processing was also economically advantageous for use in TE applications [12]. From the different sources of silk proteins, *Bombyx mori* silk produced by silkworms became the most investigated for diverse TE applications, holding impressive mechanical properties, biocompatibility, biodegradability, low immunogenicity, and suitable processability [12]. It is synthesized in a liquid state in the epithelial cells of the insects' glands, secreted in the lumen and converted (spun) into a liquid-to-solid state (fibers) when in contact with the external air, being mechanically drawn in the form of cocoons. The spun fibers are composed by two animal-based proteins: a core protein named fibroin, surrounded by a glue-like protein named sericin [13]. Even it has been found that sericin may contain some biocompatibility problems [12], several studies have been proposing both silk fibroin (SF) [14-17] and silk sericin [18-20] for diverse biomedical and TE applications. SF has been recognized for presenting favorable biocompatibility, tunable molecular structure, and remarkable mechanical properties with controllable degradation rates, and for that reason it remains the most extensively studied silk protein as promising candidate for several structural [21], biomedical [16, 17], and TE applications [14, 15, 22]. Until now, several forms have been used to fabricate scaffolds made of SF, including films [23], membranes [16], fibers [16], textiles [15, 22], sponges [14], and hydrogels [24], used for the regeneration of soft tissues, like skin [23], ligament and tendon [25], and different hard tissues, including bone [15], cartilage [26], and osteochondral (OC) tissue [14].

The natural OC tissue existing in all human body joints is composed by two main tissues, the articular cartilage and subchondral bone, connected by a stable interface that unifies both elements as a single and complex tissue [27]. The great challenge of OC TE is the design of structures able to meet all the physicochemical and biological requirements for the repair/replacement of bone and cartilage tissues, and at the same time ensure a good compatibility between these two phases.

OC defects or damage can happen in any joint in human body, and affect both the articular cartilage, the underlying subchondral bone, as well its interface [27]. Moreover, the OC tissue repair involves a deep understanding of how the OC interface is combined in terms of structure, and mechanical and biological properties. Over the past years, several studies have been reported towards the repair/regeneration of these tissues, by creating single-phase structures able to fit into the defected area [26, 28-32].

Considering the heterogeneity of OC tissue, innovative 3D structures comprising different mechanical properties and biological performances, according to the target OC tissue layer, are strongly required. The recent development of bilayered scaffolds and improved multi-phased, or stratified, scaffolds with distinct subchondral bone and cartilage layers have been applied for this purpose [33, 34]. In general, OC TE strategies can be categorized into monophasic, biphasic, and triphasic depending on the physicochemical and cellular/biological characteristics of the scaffolds (Table 3-1) [35]. Bilayered hydrogels [36] and complex bilayered scaffolds have been reported for OC regeneration applications [37]. Recent studies in the field are leading to promising approaches to use SF-based biomaterials for OC tissue repair and regeneration strategies [38, 39]. The most recent and relevant studies focused on SF-based structures, namely hydrogels and scaffolds, targeting bone, cartilage, and OC tissue repair and regeneration are overviewed. Additionally, it is summarized developed strategies, processing methodologies, and final properties of the structures.

Table 3-1. Osteochondral TE scaffolding design approaches.

	Physicochemical properties		Biological properties	
Monophasic	One material with same porosity		One cell type	
Biphasic	Two layers with different material composition and porosity		Two different cell types, with bioactive molecules/growth factors	
Triphasic	Three layers with different material composition and porosity		Three different cell types, with bioactive molecules/growth factors	

3.3. Characteristics of silk fibroin

Silk fibroin (SF) from *Bombyx mori* is composed by three protein components. A heavy (H) and a light (L) chain polypeptides of ~350 kDa and ~26 kDa, respectively, form the H-L complex linked by a single disulfide bond at the C-terminus of the H-chain (Figure 3-1a). This H-L complex is also non-covalently linked to a glycoprotein (P25) of ~25 kDa in a ratio of 6:6:1 to form micellar units [40]. The H-chains are composed by hydrophobic domains containing highly ordered amino acid sequences repeats, capable of organizing themselves together into β-sheet or crystalline structures through intramolecular or intermolecular forces, including hydrogen bonding, van der Walls forces, and hydrophobic interactions, forming the basis for the tensile strength of SF (Figure 3-1b) [41, 42]. The L-chains are hydrophilic, smaller and less ordered than the H-chains, relatively elastic, and its sequence is not involved in the formation of the crystalline region in SF (amorphous region) (Figure 3-1c) [40]. The hydrophobic repetitive domains that compose a H-chain are also interspaced by hydrophilic regions (Figure 3-1a) [43]. These repeating units are known as Ala-Gly-Ser-Gly-Ala-Gly, where glycine (Gly, ~43–46%), alanine (Ala, ~25–30%), and serine (Ser, ~12%) are the three simplest and most abundant amino acids. The next most abundant amino acids in H-chain are tyrosine (~5%), the larger amino acid with a polar side chain (semi-crystalline), valine (~2%), followed by aspartic acid, phenylalanine, glutamic acid, threonine, isoleucine, leucine, proline, arginine, lysine, and histidine, present in much smaller percentages (less than 2%) [40, 44].

The complexity of SF can be demonstrated by their four different structures (silk I, silk II, silk III, and random coil), formed through different physicochemical stimuli, and that can be transformed to each other under proper conditions [45]. Silk I is formed alternatively by α-helix and β-sheet main conformations, while silk II is rich in β-sheet content and corresponds to the main structural configuration of SF providing high mechanical and physicochemical properties. Silk III is formed by a threefold α-helix crystal structure, and the random coil structure usually exists in the SF solution [44, 46]. By controlling the crystalline and amorphous domains of SF structures (size, number, distribution, orientation, and spatial arrangement), it is possible to produce SF-based matrices with distinct mechanical properties, degradation profile, and aqueous processability, which makes this protein attractive for distinct biomedical and TE applications [12].

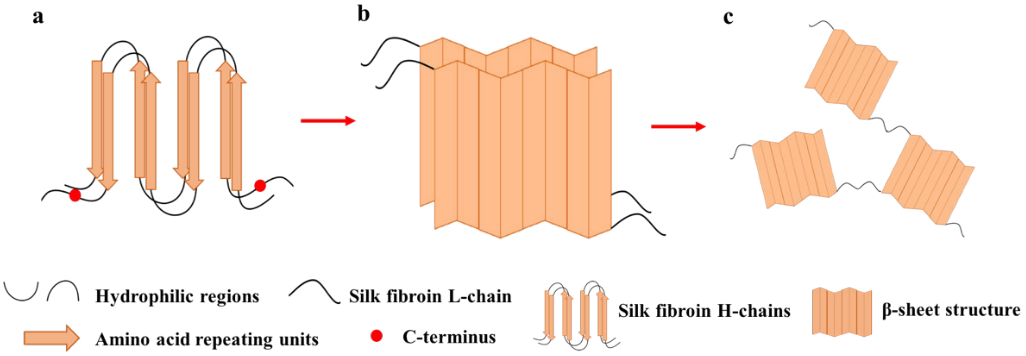

Figure 3-1. Schematic illustration of the natural SF protein composition. (a) H-L complex formation. (b) H-chains organizing themselves together into β-sheet structures. (c) β-sheet structures linked by amorphous domains.

3.4. Silk fibroin-based hydrogels

Hydrogels formation follows several distinctive requirements that mimic the natural ECM microenvironment of tissues [47]. The hydrophilic nature of the ECM is represented by the hydrophilic crosslinking of polymer-based hydrogels, formed by the reaction of one, or more monomers connected by hydrogen bonds or/and van der Waals interactions between the chains [48]. One of the most important advantages of hydrogel systems is their aqueous environment that not only protects cells, but can also be sensitive for drugs and biological agents incorporation, transport, and delivery at the injury site [47]. Moreover, they can present tailored mechanical properties, degradation profiles, and swelling abilities according to their final applications [24, 49]. Facing the traditional scaffolding strategies, hydrogel networks have also been proposed as injectable systems not only for TE strategies, but also for other clinical applications [50].

The naturally derived hydrogels have desirable biological properties as compared to synthetic hydrogels; however, they can present rapid degradation profiles for hard tissues regeneration, not to mention the chemical and molecular instability, which usually limits the reproducibility of natural-based materials [51]. Such limitations can be overcome through hydrogels formed from regenerated aqueous SF solutions, that when submitted to different physical and chemical treatments, including mechanical agitation, ultrasonication, thermal treatment, pH adjustments, organic solvents, crosslinking using ionic species (Ca^{2+} ions) or biological agents (enzymes), acquire a sol-gel transition (Figure 3-2) [24, 52-54].

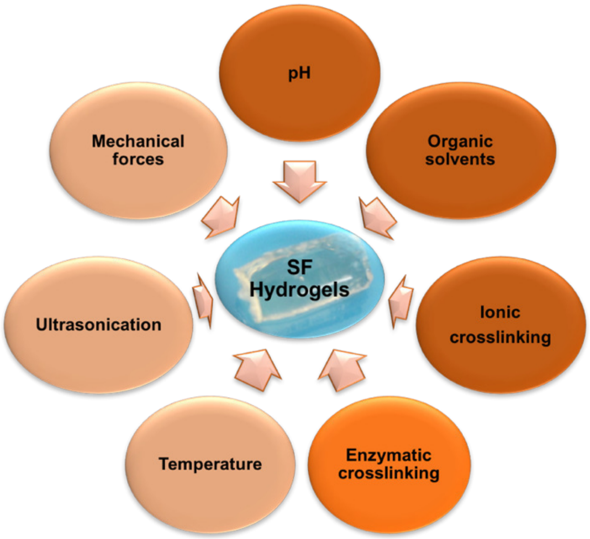

Figure 3-2. Schematic illustration of the physicochemical processes used to prepare SF hydrogels.

During the structural transition process, an interconnected network is formed in the aqueous solution either by the β-sheet aggregates formation (transition from random coil to β-sheet) [55] or by the crosslinking of fibroin molecules [56]. Yan *et al*. [50] proposed a horseradish peroxidase (HRP)-mediated crosslinking approach to produce novel SF hydrogels in a random coil conformation, that can undergo intrinsic conformational changes from amorphous to β-sheet (Figure 3-3). These hydrogels can be adjusted in terms of gelation time, mechanical properties, and degradation profile, only by changing the SF concentration and the crosslinker (HRP/H_2O_2) ratio. This will allow producing different hydrogel networks according to its final application. Moreover, the enzymatic crosslinking of SF was conducted at physiological conditions, envisioning their application as injectable systems for drug delivery purposes. In a recent study [57], the potential applications of SF-based hydrogels were magnified by the production of agarose-SF sponges, processed by freeze-drying agarose-SF blended hydrogels.

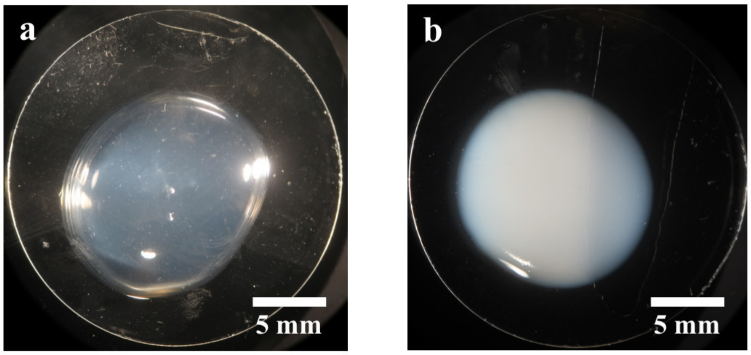

Figure 3-3. Macroscopic images of the horseradish peroxidase-mediated crosslinked SF hydrogels. (a) Analysis in a random coil conformation at day 1 and (b) after β-sheet conformational transition at day 14.

The traditional approach for TE and regenerative medicine involve the culture of cells, withdrawn from the host tissue, into a pre-established structural matrix and subsequent implantation into the defect site [1]. Structures designed to mimic the natural ECM microenvironment of the replacing tissues usually involve the engineering of matrices at several levels, depending on the physical, chemical, and biological properties of the host tissue, and SF has been proven to be a suitable material to engineer different tissues [4, 12, 58]. Combining polymeric scaffolds for osteogenesis induction with a cartilaginous-like hydrogel matrix has been one of the most studied strategies for OC tissue engineering [37, 59]. Furthermore, the mechanical strength and high biocompatibility of SF make this material a rational choice as injectable fillers or as scaffolds for bone TE purposes [60, 61]. Fini *et al*. [60] have tested the *in vitro* behavior of injectable SF hydrogels, through osteoblast culture, and after *in vivo* implantation into critical-sized defects of rabbit distal femurs. The proposed SF hydrogels were obtained by adding citric acid into aqueous SF solution, and a commercial synthetic poly(D,L lactide-glycolide) (PLGA) copolymer was used as control material [62]. *In vitro* tests showed a significant increase of cell proliferation in the SF hydrogels and a higher bone remodeling capability was observed after *in vivo* implantation into the femoral defects, as compared to the synthetic PLGA control. Sonication-induced SF hydrogels were also proposed by Zhang *et al*. [63] as injectable bone replacement biomaterials (Figure 3-4). These hydrogels were combined with the osteogenic-related growth factors, vascular endothelial growth factor (VEGF), and bone morphogenic protein-2 (BMP-2), and evaluated as vehicles for the encapsulation and release of biological agents. The dual factors were slowly released from the injectable SF hydrogels promoting angiogenesis and new bone formation after *in vivo* implantation in rabbit maxillary sinus. The authors concluded that the proposed SF hydrogels can be used as injectable matrices in a minimally invasive approach to fill and regenerate bone tissue. Moreover, the possibility of being used as vehicles to deliver multiple growth factors was also a great achievement.

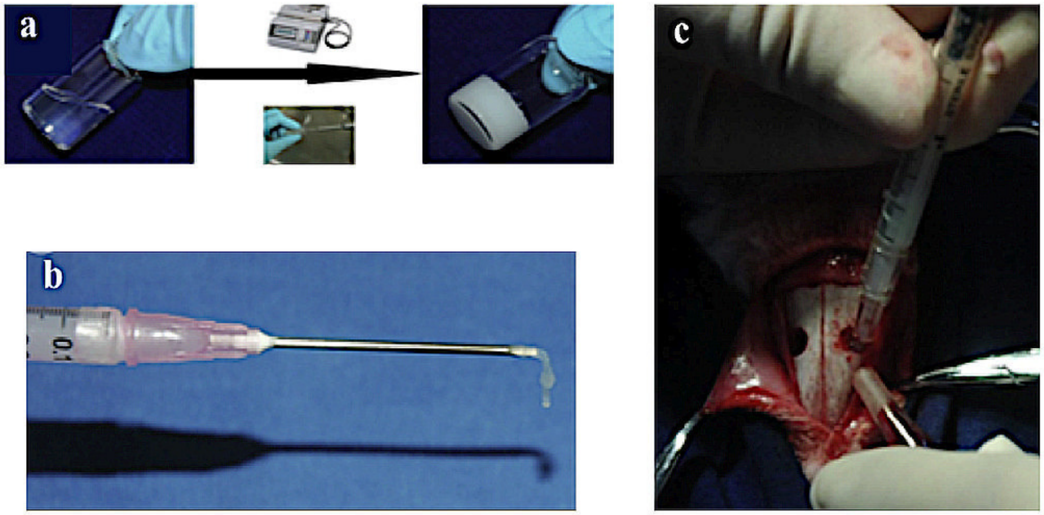

Figure 3-4. Photographs of the sonication-induced SF hydrogels and rabbit maxillary sinus surgery. (a) Aqueous SF solution transforming into SF hydrogels by ultrasonication. (b) Injectable property of the SF hydrogels. (c) SF hydrogel injection into the rabbit maxillary sinus cavity. Adapted with permission [63]. Copyright 2011, Elsevier.

Considering the high incidence of articular cartilage-related injuries [64], hydrogels are particularly desired matrices for cartilage TE, since these are water-swollen materials capable of retaining and absorbing large volumes of water and maintaining sufficient mechanical properties to support loading forces. Moreover, hydrogels have shown to be capable of encapsulating cells, biomolecules, and growth factors, for controlled drug delivery approaches after implantation in cartilage defects [65, 66]. SF-based hydrogels have also shown great potential for cartilage regeneration applications [67]. Sonication-induced SF hydrogels were proposed by Chao *et al.* [68] as an alternative approach to the commonly accepted agarose hydrogels [69] that yield the ability to sustain immature chondrocytes with biomechanical properties comparable to the native cartilage tissue. However, the non-degradability and lack of possibilities to modify the agarose's structure, composition, and mechanical properties increased the author's interest of using biocompatible, biodegradable, and highly tuned SF hydrogels to prepare cartilaginous constructs. These hydrogels presented a variety of structural and mechanical properties according to the SF extraction method, concentration, and gelation conditions. Moreover, the rapid encapsulation of chondrocytes and full maintenance of cell viability for 42 days with ECM formation (collagen and glycosaminoglycans) suggests that these hydrogels can be used as 3D models of cartilage tissue formation and maturation. In a different study, Park *et al.* [70] proposed novel sonication-induced SF composite hydrogels with fibrin/hyaluronic acid for nucleus pulposus cartilage formation. The authors demonstrated that the composite hydrogels allowed the chondrogenic differentiation in 5 different groups made of fibrin/hyaluronic acid and different SF concentrations. Importantly, the mechanical strength measurements also showed that SF induced a stronger mechanical support for cartilage tissue on composite hydrogels than fibrin/hyaluronic acid hydrogels alone. Yodmuang *et al.* [71] have proposed SF-based composites made by combining silk microfibers with SF hydrogels as a potential support material for cartilage TE. SF fiber-agarose hydrogel composite materials were used as control condition, showing that the 100% SF-based composites presented better and similar mechanical properties to those of native cartilage tissue (Figure 3-5). The SF fiber reinforcement significantly influenced the mechanical and biological properties of composite materials supporting chondrocytes maturation and cartilage matrix deposition. Once again, the versatility of SF as a composite material came to overcome the limitations presented by the "gold standard" agarose-based biomaterials. The same recognition was done by Singh *et al.* [57] that demonstrated higher levels of cartilaginous tissue formation (glycosaminoglycans and collagen matrix deposition) within micro-porous hydrogels of SF blended with agarose, as compared with the micro-porous hydrogels of agarose used as control.

Lately, bilayered hydrogels combining different polymeric materials [36, 72], or encapsulating growth factors and/or cell populations, have also shown promising results in OC tissue repair/regeneration [73-75]. SF biomaterials can be particularly attractive for these strategies due to the self-assembly properties and controlled processing of the β-sheet crystalline content, which enable to modulate the degradation rate and mechanical properties of SF structures according to the target OC tissue [76]. In a recent study, a 3D bio-printing method was used to create SF-Gelatin (SF-G) bioinks incorporated with human mesenchymal stem cells [77]. Enzymatic and physical crosslinking methods were applied after cell incorporation for post-printing stabilization, showing that both developed constructs supported multilineage differentiation and specific tissue formation according to the applied crosslinking method. These results provide a proof-of-concept for the fabrication of 3D heterogeneous tissue constructs using different crosslinking methods of SF-G hydrogels with different mechanical properties and biological effects, especially required for OC tissue regeneration. Moreover, the possibility of creating a printed construct for a target tissue in a patient-specific approach would be the answer for personalized OC therapy and regeneration.

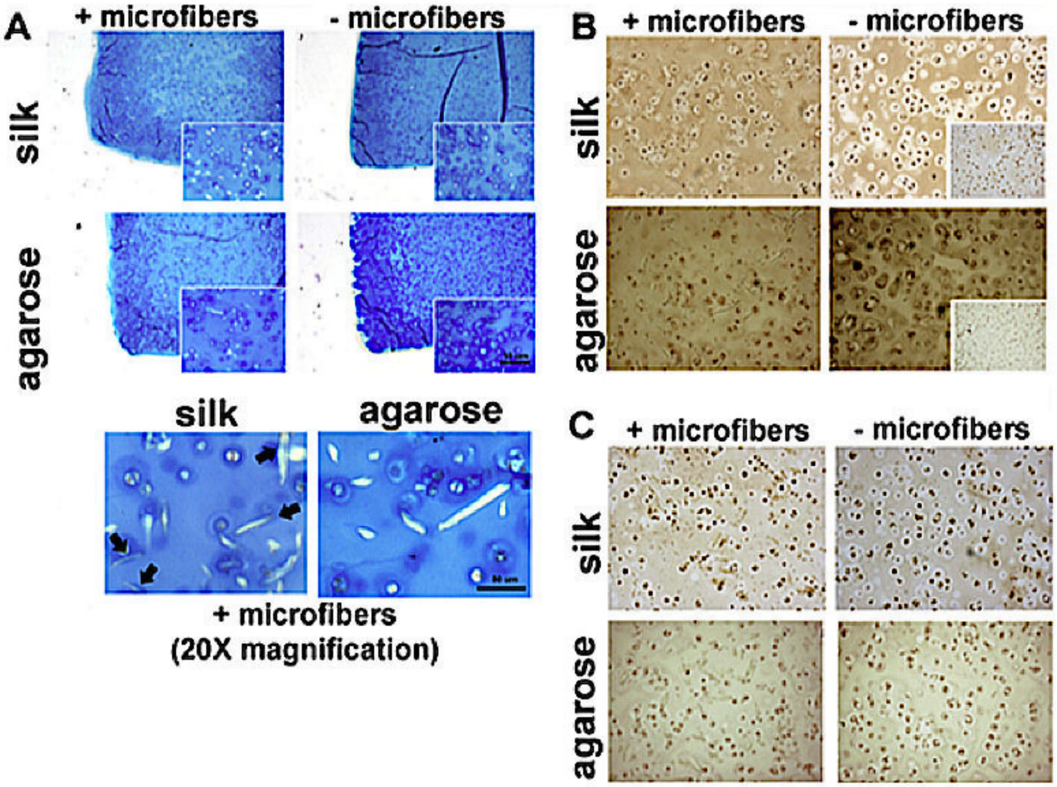

Figure 3-5. Histological analysis of the SF- and agarose-based hydrogels combined with silk microfibers. (A) Alcian blue staining used to visualize the glycosaminoglycans (GAGs) content within the hydrogels. The black arrows indicate the localization of GAGs surrounding the silk microfibers within the SF-based hydrogels. Immunohistochemical analysis of (B) type II collagen and (C) type I collagen content. The inset images represent the negative staining. Adapted with permission [71]. Copyright 2014, Elsevier.

3.5. Silk fibroin-based scaffolds

Scaffolds are 3D porous matrices developed to provide a defined microenvironment that promotes tissue repair and regeneration. Ideally, scaffolds should be able to: (i) stimulate cell-biomaterial interactions, cell attachment, growth, and migration, (ii) facilitate transport of mass, nutrients, and regulatory factors for cell survival, proliferation, and differentiation, (iii) afford structural mechanical support, as tensile strength and elasticity, (iv) degrade at a controlled rate, and (v) present minimal degree of inflammation or toxicity *in vivo* [78]. Further, scaffolds have desired characteristics for cell transfer into a defect site and to limit cell loss, instead of simple cells injection to the defects.

Layered scaffolds aiming bone and OC TE applications, where both underlying bone and cartilage tissues are damaged, are able to promote regeneration with specific properties and biological requirements [49,55-57]. The strategy is the fabrication of stratified scaffolds consisting of separate osteogenic and chondrogenic regions, which can be manufactured in a single integrated implant, or fabricated independently and joined together with sutures or sealants. It is pretended to ensure a good compatibility between the regions by keeping the porous structure and the mechanical strength. Porosity and pore sizes, respectively, of 50-90% and 300 µm are required for an improved osteogenesis, whereas a pore size between 90 and 120 µm is recommended for chondrogenesis [79]. Several technologies have been applied to produce scaffolds with organized porosity and pore size, namely foam replica, salt-leaching/solvent casting, freeze-drying, phase separation, gas foaming, rapid prototyping, supercritical fluid technology, additive manufacturing, photolithography, microfluidics, and electrospinning [14, 26, 31, 33, 80-86]. These techniques also allow envisioning the encapsulation of pharmaceutical agents/drugs and cells.

Considering the unique properties of SF for biomedical applications as abovementioned, the fabrication of useful scaffold SF-based systems, as well as constructs, has been extensively investigated with very positive results, to repair and regenerate the bone, cartilage, and OC tissues [26, 31, 39, 87, 88]. Saha *et al.* [39] evaluated the osteo-/chondro-inductive ability of acellular mulberry and non-mulberry SF scaffolds as an implantable platform in OC therapeutics. It was shown that SF scaffolds of *Antheraea mylitta* (non-mulberry) were more chondro-inductive, while those of *Bombyx mori* (mulberry) were more osteo-inductive in similar conditions. The *in vitro* culture in chondro- and osteo-inductive media, showed that non-mulberry constructs seeded with human bone marrow stromal cells, exhibited chondrocyte-like cells behavior up to 8 weeks of culture, whereas mulberry constructs seeded with human bone marrow stromal cells formed bone-like nodules. *In vivo* neomatrix formation on the scaffolds, absorbed with transforming growth factor β-3 or recombinant human BMP-2, was demonstrated after implantation for 8 weeks, in OC defects of the knee joints of Wistar rats. The neomatrix formed comprised collagen and glycosaminoglycans except in mulberry silk without growth factors, where a predominantly collagenous matrix was observed.

A different strategy was reported by Chen *et al.* [89] where they used SF sponge scaffolds seeded with rabbit bone marrow stromal cells (BMSC) aiming to engineer a multilayered OC construct. BMSC-seeded scaffolds were first cultured separately in osteogenic and chondrogenic stimulation media. Then, the differentiated pieces were combined with RADA self-assembling peptides and subsequently co-cultured. It was shown that after co-culture, the GAG production in the chondrogenic region was down-regulated compared with the chondrogenic control group, while the GAGs production in the osteogenic region was greater than from the osteogenic control group. Furthermore, in the intermediate region of co-cultured samples, hypertrophic chondrogenic gene markers collagen type X and MMP-13 were found on both chondrogenic and osteogenic sections. However, significant differences of gene expression profile were found in distinct zones of the constructs co-cultured, and the intermediate region had significantly higher hypertrophic chondrocyte gene expression. Moreover, results showed that specific stimulation from osteogenic and chondrogenic BMSCs affected both layers inducing the formation of an OC interface. Another interesting work investigated the capability of regenerated SF/natural degummed silk fiber composite scaffolds, combined with fibrin glue, with and without autologous chondrocytes for the repair of OC lesions [90, 91]. The scaffolds showed very good mechanical properties and porosity due to the incorporation of silk fibers into the SF. *In vivo* biocompatibility tests of the scaffolds after implantation in OC defects of rabbit knees demonstrated good healing, regular chondrocyte arrangement, great connection to native tissues, and complete degradation 36 weeks post-implantation.

In order to improve the rapid degradation and low mechanical strength of pure chondroitin sulfate (CS), Zou *et al*. [92] developed a scaffold combining SF with CS, using salt-leaching, freeze-drying, and crosslinking methodologies, for cartilage tissue repair. The scaffolds exhibited a porous and interconnected structure with pores sizes of approximately 100–300 μm (Figure 3-6I). *In vitro* biocompatibility tests using human articular chondrocytes (hACs) cultured on the scaffolds showed the formation of clusters inside the pores of SF scaffold, but better adhesion in SF/CS scaffold (Figure 3-6II). After 12 weeks post-implantation in a rabbit OC defect model, the defects in SF scaffolds were repaired with fibrocartilage tissue and cartilage-like tissue, generated a thinner layer compared to the surrounding normal cartilage tissue. The defects in SF/CS scaffolds were repaired by thicker cartilage-like tissue, and well-organized subchondral bone (Figure 3-6III). It was also observed that SF/CS scaffolds maintained better chondrocyte phenotype than SF scaffold, and silk-CS scaffolds reduced chondrocyte inflammatory response that was induced by interleukin (IL)-1β, consistent with the well-reported anti-inflammatory activities of CS.

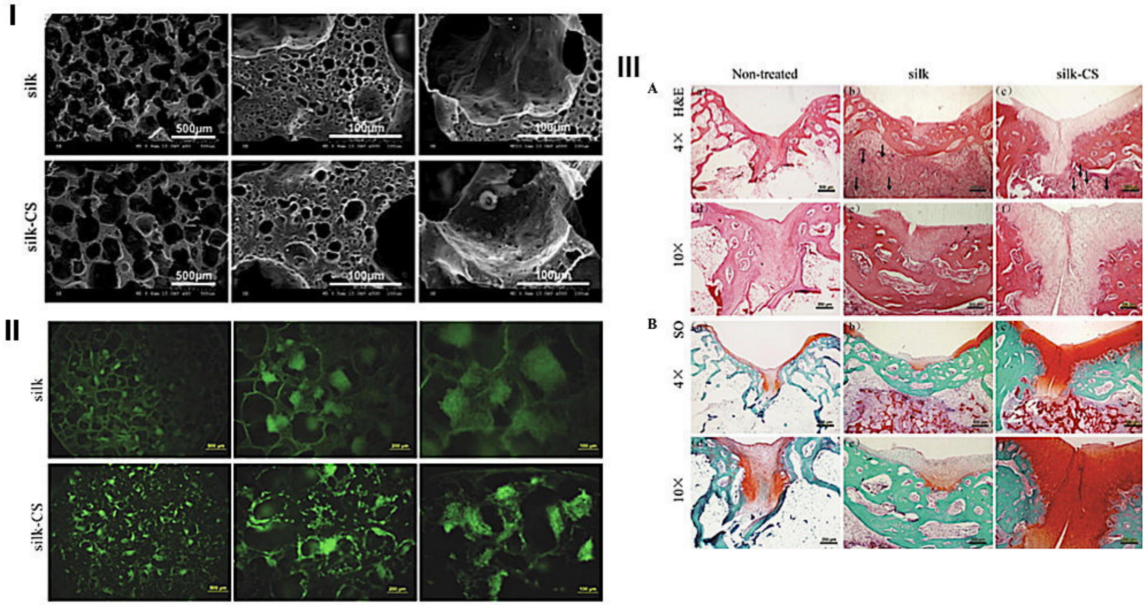

Figure 3-6. (I) Microstructure of SF and SF/CS scaffolds observed by scanning electron microscopy. **(II)** Cytocompatibility of SF and SF/CS scaffolds with hACs (scale bars: 500, 200, and 100 μm). **(III)** Histological evaluation after 12 weeks post-implantation: (A) Hematoxylin and eosin (H&E) histological images. (a, d) Non-treated group; (b, e) SF group; (c, f) SF/CS group. Arrows indicate rudimental scaffold materials. (B) Safranin-O staining of histological sections. (a, d) Non-treated group; (b, e) SF group; (c, f) SF/CS group. (Aa–c) and (Ba–c), scale bar: 500 mm. (Ad–f) and (Bd–f), scale bar: 200 mm. (A, B) Images of the bottom row represent the top row images at higher magnification. Adapted with permission [92]. Copyright 2017, Elsevier.

Alternative approaches for OC TE involve SF-based structures combined with other functional materials, as the case of calcium phosphates (CaPs), can significantly enhance its biofunctionalities, and hence improved advantages of the final composites [14, 31, 87]. Yan *et al*. [14] prepared bilayered scaffolds for OC defects regeneration, consisting of SF and SF/CaP, respectively, for cartilage and bone regions, using salt-leaching/freeze-drying techniques (Figure 3-7A). The scaffolds showed improved micro/macrostructure able to promote cell attachment and proliferation, as well as enhanced osteoconductivity and mechanical strength by the incorporation of calcium phosphate in SF. Also, good adhesion and proliferation of rabbit bone marrow mesenchymal stromal cells (RBMSCs) cultured on the scaffolds during 7 days were observed. The scaffolds were implanted subcutaneously and in critical sizes of OC defects in the rabbit knee for 4 weeks, showing a fully integration into the host tissue with no inflammation (Figure 3-7B). Moreover, the ingrowth of the subchondral bone in the bottom domain and the regeneration of cartilage in the surface area of the implant were observed. The quantitative results of CaP content and porosity of different regions showed much higher void space in the defect controls than in the defects with implant, with CaP content of 20% higher in SF/CaP layer than in the SF. From Figure 3-7C, it can be observed that the connective tissues were tightly integrated in the implants, and filled the inner pores of the scaffolds, with visible vessels formed inside the scaffolds, and some fibroblasts presented in the SF/CaP layer.

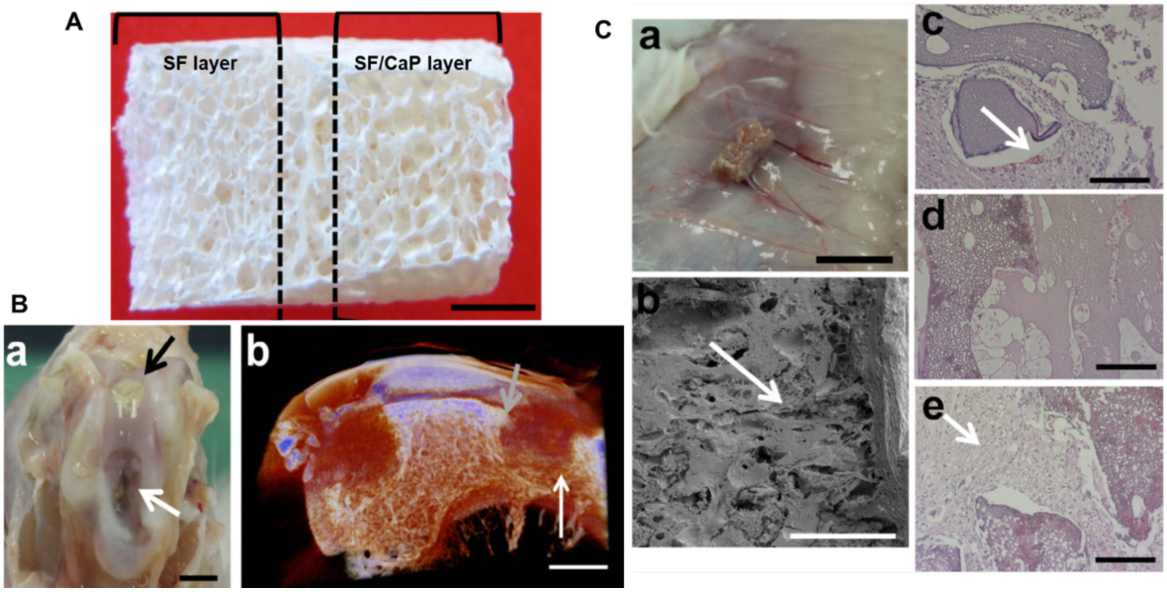

Figure 3-7. (A) Macroscopic image of the bilayered scaffolds (scale bar: 3 mm). (B) Images of the bilayered explants after implantation in rabbit OC defects: (a) Macroscopic image of the explants, the black arrow indicates the implanted scaffold and the white arrow indicates the defect control (scale bar: 5 mm); (b) micro-CT analysis of the explants, the grey arrow indicates neocartilage, and the white arrow indicates new subchondral bone formation (scale bar: 4 mm). (C) Images of the bilayered explants after subcutaneous implantation in rabbit: (a) Macroscopic image of the explants (scale bar: 1 cm); (b) SEM image of the explants (scale bar: 1 mm), the arrow indicates the interface; (c-e) H&E staining of the SF layer, interface, and SF/CaP layer in the explants, respectively (scale bar: 200 μm). The arrow in (c) indicates vessels, and the arrow in (e) indicates fibroblasts. Adapted with permission [14]. Copyright 2014, Elsevier.

Recently, in a work developed by our group, biofunctional scaffolds composed of SF and β-tricalcium phosphate, incorporating different ions, reported enhanced mechanical properties, improved cell proliferation, and higher osteogenic potential, which can also be used to engineer the bone layer in OC applications [93]. The scaffolds showed macropores highly interconnected with a size around 500 μm, and micro-porous structure pores with a size range of 1- 10 μm (Figure 3-8A). The biomineralized SF scaffolds, after immersion in SBF for 15 days, showed globule-like structures of apatite crystals, while the incorporation of ceramic powders into SF leads to the formation of porous spherulites-like structures (Figure 3-8B). Interestingly, *in vitro* assays using hASCs presented different responses on cell proliferation/differentiation when varying the ionic agents in the biofunctional scaffolds (Figure 3-8C). The incorporation of Zn into the scaffolds led to improved proliferation, while the Sr- and Mn-doped scaffolds presented higher osteogenic potential as demonstrated by DNA quantification and ALP activity. The combination of Sr with Zn led to an influence on cell proliferation and osteogenesis when compared with single ions.

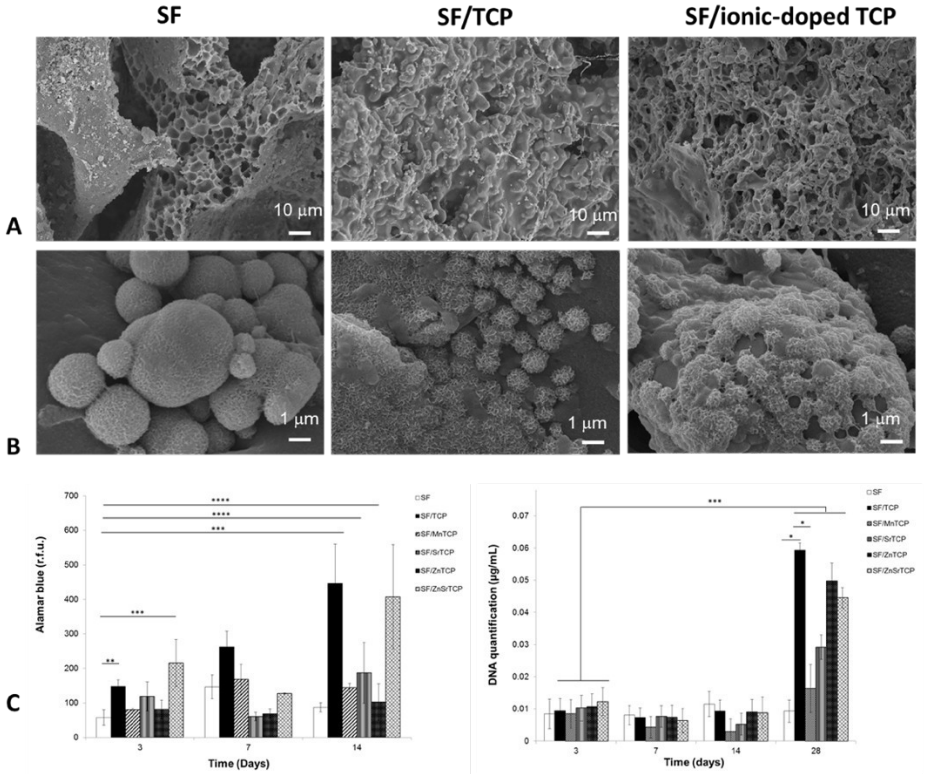

Figure 3-8. Scanning electron micrographs of SF, SF/TCP, and SF/ionic-doped TCP scaffolds. (A) Before and (B) after 15 days of mineralization. (C) Viability and proliferation of hASCs seeded in the scaffolds: Alamar blue assay of hASCs cultured for 14 days (left), and DNA quantification at different time points (right). *significant differences compared with SF and SF/MnTCP and with SF/MnTCP and SF/SrTCP ($p<0.05$), **significant differences compared between SF and SF/TCP ($p<0.005$), ***significant differences compared between SF at day 3 and the different compositions at day 28 ($p<0.0005$), ****significant differences compared between with SF and SF/SrTCP and SF/ZnTCP ($p < 0.0001$). Adapted with permission [93]. Copyright 2017, S. Karger AG, Basel.

As mentioned earlier, biomimetic OC multilayered systems, with specific microstructures and properties, have the potential clinical benefit in promoting bone and cartilage tissue repair and replacement. Taking an OC approach, Çakmak *et al*. [94] designed a SF-based trilayered scaffold suitable for both bone and cartilage, fabricated by salt-leaching process. For this purpose, the bone side was prepared with 4% (w/v) SF plus 5% (w/w) hydroxyapatite, the interface was obtained from 4% (w/v) SF, and for the cartilage layer were used arginine-glycine-aspartic acid-serine (RGDS)-containing peptide amphiphile hydrogels. The final mean pore size obtained for bone and OC interface layers was, respectively, 416 ± 87 μm and 194 ± 67 μm. Osteogenic and chondrogenic activity were evaluated by hBMSCs cultured in the SF scaffold in osteogenic media, while hACs were encapsulated and cultured inside the PA-RGDs in chondrogenic media, without using selective growth factors. After 2 weeks of growing separately, the bone and cartilage layers were combined with the interface layer by the soft silk scaffolds, followed by co-cultured in an OC cocktail medium. Results showed that the presence of hACs in the co-cultures significantly increases the osteogenic differentiation of hBMSCs, whereas hACs produces a significant amount of glycosaminoglycans (GAGs) for the cartilage region. Moreover, the effect of hBMSCs on chondrogenic differentiation of hACs was less effective than that of hACs on hBMSCs, and the hACs in the co-culture preserved the amount of synthesized chondrogenic ECM. Ding *et al*. [38] developed a trilayered scaffold combining SF/hydroxyapatite and paraffin-sphere leaching with a modified temperature gradient-guided thermal-induced phase separation (TIPS) technique. The bone layer and interface are constituted respectively by a porous and dense structure (Figure 3-9). Live/dead tests indicated good biocompatibility for supporting the growth, proliferation, and infiltration of adipose-derived stem cells (ASCs) in the scaffolds. Histological and immunohistochemical stainings confirmed that the ASCs could be induced to differentiate towards chondrocytes or osteoblasts *in vitro* at chondral and bony layers in the presence of chondrogenic or osteogenic culture medium, respectively. Moreover, the intermediate layer could play an isolating role for preventing the cells within the chondral and bone layers from mixing with each other.

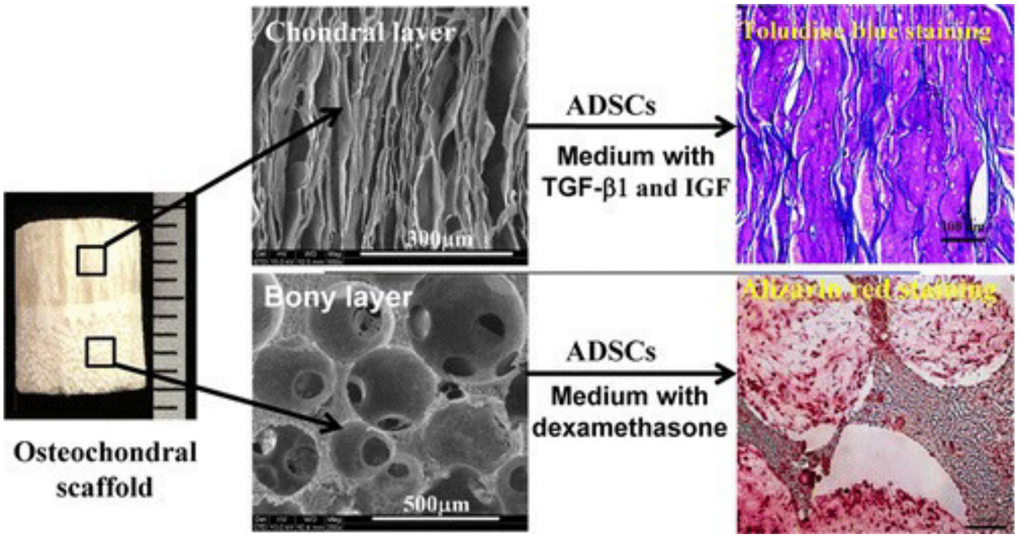

Figure 3-9. Macroscopic image of the OC scaffold showing the microstructure of bone and chondral layers. Adapted with permission [38]. Copyright 2014, American Chemical Society.

3.6. Concluding remarks and research efforts

Many progresses have been made over the past few decades in order to fully treat and replace the damaged or non-functional OC tissues. TE is an essential approach for that, which can combine different biomaterials, bioactive molecules, and cells. Repairing OC lesions remains a formidable challenge due to the high complexity of native OC tissue, and the limited self-repair capability of cartilage. Innovative strategies, such as the ones aforementioned, present solutions for specific OC challenges, and take important roles in cell proliferation and differentiation, envisioning the formation of new tissues. Such approaches will provide the production of hybrid constructs that act as bioresorbable temporary implants and resemble the physical characteristics of the ECM. Hydrogels are defined as possessing high water content and viscoelastic nature. On the other hand, scaffolds have mechanical strength necessary to temporarily offer structural support until new tissue ingrowth.

Among all the natural biopolymers presently available, SF has shown remarkable potential for biomedical applications due to its favorable structural and mechanical properties, as well good biocompatibility, biodegradability, and thermal stability. The design of 3D structures involving SF results in biomaterials with structural integrity for self-healing and load-bearing for future applications in OC TE. Furthermore, multiphasic structures, with distinct subchondral bone and cartilage regions and well-integrated interface, can overcome the common problems experienced with monolayered scaffolds, and be an effective approach for the effective regeneration of OC tissue.

3.7. References

[1] R.M. Nerem, A. Sambanis, Tissue engineering: from biology to biological substitutes, Tissue engineering 1(1) (1995) 3-13.

[2] R. Langer, et al., Tissue engineering: biomedical applications, Tissue engineering 1(2) (1995) 151-161.

[3] J.A. Hubbell, Biomaterials in tissue engineering, Nature Biotechnology 13(6) (1995) 565-576.

[4] P.X. Ma, Biomimetic materials for tissue engineering, Advanced drug delivery reviews 60(2) (2008) 184-198.

[5] M.E. Furth, et al., Smart biomaterials design for tissue engineering and regenerative medicine, Biomaterials 28(34) (2007) 5068-5073.

[6] H. Shin, et al., Biomimetic materials for tissue engineering, Biomaterials 24(24) (2003) 4353-4364.

[7] B. Seal, et al., Polymeric biomaterials for tissue and organ regeneration, Materials Science and Engineering: R: Reports 34(4) (2001) 147-230.

[8] M. Lutolf, J. Hubbell, Synthetic biomaterials as instructive extracellular microenvironments for morphogenesis in tissue engineering, Nature biotechnology 23(1) (2005) 47-55.

[9] L.S. Nair, C.T. Laurencin, Polymers as biomaterials for tissue engineering and controlled drug delivery, Tissue engineering I, Springer2005, pp. 47-90.

[10] L.S. Nair, C.T. Laurencin, Biodegradable polymers as biomaterials, Progress in polymer science 32(8) (2007) 762-798.

[11] P.B. Malafaya, et al., Natural–origin polymers as carriers and scaffolds for biomolecules and cell delivery in tissue engineering applications, Advanced drug delivery reviews 59(4) (2007) 207-233.

[12] B. Kundu, et al., Silk fibroin biomaterials for tissue regenerations, Advanced Drug Delivery Reviews 65(4) (2013) 457-470.

[13] M. Mondal, The silk proteins, sericin and fibroin in silkworm, Bombyx mori Linn. - a review, Caspian Journal of Environmental Sciences 5(2) (2007) 63-76.

[14] L.-P. Yan, et al., Bilayered silk/silk-nanoCaP scaffolds for osteochondral tissue engineering: In vitro and in vivo assessment of biological performance, Acta Biomaterialia 12 (2015) 227-241.

[15] V.P. Ribeiro, et al., Silk-based anisotropical 3D biotextiles for bone regeneration, Biomaterials 123 (2017) 92-106.

[16] T.V. Chirila, et al., Bombyx mori silk fibroin membranes as potential substrata for epithelial constructs used in the management of ocular surface disorders, Tissue Engineering Part A 14(7) (2008) 1203-1211.

[17] Z.-X. Cai, et al., Fabrication of chitosan/silk fibroin composite nanofibers for wound-dressing applications,

International journal of molecular sciences 11(9) (2010) 3529-3539.

[18] B. Kundu, S.C. Kundu, Silk sericin/polyacrylamide in situ forming hydrogels for dermal reconstruction, Biomaterials 33(30) (2012) 7456-7467.

[19] B.B. Mandal, et al., Non-mulberry silk sericin/poly (vinyl alcohol) hydrogel matrices for potential biotechnological applications, International journal of biological macromolecules 49(2) (2011) 125-133.

[20] Y.-Q. Zhang, Applications of natural silk protein sericin in biomaterials, Biotechnology advances 20(2) (2002) 91-100.

[21] J. Sirichaisit, et al., Molecular deformation in spider dragline silk subjected to stress, Polymer 41(3) (2000) 1223-1227.

[22] V.P. Ribeiro, et al., Influence of different surface modification treatments on silk biotextiles for tissue engineering applications, Journal of Biomedical Materials Research Part B: Applied Biomaterials (2015).

[23] W. Luangbudnark, et al., Properties and biocompatibility of chitosan and silk fibroin blend films for application in skin tissue engineering, The Scientific World Journal 2012 (2012).

[24] L.P. Yan, et al., Core-shell silk hydrogels with spatially tuned conformations as drug-delivery system, Journal of tissue engineering and regenerative medicine (2016).

[25] S. Sahoo, et al., A bFGF-releasing silk/PLGA-based biohybrid scaffold for ligament/tendon tissue engineering using mesenchymal progenitor cells, Biomaterials 31(11) (2010) 2990-2998.

[26] L.-P. Yan, et al., Macro/microporous silk fibroin scaffolds with potential for articular cartilage and meniscus tissue engineering applications, Acta biomaterialia 8(1) (2012) 289-301.

[27] S.P. Nukavarapu, D.L. Dorcemus, Osteochondral tissue engineering: current strategies and challenges, Biotechnology advances 31(5) (2013) 706-721.

[28] C.G. Jeong, et al., Three-dimensional polycaprolactone scaffold-conjugated bone morphogenetic protein-2 promotes cartilage regeneration from primary chondrocytes in vitro and in vivo without accelerated endochondral ossification, Journal of Biomedical Materials Research Part A 100(8) (2012) 2088-2096.

[29] J. Malda, et al., The effect of PEGT/PBT scaffold architecture on the composition of tissue engineered cartilage, Biomaterials 26(1) (2005) 63-72.

[30] J. Zhou, et al., In vitro generation of osteochondral differentiation of human marrow mesenchymal stem cells in novel collagen–hydroxyapatite layered scaffolds, Acta Biomaterialia 7(11) (2011) 3999- 4006.

[31] L.-P. Yan, et al., De novo bone formation on macro/microporous silk and silk/nano-sized calcium phosphate scaffolds, Journal of Bioactive and Compatible Polymers 28(5) (2013) 439-452.

[32] H. Tan, et al., Injectable in situ forming biodegradable chitosan–hyaluronic acid based hydrogels for cartilage tissue engineering, Biomaterials 30(13) (2009) 2499-2506.

[33] J.M. Oliveira, et al., Novel hydroxyapatite/chitosan bilayered scaffold for osteochondral tissue-engineering applications: Scaffold design and its performance when seeded with goat bone marrow stromal cells, Biomaterials 27(36) (2006) 6123-6137.

[34] J. Chen, et al., Simultaneous regeneration of articular cartilage and subchondral bone in vivo using MSCs induced by a spatially controlled gene delivery system in bilayered integrated scaffolds, Biomaterials 32(21) (2011) 4793-4805.

[35] J.E. Jeon, et al., Perspectives in Multiphasic Osteochondral Tissue Engineering, The Anatomical Record 297(1) (2014) 26-35.

[36] D.R. Pereira, et al., Gellan gum-based hydrogel bilayered scaffolds for osteochondral tissue engineering, Key Engineering Materials, Trans Tech Publ, 2014, pp. 255-260.

[37] M.T. Rodrigues, et al., Bilayered constructs aimed at osteochondral strategies: the influence of medium supplements in the osteogenic and chondrogenic differentiation of amniotic fluid-derived stem cells, Acta biomaterialia 8(7) (2012) 2795-2806.

[38] X. Ding, et al., Integrated Trilayered Silk Fibroin Scaffold for Osteochondral Differentiation of Adipose-Derived Stem Cells, ACS Applied Materials & Interfaces 6(19) (2014) 16696-16705.

[39] S. Saha, et al., Osteochondral Tissue Engineering In Vivo: A Comparative Study Using Layered Silk Fibroin Scaffolds from Mulberry and Nonmulberry Silkworms, PLOS ONE 8(11) (2013) e80004.

[40] L.-D. Koh, et al., Structures, mechanical properties and applications of silk fibroin materials, Progress in Polymer Science 46 (2015) 86-110.

[41] A.H. Simmons, et al., Molecular orientation and two-component nature of the crystalline fraction of spider dragline silk, Science 271(5245) (1996) 84.

[42] Q. Zhang, et al., Silk fibroin based porous materials, Materials 2(4) (2009) 2276-2295.

[43] M. McGill, et al., Molecular and macro-scale analysis of enzyme-crosslinked silk hydrogels for rational biomaterial design, Acta Biomaterialia 63 (2017) 76-84.

[44] Y. Hu, et al., The relationship between secondary structure and biodegradation behavior of silk fibroin scaffolds, Advances in Materials Science and Engineering 2012 (2012).

[45] D. Wilson, et al., Conformational transitions in model silk peptides, Biophysical journal 78(5) (2000) 2690-2701.

[46] R. Valluzzi, et al., Trigonal crystal structure of Bombyx mori silk incorporating a threefold helical chain

conformation found at the air– water interface, Macromolecules 29(27) (1996) 8606-8614.

[47] H. Geckil, et al., Engineering hydrogels as extracellular matrix mimics, Nanomedicine 5(3) (2010) 469-484.

[48] V. Guarino, et al., Hydrogel-based platforms for the regeneration of osteochondral tissue and intervertebral disc, Polymers 4(3) (2012) 1590-1612.

[49] O. Jeon, et al., Photocrosslinked alginate hydrogels with tunable biodegradation rates and mechanical properties, Biomaterials 30(14) (2009) 2724-2734.

[50] L.-P. Yan, et al., Tumor growth suppression induced by biomimetic silk fibroin hydrogels, Scientific Reports 6 (2016).

[51] S. Huang, X. Fu, Naturally derived materials-based cell and drug delivery systems in skin regeneration, Journal of Controlled Release 142(2) (2010) 149-159.

[52] X. Chen, et al., pH sensitivity and ion sensitivity of hydrogels based on complex-forming chitosan/silk fibroin interpenetrating polymer network, Journal of Applied Polymer Science 65(11) (1997) 2257-2262.

[53] N. Guziewicz, et al., Lyophilized silk fibroin hydrogels for the sustained local delivery of therapeutic monoclonal antibodies, Biomaterials 32(10) (2011) 2642-2650.

[54] T. Yucel, et al., Vortex-induced injectable silk fibroin hydrogels, Biophysical journal 97(7) (2009) 2044-2050.

[55] U.-J. Kim, et al., Structure and properties of silk hydrogels, Biomacromolecules 5(3) (2004) 786-792.

[56] L.S.M. Teixeira, et al., Enzyme-catalyzed crosslinkable hydrogels: emerging strategies for tissue engineering, Biomaterials 33(5) (2012) 1281-1290.

[57] Y.P. Singh, et al., Potential of Agarose/Silk Fibroin Blended Hydrogel for in Vitro Cartilage Tissue Engineering, ACS Applied Materials & Interfaces 8(33) (2016) 21236-21249.

[58] N. Kasoju, U. Bora, Silk fibroin in tissue engineering, Advanced healthcare materials 1(4) (2012) 393-412.

[59] W. Zhang, et al., Cartilage repair and subchondral bone migration using 3D printing osteochondral composites: a one-year-period study in rabbit trochlea, BioMed research international 2014 (2014).

[60] M. Fini, et al., The healing of confined critical size cancellous defects in the presence of silk fibroin hydrogel, Biomaterials 26(17) (2005) 3527-3536.

[61] H.J. Kim, et al., Bone tissue engineering with premineralized silk scaffolds, Bone 42(6) (2008) 1226-1234.

[62] P. Gentile, et al., An overview of poly (lactic-co-glycolic) acid (PLGA)-based biomaterials for bone tissue engineering, International journal of molecular sciences 15(3) (2014) 3640-3659.

[63] W. Zhang, et al., The use of injectable sonication-induced silk hydrogel for VEGF 165 and BMP-2 delivery for elevation of the maxillary sinus floor, Biomaterials 32(35) (2011) 9415-9424.

[64] E.S. Tetteh, et al., The basic science and surgical treatment options for articular cartilage injuries of the knee, journal of orthopaedic & sports physical therapy 42(3) (2012) 243-253.

[65] V. Ribeiro, et al., Fundamentals on Osteochondral Tissue Engineering, Regenerative Strategies for the Treatment of Knee Joint Disabilities, Springer2017, pp. 129-146.

[66] P. Weiss, et al., Hydrogels for cartilage tissue engineering, Biomedical Applications of Hydrogels Handbook, Springer2010, pp. 247-268.

[67] M. Floren, et al., Processing Techniques and Applications of Silk Hydrogels in Bioengineering, Journal of Functional Biomaterials 7(3) (2016) 26.

[68] P.H.G. Chao, et al., Silk hydrogel for cartilage tissue engineering, Journal of Biomedical Materials Research Part B: Applied Biomaterials 95(1) (2010) 84-90.

[69] R.L. Mauck, et al., Functional tissue engineering of articular cartilage through dynamic loading of chondrocyte-seeded agarose gels, Journal of biomechanical engineering 122(3) (2000) 252-260.

[70] S.-H. Park, et al., Silk-fibrin/hyaluronic acid composite gels for nucleus pulposus tissue regeneration, Tissue Engineering Part A 17(23-24) (2011) 2999-3009.

[71] S. Yodmuang, et al., Silk microfiber-reinforced silk hydrogel composites for functional cartilage tissue repair, Acta biomaterialia 11 (2015) 27-36.

[72] T.A. Holland, et al., Osteochondral repair in the rabbit model utilizing bilayered, degradable oligo (poly (ethylene glycol) fumarate) hydrogel scaffolds, Journal of biomedical materials research Part A 75(1) (2005) 156-167.

[73] X. Guo, et al., In vitro generation of an osteochondral construct using injectable hydrogel composites encapsulating rabbit marrow mesenchymal stem cells, Biomaterials 30(14) (2009) 2741- 2752.

[74] K. Kim, et al., Osteochondral tissue regeneration using a bilayered composite hydrogel with modulating dual growth factor release kinetics in a rabbit model, Journal of Controlled Release 168(2) (2013) 166-178.

[75] S. Lu, et al., Dual growth factor delivery from bilayered, biodegradable hydrogel composites for spatially-guided osteochondral tissue repair, Biomaterials 35(31) (2014) 8829-8839.

[76] W.L. Grayson, et al., Engineering custom-designed osteochondral tissue grafts, Trends in biotechnology 26(4) (2008) 181-189.

[77] S. Das, et al., Bioprintable, cell-laden silk fibroin–gelatin hydrogel supporting multilineage differentiation

of stem cells for fabrication of three-dimensional tissue constructs, Acta biomaterialia 11 (2015) 233-246.

[78] L. Thorrez, et al., Growth, differentiation, transplantation and survival of human skeletal myofibers on biodegradable scaffolds, Biomaterials 29(1) (2008) 75-84.

[79] V. Karageorgiou, D. Kaplan, Porosity of 3D biomaterial scaffolds and osteogenesis, Biomaterials 26 (2005) 5474-5491.

[80] P. vandeWitte, et al., Phase separation processes in polymer solutions in relation to membrane formation, J Memb Sci 117 (1996) 1-31.

[81] A. Marrella, et al., Rapid Prototyping for the Engineering of Osteochondral Tissues, in: J.M. Oliveira, R.L. Reis (Eds.), Regenerative Strategies for the Treatment of Knee Joint Disabilities, Springer International Publishing, Cham, 2017, pp. 163-185.

[82] A.L. Oliveira, et al., Controlled mineralization of nature-inspired silk fibroin/hydroxyapatite hybrid bioactive scafolds for bone tissue engineering applications, 20th European Conference on Biomaterials, Nantes, France, 2006.

[83] O. Abdelaal, S. Darwish, Fabrication of tissue engineering scaffolds using rapid prototyping techniques, World Academy of Science, Engineering and Technology 59 (2011) 577-85.

[84] T. Chae, et al., Novel biomimetic hydroxyapatite/alginate nanocomposite fibrous scaffolds for bone tissue regeneration, J Mater Sci Mater Med 24 (2013) 1885-94.

[85] L. Cui, et al., A novel nano/micro-fibrous scaffold by melt-spinning method for bone tissue engineering, Journal of Bionic Engineering 12(1) (2015) 117-128.

[86] S. Cardea, et al., Supercritical fluid assisted process for the generation of cellulose acetate loaded structures, potentially useful for tissue engineering applications, Materials Science and Engineering: C 59 (2016) 480-487.

[87] L. Yan, et al., Silk Fibroin/Nano-CaP Bilayered scaffolds for Osteochondral Tissue Engineering, Key Eng Mater 587 (2014) 245.

[88] L.P. Yan, et al., In vitro evaluation of the biological performance of macro/micro-porous silk fibroin and silk-nano calcium phosphate scaffolds, Journal of Biomedical Materials Research Part B: Applied Biomaterials 103(4) (2015) 888-898.

[89] K. Chen, et al., In vitro generation of a multilayered osteochondral construct with an osteochondral interface using rabbit bone marrow stromal cells and a silk peptide-based scaffold, Journal of Tissue Engineering and Regenerative Medicine 10(4) (2016) 284-293.

[90] S. Kazemnejad, et al., Comparative repair capacity of knee osteochondral defects using regenerated silk fiber scaffolds and fibrin glue with/without autologous chondrocytes during 36 weeks in rabbit model, Cell and Tissue Research 364(3) (2016) 559-572.

[91] S. Mobini, et al., Fabrication and characterization of regenerated silk scaffolds reinforced with natural silk fibers for bone tissue engineering, Journal of Biomedical Materials Research Part A 101A(8) (2013) 2392-2404.

[92] F. Zhou, et al., Silk fibroin-chondroitin sulfate scaffold with immuno-inhibition property for articular cartilage repair, Acta Biomaterialia 63(Supplement C) (2017) 64-75.

[93] S. Pina, et al., Biofunctional Ionic-Doped Calcium Phosphates: Silk Fibroin Composites for Bone Tissue Engineering Scaffolding, Cells Tissues Organs 204(3-4) (2017) 150-163.

[94] S. Çakmak, et al., A Silk Fibroin and Peptide Amphiphile-Based Co-Culture Model for Osteochondral Tissue Engineering, Macromolecular Bioscience 16(8) (2016) 1212-1226.

SECTION II

EXPERIMENTAL SECTION

CHAPTER 4.

Materials and Methods

CHAPTER 4.

Materials and Methods

This chapter intends to provide a detailed overview on the experimental procedures behind the results presented in Sections III and IV. Moreover, some considerations will be made regarding the selection of the materials, the scaffolds and hydrogels processing methodologies, and the physicochemical and biological characterization techniques used to sustain the proposed methodologies. With this, it is expected to present a clearer perspective of the developed work in this thesis and how it can be correlated.

4.1. Materials

4.1.1. Silk fibroin (SF)

Silk proteins are present in the glands of silk producing arthropods, including silkworms, before spinning in the form of fibers [1]. The silk studied in this thesis was derived from domesticated mulberry *Bombyx mori* silkworm, which is the most famous member of the family *Bombycidae* (Figure 4-1a). The non-mulbery silkworms are from Indian origin and belong to the family *Saturniidae* [2]. Depending on the silkworm sources, different processing methodologies are used for silk purification. In the case of the *Bombyx mori* silk this process is routinely established, involving a simple alkali- or enzyme-mediated degumming procedure to extract sericin from the cocoons and obtain SF at 70% off the original cocoon mass (excluding the worm weight) (Figure 4-1b) [3, 4]. In contrast, the SF produced from silkworms belonging to the family *Saturniidae* can only be efficiently obtained directly from the silkworm glands [5].

Sericin (20-310 kDa) is a gum-like protein produced with silk, currently suggested as an inducer of *in vivo* inflammatory response in its native state [6], justifying the need for extracting this protein from the cocoons before processing SF for biomedical applications. Nevertheless, recent studies employing isolated silk sericin-based biomaterials have shown no clear evidences that suggest sericin as the source of these effects [7].

The SF from *Bombyx mori* is composed of heavy (H) and light (L) chains, distinguished by the hydrophobic domains of the H-chains interspaced by hydrophilic regions at the L-chains. The hydrophobic domains contain highly ordered Glycine-X (X being Alanine, Serine, tyrosine, valine) repeats that form stacked anti-parallel β-sheets (silk II) of crystalline structure. The hydrophilic regions constitute the amorphous phase of the protein.

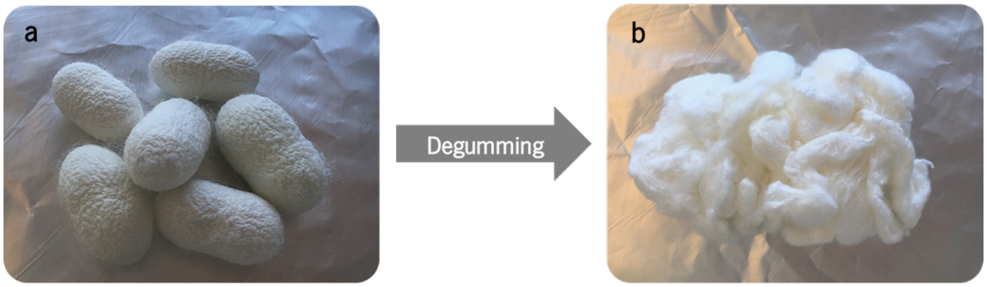

Bombyx mori cocoons

Silk fibroin

Figure 4-1. Silk cocoons purification process. (a) *Bombyx mori* silk cocoons. (b) Purified SF after sericin extraction through degumming procedure.

The degummed SF fibers can be directly used as sutures [8], or processed to form biomaterials for tissue engineering (TE) applications, including membranes [9], films [10], scaffolds [11], hydrogels [12] or even textiles [13]. For that, the SF raw material can be dissolved in order to form regenerated SF solutions, using the organic solvent hexafluoroisopropanol (HFIP), concentrated lithium bromide solution [14], ionic liquids [15], lithium thiocyanate [16], a calcium chloride/ethanol/water ternary solvent (in a 1:2:8 molar ratio) [17], or a calcium nitrate-methanol system [18]. The constructs produced from these solutions, would naturally acquire β-sheet conformation [19]. However, this process can be temporarily controlled using different chemical and physical methods, including the addition of sodium chloride [20], immersion in alcohol solutions [21], organic solvents, temperature and pH variations [22], ultrasonication [23], or vortex induction [12]. The presence of β-sheet crystalline structure in SF has shown to significantly improve the mechanical properties, water insolubility and degradability of the SF-based structures [21]. However, SF hydrogels and membranes prepared in an amorphous state, also showed good specificities for soft tissues clinical application [24]. Thus, SF has been exploited with different biomedical purposes, as a result of its processing versatility and extensive knowledge on how to control its properties, including mechanical strength, elasticity, biocompatibility, and controlled biodegradability [8]. Therefore, in this thesis, *Bombyx mori* silk cocoons were used in two ways: (i) directly processed to form twisted silk yarns used to produce textile-based scaffolds; (ii) purified in order to isolate SF used for preparing SF-based scaffolds and hydrogels. The cocoons were supplied by the Portuguese Association of Parents and Friends of Mentally Disabled Citizens (APPACDM, Castelo Branco, Portugal).

4.1.2. Polyethylene terephthalate (PET)

Polyethylene terephthalate (PET), is the condensation product of terephthalic acid (TPA) and etlhylene glycol (Figure 4-2) [25]. This thermoplastic polymer can be easily obtained by thermal treatment in different stages of order, which determines the physical and chemical properties the polymer. Depending on its processing conditions, PET can exist in both amorphous and semi-crystalline stages, appearing with a transparent, opaque or white morphology [26]. In addition to the several plastic containers produced using this polymer, PET is the first synthetic fiber-forming polyester of economic importance, presenting stable physicochemical properties and suitable biocompatibility for biological and TE application [27-29].

In this thesis, PET-based monofilament and multifilament yarns were created to produce textile-based scaffolds, aiming for bone TE applications. The details regarding the processing methodologies used for preparing the textile-based scaffolds will be described in the Section 4.3.2. of this Chapter.

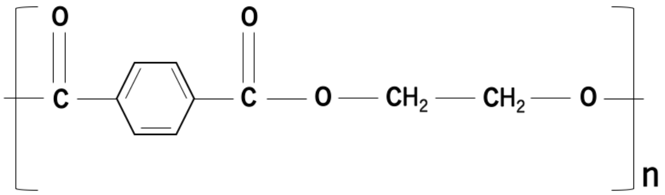

Figure 4-2. Chemical structure of Polyethylene terephthalate.

4.1.3. β-Tricalcium phosphate (β-TCP)

Calcium phosphates (CaPs) are chemical compounds of special interest for TE applications due to their close resemblance with the inorganic compounds that compose normal and pathological calcified human tissues [30]. These CaPs bioceramics are based on hydroxyapatite (HAp), β-tricalcium phosphate (β-TCP), α-tricalcium phosphate (α-TCP) or biphasic calcium phosphate (BCP) [31], and hold exceptional biological performances in terms of biocompatibility, osteoconductivity, and bioresorbability.

In the biomedical field, a great deal of attention has been attributed to β-TCP, which is high temperature phase of CaPs, obtained by thermal decomposition at temperatures above 800°C. β-TCP is biodegradable and has been extensively used as bone substitute, either as granules or blocks [32], or even in composite-polymer scaffolds to promote new bone formation *in vivo* [33]. Even if the HAp and β-TCP present similar chemical composition, the biological resorption of HAp is slower and it can be integrated within the regenerated bone tissue, whereas the β-TCP is completely reabsorbed [33, 34].

The incorporation of foreign ions (e.g., strontium (Sr) and zinc (Zn)), into the structure of β-TCP, can alter a series of structural, physicochemical, and biological properties, such as, crystallinity, mechanical properties, resorption rate, and bone bonding capability, as well as, the osteogenesis and neovascularization of the TE scaffolds [35, 36]. For example, Sr has presents bone-seeking behavior stimulating bone formation and an inhibitory role on bone resorbing osteoclast cells [37]. On the other hand, Zn is able to stimulate osteoblastic cells proliferation and differentiation, interrupts the bone resorption process induced by osteoclastic cells, and inhibit the expression of genes and growth factors involved in angiogenesis [38].

In this thesis, pure β-TCP and ZnSr-doped β-TCP particles were produced aiming for subchondral bone regeneration in an osteochondral TE strategy. The details of the synthesis and processing of the β-TCP and ZnSr-doped β-TCP particles will be described in the Section 4.3.6. of this Chapter.

4.2. Reagents

Unless addressed otherwise, all the reagents used in this thesis were purchased from Sigma-Aldrich (St. Louis, MO, USA).

4.3. Scaffolds and hydrogels preparation

4.3.1. Methodologies for scaffold and hydrogel processing: Overview

4.3.1.2. Scaffolds

There is no ideal methodology or universal biomaterial that meets all the scaffolding requirements for tissue regeneration. Different tissues require biomaterials with specific physical, mechanical and degradation properties. Nowadays, several processing techniques can be used in order to create porous SF scaffolds that can meet such specificities, including salt-leaching [20], gas foaming [14], freeze-drying [39], fiber-bonding [40], and rapid-prototyping [41, 42].

Fiber-based networks have been showing tunable surface properties with particular interest for developing scaffolds for tissue engineering (TE) applications [43, 44]. At the same time, the textile technologies have been evolving in the medical field, and its application in TE approaches has grown in the recent years [45]. The specific use of silk to prepare textile-based scaffolds is of special interest, not only due to the well-known biocompatible, structural and mechanical properties of the SF protein, but also because the silkworm's silk has been extensively used in the textile industry for centuries. This means that there is a steady silk production to serve as raw material platform and very sophisticate textile processing technologies which can be useful to create new biomaterial architectures. These are great advantages of using silkworm's silk as compared to other sources. From the silkworm's silk, high amount of fibers can be yielded from a single cocoon (600–1500 m), as compared to the ~137 m reached from the spider's glands or the ~12 m from the spider's web [5]. Moreover, the easy and non-invasive process of silk extraction together with the homogeneous behavior of the silkworms during their lifetime also influence their choice [46]. From the different textile producing systems, the knitted SF textile technologies are of particular interest for developing SF scaffolds [47]. Through these technologies, it is possible to obtain structures with controlled porosity, a certain flexibility and adjustment, as well as, high resistance to deformation, being ideal for bone TE applications. In the knitting process, the needles form symmetric and continuous series of inter-looping stitches that connected together form the final fabric [48]. In these structures, the rows formed across the width of the fabric are called courses, and the columns designed along the length of the fabric are known as wales [47]. Depending on the direction of the formed loops, the knitted fabrics can be classified weft-knitted and warp-knitted fabrics. In the weft-knitting, the wales are perpendicular to the course of the yarn (Figure 4-3a), whereas in the warp-knitting the wales run parallel to the courses (Figure 4-3b) [49]. The weft-knitted structures can be classified as jersey fabrics, rib fabrics and purl fabrics [50]. More importantly, is that the entire fabric can be fabricated from one single yarn, in contrast to the warp-knitted structures that require a different yarn in each wale. The warp-knitting processing can be performed by *Tricot* or *Raschel* knitting machines, whereas the weft-knitted fabrics can be created by *circular* and *at-bed* knitting machines [47].

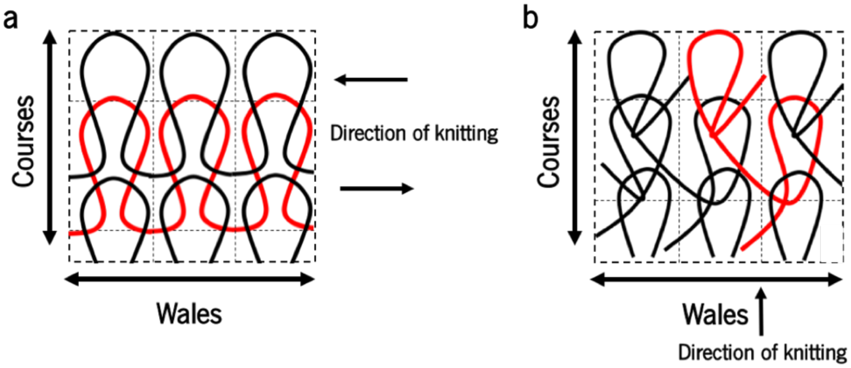

Figure 4-3. Schematic illustration of the wales and courses components of the knitted fabrics. The principles of (a) weft- and (b) warp-knitting technologies.

Focusing on increasing the fabrics three-dimensionality and create specific bulk properties, knitted spacer fabrics were engineered for different biomedical applications [51]. These fabrics can be created with different choices of yarns to meet a wide range of specifications in each layer. Different researchers [50, 52], describe the knitted spacer fabrics as two ground knitted layers connected together to form a structure in three directions in a single process. The external upper and lower knitted layers are interconnected by a resilient monofilament yarn in the z direction, which represents the adjustable height of the spacer fabric [51].

Monofilament polyester fibers have been specially used for this purpose, holding a marked stiffness that provides higher compression resistance to the fabric [53].

The salt-leaching method is widely used to prepare silk-based scaffolds, being an effective, efficient, low cost and easy processing technique. A controlled pore size can be achieved, with high interconnectivity and homogeneity. This approach is applied to aqueous SF solutions, in which the dissolved SF is transferred to molds, followed by the addition of sodium chloride particles (pre-established). After drying, the salt particles incorporating the SF structures are leached out in water, in order to form porous SF scaffolds. In this approach, the pore size will be dependent on the sodium chloride particles size [20]. Moreover, the β-sheet crystal formation is implicit when the sodium chloride particles are added to aqueous SF solutions, which is not observed in the salt-leached HFIP-derived SF scaffolds [54]. The stiffness of the salt-leached aqueous-derived SF scaffolds can significantly increase by the formation of crystalline SF structures, leaving a limitation in the utility for some soft tissues [14, 54]. SF hydrogels have generally been used for such needs, however, they also present poor stability for cell and tissue cultures. Therefore, the development of new options that match the elastic and resilient behavior of tissues with the porous and mechanically stable properties of salt-leached SF scaffolds, would provide additional options for applying SF biomaterials in different tissue engineering strategies.

Many attempts have been made to develop bioactive bone scaffolds consisting of natural biomaterials, with biocompatible, biodegradable and tunable structural properties, incorporating particles to improve the mechanical behavior and tune the topographical features of the bone-like scaffolds [55, 56]. SF as a natural protein polymer has shown potential properties for creating such structures [57]. Moreover, it owns extraordinary properties for stimulating bone repair by itself. For example, the fibrous structure of SF reminds the structure of type I collagen, and the amorphous links between the β-sheet crystals of SF structure can act as sites for the CaPs nanocrystals deposition, by mimicking the anionic structure of the non-collagenous proteins [58]. On the other hand, different reports also stated that the β-sheet crystals can alone act as nucleators for the deposition of CaPs [59]. β-TCP with similar properties to the HAp of bone tissue and suitable biocompatibility has been introduced as an appropriate bioceramic phase that can be easily incorporated in different polymeric phases. Several natural polymers, have been used in combination with β-TCP to stimulate bone regeneration [60, 61]. Some of these structures were based on SF/β-TCP composites alone [62-64], or incorporating ionic-dopants in the β-TCP structure, which significantly improved the osteoconductivity of the SF/β-TCP composites [65].

In this thesis, textile-based technologies, and a salt-leaching approach allied to freeze-drying technique, were used to prepare mechanically stable and suitable SF-based scaffolds for cartilage, bone, and osteochondral regeneration. Raw silk yarns and a highly concentrated aqueous SF solutions were used for that purpose. Three kinds of SF-based scaffolds were successfully developed: (i) a weft-knitted textile technology was used on raw silk yarns to prepare SF scaffolds alone, or in combination with a monofilament of polyethylene terephthalate (PET), aiming for TE applications and bone regeneration; (ii) Pure salt-leached SF scaffolds were prepared by using a 16 wt.% aqueous SF solution enzymatically cross-linked by a horseradish peroxidase (HRP)/hydrogen peroxide (H_2O_2) system, aiming for articular regeneration; (iii) Based on this previous work, salt-leached bilayered SF scaffolds were created for osteochondral regeneration: The HRP-crosslinked SF solution was mixed in an 80/20 ratio with β-TCP and ZnSr-doped β-TCP particles, and then salt-leached SF/β-TCP and SF/ZnSr-doped β-TCP scaffolds were generated for bone tissue engineering. These scaffolds were combined with the HRP-crosslinked SF scaffolds developed for articular cartilage regeneration, in order to create the bilayered structures.

4.3.1.3. Hydrogels

Hydrogels have been studied for several TE applications, involving cell encapsulation strategies or drug delivery systems, presenting structural similarities to the extracellular matrix (ECM) of tissue [66]. For instance, hydrogel systems have been one of the first choices to be used as fillers, or combined with cells or bioactive agents in different cartilage, or bone regeneration applications. In this sense, the injectable hydrogels are attracting much interest in this sense [67]. Several methodologies have been applied to produce injectable hydrogels, including photo-polymerization [68], ionic or thermal gelation [69], and enzymatic reactions [70]. The enzymatic crosslinking reactions can be advantageous for several reasons, including the reaction process occurs at physiological conditions, without need any external stimuli and taking only a few minutes to induce gelation. From the different enzymatic crosslinking methods applied for TE purposes, it was reported that water-soluble polymers containing phenol groups, aminophenol, tyramine or tyrosine can be crosslinked by the horseradish peroxidase (HRP)/hydrogen peroxide (H_2O_2) complex system [70]. In this sense, the SF protein can take advantage of its ~5% tyrosine groups to form enzymatically crosslinked SF hydrogels via a peroxidase mediated system [21, 71]. This is another goal of this thesis, to take advantage of the easy processing of enzymatically crosslinked SF to create hydrogel-based systems for TE and cancer research applications.

SF hydrogels previously proposed were prepared from a conformational transition of the SF protein from random coil to β-sheet, using extreme physical treatments [12, 22, 23] or chemical reagents [20], which in many cases involved long gelation times and harsh preparation conditions that limited their use as injectable systems. At the same time, these hydrogels showed homogeneous and stable physicochemical properties for hard tissues application, including bone or cartilage.

Another purpose of this thesis was to take advantage from the peroxidase-mediated crosslinked SF hydrogels and in combination with salt-leaching and freeze-drying methodologies create novel SF porous scaffolds of controlled conformation and mechanical properties.

4.3.2. Production of textile-based scaffolds

Textile-based scaffolds were proposed in this thesis in Chapters 5 and 6. A weft-knitting technology was used to produce SF-based scaffolds using raw silk yarns. The raw silk thread was obtained from the combination of 4-8 *Bombyx mori* silk cocoons and processed by twisting into silk yarns used to produce the weft-knitted SF fabrics. These structures are classified as jersey fabrics and were textured using *circular* knitting machines. A *Raschel* knitting machine was used to produce warp-knitted PET scaffolds, used for comparative analysis in Chapter 6 (see Section 4.3.1.2. of this Chapter).

Textile-based scaffolds were first cut into pieces of 5 g each and washed in a 0.15% (w/v) natural soap aqueous solution for 2 hours. Then the fabrics were rinsed in distilled water to remove the excess of impurities that resulted from the manufacturing machines. The textile-based SF scaffolds underwent a subsequent purification process, in order to remove the coating protein sericin (see Section 4.1.1. of this Chapter). Thus, each 5 g of SF fabrics were boiled for 1 hour in 2 L of sodium carbonate (Na_2CO_3) solution (0.03 M), and rinsed in 1 L of boiling distilled water for 1 hour to fully remove the excess of sericin.

In Chapter 5, the 3D jersey weft-knitted SF scaffolds were textured in a Tricolab machine (Sodemat, SA, Germany) and used as untreated textile scaffolds (Figure 4-4).

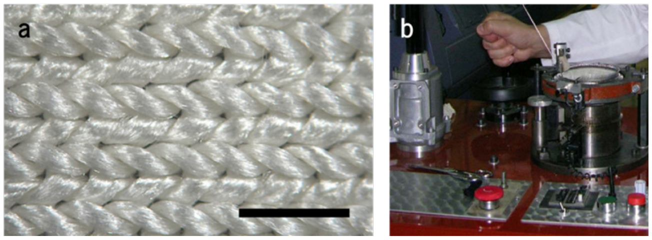

Figure 4-4. (a) Macroscopic images of the 3D weft-knitted SF scaffolds (scale bar: 2 mm). (b) Tricolab machine used for the fabrication of the jersey weft-knitted SF fabrics (collaboration established with the Technological Centre CITEVE in the frame of the FCT project Tissue2Tissue).

Several surface treatments were applied to the weft-knitted SF scaffolds, namely:

Etching with NaOH: The wet chemical treatment with sodium hydroxide (NaOH) is largely applied to activate the surface of structures, from metals to polymers, by creating free hydroxyl groups and developing bioactive surfaces [72]. This treatment has shown to affect the self-adhesion properties of polymer surfaces, and as consequence influenced cell adhesion capacity and morphology [73].

In this thesis, the wet chemical treatment with NaOH was performed by immersing the SF textile structures in 0.5 mol/L NaOH solution for 60 minutes at 30°C. Then scaffolds were washed with distilled water and used for further characterization.

Exposure to ultraviolet radiation in an ozone atmosphere (UV/O_3): Contrary to the NaOH etching surface treatment, the UV/O_3 treatment is better restricted to the surface of polymers. Herein, the treatment was performed by exposing the SF textile surfaces to 185 nm of UV radiation in a UV/ozone cleaner chamber (ProCleaner™ 220; BioForce Nanosciences, Ames, IA, USA). The principle of UV/O_3 surface treatment is a physical etching of the surfaces by the UV radiation and subsequent strong oxidation induced during de formation of O_3. When the atmospheric oxygen (O_2) is irradiated with UV radiation with a wavelength of 185 nm, it absorbs the UV rays to form O_3. During the process of O_3 formation, atomic oxygen is formed having strong oxidizing ability [74]. The direct biofunctionalization of polymer surfaces with proteins and oligonucleotides have been proposed after UV/O_3 treatment [75], being classified as one of the most convenient methods for treating surfaces at low temperature bonding.

Plasma grafting: The oxygen plasma treatment is another free-solvent method for surface modification of polymer surfaces. As the UV/O_3 modification method, plasma treatment has its only action at the very top surface of the polymers. Thus, the bulk properties of materials, including mechanical properties and degradation profile, remain intact [74]. Through this treatment, different types of gases can be introduced to produce unique surface properties required for different applications. In this thesis, the oxygen (O_2) plasma treatment was first applied for the pre-activation of the SF textile surfaces. Samples were exposed to O_2 plasma at 30 W of power for 15 minutes, using a radio frequency (13.56 MHz) plasma reactor (PlasmaPrep5, Gala Instruments, Germany). During the treatment, the gas flow was adjusted in order to keep a constant pressure of 20 Pa inside the reactor. This treatment is known for increasing the surface energy of polymers and their hydrophilicity, positively affecting cell adhesion and morphology [76]. Immediately after oxygen surface activation, samples were immersed in three different solutions, in order to grafting the surfaces with functional moieties of carboxylic groups (5% (v/v) acrylic acid (AAc)), sulfonic groups (10% (v/v) vinyl sulfonic acid (VSA)), and phosphonic groups (100 mM vinyl phosphonic acid (VPA)/2-propanol). The charge of the introduced functional groups has shown to influence the behavior of proteins and induce cell adhesion at the modified surfaces [77, 78]. These solutions were applied for 2 hours at room temperature (RT), but first were degassed by nitrogen bubbling to avoid the reaction between the induced functional groups and the O_2 present in the solutions. After each reaction, samples were washed with the solvent used to prepare the solutions, distilled water or 2-propanol, followed by dehydration in absolute ethanol and over drying at 37°C for 24 hours.

In Chapter 6, the 3D jersey weft-knitted SF scaffolds were processed using a Terrot machine (UP472T model, Germany). In order to increase the scaffolds three-dimensionality, the weft-knitted SF fabrics were incorporated with a 100D/1F polyester PET monofilament (Putian Shuangyan Chemical Fiber Co., Ltd.) introduced on the knitting machine to form 3D weft-knitted SF spacer scaffolds with 3 mm height.

The 100% PET textile scaffolds, were produced on a warp-knitting machine (COMEZ, model DNB/EL-800-8B) with a working width of 812.8 mm and stitch density between 1 and 40 stitches/cm. The polyester filaments were produced in a pilot spinning line (Hills Inc., Pretoria, South Africa), using PET Type RT52 with 0.64 of intrinsic viscosity (INVISTA™ Resins & Fibers, Kansas, USA) as raw material. The temperatures of the spinning line were maintained between 250°C and 270°C, the spinning speed was 1500 m/min for a throughput of 1.3 kg/h with a draw ratio of 3.75. Yarns with 36 continuous filaments were obtained, with 3.6 of denier per filament equivalent to about 15 μm per filament. The warp-knitted PET spacer scaffolds were created with 2.5 mm height, using the same monofilament of PET used to interconnect the external weft-knitted SF fabrics.

The prepared 3D weft-knitted SF spacer scaffolds are herein designed as SF-PET scaffolds, whereas the 3D warp-knitted PET spacer scaffolds are designed PET scaffolds (Figure 4-5).

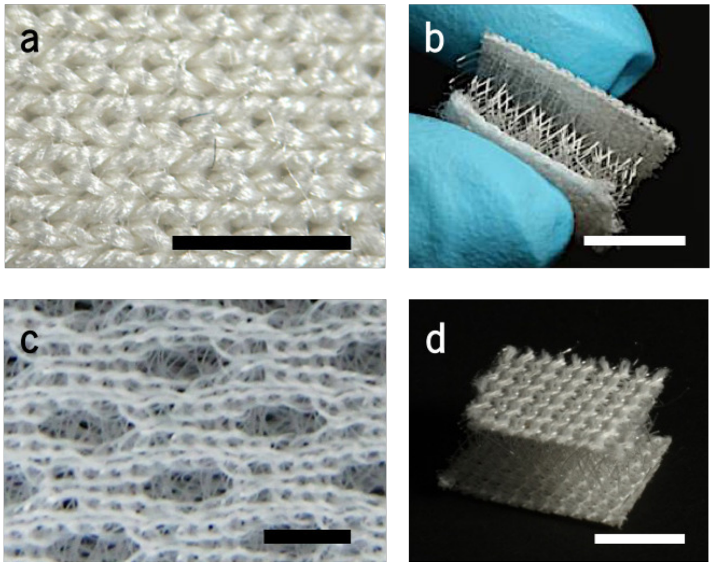

Figure 4-5. Macroscopic images of the (a, b) SF-PET scaffolds and (c, d) PET scaffolds. (a, c) Top view perspective

and (b, d) respective cross-sections (scale bars: 5 mm for the low magnification images and 2 mm for the high magnification images).

4.3.3. Production of SF membranes

In Chapter 5, SF membranes were prepared and surface modified according to the procedure previously described in Section 4.3.2. of this Chapter. Unfortunately, the porous nature of the textile-based scaffolds can limit its use for certain surface characterization assays. In fact, there are not many characterization techniques with enough sensitivity to allow surface analysis of such samples with complex shape. Therefore, SF membranes were created as "models", trying to recapitulate some of the surface properties of the textile samples.

SF was purified from the *Bombyx mori* cocoons in order to extract the glue-like protein sericin and wax [6] (see Section 4.1.1. of this Chapter). For that, 5 g of cocoons were previously cut and cleaned into several pieces and boiled for 1 hour in 2 L of sodium carbonate solution (0.02 M). Then, the purified SF was washed for 1 hour in 1 L of boiling distilled water, followed by washing in distilled water several times. Afterwards, SF was dried in a clean place. In order to obtain aqueous SF solution, 5 g of purified SF were dissolved in 25 mL of lithium bromide solution (9.3M) at 70°C for 1 hour, yielding a solution around 20% (w/v) [79]. The solution was dialyzed in distilled water for 2 days, using a benzoylated dialysis tubing (MWCO: 2 kDa), changing the distilled water at least 3 times per day. The prepared SF solution yielded around 8 wt.% and was stored at 4°C until further use.

SF membranes were obtained by casting 600 μL of SF solution in 24-well culture plates (BD Biosciences, San Jose, CA, USA) and slow dried at RT for at least 2 days. In order to induce the β-sheet conformation to the membranes, increasing concentrations of methanol/water solutions (from 30% to 100% v/v) were applied to immerse the membranes for 10 minutes, twice each concentration. At the highest concentration of ethanol solution, SF membranes were left to dry at RT in order to preserve the structural integrity during the drying process.

4.3.4. Production of SF hydrogels

The purification of SF from the *Bombyx mori* cocoons was performed as mentioned above (see Section 4.3.3. of this Chapter).

After obtaining the purified SF, a 9.3 mol/L lithium bromide solution was used to dissolve SF in an over at 70°C for 1 hour, followed by dialysis against distilled water for 2 days in a benzoylated dialysis tubing

(MWCO: 2 kDa). At the end of this process, the SF solution was dialyzed in 0.2 time phosphate buffer saline solution (PBS, without calcium and magnesium ions) for 12 hours, followed by concentration in a 20 wt.% poly(ethylene glycol) solution (20,000 g/mol) for at least 6 hours [1]. The dialysis tubing was carefully washed in distilled water and the solution collected to a 50 mL centrifuge tube (Thermo Fisher Scientific, Waltham, MA, USA) (Figure 4-6). The final concentration of the SF solution was determined by weight measurement. For that, around 500 μL of SF solution were weighted (wet weight) and dried overnight at 70°C in an over. Then, the dry weight of the sample was determined and the concentration obtained by dividing the dry weight by the wet weight. The SF solution was stored at 4°C until further use.

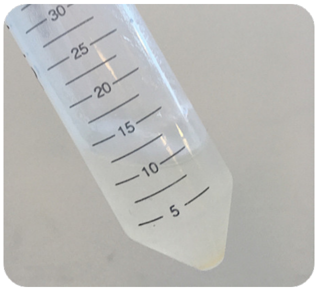

Figure 4-6. Concentrated aqueous SF solution.

Horseradish peroxidase (HRP) solution (0.84 mg/mL) and hydrogen peroxide (H_2O_2) solution (0.36 wt.%) were both prepared in PBS solution. The SF solutions (pH ~7.0) were diluted into 16 wt.% by PBS and used for the hydrogels preparation. Micropipettes M100 and M1000 (Gilson, Middleton, WI, USA) and corresponding tips were used for preparing the reaction mixtures.

In Chapters 7 and 8, 1 mL of SF solution was mixed with 50 μL of HRP and 65 μL of H_2O_2 solutions (1/0.26‰/1.45‰) in a 1.5 mL centrifuge tube (Eppendorf, Hamburg, Germany). Then, 1 mL of the SF/HRP/H_2O_2 solution was transferred into a cylindrical shaped silicone mold (9 mm inner diameter) in order to prepare the enzymatically crosslinked SF scaffolds proposed in Sections 4.3.5. and 4.3.6. of this Chapter. In Chapter 9, SF hydrogels were prepared by mixing 1 mL of SF solution with 100 μL of HRP and 65 μL of H_2O_2 solutions (1/0.52‰/1.45‰) in a 1.5 mL centrifuge tube, followed by warming in the oven at 37°C (Figure 4-7). The gelation time was determined by inverting the tube and if now flow was observed within 1 hour it was considered the hydrogel status. SF hydrogels were prepared by the deposition of 100 μL of SF/HRP/H_2O_2 solution in tissue culture polystyrene (TCPs) coverslips (22 mm diameter, Sarstedt, Nümbrecht, Germany), in polydimethylsiloxane (PDMS; Sylgard 184 Silicone Elastomer Kit, Dow Corning, Belgium) silicone molds (8 mm diameter and 2 mm height), or in fluorinated ethylene propylene (FEP) tubes, according to the characterization technique. After the complete gelation in the oven at 37°C, SF hydrogels were kept in PBS solution in an incubator with 5% CO_2 atmosphere at 37°C (Sanyo Incubator, MCO-18AIC (UV), Osaka, Japan), and further characterized after 1, 3, 7, 10 and 14 days of hydrogels formation.

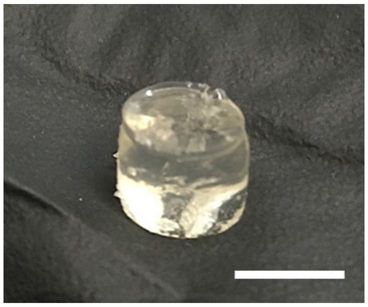

Figure 4-7. Macroscopic image of the HRP-crosslinked SF hydrogels (scale bar: 5 mm).

The SF solutions used for producing the SF hydrogel-based scaffolds proposed in Sections 4.3.5. and 4.3.6. of this Chapter, could be prepared without dialysis in PBS. However, this choice was made in order to standardize the protocol used for preparing the aqueous SF solutions. The dialysis of SF against PBS was aimed to maintain the pH value close to that of physiological conditions for further cell encapsulation studies.

4.3.5. Salt-leached enzymatically crosslinked SF scaffolds

The purification of SF from the *Bombyx mori* cocoons, the dialysis process, and the concentration of SF solution were performed as described above (see Sections 4.3.3. and 4.3.4. of this Chapter).

Granular sodium chloride in a range of 500-1000 μm was prepared by sieving a commercial grade of sodium chloride (Portugal) in an analytic sieve shaker (AS 200 Digit, Retsch, Germany) [20]. The enzymatically crosslinked SF scaffolds were prepared by the addition of 2 g of granular sodium chloride to 1 mL of SF/HRP/H_2O_2 solution previously transferred into a cylindrical shaped silicone mold (9 mm inner diameter), as mentioned above in Section 4.3.4. of this Chapter. The sodium particles were slowly added into the silicone tubing, and with the help of a glass rod gently and uniformly distributed inside the mold facilitating the precipitation of the salt particles. Afterwards, the silicon mold was placed in the oven at 37°C until complete gelation. The tubing was then immersed in distilled water for 3 days and the sodium chloride particles were leached out (porogen). Finally, the scaffolds were removed from the molds by using a biopsy punch (8 mm inner diameter; Smith & Nephew, Portugal). Through this punching the outer skin formed by the contact of the scaffolds with the inner walls of the molds was removed. The prepared scaffolds were then frozen at -80°C overnight and freeze-dried (Telstar Cryodos-80, Barcelona, Spain) for 7 days. The prepared enzymatically crosslinked SF scaffolds are herein designed as HRP-crosslinked SF scaffolds (Figure 4-8).

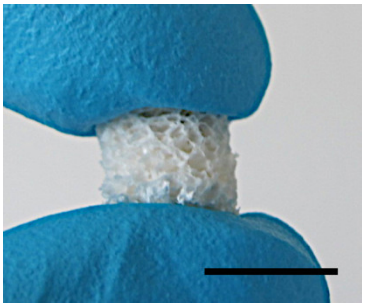

Figure 4-8. Macroscopic image of the HRP-crosslinked SF scaffolds prepared by salt-leaching/freeze-drying technologies (scale bar: 8 mm).

4.3.6. Salt-leached enzymatically crosslinked bilayered SF/SF-β-TCP scaffolds

The purification of SF from the *Bombyx mori* cocoons, the dialysis process, and the concentration of SF solution were performed as described above (see Sections 4.3.3. and 4.3.4. of this Chapter).

For the preparation of the bilayered scaffolds (Figure 4-9), the cartilage-like layer was produced using the HRP-crosslinked SF solution (SF/HRP/H_2O_2) processed by salt-leaching/freeze-drying technologies as previously described in Section 4.3.5. of this Chapter. Two different bone-like layers were proposed using powders of pure β-TCP and doped with 10 mol.% of Zn and Sr (with respect to Zn and Sr molar ratio). The ionic-doped β-TCP powders were synthesized by aqueous precipitation using zinc nitrate ($Zn(NO_3)$), and strontium nitrate ($Sr(NO_3)$) as starting chemical precursors, respectively for Zn and Sr [35, 80]. The molar ratio of (Ca+X)/P = 1.48 (being X Zn or Sr) was used in order to avoid hydroxyapatite (HAp) formation and the pH adjusted to 7.0. The precipitated suspensions were kept for 4 hours under constant agitation and then matured for 20 hours at 50°C under static conditions. The resulting precipitates were vacuum filtered, dried at 100°C, and heat treated for 2 hours at 1100°C. Afterwards, the powders were milled and sieved in an analytic sieve shaker by a mesh size of 63 µm, having a particle size distribution of 1-10 µm determined using a light scattering instrument (Coulter LS 230, UK, Fraunhofer optical model). A higher reactivity of the powders was expected using low particles size [65]. The powders containing Zn and Sr were designed as ZnSr-β-TCP. For comparative analysis, the pure β-TCP powders were also produced following the same procedure.

Firstly, the bone-like layers were produced by mixing in 5 mL tubes (Thermo Fisher Scientific, Waltham, MA, USA) 1 mL of SF/HRP/H_2O_2 solution (designed herein as HSF solution) with ZnSr-β-TCP or β-TCP powders in an 80/20 (w/w) ratio. Then, 1 mL of the HSF/ZnSr-β-TCP and HSF/β-TCP suspensions were transferred into cylindrical shaped silicone molds (9 mm inner diameter) followed by adding 2 g of granular sodium chloride low in endotoxins (EMPROVE®, VWR BDH Prolabo, Briare, France), with a particle size of

500-1000 μm and previously prepared in an analytical sieve shaker. Then, the silicone molds were left at 37°C in the oven until complete gelation. Sodium chloride was extracted overnight in distilled water and in the following day the HSF/ZnSr-β-TCP and HSF/β-TCP scaffolds were cut into pieces after removal from the molds. Each piece of the scaffolds was placed in the bottom of new silicon molds (8 mm inner diameter) and 600 μL of HSF solution were transferred to the top of the HSF/ZnSr-β-TCP and HSF/β-TCP scaffolds. Then, sodium chloride particles (500-1000 μm) were immediately added to the suspensions in the molds. After complete gelation at 37°C in the oven, the bilayered scaffolds were extracted in distilled water to remove the sodium chloride and by-products. Afterwards, the length of the bilayered scaffolds, for the HSF, HSF/ZnSr-β-TCP and HSF/β-TCP layers, was tailored according to the characterization procedure. The outer skin of the scaffolds was removed by the biopsy punch (8 mm inner diameter). Finally, the scaffolds were obtained by freeze-drying for 7 days after freezing at -80°C overnight. As controls, monolayers of HSF scaffolds, HSF/ZnSr-β-TCP (designed herein as HSF-dTCP) and HSF/β-TCP (designed herein as HSF-TCP) scaffolds were also prepared by using the same SF/HRP/H_2O_2 solution and introducing ZnSr-β-TCP and β-TCP powders in the same 80/20 (w/w) ratio. The bilayered scaffolds were abbreviated as BdTCP for bilayered HSF/HSF-dTCP scaffolds and BTCP for bilayered HSF/HSF-TCP scaffolds.

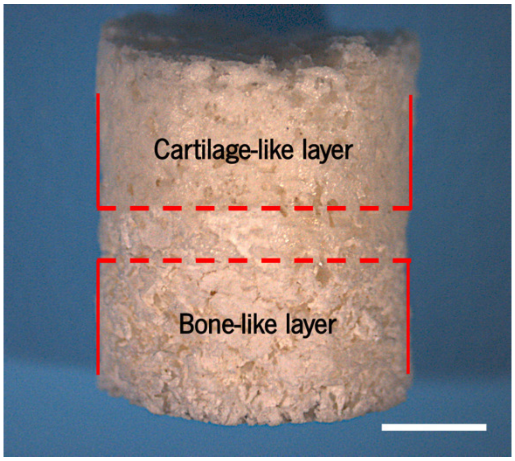

Figure 4-9. Macroscopic image of the bilayered scaffolds prepared by combining a HSF cartilage-like layer with a HSF/ZnSr-β-TCP or HSF/β-TCP bone-like layer (scale bar: 2 mm).

4.4. Physicochemical Characterization

4.4.1. Morphology and microstructure evaluation

4.4.1.1. Scanning Electron Microscopy (SEM) and Energy Dispersive Spectroscopy (EDS) analysis

Scanning Electron Microscopy (SEM), is an imaging technique that produces images of a sample by scanning the surface with focused beam of electrons. When in contact with the atoms at the sample's surface, the electrons produce several signals containing the collected information [81]. Thus, the qualitative information regarding the surface morphology of samples and elemental information can be obtained.

In Chapters 5 and 6, the morphology of the produced textile scaffolds was observed using the scanning electron microscope (Leica Cambridge S-360, United Kingdom). Prior to the analysis, samples were sputter-coated with gold (Fisons Instruments, Sputter Coater SC502, United Kingdom) and the micrographs were taken at an accelerating voltage of 15 kV at different magnifications.

In Chapter 7, the surface and cross-sectional morphology of the prepared HRP-crosslinked SF scaffolds was observed under a JEOL JSM-6010LV (Tokyo, Japan) scanning electron microscope. Prior analysis, samples were sputter-coated with gold using a Leica EM ACE600 coater (Leica Microsystems, Wien, Austria).

In Chapter 8, the morphology of the BdTCP and BTCP scaffolds was observed by SEM, using the same equipment and coating treatment described for Chapter 7. The elemental characterization was performed with an Energy Dispersive Spectrometer (EDS; Pegasus X4M) coupled to the SEM, in three independent areas selected in the bilayered scaffolds, corresponding to the HSF layer, interface, and HSF-dTCP or HSF-TCP layer. The EDS analyzer, qualitatively calculates the relative percentage of the atomic elements present in a sample creating an elemental map with the elements distribution. In this Chapter, the same samples undergone *in vitro* mineralization for 30 days and further analyzed by SEM and EDS. Three samples of each group were tested for each time point and HSF, HSF-dTCP and HSF-TCP scaffolds were used as controls.

4.4.1.2. Transmission Electron Microscopy (TEM)

Transmission Electron Microscopy (TEM) is a destructive imaging system that provides high resolution images of samples. The principle of the technique consists of electron beams that passes through the samples and interact with the atoms at different depths. The transmitted electrons originate signals which are detected by the TEM equipment and converted into a two-dimensional (2D) image. The resolution of TEM is about 0.2 nm, which is more than a thousand-fold greater than the resolution of the light microscope.

Moreover, the sections prepared for TEM analysis are much thinner and require techniques of heavy metal precipitation rather than the water-soluble staining of samples [82].

In Chapter 9, a JEOL JEM 1400 TEM (Tokyo, Japan) equipment was used to evaluate the natural ability of SF to form β-sheet nanofibrils. SF hydrogels were prepared in TCPs coverslips (22 mm diameter). For the analysis, samples were mounted on a 200-mesh copper or nickel grids, stained with 2% uranyl acetate for 5 seconds and examined. Images were digitally recorded using a CCD digital camera (Orious 1100W Tokyo, Japan).

4.4.1.3. Micro-Computed Tomography (Micro-CT)

Micro-CT analysis is a powerful and invasive tool used to analyze the microstructure of scaffolds in a 3D perspective. Micro-CT uses X-ray to scan and obtain the 3D reconstruction of samples and reach cross-section information of the object. The obtained data set, when processed by the software allow to quantify the microstructure data of scaffolds, including pore size, porosity, interconnectivity, pore-wall size, and phase distribution [83].

In Chapters 6 and 7, the architecture of the textile scaffolds was evaluated using a high-resolution X-ray microtomography system Skyscan 1072 scanner (Skyscan, Kontich, Belgium).

In Chapter 6, both SF-PET and PET scaffolds were scanned for the external sheets (Top) and for the internal monofilament of PET (Bulk). The SF-PET samples were scanned using a pixel size of 11.31 μm x/y/z and an X-ray source fixed at 41 keV of energy and 215 μA of current. For the PET scaffolds the pixel size used was 14.71 μm x/y/z and the X-ray source was set at 40 keV and 154 μA. Representative serial images in each data set (Top and Bulk) were transferred into binary images with a dynamic threshold of 60-225 for SF-PET scaffolds, and 59-255 for PET scaffolds (grey values). Then, the binary images were used for morphometric analysis (CT Analyzer v1.5.1.5, SkyScan, Kontich, Belgium), which included the quantification of porosity, mean pore size and mean pore thickness, and to build the 3D virtual models of the spacer structures (Data Viewer and CT-Vox, Kontich, Belgium). A minimum number of three specimens were used for each scaffold.

In Chapter 7, the HRP-crosslinked SF scaffolds were scanned using a pixel size of 8.79 µm x/y/z and an X-ray source fixed at 40 keV of energy and 248 µA of current. After acquisition, reconstructed grey-scale images were converted into binary images with a dynamic threshold of 40-255. Then, the binary images were used for morphometric analysis (CT Analyzer v1.12.0.0), quantifying the porosity, mean pore size, mean wall thickness and interconnectivity, and to create the scaffolds 3D virtual models (Data Viewer v1.6.6.0 and CT-

Vox v2.0.0). Three samples were used for the qualitative and quantitative microstructure evaluation.

In Chapter 9, an updated model of the micro-CT instrument (Skyscan 1272 scanner, Kontich, Belgium) was used for the qualitative and quantitative evaluation of the BdTCP and BTCP scaffolds. The scanning of the scaffolds was conducted using a pixel size of 3.5 μm and an X-ray source fixed at 50 keV and 200 μA. Both the diameter and height of the scaffolds were 8 mm (HSF layer: 3 mm in height; HSF-dTCP and HSF-TCP layer: 5mm in height). The 2D images in each data set (HSF layer, HSF-dTCP layer and HSF-TCP layer) were binarized automatically using the manufacturer's software (CT Analyzer v1.17, SkyScan, Kontich, Belgium), and used for morphometric analysis by quantification of the mean porosity, mean pore size, mean wall thickness and interconnectivity. The porosity and TCP content distribution profiles were also determined on the 2D images. 2D and 3D qualitative visualization of the different phases at the BdTCP and BTCP scaffolds were obtained with the software's Data Viewer (v1.7.1.0) and CT-Vox (v3.3.0.r1412) (SkyScan, Kontich, Belgium), respectively. Three samples were used for the qualitative and quantitative microstructure evaluation.

4.4.1.4. Thioflavin T staining

In Chapter 9, the qualitative evidence of the β-sheet structure and nanofibrils formation on the SF hydrogels was determined using the dye thioflavin T. Thioflavin T, is a benzothiazole salt obtained by the methylation of dehydrothiotoluidine with methanol in the presence of hydrochloric acid [84]. This dye, is extremely used to visualize the presence of protein aggregates with β-sheet structure in pathological samples, for example, in the brains of diseased Alzheimer's patients, or for *in vitro* samples. When it binds to β-sheet-rich structures, including those in the amyloid aggregates, the dye shows enhanced green fluorescence [85]. SF hydrogels were prepared in TCPs coverslips (22 mm diameter), and at each time point stained with 1% (w/v) thioflavin T for 10 minutes, followed by rinsing in 70% ethanol solution and washed with distilled water. Samples were then observed under transmitted and fluorescence microscopy (ex/em 495/515 nm) using a transmitted and reflected light microscope (Axio Imager Z1m, Zeiss, Jena, Gernamy). These are non-destructive imaging techniques, used to obtain high resolution 2D and 3D images of samples. In the specific case of fluorescence microscopy, the specimens are illuminated with light of a specific wavelength, which is absorbed by fluorophores that immediately emit light of longer wavelengths (i.e. with a different color that the absorbed light). In this manner, the distribution of the different fluorophore in the samples will be imaged showing a specific pattern of interest. Images acquisition was then completed using the digital cameras AxioCam MRc5 or MR3 (Zeiss, Jena, Germany), respectively, connected to the Zen microscope processing software (Zeiss, Jena, Germany).

4.4.1.5. Optical Projection Tomography (OPT)

Optical Projection Tomography (OPT) system was used in Chapter 9 to analyze the 3D microstructure of the SF hydrogels. This new technique is particularly interesting for reconstructing and examining large 3D shapes of specific structures using a high-resolution imaging system that allows the computer to automatically determine the outline of the desired structure [86]. SF hydrogel samples were prepared in FEP tubes and immersed in an index-matching liquid (distilled water) for analysis. Specimens were rotated through a series of angular positions. The center of rotation and the alignment of the samples were adjusted using a manual x-y-stage (Standa, Lithuania) in conjunction with the sample-positioning module (Standa, Lithuania) by using the 4 available axes (3 translational, 1 rotational). The acquisition consists of rotating a sample 360° in 0.9° steps and capturing an image at each rotation angle, ranging from 0° to 359.1°. A total of 400 images were acquired per sample. The OPT system was used in brightfield mode. The images were captured with an sCMOS camera (Hamamatsu, Japan) and the exposure time was adjusted from 4 ms to 20 ms depending on the transparency of the sample. Projections collected in each orientation were used to create the 3D reconstructions of each sample and the visualization of the 3D-volume was obtained using Avizo software (FEI, USA).

4.4.2. Chemical analysis

4.4.2.1. X-ray Photoelectron Spectroscopy (XPS)

X-ray Photoelectron Spectroscopy (XPS) is a surface-sensitive quantitative spectroscopic technique that allows to measure the surface energy of a material, in its original state or after a surface treatment. XPS spectra are obtained by irradiating the sample with a beam of X-rays that measure the kinetic energy and the number of electrons that scape from the top 0 to 10 nm of the material surface. Through this analysis, it is possible to specifically detect the chemical state of elements present in materials [87].

In Chapter 5, a Thermo Scientific K-Alpha ESCA XPS instrument was used to perform the analysis using monochromatic Al-Kα radiation ($h\nu = 1486.6$ eV) for the measurements. The photoelectrons were collected from a take-off angle of 90° relative to the samples surface. The spectrometer was operated in a constant analyzer energy (CAE) mode with 100 eV pass energy for the survey spectra and 20 eV pass energy for the high-resolution spectra. Charge referencing was adjusted by setting the lower binding energy of C1s peak at 285.0 eV. Overlapping peaks were resolved into their individual components by using the XPSPEAK 4.1 software.

4.4.2.2. X-Ray Diffraction (XRD)

X-Ray Diffraction (XRD) technique enables to detect the crystalline or amorphous structure of materials. The principle of this technique is based on the diffraction of the X-ray radiation into a specific direction, depending on the crystalline atoms or molecules of materials. By measuring the intensity and angles of these signals, it is possible to know the crystallinity and arrangement of the atoms in the crystals [88].

In Chapters 8 and 9, the XRD analysis was performed using a high-resolution Bragg–Brentano diffractometer (Bruker D8 Advance DaVinci, Karlsruhe, Germany) equipped with CuKα radiation (λ = 1.542 Å), produced at 40 kV and 40 mA.

In Chapter 8, data sets of the HSF, HSF-dTCP and HSF-TCP scaffolds were collected in the 2θ range of 10–60° with a step size of 0.02° and 1 second for each step. The analysis of each condition was repeated three times independently.

In Chapter 9, the SF hydrogel samples were prepared in PDMS silicone molds (8 mm diameter and 2 mm height), and data sets at the different time points were collected in the 2θ range of 10–50° with a step size of 0.02° and 1s for each step. XRD measurements were repeated three times independently.

4.4.2.3. Fourier Transform Infrared Spectroscopy (FTIR)

Fourier Transform Infrared Spectroscopy (FTIR) is a cost-effective technique that acts as a fingerprint used to identify the chemical groups in materials. Similar chemical groups absorb in the IR at similar frequencies, which enables to screen the ratio of the components in the tested material. Fourier transformation algorithm allied to IR spectroscopy gives a spectrum of IR absorption per frequency/wavelength [89].

In Chapters 7 and 9, the HRP-crosslinked SF scaffolds conformation and SF hydrogels composition information were evaluated by an Attenuated Total Reflectance (ATR) model (IRPrestige-21, Shimadzu, Japan) in a FTIR equipment (Perkin-Elmer 1600 series equipment, CA, USA) equipped with a Germanium crystal.

In Chapter 7, the analysis was performed to three samples independently and all spectra were obtained between 4500 to 800 cm^{-1} at a 4 cm^{-1} resolution with 32 scans. The spectrum of the atmosphere was used as the background for all the samples.

In Chapter 9, SF hydrogel discs were prepared in PDMS silicone molds (8 mm diameter and 2 mm height) and after each time point samples were scanned 50 times from 4600 to 800 cm^{-1} with a resolution of 4 cm^{-1}. Each sample was examined for at least 3 times and PBS was used as background.

4.4.2.4. Atomic Force Microscopy and Infrared Spectroscopy (AFM-IR)

The combination of IR spectroscopy and atomic force microscopy (AFM) has provides a new technique denominated AFM-IR. This technology is becoming one of the most relevant developments in the field of IR spectroscopy and chemical imaging, representing major advances over the conventional FTIR microspectroscopy [90]. FTIR is well established as a chemical characterization technique, however it has a diffraction-imposed size limit, which prevent its application to smaller analysis regions. AFM-IR technique uses a AFM probe as the IR absorbance sensor, which significantly improves the spatial resolution and provides chemical information from nanoscale regions of materials. Briefly, a pulsed and tunable IR source is used to exercise molecular vibrations in the sample previously mounted on IR-sampling substrates. The incident light is totally reflected at the interface between the substrate and the sample creating an evanescent field that is extended over the sample. As the sample absorbs radiation, it heats up, creating a thermal expansion that causes oscillations of the cantilever. Importantly, the internal reaction conditions of the experiment reduce the background of the source radiation with the AFM cantilever, which creates an illumination configuration similar to conventional ATR spectroscopy [91].

In Chapter 9, a resonance enhanced mode on a NanoIR-2 system by Anasys Instruments (CA, USA), equipped with a Quantum Cascade Laser (QCL) as the IR source, was used for AFM-IR analysis. SF hydrogel samples were prepared by spin-coating (Spin Coater Model WS-650-23, Laurell Technologies, PA, USA) zinc sulfide (ZnS) sampling flat substrates (Anasys Instruments, CA, USA). The spectra were acquired in a 1000-1800 cm^{-1} range with a spectral resolution of 2 cm^{-1}. Multiple spectra were acquired for each sample, averaged and smoothed using Savitzky-Golay filter.

4.4.3. Surface characterization

4.4.3.1. Atomic Force Microscopy (AFM)

Atomic Force Microscopy (AFM) technique allows to see and measure the surface structure of samples with an unprecedented resolution and accuracy. Through this analysis, it is possible to obtain images showing the arrangement of individual atoms in a surface sample, or to see the structure of individual molecules [92]. Comparing to the optical or electron microscopes, AFM does not form an image by focusing light or electrons onto a surface. It “feels” the samples surface with a sharp probe or cantilever and builds a map covering the height or topography of the samples surface. The type of images generated by this microscope can reach a magnification greater than 1000 x. On the other hand, from an imaging microscope, only a 2D projection of a samples surface can be reached without any height information included. Furthermore, besides being an imaging tool AFM has several spectroscopic modes that measure other samples properties as nanoscale [93].

In Chapter 5, AFM analysis was performed on SF membranes rather than to the SF textile scaffolds, due to its better application on 2D plan surfaces. The analysis was performed for three regions per sample (5 x 5 μm^2) using tapping mode (Veeco, NY, USA) connected to a NanoScope III (Veeco, NY, USA) with non-contacting silicon nanoprobes (ca. 300 kHz, set point 2–3 V) from Nanosensors (Neuchâtel, Switzerland). All images were fitted to a plan using the 3rd degrees flatten procedure included in the NanoScope software version 4.43r8. The surface roughness was calculated as Ra (mean absolute distance from mean flat surface). The values are presented as mean ± standard deviation.

4.4.3.2. Contact angle and surface energy

Contact angle (θ) and surface energy measurements were obtained in Chapter 5, to evaluate the wettability of untreated and surface treated SF membranes (Figure 4-10). The irregular surface morphology of the SF textile scaffolds creates a capillary effect that limits the direct determination of the surfaces contact angle with enough precision. The contact angle depends on several interconnected parameters, such us, surface chemistry, roughness and crystallinity. While the roughness of the membranes is certainly different from the textiles, the crystallinity and surface chemistry can be reproduced in the chosen model using the same treatment procedures.

Static contact angle measurements of the SF membranes were obtained by the sessile drop method using a standard contact angle apparatus (Model OCA 151) incorporating a high-performance image processing system (DataPhysics Instruments, Germany). All the measurements were made at RT and the probe liquids were ultrapure water (upH_2O) and diiodomethane (CH_2I_2; 1 mL, HPLC grade), added by a motor-driven syringe. Two samples of each condition were used and five measurements were recorded per sample. The average values were recorded after 5 seconds of the drop deposition (settling time). The obtained results from both liquids were used to calculate the surface free energy (γ) according to a method proposed by Owens, Went, Rabel and Kaelble (OWRK) [94, 95], which is particularly indicated for the determination of low energy surfaces (polymers). According to this method the surface tension can be determined into a polar (γ^p) and disperse (γ^d) component, whose contribution to the surface energy calculation, is dependent on the intermolecular attraction that results from a variety of intermolecular forces according to an additive rule.

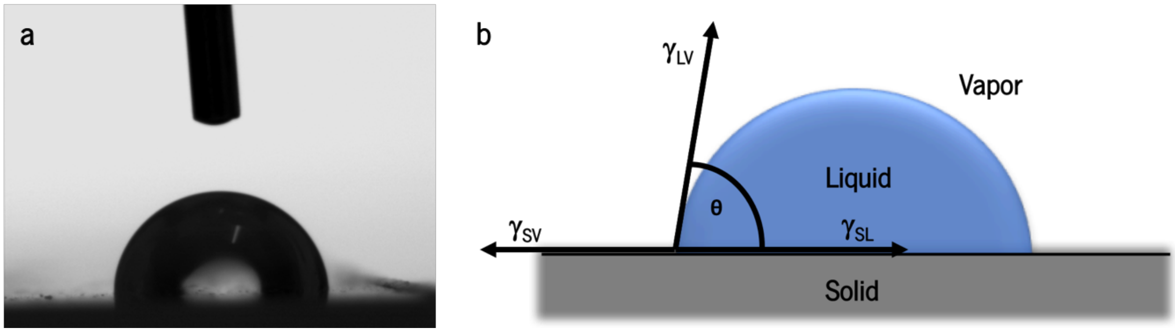

Figure 4-10. Interfacial tension at the 3-phase contact line. (a) Contact angle on a solid surface and (b) Vectorial equilibrium for a drop resting on a solid surface to balance three forces (contact angle forces): the interfacial tensions between, solid and liquid (γ_{SL}), solid and vapor (γ_{SV}), and liquid and vapor (γ_{LV}), are used to measure what is referred to as surface energy.

4.4.4. Mechanical properties

4.4.4.1. Tensile test

Tensile testing, is a fundamental materials science and engineering test, in which a sample material is subjected to a controlled tension until failure. Different properties can be directly measured, including ultimate tensile strength, breaking strength and maximum elongation of biomaterials. From these measurements, the Young's modulus can also be determined [96]. The importance of determine the elastic and failure properties of scaffold materials to be applied in biological tissues like cartilage, bone, tendon or ligament is of great clinical importance. These structures should hold sufficient mechanical properties to support tissue regeneration without breaking, and understanding their mechanical behavior properties prior *in vivo* implantation will bring a great advantage to anticipate its behavior.

In Chapter 5, the tensile properties of the SF textile scaffolds were determined by performing quasi-static tensile tests in a Instron 4505 Universal Machine (Instron Corporation, MA, USA). Instron electromechanical universal testing machines are able to perform tensile, compression, bend, peel, tear, and other mechanical tests on materials. These systems are available in a wide range of sizes, and with several force capacities depending on the testing material and final application. The tensile modulus, ultimate tensile strength and strain at maximum load were measured using a load cell of 1 kN at crosshead speed 5 mm/min. The tensile modulus was determined in the most linear region of the stress-strain curve using the secant method. The test was performed using dry and hydrated samples. Dry samples were tested at 25°C and 50% humidity, whereas the hydrated samples were prepared by immersion in PBS solution for 3 days. Five samples of 15 x 40 mm were analyzed per condition.

4.4.4.2. Compression test

Uniaxial compression tests are very common to measure the deformation of a materials under several compressive forces. This gives the ability of a material to recover after an applied compressive force and within a defined period of time. From the compressive tests, it is possible to obtain both the compressive modulus and compressive strength of a sample. Regarding bone and cartilage TE, the implanted scaffolds would undergo constant compressive forces *in vivo.* Therefore, understand the compression data of a material prior implantation is critical to better select the most appropriate implants according to its final application.

In Chapters 6, 7 and 8, the compressive tests were performed under quasi-static compression mode using the same equipment already described above in Section 4.4.4.1 of this Chapter. The scaffolds were submitted to a pre-load of 1 kN at RT. The cross-head speed was fixed at 2 mm/min and tests were run until a 60% deformation in sample height has been achieved. The size of the samples was measured with a micrometer before analysis. The elastic modulus (E) of samples was defined by the slope of the initial linear section of the stress-strain curve.

In Chapter 6, SF-PET and PET scaffolds were tested in dry state and specimens were cut into cuboid shapes of approximately 10 x 10 x 3 mm and 10 x 10 x 2.5 mm, respectively. The average compressive modulus was determined based on ten specimens examined for each group.

In Chapter 7, HRP-crosslinked SF scaffolds were tested in dry and hydrated conditions, after immersion in PBS solution overnight (until equilibrium was reached). Before the test, the absorbed liquid in the specimens was removed by a tissue, followed by immediate analysis. The diameter and height of the HRP-crosslinked SF scaffolds were 8 and 4 mm, respectively. The average compressive modulus and compressive strength were determined based on five samples measured for each group.

In Chapter 8, the BdTCP and BTCP scaffolds were also tested in wet state and prepared as described above for Chapter 7. Both the diameter and height of the scaffolds were 8 mm (HSF layer: 3 mm in height; HSF-dTCP and HSF-TCP layer: 5mm in height). The average compressive modulus and compressive strength were determined based on five samples measured for each group, using HSF, HSF-dTCP and HSF-TCP scaffolds as controls (4 mm in height, 8 mm in diameter).

4.4.4.3. Dynamic Mechanical Analysis (DMA)

When a scaffold is implanted *in vivo* (such us, in cartilage or bone) it is expected that it will be under constant physical load with different frequencies. Thus, it is important to understand the performance of the scaffolds under dynamic loading, prior implantation. Dynamic mechanical analysis (DMA) is a helpful tool to reveal this information. Through this technique, the materials' properties are characterized as a function of temperature, time, stress, atmosphere, frequency, or by the combination of these parameters. DMA apparatus works by applying a sinusoidal deformation to a sample of pre-established geometry and size, which can under a controlled stress and strain. The deformation of the sample is directly related to its stiffness, measuring the stiffness and damping properties of samples, reported as modulus (E') and tan delta (tan δ). This modulus can be expressed as storage modulus, which measures the elastic behavior of samples, and loss modulus. The ratio between the loss and storage modulus will give the tan delta that is often called damping factor, measuring the energy dissipation of materials.

In Chapters 6 and 8, the DMA analysis was performed using a TRI-TEC8000B model from Triton Technology manufacturer (Lincolnshire, UK) in the compressive mode. The measurements were carried out at 37°C in the hydrated state, by immersing the samples in PBS solution in a Teflon® reservoir and clamped in the DMA apparatus. After equilibration at 37°C, the DMA spectra were obtained in a frequency scan between 0.1 and 10 Hz. The experiments were performed under a constant strain amplitude of 30 μm (Chapter 6) and 50 μm (Chapter 8). Both storage modulus (*E'*) and loss factor (*tan δ*) were obtained in the frequency range. Before the analysis, a small pre-load was applied to each sample to ensure that the entire surface of the scaffold was in contact with the compression plates, being the distance between plates equal for all tested samples.

In Chapter 6, three specimens of each condition were tested, by cutting the SF-PET and PET scaffolds with cuboid shapes of approximately 10 x 10 x 3 mm and 10 x 10 x 2.5 mm, respectively.

In Chapter 8, five samples of BdTCP and BTCP scaffolds were tested after immersing in PBS solution overnight, at 37°C in the CO_2 incubator. The diameter and height of the samples was 8 mm and 4 mm, respectively, and monolayered HSF, HSF-dTCP and HSF-TCP scaffolds were tested as controls.

4.4.4.4. Rheological analysis

Rheology is the study of deformation and flow in matter, being in a liquid state or as "soft" solids [97]. This technique gives the elasticity, viscosity and plastic behavior of materials under changes of strain, frequency, time, or temperature. Moreover, the existence of any chemical reactions in the flows that induce gelation or polymerization, can also be detected with high sensitivity through this technology.

In Chapter 9, three different rheological experiments were performed to characterize the SF hydrogels using a Kinexus pro$^+$ rheometer (Malvern Instruments, UK), equipped with the acquisition software rSpace (Malvern Instruments, UK). SF hydrogel discs were first prepared in PDMS silicone molds (8 mm diameter and 2 mm height), and after each time point were analyzed by oscillatory experiments. For that, the measuring system was equipped with stainless steel (316 grade) parallel plates: an upper measurement geometry plate (8 mm diameter) and a lower pedestal (20 mm diameter) with roughened finish. The measurements were obtained by plot the frequency (Hz) as function of modulus (Pa) and with a predefined shear strain (0.53%). Three samples were measured for each time point. Temperature and time sweep experiments were also performed to the SF/HRP/H_2O_2 solution, in order to evaluate the temperature in which the SF hydrogels are formed, using a range of 25°C to 45°C, as well as, the gelation time of the hydrogels under a pre-established temperature of 37°C. The measurements were performed by oscillatory experiments using a large upper geometry plate of 20 mm diameter, at 1 Hz of frequency and 0.53% of shear strain during 100 minutes (6000 seconds). When the gel was formed, and reached a stable state, a plateau state was reached in the storage and loss moduli curves. The shear viscosity and shear stress of the SF/HRP/H_2O_2 solution were also determined, in order to screen the characteristics of the hydrogels as injectable systems. More specifically, to measure the shear that is induced by the syringe injection. For that, rotational experiments were performed using an upper measurement geometry cone of 40 mm diameter and 4° angle. Both shear viscosity and stress were determined as a function of the shear rate (0.01 s^{-1} to 100 s^{-1}). These experiments were performed at 37°C and all plots were averaged using at least 3 measurements.

4.4.5. Swelling ratio

Understanding the behavior of a biomaterial in contact with hydrated medium is of great importance to predict their interactions with the surrounding tissues, especially in terms of adjustability to the defect sites. These parameters are determined, in general, by means of water-uptake studies [57], that in some cases can also address the biodegradability of a material. The hydration degree was investigated in Chapter 7, since the applied biomimetic strategy relies on the capacity of these materials to uptake ions from the surrounding fluid. For that, the HRP-crosslinked SF scaffolds were immersed in 5 mL of PBS solution (5 mL tube) for time periods ranging from 1 hours up to 30 days. The solutions were weekly renewed. The experiments were conducted at 37°C and dynamic condition (60 rpm) in a water bath (GFL 1086; GFL, Burgwedel, Germany). The initial dry weight of the samples was measured before immersing in PBS solution. After each time point, the samples were removed from the solution and absorbed in filter paper to remove the excess of surface water. The wet weight of each sample was immediately measured. The swelling ratio was calculated according to the Equation 4-1:

$$\text{Water uptake (\%)} = \frac{mw-mi}{mi} \times 100$$

In Equation 4-1, the and m_i is the initial weight of the sample before hydration, and m_W is the weight of the sample after removal from the solution at each tested period. Six samples were used for analysis.

4.4.6. Degradation profile

When implanted, a biomaterial will be inevitably in the presence of body fluids containing various ECM modulatory enzyme, that in some cases can induce the degradation process of biomaterial. In human body, the enzymes that conduct proteolysis can degrade proteins in high efficiency. Some of those enzymes, have shown to degrade SF biomaterials at similar levels to those observed in the presence of protease XIV, which is not present in the human body and has no specific function in the chemical or amino acid structure of the protein [98]. Thus, in order to achieve the same functional performance offered by these enzymes, protease XIV was chosen to carry out the degradation studies *in vitro.* Protease XIV was derived from *Streptomyces griseus* (3.5 U/mg) and prepared at different concentrations by dissolving in PBS solution and each sample was immersed in 5 mL of solution into 5 mL tubes. The experiments were conducted at 37°C and dynamic condition (60 rpm) in a water bath. All the enzyme solutions were refreshed every 24 hours. Samples immersed in PBS solution were used as controls.

In Chapter 7, the HRP-crosslinked SF scaffolds were immersed in protease XIV solutions prepared at 3.5 U/mL and 0.2 U/mL [99]. The initial dry weight of each sample was determined and the degradation profile was investigated from 3 hours up to 30 days. After each time point, the samples were removed from the enzyme solution and rinsed in distilled water. The remaining mass of the specimen was measured after drying it at 70°C in the oven overnight. The weight loss ratio (%) was calculated as Equation 4-2:

$$\text{Weight loss (\%)} = \frac{mi-mf}{mi}\times 100$$

In Equation 4-2, the and m_i is the initial weight of the sample before degradation, and m_f is the dry weight of the sample been degraded for a certain period of time and after drying until constant weight is reached. Three specimens were used for each tested concentration at each time point.

In Chapter 8, the BdTCP and BTCP scaffolds analyzed by immersing in protease XIV solutions prepared at 2 U/mL and 0.0035 U/mL [100, 101]. The initial wet weight of each sample was determined after hydration in PBS solution for 3 hours at 37°C in the oven. The study was conducted for a time period ranging from 3 hours to 30 days. At the end of each time point, the wet weight of each sample was measured after washing the samples in distilled water and removing the excess of surface water in filter paper. The weight loss ratio (%) was calculated as Eq. 4-2, where mi is the initial wet weight of the sample before degradation and mf is the wet weight measured after degradation for a certain period of time. Three specimens of each group were tested and at each tested concentration. HSF, HSF-dTCP and HSF-TCP scaffolds were used as controls.

4.4.7. *In vitro* mineralization

The bone-bonding ability of a material can be evaluated by examining the apatite formation on the surface of materials immersed in simulated body fluid (SBF) with ions concentrations nearly equal to those of human blood plasma. This is useful for predicting the *in vivo* bone bioactivity of such materials, assisting for an efficient development of new types of bioactive materials.

In Chapter 8, the *in vitro* bioactivity evaluation of the BdTCP and BTCP scaffolds was performed by immersing the scaffolds in SBF solution up to 15 and 30 days in an oven at 37°C and dynamic condition (60 rpm), following the method proposed by Tas *et al.* [102] and adapted by Pina *et al.* [65]. Briefly, SBF solution containing ionic concentrations (Na^+ 142.0, K^+ 5.0, Ca^{2+} 2.5, Mg^{2+} 1.5, Cl^- 148.8, HPO_4^- 1.0, HCO_3^{2+} 4.2, SO_4^{2-} 0.5 mM/L, pH 7.4) similar to those of human blood plasma, was prepared and placed in 50 mL centrifuge tubes for pre-heating at 37°C. Then, each specimen was transferred to an individual tube and submerged in the SBF solution, as shown in Figure 4-11. At each time point, the specimens were removed from the SBF solution, washed with distilled water and absorbed in filter paper to remove the excess of surface water. Then, the samples were dried at 37°C in the oven for 3 days and further analyzed by SEM and EDS. Three specimens of each group were tested at each time point. HSF, HSF-dTCP and HSF-TCP scaffolds were used as controls.

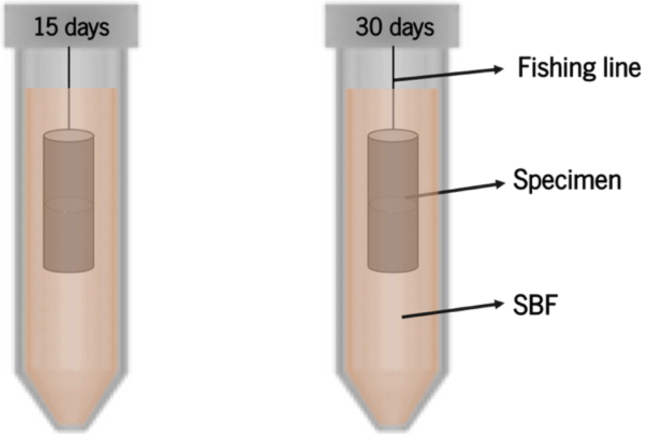

Figure 4-11. Illustrative image of the specimens immersed into the SBF solution.

4.5. *In vitro* biological characterization

In this thesis, all cell-based models were used in a cell-scaffold approaches for different TE strategies. For that, the cell sources and all the aspects related to the cell culture procedures are herein described.

4.5.1. Cell sources

4.5.1.1. L929 cell line

A L929 cell line from mouse C3H/An connective tissue (purchased from ECACC, UK) was cultured in low glucose Dulbecco's modified Eagle's medium (DMEM), supplemented with 44 mM of sodium bicarbonate, 10% (v/v) of fetal bovine serum (FBS; Biochrom, Berlin, Germany), and 1% (v/v) of antibiotic/antimycotic solution (prepared with 10,000 units/mL penicillin G sodium, 10.000 µg/mL streptomycin sulfate, and 25 µg/mL amphotericin B as Fungizone (R) in 0.85% saline; Gibco®, Life Technologies, Carlsbad, CA, USA). The L929 cells were incubated in an atmosphere containing 5% CO_2 at 37°C, and the medium changed every 2-3 days. Cells were routinely trypsinized (0.25% trypsin–EDTA solution; Life Technologies, Carlsbad, CA, USA) for 2-3 minutes at 37°C, centrifuged at 300 g for 5 minutes (Eppendorf 5810R centrifuge equipped with an A-4-62 rotor), and re-suspended at a density of 1 x 10^6 cells in T150 cell culture flasks (BD Biosciences, Enzifarma, Porto, Portugal).

4.5.1.2. Human adipose-derived stem cell (hASCs)

The human adipose-derived stem cells (hASCs) were isolated from the adipose fat tissue, which was obtained from liposuction procedures. The use of the hASCs was approved by the Ethics Committee of University of Minho.

Fat tissue was harvested from the lipoaspirates of at least two independent healthy donors undergoing abdominoplasties. The tissue was digested with 0.05% (w/v) of Collagenase type II (Sigma, USA) under agitation for 45 minutes at 37°C. The stromal vascular fraction (SVF) pellet was obtained after filtrate and centrifuge (800 g, 10 minutes, 4°C) the tissue sample, and then re-suspended in red blood cell lysis buffer (155 mM of ammonium chloride, 12 mM of potassium bicarbonate and 0.1 mM of ethylenediaminetetraacetic acid, all from Sigma-Aldrich, Germany) for 10 minutes at RT. After centrifugation (300 g, 5 minutes, RT), the supernatant was discarded and the cell pellet re-suspended and cultured in MEM alpha medium (α-MEM; Gibco®, Life Technologies, Carlsbad, CA, USA), supplemented with 2.2 g/L of sodium bicarbonate, 10% (v/v) of FBS and 1% (v/v) of antibiotic/antimycotic solution (complete **α**-MEM medium) and maintained at 37°C in an incubator with 5% CO_2 atmosphere. Human ASCs were selected by plastic adherence and harvested (P0) 7 days after isolation at 90% confluence. Then, cells were routinely trypsinized for 2-5 minutes at 37°C with TrypIE™ Express (Life Technologies, UK), centrifuged (300 g, 5 minutes) and re-suspended at a cell density of 1×10^6 cells in T150 cell culture flasks. The medium was refreshed every 2-3 days, and when cells reached around 90% confluence were detached from the culture flask (TrypIE™ Express) and stored in liquid nitrogen for long-term use.

The phenotype of hASCs has been extensively characterized using tissue samples obtained from the same anatomic region (abdominal subcutaneous adipose tissue), collected using similar techniques and isolated following the same procedure [103, 104].

4.5.1.3. Human osteoblast (hOBs)

Primary human osteoblasts (hOBs) were obtained from the femoral bone tissue (Ref. P10979; purchased from Innoprot, Derio, Spain), cryopreserved (liquid nitrogen) at a cell density of 5×10^5 cells/vial (1 mL) as primary cultures and delivered by the company frozen. The cell content in each vial was dispensed into a T75 cell culture flask at a density of 5×10^3 cells/cm^2 and cultured in osteoblast medium (Ref. P60119, purchased from Innoprot, Derio, Spain). Culture medium was changed every 3 days, until reaching approximately 70% confluence. Cells were routinely trypsinized (0.25% trypsin–EDTA solution) for 2-3 minutes at 37°C, centrifuged (200 g, 5 minutes) and re-suspended at a density of 1×10^6 cells in T150 cell culture flasks.

4.5.1.4. Human articular chondrocytes (hACs)

Human articular chondrocytes (hACs) from knee articular cartilage were purchased from Innoprot (Ref. P10970; Derio, Spain), cryopreserved (liquid nitrogen) at a cell density of 5×10^5 cells/vial (1 mL) as primary cultures and delivered by the company frozen. The cell content in each vial was dispensed into a T75 cell culture flask at a density of 5×10^3 cells/cm^2 and cultured in chondrocyte medium (Ref. P60137, purchased from Innoprot, Derio, Spain). Culture medium was changed every 3 days, until reaching approximately 70% confluence. Cells were routinely trypsinized (0.25% trypsin–EDTA solution) for 2-3 minutes at 37°C, centrifuged (200 g, 5 minutes) and re-suspended at a density of 1×10^6 cells in T150 cell culture flasks.

4.5.1.5. U251 glioma cell line

Human neuronal glioblastoma (U251) cell line was generously donated by Prof. Joseph Costello (California University, Neurosurgery Department, San Francisco, USA) and further provided by Prof. Rui M. Reis (Life and Health Science Research Institute, University of Minho, ICVS/3B's – PT Government Associate

Laboratory, Portugal). The use of U251 cell line was approved by the Ethics Committee of University of Minho. Cells were cultured in low glucose Dulbecco's modified Eagle's medium (DMEM), supplemented with 44 mM of sodium bicarbonate, 10 % (v/v) of fetal bovine serum (FBS; Life Technologies, Carlsbad, CA, USA), and 1% (v/v) of antibiotic/antimycotic solution. The U251 cells were incubated in an atmosphere containing 5% CO_2 at 37°C, and the medium changed every 2-3 days. Cells were routinely trypsinized (TrypIE™ Express) for 5 minutes at 37°C, centrifuged at 300 g for 5 minutes, and re-suspended at a density of 1×10^6 cells in T75 cell culture flasks.

4.5.2. Cryopreservation

The cryopreservation of the cells used in this thesis was performed using a Statebourne Biosystem 24 cryogenic tank (Statebourne Cryogenics Ltd., UK). Briefly, cell suspensions of 1×10^6 cells/mL were prepared in a cryopreservation solution, consisting of 10% (v/v) DMSO - Dimethyl Sulfoxide (N182, VWR, Radnor, PA, USA) in FBS, and transferred into 1.5 mL cryovials (479-6841, VWR, Radnor, PA, USA). Then, cell suspensions were gently cooled down, first at -20°C for at least 2 hours and then moved to -80°C freezer for a minimum period of 12 hours. The cryovials were subsequently stored at -176°C in the gas nitrogen phase of the cryogenic tank.

4.5.3. Cell seeding procedures

4.5.3.1. Seeding of L929 cell line on the textile-based scaffolds

In Chapter 5, confluent L929 cells were used to assess the eventual cytotoxicity of the SF textile scaffolds, by using the cells in direct contact with materials. The untreated and surface modified SF textile scaffolds were cut into 16 mm diameter discs using a punch (16 mm inner diameter; Macfer, Portugal) and sterilized by ethylene oxide (ETO; Gas Sterilizer/Aerator, Steri-Vac 5XL, 3M company, St. Paul, MN, USA) before biological examination. The textile scaffolds were immobilized into the bottom of 24-well suspension culture plates (Cellstar, Greiner Bio-One, Austria) using CellCrown™ inserts (Scaffdex, Tampere, Finland). All the procedures were performed under aseptic condition. The confluent cells were detached from the T150 cell culture flasks using trypsin (0.25% trypsin–EDTA solution), centrifuged at 300 g for 5 minutes, counted in a cell counter KOVA® Glasstic® slide 10 chamber with grids (Garden Grove, CA, USA) and diluted in a new cell suspension. The cells were seeded in the scaffolds at a density of 3×10^4 cells/sample using 1 mL of medium/well. The cell-seeded scaffolds were incubated at 37°C, in an incubator with 5% CO_2 atmosphere, for 1, 5, and 24 hours. As controls, TCPs coverslips (13 mm diameter, Sarstedt, Nümbrecht, Germany) and untreated SF membranes were seeded with the L929 cells at 3 x 10^4 cells/sample/mL, using 24-well suspension culture plates. SF membranes were prepared as described above (in Section 4.3.3. of this Chapter) and left 24 hours in PBS solution (the solution was renewed at least 3 times during the process) before cell seeding. The number of cell-seeded scaffolds and controls (TCPs and SF membranes) used for testing with different characterization techniques will be described below.

4.5.3.2. Seeding and osteogenic differentiation of hASCs on the textile-based scaffolds

In Chapter 6, hASCs were cultured in the SF-PET and PET scaffolds in order to evaluate the osteogenic differentiation potential within the proposed scaffolds. The structures were cut into 10 mm diameter discs using a punch (10 mm inner diameter; Macfer, Portugal) and sterilized by ETO before the biological examination. All the procedures were performed under aseptic condition. Before cell seeding, all samples were hydrated in PBS solution overnight in an incubator with 5% CO_2 atmosphere. In the following day, the PBS solution was removed from the scaffolds transferred to 48-well suspension culture plates (Cellstar, Greiner Bio-One, Austria). Confluent hASCs at passage 4 (P4) were detached from the T150 cell culture flasks (TrypIE™ Express), centrifuged at 300 g for 5 minutes, and a cell suspension (P5) was prepared in complete α-MEM medium. The number of cells was counted in a cell counter KOVA® Glasstic® slide 10 chamber with grids. Each scaffold was seeded with 200 µL cell suspension, at a pre-defined density of 4 x 10^5 cells/SF-PET scaffold and 3 x 10^5 cells/PET scaffold, according to the diameter and thickness of each scaffold. The constructs were kept in the CO_2 incubator at 37°C for 3 hours, and then 500 µL of complete α-MEM medium were added to each well. Cell-seeded constructs were left 24 hours in basal complete α-MEM alpha medium, and then 700 µL of fresh culture medium were added to the scaffolds cultured under basal culture conditions. For constructs tested in osteogenic differentiation medium, 700 µL of complete α-MEM medium supplemented with 1 x 10^{-8} mol/L dexamethasone, 50 µg/mL ascorbic acid and 10 mmol/L β-glycerophosphate were added to each well. The culture medium was changed every 2-3 days and samples were retrieved after 1, 7, 14, 21 and 28 days of culture in osteogenic and basal culture conditions. The number of cell-seeded scaffolds used for testing with different characterization techniques will be described below. Scaffolds without cells were kept under the same culture conditions and used as controls.

4.5.3.3. Seeding and chondrogenic differentiation of hASCs on the salt-leached enzymatically crosslinked SF scaffolds

In Chapter 7, hASCs were cultured in the HRP-crosslinked SF scaffolds for chondrogenic differentiation analysis. The scaffolds used for cell seeding were of 8 mm in diameter and 4 mm in height. The scaffolds were sterilized by ETO and before cell seeding were hydrated in Dulbecco's modified Eagle's medium-high glucose (DMEM-HG; Gibco®, Life Technologies, Carlsbad, CA, USA) supplemented with 1% (v/v) antibiotic/antimycotic solution, overnight in the CO_2 incubator at 37°C. In the following day, the scaffolds were transferred to 48-well suspension culture plates after removing the excess of hydration culture medium.

The hASCs used for cell seeding were previously characterized for the expression of the mesenchymal stem cells (MSCs) surface markers CD73, CD90, CD105, CD45 and CD34 by flow cytometry (FACSCalibur flow cytometer, BD Biosciences, San Jose, CA, USA) [105]. Flow cytometry is qualitative and quantitative method for the detection of specific antigens. This method follows the antigen-antibody binding principle, but instead of analyzing the antigen under a fluorescence microscope, it is quantified by flow cytometry. Briefly, the optical detectors of the equipment convert all the detected light into electric signals subsequently converted into the digital data. After the immunostaining process, the single cells pass through a liquid stream, and the fluorophore-labeled antigens are excited by a laser emitting light at specific wavelengths, which are detected and recorded at an optical-to-electronic coupling system [106]. Confluent hASCs (passage 2) were detached with TrypIE™ Express, centrifuged at 300 g for 5 minutes and counted in a cell counter KOVA® Glasstic® slide 10 chamber with grids. A minimum number of 2×10^5 cells was transferred into a 5 mL polystyrene round-bottom tube (Corning Incorporated, Durham, NC, USA) using 100 µL of complete α-MEM medium. Then, 10 µL of each anti-body, anti-CD73 PE, anti-CD90 APC, anti-CD45 FITC, and anti-CD34 PE (BD Biosciences, San Jose, CA, USA), were transferred to the tubes and gently mixed with the cell suspensions. The tubes were left to incubate at RT for 20 minutes in the dark. After incubation, 2 mL of 2% FBS/PBS solution were transferred into each tube and centrifuged at 300 g for 5 minutes. The supernatant was discarded, 500 µL of acquisition buffer (1% formalin/PBS; Thermo Fisher Scientific, Waltham, MA, USA) were mixed in the solutions and tubes were keep at 4°C and protected from light until the analysis. After analysis at the flow cytometer, the results were analyzed with a BD CellQuest software v3.3 and expressed as a percentage of the total number of cells collected within the hASCs population.

For hASCs seeding onto the surface of the hydrated HRP-crosslinked SF scaffolds, a 20 µL cell suspension (P3) was prepared at a density of 3×10^5 cells/scaffold. After 3 hours of incubation at 37°C in the CO_2 incubator, the cell-seeded constructs were completed with 1 mL of DMEM-HG supplemented with 10% (v/v) FBS and 1% (v/v) antibiotic/antimycotic solution, and kept for 24 hours in the CO_2 incubator at 37°C. Cultures were performed both under basal culture conditions (DMEM-HG supplemented with 10% (v/v) FBS and 1% (v/v) antibiotic/antimycotic solution) and in chondrogenic differentiation medium, consisting of DMEM-HG supplemented with 50 µg/mL Ascorbic acid, 40 µg/mL L-Prolin, 1% Insulin-Transferrin-Selenium-G (ITS-G;

Life Technologies, Carlsbad, CA, USA), 100 nM Dexamethasone, 10 ng/mL recombinant human TGF-β1 (PeproTech, London, UK) and 1% (v/v) antibiotic/antimycotic solution. The culture medium was changed every 2-3 days and samples were retrieved after 1, 7, 14, 21 and 28 days of culture in chondrogenic and basal culture conditions. The number of cell-seeded scaffolds used for testing with different characterization techniques will be described below. Scaffolds without cells were kept under the same culture conditions and used as controls.

4.5.3.4. Seeding and co-culture of hOBs and hACs on the bilayered scaffolds

In Chapter 8, the BdTCP and BTCP scaffolds were co-cultured with the hOBs and hACs to simultaneously evaluate the osteogenic and chondrogenic potential within the bilayered structures. As control conditions, monolayered HSF scaffolds were cultured with hACs, and monolayered HSF-dTCP and HSF-TCP scaffolds were cultured with hOBs. The bilayered scaffolds were of 8 mm in diameter and height (HSF layer: 3 mm in height; HSF-dTCP and HSF-TCP layer: 5mm in height). Monolayered HSF scaffolds (8 mm in diameter and 3 mm in height), and monolayered HSF-dTCP and HSF-TCP scaffolds (8 mm in diameter and 5 mm in height) were seeded with hACs and hOBs, respectively, and used as monoculture controls. The scaffolds were sterilized by β-radiation (IONMED sterilization SA, Tarancón, Cuenca, Spain), and before cell seeding were hydrated overnight in the CO_2 incubator in DMEM/F12 (Dulbecco's modified Eagle's medium/Nutrient Mixture F12) GlutaMAX supplement (Gibco®, Life Technologies, Carlsbad, CA, USA), supplemented with 1% (v/v) antibiotic/antimycotic solution. Afterwards, the scaffolds were placed into 24-well culture plates, after removing the excess of medium. Confluent hOBs at P5 were detached from the T150 cell culture flasks (0.25% trypsin–EDTA solution), centrifuged at 200 g for 5 minutes, and a cell suspension (P6) was prepared in DMEM/F12 GlutaMAX supplement, supplemented with 10% (v/v) FBS, 1% (v/v) antibiotic/antimycotic solution, 50 mmol/L Dexamethasone, 1% (v/v) MEM-NEAA (Gibco®, Life Technologies, Carlsbad, CA, USA) and 150 μg/mL Ascorbic acid. The number of cells was counted in a Countess Automated Cell Counter (Invitrogen, Thermo Fisher Scientific, Waltham, MA, USA). HSF-dTCP and HSF-TCP layers were seeded with 10 μL cell suspension at a density of 3 x 10^5 cells/scaffold. The cell-seeded layers and monolayered HSF-dTCP and HSF-TCP constructs were kept in the CO_2 incubator for 3 hours and then completed with 2 mL of supplemented DMEM/F12 Glutamax. The constructs were left in culture for 24 hours for allowing cell adhesion, and then the hACs were seeded (P6) onto the surface of the HSF layers and monolayred HSF scaffolds, following the same procedure and the same cell density described for seeding the hOBs. Then, the co-culture and monoculture systems were left at 37°C in the CO_2 incubator, changing the culture medium every 2-3 days. Samples were harvested after 1, 7 and 14 days of culture and scaffolds without cells were kept under the same culture conditions for being used as controls. The number of scaffolds used for testing with different characterization techniques will be described below.

4.5.3.5. Encapsulation of U251 cells on the SF hydrogels

In Chapter 9, the U251 cells were used to screen the cell encapsulation potential and cytotoxicity within the SF hydrogels. The aqueous SF solution prepared at 16 wt.% was sterilized by UV radiation for 10 minutes in a sterile vertical laminar airflow cabinet (BH-EN 2000 S/D; Faster, Cornaredo, Italy), and stored at 4°C for later use in cell encapsulation. The HRP solution (0.84 mg/mL) and the H_2O_2 solution (0.36 wt.%) were sterile by using filters 0.22 μm sterile (Techno Plastic Products AG, Trasadingen, Switzerland). To perform the cell encapsulation, a shaking water bath (SW23, Julabo, Seelbach, Germany) was necessary to pre-heat the HRP-crosslinking SF solution. U251 cells were detached from the T150 cell culture flasks with TrypIE™ Express, the number of cells was counted using a cell counter KOVA® Glasstic® slide 10 chamber with grids, and a suspension containing 1 x 10^6 cells was placed in a 15 mL centrifuge tube (Thermo Fisher Scientific, Waltham, MA, USA). The cells were subsequently centrifuged at 300 g for 5 minutes, and the supernatant was discarded. In the meantime, the SF/HRP/H_2O_2 solution was prepared in a 5 mL tube (see Section 4.3.4. of this Chapter), and warmed in the water bath at 37°C for about 6 minutes. Then, 1 mL of the warmed solution was transferred to a new 5 mL tube and mixed with the cell pellet in order to obtain a homogeneous cell suspension at 1 x 10^6 cells/mL. The cell-encapsulated SF hydrogels were then produced by transferring 100 μL of the cell suspension into TCPs coverslips (22 mm diameter, Sarstedt, Nümbrecht, Germany), or FEP tubes, placed in 12-well suspension culture plates. The cell suspensions were allowed to completely gelify, at 37°C in the CO_2 incubator for 15 minutes, and then 3 mL of complete low glucose DMEM were transferred into each well. The cell-laden hydrogels were cultured in the CO_2 incubator for 1, 7, 10 and 14 days, and culture medium was changed every 2-3 days. The number of cell-laded hydrogels used for testing with different characterization techniques will be described below. SF hydrogels without cells were kept under the same culture conditions and used as controls.

4.5.4. Metabolic activity and cell viability examination

4.5.4.1. Alamar blue assay

Alamar blue assay was used to evaluate the metabolic activity of cells. Alamar blue is a cell viability reagent that function by using the reducing power of living cells to quantitatively measure their metabolic activity. When cells are metabolically active they maintain a reducing environment within the cytosol. Resazurin, is the active ingredient of AlamarBlue® reagent, blue in color, non-toxic and cell permeable. Upon within the cells, resazurin is reduced to resorufin, a compound that is red in color and highly fluorescent. Viable cells continuously convert resazurin to resorufin, increasing the overall fluorescence and color of the media surrounding the cells [107].

In Chapters 7 and 8, a Alamar blue working solution containing 10% (v/v) AlamarBlue® (BioRad, Hercules, CA, USA) solution and 90% culture medium was prepared and protected from light. At the end of each time-point, constructs washed with PBS solution and transferred to new culture plates. Then, the HRP-crosslinked SF constructs were immersed in 500 µL Alamar blue working solution, whereas the bilayered and monolayered control scaffolds were supplemented with 1 mL/construct. The culture plates were kept in the dark, at 37°C in the CO_2 incubator for 3 hours. The reacted AlamarBlue® was read in a microplate reader (Synergy HT, BioTek, Instruments, USA) using 100 µL supernatant per well, at an excitation wavelength of 530/25 nm and at an emission wavelength of 590/35 nm. Meanwhile, the constructs were washed with PBS solution and returned to the wells in the original culture plates, supplemented with the corresponding culture medium. Three specimens of each group were tested at each time-point. Three independent experiments were performed.

4.5.4.2. ATP bioluminescence assay

In Chapter 9, a CellTiter-Glo® Luminescent Cell Viability Assay (Promega, WI, USA) was used to evaluate the viability and metabolic activity of the U251 cells. This is a homogeneous and reproducible method for the determination of cell viability based on the quantification of the existing Adenosine Triphospate (ATP), which directly quantifies the metabolic activity of cells. This assay was designed for direct use in multi-well culture plates, making it ideal for an automated screening of cells cytotoxicity, and highly reproducible. This assay involves adding a single reagent (CellTiter-Glo® Reagent) directly to the cultured cells, prepared in the corresponding serum-free culture medium. The contact with this reagent, will induce cell lysis and generation of a luminescent signal proportional to the amount of the present ATP. The amount of ATP is directly proportional to the number of cells in culture [108].

The cell-laden hydrogels were prepared in TCPs coverslips (22 mm diameter) were washed with PBS solution and incubated in 1 mL ATP working solution, consisting of CellTiter-Glo® Reagent and serum-free cell culture medium DMEM (without phenol red), in a 1:1 ratio. The specimens were incubated for 30 minutes at RT, in an orbital shaker (KS 260 control, Wilmington, NC, USA). The reacted ATP solution was read in the microplate reader using 100 µL supernatant per well, and the emitted luminescence was detected using a sensivity of 120. Different concentrations of ATP disodium salt solution, ranging between 0 and 2 µmol/L, were used to prepare a standard curve for the calculation of ATP concentration, relating quantity of ATP and luminescence intensity. Three specimens were tested at each time-point. Three independent experiments were performed.

4.5.4.3. Live/Dead staining assay

Calcein-AM/Propidium iodide (PI) staining is a method for the visualization of cell viability and death. In this method, cells are incubated with calcein acetoxymethyl (Calcein-AM), which is a non-fluorescent and cell-permeant derivative of calcein, transported through the cellular membrane. When the intracellular esterases of living cells remove the acetomethoxy group, this probe became green fluorescent. However, it stays non-fluorescent when the acetoxymethyl ester is intact because of the non-active esterases of dead cells. The specific visualization of dead cells, can be performed by incubation with fluorescent (PI), which shows enhanced fluorescence when binding with high affinity to DNA. Contrary to calcein-AM, PI does not permeant the cellular membrane, it binds to the cytoplasmic DNA when the cellular membrane of dead cells is disrupted.

In Chapters 7 and 9, the cell viability and assessed by staining the cells with calcein-AM (1 μg/mL) and propidium iodide (PI; 2 μg/mL), followed by incubation for 10-30 minutes in the dark, at 37°C in the CO_2 incubator. The HRP-crosslinked SF constructs and cell-laded SF hydrogels, prepared in TCPs coverslips (22 mm diameter), were washed with PBS solution and immediately observed under fluorescence microscopy (Calcein-AM ex/em 495/515 nm; PI ex/em 495/635 nm) in the transmitted and reflected light microscope. Images were acquired using the Zen microscope processing software, connected to the digital camera AxioCam MR3. A Z-stack function was used to combine images at different depths into one final image.

4.5.4.4. TUNEL assay

In Chapter 9, the *in situ* Cell Death Detection Kit, Fluorescein (Roche, Basel, Switzerland) was used to assess the U251 cell apoptosis in the cell-laded SF hydrogels and sections of cell-laded hydrogels, in order to evaluate the apoptotic behavior of cells.

This is designed as a precise, fast and simple, non-radioactive technique to detect and quantify apoptotic cell death at a single cell level. This kit can be used in different assay systems, including the one proposed in this thesis, for the detection of individual apoptotic cells in formalin fixed tissue sections. According to this assay, the genomic DNA that is cleaved during apoptosis can be identified by labeling the free 3'-OH termini with modified nucleotides in an enzymatic reaction. Also called as TUNEL reaction, this method is conducted by the terminal deoxynucleotidyl transferase (TdT), which catalyzes the polymerization of the labeled nucleotides to the free 3'-OH DNA ends in a template-independent manner (TdT-mediated dUTP nick end labeling) [109]. The fluorescein labels incorporated in the nucleotides are detected by fluorescence microscopy or flow cytometry.

The cell-laded SF hydrogels prepared in TCPs coverslips (22 mm diameter) were washed with PBS solution and fixed in 10% (v/v) formalin for 1 hour at RT. Samples were permeabilized for 5 minutes with 0.1% (v/v) of Triton X-100/0.1% (w/v) of sodium citrate (Thermo Fisher Scientific, Waltham, MA, USA) solution, on ice, and repeatedly washed in PBS solution before labeling.

Sections of cell-laded hydrogels were prepared with 3.5 μm thick, using a microtome (HM355S Microtome; Thermo Fisher Scientific, Waltham, MA, USA). All samples were first fixed in 10% (v/v) formalin, dehydrated in a graded series of alcohol baths and embedding in paraffin. After sectioning, the paraffin-embedded slides were deparaffinized in xylene (Thermo Fisher Scientific, Waltham, MA, USA), rehydrated, and boiled for 4-5 min in sodium citrate buffer (10 mmol/L Sodium Citrate, pH 6.0) for antigen retrieval.

A TUNEL reaction mixture (label solution and enzyme solution mixed according to the manufacturer's instructions) was applied in the dark to the cell-laded hydrogels and sectioned cell-laded hydrogels in 50 μL/sample, and incubated for 1 hour at 37°C in the CO_2 incubator. The negative controls were incubated in label solution (without TdT) and positive controls were incubated with DNase I recombinant (Amresco, VWR, Radnor, PA, USA) at 20 U/mL, in 50 mmol/L Tris(hydroxymethyl) aminomethane buffer, pH 7.5, 1 mg/mL bovine serum albumin. Samples were conterstained with 4,6-Diamidino-2-phenyindole, dilactate (DAPI; 1 μg/mL, Biotium, CA, USA), and after washing with PBS solution the sectioned cell-laded hydrogels were mounted with a Fluoromount Aqueous Mounting Medium. All samples were observed under fluorescence microscopy (Apoptotic cells ex/em 495/515 nm; DAPI ex/em 358/461 nm) in the transmitted and reflected light microscope. Images were acquired using the Zen microscope processing software, connected to the digital camera AxioCam MR3. A Z-stack function was used to combine images at different depths into one final image.

4.5.5. Cell attachment, morphology and arrangement on the scaffolds and hydrogels

4.5.5.1. Scanning Electron Microscopy (SEM) and Energy Dispersive Spectroscopy (EDS) analysis

In Chapters 5, 6 and 8, cell morphology and distribution were assessed by SEM, as described above in Section 4.4.1.1. of this Chapter. At the end of each time-point, the cell-seeded constructs were washed with PBS solution and fixed in 2.5% (v/v) glutaraldehyde solution prepared in PBS, for 1 hour at 4°C. Samples were further dehydrated through increasing concentrations of ethanol solutions (30% - 100% v/v) for 15 minutes each concentration, treated with hexamethylidisilazane (HMDS; Electron Microscopy Sciences, USA) and left to dry at RT in the hood. Prior observations, samples were sputter-coated with gold (Fisons Instruments, Sputter Coater SC502, United Kingdom) in Chapters 5 and VI, or gold-palladium (60:40; Polaron SC 7640, Watford, UK) in Chapter 8. The same SF-PET and PET constructs used for SEM analysis in Chapter 6, were coated with graphite for elemental characterization using EDS analysis (ink-eXL-II, Oxford, UK). Three samples of each group were tested for each time-point.

4.5.5.2. Optical Projection Tomography (OPT)

In Chapter 9, an OPT system was used to evaluate the U251 cells distribution within the SF hydrogels, following the same procedure described in Section 4.4.1.5 of this Chapter. At the end of each time-point, the cell-laded SF hydrogels prepared in FEP tubes were removed from the culture medium, rinsed with PBS solution and fixed in 10% (v/v) formalin for 10 minutes at 4°C. Afterwards, the specimens were washed in PBS solution and immersed in an index-matching liquid (distilled water) until further analysis. Two samples were prepared for each time-point.

4.5.5.3. Selective Plane Illumination Microscopy (SPIM)

Selective Plane Illumination Microscopy (SPIM) was used in Chapter 9 to analyze the U251 cells arrangement within the SF hydrogels by tracking the cells using fluorescence labeling. SPIM technique allows to achieve high resolution 3D images and reconstructions of samples using high penetration depths and high imaging speeds. At the same time, this technique can offer an improvement to other fluorescence microscopy techniques, in which only a focused sheet of light serves to illuminate the sample. Using SPIM, the high depth penetration, low bleaching and high acquisition speeds make the light-sheet microscopy ideally suited for extended time-lapse experiments in biological samples [110].

Cell-laded SF hydrogel samples were prepared in FEP tubes and after each time-point, were removed from the culture medium and washed with PBS solution. Then, samples were incubated with calcein-AM (1 μg/mL) for 30 minutes in the dark, at 37°C in the CO_2 incubator. After incubation, samples were washed in PBS solution, fixed with 10% (v/v) formalin for 10 minutes at 4°C, and washed again with PBS solution. Afterwards, samples were incubated with phalloidin-TRITC (5 μg/mL) for 1 hour at 37°C in the CO_2 incubator, in order to visualize the cytoskeleton of cells. Phalloidin is a rigid bicyclin heptapeptide lethal toxin which binds and stabilizes actin filaments (F-actin). After washing with PBS solution, the cell-laded hydrogels inside

FEP tubes were stored in the dark, in 5 mL tubes completely immersed in PBS solution. For SPIM analysis, the FEP tubes were supported by a 4 axis-positioning device (Picard Industries, USA) and the plane of interest in each sample was found by using the 4 available axes (3 translational, 1 rotational). The fluorophore distribution in the samples was acquired my translating the sample along the detection axis while taking images at constant intervals (Calcein-AM ex/em 495/515 nm; Phalloidin-TRITC ex/em 550/575 nm). The images were collected with an sCMOS camera. The samples were imaged using an exposure time of 300 ms, except for samples from day 10 and day 14 (exposure time of 100 ms to avoid overexposure). Images were taken in 3 µm z-steps across depth of 500 µm. Due to narrow field of view, separate stacks were acquired to cover the width of the sample. The stacks were stitched together in post processing to create a wider field of view. The stitched stacks were then visualized using Avizo software.

4.5.6. Biochemical characterization

4.5.6.1. DNA quantification

In Chapters 5, 6, 7, 8 and 9, the proliferation of the seeded cells into the scaffolds and encapsulated cells within the SF hydrogels was analyzed by the total double strained DNA (dsDNA) content using the Pico-Green® dsDNA quantification assay. This colorimetric assay employs fluorescence to evaluate cell proliferation through the measurement of the dsDNA of samples. When the PicoGreen® fluorescent marker is added to the solution, it specifically binds to the double-stranded DNA emitting fluorescence, read at 480 nm (excitation) and 520 (emission). DNA content was further determined through a DNA standard curve, prepared using standard dsDNA solutions with concentrations ranging from 0 to 2 µg/mL.

In Chapters 5, 6, 7 and 8, constructs were removed from the culture medium at the end of each time-point, washed with PBS solution, and transferred into 1.5 mL centrifuge tubes containing 1 mL of ultrapure water. The samples were placed for 1 hour at 37°C in the CO_2 incubator, and stored at -80°C in the freezer until further analysis (at least 6 hours befor the DNA quantification assay).

In Chapter 9, the cell-loaded SF hydrogels prepared in TCPs coverslips (22 mm diameter) were washed with PBS solution, transferred into 1.5 mL centrifuge tubes, incubated at 70°C in the oven for 30 minutes, and then frozen at -80°C in 1 mL of ultrapure water.

For the DNA quantification, the samples were defrosted at RT, and then underwent ultrasonication treatment for 1 hour at 37°C, controlled temperature, to release the DNA from the scaffolds. The double-stranded DNA (dsDNA) was quantified by using the Quant-iT™ Pico-Green® dsDNA kit 2000 assays (Thermo Fisher Scientific, Waltham, MA, USA) according to the manufacturer's instructions. Briefly, 28.7 µL of sample or standard were added to a 96-well white opaque plate, mixed with 100 µL of 1X Tris-EDTA buffer (10 mmol/L Tris-HCl, 1 mmol/L EDTA, pH 7.5) and 71.3 µL of 1X Quant-iT™ PicoGreen® reagent, in a total volume of 200 µL. The plate was incubated at RT for 10 minutes and read in the microplate reader (ex/em 485/528). Three specimens of each group were tested at each time-point. Three independent experiments were performed.

4.5.6.2. Alkaline phosphatase (ALP) activity

In Chapters 6 and 8, the same lysates used for DNA quantification were used for ALP activity quantification. ALP activity from the constructs was quantified by the specific conversion of p-nitrophenyl phosphate (pNPP) into p-nitrophenol (pNP) [111]. The pNPP solution was prepared by dissolving in 1 mol/L diethanolamine buffer solution (pH 9.8, adjusted by hydrochloric acid). During reaction, the pNPP is hydrolyzed by the ALP of the supernatants and the yellow pNP is formed. For this, 20 µL of supernatant were mixed with 60 µL 0.2% (w/v) pNPP in a 96-well culture plate, and incubated for 45 minutes at 37°C in the CO_2 incubator. After reaction, 80 µL of stop solution, consisting of 2 mol/L NaOH solution (Merck, Berlin, Germany) solution and 0.2 mmol/L ethylenediaminetetraacetic acid (EDTA) in distilled water, were added to each well. The absorbance of pNP in each well was read at 405 nm in the microplate reader, and ALP concentration was determined from a standard curve prepared using standard solutions ranging from 0 to 0.2 µmoL/mL. For ALP activity determination, the ALP concentration of each sample was normalized by their corresponding DNA contents. Three specimens of each group were tested at each time-point. Three independent experiments were performed.

4.5.6.3. Calcium quantification

In Chapter 6, the inorganic calcium produced at the SF-PET and PET constructs was determined by using a o-cresolphthalein-complexon method with colorimetric detection (Roche Cobas kit, Roche Diagnostics, Germany). This method is used for the quantitative determination calcium from *in vitro* samples, and is based on the reaction of the calcium present in the samples with the o-cresolphthalein-complexon in alkaline environment. This reaction will be noticed by the formation of a purple complex, quantified photometrically at 570 nm [112].

At the end of each time-point, samples were removed from the culture medium, washed with PBS solution, and transferred into 1.5 mL centrifuge tubes containing 1 mL hydrochloric acid (HCl; 6 mol/L, Analar Normapur, Germany). The dissolved samples were stored at 4°C until further analysis. In a 96-well culture plate, 175 µL of ethanolamine (1 mol/L, pH 10.6) were mixed with 10 µL of sample and incubated for 5 min at RT. Then, 70 µL of o-cresolphthalein-complexon (0.3 mmol/L, hydroxy-8-quinoleine 13.8 mmol/L, HCl 122 mmol/L) were added to each well and incubated for 2 minutes at 37°C in the microplate reader. The absorbance in each well was read at 570 nm, and calcium concentration was determined from a standard curve prepared using serial dilutions of a 200 mg/L calcium chloride ($CaCl_2$) stock solution (Merck, Berlin, Germany). Three samples were tested in each group at every time-points. Three independent experiments were performed.

4.5.6.4. Glycosaminoglycans (GAGs) quantification

The glycosaminoglycans (GAGs) matrix production was evaluated in Chapters 7 and 8, by performing a dimethylmethylene blue (DMB) assay. Using this method, the GAGs produced in the constructs are solubilized through exhaustive proteolytic digestion using papain. This enzyme acts by cleaving the core protein of GAGs and then the GAGs content is measured by using the dimethyl methylene blue (DMB) colorimetric assay [113].

In Chapter 7, the GAGs quantification was performed using the same samples prepared for DNA assay. After removing from the lysates used for DNA quantification, the constructs were transferred into new 1.5 mL centrifuge tubes containing 1 mL papain digestion solution prepared by dissolving in 50 mL of digestion buffer (200 mmol/L of phosphate buffer containing 1mmol/L EDTA, pH 6.8), 25 mg of papain and 48 mg of n-acetyl cysteine. In Chapter 8, the BdTCP, BTCP and monolayered control samples, after removed from the culture medium and washed with PBS solution, were transferred into 1.5 mL centrifuge tubes containing 1 mL papain digestion solution. Afterwards, samples were digested overnight at 60°C in a shaking water bath (100 rpm). Then, the samples were centrifuged at 13,000 rpm for 10 minutes and the supernatants collected to new 1.5 mL centrifuge tubes. The GAGs content in each sample was determined by spectrophotometry with a DMB solution. This solution was prepared by dissolving 16 mg DMB powder in 900 mL distilled water containing 3.04 g glycine and 2.73 g of sodium chloride (NaCl; Panreac Química SAU, Barcelona, Spain), pH 3.0. Briefly, the 900 mL of distilled water were mixed with 3.04 g glycine and 2.73 g of sodium chloride. In the meantime, 16 mg of DMB were dissolved in 5 mL of absolute ethanol in a dark glass beaker, for a least two hours. The dissolved DMB was added to the NaCl-glycine solution, and pH adjusted to 3.0 with 1 mol/L of HCl. The final volume was adjusted to 1 L with distilled water, and the solution was stored at RT in the dark. For GAGs detection, 20 µL of sample or standard were transferred to a 96-well culture plate, and mixed with 250 µL of DMB solution. The optical density (OD) was measured in each well plate at 530 nm, and GAGs content was determined from a standard curve prepared using serial dilutions of a 50 µg/mL chondroitin sulfate stock solution. Three samples of each group were tested at each time-point. Three independent experiments were performed.

4.5.6.5. Collagenous proteins quantification

In Chapters 7, a Sirius red/Fast Green collagen staining kit (Chondrex, Redmond, WA, USA) was used to for the semi-quantification of collagen and non-collagenous proteins in the cell-seeded HRP-crosslinked SF constructs, according to the manufacturer's instructions. In this assay, Sirius red dye specifically binds to the helical structure of fibrillary collagen, whereas Fast green binds to the non-collagenous proteins of cultured cells. After each time-point, samples were removed from the culture medium, washed with PBS solution and fixed with 10% (v/v) formalin for 20 minutes at RT. Samples were stored in PBS solution at 4°C, until analysis. Sirius red/Fast Green staining was performed by immersing the samples in 500 μL of dye solution (0.1% (v/v) Sirius red and 0.1% (v/v) Fast green solution saturated with picric acid), incubated for 30 minutes at RT. The dye solution was carefully removed from the samples by washing with distilled water until the fluid is colorless. Then, samples were transferred to new 48-well culture plates and a total volume of 2 mL of dye extraction buffer (0.05 mol/L NaOH solution in methanol) were applied to the samples in 500 μL each time, until the color was completely eluted from the samples. The eluted dye solutions were collected to 5 mL tubes, and read in a microplate reader using 100 μL supernatant per well, using a OD of 540 nm and 605 nm. To calculate collagen content, the OD 540 was first corrected by subtracting the contribution of the Fast Green at 540, which is 29.1% of the OD 605. The color equivalence (OD value/μg collagen) is 0.0378 at OD 540. Three samples of each group were tested at each time-point. Three independent experiments were performed.

4.5.7. Gene expression profiles

4.5.7.1. RNA isolation and first-strand cDNA synthesis

The expression of mRNA for specific osteogenic and chondrogenic-related genes of interest, was measured by real-time PCR analysis. Different extraction kits were used for total RNA isolation in Chapters 6 and 7. Extraction of high-quality RNA is a crucial step in gene expression profiling, and previous studies have shown that using kits for RNA extraction allows to obtain a higher purity and efficiency in the process [114].

In Chapter 6, a RNeasy Mini Kit (Qiagen, Hilden, Germany) was used for total RNA extraction from the SF-PET and PET constructs, following the manufacturer's instructions. After each time-point, constructs were washed with PBS solution, and collected to 500 μL of β-mercaptoethanol solution in RLT buffer (dilution

1:100) and stored at -80°C until further analysis. Afterwards, samples were defrosted at RT and then underwent ultrasonication treatment for 15 minutes at 20°C to ensure complete lysis and collection of the cells from constructs. Briefly, 500 µL of 70% (v/v) ethanol solution were added to the lysates, and the total volume in each tube transferred to RNeasy spin columns, attached to 2 mL collection tubes. The solutions were centrifuged for 30 seconds at 8,000 rpm. Then, a series of buffer solutions were added to the columns, 700 µL of RW1 buffer solution and 500 µL RPE washing buffer, and centrifuged for 30 seconds at 8,000 rpm. This last step was repeated, but with 2 minutes of RPE washing buffer centrifugation in order to completely remove the ethanol used for diluting the buffer and completely dry the columns membrane. The flow collected in the tubes was discarded during the process. As last step, the RNA of each sample was eluted by placing the RNeasy spin columns in 1.5 mL centrifuge tubes and adding 30 µL of RNAse-free water (Gibco®, Life Technologies, Carlsbad, CA, USA), centrifuged for 1 minute at 8,000 rpm.

In Chapter 7, a Direct-zol™ RNA MiniPrep kit (Zymo Research, Irvine, CA, USA) was used to extract the total RNA from the HRP-crosslinked SF constructs, following the manufacturer's instructions. After each time-point, constructs were washed with PBS solution, and collected to 700 µL of TRI Reagent® (T9424) and stored at -80°C until further analysis. Afterwards, samples were defrosted at RT and ultrasonicated for 15 minutes at 20°C. For RNA extraction, 700 µL of absolute ethanol were added to the lysates, and the total volume in each tube transferred to spin columns. The solutions were centrifuged for 30 seconds at 16,000 rpm. Then, 400 µL of RNA wash buffer and Direct-zol RNA pre-wash buffer were added to the columns and centrifuged for 30 seconds at 16,000 rpm. The Direct-zol RNA pre-wash buffer was added twice, followed by 700 µL of RNA wash buffer centrifuged for 2 minutes at 16,000 rpm. The flow collected in the tubes was discarded during the process. As last step, the RNA of each sample was eluted by placing the RNeasy spin columns in 1.5 mL centrifuge tubes and adding 25 µL of RNAse-free water, centrifuged for 30 seconds at 16,000 rpm.

In Chapters 6 and 7, the RNA quantity and purity were assessed with a NanoDrop ND-1000 spectrophotometer (NanoDrop Technologies, USA). Samples with a 260/280 ratio between 1.6 and 2.0 were used for first-strand complementary DNA (cDNA) synthesis, performed with the qScript cDNA Synthesis kit (Quanta Biosciences, MD, USA) and using a MiniOpticon real-time PCR detection system (BioRad, CA, USA). Briefly, 100 ng of the total RNA of each sample were used to generate single-stranded cDNA by random priming with qScript Reverse Transcriptase (RT). A reaction mixture consisting of 4 µL qScript Reaction Mix, 1 µL qScript Reverse Transcriptase (RT), RNA template (100 ng) and nuclease-free water was prepared, in a final volume of 20 µL. The single-strand cDNA synthesis occurred by incubating the complete reaction mixture for 5 minutes at 22°C, followed by 30 minutes at 42°C and terminated with an incubation of 5 minutes at 85°C.

4.5.7.2. Real-time polymerase chain reaction (Real-time PCR)

Real time polymerase chain reaction (PCR) was used in Chapters 6 and 7, as technique for detecting and measuring PCR products of interest [115]. For starting the RNA is reverse-transcripted into a single-strand cDNA chain using a reverse transcriptase polymerase chain reaction (RT-PCR), as described above in Section 4.5.7.1. of this Chapter. Afterwards, the oligonucleotide primers (specific for the target genes) are allowed to anneal to the template cDNA, and with a Taq polymerase starting reaction, a double-strand cDNA is produced. The three steps process of denaturation, primer annealing and extension are repeated in at least 40 cycles to yield PCR products, detected in real-time as the reaction progresses. The real-time detection of PCR products is made by including in the reaction a fluorescent molecule that reports an increase in the amount of DNA. The measured fluorescence reflects the amount of amplified product in each reaction cycle.

In Chapters 6 and 7, the amplification of the target cDNA for real-time PCR quantification was performed using the PerfeCta SYBR Green FastMix kit (Quanta Biosciences, Gaithersberg, MD, USA), according to the manufacturer's instructions. Briefly, 1 μL of single-strand cDNA products, 1 μmol/L of primer forward and reverse, 10 μL PerfeCta SYBR Green FastMix and nuclease-free water, in a final volume of 20 μL, were prepared as reaction mixture. The primers sequence, specific for each gene of interest, are described in Table 4-1. Each real-time PCR run was carried out with an initial incubation at 95°C for 2 minutes, followed by 45 cycles of denaturation (95°C, 10 seconds), annealing (specific for each gene, 25 seconds) and extension (72°C, 30 seconds) in a Mastercycle® ep realplex real-time PCR system (Eppendorf, Hamburg, Germany). The transcripts expression data were normalized to the endogenous housekeeping gene glyceralde-hyde-3-phosphate-dehydrogenase (GAPDH) and the relative quantification was calculated using as calibrators he results obtained for each target gene at day 7 (Chapter 6) and day 1 (Chapter 7) in basal culture conditions, according to the Livak ($2^{-\Delta\Delta CT}$) method [116]. Briefly, the ΔCt values were obtained by the difference between the Ct values of the target genes and the GAPDH gene. These values were then normalized by subtracting the ΔCt value of the calibrator samples, in order to obtain the ΔΔCt values.

Table 4-1. Primers list for the studied genes.

Gene	Forward Primer	Reverse Primer	Accession number
GAPDH	TGCACCACCAACTGCTTAGC	GGCATGGACTGTGGTCATGAG	NM_001256799.2
Osteocalcin (OCN)	CTGGAGAGGAGCAGAACTGG	GGCAGCGAGGTAGTGAAGAG	NM_199173.5
Osteopontin (OPN)	TGAAACGAGTCAGCTGGATG	TGAAATTCATGGCTGTGGAA	NM_000582.2
Sox-9 (SOX9)	TACGACTACACCGACCACCA	TTAGGATCATCTCGGCCATC	NM_000346.3
Aggrecan (ACAN)	TGAGTCCTCAAGCCTCCTGT	TGGTCTGCAGCAGTTGATTC	NM_001135.3
Collagen type I/Col I (COL1A1)	AAGAACCCCAAGGACAAGAG	GTAGGTGATGTTCTGGGAGG	NM_000088.3
Collagen type II/Col II (COL2A1)	GACAATCTGGCTCCCAAC	ACAGTCTTGCCCCACTTAC	NM_001844.4

4.5.8. Histological analysis

Histological analysis was performed on *in vitro* samples in Chapters 7 and 8. This analysis provides increased contrast to better evaluate the morphology, structure and distribution of biological samples. All samples were first fixed in 10% (v/v) formalin, dehydrated in a graded series of ethanol baths and xylene, and embedding in paraffin. Sections of 20 μm thick were prepared using the microtome. After sectioning, the specimens were transferred to glass slides and stored until further analysis. Paraffin-embedded sections were deparaffinized in xylene (Thermo Fisher Scientific, Waltham, MA, USA), rehydrated and stained following the protocols described below. As last step, sections were washed in distilled water, dehydrated and mounted in Entelan (Millipore, USA), unless otherwise stated. Slides were observed under transmitted microscopy, using the transmitted and reflected light microscope. Images were acquired using the Zen microscope processing software, connected to the digital camera AxioCam MRc5.

4.5.8.1. Haematoxylin and Eosin (H&E) staining

Hematoxylin and eosin (H&E) is the most common staining used in histology, since it can be used for visualizing different cell components. Hematoxylin is a base that preferentially colors the acidic components of cells in blue, including some proteins, nuclei, DNA and RNA, or the endoplasmic reticulum. Eosin, as an acid, dyes the basic components of cells with a pink color, such us, the cytoplasm or collagen fibrils. In Chapter 8, representative sections of the BdTCP, BTCP and monolayered constructs (control) were stained with H&E following standard protocol.

4.5.8.2. Alizarin red staining

Alizarin red staining is performed to detect calcium deposition and the mineralization pattern on bone matrix producing samples. This method can be applied for *in vitro* cell cultured fixed in formalin, or paraffin embedded tissue sections.

In Chapter 6, this staining was used as a complementary test to the inorganic calcium quantification method, in order to assess the ECM mineralization in the SF-PET and PET constructs. After each time-point, samples were carefully washed with PBS solution and fixed in 10% (v/v) formalin for 1 hour at RT. Afterwards, samples were rinsed in PBS solution and stained for 5 minutes with 2% (w/v) alizarin red solution (Merck, Berlin, Germany) in ultrapure water, followed by washing with distilled water until remove the excess of dye and the fluid is colorless. Samples were observed under a stereo microscope (Stemi 1000, Zeiss, Jena, Gernamy), using the light reflected from the surface of samples and images captured using a digital camera (Canon PowerShot, G11).

In Chapter 8, representative sections of the BdTCP, BTCP and monolayered control constructs were stained with alizarin red, following the same protocol. After washing in distilled water, slides were dehydrated in acetone (VWR BDH Prolabo, Briare, France), acetone-xylene (1:1), and xylene.

4.5.8.3. Masson's trichrome staining

In Chapter 7, representative sections of the HRP-crosslinked SF constructs were stained with Masson's trichome, using a Bio-Optica staining kit (Milan, Italy) according to the manufacturer's instructions. In this kit, four different dyes are used, weigert's iron hematoxylin for nuclei, picric acid for erythrocytes, a mixture of acid dyes for cytoplasm and aniline blue for connective tissue. As results, usually the biological samples are stained in black for nuclei, red for cytoplasm and blue or green for collagen. Briefly, the sections were stained with six reagents from the kit, using different staining periods and intermediate washes with distilled water.

4.5.8.4. Sirius red/Fast green staining

In Chapters 7 and 8, the Sirius red/Fast green collagen kit was also applied as described above in Section 4.5.6.5 of this Chapter, for staining the collagen content in representative sections of the constructs with Sirius Red dye and counterstain the non-collagenous proteins with Fast Green.

4.5.8.5. Alcian blue staining

In Chapter 7, representative sections of the HRP-crosslinked SF constructs were stained with Alcian Blue

8GX (1% v/v in 0.5 mol/L acetic acid glacial; VWR BDH Prolabo, Briare, France), following standard protocol. Alcian Blue 8GX is a polyvalent basic dye, used to stain acidic polysaccharides such us GAGs in cartilage tissue or cartilage matrix producing samples.

4.5.8.6. Safranin-O staining

In Chapters 7 and 8, complementarily to the Alcian blue staining, Safranin-O (0.1% v/v; Honeywell Fluka, Morris Plains, NJ, USA) was also used to stain the GAGs in the constructs ECM. This is a basic dye that stains with varying shades of red the growth plate of cartilage or articular cartilage tissue, including proteoglycans, chondrocytes and type II collagen. The intensity of the red staining will be proportional to the proteoglycans content in the tissue or cell matrix. Sections were counterstained with Gill-2 hematoxylin (Thermo Scientific, Waltham, MA, USA; dilution 1:2 in distilled water) and Fast green (0.02% v/v; Honeywell Fluka, Morris Plains, NJ, USA), to simultaneously distinguish the nuclei of cells and the non-collagenous proteins of the ECM.

4.5.9. Immunocytochemistry

Immunocytochemistry is a detection method used for the visualization of specific antigens in cells, detected by antigen-antibody binding [117]. The principle of this technique can rely in the use of specific fluorescent-labeled secondary antibodies that bind to the primary antibodies, visualized under a fluorescence microscope. This procedure involves some preliminary steps after cell culturing, including cell fixation, cell membrane permeabilization, enables the antibodies to enter into the cells when searching for intracellular antigens, and a blocking step that blocks unspecific bindings of antibodies. These steps are intercalated with washing steps to remove unbound antibodies.

In Chapter 6, the SF-PET and PET constructs were permeabilized with 0.2% (v/v) of Triton X-100/PBS for 15 minutes, except those prepared for collagen type I (Col I) identification, and blocked with 3% (w/v) bovine serum albumin solution (BSA) in PBS for 45 minutes at RT. Constructs were incubated with 50 µL of primary antibodies (Table 4-2) overnight at 4°C and with 50 µL of secondary antibodies Alexa Fluor 488 or 594 for 2 hours in the dark, according to the host of the primary antibody. All antibodies were prepared in 1% (w/v) BSA/PBS solution. Between antibodies incubations, the constructs were washed twice with PBS solution for 10 minutes. Constructs were counterstained with DAPI (1 µg/mL), incubated for 10 minutes in the dark. Samples were observed under a Zeiss LSM 510 Meta confocal laser scanning microscope. Confocal microscopy is based on the same principle as the fluorescence microscope, but it has a special pinhole in the detector system that eliminates out-of-focus (background), being ideal for analyzing natural origin materials with auto-fluorescence, including silk.

Table 4-2. Antibodies used for immunocytochemistry of *in vitro* samples.

Antibody	**Type**	**Reference**	**Host**	**Dilution**	**Clonality/Reactivity**
OCN (Abcam, Cambridge, UK)	Primary	Ab13418	Mouse	1:25	Monoclonal mouse/Human
OPN (Abcam, Cambridge, UK)	Primary	Ab14175	Rabbit	1:25	Monoclonal rabbit/Human
Col I (Abcam, Cambridge, UK)	Primary	Ab292	Rabbit	1:50	Polyclonal Rabbit/Human
Antibody to Rabbit IgG – H&L (Alexa Fluor 488) Thermo Scientific, Waltham, MA, USA)	Secondary	A21206	Donkey	1:100	Polyclonal Donkey/Rabbit
Antibody to Mouse IgG – H&L (Alexa Fluor 594) (Thermo Scientific, Waltham, MA, USA)	Secondary	A21203	Donkey	1:100	Polyclonal Donkey/Mouse

4.5.10. Immunohistochemistry

Immunohistochemistry is a method that also enables the visualization of specific antigens in cells, using the same principle of antigen-antibody binding, combined with fluorescent-labeled secondary antibodies, as in the immunofluorescence technique [117]. However, this technique involves an additional step of antigen retrieval, to unmask the antigen (masked by fixation) and enable antigen-antibody binding.

In Chapters 7 and 8, the antigen retrieval on the representative sections of the constructs was performed with 50 µL of 0.5% (w/v) pepsin in 5 mmol/L HCl for 30 minutes at 37°C. Sections were permeabilized with 1% (v/v) Triton X-100/PBS for 10 minutes, and blocked in 3% (w/v) BSA/PBS for 1 hour at RT. Sections were incubated with 50 µL of primary antibodies (Table 4-3) overnight at 4°C (18 hours minimum), and with 50 µL of secondary antibodies Alexa Fluor 488 or 594 for 2 hours and 30 minutes in the dark, according to the host of the primary antibody. All antibodies were prepared in 1% BSA/0.2%Triton in PBS. Between antibodies incubations, the constructs were washed twice with PBS solution for 10 minutes. Sections were counterstained with DAPI (2 µg/mL), incubated for 15 minutes in the dark. After washing with PBS solution, sections were mounted with a Fluoromount Aqueous Mounting Medium and observed under fluorescence microscopy (Alexa Fluor 488 ex/em 488/517 nm; Alexa Fluor 594 ex/em 594/618 nm) in the transmitted and reflected light microscope. Images were acquired using the Zen microscope processing software, connected to the digital camera AxioCam MR3.

Table 4-3. Antibodies used for immunohistochemistry of *in vitro* samples.

Antibody	Type	Reference	Host	Dilution	Clonality/Reactivity
OPN (Abcam, Cambridge, UK)	Primary	Ab14175	Rabbit	1:25	Monoclonal rabbit/Human
Sox-9 (Milipore S.A.S, Molsheim, France)	Primary	AB5535	Rabbit	1:10	Polyclonal rabbit/Human
ACAN (Thermo Scientific, Waltham, MA, USA)	Primary	MA316888	Mouse	1:5	Monoclonal mouse/Human
Col II (Chemicon, Temecula, CA, USA)	Primary	MAB1330	Mouse	1:5	Monoclonal Mouse/Human
Antibody to Mouse IgG – H&L (Alexa Fluor 488) (Thermo Scientific, Waltham, MA, USA)	Secondary	A21202	Donkey	1:100	Polyclonal Donkey/Mouse
Antibody to Rabbit IgG – H&L (Alexa Fluor 488) (Thermo Scientific, Waltham, MA, USA)	Secondary	A21206	Donkey	1:100	Polyclonal Donkey/Rabbit
Antibody to Rabbit IgG – H&L (Alexa Fluor 594) (Thermo Scientific, Waltham, MA, USA	Secondary	A21207	Donkey	1:100	Polyclonal Donkey/Rabbit

4.5.11. Biomechanical analysis

In Chapter 7, the DMA analysis was performed on the HRP-crosslinked SF constructs after culturing for 28 days with human adipose-derived stem cells in chondrogenic differentiation medium (procedure described in Section 4.5.3.3. of this Chapter). The DMA equipment and measurement parameters were the same as described above (see Section 4.4.4.3. of this Chapter). The experiments were performed under a constant strain amplitude of 50 μm. HRP-crosslinked SF were kept under the same culture conditions and used as controls. At least four samples were tested in each group, presenting a diameter and height of 8 and 4 mm, respectively.

4.6. *In vivo* studies

Animal manipulation for *in vivo* studies was performed only be qualified personnel and following the Principle of the 3Rs. The host institution is authorized by the DGVA (Direção Geral de Alimentação e Veterinária) to perform animal experimentation. All animal protocols were conducted in accordance with the Portuguese legislation (Portaria no1005/92) and international standards on animal welfare as defined by the EC Directive 2010/63/EU.

4.6.1. Chick chorioallantoic membrane (CAM) assay

Chick chorioallantoic membrane (CAM) is composed of a multilayer epithelium, including the ectoderm at the air interface, mesoderm or stroma and endoderm at the interface with the allantoic sac. This membrane contains ECM proteins, such us, fibronectin, laminin, collagen type I and integrins, and the presence of such proteins mimics the physiological cancer environment. For that reason, CAM assay have been widely used to study tumor cell invasion and angiogenesis. The highly-vascularized nature of the CAM greatly promotes efficiency for materials grafting, high reproducibility, simplicity and cost effectiveness, being an attractive and well established model for studying angiogenesis and cell invasion [118].

In Chapter 6, CAM assay was performed to evaluate the angiogenic potential of the SF-PET and PET scaffolds. SF-PET scaffolds with 9 mm diameter and 3 mm height, and PET scaffolds with 9 mm diameter and 2.5 mm height, were used for CAM implantation. The scaffolds were sterilized by ETO and all the procedures were performed in aseptic conditions, in a sterile vertical laminar airflow cabinet to minimize contaminations. Gelatin sponges with 9 mm diameter and 3 mm height were prepared from sterile Cutanplast® sponge (Mascia Brunelli S.p.a., Milan, Italy) and used as negative control for angiogenesis. A total number of 120 white fertilized chicken eggs (Pintobar, Amares, Portugal) were incubated at 37°C (Laboratory Incubator model B8420; Termaks, Bergen, Norway) for 3 days for embryonic growth. A small hole was created in the pointed end of the eggs to allow dissociation of the CAM from the shell membrane. Then, a circular window was made into the egg shell, in order to evaluate embryo viability and access the CAM. The shell opening was sealed with transparent tape (50 x 30 mm, Staples) to prevent dehydration and the eggs were returned to the incubator at 37°C until implantation of the scaffolds. After 10 days of embryonic development, the sterile scaffolds were implanted into the CAM and the shell windows were again sealed with transparent tape for incubation until day 14. Afterwards, the embryos and their membranes were fixed *in ovo*, using 4% (v/v) paraformaldehyde (PFA; Merck, Berlin, Germany) solution onto the CAM surface, for 10 minutes at -80°C in a ultra-low freezer. The implanted specimens and adjacent CAM region were dissected using surgical forces and scissors, and transferred to 6-well culture plates in 4% (v/v) PFA for analysis. *Ex ovo* images were acquired using the AxioVision imaging software (release 4.8; Zeiss, Jena, Gernamy) connected to an AxioCAM ICc1 digital camera (Zeiss, Jena, Gernamy) attached to a stereomicroscope (Stemi 2000-C; Zeiss, Jena, Gernamy). A minimum number of 18 samples were tested for each group. Three independent CAM experiments were performed.

4.6.2. Subcutaneous implantation

In Chapters 6 and 7, scaffolds were tested for the *in vivo* biological performance by subcutaneous implantation in Hsd:ICR (CD-1) mice, for 14 and 28 days. Mice of 5 weeks old were used in the studies, always manipulated in aseptic conditions.

In Chapter 6, six mice with an average weight of 25-30 g were used for the implantation of the SF-PET scaffolds (9 mm in diameter and 3 mm in height) and PET scaffolds (9 mm in diameter and 2.5 mm in height). Each mouse was anesthetized by intraperitoneal injection of ketamine (25 mg/kg) and medetomidine (0.15 mL/kg) for anesthesia, cephalexin (15 mg/kg) as antibiotic, and bupivacaine and pethidine (5-10 mg/kg) as analgesic. The hair of the mice was shaved in the area of implantation and disinfected with 70% (v/v) ethanol and iodine. In each mouse, four skin incisions (1 cm length) were made in the dorsal midline, two close from the head (CH) and two far from the head (FH). Afterwards, two sterile scaffolds from each group were implanted subcutaneously into the respective pocket, followed by skin suture. A total number of twelve scaffolds from each group were used for implantation. After each time-point, the mice were euthanized by injection of overdose pentobarbital sodium (250 mg/kg) and the implanted specimens were collected for analysis.

In Chapter 7, twelve mice with an average weight of 27-32 g were implanted with the HRP-crosslinked SF scaffolds (8 mm in diameter and 4 mm in height). The anesthetic solution administered intraperitoneally was composed of Domitor INJ 1mg/mL (Medetomidine 1 mg/Kg) and Imalgene 1000 INJ 100 mg-mL (Ketamine 75 mg/Kg). The hair of the mice was shaved in the area of implantation and disinfected with iodine. In each mouse, two skin incisions (1 cm length) were made in the dorsal midline, CH and FH, and the specimens were implanted on both right and left sides into the respective pockets, followed by skin suturing. A total number of 12 scaffolds were used for implantation. At the end of each time-point, the mice were euthanized by injection of Eutasil (200 mg/mL) and the specimens collected for analysis.

4.6.3. Explants characterization

4.6.3.1. Analysis of blood vessels convergence

In Chapter 6, a semi-quantitative method was used to evaluate the total number of macroscopic blood vessels converging toward the implanted SF-PET and PET scaffolds, and control gelatin sponges in the CAM assay. This method has been previously described by Ribatti *et al.,* [119] for the quantification of angiogenesis in the CAM of chicken eggs, using gelatin sponges as implanted materials. In this thesis, the *ex ovo* images of the explants obtained after 14 days of embryonic development, were processed according to Silva-Correia *et al.,* [120] and a new method based on the work of Nowak-Sliwinska *et al.*, [121]. Both methods of imaging processing were automated in macro files for analysis at the ImageJ software program (US National Institutes of Health) and compared. The magnification of the stereomicrocope images was kept constant (7x), as well as, the image-processed area (1000 x 1000 pixels). The total number of blood vessels converging toward the implants was counted blindly for each egg by three independent observers.

4.6.3.2. Histological examination

In Chapters 6 and 7, histological analysis was performed to the explants after CAM assay and subcutaneous implantation in mice. The collected explants were sectioned with 3.5-4.0 μm thick in a microtome and processed for histological analysis following the procedure described above (Section 4.5.8. of this Chapter). Representative sections of the explants were stained with H&E following standard protocol.

4.6.3.3. Immunohistochemistry

In Chapter 6, representative CAM sections of 4.0 μm thick were used for immunohistochemical detection of the endothelial cells marker SNA-lectin (Vector Laboratories, Burlingame, CA, USA). Sambucus Nigra Lectin (SNA, EBL) has been used to identify vascular beds in chick CAMs. It specifically binds to the endothelial cells that surround and infiltrate the CAM implants, being useful for angiogenesis assays [120]. Briefly, after paraffin dewaxing and rehydration, sections were submitted to a heat-induced antigen retrieval using 10 mmol/L sodium citrate buffer (Merck, Berlin, Germany) pH 6, for 20 minutes at 98°C in the water bath. Sections were incubated with 50 μL of 3% (v/v) H_2O_2 for 10 minutes at RT, in order to inactivate block tissue endogenous peroxidase activity, which may induce a high and non-specific background when using HRP conjugated antibodies. After soaking in PBS solution, sections were incubated in protein blocking solution (Ultra V block), from the UltraVision Detection System kit (Lab Vision, Thermo Scientific, CA, USA), for 10 minutes at RT. Afterwards, 50 μL of SNA-lectin (Vector Laboratories, Burlingame, CA, USA; dilution 1:750 in

Ultra V block) were added to each section and incubated for 10 minutes at RT. Sections were then washed with PBS solution and incubated in streptavidin-peroxidase complex, from the UltraVision Detection System kit, for 10 minutes at RT. A 3,3'-diamoonobenzidine (DAB) solution was prepared using the Peroxidase Substrate Kit – DAB* (Vector Laboratories, Burlingame, CA, USA) and incubated for 2-3 minutes at RT. Sections were washed for 5 minutes in running water, to completely remove the DAB solution, and counterstained with Gill-2 hematoxylin (Merck, Berlin, Germany; dilution 1:2 in distilled water) solution. After washing with distilled water, sections were dehydrated and mounted in Entelan. Slides were observed under transmitted microscopy, using the transmitted and reflected light microscope. Images were acquired using the Zen microscope processing software, connected to the digital camera AxioCam MRc5.

*DAB Solution: 5 mL of distilled water, 2 drops of buffer stock solution, 4 drops of DAB stock solution, 2 drops of H_2O_2.

4.7. Statistical analysis

GraphPad Prism 5.0 software (GraphPad Software, La Jolla, CA, USA) was used to perform the statistical analysis. Statistical significance was set to *p<0.05, **p<0.01, ***p<0.001.

In Chapter 5, all the numerical results are presented as mean ± standard deviation. Statistical analysis was performed using a one-way ANOVA test followed by Tukey's method as a post hoc pair-wise comparison method, or a two-way ANOVA test followed by Bonferroni's as multiple comparison analysis method for the comparisons between more than two groups.

In Chapters 6, 8 and 9, all the numerical results are presented as mean ± standard deviation. First, a Shapiro-Wilk normality test was used to ascertain about the data normality. Data that followed a normal distribution was analyzed using the unpaired *t*-test. Data that did not follow a normal distribution was analyzed using the Kruskal-Wallis test followed by Dunn's multiple comparison test, for the comparisons between more than two groups.

In Chapter 7, the numerical results are presented as mean ± standard deviation or madian and interquartile range. Data normality was first assessed by a Shapiro-Wilk normality test. The results indicated that non-parametric tests should be used for all comparisons, using a two-tailed Mann-Whitney test or a Kruskal-Wallis test followed by Dunn's multiple comparison test for the comparisons between more than two groups.

4.8. References

[1] H.-J. Jin, D.L. Kaplan, Mechanism of silk processing in insects and spiders, Nature 424(6952) (2003) 1057-1061.

[2] J.G. Hardy, T.R. Scheibel, Silk-inspired polymers and proteins, Portland Press Limited, 2009.

[3] C. Vepari, D.L. Kaplan, Silk as a biomaterial, Progress in polymer science 32(8) (2007) 991-1007.

[4] A.R. Murphy, D.L. Kaplan, Biomedical applications of chemically-modified silk fibroin, Journal of materials chemistry 19(36) (2009) 6443-6450.

[5] B. Kundu, et al., Silk fibroin biomaterials for tissue regenerations, Advanced drug delivery reviews 65(4) (2013) 457-470.

[6] N. Du, et al., Structural Origin of the Strain-Hardening of Spider Silk, Advanced Functional Materials 21(4) (2011) 772-778.

[7] B. Kundu, S.C. Kundu, Silk sericin/polyacrylamide in situ forming hydrogels for dermal reconstruction, Biomaterials 33(30) (2012) 7456-7467.

[8] F.G. Omenetto, D.L. Kaplan, New opportunities for an ancient material, Science 329(5991) (2010) 528-531.

[9] Y. Cai, et al., Silk fibroin membrane used for guided bone tissue regeneration, Materials Science and Engineering: C 70 (2017) 148-154.

[10] M. Yang, et al., Ice-Templated Protein Nanoridges Induce Bone Tissue Formation, Advanced Functional Materials 27(44) (2017).

[11] S. Font Tellado, et al., Fabrication and characterization of biphasic silk fibroin scaffolds for tendon/ligament-to-bone tissue engineering, Tissue Engineering Part A (2017).

[12] T. Yucel, et al., Vortex-induced injectable silk fibroin hydrogels, Biophysical journal 97(7) (2009) 2044-2050.

[13] V.P. Ribeiro, et al., Silk-based anisotropical 3D biotextiles for bone regeneration, Biomaterials 123 (2017) 92-106.

[14] R. Nazarov, et al., Porous 3-D scaffolds from regenerated silk fibroin, Biomacromolecules 5(3) (2004) 718-726.

[15] S.S. Silva, et al., Silk hydrogels from non-mulberry and mulberry silkworm cocoons processed with ionic liquids, Acta biomaterialia 9(11) (2013) 8972-8982.

[16] M. Li, et al., Compliant film of regenerated Antheraea pernyi silk fibroin by chemical crosslinking, International Journal of Biological Macromolecules 32(3) (2003) 159-163.

[17] C. Du, et al., Novel silk fibroin/hydroxyapatite composite films: structure and properties, Materials Science and Engineering: C 29(1) (2009) 62-68.

[18] A.B. Mathur, et al., The dissolution and characterization of Bombyx mori silk fibroin in calcium nitrate-methanol solution and the regeneration of films, Biopolymers 42(1) (1997) 61-74.

[19] X. Chen, et al., Conformation transition kinetics of Bombyx mori silk protein, Proteins: Structure, Function, and Bioinformatics 68(1) (2007) 223-231.

[20] L.-P. Yan, et al., Macro/microporous silk fibroin scaffolds with potential for articular cartilage and meniscus tissue engineering applications, Acta biomaterialia 8(1) (2012) 289-301.

[21] L.P. Yan, et al., Core-shell silk hydrogels with spatially tuned conformations as drug-delivery system, Journal of tissue engineering and regenerative medicine (2016).

[22] M. Fini, et al., The healing of confined critical size cancellous defects in the presence of silk fibroin hydrogel, Biomaterials 26(17) (2005) 3527-3536.

[23] X. Wang, et al., Sonication-induced gelation of silk fibroin for cell encapsulation, Biomaterials 29(8) (2008) 1054-1064.

[24] D.G. Harkin, et al., Silk fibroin in ocular tissue reconstruction, Biomaterials 32(10) (2011) 2445-2458.

[25] K. Illers, H. Breuer, Molecular motions in polyethylene terephthalate, Journal of Colloid science 18(1) (1963) 1-31.

[26] B. Demirel, et al., Crystallization behavior of PET materials, Balıkesir Üniversitesi Fen Bilimleri Enstitüsü Dergisi 13(1) (2016) 26-35.

[27] J. Mayer, et al., Matrices for tissue engineering-scaffold structure for a bioartificial liver support system, Journal of controlled release 64(1) (2000) 81-90.

[28] Z. Ma, et al., Surface engineering of electrospun polyethylene terephthalate (PET) nanofibers towards development of a new material for blood vessel engineering, Biomaterials 26(15) (2005) 2527-2536.

[29] Y. Li, et al., Thermal compression and characterization of three-dimensional nonwoven PET matrices as tissue engineering scaffolds, Biomaterials 22(6) (2001) 609-618.

[30] S.V. Dorozhkin, Calcium orthophosphates in nature, biology and medicine, Materials 2(2) (2009) 399-498.

[31] M. Farokhi, et al., Silk fibroin/hydroxyapatite composites for bone tissue engineering, Biotechnology advances (2017).

[32] T. Matsuno, et al., Preparation of injectable 3D-formed β-tricalcium phosphate bead/alginate composite for bone tissue engineering, Dental materials journal 27(6) (2008) 827-834.

[33] Y. Takahashi, et al., Osteogenic differentiation of mesenchymal stem cells in biodegradable sponges composed of gelatin and β-tricalcium phosphate, Biomaterials 26(17) (2005) 3587-3596.

[34] M.-P. Ginebra, et al., Calcium phosphate cements as bone drug delivery systems: a review, Journal of Controlled Release 113(2) (2006) 102-110.

[35] S. Pina, et al., In vitro performance assessment of new brushite-forming Zn-and ZnSr-substituted β-TCP bone cements, Journal of Biomedical Materials Research Part B: Applied Biomaterials 94(2) (2010) 414-420.

[36] S. Pina, J.M. Ferreira, Brushite-forming Mg-, Zn-and Sr-substituted bone cements for clinical applications, Materials 3(1) (2010) 519-535.

[37] Z. Saidak, P.J. Marie, Strontium signaling: molecular mechanisms and therapeutic implications in osteoporosis, Pharmacology & therapeutics 136(2) (2012) 216-226.

[38] M. Kandaz, et al., The effects of zinc sulfate on the levels of some elements and oxidative stress occurring in lenses of rats exposed to total cranium radiotherapy, The Eurasian journal of medicine 41(2) (2009) 110.

[39] B.B. Mandal, et al., High-strength silk protein scaffolds for bone repair, Proceedings of the National Academy of Sciences 109(20) (2012) 7699-7704.

[40] N. Kasoju, et al., Preparation and characterization of Antheraea assama silk fibroin based novel non-woven scaffold for tissue engineering applications, Journal of tissue engineering and regenerative medicine 3(7) (2009) 539-552.

[41] S. Ghosh, et al., Direct-Write Assembly of Microperiodic Silk Fibroin Scaffolds for Tissue Engineering Applications, Advanced Functional Materials 18(13) (2008) 1883-1889.

[42] J.B. Costa, et al., Fast Setting Silk Fibroin Bioink for Bioprinting of Patient-Specific Memory-Shape Implants, Advanced healthcare materials 6(22) (2017).

[43] A. Martins, et al., The influence of patterned nanofiber meshes on human mesenchymal stem cell osteogenesis, Macromolecular bioscience 11(7) (2011) 978-987.

[44] W.J. Li, et al., Electrospun nanofibrous structure: a novel scaffold for tissue engineering, Journal of Biomedical Materials Research Part A 60(4) (2002) 613-621.

[45] A. Walther, et al., Novel textile scaffolds generated by flock technology for tissue engineering of bone and cartilage, Materials 5(3) (2012) 540-557.

[46] B. Kundu, et al., Silk proteins for biomedical applications: bioengineering perspectives, Progress in Polymer Science 39(2) (2014) 251-267.

[47] X. Wang, et al., Applications of knitted mesh fabrication techniques to scaffolds for tissue engineering and regenerative medicine, Journal of the mechanical behavior of biomedical materials 4(7) (2011) 922-932.

[48] K.H. Leong, et al., The potential of knitting for engineering composites—a review, Composites Part A: applied science and manufacturing 31(3) (2000) 197-220.

[49] D.J. Spencer, Knitting technology: a comprehensive handbook and practical guide, Crc Press2001.

[50] S.M. Bruer, et al., Three-dimensionally knit spacer fabrics: a review of production techniques and applications, Journal of Textile and Apparel, Technology and Management 4(4) (2005) 1-31.

[51] A. Davies, J. Williams, The Use of spacer fabrics for absorbent medical applications, (2009).

[52] J. Yip, S.-P. Ng, Study of three-dimensional spacer fabrics:: Physical and mechanical properties, Journal of materials processing technology 206(1) (2008) 359-364.

[53] U. Wollina, et al., Functional textiles in prevention of chronic wounds, wound healing and tissue engineering, Textiles and the Skin, Karger Publishers2003, pp. 82-97.

[54] U.-J. Kim, et al., Three-dimensional aqueous-derived biomaterial scaffolds from silk fibroin, Biomaterials 26(15) (2005) 2775-2785.

[55] M. Abadi, et al., Synthesis of nano β-TCP and the effects on the mechanical and biological properties of β-TCP/HDPE/UHMWPE nanocomposites, Polymer Composites 31(10) (2010) 1745-1753.

[56] M. Swetha, et al., Biocomposites containing natural polymers and hydroxyapatite for bone tissue engineering, International journal of biological macromolecules 47(1) (2010) 1-4.

[57] L.-P. Yan, et al., De novo bone formation on macro/microporous silk and silk/nano-sized calcium phosphate scaffolds, Journal of Bioactive and Compatible Polymers 28(5) (2013) 439-452.

[58] B. Marelli, et al., Silk fibroin derived polypeptide-induced biomineralization of collagen, Biomaterials 33(1) (2012) 102-108.

[59] J.R. Vetsch, et al., Effect of fetal bovine serum on mineralization in silk fibroin scaffolds, Acta biomaterialia 13 (2015) 277-285.

[60] T. Arahira, M. Todo, Effects of proliferation and differentiation of mesenchymal stem cells on compressive mechanical behavior of collagen/β-TCP composite scaffold, Journal of the mechanical behavior of biomedical materials 39 (2014) 218-230.

[61] M. Kucharska, et al., Fabrication of in-situ foamed chitosan/β-TCP scaffolds for bone tissue engineering application, Materials Letters 85 (2012) 124-127.

[62] J. Ou, et al., Preparation and Characterization of Nano-β-Tricalcium Phosphate/Silk Fibroin Scaffold for Tissue Engineering Applications, Advanced Materials Research, Trans Tech Publ, 2012, pp. 882-888.

[63] C. Dararutana, et al., Characteristics and Osteoconductivity of Bone Composite Scaffolds Made of Thai Silk Fibroin, Gelatin and Inorganic Compounds: A Comparative Study of β-Tricalcium Phosphate and Hydroxyapatite, Macromolecular Symposia, Wiley Online Library, 2015, pp. 258-264.

[64] D.H. Lee, et al., Enhanced osteogenesis of β-tricalcium phosphate reinforced silk fibroin scaffold for bone tissue biofabrication, International journal of biological macromolecules 95 (2017) 14-23.

[65] S. Pina, et al., Biofunctional Ionic-Doped Calcium Phosphates: Silk Fibroin Composites for Bone Tissue Engineering Scaffolding, Cells Tissues Organs 204 (2017).

[66] A.S. Hoffman, Hydrogels for biomedical applications, Advanced drug delivery reviews 64 (2012) 18-23.

[67] H. Tan, et al., Injectable in situ forming biodegradable chitosan–hyaluronic acid based hydrogels for cartilage tissue engineering, Biomaterials 30(13) (2009) 2499-2506.

[68] J. Kundu, et al., Silk fibroin/poly (vinyl alcohol) photocrosslinked hydrogels for delivery of macromolecular drugs, Acta biomaterialia 8(5) (2012) 1720-1729.

[69] H.-F. Liang, et al., Novel method using a temperature-sensitive polymer (methylcellulose) to thermally gel aqueous alginate as a pH-sensitive hydrogel, Biomacromolecules 5(5) (2004) 1917-1925.

[70] L.S.M. Teixeira, et al., Enzyme-catalyzed crosslinkable hydrogels: emerging strategies for tissue engineering, Biomaterials 33(5) (2012) 1281-1290.

[71] L.P. Yan, et al., Tumor Growth Suppression Induced by Biomimetic Silk Fibroin Hydrogels, Scientific Reports 6 (2016) 31037.

[72] X.D. Liu, et al., Surface modification of nonporous glass beads with chitosan and their adsorption property for transition metal ions, Carbohydrate Polymers 49(2) (2002) 103-108.

[73] G.E. Park, et al., Accelerated chondrocyte functions on NaOH-treated PLGA scaffolds, Biomaterials 26(16) (2005) 3075-3082.

[74] I. Pashkuleva, et al., Surface modification of starch based biomaterials by oxygen plasma or UV-irradiation, Journal of Materials Science: Materials in Medicine 21(1) (2010) 21-32.

[75] J. Schütte, et al., A method for patterned in situ biofunctionalization in injection-molded microfluidic devices, Lab on a Chip 10(19) (2010) 2551-2558.

[76] C. Oehr, Plasma surface modification of polymers for biomedical use, Nuclear Instruments and Methods in Physics Research Section B: Beam Interactions with Materials and Atoms 208 (2003) 40-47.

[77] E. Ostuni, et al., A survey of structure– property relationships of surfaces that resist the adsorption of protein, Langmuir 17(18) (2001) 5605-5620.

[78] H.M. Kowalczyńska, M. Nowak-Wyrzykowska, Modulation of adhesion, spreading and cytoskeleton organization of 3T3 fibroblasts by sulfonic groups present on polymer surfaces, Cell biology international 27(2) (2003) 101-114.

[79] S. Sofia, et al., Functionalized silk-based biomaterials for bone formation, Journal of Biomedical Materials Research Part A 54(1) (2001) 139-148.

[80] S. Pina, et al., Newly developed Sr-substituted α-TCP bone cements, Acta biomaterialia 6(3) (2010) 928-935.

[81] R. Reichelt, Scanning electron microscopy, Science of microscopy, Springer2007, pp. 133-272.

[82] L. Reimer, Transmission electron microscopy: physics of image formation and microanalysis, Springer2013.

[83] A. Oliveira, et al., Micro-computed tomography (μ-CT) as a potential tool to assess the effect of dynamic coating routes on the formation of biomimetic apatite layers on 3D-plotted biodegradable polymeric scaffolds, Journal of Materials Science: Materials in Medicine 18(2) (2007) 211-223.

[84] M. Biancalana, S. Koide, Molecular mechanism of Thioflavin-T binding to amyloid fibrils, Biochimica et Biophysica Acta (BBA)-Proteins and Proteomics 1804(7) (2010) 1405-1412.

[85] M.M. Picken, G.A. Herrera, Thioflavin T stain: an easier and more sensitive method for amyloid detection, Amyloid and Related Disorders, Springer2012, pp. 187-189.

[86] J. Sharpe, Optical projection tomography, Annu. Rev. Biomed. Eng. 6 (2004) 209-228.

[87] H.-L. Lee, N.T. Flynn, X-ray photoelectron spectroscopy, Handbook of Applied Solid State Spectroscopy (2006) 485-507.

[88] P. Thibault, et al., High-resolution scanning x-ray diffraction microscopy, Science 321(5887) (2008) 379-382.

[89] T. Theophanides, Introduction to infrared spectroscopy, Infrared Spectroscopy-Materials Science, Engineering and Technology, InTech2012.

[90] A. Dazzi, et al., AFM–IR: combining atomic force microscopy and infrared spectroscopy for nanoscale chemical characterization, Applied Spectroscopy 66(12) (2012) 1365-1384.

[91] C. Marcott, et al., Applications of AFM-IR—Diverse Chemical Composition Analyses at Nanoscale Spatial Resolution, Microscopy Today 20(6) (2012) 16-21.

[92] D. Rugar, P. Hansma, Atomic force microscopy, Physics today 43(10) (1990) 23-30.

[93] P. Eaton, P. West, Atomic force microscopy, Oxford University Press2010.

[94] D.K. Owens, R. Wendt, Estimation of the surface free energy of polymers, Journal of applied polymer science 13(8) (1969) 1741-1747.

[95] D. Kaelble, Dispersion-polar surface tension properties of organic solids, The Journal of Adhesion 2(2) (1970) 66-81.

[96] H. Czichos, Materials and Their Characteristics: Overview, Springer Handbook of Materials Measurement Methods, Springer2006, pp. 95-102.

[97] H.A. Barnes, et al., An introduction to rheology, Elsevier1989.

[98] M. Li, et al., Enzymatic degradation behavior of porous silk fibroin sheets, Biomaterials 24(2) (2003) 357-365.

[99] R.L. Horan, et al., In vitro degradation of silk fibroin, Biomaterials 26(17) (2005) 3385-3393.

[100] L.-P. Yan, et al., Bilayered silk/silk-nanoCaP scaffolds for osteochondral tissue engineering: in vitro and in vivo assessment of biological performance, Acta biomaterialia 12 (2015) 227-241.

[101] P.J. Reardon, et al., Mimicking Hierarchical Complexity of the Osteochondral Interface Using Electrospun Silk–Bioactive Glass Composites, ACS Applied Materials & Interfaces 9(9) (2017) 8000-8013.

[102] A.C. Tas, Synthesis of biomimetic Ca-hydroxyapatite powders at 37 C in synthetic body fluids, Biomaterials 21(14) (2000) 1429-1438.

[103] P.P. Carvalho, et al., The effect of storage time on adipose-derived stem cell recovery from human lipoaspirates, Cells Tissues Organs 194(6) (2011) 494-500.

[104] M. Cerqueira, et al., Human adipose stem cells cell sheet constructs impact epidermal morphogenesis in full-thickness excisional wounds, Biomacromolecules 14(11) (2013) 3997-4008.

[105] M. Dominici, et al., Minimal criteria for defining multipotent mesenchymal stromal cells. The International Society for Cellular Therapy position statement, Cytotherapy 8(4) (2006) 315-317.

[106] H.M. Shapiro, H.M. Shapiro, Practical flow cytometry, (2003).

[107] J. O'brien, et al., Investigation of the Alamar Blue (resazurin) fluorescent dye for the assessment of mammalian cell cytotoxicity, The FEBS Journal 267(17) (2000) 5421-5426.

[108] S. Crouch, et al., The use of ATP bioluminescence as a measure of cell proliferation and cytotoxicity, Journal of immunological methods 160(1) (1993) 81-88.

[109] C. Lebon, et al., On the use of an appropriate TdT-mediated dUTP–biotin nick end labeling assay to identify apoptotic cells, Analytical biochemistry 480 (2015) 37-41.

[110] J. Huisken, D.Y. Stainier, Selective plane illumination microscopy techniques in developmental biology, Development 136(12) (2009) 1963-1975.

[111] S. Qin, et al., Electrochemical Determination of Alkaline Phosphatase as a Potential Marker of Reperfusion Injury, Int J Electrochem Sci 12(10) (2017) 8908-8917.

[112] R.P. Pirraco, et al., Development of osteogenic cell sheets for bone tissue engineering applications, Tissue Engineering Part A 17(11-12) (2011) 1507-1515.

[113] C.J. Billington, Cartilage proteoglycan release assay, Matrix Metalloproteinase Protocols (2001) 451-456.

[114] J.-H. Kim, et al., Comparison of three different kits for extraction of high-quality RNA from frozen blood, Springerplus 3(1) (2014) 76.

[115] M. Arya, et al., Basic principles of real-time quantitative PCR, Expert review of molecular diagnostics 5(2) (2005) 209-219.

[116] K.J. Livak, T.D. Schmittgen, Analysis of relative gene expression data using real-time quantitative PCR and the 2– ΔΔCT method, methods 25(4) (2001) 402-408.

[117] E. Molnár, Immunocytochemistry and immunohistochemistry, Essential Guide to Reading Biomedical Papers: Recognising and Interpreting Best Practice (2013) 117-127.

[118] N.A. Lokman, et al., Chick chorioallantoic membrane (CAM) assay as an in vivo model to study the effect of newly identified molecules on ovarian cancer invasion and metastasis, International journal of molecular sciences 13(8) (2012) 9959-9970.

[119] D. Ribatti, et al., The gelatin sponge-chorioallantoic membrane assay, Nature protocols 1(1) (2006) 85.

[120] J. Silva-Correia, et al., Angiogenic potential of gellan-gum-based hydrogels for application in nucleus pulposus regeneration: in vivo study, Tissue Engineering Part A 18(11-12) (2012) 1203-1212.

[121] P. Nowak-Sliwinska, et al., Processing of fluorescence angiograms for the quantification of vascular effects induced by anti-angiogenic agents in the CAM model, Microvascular research 79(1) (2010) 21-28.

SECTION III

EXPERIMENTAL STUDIES

CHAPTER 5

Influence of Different Surface Modification Treatments on Silk Biotextiles for Tissue Engineering Applications

CHAPTER 5.

Influence of different surface modification treatments on silk biotextiles for tissue engineering applications*

5.1. Abstract

Biotextile structures from silk fibroin have demonstrated to be particularly interesting for tissue engineering (TE) applications due to their high mechanical strength, interconnectivity, porosity, and ability to degrade under physiological conditions. In this work, we described several surface treatments of knitted silk fibroin (SF) scaffolds, namely sodium hydroxide (NaOH) solution, ultraviolet radiation exposure in an ozone atmosphere (UV/O_3) and oxygen (O_2) plasma treatment followed by acrylic acid (AAc), vinyl phosphonic acid (VPA), and vinyl sulfonic acid (VSA) immersion. The effect of these treatments on the mechanical properties of the textile constructs was evaluated by tensile tests in dry and hydrated states. Surface properties such as morphology, topography, wettability and elemental composition were also affected by the applied treatments. The *in vitro* biological behavior of L929 fibroblasts revealed that cells were able to adhere and spread both on the untreated and surface- modified textile constructs. The applied treatments had different effects on the scaffolds' surface properties, confirming that these modifications can be considered as useful techniques to modulate the surface of biomaterials according to the targeted application.

*This chapter is based on the following publication:

Ribeiro VP, Almeida LR, Martins AR, Pashkuleva I, Marques AP, Ribeiro AS, Silva CJ, Bonifácio G, Sousa RA, Reis RL, Oliveira AL. Influence of different surface modification treatments on silk biotextiles for tissue engineering applications. Journal of Biomedical Materials Research Part B: Applied Materials. 2015, 104(3):496-507. doi: 10.1002/jbm.b.33400.

5.2. Introduction

The field of tissue engineering involves the use of scaffold materials that are ideally able to contribute to the necessary microenvironment for stimulating neotissue morphogenesis [1,2]. The combination of chemical, biological, and mechanical properties of the scaffold must provide instructive cues for cells to develop into a functional tissue *in vivo* [3-5]. Three-dimensional (3D) polymeric structures are the main scaffolding materials in various tissue engineering approaches because of their versatility and the possibility of tailoring their properties.

Several strategies have been proposed to prepare polymeric porous 3D biodegradable scaffolds for tissue engineering (TE) [1,6]. Among these, fiber-based structures have demonstrated to be particularly interesting as they present higher porosity, interconnectivity and surface area, which can facilitate cellular attachment and consequently improve scaffold cell colonization and new tissue formation [7-11]. Textile technologies constitute an attractive route to develop fiber-based matrices. These technologies allow for the production at an industrial scale and they can offer a superior control over the material design (size, shape, porosity, and fiber orientation) and the manufacturing processing conferring a high degree of reproducibility without involving the use of toxic solvents [12-14]. In particular, knitting-based technologies are known to exhibit better extensibility or compliance as compared to other woven substrates, with an enhanced porosity/volume, although with limited thickness [15]. In the literature, a few knitted structures from synthetic or natural materials have been already proposed, either alone [16] or in a synergistic combination with other types of biomaterials/structures for the construction of functional 3D scaffolds, applicable in the repair/replacement and regeneration of tissues or organs such as blood vessels and heart valves [17-19], tendons and ligaments [17, 20-25], cartilage [26-28], and skin [29]. As this is a new field of application for knitting technologies, most of these devices are still in exploratory stages. In this work, we have applied a knitting technology to fabricate highly reproducible biodegradable porous architectures using silk fibers [30].

Silk fibroin (SF) is a natural protein that is spun into fibers by a variety of species including silkworms and spiders [31,32]. This naturally occurring polymer has been clinically used as sutures for centuries. Long standing FDA regulatory approval of silk-based sutures, its abundance as raw fiber material and controlled proteolytic degradability *in vitro* and *in vivo* have established silk fibroin as a widely-applied biomaterial. Moreover, silk-based biomaterials have been proposed for a range of tissue engineering applications, including bone [30, 33, 34], cartilage [35,36], tendon/ligament [37-40], and skin [41,42], regeneration. In all of these approaches, the use of silk fibroin is associated with targeted functional microenvironments supporting tissue morphogenesis.

SF is mainly composed by glycine and alanine and also contains significant quantities of serine, threonine, aspartic and glutamic acid, and tyrosine [43]. The biomedical applications of SF can be broadened by chemical modifications, allowing for further biofunctionalization such as immobilization of growth factors or cell binding domains able to modulate cell behavior [32,44]. There are several examples of SF matrices successfully modified by various surface treatments for advanced biological and therapeutic applications [45-50]. Nonetheless, from those none involved a knitting processing technique combined with surface treatments. The main advantage of a surface modification is the possi- bility to alter the surface properties that indirectly dictate cell response, and at the same time preserve the bulk material features, such as, the mechanical properties and/or biodegradation. Polymeric scaffolds modified by radiofrequency (RF) argon plasma treatments have shown enhanced cell attachment, spreading and proliferation [45,46]. Surface modifications of SF by plasma treatment using different working gases (SO_2, NH_3, and O_2) have demonstrated to increase the antithrombogenicity and the cellular activity of human epidermal keratinocytes and fibroblasts, suggesting that these structures might be potentially used as blood-contacting biomaterials or as novel extracellular matrices for other tissue engineering applications [47,48]. Sulfonic acid is another compound recently used to tailor the surface chemistry of SF [49, 50]. As a result of the introduced changes, SF decorated with sulfonated moieties could mimic the natural ECM environment and lead to further immobilization of biomolecules.

In the present study, we explore several treatments to tailor the surface of SF knitted scaffolds: (i) wet chemical etching using NaOH (a method largely applied at the industrial scale, although not only surface confined); (ii) physical etching/oxidation (treatment with UV ozonator), which is better restricted to the surface; and (iii) the grafting of functional moieties after preactivation by plasma—this modification method is commonly applied for further biofunctionalization. We have chosen plasma among the possibilities for activation as it is very effective and the most surface confined modification method (few angstroms in depth). Additional, air plasma can be easily scaled-up; this versatile method can be used to easily decorate 3D scaffolds with various functional groups including sulfonic, phosphonic and carboxylic ones. This preliminary work reports on the effectiveness of the treatments and evaluates the effect of surface properties changes over early cell behavior. This study is a first step toward the development of surfaces that are able to easily bind to biomolecules that can stimulate ECM formation.

5.3. Materials and Methods

5.3.1. Production of the textile constructs and membranes

Silk derived from silkworm *Bombyx mori* was used in the form of cocoons and yarns supplied by the

Portuguese Association of Parents and Friends of Mentally Disable Citizens (APPA-CDM, Portugal). Plain 3D Jersey constructs were produced through weft knitting using the raw silk fibers (Tricolab machine, Sodemat, SA, Germany). The diameters of the fibers were measured and the average of five fibers calculated as 9.1 ± 2.2 μm. The measured thickness of the silk textile matrix was ~0.8 mm. A detailed analysis of the 3D morphology of the textile constructs was previously performed through microcomputed tomography (micro-CT) [30]. The calculated average porosity, mean wall thickness, and mean pore size were 68.4 ± 3.7%, 37.8 ± 14.9 μm, and 54.5 ± 9.4 μm, respectively.

Textile constructs were washed in a 0.15% (w/v) natural soap aqueous solution for 2 h and then rinsed with distilled water. Silk structures underwent a subsequent purification process since *Bombyx mori* silkworm fibers are composed by a core protein called fibroin that is naturally coated by sericin, which is known to present cytotoxicity [51]. Thus, SF textiles were consecutively boiled for 60 minutes in a 0.03 M sodium carbonate (Na_2CO_3) solution and rinsed with distilled water to ensure the full extraction of the sericin.

Because some of the used characterization techniques [e.g., atomic force microscopy (AFM), contact angle] are better applied to 2D plan surfaces, SF membranes were also prepared and modified using the same procedures as the ones used for the textile constructs. SF membranes were cast from a water-based silk fibroin solution prepared as previ- ously described by Yan *et al.* [36]. Briefly, the cocoons were consecutively boiled in an aqueous solution of 0.02 M sodium carbonate for 60 minutes. The extracted SF was washed with distilled water. After drying, SF was dissolved in 9.3 M LiBr solution at 70°C for 1 hour. This solution was dialysed for 2 days. The SF membranes were obtained by casting the solution in 24-well culture plates (BD Biosciences, San Jose, CA, USA) and slow dried at room temperature (RT). In order to induce β-sheet conformation the membranes were immersed in methanol/water solutions with increasing concentration of methanol, up to 100% (v/v) to preserve the structural integrity during the drying process. Ideally it would be preferable to produce a membrane through self-assembly processes as a way to recreate the natural process of SF fiber formation and mimic the natural silk structure. However, these processes remain poorly understood which makes the reconstitution of silk solutions into materials with properties comparable to the native state problematic [52]. Therefore, we decided to induce β-sheet through methanol treatment in order to achieve reproducible surfaces that could be comparable to those found in the native SF fibers.

5.3.2. Surface treatments

5.3.2.1. Etching with NaOH

SF structures were immersed in 0.5 M NaOH solution for 60 minutes at 30°C.

5.3.2.2. Exposure to ultraviolet radiation in an ozone atmosphere (UV/O_3)

The UV/O_3 treatment was performed by exposing the SF surfaces to 185 nm of UV radiation using a UV/ozone cleaner (ProCleaner™ 220; BioForce Nanosciences, Ames, IA, USA).

5.3.2.3. Plasma grafting

The most attractive aspect of plasma-based surface treatments is that several gases can be employed to produce plasma and thus activate the surface functionality of structures, without requiring high chemical consumption. In this study, plasma treatment was performed using a radio frequency (13.56 MHz) plasma reactor (PlasmaPrep5, Gala Instruments, Germany). Samples were exposed to O_2 plasma at 30 W of power for 15 minutes. During the treatment, the gas flow was adjusted in order to keep a constant pressure of 20 Pa inside the reactor. Immediately after plasma treatment, the activated surfaces were immersed in three different solutions 5% (v/v) acrylic acid (AAc), 100 mM vinyl phosphonic acid (VPA)/2-propanol and 10% (v/v) vinyl sulfonic acid (VSA) for 2 hours at RT, in order to induce carboxylic, phosphonic or sulfonic groups' formation. Solutions were previously degassed by nitrogen (N_2) bubbling to avoid the reaction between the induced functional groups and the O_2 present in the solutions. After each reaction, samples were washed with the solvent used to prepare the solutions, distilled water or 2-propanol, followed by dehydration in absolute ethanol and over drying at 37°C for 24 hours.

5.3.3. Mechanical properties

The mechanical properties of the produced SF textile constructs were determined by performing quasi-static tensile tests (Instron 4505 Universal Machine). The tensile modulus, ultimate tensile strength and strain at maximum load were measured using a load cell of 1 kN at crosshead speed 5 mm/minute. The tensile modulus was determined in the most linear region of the stress-strain curve using the secant method. Both dry and hydrated samples were tested. The tests with dry samples were conducted at RT. Hydrated samples were prepared by immersion in a phosphate-buffer saline solution (PBS) at pH of 7.4 for 3 days. Five samples with dimensions of 15 x 40 mm were analyzed per condition.

5.3.4. Scanning electron microscopy

The surface morphology of the produced SF textile constructs was analyzed before and after the different surface treatments using a Leica Cambridge S-360 (United Kingdom) Scanning Electron Microscope.

After cultures, cell morphology and distribution on the surface of the 2D membranes and 3D textile scaffolds were also analyzed by scanning electron microscopy (SEM). After each predefined time point, the cell-seeded structures were washed with PBS and fixed with 2.5% glutaraldehyde (Sigma-Aldrich, MO, USA) solution in PBS. Samples were again rinsed with PBS and dehydrated using a series of ethanol solutions (30%, 50%, 60%, 70%, 80%, 90%, and 100%, v/v). Finally, the samples were treated with hexamethylidisilazane (HMDS; Electron Microscopy Sciences) and air dried overnight at RT. Prior observation all samples were sputter-coated with gold (Fisons Instruments, Sputter Coater SC502, United Kingdom) and the micrographs were taken at an accelerating voltage of 15 kV at different magnifications.

5.3.5. Atomic force microscopy

The surface roughness of the samples was determined by AFM. The analysis was performed for three regions per sample (5 x 5 μm^2) using tapping mode (Veeco) connected to a NanoScope III (Veeco) with non-contacting silicon nanoprobes (ca. 300 kHz, set point 2–3 V) from Nanosensors (Switzerland). All images were fitted to a plan using the 3rd degrees flatten procedure included in the NanoScope software version 4.43r8. The surface roughness was calculated as Ra (mean absolute distance from mean flat surface). The values are presented as mean 6 standard deviation.

5.3.6. Contact angle and surface energy

Understanding the surface behavior of a biomaterial in contact with hydrated media is of great importance to predict its interactions with cells, when applied in a particular biomedical application. The wettability of untreated and surface modified SF was assessed by contact angle (θ) measurements. Unfortunately, the morphology (porous irregular surface creating a capillary effect) of the present samples/textiles did not allow direct determination of the contact angle with enough precision. In fact, there are not many characterization techniques with enough sensitivity to allow surface analysis of such samples with complex shape. Therefore, "models" have been prepared in the form of membranes, trying to recapitulate some of the surface properties of the textiles. The contact angle depends on several parameters such as surface chemistry, roughness and crystallinity among others that can't be controlled separately. While the roughness of the membranes and the textiles is obviously different, the crystallinity and surface chemistry can be reproduced using the same procedure. Because of these differences between membranes and textiles the discussion will not be solely based on the contact angle measurements. The results are complemented with the other characterization techniques presented in this study.

Static contact angle measurements of the untreated and surface modified SF membranes were obtained by the sessile drop method using a contact angle meter OCA 151 with a high-performance image processing system (DataPhysics Instruments, Germany). Two different liquids were used: ultrapure water (upH_2O; 1 µL) and diiodomethane (CH_2I_2; 1 µL, HPLC grade), added by a motor-driven syringe at RT. Two samples of each material were used and five measurements were carried out for each sample. The surface free energy (γ) of the treated and untreated samples was calculated using the Owens, Wendt, Rabel, and Kaelble (OWRK) equation [53,54].

5.3.7. X-ray photoelectron spectroscopy

X-ray photoelectron spectroscopy (XPS) analysis was performed to characterize the surface elemental composition of the modified and unmodified samples using a Thermo Scientific K-Alpha ESCA instrument. Monochromatic Al-Kα radiation ($h\nu$ = 1486.6 eV) was used to perform the XPS measurements and the photoelectrons were collected from a take-off angle of 90° relative to the samples surface. The spectrometer was operated in a constant analyzer energy (CAE) mode with 100 eV pass energy for the survey spectra and 20 eV pass energy for the high-resolution spectra. Charge referencing was adjusted by setting the lower binding energy of C1s peak at 285.0 eV. Overlapping peaks were resolved into their individual components by using the XPSPEAK 4.1 software.

5.3.8. Cell culture

A mouse fibroblast cell line (L929), acquired from the European Collection of Cell Cultures (ECACC, United Kingdom), was used to assess the eventual cytotoxicity of the developed scaffolds. For that purpose, the 3D textile materials were cut into 16 mm diameter discs, and immobilized into the bottom of 24-well culture plates (BD Biosciences) using CellCrown® inserts (Scaffdex, Finland). Cells were grown as monolayer cultures in Dulbecco's Modified Eagle's Medium (DMEM; Sigma-Aldrich, MO, USA) supplemented with 10% fetal bovine serum (FBS; Biochrom, Berlin, Germany) and 1% antibiotic/antimycotic solution (Gibco®, Life Technologies, USA). At confluence cells were detached from the culture flasks using trypsin (Sigma Aldrich, MO, USA), centrifuged, resuspended in the cell-culture medium, and seeded in the scaffolds at a density of 3×10^4 cells/sample. The cell-seeded scaffolds were incubated at 37°C, 5% CO_2 and 95% humidity, for 1, 5, and 24 hours. Tissue culture polystyrene (TCPs; Sarstedt) coverslips and SF membranes were used as control surfaces.

5.3.9. DNA quantification assay

The L929 cell proliferation onto the developed 3D textile constructs was assessed by using a fluorimetric double-strand DNA quantification kit (PicoGreen, Molecular Probes, Invitrogen Corporation) following manufacturer's instructions. After each time point, scaffolds were rinsed with PBS and transferred into 1.5 mL microtubes, containing 1 mL of ultrapure water, to induce an osmotic shock. An additional thermal shock was provoked by placing the scaffolds at 37°C for 1 hour prior to -80°C freezing. Prior to dsDNA quantification, samples were thawed and sonicated for 1 hour. A PicoGreen solution was mixed with the samples and the standards (ranging from 0 to 2 μg/mL) in a 200:1 ratio and placed into opaque 96-well plates. Each sample or standard was made in triplicate. After 10 minutes of incubation in the dark, the fluorescence was read into a microplate enzyme-linked immunosorbent assay reader (BioTek, USA) at 485/528 nm of excitation/emission. To exclude the materials autofluorescence, the same quantification assay was performed for samples without cells but subjected to the same culture conditions.

5.3.10. Statistical analysis

All the numerical results are presented as mean ± standard deviation. Statistical tests were performed with GraphPad Prism 5.0 (GraphPad Software). A one-way analysis of var- iance (ANOVA) was used to evaluate the AFM and contact angle results, using the Tukey's method as a post hoc pair- wise comparison test. Statistical significance of DNA quantification, obtained from three independent experiments, and tensile tests results were determined with a two-way ANOVA test followed by Bonferroni's as multiple comparasion analysis method. The significance level was *$p<0.05$, **$p < 0.01$, and ***$p < 0.001$.

5.4. Results and Discussion

When developing biomaterials to be used in tissue engineering that intend to direct cellular behavior, the ability to tailor their surface properties becomes an issue of great importance. Slight changes in the surface topography and chemistry can be responsible for significant changes on cell behavior.

5.4.1. Mechanical properties

SF fibers are known for their extraordinary mechanical properties that rival most of the high performance synthetic fibers. This behavior results from their unique molecular structure and protein conformation [55]. In a previous study [30], the mechanical properties of the produced knitted SF matrices were measured in the longitudinal and transversal direction confirming their anisotropic character. Anisotropy is particularly interesting when considering that most tissues present a high degree of anisotropy. Herein, the mechanical properties of the untreated and surface modified SF textile constructs were investigated by performing quasi-static tensile tests in the longitudinal direction, as presented in Figure 5-1.

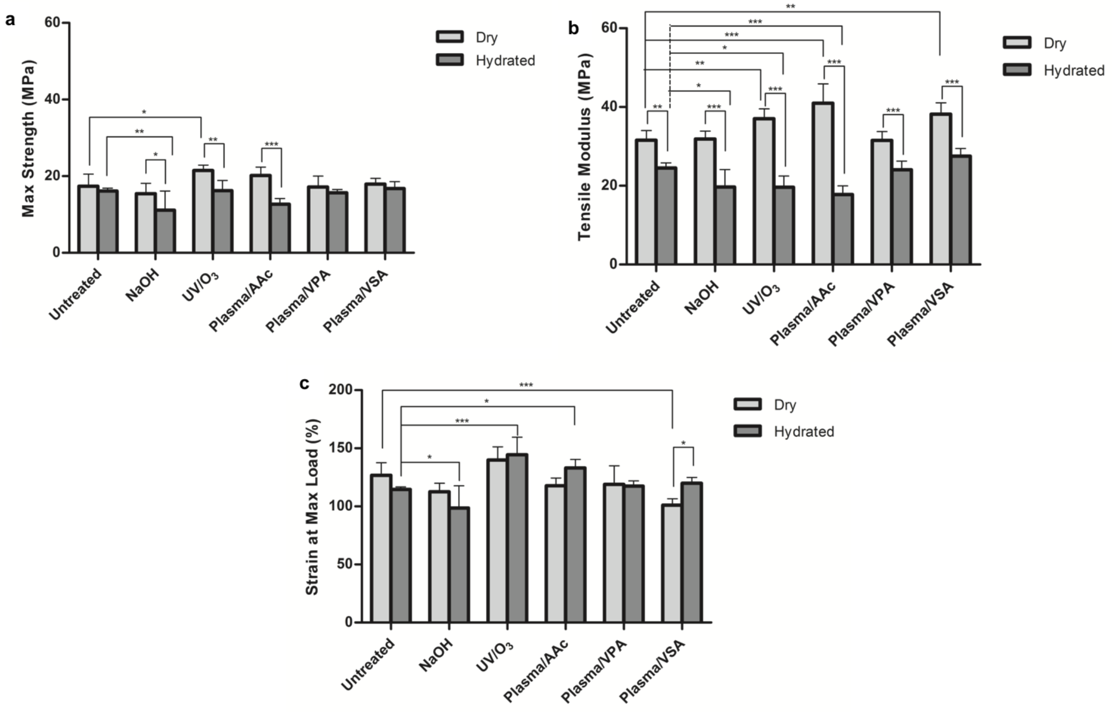

Figure 5-1. Effect of the different surface modifications on (a) maximum strength (MPa), (b) E modulus (MPa), and (c) strain at maximum load (%) obtained for SF textile matrices in dry and hydrated state (PBS; 37°C), in the longitudinal direction (* $p<0.05$; ** $p<0.01$, and *** $p<0.001$).

As expected, when comparing the untreated and the surface-treated textile constructs in the dry state no relevant changes were detected in terms of maximum strength and elongation at break. Even though, when considering the modulus, a slight increase was observed for UV/O_3, plasma/AAc and plasma/VSA, indicating that these structures have become stiffer.

By analysing the mechanical properties of the untreated SF textiles in the dry and hydrated states it was possible to see that while the changes on the maximum strength and elongation at break were not significant, a significant decrease (**$p < 0.01$) in the tensile modulus was observed in the presence of PBS solution. Considering the properties of the treated textile matrices, a significantly lower maximum strength was observed for hydrated samples treated with NaOH (*$p < 0.05$), UV/O_3 (**$p < 0.01$), and plasma/AAc (***$p < 0.001$). The hydration process induced an even higher difference for the modulus, indicating that all the surface treatments had impacted the mechanical performance in the wet state. In opposition, strain at break was significantly higher (*$p < 0.05$) for the plasma/VSA-treated hydrated samples in comparison to the dried ones. No significant differences were observed between the hydrated and dried samples treated with the remaining treatments. A decrease in the modulus was observed for the hydrated samples treated with NaOH, UV/O_3, and plasma/AAc as compared with the untreated samples while an increase in the maximum strain at break was observed for the samples treated with UV/O_3 and plasma/AAc. The differences in mechanical properties of the SF textile constructs when these are in the hydrated state, are related with the effect of water molecules incorporating the structure of the fibers, as reported by Perez-Rigueiro *et al.* [56] β-sheet platelets in SF constitute around 50–60% of the total volume of the fiber [51]. It is accepted that this crystalline domain is not affected by water molecules. Thus, the observed changes between the elastic modulus of samples tested in air and in the buffered solution can be attributed to alterations in the amorphous regions. Immersion in water disrupts the hydrogen bonds between chain segments in the amorphous phase, leaving van der Waals bonds to dominate, thus reducing the initial modulus. In this sense, it is expected that the surface treatments in wet conditions might attack preferentially the amorphous phase, corresponding to a general increase in the ductility with more impact in case of the scaffolds treated with plasma/AAc and UV/O_3 treatments, as observed by the general decrease in the modulus from the dry to the wet state. In case of UV/O_3 it is known that SF has a high permeability to oxygen [57], which has favored the modification of the fibers beyond the surface. In general, it is possible to affirm that the impact of the treatments in the final mechanical performance of the textile constructs was not severe.

5.4.2. Surface morphology and topography

The morphology of the surface of the scaffolds, as well as, of the surface of the fibers that form the 3D structure were analyzed by SEM. Figure 5-2, presents the scanning electron micrographs of side A and B of the SF knitted structure and magnifications of the fibers before and after the surface treatments.

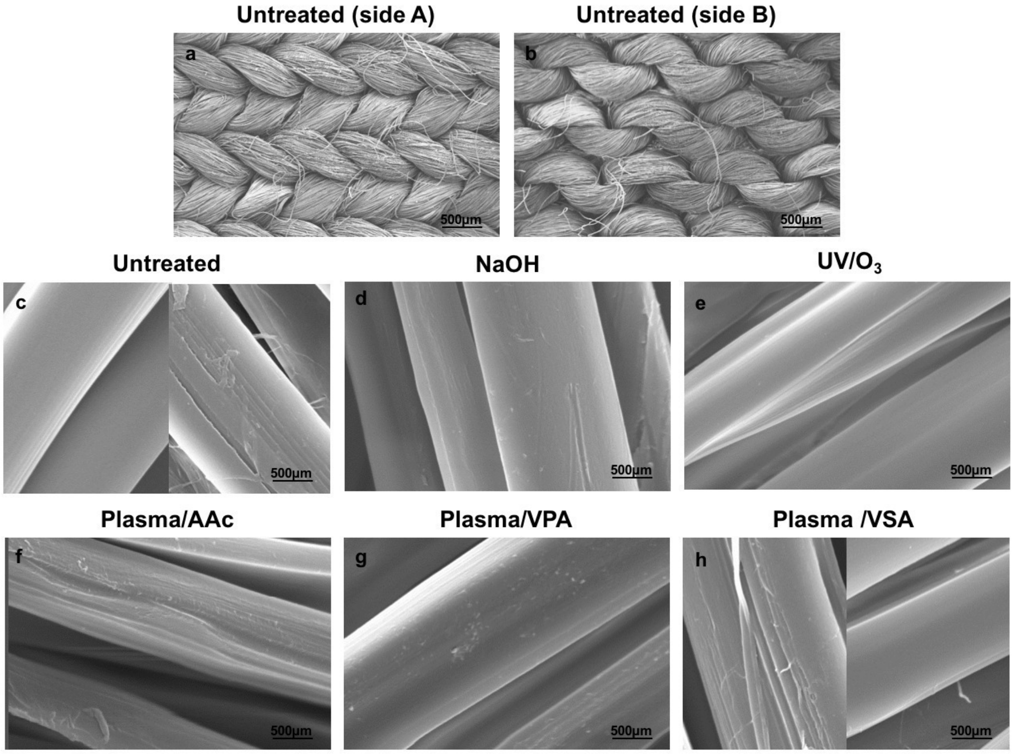

Figure 5-2. Scanning electron micrographs of (a) side A and (b) side B of the SF knitted structure and magnifications of the fibers on the top side (c) before and (d–h) after the different surface treatments.

Scanning electron micrographs of the untreated SF fibers revealed in general a smooth surface without pores or defects (Figure 5-2c). The SEM analysis of the treated fibers reveals some surface irregularities especially in the case of plasma/AAc and plasma/VSA treatments (Figure 5-2f and h). Nevertheless, it is difficult by using only SEM analysis to clearly differentiate the surface treatments based on the fiber morphology. In some cases, it was possible to observe areas with fibers exhibiting smooth surfaces and others with fibers presenting more irregular surfaces in the same sample, as for instances in case of untreated samples and after treatment with plasma/VSA (Figure 5-2c and h). It is important to state that degumming process can cause per se some physical changes in the fibers (Figure 5-2c).

The characterization of the surface of the SF fibers and the influence of the several surface modifications was done indirectly, through the analysis of SF membranes. Although it was clear that the starting surface of the membranes casted from regenerated SF can be different from the surface fibers in terms of crystalinity, it is plausible to correlate the effect of the proposed treatments in both scenarios.

Figure 5-3 presents the AFM images of the membrane surfaces before and after different surface treatments. The correspondent average roughness for each surface is presented in Figure 5-4.

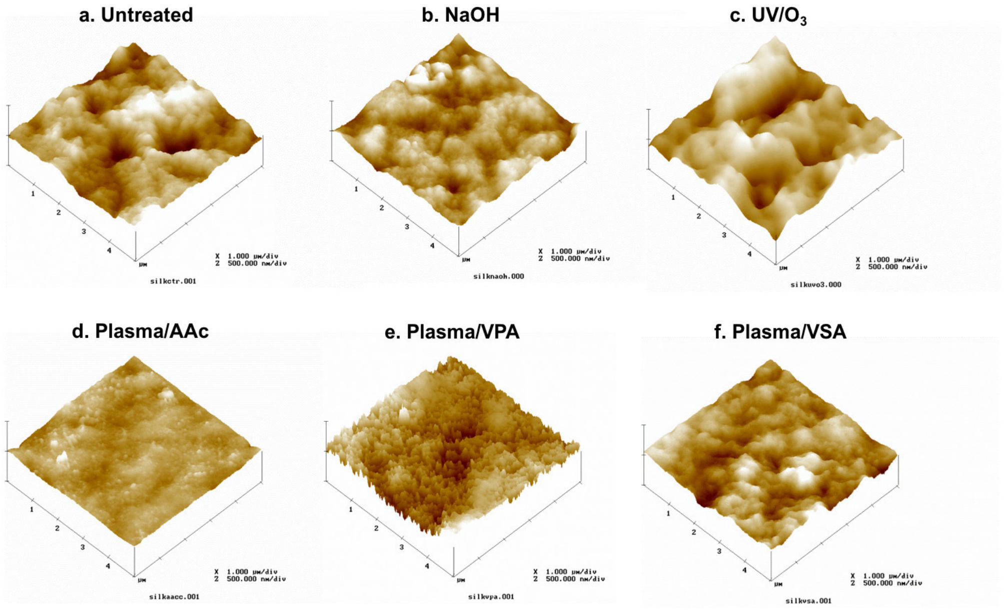
a. Untreated
b. NaOH
c. UV/O$_3$
d. Plasma/AAc
e. Plasma/VPA
f. Plasma/VSA
1
2
3
4
μm
X 1.000 μm/div
Z 500.000 nm/div
silkctr.001
silknaoh.000
silkuvo3.000
silkaacc.001
silkvpa.001
silkvsa.001

Figure 5-3. AFM images of the SF surfaces (a) before and (b–f) after the different surface treatments.

The wet chemical treatment with NaOH resulted in a smoother surface as compared to the untreated sample. In contrast, the UV/O$_3$ treatment significantly increased the roughness of the surface. Regarding the modifications following plasma preactivation only the treatment with acrylic acid was able to considerably smooth the surface. Nevertheless, etching processes are unavoidable when polymers are exposed to plasma. In general, the surface nanotopography and the average roughness were affected by the applied treatments. It is well recognized that small changes in the surface topography can affect cell behavior [58]. However, it is not possible to dissociate this physical modification from those occurring in due to changes in the wettability and chemical composition.

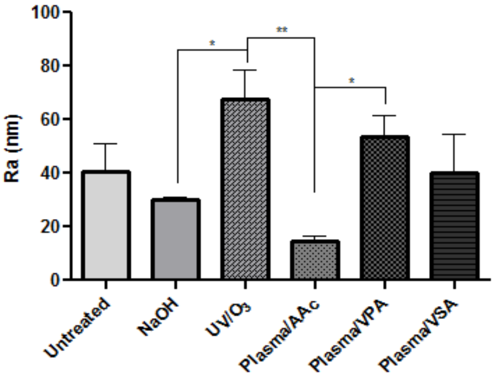

Figure 5-4. Average roughness (R_a) of the SF surfaces before and after the different surface treatments (*$p < 0.05$; ** $p < 0.01$).

5.4.3. Surface wettability and composition

The contribution of the dispersion and polar interactions to the surface energy was calculated by considering that the intermolecular attraction, which causes surface energy, results from a variety of intermolecular forces. Most of these forces are function of the specific chemical nature of a particular material, and the surface energy can be compiled as γ_p (polar interactions), taking into consideration that the dispersion forces (γ_d) are always present in all systems, independently of their chemical nature. The water contact angle values obtained for the untreated and surface-treated SF membranes are plotted in Figure 5-5 and the respective calculated surface energies are presented in Table 5-1.

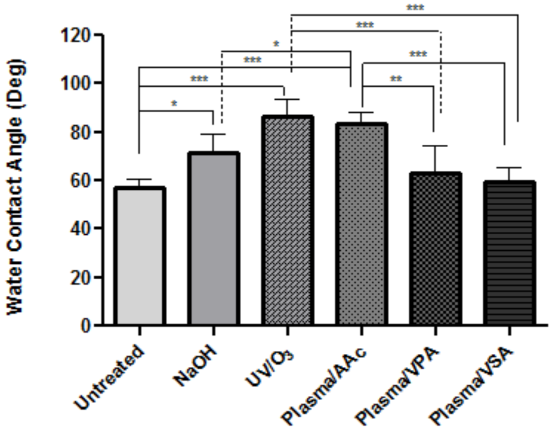

Figure 5-5. Water contact angles obtained for the untreated and treated SF surfaces. The significance level is $^{*}p < 0.05$, $^{**}p < 0.01$, and $^{***}p < 0.001$.

In Figure 5-1, it is possible to observe a general trend toward an increase in the hydrophobicity of the treated surfaces with significantly different values for NaOH etching, UV/O_3 and plasma/AAc treatments. Consequently, a decrease in the surface energy was registered due to a general decrease in the polar component most significant for UV/O_3 and plasma/AAc treatments (Table 5-1). In the case of NaOH treatment, the decrease in surface energy was also due to a decrease in the dispersive component. Generally, all treatments can result in simultaneous etching and modification that is expected to mainly affect the amorphous phase in SF. SF crystalline phase (β-sheet) represents near half of the total composition while the remaining amorphous phase is majorly composed of random coil, α-helix and turn secondary structures [51]. An increase in the surface crystallinity as a result of conformational change in the amorphous domains to silk II and/or the exposure of the crystalline phase due to an etching effect might be also contributing to an increase in the surface hydrophobicity. Further studies need to be conducted in order to confirm this possibility.

Table 5-1. Contact angle values (θ) measured for the untreated and treated surfaces and respective calculated surface energies (γ_s).

Treatment	Contact Angle (θ)		Surface Energy (mN.m^{-1})	Ratio
	H_2O	CH_2I_2	γ_s (γ_s^d +γ_s^p)	(γ_s^d/γ_s^p)
Untreated	57.34 ±3.27	46.22 ± 5.95	45.31 (25.66 + 19.66) ± 0.04	1.30
NaOH	71.78 ± 7.70	56.56 ± 8.62	35.36 (20.44 + 14.92) ± 0.06	1.37
UV/O_3	86.62 ± 7.14	48.5 ± 4.99	32.39 (27.61 + 3.82) ± 0.02	7.22
Plasma/AAc	83.34 ± 5.04	55.28 ± 9.52	30.02 (24.36 + 5.72) ± 0.02	4.26
Plasma/VPA	63.18 ± 11.36	58.76 ± 10.14	40.33 (24.00 + 16.33) ± 0.07	1.47
Plasma/VSA	59.48 ± 6.09	42.44 ± 7.91	45.92 (26.90 + 19.02) ± 0.07	1.41

The surface composition and atomic ratios of the untreated and treated samples, investigated by XPS, are presented in Table 5-2. The wet chemical treatment with NaOH resulted in etching as confirmed by the surface analysis. XPS results showed lower oxygen content on the NaOH-treated surface (Table 5-2). The obtained result might be associated to the higher sensitivity of the oxygen containing moieties (related with the amorphous domains) to degradation/hydrolysis processes, that is, the scission of the chains that occur predominantly at the places where those functionalities are. As expected, the lower oxygen content was associated with higher water contact angle value (less hydrophilic surface, Figure 5-4, Table 5-1) and smoother surface after the treatment.

Table 5-2. Surface composition and atomic ratios of modified and nonmodified SF samples determined by XPS.

Modification	O	N	C	S	P	O/C
Untreated	19.6	14.9	63.5	-	-	0.31
NaOH	15.3	11.9	72.6	-	-	0.21
UV/O_3	25.1	11.9	59.0	-	-	0.43
Plasma/AAc	21.3	15.2	61.5	-	-	0.35
Plasma/VPA	28.4	11.0	49.8	-	2.7	0.57
Plasma/VSA	19.6	6.1	73.2	0.1	-	0.27

The modification with UV/O_3 resulted in higher oxygen content in the XPS spectrum of the modified material (Table 5-2). This result is in agreement with previous reports for different polymers treated by UV/O_3 and with the expected ongoing oxidation induced by the ozone presence [59-61]. Surprisingly, the water contact angle for the treated samples was significantly higher when compared to the untreated samples. The significant increase in roughness (Figure 5-4) resulting from the surface etching can be a possible explanation for the obtained results, most probably due the Cassie-Baxter effect [62].

AAc grafted surfaces presented a slight increase in the oxygen to carbon rate content (Table 5-2), together with a significant smoothening of the surface (Figures 5-3d and 5-4). This smoothening may indicate that upon grafting, acrylic acid monomers started to fill the valleys similarly to the phenomenon recently reported by Gupta *et al.* [63] for the grafting of AAc onto plasma-treated polycaprolactone monofilament surface. It is known that the etching by plasma treatment can contribute per se to an increase in the hydrophobicity of silk surfaces [64], while the subsequent grafting with acrylic acid monomers is expected to functionalize the surface and increase its wettability. Thus, the measured significant increase in the hydrophobicity was unexpected. It is difficult to confirm the AAc grafting by XPS because all functionalities characteristic for acrylic acid (CHCOO-, COO-) are already present in the silk structure. However, the C1s high resolution spectra for plasma/AAc-treated surfaces is quite different from the untreated ones, showing less intensive peaks for –CO and –COO (Supplementary Figure 5-1). This result seems to confirm that most probably etching and not grafting is preferentially occurring on the surface during plasma/AAc treatment. In case of VPA and VSA-treated samples P and S, respectively, were detected in their surfaces by XPS (Supplementary Figure 5-2), confirming the successful grafting although with different effec- tiveness. Lopez-Perez *et al.* [65] have reported higher grafting efficiency for VPA-grafted surfaces that has resulted in higher number of adherent cells (SaOs-2) and higher prolif- eration rate. Here, it was not observed a significant change on the surface wettability leading to the assumption that the grafting yield was lower than expected. The equilibrium degree of grafting is dependent on monomer concentration, reaction temperature and the concentration of active regions created upon plasma exposure, thus further optimization of these parameters are necessary for increasing the grafting yield in this particular reaction.

5.4.4. Cell morphology

The effect of the applied surface treatments over initial cell adhesion was analyzed based on the morphology of L929 cells observed by SEM (Figure 5-6). After 1 hour of cell culture, extensive cell colonization can be observed for the studied materials. However, the majority of the attached cells were not spread (Figure 5-6a, d, g, j, m, p and s). After 5 hours of culture, cells presented typical spindle-like fibroblast morphology, showing a higher degree of spreading with some extended lamellipodia over the surface of all modified materials (Figure 5-6h, k, n, q, and t). This effect was even more notorious after 24 hours of culture (Figure 5-6i, l, o, r and u). The adhered cells presented an elongated morphology and a high degree of spreading over the modified surfaces was observed, interacting and integrating well with the fibers. In agreement with these findings, Park *et al.* [66] have reported that surfaces of poly(glycolic acid), poly(L-lactic acid), and poly(lactic-co- glycolic acid) chemically modified using air plasma treatment followed by acrylic acid grafting, improved fibroblast-like cells spreading over the nanofibrous surfaces, suggesting that the carboxylic functional groups could be successfully immobilized at the scaffolds' surface improving cell attachment and proliferation *in vitro*. A different study using human bone marrow-derived mesenchymal stem cells (hMSCs) showed a similar cell behavior after 5 days of culture on SF films modified with sulfonic acid [49]. Cells grew across the surface, exhibiting spindle-like fibroblast morphology, typical of undifferentiated hMSCs. For the untreated SF textile scaffolds, L929 cells clearly presented their typical fibroblastic morphology, attaching and stretching over the scaffolds surface (Figure 5-6e and f). This expected cell behavior [30] can be justified by the silk conformation at the scaffolds' surface as well as the presence of –COOH and –OH polar groups that confer a more hydrophilic character to the fibers, known to directly mediate and control cell adhesion, cell–surface interactions, cytoskeleton organization and cell shape [67, 68]. Cells were also able to adhere on the SF membranes (Figure 5-6a–c) showing evident lamellipodia and filopodia over the surfaces (Figure 5-6b and c). Nevertheless, higher cell–surface interactions were observed on the untreated fibers, which can be eventually justified by the high porosity and surface area of the fiber-based scaffolds that improve cell attachment and proliferation [9-11].

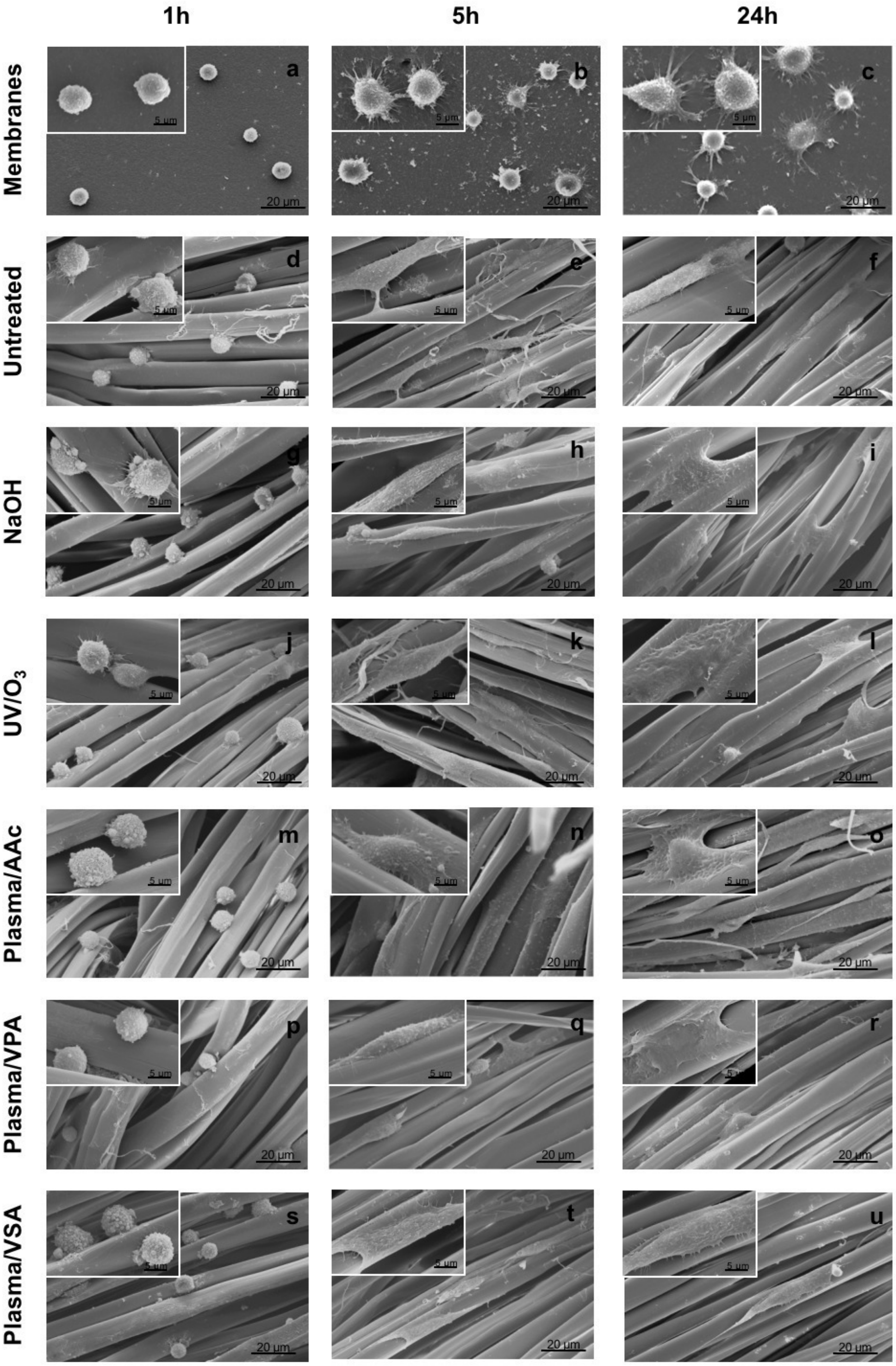

1h
5h
24h
Membranes
Untreated
NaOH
UV/O3
Plasma/AAc
Plasma/VPA
Plasma/VSA
a
b
c
d
e
f
g
h
i
j
k
l
m
n
o
p
q
r
s
t
u
5 µm
20 µm

Figure 5-6. Scanning electron micrographs showing the L929 cell morphology and adhesion at the surface of (a–c) 2D silk membranes, 3D silk textile scaffolds (d–f) untreated and after the different surface modifications: (g–i) NaOH; (j–l) UV/O$_3$; (m–o) plasma/AAc; (p–r) plasma/VPA; (s–u) plasma/VSA, for (a, d, g, j, m, p, and s) 1 hour, (b, e, h, k, n, q, and t) 5 hours, and (c, f, i, l, o, r, and u) 24 hours of culture.

5.4.5. Cell adhesion

Cell adhesion rate was evaluated by quantifying the DNA content along the culture time (Figure 5-7). The obtained results showed that after 1 hour, L929 cells adhered in significantly higher numbers (***$p < 0.001$) to untreated scaffolds, possibly indicating a cell adaptation to the induced surface modifications. Moreover, no significant differences were identified between the scaffolds treated under different conditions. After 5 hours of culture the number of cells adhered to the untreated structures remained the same while a significantly higher number (***$p < 0.001$, except for plasma/VPA: **$p < 0.01$) in comparison to 1 hour of culture, reaching a value similar to the untreated condition, was quantified in the treated scaffolds. Nonetheless, the DNA values obtained for plasma/VPA-treated surfaces were significantly lower than those reached for structures treated by NaOH (**$p < 0.01$), plasma/AAc (***$p < 0.001$), plasma/VSA and UV/O$_3$ (*$p < 0.05$). After 24 hours, plasma/VPA-treated surfaces also presented significantly lower (*$p < 0.05$) DNA values compared to the untreated and plasma/AAc structures. No further significant changes were observed between the untreated and treated conditions and between the treatments, revealing that the unmodified SF presents per se properties of great interest that can be used as a way to improve and facilitate cell adhesion. A different study comparing different biodegradable polymers with those chemically modified at the surface by Plasma/AAc treatment, also reported that after 24 hours of culture, fibroblast cells adhesion rate on the surface-treated scaffolds was similar to that on control conditions [66]. Moreover, the number of cells adhered to the untreated structures significantly increased after 24 hours in comparison to 1 hour (**$p < 0.01$) and 5 hour (*$p < 0.05$) of culture, which is not consistent with the results obtained for SF membranes whose adhesion rate did not vary after 5 hours of culture (Data not shown).

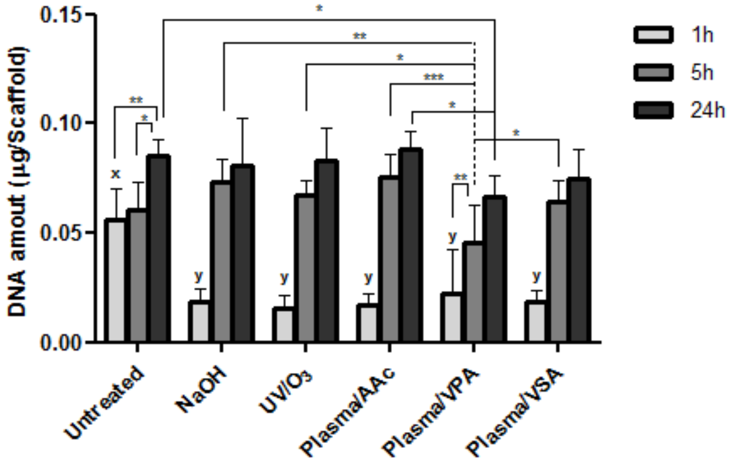

Figure 5-7. DNA amount corresponding to the number of L929 cells adhered on untreated and surface-treated 3D silk textile scaffolds after 1, 5 and 24 hours of culture. Data are shown as mean 6 standard deviation from at least n=5

(*$p < 0.05$, **$p < 0.01$, and ***$p < 0.001$). x: $p < 0.001$ for all the treatments at the same culture period. y: ***$p < 0.001$ for the same treatment after 5 and 24 hours of culture. The exceptions are represented in the graphic.

5.5. Conclusions

SF knitted matrices were successful modified using different surface treatments, NaOH solution, UV/O_3 exposure and air plasma treatment followed by AAc, VPA and VSA grafting. The impact of the treatments on the final mechanical performance of the textile constructs was not pronounced. Nevertheless, an increase in the modulus in the dry state was significant for UV/O_3, plasma/AAc and plasma/VPA treatments. This was followed by an increase in the maximum strength and elongation at break. It seems that these surface treatments had a positive impact in the bulk properties of the fibers by increasing both the strength and ductility of the textile constructs. At the surface level, AFM and XPS confirmed the modification and grafting of the surfaces, although with different effectiveness, while a significant increase in the hydrophobicity was detected for NaOH, UV/O_3 and plasma/AAc treatments. This intriguing result is presently under investigation. The *in vitro* preliminary biological studies showed that the number of adhered cells increases for all the studied surfaces over the culture time. However, the morphology of the adhered fibroblasts was found to be considerably different in the case of fiber-based constructs, since the cells tend to overspread both on the untreated and surface-treated fibers. This study validates the present treatments to be further investigated in a tissue engineering context, where more sensitive cells (stem cells).

5.6. Spplementary information

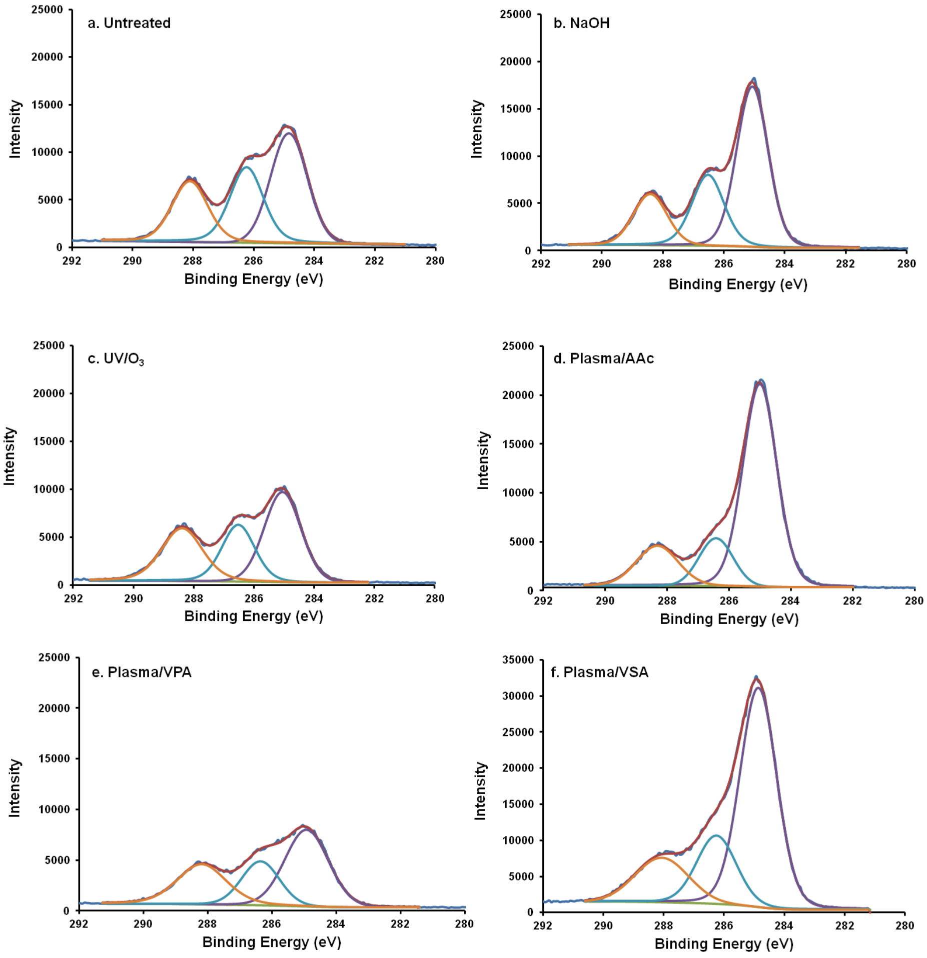

Supplementary Figure 5-1. C1s core level spectra of a) untreated and modified SF samples: b) NaOH, c) UV/O$_3$, d) plasma/AAc, e) plasma/VPA, f) plasma/VSA.

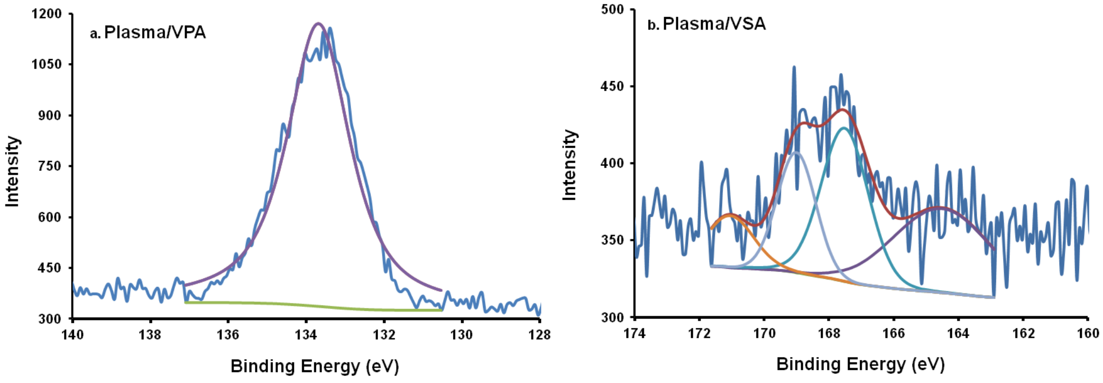

Supplementary Figure 5-2. P2p (a) and S2p (b) high resolution spectra for SF treated by plasma/VPA and plasma/VSA, respectively.

5.7. References

[1] D.W. Hutmacher, Scaffolds in tissue engineering bone and cartilage, Biomaterials 21(24) (2000) 2529-2543.

[2] C. Liu, et al., Design and development of three-dimensional scaffolds for tissue engineering, Chemical Engineering Research & Design 85(A7) (2007) 1051-1064.

[3] P.X. Ma, Biomimetic materials for tissue engineering, Adv Drug Deliv Rev 60(2) (2008) 184-98.

[4] K. Rezwan, et al., Biodegradable and bioactive porous polymer/inorganic composite scaffolds for bone tissue engineering, Biomaterials 27(18) (2006) 3413-31.

[5] A.R. Costa-Pinto, et al., Scaffolds based bone tissue engineering: the role of chitosan, Tissue Eng Part B Rev 17(5) (2011) 331-47.

[6] A.J. Salgado, et al., Bone tissue engineering: state of the art and future trends, Macromol Biosci 4(8) (2004) 743-65.

[7] K. Tuzlakoglu, R.L. Reis, Biodegradable polymeric fiber structures in tissue engineering, Tissue Eng Part B Rev 15(1) (2009) 17-27.

[8] A.L. Oliveira, et al., Micro-computed tomography (micro-CT) as a potential tool to assess the effect of dynamic coating routes on the formation of biomimetic apatite layers on 3D-plotted biodegradable polymeric scaffolds, J Mater Sci Mater Med 18(2) (2007) 211-23.

[9] M.E. Gomes, et al., Influence of the porosity of starch-based fiber mesh scaffolds on the proliferation and osteogenic differentiation of bone marrow stromal cells cultured in a flow perfusion bioreactor, Tissue Eng 12(4) (2006) 801-9.

[10] M. Chen, et al., Role of electrospun fibre diameter and corresponding specific surface area (SSA) on cell attachment, J Tissue Eng Regen Med 3(4) (2009) 269-79.

[11] M.E. Gomes, et al., Effect of flow perfusion on the osteogenic differentiation of bone marrow stromal cells cultured on starch-based three-dimensional scaffolds, J Biomed Mater Res A 67(1) (2003) 87-95.

[12] R. Sumanasinghe, M.W. King, New trends in biotextiles - the challenge of tissue engineering, Journal of Textile and Apparel, Technology and Management 3(2) (2003) 1-13.

[13] X. Tao, Smart fibres, fabrics and clothing, in textile scaffolds in tissue engineering, Woodhead Publishing2001.

[14] R. Sumanasinghe, M.W. King, The applications of biotextiles in tissue engineering, Journal of Textile and Apparel, Technology and Management 9(3) (2005) 80-90.

[15] X.G. Wang, et al., Applications of knitted mesh fabrication techniques to scaffolds for tissue engineering and regenerative medicine, J Mech Behav Biomed 4(7) (2011) 922-932.

[16] X.H. Zou, et al., Mesenchymal stem cell seeded knitted silk sling for the treatment of stress urinary incontinence, Biomaterials 31(18) (2010) 4872-4879.

[17] T. Yagi, et al., Preparation of double-raschel knitted silk vascular grafts and evaluation of short-term function in a rat abdominal aorta, Journal of Artificial Organs 14(2) (2011) 89-99.

[18] S. Gundy, et al., Human coronary artery smooth muscle cell response to a novel PLA textile/fibrin gel composite scaffold, Acta Biomater 4(6) (2008) 1734-44.

[19] M.I. Van Lieshout, et al., Electrospinning versus knitting: two scaffolds for tissue engineering of the aortic valve, J Biomat Sci-Polym E 17(1-2) (2006) 77-89.

[20] S. Sahoo, et al., A bFGF-releasing silk/PLGA-based biohybrid scaffold for ligament/tendon tissue engineering using mesenchymal progenitor cells, Biomaterials 31(11) (2010) 2990-2998.

[21] H.B. Fan, et al., Anterior cruciate ligament regeneration using mesenchymal stem cells and silk scaffold in large animal model, Biomaterials 30(28) (2009) 4967-4977.

[22] X. Chen, et al., Ligament regeneration using a knitted silk scaffold combined with collagen matrix, Biomaterials 29(27) (2008) 3683-3692.

[23] H.F. Liu, et al., The interaction between a combined knitted silk scaffold and microporous silk sponge with human mesenchymal stem cells for ligament tissue engineering, Biomaterials 29(6) (2008) 662-674.

[24] J.L. Chen, et al., Efficacy of hESC-MSCs in knitted silk-collagen scaffold for tendon tissue engineering and their roles, Biomaterials 31(36) (2010) 9438-9451.

[25] C. Vaquette, et al., Aligned poly(L-lactic-co-e-caprolactone) electrospun microfibers and knitted structure: A novel composite scaffold for ligament tissue engineering, J Biomed Mater Res A 94A(4) (2010) 1270-1282.

[26] G.P. Chen, et al., Regeneration of cartilage tissue by combination of canine chondrocyte and a hybrid mesh scaffold, Mat Sci Eng C-Bio S 24(3) (2004) 373-378.

[27] W.D. Dai, et al., The influence of structural design of PLGA/collagen hybrid scaffolds in cartilage tissue engineering, Biomaterials 31(8) (2010) 2141-2152.

[28] N. Kawazoe, et al., A Cell Leakproof PLGA-Collagen Hybrid Scaffold for Cartilage Tissue Engineering, Biotechnol Progr 26(3) (2010) 819-826.

[29] K.W. Ng, et al., In vitro characterization of natural and synthetic dermal matrices cultured with human dermal fibroblasts, Biomaterials 25(14) (2004) 2807-2818.

[30] L.R. Almeida, et al., New biotextiles for tissue engineering: development, characterization and in vitro cellular viability, Acta Biomater 9(9) (2013) 8167-81.

[31] V. Kearns, et al., Silk-based biomaterials for tissue engineering, Biomaterials and Tissue Engineering Group2008.

[32] C. Vepari, D.L. Kaplan, Silk as a biomaterial, Progress in Polymer Science 32(8-9) (2007) 991-1007.

[33] C. Correia, et al., Development of silk-based scaffolds for tissue engineering of bone from human adipose-derived stem cells, Acta Biomater 8(7) (2012) 2483-92.

[34] A.L. Oliveira, et al., Aligned silk-based 3-D architectures for contact guidance in tissue engineering, Acta Biomater 8(4) (2012) 1530-42.

[35] S.S. Silva, et al., Novel genipin-cross-linked chitosan/silk fibroin sponges for cartilage engineering strategies, Biomacromolecules 9(10) (2008) 2764-74.

[36] L.P. Yan, et al., Macro/microporous silk fibroin scaffolds with potential for articular cartilage and meniscus tissue engineering applications, Acta Biomaterialia 8(1) (2012) 289-301.

[37] T. Kardestuncer, et al., RGD-tethered silk substrate stimulates the differentiation of human tendon cells, Clin Orthop Relat Res 448 (2006) 234-9.

[38] K. Karthikeyan, et al., Fabrication of novel biofibers by coating silk fibroin with chitosan impregnated with silver nanoparticles, J Mater Sci Mater Med 22(12) (2011) 2721-6.

[39] S. Sahoo, et al., PLGA nanofiber-coated silk microfibrous scaffold for connective tissue engineering, J Biomed Mater Res B Appl Biomater 95(1) (2010) 19-28.

[40] L. Wu, et al., Preliminary study on polyvinyl alcohol/wild antheraea pernyi silk fibroin as nanofiber scaffolds for tissue engineered tendon, Zhongguo Xiu Fu Chong Jian Wai Ke Za Zhi 25(2) (2011) 181-6.

[41] W. Luangbudnark, et al., Properties and biocompatibility of chitosan and silk fibroin blend films for application in skin tissue engineering, ScientificWorldJournal 2012 (2012) 697201.

[42] A. Vasconcelos, et al., Novel silk fibroin/elastin wound dressings, Acta Biomater 8(8) (2012) 3049-60.

[43] A.R. Murphy, D.L. Kaplan, Biomedical applications of chemically-modified silk fibroin, Journal of materials chemistry 19(36) (2009) 6443-6450.

[44] Y. Wang, et al., Stem cell-based tissue engineering with silk biomaterials, Biomaterials 27(36) (2006) 6064-82.

[45] H.S. Baek, et al., Enhanced chondrogenic responses of articular chondrocytes onto porous silk fibroin scaffolds treated with microwave-induced argon plasma, Surf Coat Tech 202(22-23) (2008) 5794-5797.

[46] S. Wang, et al., Preparation, characterization and biocompatibility of electrospinning heparin-modified silk fibroin nanofibers, Int J Biol Macromol 48(2) (2011) 345-53.

[47] J. Gu, et al., Surface sulfonation of silk fibroin film by plasma treatment and in vitro antithrombogenicity study, Materials Science and Engineering: C 20(1) (2002) 199-202(4).

[48] L. Jeong, et al., Plasma-treated silk fibroin nanofibers for skin regeneration, International Journal of Biological Macromolecules 44(3) (2009) 222-228.

[49] A.R. Murphy, et al., Modification of silk fibroin using diazonium coupling chemistry and the effects on hMSC proliferation and differentiation., Biomaterials 29(31) (2008) 4260-4260.

[50] C. Zaharia, et al., Silk fibroin films for tissue bioengineering applications, J Optoelectron Adv M 14(1-2) (2012) 163-168.

[51] G.H. Altman, et al., Silk-based biomaterials, Biomaterials 24(3) (2003) 401-416.

[52] Q. Lu, et al., Silk self-assembly mechanisms and control from thermodynamics to kinetics, Biomacromolecules 13(3) (2012) 826-832.

[53] D.K. Owens, R.C. Wendt, Estimation of the surface free energy of polymers, J Appl Polym Sci 13(8) (1969) 1741–1747.

[54] D.H. Kaelble, Dispersion-Polar Surface Tension Properties of Organic Solids, J Adhesion 2 (1970) 66-81.

[55] G.H. Altman, et al., Silk-based biomaterials, Biomaterials 24(3) (2003) 401-16.

[56] J. Perez-Rigueiro, et al., Mechanical properties of silkworm silk in liquid media, Polymer 41(23) (2000) 8433-8439.

[57] N. Minoura, et al., Physico-chemical properties of silk fibroin membrane as a biomaterial, Biomaterials 11(6) (1990) 430-434.

[58] N.M. Alves, et al., Controlling Cell Behavior Through the Design of Polymer Surfaces, Small 6(20) (2010) 2208-2220.

[59] I. Pashkuleva, et al., Surface modification of starch based biomaterials by oxygen plasma or UV-irradiation, J Mater Sci Mater Med 21(1) (2010) 21-32.

[60] G.-H. Koo, J. Jang, Surface modification of poly(lactic acid) by UV/Ozone irradiation, Fiber Polym 9(6) (2008) 674-678.

[61] I. Mathieson, R.H. Bradley, Improved adhesion to polymers by UV/ozone surface oxidation, Int J Adhes Adhes 16(1) (1996) 29-31.

[62] A.B. Cassie, S. Baxter, Wettability of porous surfaces, Transactions of the Faraday Society 40 (1944) 546-551.

[63] B. Gupta, et al., Oxygen plasma-induced graft polymerization of acrylic acid on polycaprolactone monofilament, European Polymer Journal 48(11) (2012) 1940-1948.

[64] P. Chaivan, et al., Low-temperature plasma treatment for hydrophobicity improvement of silk, Surface and Coatings Technology 193(1–3) (2005) 356-360.

[65] P.M. Lopez-Perez, et al., Plasma-induced polymerization as a tool for surface functionalization of polymer scaffolds for bone tissue engineering: An in vitro study, Acta biomaterialia 6(9) (2010) 3704-3712.

[66] K. Park, et al., Surface modification of biodegradable electrospun nanofiber scaffolds and their interaction with fibroblasts, J Biomat Sci-Polym E 18(4) (2007) 369-382.

[67] N.R. Washburn, et al., High-throughput investigation of osteoblast response to polymer crystallinity: influence of nanometer-scale roughness on proliferation, Biomaterials 25(7-8) (2004) 1215-1224.

[68] Y. Arima, H. Iwata, Effect of wettability and surface functional groups on protein adsorption and cell adhesion using well-defined mixed self-assembled monolayers, Biomaterials 28(20) (2007) 3074-3082.

CHAPTER 6.

Silk-Based Anisotropical 3D Biotextiles for Bone Regeneration

CHAPTER 6.

Silk-based anisotropical 3D biotextiles for bone regeneration*

6.1. Abstract

Bone loss in the craniofacial complex can been treated using several conventional therapeutic strategies that face many obstacles and limitations. In this work, novel three-dimensional (3D) biotextile architectures were developed as a possible strategy for flat bone regeneration applications. As a fully automated processing route, this strategy as potential to be easily industrialized. Silk fibroin (SF) yarns were processed into weft-knitted fabrics spaced by a monofilament of polyethylene terephthalate (PET). A comparative study with a similar 3D structure made entirely of PET was established. Highly porous scaffolds with homogeneous pore distribution were observed using micro-computed tomography analysis. In the frequency range tested, the storage modulus values obtained for SF-PET scaffolds were higher than for the PET scaffolds. Human adipose-derived stem cells (hASCs) cultured on the SF-PET spacer structures showed the typical pattern for ALP activity under osteogenic culture conditions. Osteogenic differentiation of hASCs on SF-PET and PET constructs was also observed by extracellular matrix mineralization and expression of osteogenic-related markers (osteocalcin, osteopontin and collagen type I) after 28 days of osteogenic culture, in comparison to the control basal medium. The quantification of convergent macroscopic blood vessels toward the scaffolds by a chick chorioallantoic membrane assay, showed higher angiogenic response induced by the SF-PET textile scaffolds than PET structures and gelatin sponge controls. Subcutaneous implantation in CD-1 mice revealed tissue ingrowth accompanied by blood vessels infiltration in both spacer constructs. The structural adaptability of textile structures combined to the structural similarities of the 3D knitted spacer fabrics to craniofacial bone tissue and achieved biologial performance, make these scaffolds a possible solution for tissue engineering approaches in this area.

*This chapter is based on the following publication:

Ribeiro VP, Silva-Correia J, Nascimento AI, da Silva Morais A, Marques AP, Ribeiro AS, Silva CJ, Bonifácio G, Sousa RA, Oliveira JM, Oliveira AL, Reis RL. Silk-based anisotropical 3D biotextiles for bone regeneration. Biomaterials. 2017, 123:92-106. doi: 10.1016/j.biomaterials.2017.01.027.

6.2. Introduction

Craniofacial critical-sized bone defects can be caused by several conditions, including tumor excisions, trauma, congenital malformations, degenerative skeletal disorders and advanced bone resorption due to teeth extraction [1]. More than 1.5 million bone grafts, including autologous or allogenic grafts, xenografts or alloplastic graft materials, are performed every year in the USA and the maxillofacial region is the most affected with over then three-quarters of surgical interventions every year [2]. Nevertheless, these standard clinical practices still present significant limitations in the treatment of craniofacial defects, including the need for complex-shaped bones that may complicate the surgical process. The use of metal implants as bone substitutes came as a possible solution in some cases, however, the frequent foreign body reaction makes this solution impossible as a lifetime treatment [3]. In this sense, the craniofacial bone regeneration involving scaffolding strategies and tissue engineering (TE) approaches have emerged to fulfil the gaps presented by the current therapeutic modalities [4].

Flat bones, as those from the craniofacial region, possess an anisotropic architecture composed of two nearly parallel plates of compact bone enclosing a layer of trabecular bone [2]. Scaffolds designed for craniofacial TE must contain such specificities, two dense external layers to sustain the masticatory forces at the maxillofacial region or to protect the constant brain pressures, and a porous spongy-like inner part to facilitate scaffolds adaptability and integration from the surrounding tissues, improving neotissue formation and vascular invasion [5].

Fiber-based networks with high surface area and interconnectivity have been proven to be particularly interesting to prepare polymeric porous 3D scaffolds for TE applications [6, 7]. Computer assisted textile-based technologies constitute an attractive route for the production of more complex fibrous three-dimensional (3D) scaffolds, based on automated pre-established techniques with high reproducibility and controlled properties [8]. Different textile production systems, including stitching, braided, woven, non-woven and knitted have already been proposed as scaffolding strategies. For example, Moutos *et al.* [9] developed 3D woven composite scaffolds for cartilage TE applications by combining a chondrocyte–hydrogel mixture into tissue constructs, to achieve improved mechanical properties. Liu *et al.* [10] combined micro-porous silk sponges with knitted silk mesh fo specifc ligament TE, and Chen *et al.* [11] developed a new practical ligament scaffold based on the synergistic incorporation of a plain knitted silk structure and a collagen matrix. The application of these textile production systems have also been proposed for bone TE applications [12, 13]. Knitted textile technologies are particularly useful for the fabrication of 3D fiber-based structures, since they allow for producing structures with complex shapes using rapid manufacturing processes. Moreover, they can be successfully adjusted to the use of several types of fiber materials, present controlled internal porosity, enhanced flexibility and high resistance to deformation, which makes this technique particularly desired for TE applications [14-16]. The resulting structural similarities to the anisotropic architecture of flat bone, makes the 3D knitted spacer fabrics a possible solution for craniofacial bone scaffolding strategies.

Synthetic materials and ceramic implants composed of hydroxyapatite (HA) and calcium phosphate are still the most used, especially due to the high chemical similarity to bone [17]. However, natural-based materials have gained much attention as craniofacial bone scaffolding systems, showing high osteoconductivity and controlled degradability [18, 19]. Natural silk fibroin (SF)-based materials have been successfully used for bone TE applications [20]. For example, Meinel and co-workers [21] have demonstrated well the feasibility of silk-based implants with engineered bone for the regeneration of bone tissue as a mechanically stable option. More recently, Mandal *et al.* [22] developed a microfiber-reinforced silk scaffolds with high compressive strength as matrices for load-bearing bone applications with adequate *in vivo* response. The repair and regeneration of cranial defects have also been addressed using silk fibroin nanofibrous membranes [23] and porous scaffolds [24, 25].

Human adipose-derived stem cells (hASCs), isolated from the stromal vascular fraction (SVF) of adipose tissue have emerged as a viable possibility for bone regeneration applications due to the comparable features to bone marrow stromal cells (BMSCs), including similar morphology, differentiation capacity and phenotype [26]. In addition, they hold the advantage of being easily harvested from the adipose tissue in relative abundance and with less morbidity at the donor site [27]. There have been many recent reports indicating that hASCs can differentiate along multiple lineage pathways, including into osteogenic lineages when appropriatly stimulated [26, 28, 29]. It is also important to consider that the biological environment involves different cell interactions, which justify the use of a source of cells that can be used for several differentiation pathways [30]. Thus, the use of hASCs is relevant not only for bone TE but for other TE applications and clinical approaches. In a previous study, Correia *et al.* [20] were able to successfully explore the potential of hASC as a single cell source for osteogenic and endothelial differentiation and the assembly of bone and vascular compartments within the same scaffold, using silk porous matrices.

In the present study, a highly anisotropic scaffold was designed for bone TE applications, using natural silk yarns processed for the first time to form 3D knitted spacer fabrics. This structure is composed of two dense knitted sheets of SF spaced by a monofilament of polyethylene terephthalate (PET), the so-called SF-PET scaffolds, as a viable model for flat bone regeneration. A comparative analysis was performed using a knitted spacer scaffold entirely composed of PET. The morphology and 3D structure of the developed scaffolds were evaluated by scanning electron microscopy (SEM) and micro-computed tomography (micro-CT). The dynamic mechanical analysis (DMA) and static mechanical properties were also analyzed. Osteogenic differentiation of human adipose derived stem cells (hASCs) seeded in the SF-PET and PET scaffolds was also evaluated up to 28 days of *in vitro* culture. The *in vivo* biological response and agiogenic potential were investigated in a chick choroallontoic membrane assay and by subcutaneous implantation in a mice model.

6.3. Materials and Methods

6.3.1. Materials

Bombyx mori cocoons were supplied by the Portuguese Association of Parents and Friends of Mentally Disabled Citizens (APPACDM, Castelo Branco, Portugal).

6.3.2. Production of the textile-based scaffolds

Raw silk yarns were processed from the combination of 4-8 cocoons into threads of raw silk. The reeled silk was then combined by twisting into a silk yarn, used to produce the 3D knitted spacer fabric by weft-knitting technology (Terrot, UP472T model, Germany). A 100D/1Fpolyester monofilament (from Putian Shuangyan Chemical Fiber Co., Ltd.) was used on the knitting machine, to form the SF-PET spacer fabric.

The 100% PET warp-knitted spacer fabric was produced on a warp-knitting machine (COMEZ, model DNB/EL-800-8B), with a working width of 812.8 mm and stitch density between 1 and 40 stitches/cm. The same monofilament was used to interconnect the outer PET knitts. The polyester based filaments used in this spacer fabric construction were produced in a pilot spinning line (from Hills Inc., Pretoria, South Africa) using Polyethylene terephthalate Type RT52, with 0.64 of intrinsic viscosity (supplied by INVISTA™ Resins & Fibers, Kansas, USA) as raw material. The temperatures of the spinning line were maintained between 250°C and 270°C, the spinning speed was 1500 m/minute for a throughput of 1.3 Kg/h with a draw ratio of 3.75. A yarn with 36 continuous filaments was obtained, with 3.6 of denier per filament equivalent to about 15μm per filament.

Textile scaffolds (both SF-PET and PET) were first washed in a 0.15% (w/v) natural soap aqueous solution for 2 hours and then rinsed in distilled water to remove the impurities resulting from the manufacturing process. In this sense, SF-PET spacer fabrics underwent a subsequent purification process. Structures were boiled for 1 hour in a 0.03 M Na_2CO_3 solution (Sigma-Aldrich, MO, USA), and then rinsed in boiling distilled water to ensure the full extraction of sericin.

6.3.3. Morphological characterization

6.3.3.1. Scanning electron microscopy

Scanning Electron Microscopy (SEM) analysis was performed using a Leica Cambridge S360 (UK) to investigate the morphology of the produced spacer structures. All samples were sputter-coated with gold (Fisons Instruments, Sputter Coater SC502, UK) prior analysis and the micrographs were taken at an accelerating voltage of 15 kV at different magnifications.

6.3.3.2. Micro-computed tomography

The microstructure of the developed spacer textile structures was evaluated using a high-resolution X-ray microtomography system Skyscan 1072 scanner (Skyscan, Belgium). The different materials were scanned both for the external sheets (Top) as for the internal monofilament (Bulk). SF-PET samples were scanned using a pixel size of 11.31 µm x/y/z and an X-ray source fixed at 41 keV of energy and 215 µA of current. For PET fabrics the pixel size used was 14.71 µm x/y/z and the X-ray source was set at 40 keV and 154 µA. Representative serial images in each data set (Top and Bulk) were transferred into binary images by using a dynamic threshold of 60-225 for SF-PET and 59-255 for PET fabrics. Then, the binary images were used for morphometric analysis (CT Analyzer v1.5.1.5, SkyScan, Belgium), which included the quantification of porosity, mean pore size and mean pore thickness. The 3D virtual models of the spacer structures were also created, visualized and registered using the image processing software's Data Viewer and CT-Vox (both from SkyScan, Belgium). A minimum number of three specimens were used for the qualitative and quantitative microstructure evaluation.

6.3.4. Mechanical properties

6.3.4.1. Compressive tests

The mechanical behavior of the spacer textile structures was tested under quasi-static compression (dry state) using a Universal Testing Machine (Instron 4505, USA). SF-PET and PET specimens were cut into cuboid shapes of approximately 10x10x3 mm and 10x10x2.5 mm, respectively. Textile structures were submitted to a pre-loaded of 1 kN at room temperature (RT). The cross-head speed was fixed at 2 mm/minute and tests were run until a 60% deformation in specimen height was achieved. The elastic modulus (*E*) was defined by the slope of the initial linear section of the stress-strain curve.

6.3.4.2. Dynamic mechanical analysis

The dynamic mechanical behavior of spacer textile structures was determined using a TRI-TEC8000B dynamic mechanical analyzer (Triton Technology, UK) in the compressive mode and measurements were carried out in hydrated state at 37°C. The dimensions of the tested SF-PET and PET specimens were the same as for the compressive tests in dry state. Samples were always analyzed immersed in a liquid bath placed in a Teflon® reservoir. Prior analysis, the specimens were immersed in a phosphate-buffered saline solution (PBS, pH 7.4) for 3 days, until equilibrium was reached (37°C). Afterwards, the specimens were clamped in the DMA apparatus and kept immersed in the PBS solution during the measurements. After equilibration at 37°C, the DMA spectra were obtained in a frequency scan between 0.1 and 10 Hz. The experiments were performed under the constant strain amplitude of 30 µm. Both storage modulus (E') and loss factor (tan δ) were obtained in the frequency range. Before the analysis, a small pre-load was applied to each sample to ensure the complete contact of the structure surface with the compression plates, being the distance between plates equal for all tested samples. Three specimens of each group were tested.

6.3.5. *In vitro* cell studies

6.3.5.1. hASCs isolation and expansion

Human adipose-derived stem cells (hASCs) were isolated from subcutaneous adipose tissue samples obtained from liposuction procedures performed in patient's informed consent and using a protocol previously established with the Department of Plastic Surgery of Hospital da Prelada (Porto, Portugal). All the samples were processed within 24 hours after the liposuction procedure and human ASCs were enzymatically isolated from the subcutaneous adipose tissue, as previously described [27]. Human ASCs were expanded in basal medium consisting of MEM alpha medium (α-MEM; Gibco®, Life Technologies, Carlsbad, CA, USA) supplemented with sodium bicarbonate (Sigma-Aldrich, MO, USA), 10% (v/v) fetal bovine serum (FBS; Biochrom AG, Germany) and 1% (v/v) antibiotic/antimycotic solution (final concentration of penicillin 100 units/mL and streptomycin 100 mg/mL; Gibco®, Life Technologies, USA). Cells were cultured until confluence at 37 °C in an atmosphere of 5% CO_2 incubator, changing the culture medium every 2 days.

6.3.5.2. Seeding and osteogenic differentiation of hASCs in the textile-based scaffolds

Before the *in vitro* studies, SF-PET and PET textile scaffolds were cut into cylindrical shapes of approximately 10 mm diameter and 3 mm or 2.5 mm thickness, respectively, and sterilized by ethylene oxide. Before cell seeding, all samples were hydrated in PBS overnight in the CO_2 incubator. In the following day, the hydrated textiles were transferred to 48-well suspension cell culture plates (Cellstar, Greiner Bio-One, Austria). Confluent hASCs (passage 4) were detached with TrypLE Express (1X) (Life Technologies, Carlsbad, CA, USA) and seeded in a 200 µL cell suspension onto the SF-PET and PET spacer fabrics, at a density of $4x10^5$ cells/scaffold and $3x10^5$ cells/scaffold, respectively, according to scaffolds diameter and thickness. Each scaffold was kept in the CO_2 incubator for 3 hours, and then 500 µL of α-MEM culture medium were added to each well. After 24 hours, cell culture medium was refreshed or changed to osteogenic differentiation medium (basal medium supplemented with 10^{-8} M dexamethasone, 50 µg/mL ascorbic acid and 10 mM β-glycerophosphate). Samples were retrieved at different culture times (1, 7, 14, 21 and 28 days) and the culture medium was changed every 2-3 days.

6.3.5.3. Scanning electron microscopy and energy dispersive spectroscopy analysis

Cell morphology and distribution were observed in the 3D textile scaffolds by SEM. Constructs were rinsed in PBS and fixed with a 2.5% (v/v) glutaraldehyde solution (Sigma-Aldrich, MO, USA) for 1 hour at 4°C. Samples were further dehydrated through increasing series of ethanol concentrations (30, 50, 70, 90, 100% v/v) for 15 minutes, twice each concentration and left in hexamethylidisilazane (HMDS; Electron Microscopy Sciences, USA) overnight. Prior to SEM observation, all scaffolds were sputter-coated with gold and a graphite coating was used for energy dispersive spectroscopy (EDS; link-eXL-II) analysis to detect the elemental composition of the samples.

6.3.5.4. DNA quantification

The amount of double strained DNA (dsDNA), that is directly proportional with the cell number, was determined using a fluorimetric dsDNA quantification kit (PicoGreen, Molecular Probes, Invitrogen Corporation, USA), according to the manufacturer's instructions. After each culture time, samples were washed twice with PBS solution and kept in 1 mL of ultrapure water at −80 °C until further analysis. Constructs were thawed at RT and sonicated for 1 hour to induce complete membrane lysis. Supernatant fluorescence was measured at an excitation wavelength of 485/20 nm and at an emission wavelength of 528/20 nm, in a microplate reader (Synergy HT, BioTek Instruments, USA). The quantification of DNA was calculated according to a standard curve prepared with concentrations ranging between 0 and 2 µg/mL, relating quantity of DNA and fluorescence intensity. Samples without cells were used as control.

6.3.5.5. Alkaline phosphatase activity quantification

The alkaline phosphatase (ALP) activity was determined on the same samples used for dsDNA quantification as a marker of ostegenic differentiation. ALP activity from constructs was quantified by the specific conversion of p-nitrophenyl phosphate (pNPP; Sigma-Aldrich, MO, USA) into p-nitrophenol (pNP). A buffer solution containing 0.2% (w/v) pNPP was added to the supernatant in a 96-well plate (Corning Costar, NY, USA). The enzyme reaction was carried out at 37°C for 45 minutes and then stopped by the addition of a solution containing 2 M NaOH (Merck, Germany) and 0.2 mM EDTA (Sigma-Aldrich, MO, USA) in distilled water. The absorbance of pNP formed was read at 405 nm in a microplate reader (Synergy HT, BioTek Instruments, USA) and sample concentrations were read off from a standard curve made using pNP values ranging from 0 to 0.2 μmol/mL. The obtained ALP concentrations were normalized against the DNA concentrations of the same samples. Samples without cells were used as control.

6.3.5.6. Alizarin red staining and calcium deposition quantification

Staining with alizarin red was performed in order to assess the matrix mineralization. Constructs were rinsed with PBS and fixed in 10% (v/v) formalin (Sigma-Aldrich, MO, USA) for 1 hour. Samples were maintained in PBS until further staining with a 2% (w/v) alizarin red solution (Merck, Germany) in ultrapure water, for 5 minutes, and finally washed with distilled water. Stained structures were visualized using a stereo microscope (Stemi 1000, Zeiss) and images captured by a digital camera (Canon PowerShot, G11).

The inorganic calcium quantification was performed using the o-cresolphthalein-complexon method with colorimetric detection (Roche Cobas kit, Roche Diagnostics, Germany), according to the manufacturer's instructions. Samples were incubated in a 6 M HCl solution (Analar Normapur, Germany) to remove and dissolve the calcium. In a 96-well plate (Corning Costar, NY, USA), 175 µL of ethanolamine (1 M, pH 10.6) were mixed with 10 µL of each sample and incubated for 5 minutes at RT. Then, 70 µL of o-cresolphthalein-complexon (0.3 mM, hydroxy-8-quinoleine 13.8 mM, HCl 122 mM) were added and further incubated at 37°C for 2 minutes. The absorbance of the samples was read at 570 nm in a microplate reader. The calcium concentrations were extrapolated from the standard curve obtained using serial dilutions of a 200 mg/L $CaCl_2$ solution (Merck, Germany). Samples without cells were used as control.

6.3.5.7. Immunodetection of bone-specific proteins

Immunocytochemistry was performed using a mouse anti-human monoclonal antibody against osteocalcin (OCN; clone OC4-30, Abcam, Cambridge, UK; dilution 1:25), a rabbit anti-human polyclonal antibody against osteopontin (OPN; Abcam, Cambridge, UK; dilution 1:25), and a rabbit anti-human polyclonal antibody against collagen type I (Col I; Abcam, Cambridge, UK; dilution 1:50). Human ASCs grown both on the SF-PET and PET textile scaffolds were fixed in 10% (v/v) formalin (Sigma-Aldrich, MO, USA) for 1 hour, and stored at 4°C in PBS until further use. Cells were permeabilized with 0.2% (v/v) of Triton X-100/PBS (Sigma-Aldrich, MO, USA) and washed twice with PBS. To block unspecific reactions, samples were incubated with 3% (w/v) bovine serum albumin solution (BSA; Sigma-Aldrich, MO, USA) in PBS for 45 minutes at RT, followed by incubation with the primary antibodies overnight at 4°C in 1% (w/v) BSA/PBS solution. Samples were rinsed in PBS for 10 minutes and then incubated for 2 hours in the dark with the respective secondary fluorochrome-conjugated antibodies, anti-rabbit/mouse IgG (Invitrogen, Life Technologies, California, USA; dilution 1:100). Finally, samples were incubated for 15 minutes with DAPI solution (Sigma-Aldrich, MO, USA; dilution 1:1000) for nuclei staining and then washed with PBS for further observation under a Zeiss LSM 510 Meta confocal laser scanning microscope.

6.3.5.8. RNA isolation and real-time reverse transcriptase-polymerase chain reaction

The expression of mRNA for the genes of interest was measured by real-time PCR analysis. Total RNA was extracted using RNeasy Mini Kit (Qiagen, Germany), following the manufacturer's instructions. After each culturing time, constructs were washed with PBS, immersed in 500 µL of β-mercaptoethanol solution (β-ME; Sigma-Aldrich, MO, USA) in RLT buffer (dilution 1:100) and stored at -80°C until further use. Samples were thawed at RT and sonicated for 15 minutes at 20°C to ensure the complete lysing of the cells. After adding 500 µL of 70% (v/v) ethanol solution to the lysates, total volumes were transferred to RNeasy spin columns placed in 2 mL collection tubes and centrifuged for 30 seconds at 8.0 rpm. Then, 700 µL of RW1 buffer solution were added to the RNesay spin columns and centrifuged for 30 seconds at 8.0 rpm. The RNA pellets were washed twice with 500 µL RPE buffer (RPE buffer was previous diluted with 70% v/v ethanol according to the instructions) and centrifuged for 30 seconds and then 2 minutes at 8.0 rpm. Finally, the total RNA pellets were reconstituted in 30 µL of RNAse-free water (Gibco®, Life Technologies, Carlsbad, CA, USA), added to the RNeasy spin columns and centrifuged for 1 minute at 8.0 rpm into 1.5 mL collection tubes. RNA quantity and purity were assessed with a NanoDrop ND-1000 spectrophotometer (NanoDrop Technologies, USA). Samples with a 260/280 ratio between 1.6 and 2.0 were used for first-strand complementary DNA (cDNA) synthesis according to the protocol from the qScript™ cDNA synthesis Kit (Quanta Biosciences, MD, USA) in a MiniOpticon real-time PCR detection system (BioRad, CA, USA). Briefly, a reaction mixture consisting of 4 µL qScript Reaction Mix, 1 µL qScript Reverse Transcriptase (RT), RNA template (100 ng total RNA) and nuclease-free water was prepared, in 20 µL of final volume. The single-strand cDNA synthesis occurred by incubating the complete reaction mixture for 5 minutes at 22°C, followed by 30 minutes at 42°C and terminated with an incubation of 5 minutes at 85°C. Amplification of the target cDNA for real-time PCR quantification was performed according to the manufacturer's instructions, using 1 µL RT cDNA products, 1 µM each primer, 10 µL PerfeCta SYBR Green FastMix (Quanta Biosciences, MD, USA) and nuclease-free water, in a final volume of 20 µL. The primers sequence, specific for each gene, namely glyceraldehyde-3-phosphate dehydrogenase (GAPDH), OCN, OPN and Col I are described in Table 6-1. Each real-time PCR run was carried out with an initial incubation at 95 °C for 2 minutes, followed by 45 cycles of denaturation (95 °C, 10 seconds), annealing (specific for each gene, 25 seconds) and extension (72 °C, 30 seconds) in a Mastercycler® ep realplex real-time PCR system (Eppendorf, USA). The transcripts expression data were normalized to the endogenous housekeeping gene glyceralde- hyde-3-phosphate-dehydrogenase (GAPDH) and the relative quantification was calculated using as calibrators the results obtained for each marker at day 7 in basal culture conditions, according to the Livak ($2^{-\Delta\Delta CT}$) method [31].

Table 6-1. Primers list for the studied genes.

Gene	**Sequences**	
	Forward (5'–3')	**Reverse (5'–3')**
GAPDH	TGCACCACCAACTGCTTAGC	GGCATGGACTGTGGTCATGAG
OCN	CTGGAGAGGAGCAGAACTGG	GGCAGCGAGGTAGTGAAGAG
OPN	TGAAACGAGTCAGCTGGATG	TGAAATTCATGGCTGTGGAA
Col I	AAGAACCCCAAGGACAAGAG	GTAGGTGATGTTCTGGGAGG

6.3.6. *In vivo* angiogenesis evaluation

6.3.6.1. Chick chorioallantoic membrane assay

CAM assay was performed according to the procedure described by Silva-Correia *et al.* [32] in a laminar-flow hood to minimize contamination. Briefly, white fertilized chicken eggs (n=120; Pintobar, Portugal) were incubated at 37 °C (Laboratory Incubator model B8420; Termaks) for 3 days. A small hole was then created in the pointed end of the egg to allow dissociation of the CAM from the shell membrane. Additionally, a circular window was made into the egg shell, in order to evaluate embryo viability and access the CAM. Shell opening was then sealed with transparent tape (~50x30 mm, Staples) to prevent dehydration and the eggs were returned to the incubator at 37°C until implantation of the SF-PET and PET textile scaffolds (diameter: 9 mm; height: 3 mm and 2.5 mm, respectively).

Sterile textile scaffolds were implanted on the CAM at day 10 of embryonic development. Gelatin sponges with 9 mm diameter and 3 mm height were prepared from sterile Cutanplast® sponge (Mascia Brunelli S.p.a.) and used as negative control for angiogenesis. The shell windows were then protected with transparent tape and the eggs returned to the incubator at 37°C until day 14 of embryonic development. At the end of the assay, the embryos and their membranes were fixed *in ovo* by using freshly prepared paraformaldehyde (PFA; Merck, Germany) solution at 4% (v/v) followed by incubation at -80 °C for 10 minutes in an ultra-low freezer. The implanted specimens and the immediately adjacent CAM portions were cut and transferred to 6-well plates containing PFA solution at 4% (v/v). *Ex ovo* images were then acquired using the AxioVision imaging software (release 4.8; Zeiss) connected to a AxioCAM ICc1 digital camera (Zeiss) attached to a stereomicroscope (Stemi 2000-C; Zeiss). The excised membranes were transferred to histological cassettes, embedded in paraffin, and cut into sections of 4 μm thick using a microtome (Spencer 820, American Optical Company, NY, USA). Three independent CAM assays were performed and a minimum number of 18 specimens were used for each group.

6.3.6.2. Analysis of blood vessel convergence

A semi-quantitative method was used to evaluate the total number of macroscopic blood vessels converging toward the implanted textile scaffolds (SF-PET and PET) and gelatin sponges, as previously described [32]. The *ex ovo* images obtained at day 14 of embryonic development were analyzed by three independent observers after image processing using the WCIF ImageJ software program (US National Institutes of Health).

6.3.6.3. Hematoxylin & Eosin (H&E) staining

The CAM sections were stained with H&E (Sigma-Aldrich, MO, USA) and observed under transmitted microscopy using an Axio Imager Z1m light microscope (Zeiss, Jena, Germany). Images were acquired using the Zen microscope processing software (Zeiss, Jena, Germany) connected to a digital camera AxioCam MRc5 (Zeiss, Jena, Germany).

6.3.6.4. Immunohistochemical detection

Representative CAM sections were subjected to immunohistochemical analysis using the streptavidin-biotin peroxidase complex kit (UltraVision Large Volume Detection System Anti-Polyvalent, HRP; Lab Vision, Thermo Scientific, CA, USA). After paraffin removal, sections were rehydrated and submitted to heat-induced antigen retrieval using 10 mM citrate buffer (pH 6; Merck, Germany) for 20 minutes at 98°C. To inactivate endogenous peroxidases, the samples were incubated in a 3% (v/v) hydrogen peroxide solution (H_2O_2; Panreac Química SAU) for 10 minutes, and then soaked in PBS. Sections were incubated in protein blocking solution (Ultra V block; Lab Vision, Thermo Scientific, CA, USA) for 10 minutes followed by incubation with lectin (SNA-lectin; Vector Laboratories, Burlingame, CA, USA) for 1 hour at RT. Finally, sections were sequentially washed with PBS and incubated with the streptavidin-peroxidase complex for 10 minutes. A 3,3'-diamoonobenzidine solution (DAB; Vector Laboratories, Burlingame, USA) was used as chromogen. All sections were counterstained with Gill-2 hematoxylin (Merck, Germany). The histological sections were observed and images acquired as described in 6.3.6.3.

6.3.7. Subcutaneous implantation

The maintenance and use of animals were carried out in accordance to the Ethics Committee of University of Minho and approved by the Portuguese Licensing Authority (DGV-DSSPA). Six mice Hsd:ICR (CD-1) of 5 weeks old and average weight of 25-30 g (Harlan Laboratories, Sant Feliu de Codines, Spain) were used in this study. Each mouse was anesthetized by intraperitoneal injection of: ketamine (25 mg/kg) and medetomidine (0.15 mL/kg) for anesthesia; cephalexin (15 mg/kg) as antibiotic; bupivacaine, pethidine (5-10 mg/kg) as analgesic. The hair of the mice was removed at the implantation area by shaving, followed by disinfection with 70% (v/v) ethanol and iodine. In each mouse, four skin incisions (1 cm length) were made in the dorsal midline, two close from the head (CH) and two far from the head (FH). In the following, two sterile SF-PET textile scaffolds (diameter: 9 mm; height: 3 mm) and two sterile PET textile scaffolds (diameter: 9 mm; height: 2.5 mm) were implanted subcutaneously into the respective pocket and then the skin was sutured. Twelve specimens of both spacer fabrics were implanted. Fourteen and twenty eight days post-surgery, the mice were euthanized by injection of overdose pentobarbital sodium and the implanted materials together with the surrounded tissue retrieved. The explants were fixed with 10% (v/v) formalin solution (Sigma-Aldrich, MO, USA) for at least 5 days at RT and then transferred to histological cassettes for immersion in paraffin, after dehydration through increasing series of ethanol concentrations (from 30% up to 100% v/v). Samples were then serially sectioned using a microtome (3.5 μm thick) for H&E staining.

6.3.8. Statistical analysis

All the numerical results are presented as mean ± standard deviation (SD). Statistical analysis was performed using the GraphPad Prism 5.0 (GraphPad Software, La Jolla, CA, USA). First, a Shapiro-Wilk test was used to ascertain about the data normality. The results from static mechanical properties were analyzed by means of the unpaired t-test using ten specimens for each group. For all the biological quantification assays, the differences between the experimental results were analyzed using a Kruskal-Wallis test followed by Dunn's multiple comparison test. Three independent experiments were performed for cell differentiation studies (ALP activity, calcium deposition quantification and real-time PCR analysis), and three samples were analyzed per group in each culturing time. A minimum number of 10 specimens were analyzed in each group for analysis of blood vessels convergence after CAM assay. The significance level was set to $^{*}p < 0.05$, $^{**}p < 0.01$, $^{***}p < 0.001$.

6.4. Results

6.4.1. Morphological characterization

Figure 6-1 depicts the schematic drawings of the programmed knitted architectures to produce the SF-PET (Figure 6-1a) and PET (Figure 6-1e) textile scaffolds, and provides details of the surface morphology and cross-sections of the spacer scaffolds, obtained by SEM. The surface micrographs of SF-PET scaffolds (Figure 6-1b and c) revealed a tight knit structure formed by natural silk filaments with regular size. Some loose filaments were observed in the SF matrices, which can be related to the physical wear resulting from the degumming process applied during sericin degumming. The PET-based external layers (Figure 1f and g) showed filaments with the same size range of those present in the SF matrices, forming a loose knit structure. The cross-section micrographs of both SF-PET (Figure 6-1d) and PET (Figure 6-1h) spacer structures showed a significant three-dimensionality introduced by the resilient monofilament of PET (z direction).

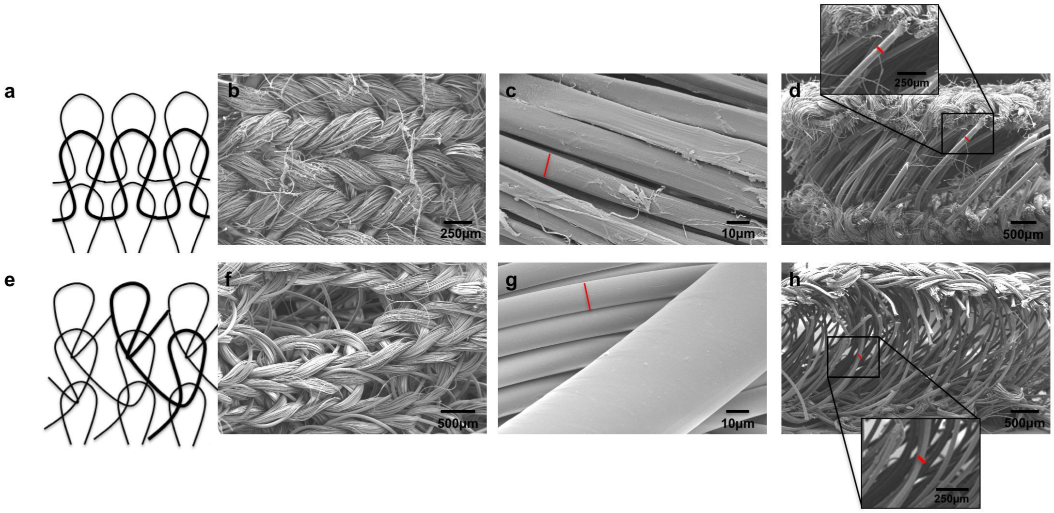

Figure 6-1. Illustrative images showing the wale and course components of the (a) weft and (e) warp knitting technologies, used for processing the SF and PET filaments in the scaffolds external layers, respectively. SEM

micrographs of (b-d) SF-PET and (f-h) PET knitted spacer fabrics showing different levels of detail. Morphology of the (b, c) SF and (f, g) PET external layers from a top view perspective and the respective (d, h) cross-sections, showing the resilient PET monofilament (z direction). The red bars indicates: (c) SF and (g) PET fibers diameter (~15 μm); (d,h) PET monofilament diameter (~100 μm).

The qualitative and quantitative analysis of porosity, mean pore size and mean pore thickness of the spacer textile fabrics were assessed by micro-CT (Table 6-2). From the 3D reconstructions it was observed that both SF-PET and PET spacer scaffolds presented high porosity and interconnected pores. Nevertheless, a higher porosity was observed at scaffolds' interior (Bulk), as compared to the external SF and PET layers (Top). Micro-CT histomorphometric analysis also revealed that the external sheets of PET spacer scaffolds presented high porosity (89.9 ± 3.6%) and mean pore size (355.6 ± 3.4 μm), as compared to the porosity (64.8 ± 1.2%) and mean pore size (179.5 ± 5.0 μm) of SF matrices. No relevant differences for porosity were found among the scaffolds interior, in contrast to the mean pore size (1351.7 ± 16.7 μm for PET, 587.6 ± 4.6 μm for SF-PET) and mean pore thickness (125.9 ± 1.7 μm for PET, 75.3 ± 1.3 μm for SF-PET) that were found to be higher in the PET scaffolds interior. As the SF-PET scaffolds porosity increased, from the top to the bulk, the mean pore thickness tends to decrease. The same pattern was not observed for PET scaffolds, but the differences between the mean porosity at the scaffolds surface (89.9 ± 3.6%) and interior (98.0 ± 1.6%), were not so pronounced as in SF-PET scaffolds (64.8 ± 1.2% at surface, 95.0 ± 1.1% at interior).

Table 6-2. 3D reconstructions of the SF-PET and PET knitted spacer fabrics, mean porosity, pore size and trabeculae thickness, calculated from the micro-CT data.

Spacer textile construct		3D reconstruction	Mean porosity (%)	Mean pore size (µm)	Mean pore thickness (µm)
SF-PET	**Top**	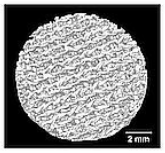	64.8 ± 1.2	179.5 ± 5.0	115.4 ± 3.7
	Bulk	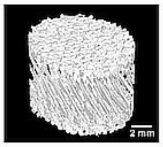	95.0 ± 1.1	587.6 ± 4.6	75.3 ± 1.3
PET	**Top**	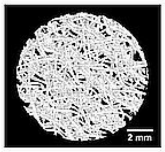	89.9 ± 3.6	355.6 ± 3.4	108.2 ± 2.1
	Bulk	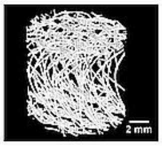	98.0 ± 1.6	1351.7 ± 16.7	125.9 ± 1.7

6.4.2. Mechanical properties

Figure 6-2 shows the mechanical behavior of both SF-PET and PET spacer textile scaffolds evaluated under compression. The quasi-static compressive modulus (Figure 6-2a) determined in dry conditions was similar for both structures (41.9 ± 17.1 kPa for SF-PET, 39.5 ± 25.7 kPa for PET). The same behavior was observed for the compressive strength of scaffolds, presented in the stress-strain plot (Figure 6-2b). The dynamic mechanical properties (wet conditions) of the SF-PET and PET spacer textile scaffolds assessed by DMA (Figure 6-2c) showed that the storage modulus (*E')* of the SF-PET scaffolds increased at lower rates with increasing testing frequencies (from 0.1 to 10 Hz), ranging from 39.1 ± 8.7 to 43.0 ± 8.9 kPa. The *E'* of PET scaffolds presented no differences in all tested frequencies, ranging from 26.5 ± 2.1 to 27.6 ± 2.5 kPa. In the frequency range tested, the storage modulus values obtained for SF-PET scaffolds were higher than for the PET scaffolds. Comparing the loss factor data, it was found that SF-PET spacer scaffolds presented higher loss factor values for the tested frequencies. Nevertheless, at higher frequencies (from 1 up to 10 Hz) the loss factor of SF-PET decreased. The tan δ of PET structures was constant in all tested frequencies.

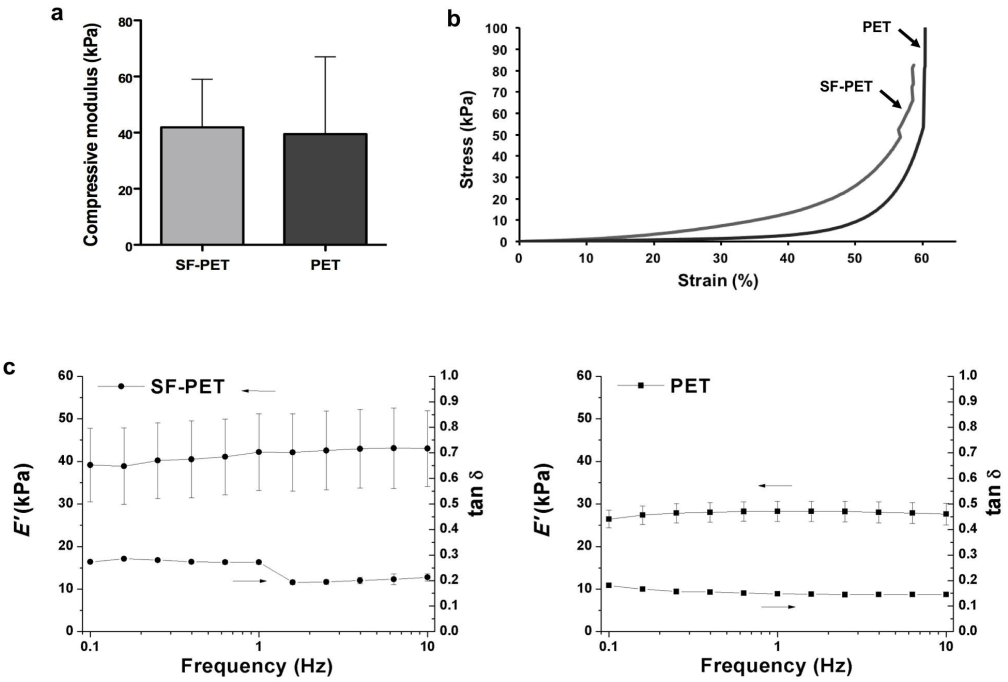

Figure 6-2. (a) Compressive modulus and (b) representative stress–strain plot of the SF-PET and PET knitted spacer fabrics measured in the dry state. (c) Storage modulus (*E′*) and loss factor (tan δ) of the SF-PET and PET knitted spacer fabrics determined in the hydrated (phosphate-buffered saline solution, 37°C) state, after 3 days of immersion.

6.4.3. *In vitro* assessment of the textile-based scaffolds

6.4.3.1. Osteogenic differentiation in the textile-based scaffolds

Quantitative analysis of ALP activity was determined up to 28 days of culturing (Figure 6-3). In osteogenic culture conditions, a significant increase of ALP activity was evidenced on the SF-PET constructs after 7 and 14 days of culture, in comparison to day 1 (*$p < 0.05$ and ***$p < 0.001$, respectively). From day 21, significantly higher activity levels were also observed as compared to day 1 (**$p < 0.01$), however the ALP activity tend to decrease when compared to day 14 reaching stable values until day 28. PET constructs presented no significant differences in ALP activity until day 28, where significantly higher levels were detected as compared to day 1 (***$p < 0.001$) and day 7 (**$p < 0.01$). Comparing the results obtained for the different textile structures under the same osteogenic culture conditions, SF-PET constructs presented significantly higher activity levels from day 7 until day 28 (a***$p < 0.001$, **$p < 0.01$), as compared to PET. Concerning the cultures in basal medium, ALP activity significantly increased over the 28 days of culture (**$p < 0.01$; ***$p < 0.001$) on the SF-PET textile structures, but the results obtained for PET structures revealed no significant differences until day 28, as compared to day 1 (***$p < 0.001$). Also in basal culture conditions, SF-PET structures displayed a significantly higher ALP activity from day 14 until day 28 (a***p < 0.001) than PET constructs.

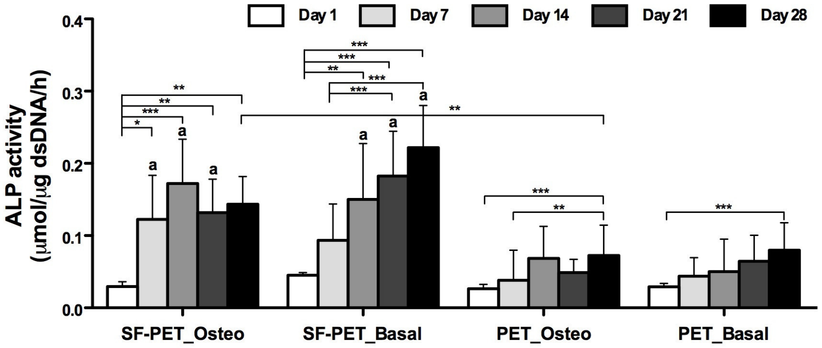

Figure 6-3. Normalized ALP activity of hASCs cultured on SF-PET and PET knitted spacer fabrics, after 1, 7, 14, 21 and 28 days in osteogenic and basal culture medium. ^{a}Statistically significant when compared to the PET constructs at the same culture period and under the same culture conditions (***p < 0.001). The exception is represented in the graphic.

6.4.3.2. Extracellular matrix mineralization and elemental composition of the deposited matrix

In figure 6-4a, a significant increase in calcium concentration was observed after 21 days of hASCs culture in osteogenic differentiation medium on both SF-PET and PET constructs, as compared to day 7 (***p < 0.001 and **p < 0.01, respectively) and day 14 (**p < 0.01). After 28 days, significantly higher calcium concentration values were detected, as compared to day 7 (***p < 0.001) and day 14 (***p < 0.001) in both textile constructs. In basal culture conditions, only a residual calcium concentration was detected and no significant differences were observed for both scaffolds over the 28 days of cuture. In fact, the calcium concentration detected on SF-PET and PET constructs cultured in osteogenic conditions was significantly higher at day 21 and day 28 (***p < 0.001), as compared to that obtained in basal conditions.

The ECM mineralization was confirmed by performing an alizarin red staining (Figure 6-4b). After 14 and 21 days of culture in osteogenic differentiation medium, evidences of ECM mineralization were observed on the SF-PET and PET constructs. The mineralization was more intense after 28 days of culture in both textile constructs, when compared to the first 21 days in the same osteogenic culture conditions. Moreover, it is visible that the stained areas are not homogeneously distributed within the scaffolds. When comparing the results obtained in osteogenic and basal culture conditions, a clear difference was observed. Both SF-PET and PET constructs showed a strong staining when cultured in osteogenic differentiation medium, while there were no evidences of ECM mineralization in basal culture conditions.

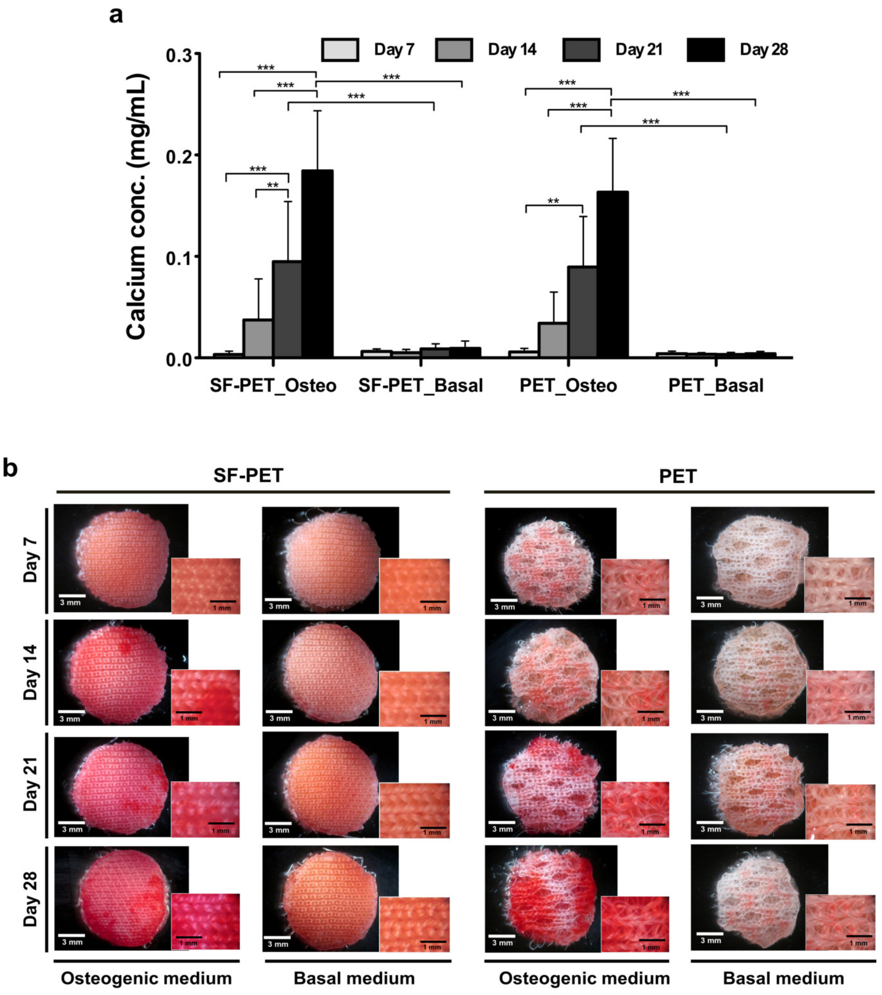

Figure 6-4. (a) Calcium quantification on the SF-PET and PET knitted spacer fabrics, cultured with hASCs in osteogenic and basal medium for 7, 14, 21 and 28 days. (b) Alizarin red staining performed directly into the textile constructs, after 7, 14, 21 and 28 days of culture in osteogenic and basal medium.

The hASCs adhesion along the SF-PET and PET textile scaffolds was analyzed by SEM (Supplementary Figure 6-1), showing that cells were able to attach, spread and deeply penetrate into the scaffolds' interior. From Figure 6-5, an increasing formation of mineralization nodules were observed on both SF-PET and PET constructs, from day 14 until day 28 in osteogenic culture conditions. Using EDS analysis it was possible to confirm that the nodules were composed mainly of calcium (Ca) and phosphorous (P), reaching Ca/P ratio values between 1.65 to 1.79 on SF-PET constructs and 1,70 to 1.79 on PET contrcuts. Similar Ca/P ratios were observed on both textile scaffolds at the different culture periods.

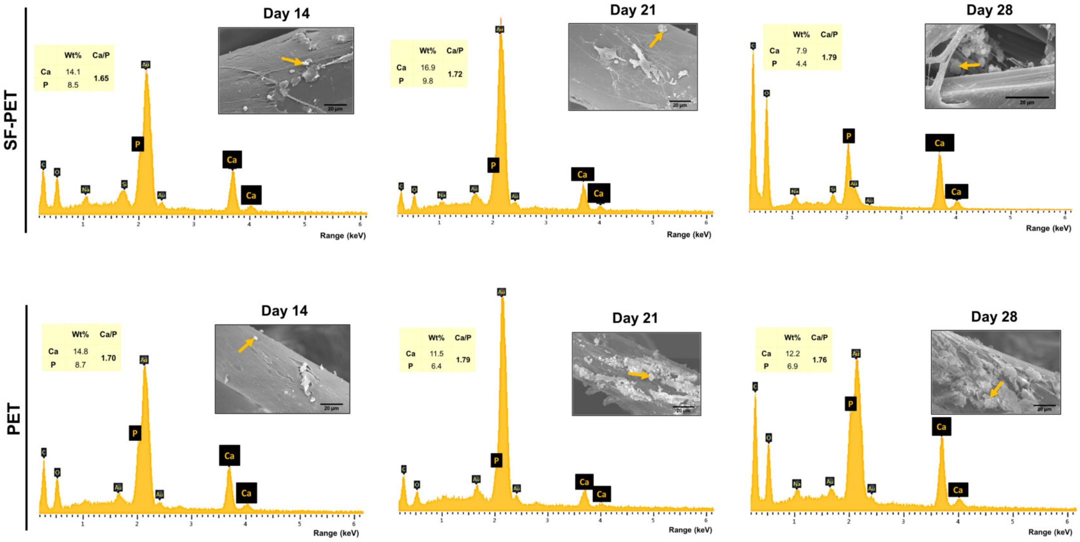

Figure 6-5. SEM micrographs (inset) and EDS spectra with Ca/P ratios determined for the SF-PET and PET knitted spacer fabrics, after 14, 21 and 28 days of culture in osteogenic medium. The yellow arrows indicate mineralization nodules.

6.4.3.3. Genotypic and phenotypic expression of osteogenic-related markers

The differentiation of hASCs seeded onto the SF-PET and PET spacer textile scaffolds was analyzed by quantifying the mRNA expression of osteocalcin (OCN), osteopontin (OPN) and collagen type I (Col I) osteogenic markers (Figure 6-6). All mRNA transcripts were observed after 28 days in osteogenic and basal culture conditions (Figure 6-6a). The OCN and OPN gene expression presented no significant differences between the SF-PET and PET constructs cultured in osteogenic differentiation medium. In basal culture conditions, no mRNA expression was detected for these osteogenic-related markers both on SF-PET and PET constructs. For Col I gene expression, no significant differences were detected between the tested textile materials cultured under osteogenic and basal conditions. However, the mRNA expression of Col I was significantly higher in basal culture culture conditions, as compared to SF-PET (*$p < 0.05$) and PET (***$p < 0.001$) constructs cultured in osteogenic differentiation medium.

Complementary to the genotypic analysis, the osteogenic phenotype of hASCs seeded onto the SF-PET and PET spacer textile scaffolds was assessed by the immunodetection of OCN and OPN bone-specific glycoproteins. The presence of Col I was also evaluated in order to determine the deposited collagenous matrix. Confocal micrographs (Figure 6-6b), indicated that in basal culture conditions only residual OCN and

OPN were detected for hASCs cultured for 28 days on both SF-PET and PET textile scaffolds. However, in the presence of osteogenic differentiation medium, higher evidences of OCN and OPN were observed. In the case of Col I an intense protein expression was observed on SF-PET and PET constructs cultured both under osteogenic and basal culture conditions. Moreover, a uniformly distributed collagen deposition seemed to be detected on both textile scaffolds.

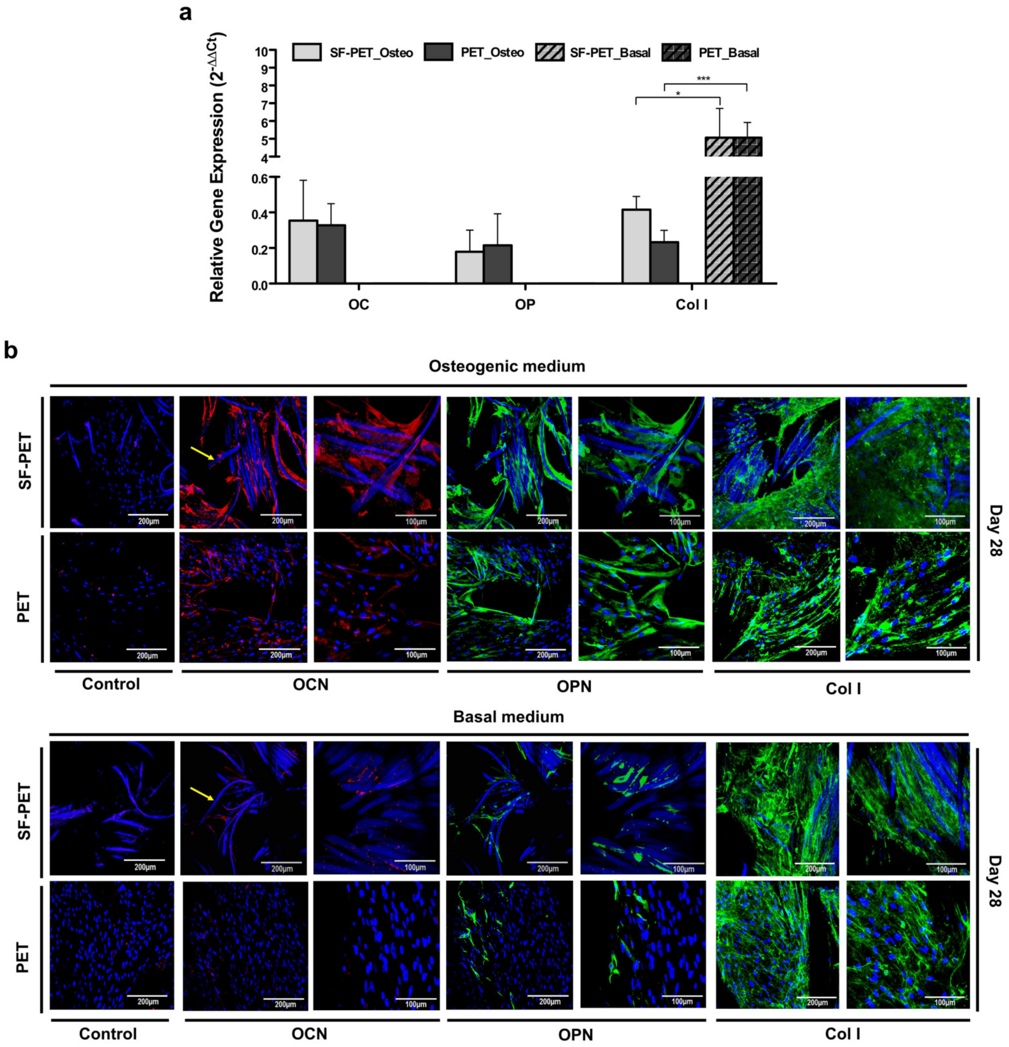
a
Relative Gene Expression ($2^{-\Delta\Delta Ct}$)
SF-PET_Osteo
PET_Osteo
SF-PET_Basal
PET_Basal
10
9
8
7
6
5
4
0.6
0.4
0.2
0.0
*
***
OC
OP
Col I
b
Osteogenic medium
SF-PET
PET
200µm
100µm
Control
OCN
OPN
Col I
Day 28
Basal medium
SF-PET
PET
Control
OCN
OPN
Col I
Day 28

Figure 6-6. Quantitative and qualitative expression of osteogenic-related markers by hASCs after 28 days of culture on the SF-PET and PET knitted spacer fabrics. (a) RT-PCR results and (b) confocal micrographs of the detection of OCN, OPN and Col I in osteogenic and basal culture conditions. # Indicate the non-expression of the OC and OP genes under basal culture conditions. In representative immunofluorescence images nuclei are stained in blue, OCN in red, OPN and Col I in green. The yellow arrows indicate SF fibers stained in blue due to autofluorescence in the blue wavelength range. Scale bars: 200 µm for low magnification images; 100 µm for high magnification images.

6.4.4. Angiogenic potential of the textile-based scaffolds

The convergence of blood vessels toward the implanted structures was investigated *ex ovo* (Figure 6-7a). Macroscopically, there were no significant differences on the number of blood vessels converging to the PET textiles and control gelatin sponges. However, a significantly higher number of blood vessels converged to the SF-PET textiles, in comparison to the PET (*$p < 0.05$) and gelatin sponges (**$p < 0.01$). The stereomicroscopy photographs and H&E staining images (Figure 6-7b) showed that both textile scaffolds were well integrated in the CAM after 4 days of implantation, allowing connective tissue infiltration. Complementarily, the immunohistochemical analysis of endothelial cells of chick origin performed with SNA-lectin (Figure 6-7b), revealed the presence of endothelial cells surrounding the textile fibers. Gelatin sponge implants were partially absorbed, as observed by the *ex ovo* and H&E staining images. Immunohistochemistry showed the presence of endothelial cells contacting and infiltrating into the control gelatin sponges.

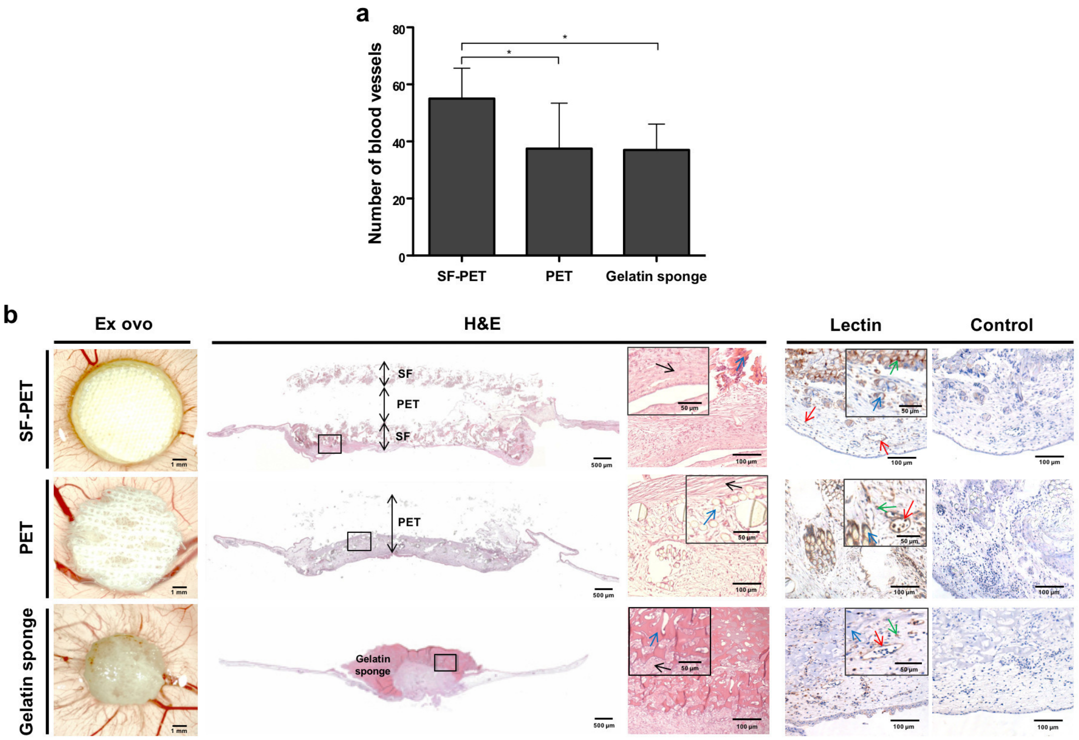

Figure 6-7. Chorioallantoic membrane (CAM) assay, after 4 days of SF-PET, PET textiles and gelatin sponges implantation. (a) Quantification of the macroscopic blood vessels converging towards the implanted structures. (b) Stereomicroscopy photographs of the explants and excised CAM sections of the implants stained with H&E and SNA-lectin. Squares represent the regions corresponding to the magnified stained images. The black arrows indicate

connective tissue, the red arrows indicate blood vessels, the green arrows indicate infiltrated endothelial cells (brown) and the blue arrows indicate SF-PET, PET fibers or gelatin sponge.

6.4.5. Subcutaneous implantation of the textile-based scaffolds

The *in vivo* biological performance of the SF-PET and PET spacer textile scaffolds was assessed after subcutaneous implantation in mice. The macroscopic images of the explants showed that both SF-PET and PET scaffolds were integrated in the subcutaneous tissue, maintaining their integrity and shape after 14 (Figure 6-8a and b) and 28 (Figure 6-8g and h) days of implantation. The H&E staining images showed the presence of connective tissue at the SF-PET (Figure 6-8c and j) and PET (Figure 6-8e and l) scaffolds surface and also infiltrating the scaffolds interior. It was also detected the presence of macrophages in the connective tissue, wrapping the fibers. Nevertheless, no signs of acute inflammation were observed, nor by the occurrence of edema after the implantation periods nor by the presence of neutrophils. Additionally, the infiltration of blood vessels was also identified on both textile structures (Figure 6-8d, f, I and k).

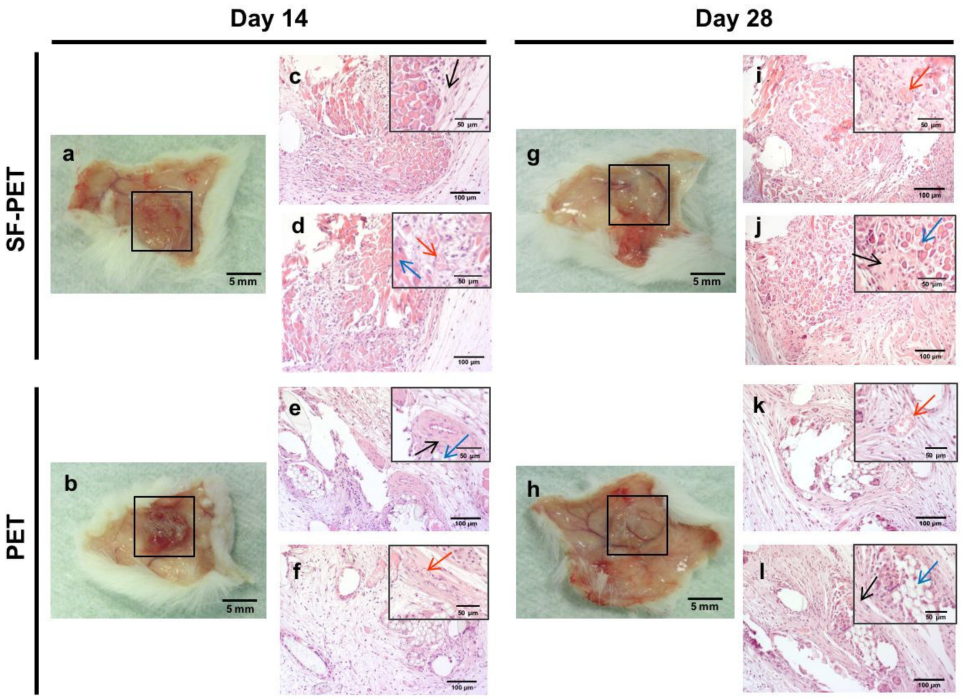

Figure 6-8. Subcutaneous implantation of the SF-PET and PET knitted spacer fabrics in mice. Macroscopic images of the explants after implantation for (a, b) 14 and (g, h) 28 days. H&E staining of the SF (c, d, i, j) and PET (e, f, k, l) explants. Squares represent the regions corresponding to the implanted SF and PET textile scaffolds. The black arrows indicate connective tissue, the red arrows indicate blood vessels and the blue arrows indicate SF-PET and PET fibers.

6.5. Discussion

Textile technologies are being increasingly adopted to generate highly precise and reproducible scaffolds for tissue engineering purposes. Different reports have proposed the use of knitting technologies as scaffolds for several TE applications, including tendons and ligaments [11], cartilage [33] or skin [34]. However, only few have proposed the use of these knitting technologies as a way to create architectures with sufficient mechanical properties according to the geometric parameters of the looms (yarn spacing and thickness) and fiber materials, for more targeted bone regeneration applications. For example, Kellomäki *et al.,* [35] developed composite plates of weft-knitted PLA meshes attached on the surface of PLA films, showing that the composite structures were able to guide new bone formation and the mechanical properties of the composites were dependent on the mesh component. In previous studies by our group [14, 15, 36], standard weft-knitted SF and polybutylene succinate (PBS) scaffolds were proposed as a platform for the functional engineering of bone, showing that the knitting textile substrates exhibit better extensibility or compliance as compared to other textile structures, including the 3D woven structures previously proposed by Moutos *et al.* [9] as a possible strategy for cartilage TE applications. This technology has been applied for TE strategies that seek to restore the biomechanical functions of damaged musculoskeletal tissues [9, 37, 38], particularly difficult to mimic in terms of biomechanical properties, as they are continualy subjected to complex loading patterns that require tissue arquitectures with preferably aligned fiber structures, as those present on knitting structures. Nevertheless, to fully recreate the necessary three-dimensionality and anisotropy found in bone tissue an increase in the three-dimensionality is required. To achieve this effect, in the herein developed scaffolds two external silk fabric layers are connected by a resilient PET monofilament (z direction) that not only increases the scaffolds' three-dimensionality but also replicates the anisotropy of flat bone [16]. Advanced materials can be reinforced by these textile plaftforms for structural applications. The control over fiber architecture is of potential interest for highly loaded structures, enabling fibers to be assembled in specific positions and with necessary orientations to optimize strength and stiffness locally [39]. The cellular components can also take advantage from this arquitecture by producing ECM to generate new tissue, while the scaffold material provides structural integrity and mechanical stability in the mean time [40]. In this study, the PET monofilament is mostly responsible for the resulting mechanical performance regardless of the composition of the external layers, as demonstrated by similar compressive modulus (Figure 6-2a) and strength (Figure 6-2b), presented by SF-PET and PET knitted spacer fabrics [41]. In a previous study, Walther *et al.* [13] observed that the compression strength of 3D textile scaffolds produced by electrostatic flocking changed depending on the fiber length that defined the scaffolds thickness, ranging from 10-36 kPa, where a higher fiber length resulted in lower compression strength. This was not the behavior presented by our samples, since the SF-PET scaffolds presented similar compressive modulus (Figure 6-2a) and strength (Figure 6-2b) to PET scaffolds, even presenting higher thickness. The anisotropic architecture of flat bone in all craniofacial region has a direct influence on its stiffness and strength. O'Mahony *et al.* [42] determined different compressive modulus on hydrated compact bones taken from an edentulous mandible, ranging from 114 to 907 MPa, depending on the tested direction. In another example, Misch *et al.* [43] observed that the ultimate compressive strength of different human mandibular trabecular bone regions in the absence of cortical plates, ranged from 1.7 to 5.38 MPa. This huge variability of available data is a consequence of testing bone in different directions, different regions and with diferent type of individuals. Therefore, the strength values obtained for the spacer scaffolds are difficult to compare with the above described values for native bone. Nevertheless, it is important to consider that bone tissue regeneration does not imply that the mechanical properties of the temporary bone substitute equal those of the natural bone. Scaffolds should present sufficient mechanical strength to support the hydrostatic pressures and to allow cells to recognize an adequate mechanical stimuli for ECM production, mineralization and reinforcement by native bone tissue. Different studies have demonstrated that a compressive modulus of only a few MPa are sufficient to meet all the requirements for an adequate bone regeneration [44, 45]. In the present study we have designed a construct with great capacity to fold and to be easily adjusted and shaped to the bone defect, facilitating the surgical intervention. Interestingly when comparing the mechanical performance of the scaffolds in the dry state with the hydrated state (as in the real scenario), SF-PET presented higher storage modulus than the PET, as well as an increase of the storage modulus with the increase of the frequency, indicating a higher stiffness of this material. These results correlate well with the SEM (Figure 6-1) and micro-CT (Table 6-2) observations, where the SF-PET scaffolds presented lower porosity and mean pore size at the surface that might induce a higher stiffness of the structures in the hydrated state. The interaction of silk with water and its effect on the mechanical properties is well-known as reported previously by us [14, 15], and correlates well with the present study. The viscoelastic nature of both SF-PET and PET spacer scaffolds was also confirmed by the loss factor results (ranging from 0.2-0.3 and 0.15-0.2, respectively), which means that the proposed scaffolds will be able to respond and recover from high physical loads before failing or breaking [46]. This is a very important concern considering that flat bones in the cranio-maxillofacial region are highly stimulated mechanically, due to the daily masticatory stresses that increase the activity in this area [5].

It is well recognized that mimic the anisotropy of bone in a scaffold can be a complex strategy for scaffold processing [47]. However, the flat bone in the maxillofacial region can constitute an interesting structure to recreate as it presents more regular architecture, which can be reproduced through 3D knitting technology.

Up to now, the 3D textile technologies employed for TE purposes are limited to the use of synthetic monofilament fibers to cope with the stability of the fabrication process [33-35]. To our knowledge, this work is the first to report the use of a natural silk yarn to generate two weft-knitted SF layers spaced by a monofilament of PET as a medical textile. The resulting construct exhibits a thickness which can be adjusted to adequately fit the defect (Supplementary Figure 6-2). In this way we were able to generate a partially degradable porous construct which in the long term will fully integrate with bone. The mean pore size at these scaffolds interior, larger than 500 µm (Table 6-2), has proved suitable for cell proliferation, nutrients exchange and capillaries formation, promoting rapid bone regeneration, correlating well with the literature [48]. Moreover, the presence of smaller pores in the outer layers, larger than 100 µm (Table 6-2), is essential for the initial cell attachment [49]. SF-PET scaffolds presented higher fiber density than PET control scaffolds, which can be related to the different formed loops according to the applied knitting technology [50].

Human ASCs have emerged as a viable possibility for bone regeneration applications [20, 51]. Osteogenic-induced hASCs expressed the typical temporal sequence for ALP activity on SF-PET scaffolds, with a rise up until day 14 and a tendency to decrease at day 21 (Figure 6-3), accompanied by a significant increase in calcium content (Figure 6-4a). This behavior has been reported in other studies [20, 51] and is also in agreement with our results obtained from calcium deposition (Figure 6-4b), SEM and EDS analysis (Figure 6-5), showing the formation of a mineralized matrix with the presence of Ca and P elements. Moreover, in both textile constructs, the Ca/P ratios (Figure 6-5) were very close to those typically found for the HA (1.67) and adult human bone (1.71) [52, 53]. In a previous study by our group, Rodrigues *et al.,* also demonstrated similar Ca/P ratios after culturing fiber-based scaffolds with hASCs for 21 days in osteogenic culture conditions. From day 7 and day 21, significantly higher levels of ALP activity were presented by the SF-PET constructs cultured under osteogenic and basal conditions, respectively, as compared to PET constructs (Figure 6-3). These results can be explained by the lower number of cells quantified on the SF-PET constructs (data not shown) and the lower porosity and mean pore size observed on the external SF layers may also corroborates to this hypothesis (Table 6-2). Moreover, the sequencial increase of ECM mineralization observed at similar levels on SF-PET and PET constructs in osteogenic culture conditions (Figure 6-4), suggests that both knitted materials are potential matrices to support new bone deposition.

The genotypic (Figure 6-6a) and phenotypic (Figure 6-6b) analysis of the osteogenic-related markers OCN and OPN, showed the expression of both markers on SF-PET and PET constructs after 28 days of osteogenic culture, which may be indicative of the hASCs osteogenic differentiation [51]. Moreover, the non-expression of these osteogenic-related markers under basal culture conditions also support this hypothesis. Considering that OCN and OPN have a strong binding capacity to the inorganic component of bone ECM [7], these results also corroborate to our ECM mineralization observations (Figures 6-4 and 6-5). The relative gene expression of Col I was significantly higher in basal culture conditions for both textile constructs, which may also be related to the ostegenic differentiation of hASCs in osteogenic culture conditions, accompanied by a continuous deposition of the collagen matrix in basal conditions [54].

All together, the obtained results demonstrated the effectiveness of the proposed textile-based scaffolds on the differentiation of hASCs into osteoblasts and in the deposition of mineralized ECM. In a previous study by our group, Correia *et al.,* [20] showed the ability of silk-based scaffolds to support hASCs osteogenic differentiation, confirmed by the typical course of ALP activity, calcium deposition and immunostaining of osteogenic-related markers. Mandal *et al.,* [22] have also shown that micron-sized silk fibers used as reinforcement in a compact fiber composite favored the differentiation of BMSCs toward bone-like cells, based on biochemical and gene expression of bone markers. Walther *et al.,* [13] presented novel 3D scaffolds generated by a flock textile technology that allowed hMSCs attachment, proliferation and differentiation along the osteoblastic lineage, revealing that the fibers' orientation and the highly porous structure had a positive influence over cell response and resulting biological mechanisms. Thus, the pre-establishment of the fibers' alignment on the development of textile-based scaffolds represents an important concert, since it can directly influence the differentiation potential of cells over the structures.

The quantification of convergent macroscopic blood vessels on CAM assay, demonstrated that SF-PET textile structures presented a significantly higher angiogenic capacity, as compared to PET textiles and gelatin sponges (Figure 6-7a). As a natural protein fiber, SF presents not only controlled degradability [14], as superior *in vivo* compatibility and angiogenic potential [55]. This is in agreement to the obtained histological results where SF-PET scaffolds presented good integration in the CAM (Figure 6-7b). These features are very important when considering a scaffold to be used as implant material. It should be well integrated in the first stage of implantation, but continuouslly absorbed to replace the new-formed tissue [32]. In fact, the chemical stability of the synthetic polymer PET [56] and the fact that gelatin sponges are often used in the CAM assay without influencing angiogenesis [32], also contribute to evidenciate the potential of SF in the present application. Both studied scaffolds allowed the infiltration of endothelial cells and the formation of microscopic blood vessels (Figure 6-7b), showing their potential as angiogenesis carriers. These textile constructs also showed good integrity and dimensional stability for the studied period of subcutaneous implantation (14-28 days) (Figure 6-8). This was expected for PET constructs [57] but in case of SF no signs of degradation were visible. In a previous study by our group [14] the degradability of SF knitted scaffolds (single layer) was studied using a solution of PBS containing 3.5 U/mL of protease XIV. These *in vitro* results present a weight loss of

5% after 5 days, which correlates well with the present study, indicating a slow proteolitically degradation of native SF fibers mostly due to its high crystalline content (β-sheet conformation). In a previous study, Dal Pra *et al.,* [58] observed that non-woven SF cords in β-sheet form presented by day 180 of mice implantation a non-appreciable biodegradation, which corroborates the results obtained in our study. These results also indicate that scaffolds are able to retain good mechanical properties *in vivo,* which is in agreement with the wet compressive modulus analysis. The observation of a thick layer of connective tissue involving the fibers and infiltrating the scaffolds was found on both textile constructs, as well as the presence of vessels formed inside the scaffolds. The high porosity and fiber alignement in the structures may have contributed for these results [40]. It has been reported that fiber-like networks can have a positive influence over cell behavior and *in vivo* implantation, as it resembles the fibrous architecture of the natural ECM environment [8]. For example, Sanders *et al.,* [59] have demonstrated that the subcutaneous implantation of textile scaffolds in mice resulted in different tissue thicknesses surrounding the structures, depending on the fibers' diameters. The results obtained for PET constructs can also evidence the positive influence of the proposed fiber-based networks with respect to *in vitro* and *in vivo* response. Unlike silk, whose surface chemistry has shown to positively influence cell behavior in different scaffolding strategies [14], the chemical stability of PET is not expected to induce any biological effects, which indicates that the cell viability, proliferation and osteogenic differentiation on the PET scaffolds and their *in vivo* performance can be related to the architecture and morphological features of the construct, as well as to the high molecular orientation on PET fibers due to shear stress during processing [60]. Besides of the promising results presented herein, the possibility of having an automated production of the proposed biotextiles represents great prospects for their possible industrialization and application in tissue engineering. We have addressed flat bone tissue engineering for modelling the presented scaffolds, but other specific applications can be considered due to the versatility of process.

6.6. Conclusions

In this study, novel 3D biotextile architectures composed of knitted SF and PET fibers spaced by a monofilament of PET, are proposed for the regeneration of bone tissue and a possible strategy for craniofacial bone scaffolding. The scaffolds presented suitable porosity and mechanical properties for bone applications, with special relevance for the superior mechanical properties of SF-PET textile scaffolds in the hydrated state. The *in vitro* osteogenic differentiation of the seeded hASCs was represented on SF-PET scaffolds by the peak of ALP activity after 14 days of osteogenic culture and subsequent deposition of mineralized ECM, also detected on PET constructs. Additionally, the genotypic expression and immunodetection of bone-specific transcripts also confirmed the osteogenic differentiation of hASCs cultured on SF-PET and PET spacer contructs. The *in vivo* studies revealed that SF-PET scaffolds induced higher angiogenic effect when performing a CAM assay and both textile structures allowed tissue ingrowth when subcutaneously implanted in mice, with minimum foreign body reaction. Although a complementary *in vivo* study is necessary to evaluate the long-term performance and stability of the scaffolds in craniofacial bone defects, the obtained results indicate that the developed 3D biotextiles are promising structures for bone regeneration applications. Moreover, the structural adaptability of the knitted spacer fabrics increase the scaffolds applicability for different regenerative strategies, including for bone regeneration at the craniofacial complex.

6.7. Supplementary information

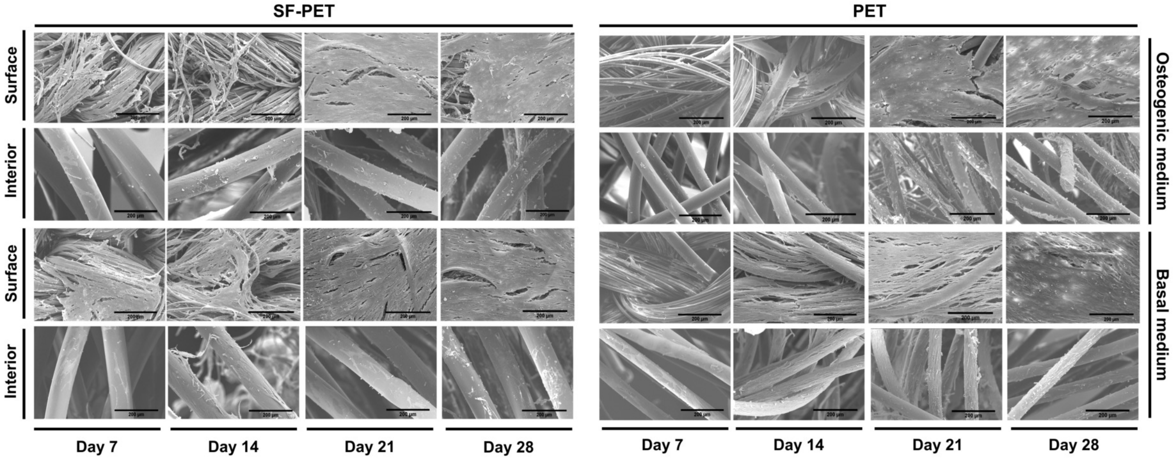
SF-PET
PET
Surface
Interior
Surface
Interior
Osteogenic medium
Basal medium
Day 7
Day 14
Day 21
Day 28
Day 7
Day 14
Day 21
Day 28

Supplementary Figure 6-1. SEM micrographs of the SF-PET and PET knitted spacer fabrics, cultured with hASCs in osteogenic and basal medium for 7, 14, 21 and 28 days. The figures show cell adhesion at the surface and cross-sections of the seeded scaffolds.

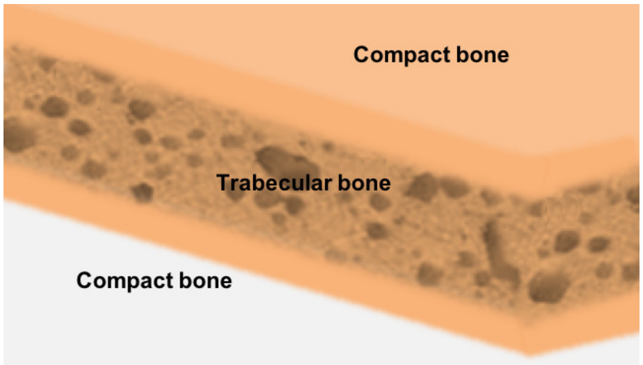
Compact bone
Trabecular bone
Compact bone

Supplementary Figure 6-2. Representative image of the structure of a flat bone.

6.8. References

[1] M. Miura, et al., Bone marrow-derived mesenchymal stem cells for regenerative medicine in craniofacial region, Oral diseases 12(6) (2006) 514-522.

[2] V. Petrovic, et al., Craniofacial bone tissue engineering, Oral Surgery, Oral Medicine, Oral Pathology and Oral Radiology 114(3) (2012) e1-e9.

[3] H. Schöning, R. Emshoff, Primary temporary AO plate reconstruction of the mandible, Oral Surgery, Oral Medicine, Oral Pathology, Oral Radiology, and Endodontology 86(6) (1998) 667-672.

[4] Y. Kinoshita, H. Maeda, Recent developments of functional scaffolds for craniomaxillofacial bone tissue engineering applications, The Scientific World Journal 2013 (2013).

[5] B. Ward, et al., Bioengineering strategies for regeneration of craniofacial bone: a review of emerging technologies, Oral diseases 16(8) (2010) 709-716.

[6] F. Yang, et al., Electrospinning of nano/micro scale poly (L-lactic acid) aligned fibers and their potential in neural tissue engineering, Biomaterials 26(15) (2005) 2603-2610.

[7] A. Martins, et al., The influence of patterned nanofiber meshes on human mesenchymal stem cell osteogenesis, Macromolecular Bioscience 11(7) (2011) 978-987.

[8] R. Sumanasinghe, M.W. King, The applications of biotextiles in tissue engineering, Research Journal of Textile and Apparel 9(3) (2005) 80-90.

[9] F.T. Moutos, et al., A biomimetic three-dimensional woven composite scaffold for functional tissue engineering of cartilage, Nature materials 6(2) (2007) 162-167.

[10] H. Liu, et al., The interaction between a combined knitted silk scaffold and microporous silk sponge with human mesenchymal stem cells for ligament tissue engineering, Biomaterials 29(6) (2008) 662-674.

[11] X. Chen, et al., Ligament regeneration using a knitted silk scaffold combined with collagen matrix, Biomaterials 29(27) (2008) 3683-3692.

[12] C. Heinemann, et al., Novel textile chitosan scaffolds promote spreading, proliferation, and differentiation of osteoblasts, Biomacromolecules 9(10) (2008) 2913-2920.

[13] A. Walther, et al., Novel textile scaffolds generated by flock technology for tissue engineering of bone and cartilage, Materials 5(3) (2012) 540-557.

[14] L.R. Almeida, et al., New biotextiles for tissue engineering: development, characterization and in vitro cellular viability, Acta Biomaterialia 9(9) (2013) 8167-8181.

[15] V.P. Ribeiro, et al., Influence of different surface modification treatments on silk biotextiles for tissue engineering applications, Journal of Biomedical Materials Research Part B: Applied Biomaterials (2015).

[16] A. Davies, J. Williams, The use of spacer fabrics for absorbent medical applications, Journal of Fiber Bioengineering and Informatics 1(4) (2009) 321-330.

[17] C. Chua, et al., Development of tissue scaffolds using selective laser sintering of polyvinyl alcohol/hydroxyapatite biocomposite for craniofacial and joint defects, Journal of Materials Science: Materials in Medicine 15(10) (2004) 1113-1121.

[18] J.L. Moreau, H.H. Xu, Mesenchymal stem cell proliferation and differentiation on an injectable calcium phosphate–chitosan composite scaffold, Biomaterials 30(14) (2009) 2675-2682.

[19] Z.S. Haidar, et al., Delivery of recombinant bone morphogenetic proteins for bone regeneration and repair. Part B: Delivery systems for BMPs in orthopaedic and craniofacial tissue engineering, Biotechnology letters 31(12) (2009) 1825-1835.

[20] C. Correia, et al., Development of silk-based scaffolds for tissue engineering of bone from human adipose-derived stem cells, Acta Biomaterialia 8(7) (2012) 2483-2492.

[21] L. Meinel, et al., Silk implants for the healing of critical size bone defects, Bone 37(5) (2005) 688-698.

[22] B.B. Mandal, et al., High-strength silk protein scaffolds for bone repair, Proceedings of the National Academy of Sciences 109(20) (2012) 7699-7704.

[23] K.H. Kim, et al., Biological efficacy of silk fibroin nanofiber membranes for guided bone regeneration, Journal of Biotechnology 120(3) (2005) 327-339.

[24] Q. Han, et al., Epigenetically Modified Bone Marrow Stromal Cells (BMSCs) in Silk Scaffolds Promote Craniofacial Bone Repair and Wound Healing, Tissue Engineering (ja) (2015).

[25] A. Woloszyk, et al., Influence of the mechanical environment on the engineering of mineralised tissues using human dental pulp stem cells and silk fibroin scaffolds, (2014).

[26] B. Levi, M.T. Longaker, Concise Review: Adipose-Derived Stromal Cells for Skeletal Regenerative Medicine, Stem cells 29(4) (2011) 576-582.

[27] M.T. Cerqueira, et al., Human adipose stem cells cell sheet constructs impact epidermal morphogenesis in full-thickness excisional wounds, Biomacromolecules 14(11) (2013) 3997-4008.

[28] J.C. Bodle, et al., Adipose-derived stem cells in functional bone tissue engineering: lessons from bone mechanobiology, Tissue Engineering Part B: Reviews 17(3) (2011) 195-211.

[29] Y.-D.C. Halvorsen, et al., Extracellular matrix mineralization and osteoblast gene expression by human adipose tissue-derived stromal cells, Tissue engineering 7(6) (2001) 729-741.

[30] S.M. Mihaila, et al., The osteogenic differentiation of SSEA-4 sub-population of human adipose derived stem cells using silicate nanoplatelets, Biomaterials 35(33) (2014) 9087-9099.

[31] K.J. Livak, T.D. Schmittgen, Analysis of relative gene expression data using real-time quantitative PCR and the 2(T)(-Delta Delta C) method, Methods 25(4) (2001) 402-408.

[32] J. Silva-Correia, et al., Angiogenic potential of gellan-gum-based hydrogels for application in nucleus pulposus regeneration: in vivo study, Tissue Engineering Part A 18(11-12) (2012) 1203-1212.

[33] G. Chen, et al., The use of a novel PLGA fiber/collagen composite web as a scaffold for engineering of articular cartilage tissue with adjustable thickness, Journal of Biomedical Materials Research Part A 67(4) (2003) 1170-1180.

[34] K.W. Ng, et al., Characterization of a novel bioactive poly [(lactic acid)-co-(glycolic acid)] and collagen hybrid matrix for dermal regeneration, Polymer international 54(10) (2005) 1449-1457.

[35] M. Kellomäki, et al., Bioabsorbable scaffolds for guided bone regeneration and generation, Biomaterials 21(24) (2000) 2495-2505.

[36] V.P. Ribeiro, et al., Modulating cell adhesion to polybutylene succinate biotextile constructs for tissue engineering applications, Journal of Tissue Engineering and Regenerative Medicine (2016).

[37] F.T. Moutos, F. Guilak, Functional properties of cell-seeded three-dimensionally woven poly(epsilon-caprolactone) scaffolds for cartilage tissue engineering, Tissue Engineering Part A 16(4) (2010) 1291-1301.

[38] Z. Ge, et al., Biomaterials and scaffolds for ligament tissue engineering, Journal of biomedical materials research Part A 77(3) (2006) 639-652.

[39] U. Wollina, et al., Functional textiles in prevention of chronic wounds, wound healing and tissue engineering, Current problems in dermatology 31 (2003) 82-97.

[40] E. Wintermantel, et al., Tissue engineering scaffolds using superstructures, Biomaterials 17(2) (1996) 83-91.

[41] J. Yip, S.-P. Ng, Study of three-dimensional spacer fabrics:: Physical and mechanical properties, Journal of materials processing technology 206(1) (2008) 359-364.

[42] A.M. O'Mahony, et al., Anisotropic elastic properties of cancellous bone from a human edentulous mandible, Clinical oral implants research 11(5) (2000) 415-421.

[43] C.E. Misch, et al., Mechanical properties of trabecular bone in the human mandible: implications for dental implant treatment planning and surgical placement, Journal of Oral and Maxillofacial Surgery 57(6) (1999) 700-706.

[44] R. Zhang, P.X. Ma, Poly (a-hydroxyl acids)/hydroxyapatite porous composites for bone-tissue engineering. I. Preparation and morphology, Journal of biomedical materials research 44(4) (1999) 446-455.

[45] J.J. Blaker, et al., Mechanical properties of highly porous PDLLA/Bioglass® composite foams as scaffolds for bone tissue engineering, Acta biomaterialia 1(6) (2005) 643-652.

[46] J.F. Mano, Viscoelastic properties of bone: mechanical spectroscopy studies on a chicken model, Materials Science and Engineering: C 25(2) (2005) 145-152.

[47] Y. Liu, et al., Review: development of clinically relevant scaffolds for vascularised bone tissue engineering, Biotechnology Advances 31(5) (2013) 688-705.

[48] V. Karageorgiou, D. Kaplan, Porosity of 3D biomaterial scaffolds and osteogenesis, Biomaterials 26(27) (2005) 5474-5491.

[49] D.W. Hutmacher, et al., State of the art and future directions of scaffold-based bone engineering from a biomaterials perspective, Journal of Tissue Engineering and Regenerative Medicine 1(4) (2007) 245-260.

[50] X. Wang, et al., Applications of knitted mesh fabrication techniques to scaffolds for tissue engineering and regenerative medicine, Journal of the mechanical behavior of biomedical materials 4(7) (2011) 922-932.

[51] V.E. Santo, et al., Enhancement of osteogenic differentiation of human adipose derived stem cells by the controlled release of platelet lysates from hybrid scaffolds produced by supercritical fluid foaming, Journal of Controlled Release 162(1) (2012) 19-27.

[52] S.V. Dorozhkin, Bioceramics of calcium orthophosphates, Biomaterials 31(7) (2010) 1465-1485.

[53] L.C. Palmer, et al., Biomimetic systems for hydroxyapatite mineralization inspired by bone and enamel, Chemical reviews 108(11) (2008) 4754-4783.

[54] E. Fiorentini, et al., Effects of osteogenic differentiation inducers on in vitro expanded adult mesenchymal stromal cells, International Journal of Artificial Organs 34(10) (2011) 998.

[55] B. Kundu, et al., Silk fibroin biomaterials for tissue regenerations, Advanced drug delivery reviews 65(4) (2013) 457-470.

[56] Z. Ma, et al., Surface engineering of electrospun polyethylene terephthalate (PET) nanofibers towards development of a new material for blood vessel engineering, Biomaterials 26(15) (2005) 2527-2536.

[57] H.K. Webb, et al., Plastic degradation and its environmental implications with special reference to poly (ethylene terephthalate), Polymers 5(1) (2012) 1-18.

[58] I. Dal Pra, et al., De novo engineering of reticular connective tissue in vivo by silk fibroin nonwoven materials, Biomaterials 26(14) (2005) 1987-1999.

[59] J. Sanders, et al., Tissue response to microfibers of different polymers: polyester, polyethylene, polylactic acid, and polyurethane, Journal of biomedical materials research 62(2) (2002) 222-227.

[60] K. Illers, H. Breuer, Molecular motions in polyethylene terephthalate, Journal of Colloid science 18(1) (1963) 1-31.

CHAPTER 7.

Combinatory Approach for Developing Silk Fibroin Scaffolds for Cartilage Regeneration

CHAPTER 7.

Combinatory approach for developing silk fibroin scaffolds for cartilage regeneration*

7.1. Abstract

Several processing technologies and engineering strategies have been combined to create scaffolds with superior performance for efficient tissue regeneration. Cartilage tissue is a good example of that, presenting limited self-healing capacity together with a high elasticity and load-bearing properties. In this work, novel porous silk fibroin (SF) scaffolds derived from horseradish peroxidase (HRP)-mediated crosslinking of highly concentrated aqueous SF solution (16 wt.%) in combination with salt-leaching and freeze-drying methodologies were developed for articular cartilage tissue engineering (TE) applications. The HRP-crosslinked SF scaffolds presented high porosity (89.3 ± 0.6%), wide pore distribution and high interconnectivity (95.9 ± 0.8%). Moreover, a large swelling capacity and favorable degradation rate were observed up to 30 days, maintaining the porous-like structure and β-sheet conformational integrity obtained with salt-leaching and freeze-drying processing. The *in vitro* studies supported human adipose-derived stem cells (hASCs) adhesion, proliferation, and high glycosaminoglycans (GAGs) synthesis under chondrogenic culture conditions. Furthermore, the chondrogenic differentiation of hASCs was assessed by the expression of chondrogenic-related markers (collagen type II, Sox-9 and Aggrecan) and deposition of cartilage-specific extracellular matrix for up to 28 days. The cartilage engineered constructs also presented structural integrity as their mechanical properties were improved after chondrogenic culturing. Subcutaneous implantation of the scaffolds in CD-1 mice demonstrated no necrosis or calcification, and deeply tissue ingrowth. Collectively, the structural properties and biological performance of these porous HRP-crosslinked SF scaffolds make them promising candidates for cartilage regeneration.

*This chapter is based on the following publication:

Ribeiro VP, da Silva Morais A, Maia FR, Canadas R, Costa JB, Oliveira AL, Oliveira JM, Reis RL. Combinatory approach for developing silk fibroin scaffolds for cartilage regeneration. 2018, Submitted.

7.2. Introduction

Articular cartilage is a highly-organized tissue with avascular properties and limited intrinsic healing capacity [1]. Injuries and degenerative conditions may compromise cartilage functions and cause pain and disability to the patients. A study performed by Widuchowski *et al.,* [2] involving 25,124 knee arthroscopies showed chondral lesions in 60% of the cases, classified as focal chondral lesions (67%), osteoarthritis (29%), ostechondritis dissecans (2%) and other types of lesions (1%). Surgical procedures remain the standard treatment for injured and degenerative joint pathologies, which may include early surgical interventions, such us osteotomy, autologous osteochondral graft transplantation and arthroscopic microfracture chondroplasty, or the total tissue replacement applied in cases of end-stage degenerative pathologies [3]. Thus, the real challenge for orthopaedic surgeons is still the management of articular cartilage defects, whose treatment options are in most cases only for symptom relief and do not ensure the long-term healing of tissue.

Bioactive substitutes emerged over the past years as possible solutions for the treatment and regeneration of articular cartilage tissue [1]. For example, a clinical success has been obtained since 1994 through the use of autologous chondrocytes implantation (ACI) techniques directly at the cartilage defects [4]. Since then, cartilage tissue engineering (TE) strategies have been proposed as cell-free or cell-based approaches, combined with biomimetic materials as supporting matrices [5]. The clinical use of scaffolds in cartilage regeneration is represented only by a few examples of commercially available products, including the Chondro-Gide® (Geistlich Pharma AG, Wolhusen, Switzerland) collagen scaffold that presented promising results for mid-long-term cartilage treatment [6]. The inclusion of interconnected porous-like structures showed to benefit cell adhesion and guided a rapid extracellular matrix (ECM) formation and infiltration within the scaffolds, which represents great advancements on cartilage tissue regeneration, especially when envisioning the use of cell-free strategies [7, 8]. On the other hand, different polymeric-based hydrogels have been investigated as injectable systems for arthroscopic insertion approaches [9]. The high-water-content that mimics the native cartilage tissue, or the ability to encapsulate cells and diffuse growth factors may benefit this technology [10]. Gelrin C® (Regentis, Haifa, Isreal) and ChonDux™ (Cartilix, CA, USA) hydrogels composed of polyethylene glycol (PEG) covalently bonded to fibrinogen chains and to hyaluronic acid, respectively, are two good examples of biocompatible and bioabsorbable injectable system that have been successfully used in clinic to fill and reinforce micro-fractured cartilage defects [11].

Silk fibroin (SF) solutions have been used to prepare hydrogels as injectable or non-injectable systems, with suitable mechanical properties for load bearing of cartilage tissue [12-14]. Most of these hydrogels are formed in a sol-gel transition, together with a structure conformation transition from amorphous to β-sheet, which can happen by means of different physical and chemical treatments [15]. Different authors have shown that the addition of organic solvents (methanol) [16], decreasing the pH value [17] or increasing the temperature/ionic species (Ca^{2+}) concentration [18] in the aqueous SF solution, can induce SF hydrogels formation with gelation times that can range from a few hours to days, depending on the applied method. Moreover, in cases where cell encapsulation is desired, some of these methods may be compromised. For example, the use of methanol as crosslinking agent imply the immersion of SF solution into the solvent until the reaction is complete and the hydrogel formed. This way, the cell encapsulation process would be compromised, since cells would not survive in the presence of methanol solution. Nevertheless, this process does not invalidate the methanol-induced SF hydrogels for cell-seeding approaches [19]. The use of external stimuli-like ultrasonication and mechanical agitation, have also been explored to produce fast-formed SF hydrogels, compatible for cell encapsulation [20, 21]. Also, several enzymatically mediated crosslinking methods have been used to prepare *in situ* formed hydrogels. Comparing to other systems, enzyme-mediated crosslinking can display several advantages. They occur at physiological conditions and the gelation time can be easily tuned to be fast, favouring cell encapsulation and the delivery of bioactive molecules [22]. Recently, the horseradish peroxidase (HRP) mediated crosslinking has received an increasing interest, since the phenol groups in tyrosine, tyramine or aminophenol, can be conjugated when catalyzed by peroxidase and hydrogen peroxide (H_2O_2) [23, 24]. Considering that SF protein contains some reactive amino acid residues of tyrosine (~5%), this was seen as a great advantage to create naturally induced SF hydrogels [16, 25]. These HRP-mediated crosslinked SF hydrogels were previously produced in a main amorphous conformation and at physiological conditions, showing promising biological results and tunable mechanical properties according to the protein/crosslinker concentration. Simultaneously, it has been recognized that the anti-parallel β-sheets formation in SF hydrogels or scaffolds can affect their stiffness, degradability and biological behavior in response to changes in surface roughness [26]. For example, Yan *et al.,* [27] combined salt-leaching and freeze-drying methodologies to produce macro-/micro-porous SF scaffolds, showing that the anti-parallel β-sheet conformation was present in the scaffolds and improved their mechanical properties for cartilage TE scaffolding strategies. Moreover, high and controlled porosity induced by the salt-leaching technique have also shown to improve cell adhesion, proliferation and chondrogenic differentiation within SF constructs [14].

On the side of the cells, the combination of three-dimensional (3D) networks with autologous chondrocytes previous implantation, represented significant clinical improvements for cartilage defects treatment (see NeoCart®, Histogenics, Waltham, MA and Hyalograft® C, Anika Therapeutics, Bedford, MA) [28, 29]. Nevertheless, great attention has been directed for cell sources able to differentiate into the chondrogenic lineage, and secret growth factors responsible for creating an ECM that can fill the chondral lesion [30]. The application of human mesenchymal stem cells (MSCs) covered a noticeable interest having shown to possess multilineage differentiation potential including for chondrogenesis induction [31]. On the other hand, human adipose-derived stem cells (hASCs) appear to present the same multilineage differentiation potential as MSCs, but also demonstrated special features regarding cell surface markers and abundance in the body. Moreover, they can be easily harvested from the adipose tissue with less pain for the donor [32]. Previous studies, were able to explore the chondrogenic differentiation potential of hASCs when cultured in SF scaffold materials, showing that the 3D porous matrices successfully induced cell-cell interactions and ECM matrix formation in a similar fashion to the forming cartilage tissue [33, 34].

In the present work, we aimed to make use of an enzymatic-mediated approach to crosslink SF combined with salt-leaching and freeze-drying technologies, towards producing robust and interconnected porous SF scaffolds for cartilage TE applications. With this strategy, it is expected to tune a large number of properties in a single HRP-crosslinked SF scaffold, while avoiding the use of harsh or toxic crosslinking agents during processing. These work reports on the effectiveness of the proposed scaffolds over *in vitro* chondrogenic differentiation and *in vivo* compatibility, being the first study to propose such combinatory approaches for the development of a more complete SF scaffold able to better recreate the requirements for the treatment of cartilage defects.

7.3. Materials and Methods

7.3.1. Materials and reagents

Silk derived from the silkworm *Bombyx mori* in the form of cocoons was provided by the Portuguese Association of Parents and Friends of Mentally Disabled Citizens (APPACDM, Castelo Branco, Portugal). Silicone tubing was purchased from Deltalab (Barcelona, Spain). Granular sodium chloride (Commercial grade, Portugal) was prepared in the range of 500-1000 µm in an analytic sieve shaker (AS 200 Digit, Retsch, Germany). All reagents were purchased from Sigma-Aldrich (St. Louis, MO, USA) unless otherwise stated.

7.3.2. Preparation of aqueous silk fibroin solution

Purified silk fibroin (SF) was prepared by removing the glue-like protein sericine from the cocoons in a boiling sodium carbonate solution (0.02 M) for 1 hour and then rinsed with distilled water in order to fully remove the degumming solution. A 9.3 M lithium bromide solution was used to dissolve the purified SF for 1 hour at 70°C and dialyzed in distilled water for 48 hours using a benzoylated dialysis tubing (MWCO: 2 kDa). Next, the aqueous SF solution was concentrated using a 20 wt.% poly(ethylene glycol) solution for at least 6 hours. The final concentration of SF (18-20 wt.%) was determined by measuring the dry weight of the SF solution placed in the oven at 70°C overnight. Meanwhile, the prepared SF solution was stored at 4°C until further use (Figure 7-1a).

7.3.3. Preparation of salt-leached enzymatically crosslinked silk fibroin scaffolds

Enzymatically crosslinked SF scaffolds were prepared by the initial mixture of SF solution, diluted to 16 wt.%, with horseradish peroxidase solution (HRP type VI, 0.84 mg/mL) and hydrogen peroxide solution (H_2O_2, 0.36 wt.%; Panreac, Barcelona, Spain), as reported previously [16]. Briefly, 1 mL SF solution, 50 µL HRP solution and 65 µL H_2O_2 solution (1/0.26‰/1.45‰) were mixed in a 1.5 mL centrifuge tube (Eppendorf, Hamburg, Germany) and before gelling, 1 mL of the SF/HRP/H_2O_2 solution was transferred into a cylindrical shaped silicone mold (9 mm inner diameter). β-sheet induced SF structures were prepared by the slow addition of 2 g of granular sodium chloride (particle size 500-1000 µm) to the solution. The sodium chloride particles were gently added to the silicon molds to facilitate the precipitation of the salt [27]. The molds were placed in the oven at 37°C to complete the enzymatic reaction at the SF/HRP/H_2O_2 complex. HRP-crosslinked SF scaffolds were formed when the undissolved sodium chloride particles were leached out (porogen) in distilled water for 72 hours. Finally, the scaffolds were removed from the molds by using a biopsy punch (8 mm inner diameter; Smith & Nephew, Portugal), followed by freezing at -80°C overnight and freeze-drying (Telstar Cryodos-80, Barcelona, Spain) for 7 days (Figure 7-1b).

7.3.4. Physicochemical characterization

7.3.4.1. Scanning electron microscopy

The surface and cross-sectional morphology of the HRP-crosslinked SF scaffolds was analyzed by analytic scanning electron microscopy (SEM) using a JEOL JSM-6010LV (Tokyo, Japan). Two samples were used for structure qualitative evaluation. Prior analysis all samples were sputter-coated with gold using a Leica EM ACE600 coater (Leica Microsystems, Wien, Austria).

7.3.4.2. Micro-computed tomography

The microstructure of the prepared HRP-crosslinked SF scaffolds was evaluated using a high-resolution X-ray microtomography system Skyscan 1072 scanner (Skyscan, Kontich, Belgium). Samples were scanned using a pixel size of 8.79 µm x/y/z and an X-ray source fixed at 40 keV of energy and 248 µA of current. After acquisition, reconstructed grey-scale images were converted into binary images by using a dynamic threshold of 40-255. Then, the binary images were used for morphometric analysis (CT Analyzer v1.12.0.0, SkyScan, Kontich, Belgium) by quantification of porosity, mean pore size, mean wall thickness and interconnectivity. The scaffolds cross-sectional images and 3D virtual models were also created, visualized and registered using the image processing and reconstruction software's Data Viewer (v1.6.6.0) and CT-Vox (v2.0.0) (SkyScan, Kontich, Belgium), respectively. Three samples were used for the qualitative and quantitative microstructure evaluation.

7.3.4.3. Fourier transform infrared spectroscopy

The infrared spectra of the HRP-crosslinked SF scaffolds were recorded by Fourier transform infrared (FTIR) spectroscopy (Perkin-Elmer 1600 series equipment, CA, USA) under an attenuated total reflectance (ATR) model (IRPrestige-21, Shimadzu, Kyoto, Japan), equipped with a germanium crystal. Prior analysis, the samples were immersed in phosphate-buffered saline (PBS, pH 7.4) solution until equilibrium was reached (overnight). All spectra were obtained between 4500 to 800 cm^{-1} at a 4 cm^{-1} resolution with 32 scans. Three samples were used for analysis and PBS was used as background.

7.3.4.4. Compressive tests

The mechanical behavior of the HRP-crosslinked SF scaffolds was tested under quasi-static compression in dry and hydrated state using a Universal Testing Machine (Instron 4505, Norwood, MA, USA). The diameter and height of the scaffolds were 8 and 4 mm, respectively. Prior analysis, the samples tested in hydrated state were immersed in PBS solution (pH 7.4) until equilibrium was reached (overnight). The cross-head speed was fixed at 2 mm/min and tests were run until a 60% reduction in sample height had been achieved. The compressive stress and strain were graphed and the average compressive modulus and compressive strength were determined based on five samples measured for each group. The elastic modulus (E) was defined by the slope of the initial linear region of the stress-strain curve. The compressive strength was determined by the maximum compressive load (N) applied in the test divided by the original area of the specimen (mm^2).

7.3.5. Swelling ratio and degradation profile

The swelling ratio of the HRP-crosslinked SF scaffolds was tested in PBS solution. The initial dry weight of each sample (n=6) was measured, and then the scaffolds were immersed in 5 mL of PBS solution. The study was conducted at 37°C for a time period ranging from 1 hour to 30 days. The solutions were changed weekly. At the end of each time point, samples were gently blotted with filter paper to remove excess liquid and the wet weight measured. The swelling ratio was determined following Equation 4-1:

$$\text{Water uptake (\%)} = \frac{mw-mi}{mi}\times 100$$

where m_W is the weight of the sample after removal from the solution and m_i is the initial weight of the sample.

The stability of the HRP-crosslinked SF scaffolds was evaluated by enzymatic degradation test. Protease XIV was derived from *Streptomyces griseus* (3.5 U/mg) and prepared at 3.5 U/mL and 0.2 U/mL by dissolving the enzyme in PBS [35]. As control condition, samples were incubated in PBS solution alone. The initial dry weight of each sample (n=3) was measured, and then the scaffolds were immersed in 5 mL of protease solution or PBS solution. The study was conducted at 37°C for a time period ranging from 3 hours to 30 days. The enzyme solutions were changed every 24 hours. The dry weight was measured after washing the samples with distilled water and drying at 70°C overnight. The weight loss was determined following Equation 4-2:

$$\text{Weight loss (\%)} = \frac{mi-mf}{mi}\times 100$$

where m_i is the initial weight of the sample and m_f is the weight of the sample after drying.

7.3.6. *In vitro* cell studies

7.3.6.1. hASCs isolation and expansion

Human abdominal subcutaneous adipose tissue samples were obtained from lipoaspiration procedures performed on healthy male and female donors with ages between 18 and 57 years, after informed consent, under established cooperative agreements between Hospital da Senhora da Oliveira (Guimarães, Portugal) and 3B's Research Group. All the samples were processed within 24 hours after the lipoaspiration procedure and human adipose-derived stem cells (hASCs) were enzymatically isolated from subcutaneous adipose tissue as previously described [36]. Human ASCs were expanded in basal medium consisting of MEM alpha medium (α-MEM; Gibco®, Life Technologies, Carlsbad, CA, USA) supplemented with sodium bicarbonate, 10% (v/v) fetal bovine serum (FBS; Life Technologies, Carlsbad, CA, USA) and 1% (v/v) antibiotic/antimycotic solution (final concentration of penicillin 100 units/mL and streptomycin 100 mg/mL, Life Technologies, Carlsbad, CA, USA). Cells were cultured until confluence at 37°C, 5% CO_2 incubator, changing the culture medium every 2-3 days.

7.3.6.2. Seeding and chondrogenic differentiation of hASCs on the HRP-crosslinked SF scaffolds

Human ASCs were characterized by flow cytometry (FACSCalibur flow cytometer, BD Biosciences, San Jose, CA, USA) for MSCs surface markers [37]. The following monoclonal antibodies conjugated to fluorochromes were used: anti-CD105 FITC (BioRad, Hercules, CA, USA), anti-CD73 PE, anti-CD90 APC, anti-CD45 FITC, anti-CD34 PE (BD Biosciences, San Jose, CA, USA). HRP-crosslinked SF scaffolds of 8 mm in diameter and 4 mm in height were used for the *in vitro* studies and sterilized by ethylene oxide (Gas Sterilizer/Aerator, Steri-Vac 5XL, 3M company, St. Paul, MN, USA). The number of cell-seeded constructs used for the different characterization techniques will be described below. Before cell seeding, all scaffolds were hydrated in Dulbecco's modified Eagle's medium-high glucose (DMEM-HG; Gibco®, Life Technologies, Carlsbad, CA, USA) supplemented with 1% (v/v) antibiotic/antimycotic solution, overnight in the CO_2 incubator. In the following day, the hydrated scaffolds were transferred to 48-well suspension cell culture plates (Cellstar, Greiner Bio-One, Kremsmuenster Austria). Confluent hASCs (passage 2) were detached with TrypIE™ Express (Life Technologies, Carlsbad, CA, USA) and seeded in a 20 µL cell suspension onto the surface of the scaffolds, at a density of 3×10^5 cells/scaffold. The constructs were kept in the CO_2 incubator for 3 hours and then completed with 1 mL of DMEM-HG supplemented with 10% (v/v) FBS (Life Technologies, Carlsbad, CA, USA) and 1% (v/v) antibiotic/antimycotic solution. After 24 hours, the culture medium was refreshed or replaced by chondrogenic differentiation medium. The chondrogenic medium was based on DMEM-HG supplemented with 50 µg/mL Ascorbic acid, 40 µg/mL L-Prolin, 1% Insulin-Transferrin-Selenium-G (ITS-G; Life Technologies, Carlsbad, CA, USA), 100 nM Dexamethasone, 10 ng/mL recombinant human TGF-β1 (PeproTech, London, UK) and 1% (v/v) antibiotic/antimycotic solution. Samples cultured in chondrogenic and basal culture medium, were harvested after culturing for 1, 7, 14, 21 and 28 days and the culture medium was changed every 2-3 days (Figure 7-1c).

7.3.6.3. Live/Dead staining

Cell viability at the HRP-crosslinked SF constructs was confirmed by performing a calcein-AM and propidium iodide (PI; Life Technologies, Carlsbad, CA, USA) staining. At the end of each time-point, three samples of each group (chondrogenic and basal medium) were incubated in 1 µg/mL calcein-AM and 5 µg/mL PI prepared in DMEM-low glucose supplemented with sodium bicarbonate and 1% (v/v) antibiotic/antimycotic solution, for 30 minutes in the dark at 37°C in the CO_2 incubator. After washing in PBS, samples were immediately examined under fluorescence microscopy (Calcein-AM in green: ex/em 495/515 nm; PI in red: ex/em 495/635 nm) in a transmitted and reflected light microscope (Axio Imager Z1 m; Zeiss, Jena, Germany). Images were acquired using the Zen microscope processing software (Zeiss, Jena, Germany) connected to a digital camera AxioCam MR3 (Zeiss, Jena, Germany). A Z-stack function was used to combine images at different depths into one final image.

7.3.6.4. Alamar blue assay

Alamar blue assay was performed to assess the metabolic activity of cells at the HRP-crosslinked SF constructs, following the manufacturer's instructions. After each culture time, the constructs were transferred to a new 48-well suspension cell culture plate and a solution of 10% (v/v) AlamarBlue® (BioRad, Hercules, CA, USA), prepared in chondrogenic or basal culture medium, was transferred to the culture plates in 500 µL/scaffold. After 3 hours of reaction with cells at 37°C in the CO_2 incubator, 100 µL of Alamar blue solution were taken from each well and placed in a 96-well white opaque plate (Corning-Costar Corporation, Acton, MA, USA) in triplicate. The fluorescence was measured in a microplate reader (Synergy HT, BioTek, Instruments, USA) at an excitation wavelength of 530/25 nm and at an emission wavelength of 590/35 nm. Three samples of each group (chondrogenic and basal medium) were tested at each time-point, in three independent experiments. Scaffolds without cells were used as control.

7.3.6.5. Quantitative DNA and glycosaminoglycans assays

The amount of double stranded DNA (dsDNA), that is directly proportional to the cell number, was determined using a Quant-IT PicoGreen dsDNA quantification kit (Life Technologies, Carlsbad, CA, USA), according to the manufacturer's instructions. After each culture time, samples were washed with PBS solution and frozen at -80°C in 1 mL of ultrapure water until further analysis. To induce complete membrane lysis, samples were sonicated for 1 hour after thawed at room temperature (RT). Supernatant fluorescence was measured using a microplate reader at an excitation wavelength of 485/20 nm and at an emission wavelength of 528/20 nm. The standard curve for DNA analysis was prepared with concentrations ranging from 0 to 2 µg/mL.

A dimethylmethylene blue (DMB) assay was performed for glycosaminoglycans (GAGs) quantification on the same samples used for dsDNA quantification. Samples were digested overnight at 60°C in 1 mL papain digestion solution, prepared by adding to each 50 mL of digestion buffer, 25 mg of papain and 48 mg of n-acetyl cysteine. Digestion buffer was composed of 200 mM of phosphate buffer (sodium phosphate monobasic) containing 1 mM ethylenediaminetetraacetic acid (EDTA) (pH 6.8). Then, samples were centrifuged at 13,000 rpm for 10 minutes and the supernatants collected. GAGs content was spectrophotometrically determined with a DMB solution, prepared by dissolving 16 mg DMB powder in 900 mL distilled water containing 3.04 g glycine and 2.73 g of NaCl (Panreac Química SAU, Barcelona, Spain) (pH 3.0). The optical density (OD) was measured in a microplate reader at an absorbance of 530 nm. A chondroitin sulphate stock solution was prepared in distilled water at 50 µg/mL in order to make a standard curve with concentrations ranging from 0 to 35 µg/mL. The obtained GAGs concentrations were normalized against the DNA concentrations of the same samples. Three samples of each group (chondrogenic and basal medium) were tested at each time-point, in three independent experiments. Scaffolds without cells were used as control.

7.3.6.6. Collagenous proteins quantification

The presence of collagen within the ECM was determined by the Sirius red/Fast green collagen staining kit (Chondrex, Redmond, WA, USA), where the Sirius red dye specifically binds to collagen and Fast green dye stains the non-collagenous proteins. After each culture time, samples were washed with PBS solution and fixed with 10% (v/v) formalin (Thermo Scientific, Waltham, MA, USA) for 20 minutes at RT, washed again with PBS solution and stored at 4°C until further analysis. A mixture of 0.1% (v/v) Sirius red and 0.1% (v/v) Fast green solution saturated with picric acid was transferred to the culture plates in 500 µL/scaffold. After 30 minutes of incubation at RT, the dye solution was carefully removed and samples were washed with distilled water. Afterwards, the dyes were extracted from the stained samples by applying 2 mL of dye extraction buffer (0.05 M NaOH solution in methanol). The OD was measured in a microplate reader at an absorbance of 540 nm and 605 nm. The amount of collagenous proteins was calculated according to the manufacturer's instructions. Three samples of each group (chondrogenic and basal medium) were tested at each time-point, in three independent experiments. Scaffolds without cells were used as control.

7.3.6.7. RNA isolation and real-time reverse transcriptase-polymerase chain reaction

The expression of mRNA for the genes of interest on the HRP-crosslinked SF constructs was measured by real-time PCR analysis. Total RNA was extracted from cells recovered from the 3D cultures using Direct-zol™ RNA MiniPrep kit (Zymo Research, Irvine, CA, USA), following the manufacturer's instructions. After each culture time, samples were washed with PBS solution, immersed in 700 µL TRI Reagent® and stored at -80°C until further use. Samples were thawed at RT and sonicated for 15 minutes at 20°C to ensure the complete lysing of the cells. RNA quantification and purity were assessed using a NanoDrop ND-1000 spectrophotometer (NanoDrop Technologies, Wilmington, DE, USA). Samples with a 260/280 ratio between 1.6 and 2.0 were used for first-strand complementary DNA (cDNA) synthesis according to the protocol from the qScriptTM cDNA synthesis Kit (Quanta Biosciences, Gaithersberg, MD, USA) in a MiniOpticon real-time PCR detection system (BioRad, Hercules, CA, USA). Briefly, 100 ng of the total RNA were used to generate single-stranded cDNA by random priming with qScript Reverse Transcriptase (RT). Afterwards, the obtained cDNA was used as template for the amplification of the target genes using the PerfeCta SYBR Green FastMix kit (Quanta Biosciences, Gaithersberg, MD, USA) according to the manufacturer's instructions. The primers sequence, specific for each gene, namely glyceraldehyde-3-phosphate dehydrogenase (GAPDH), collagen type II (Col II), Sox-9 and Aggrecan (ACAN) are described in Table 7-1. Each real-time PCR run was carried out with an initial incubation at 95°C for 2 minutes, followed by 45 cycles of denaturation (95°C, 10 seconds), annealing (specific for each gene, 25 seconds) and extension (72°C, 30 seconds) in a Mastercycler® ep realplex real-time PCR system (Eppendorf, Hamburg, Germany). The transcripts expression data were normalized to the endogenous housekeeping gene GAPDH and the relative quantification was calculated using as calibrators the results obtained for each target gene at day 1 in basal culture conditions, according to the Livak ($2^{-\Delta\Delta CT}$) method [38]. Three samples of each group (chondrogenic and basal medium) were tested at each time-point, in three independent experiments.

Table 7-1. Primers list for the studied genes.

Gene	**Sequences**	
	Forward (5'-3')	**Reverse (5'-3')**
GADPH	TGCACCACCAACTGCTTAGC	GGCATGGACTGTGGTCATGAG
Col II	GACAATCTGGCTCCCAAC	ACAGTCTTGCCCCACTTAC
Sox-9	TACGACTACACCGACCACCA	TTAGGATCATCTCGGCCATC
ACAN	TGAGTCCTCAAGCCTCCTGT	TGGTCTGCAGCAGTTGATTC

7.3.6.8. Histology and immunofluorescence staining

At the end of each time-point, three HRP-crosslinked SF constructs from each group (chondrogenic and basal medium) were fixed with 10% (v/v) formalin for 20 minutes at RT and transferred to histological cassettes for paraffin-embedding. Samples were then serially sectioned with 20 µm thick using a microtome (Spencer 820, American Optical Company, NY, USA). Representative sections of the constructs were stained with standard Masson's trichome, using a Bio-Optica staining kit (Milan, Italy) to detect the fibrous collagen content. Sirius red/Fast green collagen kit was also applied as described in 7.3.6.6, for staining the collagen content with Sirius red dye and counterstaining the non-collagenous proteins with Fast green. Sections were also stained with Alcian blue 8GX (1% v/v in 0.5 M acetic acid glacial; VWR BDH Prolabo, Briare, France) and

Safranin-O (0.1% v/v; Honeywell Fluka, Morris Plains, NJ, USA) to detect the distribution and content of sulfated GAGs. For Safranin-O staining, sections were counterstained with Gill-2 hematoxylin (Thermo Scientific, Waltham, MA, USA) and Fast green (0.02% v/v; Honeywell Fluka, Morris Plains, NJ, USA).

To detect protein expression, antigen retrieval was performed on the sections by incubating in 0.5% pepsin in 5 mM HCl (Fisher Scientific, Waltham, MA, USA) for 30 minutes at 37°C. The sections were permeabilized with 1% (v/v) Triton X-100/PBS for 10 minutes and blocked in 3% (w/v) BSA/PBS for 1 hour at RT. Immunolabeling was performed using a mouse anti-human monoclonal antibody against collagen type II (Col II; Chemicon, Temecula, CA, USA; dilution 1:5), a rabbit anti-human polyclonal antibody against Sox-9 (Milipore S.A.S, Molsheim, France; dilution 1:10) and a mouse anti-human monoclonal antibody against Aggrecan (ACAN; clone BC-3, Thermo Scientific, Waltham, MA, USA; dilution 1:5) as primary antibodies, prepared in 1% (w/v) BSA/0.2% (v/v) Triton X-100 in PBS solution and incubated overnight at 4°C. The sections were incubated for 2 hours at RT with the respective secondary fluorochrome-conjugated antibodies, anti-rabbit/mouse IgG (Invitrogen, Life Technologies, California, USA; dilution 1:100), and with 4,6-Diamidino-2-phenyindole, dilactate (DAPI; Biotium, CA, USA; dilution 1:500) for 15 minutes for nuclei staining.

Histological and immunofluorescent sections were observed under transmitted and fluorescence microscopy (Col II and ACAN in green: ex/em 488/517; Sox-9 in red: ex/em 594/618; DAPI in blue: ex/em 358/461), respectively, using a transmitted and reflected light microscope. Images were acquired using the digital cameras AxioCam MRc5 and MR3, as described in 7.3.6.6. Scaffolds without cells were used for staining control.

7.3.6.9. Dynamic mechanical analysis

A dynamic mechanical analysis (DMA) was performed on the HRP-crosslinked SF scaffolds and cell-seeded constructs after 28 days of culture in chondrogenic differentiation medium, using a TRI-TEC8000B dynamic mechanical analyzer (Triton Technology, Lincolnshire, UK) in the compressive mode [27]. The measurements were carried out in the hydrated state at 37°C. The diameter and height of the tested samples were 8 and 4 mm, respectively. The samples were placed in a Teflon® reservoir and clamped in the DMA apparatus immersed in PBS solution. After equilibration at 37°C, the DMA spectra were obtained in a frequency scan between 0.1 and 10 Hz. A constant displacement amplitude of 50 μm was maintained during the experiments. Both storage modulus (*E'*) and loss factor (*tan δ*) were obtained in the frequency range. Before the analysis, a small pre-load of 0.1 N was applied to each sample to ensure that the entire surface of the scaffold was in contact with the compression plates, being the distance between plates equal for all tested samples. At least four samples were used for analysis.

7.3.7. Subcutaneous implantation

In order to evaluate the *in vivo* biological response to the HRP-crosslinked SF scaffolds, the scaffolds were subcutaneously implanted in the back of twelve mice Hsd:ICR (CD-1) of 5 weeks old and average weight of 27-32 g at the time of implantation (Charles River Laboratories, Saint-Germain-sur-l'Arbresle, France). All animal procedures were based upon the "3Rs" policy (Replacement, Reduction and Refinement). The maintenance and use of animals were in accordance to the Ethics Committee of University of Minho, and approved by the Portuguese Licensing Authority (DGV-DSSPA).

Scaffolds of 8 mm in diameter and 4 mm in height were used for the subcutaneous implantation and sterilized by ethylene oxide. Each mouse was anesthetized by intraperitoneal injection of Domitor INJ 1mg/mL (Medetomidine 1 mg/Kg, Novavet, Braga, Portugal) and Imalgene 1000 INJ 100 mg-mL (Ketamine 75 mg/Kg, Novavet, Braga, Portugal). The hair of the mice was removed at the implantation area, followed by disinfection with iodine (Life Technologies, Carlsbad, CA, USA). In each mouse, two skin incisions (1 cm length) were made in the dorsal midline, close from the head (CH) and far from the head (FH). The HRP-crosslinked SF scaffolds were then implanted subcutaneously at both right and left sides into the respective pockets, followed by skin suturing. Twelve specimens were implanted. The mice were euthanized 14 and 28 days post-surgery by injection of Eutasil 200 mg/mL (pentobarbital sodium, Novavet, Braga, Portugal) and the implanted materials were retrieved along with the surrounding tissue (Fig. 1d). The explants were fixed with 10% (v/v) formalin for at least 5 days at RT and transferred to histological cassettes for paraffin-embedding. Samples were then serially sectioned using a microtome (3.5 μm thick) and stained with hematoxylin & eosin (H&E). The histological sections were observed and images acquired as described in 7.3.6.8.

7.3.8. Statistical analysis

Statistical analysis was performed using the GraphPad Prism 5.0 software (GraphPad Software, La Jolla, CA, USA). First, a Shapiro-Wilk test was used to ascertain about the data normality. The compressive modulus results from static mechanical properties were analyzed by means of a Mann-Whitney test. A Kruskal-Wallis test, followed by Dunn's post-test were used to analyze the hASCs metabolic activity, proliferation, GAGs/DNA quantification and collagen content. The significance level was set to $^{*}p < 0.05$, $^{**}p < 0.01$, $^{***}p < 0.001$.

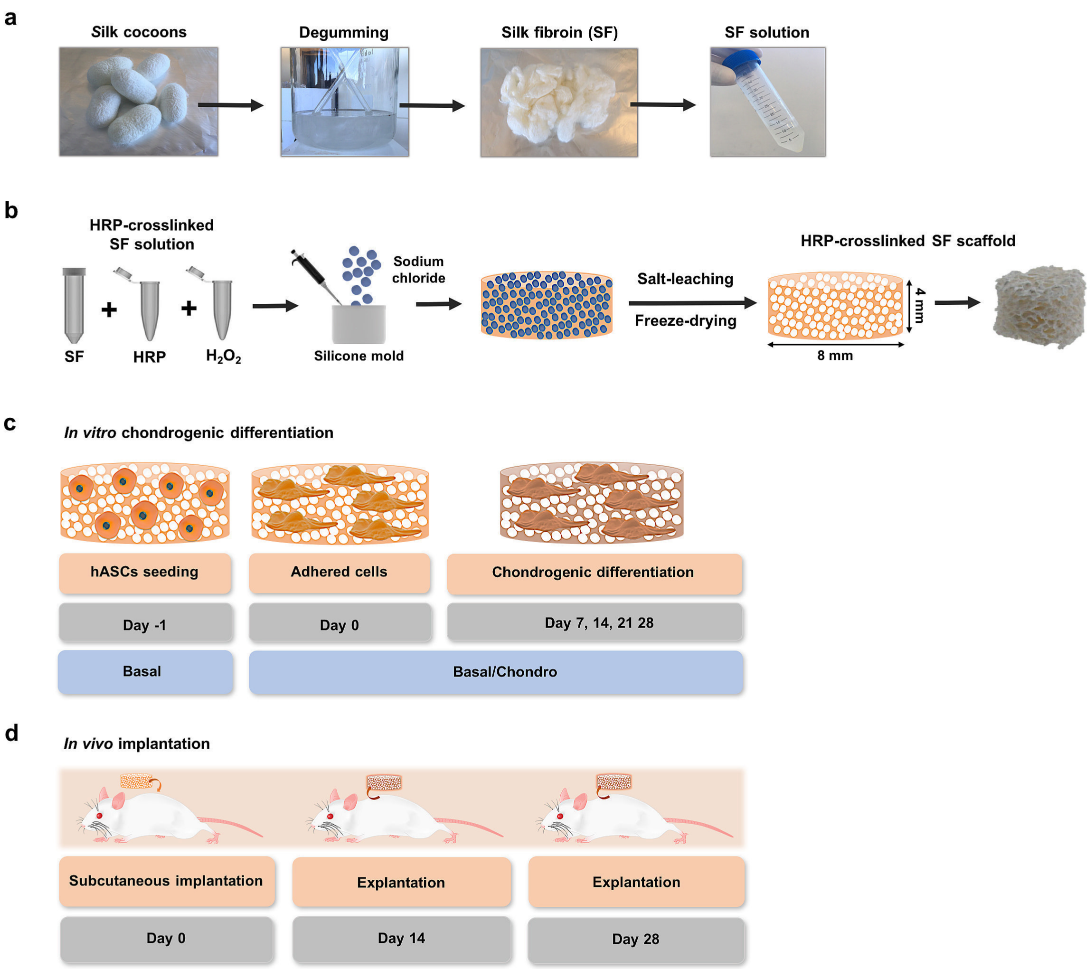
a
Silk cocoons
Degumming
Silk fibroin (SF)
SF solution
b
HRP-crosslinked SF solution
SF
HRP
H_2O_2
Sodium chloride
Silicone mold
Salt-leaching
Freeze-drying
HRP-crosslinked SF scaffold
4 mm
8 mm
c
In vitro chondrogenic differentiation
hASCs seeding
Adhered cells
Chondrogenic differentiation
Day -1
Day 0
Day 7, 14, 21 28
Basal
Basal/Chondro
d
In vivo implantation
Subcutaneous implantation
Explantation
Explantation
Day 0
Day 14
Day 28

Figure 7-1. Schematic illustration of the experimental setup proposed in this study. (a) Purification process for producing aqueous SF solution. (b) Methodology used for preparing the HRP-crosslinked SF scaffolds, combining the HRP-mediated crosslinking of highly concentrated SF solution (16 wt.%) with salt-leaching and freeze-drying technologies. Temporal approach followed (c) to induce the chondrogenic differentiation of hASCs into the scaffolds, and (d) for *in vivo* evaluation of the subcutaneously implanted HRP-crosslinked SF scaffolds. The diameter and height of scaffolds were 8 mm and 4 mm, respectively.

7.4. Results

7.4.1. Morphology and microstructure characterization

In this study, the detailed pore morphology at the HRP-crosslinked SF scaffolds surface (Figure 7-2a and b) and cross-sections (Figure 7-2c and d) were analyzed by SEM. It was observed a similar macro-/micro-porous structure both at the scaffolds surface and interior, mainly with two types of pore size. From Figure 7-2a and c, macro-pores with more than 500 μm in size were observed. There were also micro-pores with less than 50 μm distributed inside the thick macro-pore walls (Figure 7-2b and d).

The qualitative and quantitative analysis of scaffolds architecture were investigated by micro-CT. Table 7-2 demonstrates that the HRP-crosslinked SF scaffolds presented a high porosity (89.3 ± 0.6%) and mean pore size (361.4 ± 20.3 µm), with interconnected pores (95.9 ± 0.8%) and thick pore walls (51.7 ± 2.9 µm). The two-dimensional (2D) horizontal cross-section (Figure 7-2e) and 3D reconstruction of top and side views (Figure 7-2f and g) also showed the interconnectivity and porous structure of scaffolds, confirming the SEM observations. The micro-CT morphometric analysis revealed a widespread pore size and wall thickness distribution ranging from 8.79 µm to 747.32 and 114.30 µm within the scaffolds, respectively (Figure 7-2h and i).

Table 7-2. Microstructure of the HRP-crosslinked SF scaffolds determined from the micro-CT data.

	Mean porosity (%)	Mean pore size (µm)	Mean interconnectivity (%)	Mean wall thickness (µm)
HRP-crosslinked SF scaffold	89.3 ± 0.6	361.4 ± 20.3	95.9 ± 0.8	51.7 ± 2.9

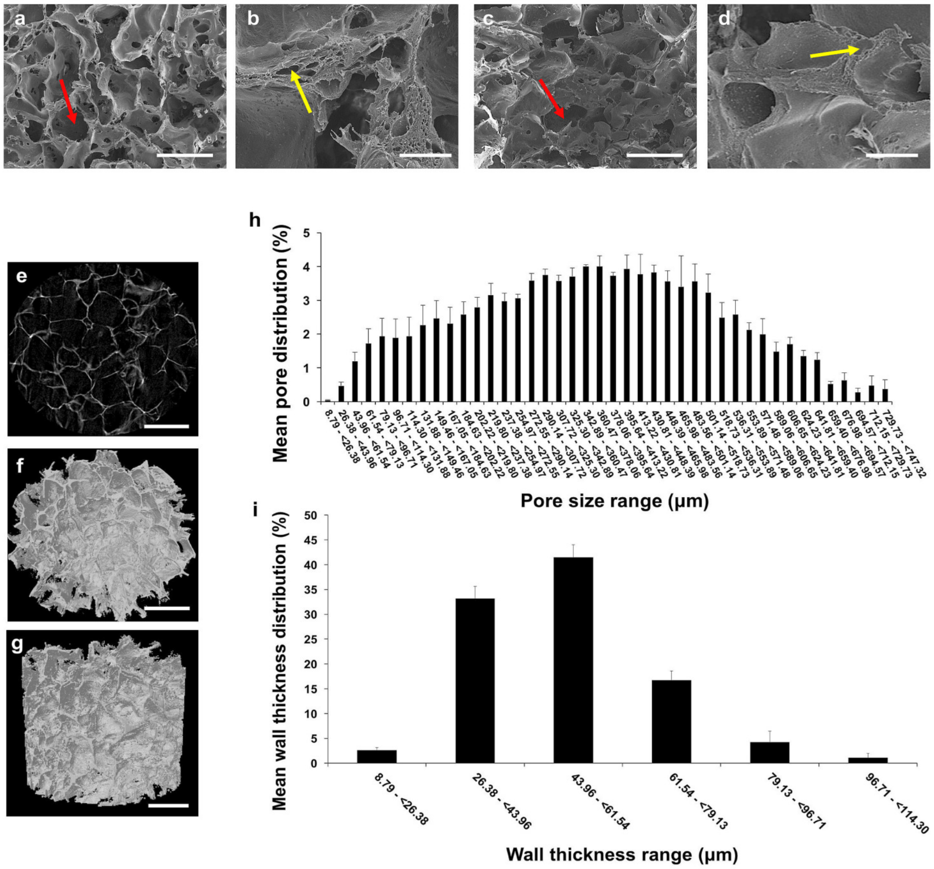

Figure 7-2. SEM micrographs of the (a, b) surface and respective (c, d) cross-sections of the HRP-crosslinked SF scaffolds (scale bars: 1 mm for low magnification images and 100 µm for high magnification images). The red arrows

indicate macro-pores and the yellow arrows indicate micro-pores (< 100 μm). Micro-CT analysis showing the (e) 2D cross-sectional image for porosity representation, (f, g) 3D reconstruction of top and side views, respectively (scale bar: 2 mm), (h) mean pore size distribution, and (i) mean wall thickness distribution of the HRP-crosslinked SF scaffolds.

7.4.2. Chemical structure and protein conformation

The SF conformation and chemical composition in the scaffolds were analyzed by ATR-FTIR (Figure 7-3). The FTIR spectra showed two strong absorbance peaks at 1624 and 1528 cm^{-1}. These two absorbance peaks are in the range assigned to amide-I and amide-II, respectively, and can be attributed to the β-sheet conformation of SF. A very small and hardly pronounced shoulder peak corresponding to the amorphous or silk-I conformation was detected at ~1650 cm^{-1} [39].

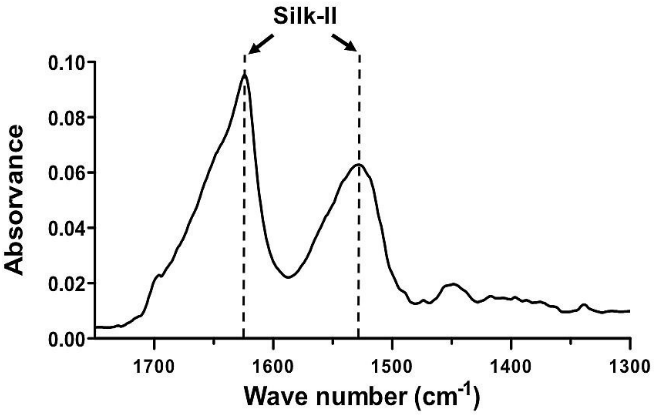

Figure 7-3. ATR-FTIR spectra of the HRP-crosslinked SF scaffolds.

7.4.3. Mechanical properties, swelling ratio and degradation profile

As shown in Figure 7-4a, the static compressive modulus of the dried HRP-crosslinked SF scaffolds was 2.97 ± 0.90 MPa, significantly higher than the wet state modulus of 0.11 ± 0.07 MPa ($^{***}p < 0.01$). The representative stress-strain plot (Figure 7-4b) shows the same behavior for the compressive strength of scaffolds in dry (0.54 ± 0.05 MPa) and wet (0.03 ± 0.006 MPa) conditions.

Figure 7-4c shows that the swelling ratio of the HRP-crosslinked SF scaffolds reached an equilibrium after 6 hours of immersion in PBS (~585%) solution, maintaining their weights up to 30 days. In this study, the enzymatic degradation of the HRP-crosslinked SF scaffolds was analyzed by using protease XIV [40]. It was observed that the degradation rate of scaffolds was faster in the presence of protease XIV at both tested concentrations (3.5 U/mL and 0.2 U/mL), as compared to the control condition in which scaffolds maintained their original weights after soaking in PBS solution for 30 days. In the first 12 hours, the degradation rate of scaffolds immersed in protease XIV at 3.5 U/mL was higher than 50%, as compared to the ~20% weight loss in protease XIV at 0.2 U/mL. After 14 days of degradation in protease XIV at 3.5 U/mL, scaffolds reached 100% weight loss, while the scaffolds immersed in protease XIV at 0.2 U/mL presented ~60% weight loss only after 30 days of degradation.

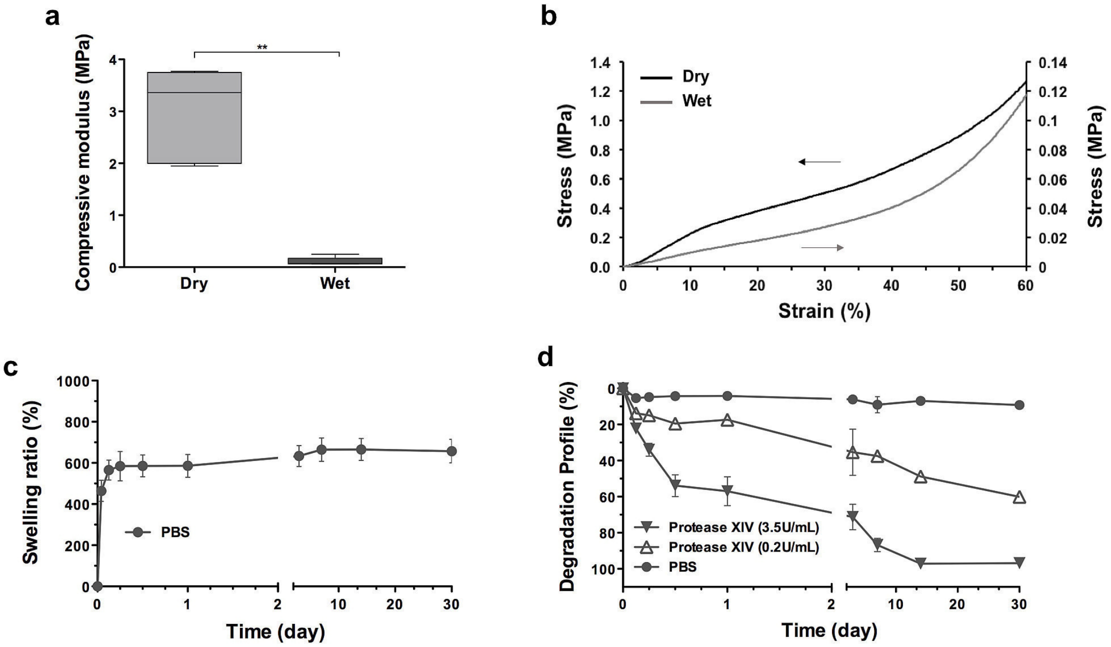

Figure 7-4. (a) Box and whisker graph plot of the compressive modulus and (b) representative stress-strain plot of the HRP-crosslinked SF scaffolds measured in the dry and hydrated state. The left and right arrows indicate the respective y-axis (compressive stress) of the dry and hydrated samples. (c) Swelling ratio, and (d) enzymatic degradation profile of the HRP-crosslinked SF scaffolds for a period of 30 days (% weight).

7.4.4. *In vitro* characterization of the HRP-crosslinked SF scaffolds

Prior differentiation, hASCs were characterized for the expression of MSCs surface markers, CD105, CD90, CD73, CD45 and CD34. The cells showed a mesenchymal-like phenotype, exhibiting the typical panel of markers: CD105$^+$/CD73$^+$/ CD90$^+$/CD45$^-$/CD34$^-$ [37] (Supplementary Figure 7-1).

7.4.4.1. Metabolic activity and cell viability

The Alamar blue assay was performed to evaluate the metabolic activity of cells up to 28 days of culturing (Figure 7-5a). In basal culture conditions, cells presented a significant increase of metabolic activity over the

28 days of culture (*$p < 0.05$ from day 7 to day 14; **$p < 0.01$ from day 1 to day 21; ***$p < 0.001$ from day 7 to day 21 and from day 1, 7, 14 to day 28). Concerning the cultures in chondrogenic differentiation medium, stable metabolic activity levels were observed from day 1 to day 28. However, at day 1 and day 7, cells presented a significantly higher metabolic activity as compared to that detected in basal culture conditions ($a^{***}p < 0.001$). From the live/dead staining, it was found that cells adhered to the highly porous scaffolds and were alive over the 28 days of culture in chondrogenic and basal conditions (Figure 7-5b). From day 7, a dense cell layer spreading over the HRP-crosslinked SF constructs was observed in both culture media. Nevertheless, at day 21 and day 28 the presence of self-aggregated cells clusters was observed in chondrogenic culture conditions, replacing the dispersive and elongated morphology of cells observed in basal medium at the same culture periods.

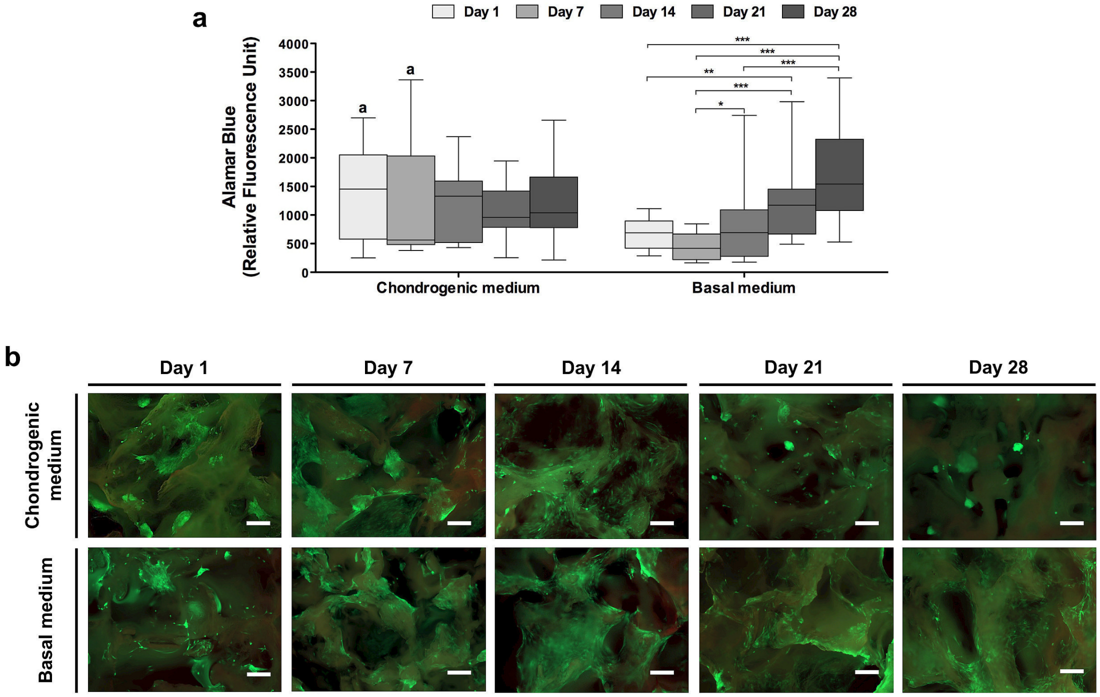

Figure 7-5. (a) Box and whisker graph plot of the alamar blue metabolic activity and (b) live/dead staining (scale bar: 200 μm) of the hASCs cultured on the HRP-crosslinked SF scaffolds for 1, 7, 14, 21 and 28 days in chondrogenic and basal culture medium. ^{a}Statistically significant when compared to the HRP-crosslinked SF constructs at the same culture period under basal culture conditions ($^{***}p < 0.001$).

7.4.4.2. Biochemical characterization

Cell proliferation was screened by DNA content analysis (Figure 7-6a). It was observed that no significant differences in cell proliferation were observed from day 1 to day 28 for cells cultured in chondrogenic differentiation medium. The DNA content significantly increased in basal culture conditions from day 1 to day 28 (*$p < 0.05$: from day 7 to day 21; **$p < 0.01$: from day 1 to day 28; ***$p < 0.001$: from day 7 to day 28) presenting at day 21 (a$^{**}p < 0.01$) and day 28 (b$^{***}p < 0.001$) significantly higher DNA content than in chondrogenic culture conditions.

The GAGs production from the cells seeded on the HRP-crosslinked SF scaffolds was normalized by their respective DNA content (Figure 7-6b). It was found a significant increase of GAG/DNA ratio after 7 days of culture in chondrogenic differentiation medium, in comparison to day 1 (**$p < 0.01$). No significant differences were observed at day 14. However, after 21 days and 28 days in chondrogenic culture conditions the GAG/DNA ratio significantly increased as compared to day 1 (***$p < 0.001$). In basal culture medium, only a residual GAG/DNA ratio was determined and no significant differences were observed over the 28 days of culture. In fact, the GAG/DNA ratio determined on the HRP-crosslinked SF constructs cultured in chondrogenic differentiation medium was significantly higher at day 21 (b$^{***}p < 0.001$) and day 28 (a$^{***}p < 0.01$), as compared to that obtained in basal culture conditions.

The quantification of the proteins that integrate the ECM was performed by Sirius red/Fast green staining kit, aiming at discriminate the collagen content on the HRP-crosslinked SF constructs. In Figure 7-6c, a non-significant increase of the collagen content was determined after 21 days of culture in chondrogenic differentiation medium. For the HRP-crosslinked SF constructs cultured in basal conditions, a significant increase of the collagenous proteins was observed after 21 and 28 days of culture, as compared to day 1 (*$p < 0.05$), day 7 (**$p < 0.01$) and day 14 (***$p < 0.001$). When comparing the chondrogenic and basal culture conditions at the same culture period, no significant differences were detected for the collagen deposition at the HRP-crosslinked SF constructs.

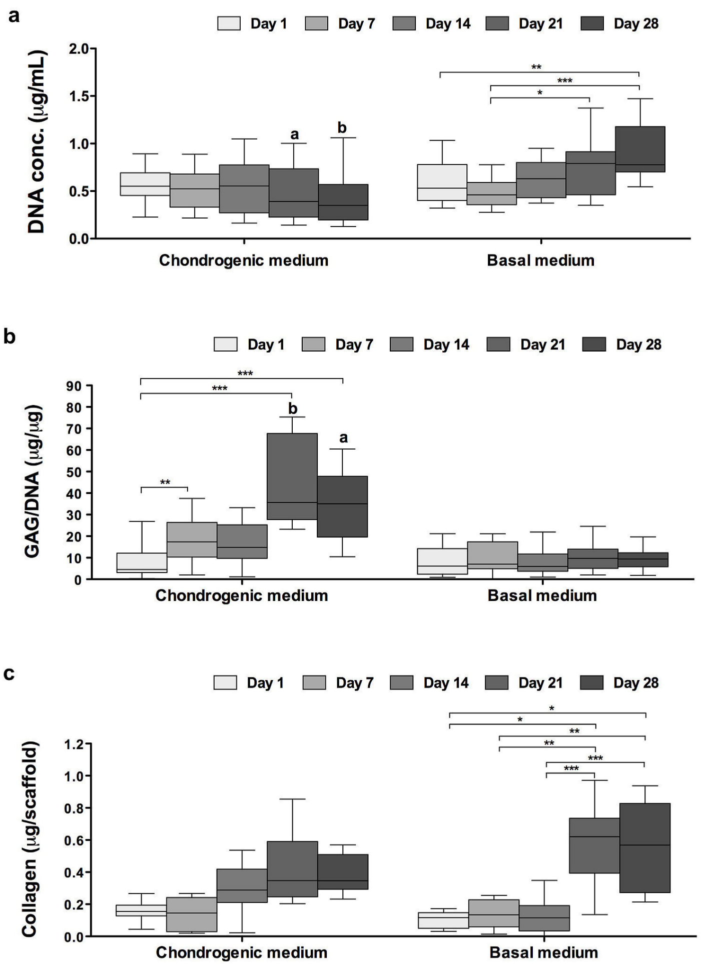

Figure 7-6. Box and whisker graph plot of the (a) DNA quantification, (b) GAGs content normalized against the amount of DNA, and (c) collagenous proteins quantification at the HRP-crosslinked SF scaffolds cultured with hASCs in chondrogenic and basal medium for 1, 7, 14, 21 and 28 days. ^{a,b}Statistically significant when compared to the HRP-crosslinked SF constructs at the same culture period under basal culture conditions (a***p < 0.01, b***p < 0.001).

7.4.4.3. Chondrogenic-related markers expression, extracellular matrix composition and dynamic mechanical properties after culturing

The differentiation of hASCs seeded onto the HRP-crosslinked SF scaffolds was evaluated by quantifying the mRNA expression of the chondrogenic-related markers, collagen type II (Col II), Sox-9 and Aggrecan (ACAN) (Figure 7-7a). The mRNA transcripts evaluated after 28 days of culture in basal and chondrogenic differentiation medium, revealed the expression of all chondrogenic-related markers after culturing the HRP-crosslinked SF constructs in chondrogenic differentiation medium. In contrast, no mRNA expression was detected for the same markers in basal culture conditions.

Complementary, the immunodetection of Col II, Sox-9 and ACAN at the HRP-crosslinked SF constructs was also evaluated (Figure 7-7b). The immunofluorescence images show an intense protein expression of all chondrogenic-related markers after 28 days of culture in chondrogenic differentiation medium. However, in basal culture conditions only a residual expression of Col II, Sox-9 and ACAN was detected.

The newly formed ECM at the HRP-crosslinked SF constructs was evaluated and sections stained to visualize the GAGs secretion and collagen deposition (Figure 7-7c). After 28 days of culture, only the ECM formed on the HRP-crosslinked SF constructs cultured in chondrogenic differentiation medium was intensely stained for GAGs, as observed from the intense Alcian blue and positive staining for Safranin-O. Moreover, from the Masson's trichome and Sirius red staining's it was possible to observe a well pronounced collagen matrix deposited on the HRP-crosslinked SF constructs cultured both under chondrogenic and basal culture conditions.

The dynamic viscoelastic properties of the HRP-crosslinked SF scaffolds and constructs after 28 days of culture in chondrogenic differentiation medium were assessed by DMA (Figure 7-7d), in order to evaluate and compare the dynamic mechanical behavior of scaffolds for cell-free and cell-based approaches in cartilage TE applications. It was observed that the storage modulus (E') of the HRP-crosslinked SF scaffolds and constructs slightly increased from 0.17 ± 0.06 to 0.22 ± 0.10 MPa and 0.19 ± 0.02 to 0.27 ± 0.03 MPa, respectively, as the frequency increased from 0.1 to 10 Hz. In the frequency range tested the E' values of the HRP-crosslinked SF constructs were higher than those obtained for the scaffolds. Comparing the loss factor (tan δ) results, it was found that both groups presented stable and high tan δ values for the tested frequencies. Nevertheless, it was found that the HRP-crosslinked SF scaffolds presented higher tan δ values than constructs.

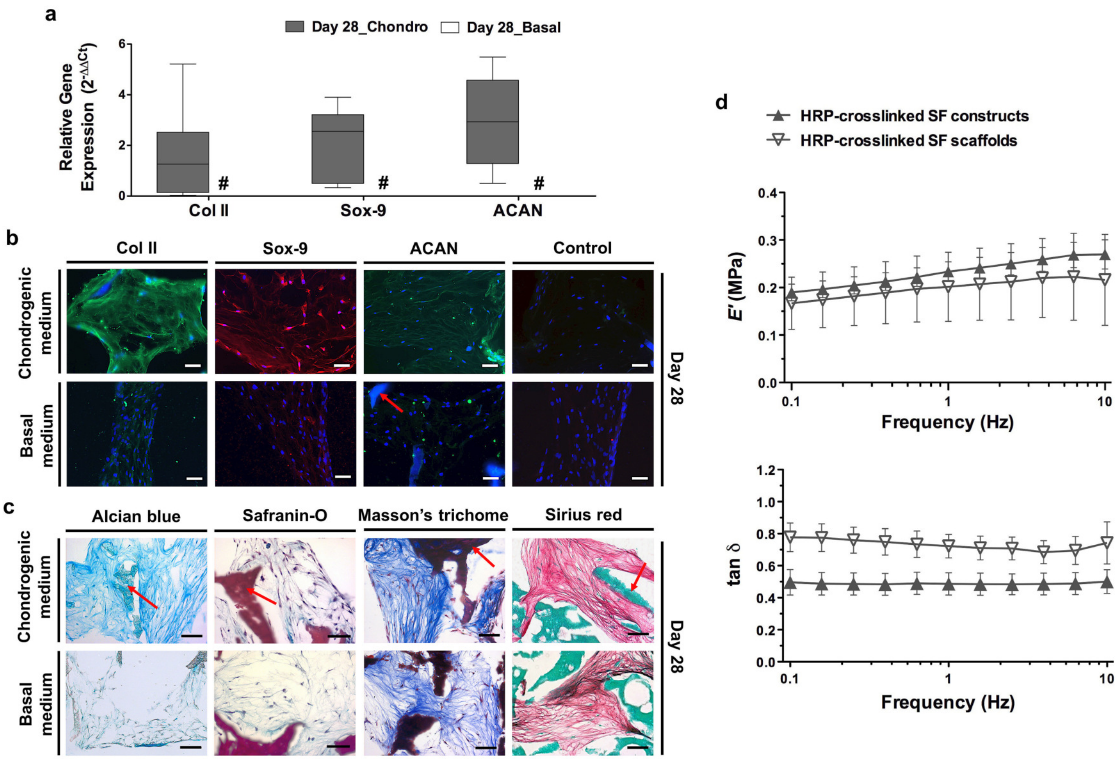

Figure 7-7. HRP-crosslinked SF scaffolds after 28 days of culturing with hASCs in chondrogenic and basal medium. (a) Box and whisker graph plot of the real-time PCR results of Col II, Sox-9 and ACAN. Relative gene expression was normalized to the reference gene GAPDH and calibrated to the data of each gene at day 1 in basal conditions. # Indicate the non-expression of the target genes under basal culture conditions. (b) Immunofluorescence analysis of the chondrogenic-related markers. Nuclei are stained in blue, Col II and ACAN in green, and Sox-9 in red (scale bar: 50 µm). (c) Histological analysis of the HRP-crosslinked SF constructs. Alcian blue (blue) and Safranin-O (red) staining were used to detect GAGs formation, Masson's trichome (blue) and Sirius red (red) staining were used for the visualization of collagen at the ECM (scale bar: 100 µm). The red arrows indicate the stained scaffolds. (d) Storage modulus (*E'*) and loss factor (*tan δ*) of the HRP-crosslinked SF scaffolds and constructs determined in chondrogenic differentiation medium.

7.4.5. Subcutaneous implantation of the HRP-crosslinked SF scaffolds

The *in vivo* compatibility of the HRP-crosslinked SF scaffolds was assessed by subcutaneous implantation in a mice model (Figure 7-8). The macroscopic images of the explants showed that scaffolds were still integrated in the subcutaneous tissue after 14 (Figure 7-8a) and 28 (Figure 7-8b) days of implantation, maintaining their shape and integrity over the implantation periods. From the low magnification H&E staining images (Figure 7-8c and d), it was observed that a thick layer of connective tissue adhered on the entire surface of the scaffolds and deeply infiltrated into the porous structures. The high magnification H&E staining images (Figure 7-8e-h) allowed confirming the presence of connective tissue filling the inner pores of the scaffolds. The absence of edema or signs of neutrophils after the implantation periods, revealed that no acute inflammation was induced by the HRP-crosslinked SF scaffolds.

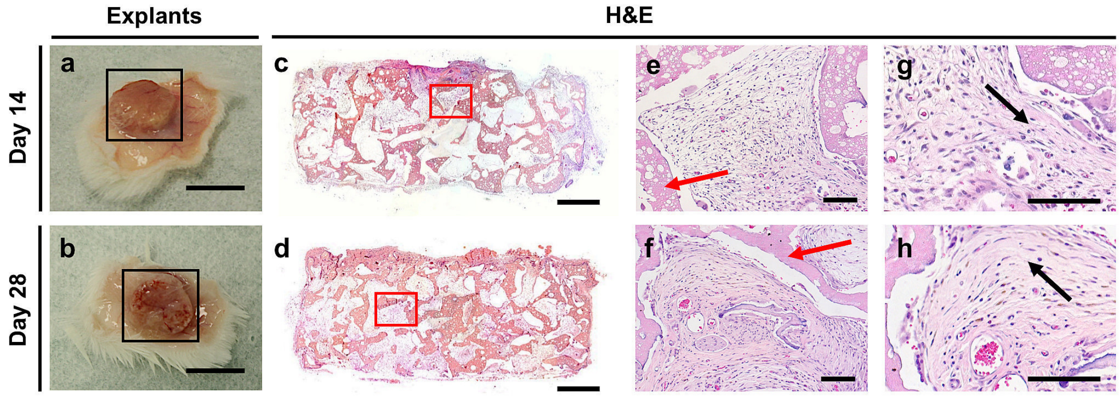

Figure 7-8. Subcutaneous implantation of the HRP-crosslinked SF scaffolds in mice. Macroscopic images of the explants after implantation for (a) 14 days and (b) 28 days (scale bar: 10 mm). H&E staining of the SF scaffold explants after (c, e, g) 14 days and (d, f, h) 28 days of implantation (scale bars: 1 mm for low magnification images and 100 µm for high magnification images). Black squares represent the regions corresponding to the implanted HRP-crosslinked SF scaffolds. Red squares represent the regions corresponding to the magnified stained images (e-h). The black arrows indicate connective tissue, the red arrows indicate the stained scaffolds.

7.5. Discussion

In natural cartilage tissue, the ECM provides a complex environment of physical, chemical and mechanical cues that directly affect and guide cell behavior. In the recent years, SF has demonstrated to be a robust natural material widely explored for bone [41], cartilage [27] and osteochondral [42] TE. Its processing versatility allowed to extend the use of SF for TE applications of ligament [43], blood vessels [44] or skin [45]. Several methods have been individually applied to prepare silk scaffolds [41, 44, 46], frequently with the limitation of poorly mimicking the structural and mechanical complexity of tissues like cartilage. The salt-leaching method is widely used due to the effective processing and generated controlled porosity in a wide range of pore sizes [47]. Moreover, the behavior of SF in the presence of NaCl is affected by the salt ions extracting the water that usually coat the hydrophobic domains in the β-sheet structure of the protein. This would promote chain-chain interactions resulting in protein folding and β-sheet formation [48, 49]. Salt-leached silk scaffolds generally present high stiffness due to the presence of silk II (β-sheet conformation)

formation. For example, Kim *et al.* [48] developed aqueous-derived SF scaffolds prepared using salt-leaching and freeze-drying methodologies, showing that scaffolds had controlled pore size, interconnectivity and adjustable mechanical properties. In a different study, Nazarov *et al.* [46] individually applied the salt-leaching and freeze-drying techniques to form porous 3D silk biomaterials, stating that different matrices can be produced according to the processing method and conditions. Moreover, these authors also showed that to induce β-sheet structure and water insolubility after lyophilization, a methanol treatment was induced to the aqueous SF before freeze-drying processing. In our study, the crystallinity of the HRP-crosslinked SF solution was ensured with the salt-leaching processing, avoiding the return to an amorphous and gel state after re-hydration of the freeze-dried scaffolds, as confirmed by FTIR analysis (Figure 7-3). According to different authors [13, 14], scaffolds designed for cartilage TE should include optimal structural and mechanical properties, controlled degradability rate and good adaptability to the defect site, showing that highly porous SF scaffolds developed by salt-leaching and freeze-drying methodologies can fit to these criteria. In a previous study by our group [27], salt-leached and freeze-dried SF scaffolds prepared in a range of high-concentration aqueous SF solutions, showed stable degradability and improved mechanical properties for meniscus and cartilage regeneration. Nevertheless, to fully recreate the microenvironment found in cartilage tissue, there is a need to better control the stiffness of the salt-leached SF scaffolds. Until now, SF hydrogels have been seen as potential matrices for cartilage applications presenting a biomimetic aqueous matrix responsible for its resilient and elastic behavior [12]. However, these matrices can also be less stable for cell culture applications, raising the hypothesis of creating novel SF biomaterials that match the stiffness of soft SF hydrogels with the porosity and mechanical stability of salt-leached SF scaffolds. In a recent study, agarose/SF blended hydrogels were structured by freeze-drying methodology to create porous structure of hydrogels, showing the typical elastic behavior of blended hydrogels but at the same time a reinforcement and stability induced by the micro-porous structures [7]. Moreover, the cellular studies demonstrated that chondrocytes cultured in the structures with larger pores induced higher cartilage-specific ECM production. To achieve this effect, the herein proposed scaffolds resulted from a combination of enzymatically crosslinked SF hydrogels with salt-leaching and freeze-drying technologies to create a highly porous, stable and yet stiff hydrogel-based system for specific cartilage TE applications. As demonstrated by the SEM (Figure 7-2a-d) and micro-CT (Figure 7-2e-i and Table 7-2) analysis not only a high porosity was observed within the HRP-crosslinked SF scaffolds, as different pores sizes were achieved. Considering the wide size range of the sodium chloride particles used for salt-leaching processing, it was expected that the pore size of the scaffolds would not be homogeneous, even presenting a homogeneous distribution along the scaffolds (Figure 7-2h). Moreover, the thick pore walls (51.7 ± 2.9 μm) induced by the highly concentrated aqueous SF solution, also demonstrated small pores (< 50 μm) distributed inside the structures (Figure 7-2b and d) that can result from the recrystallization of the dissolved salt particles (leaching process) combined with the freeze-drying process [27]. This wide range of pore size is of great interest for cartilage TE, especially due to the lack of self-remodeling capacity of cartilage tissue that naturally present small pores (2.5 to 6.5 nm). Pores with sizes inferior to 50 μm are recommended to improve cell adhesion and seeding efficiency, whereas larger and interconnected pores improve cellularity and ECM ingrowth for faster constructs development [50]. As reported by Vikingsson *et al.* [51] different pore sizes and wall thickness within the micro-architecture can directly affect the mechanical properties and degradation profile of scaffolds. In a previous study, Han *et al.* [8] observed that the compressive strength of salt-leached/freeze-dried SF scaffolds produced with aqueous SF solutions of 4-5 wt.%, decreased from 1.6 to 1.09 MPa as the pore size increased (90-180 μm to 355-425 μm). This was an expected result, since a lower macro-porosity induce the formation of denser structures that can withstand higher loads. As observed in our study, Kim *et al.* [48] also showed a compressive modulus of 3.33 ± 0.5 MPa and a compressive strength of 0.32 ± 0.01 MPa on dried salt-leached/freeze-dried SF scaffolds, produced with high concentration SF solution (10 wt.%) and bigger particle sizes (1,000 to 1,180 μm). An important role is also attributed to the β-sheet content of SF scaffolds. In the present study, superior β-sheet content and less amount of amorphous conformation was detected by FTIR (Figure 7-3), which may have influenced the mechanical properties of the produced scaffolds. In a different study performed by Yao *et al.* [52], the compressive modulus and compressive strength of salt-leached SF scaffolds was higher on samples with higher silk II (β-sheet crystal) formation. Yan *et al.* [16], also showed that the compressive modulus of the HRP-crosslinked SF hydrogels with β-sheet conformation (1.12 MPa), was significantly higher than that of random coil hydrogels (0.022 MPa). When compared to the compressive modulus of the crystalline HRP-crosslinked SF scaffolds, both presented similar compressive modulus to the native human articular cartilage tissue (ranging from 1.16 to 7.75 MPa in deep, from the articular surface) [53].

It is well-established that implantable scaffold materials should be able to absorb the nutrients and metabolites from the adjacent tissue. Moreover, the swelling process is also necessary to press-fit the construct at the implantation site, improving the fluidic exchanges [40]. At the same time, the constructs should be able to restore the biomechanical function and maintain a controllable degradation during the stages of manipulation and thereafter.

Biomaterials degradation in the living environment is a complex phenomenon that involves several synergistic pathways, either enzymatic or chemical [54]. Thus, the *in vitro* degradation should provide a realistic clue of the functional interaction between the construct and the biological environment. Protease XIV have been used for *in vitro* degradation studies involving SF structures [42, 54]. This enzyme has no specific activity towards the chemical structure and amino acid sequence of SF, which makes it more aggressive to better mimic the *in vivo* conditions that simultaneously involve the activity of several enzymes (chymotrypsin, collagenase, etc.) [55]. In the present study, we have proposed HRP-crosslinked SF scaffolds with large swelling capacity and able to maintain a swelling stability and structural integrity over 30 days (Figure 7-4c). In our previous study, we also found that the HRP-mediated SF hydrogels are pH responsive maintaining their original weights and structure at physiological conditions [25]. In a different study, Yan *et al.* [16] observed that random coil SF hydrogels presented higher swelling capacity than the crystalline SF hydrogels, due to the aggregated SF molecules formed with the β-sheet induction that make the hydrogels more hydrophobic. Moreover, these strong hydrophobic interactions may have rendering the protease XIV more inaccessible for proteolytic cleavage, affecting the degradation of the crystalline SF hydrogels, which presented only 5% weight loss after 12 hours in protease XIV solution (0.2 U/mL), as compared to the faster degradation of the random coil SF hydrogels. Our results showed a greater impact on the HRP-crosslinked SF scaffolds degradation at the highest tested concentration of protease XIV (3.5 U/mL), reaching 100% weight loss after 14 days in degradation solution. However, the degradation profile tested with 0.2 U/mL of enzyme, showed a 19% weight loss within 12 hours, which can be explained by the high porosity and mean pore size (Table 7-2) attributed to the salt-leaching processing [56]. In a previous study by our group [42], it was observed that SF scaffolds derived from highly concentrated aqueous SF solution (16 wt.%) and processed through salt-leaching (500 to 1,000 μm sodium chloride particles size) and freeze-drying technologies, presented a much faster degradation rate as compared to the HRP-crosslinked SF scaffolds. In this case, the covalent bonds established between the tyrosine groups in the enzymatic crosslinking process can difficult the proteolytic cleavage induced by the protease XIV, making the degradation process slower and more controlled [16, 25]. These results correlate well with the literature, stating that the degradation properties of scaffolds should be tailored to match the target tissue regeneration [1]. Considering the limited self-remodeling capacity of cartilage tissue, a slower degradation profile of the HRP-crosslinked SF scaffolds can be appropriate for cartilage scaffolding strategies.

Successful cell-based TE strategies for the repair of critical-sized cartilage defects also require a safe and easily accessible cell source for *in vitro* chondrogenesis and eventually functional integration *in vivo* [57]. Human ASCs have demonstrated a significant potential for chondrogenic differentiation, using different scaffolding strategies as platforms [33, 58]. Nevertheless, as reported in previous studies, a wide range of scaffolds pore size can induce different cell behaviors [7, 8]. In this study, we were able to observe the effects of scaffolds micro-porosity on a good cell adhesion and spreading at the surface, as well as, cells infiltrating the interconnected large pores to colonize the scaffolds interior (Figure 7-5b). In chondrogenic differentiation medium it was possible to observe that the porous 3D environment induced cell clusters formation, typically found during cartilage development [59]. Han *et al.* [8] also observed that salt-leached SF scaffolds produced with different pore size had distinct influence on chondrocytes behavior. Scaffolds with smaller pore size improved cell adhesion and presented the highest levels of GAGs and collagen content, whereas the scaffolds with higher pore size provided the best environment for cell proliferation. In our study, cell proliferation was stable until day 14 on both chondrogenic and basal culture conditions, however, at day 21 and day 28 significantly higher DNA values were detected in basal culture conditions, as compared to HRP-crosslinked SF constructs in chondrogenic differentiation medium (Figure 7-6a). These results corroborate the metabolic activity (Figure 7-5a) and live/dead (Figure 7-5b) observations, suggesting the differentiation of hASCs in the HRP-crosslinked SF constructs under chondrogenic culture conditions. Confirming these observations, the amount of released GAGs by the chondrogenic-induced hASCs at day 21 and day 28 was significantly higher than that in basal culture conditions (Figure 7-6b). Moreover, the quantification of collagen content showed the same tendency for an increase of protein deposition until day 21 (Figure 7-6c). Previous studies, showed the positive influence of the porous-like structure of SF scaffolds on hASCs chondrogenic differentiation and cartilage-specific ECM production [33, 34]. For example, Kim *et al.* [33] observed that chondrogenic-induced hASCs were able to produce higher GAGs and collagen content on salt-leached SF scaffolds, as compared to those in the conventional micromass pellet culture system [60].

In vitro chondrogenic differentiation is characterized by the genotypic (Figure 7-7a) and phenotypic (Figure 7-7b) expression of cartilage-specific markers. Col II is the most common type of collagen at the hyaline cartilage, and together with ACAN are two of the most important components of cartilage ECM. Sox-9 is a key transcription factor in chondrogenesis able to directly regulate the expression of Col II and ACAN [14]. In this study, the analysis of Col II, Sox-9 and ACAN showed their expression after 28 days of culturing in chondrogenic differentiation medium, which may be indicative of hASCs chondrogenic differentiation on the HRP-crosslinked SF constructs. This behavior has been reported in other studies [33, 34] and is also in agreement to the GAGs (Figure 7-6b) and collagen (Figure 7-6c) quantification results. Moreover, the non-expression of these markers under basal culture conditions also corroborates to this hypothesis.

The GAGs secreted by the chondrogenic-induced hASCs were also confirmed by histological analysis (Figure 7-7c). However, the collagen deposition was shown at similar levels on both chondrogenic and basal culture conditions, which is not in agreement to the results obtained for Col II expression (Figure 7-7a and b). In fact, it is well known that other type of collagen is associated with the ECM of undifferentiated cells

[61]. Therefore, the total collagen quantified (Figure 7-6c) and visualized (Figure 7-7c) at the ECM of the HRP-crosslinked SF constructs cultured in basal medium may not correspond to the Col II observed in chondrogenic culture conditions. After 28 days of culture in chondrogenic differentiation medium, a slight increase of the storage modulus was determined on the HRP-crosslinked SF constructs, as compared to the non-seeded scaffolds (Figure 7-7d), which can be explained by the presence of the newly formed ECM. Nevertheless, there were no statistical differences in respect to the mechanical properties with or without chondrogenic cell culture, which represents the ability of scaffolds to maintain their mechanical performance during tissue regeneration [27]. Considering that a healthy articular cartilage sustains physiological stresses that can range from 1 to 10 MPa, the proposed HRP-crosslinked SF constructs can be suggested as temporary cartilage tissue substitutes [62]. The loss factor results (Figure 7-7d), also confirmed the viscoelastic nature of both HRP-crosslinked SF scaffolds (ranging from 0.8 to 0.74) and constructs (ranging from 0.49 to 0.50), which means that the proposed structures can completely recover from high physical loads, which is an important concern considering that articular cartilage of joints are highly stimulated mechanically, from the daily walking to the active loading sports [2]. Moreover, these results suggest that these structures can be easily adjusted to fulfill cartilage defects and facilitate surgical interventions.

The compatibility between the HRP-crosslinked SF scaffolds and *in vivo* tissues evaluated by subcutaneous implantation, showed good scaffolds integrity and dimensional stability during the implantation periods (Figure 7-8a,b). The crystalline structure of scaffolds, confirmed by FTIR (Figure 7-3) analysis, may have influenced the obtained results. Moreover, the stable degradation profile of the HRP-crosslinked SF scaffolds (Figure 7-4d), also corroborates to this hypothesis. In a previous study by our group [42], the *in vivo* compatibility of bilayered SF/SF-nanoCaP scaffolds was also tested by subcutaneous implantation up to 28 days, showing that the crystalline structure of SF allied to the suitable mechanical properties of scaffolds maintained their stability and shapes during the implantation period. A thick layer of connective tissue was observed surrounding and deeply infiltrating the HRP-crosslinked SF scaffolds (Figure 7-8e-h). The high porosity and interconnectivity revealed by SEM (Figure 7-2a-d) and micro-CT (Figure 7-2e-i and Table 7-2) analysis may have contributed to these results [41, 42]. For example, Yan *et al*. [42] have also demonstrated the positive influence of highly porous structures to support tissue ingrowth on bilayered SF/SF-nanoCaP scaffolds. The surface chemistry of SF is known for providing good cell behavior and biocompatibility *in vivo* [41], showing that the *in vitro* and *in vivo* performance of the HRP-crosslinked SF scaffolds may not be only related to the architecture and morphological features of constructs, but also to the physical and chemical properties of SF [63]. The versatility of the present combined technologies, and the possibility of incorporating inorganic materials can encourage extending their application in different regenerative strategies, in particular, for developing monolithic and hierarchical structures for osteochondral regeneration.

7.6. Conclusions

This study proposed novel HRP-crosslinked SF scaffolds developed in combination with the salt-leaching and freeze-drying technologies, for cartilage regeneration applications. These scaffolds presented suitable porosity and mechanical properties for cartilage scaffolding strategies, as well as, large swelling capacity and structural integrity after 30 days at physiological conditions. The scaffolds supported the attachment, viability and proliferation of human adipose-derived stem cells (hASCs) *in vitro*. The chondrogenic differentiation on the HRP-crosslinked SF scaffolds was represented by the peak of GAGs produced by the seeded hASCs after 21 days of chondrogenic culture. Additionally, the genotypic and phenotypic expression of chondrogenic-related markers, allied to the deposition of cartilage-specific ECM, also confirmed these observations. The HRP-crosslinked SF scaffolds maintained their original morphology and allowed tissue ingrowth when subcutaneously implanted in mice. Although complementary studies are necessary to biomechanically evaluate the anisotropic properties of the scaffolds, as well as, *in vivo* validate their efficacy and stability in articular cartilage defects. The scaffolds characterization, *in vitro* chondrogenic differentiation of hASCs at the HRP-crosslinked SF scaffolds and preliminary *in vivo* data, confirm that these can be promising structures for cartilage regeneration applications. Moreover, the multitude of structural, mechanical and biological parameters that can be achieved through these combined technologies can also encourage to extend their applicability for different TE strategies, including for osteochondral regeneration.

7.7. Supplementary information

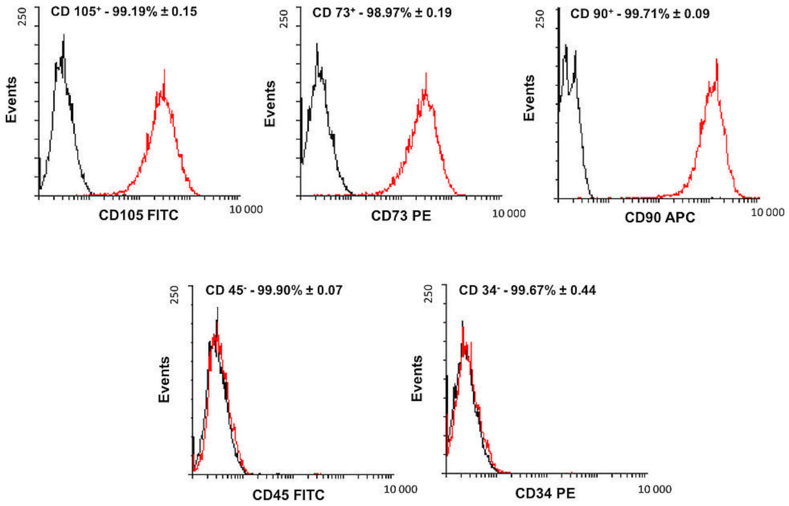

Supplementary Figure 7-1. Human ASCs characterization by flow cytometry prior differentiation assays. The graphics show a mesenchymal-like phenotype with cells displaying the characteristic multiple-parametric patter: CD105^{+}/CD73^{+}/ CD90^{+}/CD45^{-}/CD34^{-}.

7.8. References

[1] E.A. Makris, et al., Repair and tissue engineering techniques for articular cartilage, Nature Reviews Rheumatology 11(1) (2015) 21-34.

[2] W. Widuchowski, et al., Articular cartilage defects: study of 25,124 knee arthroscopies, The Knee 14(3) (2007) 177-182.

[3] C.J. Moran, et al., Restoration of articular cartilage, JBJS 96(4) (2014) 336-344.

[4] M. Brittberg, et al., Treatment of deep cartilage defects in the knee with autologous chondrocyte transplantation, New england journal of medicine 331(14) (1994) 889-895.

[5] J. Gille, et al., Cell-laden and cell-free matrix-induced chondrogenesis versus microfracture for the treatment of articular cartilage defects: a histological and biomechanical study in sheep, Cartilage 1(1) (2010) 29-42.

[6] J. Gille, et al., Outcome of Autologous Matrix Induced Chondrogenesis (AMIC) in cartilage knee surgery: data of the AMIC Registry, Archives of orthopaedic and trauma surgery 133(1) (2013) 87-93.

[7] Y.P. Singh, et al., Potential of Agarose/Silk Fibroin Blended Hydrogel for in Vitro Cartilage Tissue Engineering, ACS applied materials & interfaces 8(33) (2016) 21236-21249.

[8] K.-S. Han, et al., Effect of pore sizes of silk scaffolds for cartilage tissue engineering, Macromolecular Research 23(12) (2015) 1091-1097.

[9] W. Zhao, et al., Degradable natural polymer hydrogels for articular cartilage tissue engineering, Journal of Chemical Technology and Biotechnology 88(3) (2013) 327-339.

[10] B. Mollon, et al., The clinical status of cartilage tissue regeneration in humans, Osteoarthritis and cartilage 21(12) (2013) 1824-1833.

[11] Y.J. Chuah, et al., Hydrogel based cartilaginous tissue regeneration: recent insights and technologies, Biomaterials Science 5(4) (2017) 613-631.

[12] P.H.G. Chao, et al., Silk hydrogel for cartilage tissue engineering, Journal of Biomedical Materials Research Part B: Applied Biomaterials 95(1) (2010) 84-90.

[13] K. Makaya, et al., Comparative study of silk fibroin porous scaffolds derived from salt/water and sucrose/hexafluoroisopropanol in cartilage formation, Journal of bioscience and bioengineering 108(1) (2009) 68-75.

[14] Y. Wang, et al., In vitro cartilage tissue engineering with 3D porous aqueous-derived silk scaffolds and mesenchymal stem cells, Biomaterials 26(34) (2005) 7082-7094.

[15] U.-J. Kim, et al., Structure and properties of silk hydrogels, Biomacromolecules 5(3) (2004) 786-792.

[16] L.P. Yan, et al., Core-shell silk hydrogels with spatially tuned conformations as drug-delivery system, J Tissue Eng Regen Med 11(11) (2016) 3168-3177.

[17] M. Fini, et al., The healing of confined critical size cancellous defects in the presence of silk fibroin hydrogel, Biomaterials 26(17) (2005) 3527-3536.

[18] X. Hu, et al., Regulation of silk material structure by temperature-controlled water vapor annealing, Biomacromolecules 12(5) (2011) 1686.

[19] K. Numata, et al., State of water, molecular structure, and cytotoxicity of silk hydrogels, Biomacromolecules 12(6) (2011) 2137-2144.

[20] T. Yucel, et al., Vortex-induced injectable silk fibroin hydrogels, Biophysical journal 97(7) (2009) 2044-2050.

[21] X. Wang, et al., Sonication-induced gelation of silk fibroin for cell encapsulation, Biomaterials 29(8) (2008) 1054-1064.

[22] I. Karakutuk, et al., Diepoxide-triggered conformational transition of silk fibroin: formation of hydrogels, Biomacromolecules 13(4) (2012) 1122-1128.

[23] S.J. Sofia, et al., Peroxidase-catalyzed crosslinking of functionalized polyaspartic acid polymers, Journal of Macromolecular Science, Part A 39(10) (2002) 1151-1181.

[24] S. Sakai, et al., Peroxidase-catalyzed cell encapsulation in subsieve-size capsules of alginate with phenol moieties in water-immiscible fluid dissolving H2O2, Biomacromolecules 8(8) (2007) 2622-2626.

[25] L.-P. Yan, et al., Tumor growth suppression induced by biomimetic silk fibroin hydrogels, Scientific reports 6 (2016) 31037.

[26] C.-H. Chen, et al., Cartilage tissue engineering with silk fibroin scaffolds fabricated by indirect additive manufacturing technology, Materials 7(3) (2014) 2104-2119.

[27] L.-P. Yan, et al., Macro/microporous silk fibroin scaffolds with potential for articular cartilage and meniscus tissue engineering applications, Acta biomaterialia 8(1) (2012) 289-301.

[28] M. Marcacci, et al., Articular Cartilage Engineering with Hyalograft (R) C: 3-Year Clinical Results, Clinical orthopaedics and related research 435 (2005) 96-105.

[29] D.C. Crawford, et al., An autologous cartilage tissue implant NeoCart for treatment of Grade III Chondral injury to the distal femur, The American journal of sports medicine 37(7) (2009) 1334-1343.

[30] B.T. Estes, et al., Isolation of adipose-derived stem cells and their induction to a chondrogenic phenotype, Nature protocols 5(7) (2010) 1294-1311.

[31] A.I. Caplan, S.P. Bruder, Mesenchymal stem cells: building blocks for molecular medicine in the 21st century, Trends in molecular medicine 7(6) (2001) 259-264.

[32] G.-I. Im, et al., Do adipose tissue-derived mesenchymal stem cells have the same osteogenic and chondrogenic potential as bone marrow-derived cells?, Osteoarthritis and cartilage 13(10) (2005) 845-853.

[33] H.J. Kim, et al., In vitro chondrogenic differentiation of human adipose-derived stem cells with silk scaffolds, Journal of tissue engineering 3(1) (2012) 2041731412466405.

[34] M. Naeimi, et al., Incorporation of chitosan nanoparticles into silk fibroin-based porous scaffolds: Chondrogenic differentiation of stem cells, International Journal of Polymeric Materials and Polymeric Biomaterials 65(4) (2016) 202-209.

[35] R.L. Horan, et al., In vitro degradation of silk fibroin, Biomaterials 26(17) (2005) 3385-3393.

[36] M. Cerqueira, et al., Human adipose stem cells cell sheet constructs impact epidermal morphogenesis in full-thickness excisional wounds, Biomacromolecules 14(11) (2013) 3997-4008.

[37] M. Dominici, et al., Minimal criteria for defining multipotent mesenchymal stromal cells. The International Society for Cellular Therapy position statement, Cytotherapy 8(4) (2006) 315-317.

[38] K.J. Livak, T.D. Schmittgen, Analysis of relative gene expression data using real-time quantitative PCR and the 2– ΔΔCT method, methods 25(4) (2001) 402-408.

[39] H.J. Jin, et al., Water-Stable Silk Films with Reduced β-Sheet Content, Advanced Functional Materials 15(8) (2005) 1241-1247.

[40] P.J. Reardon, et al., Mimicking Hierarchical Complexity of the Osteochondral Interface Using Electrospun Silk–Bioactive Glass Composites, ACS Applied Materials & Interfaces 9(9) (2017) 8000-8013.

[41] V.P. Ribeiro, et al., Silk-based anisotropical 3D biotextiles for bone regeneration, Biomaterials 123 (2017) 92-106.

[42] L.-P. Yan, et al., Bilayered silk/silk-nanoCaP scaffolds for osteochondral tissue engineering: in vitro and in vivo assessment of biological performance, Acta biomaterialia 12 (2015) 227-241.

[43] H. Liu, et al., The interaction between a combined knitted silk scaffold and microporous silk sponge with human mesenchymal stem cells for ligament tissue engineering, Biomaterials 29(6) (2008) 662-674.

[44] X. Zhang, et al., In vitro evaluation of electrospun silk fibroin scaffolds for vascular cell growth, Biomaterials 29(14) (2008) 2217-2227.

[45] N. Bhardwaj, et al., Silk fibroin–keratin based 3D scaffolds as a dermal substitute for skin tissue engineering, Integrative Biology 7(1) (2014) 53-63.

[46] R. Nazarov, et al., Porous 3-D scaffolds from regenerated silk fibroin, Biomacromolecules 5(3) (2004) 718-726.

[47] G. Chen, et al., Scaffold design for tissue engineering, Macromolecular Bioscience 2(2) (2002) 67-77.

[48] U.-J. Kim, et al., Three-dimensional aqueous-derived biomaterial scaffolds from silk fibroin, Biomaterials 26(15) (2005) 2775-2785.

[49] H.J. Park, et al., Fabrication of microporous three-dimensional scaffolds from silk fibroin for tissue engineering, Macromolecular Research 22(6) (2014) 592-599.

[50] D.J. Griffon, et al., Chitosan scaffolds: interconnective pore size and cartilage engineering, Acta biomaterialia 2(3) (2006) 313-320.

[51] L. Vikingsson, et al., Relationship between micro-porosity, water permeability and mechanical behavior in scaffolds for cartilage engineering, Journal of the mechanical behavior of biomedical materials 48 (2015) 60-69.

[52] D. Yao, et al., Salt-leached silk scaffolds with tunable mechanical properties, Biomacromolecules 13(11) (2012) 3723-3729.

[53] S. Chen, et al., Depth-dependent compressive properties of normal aged human femoral head articular cartilage: relationship to fixed charge density, Osteoarthritis and Cartilage 9(6) (2001) 561-569.

[54] L.R. Almeida, et al., New biotextiles for tissue engineering: Development, characterization and in vitro cellular viability, Acta biomaterialia 9(9) (2013) 8167-8181.

[55] P. Gupta, et al., Mimicking form and function of native small diameter vascular conduits using mulberry and non-mulberry patterned silk films, ACS applied materials & interfaces 8(25) (2016) 15874-15888.

[56] L. Wu, J. Ding, Effects of porosity and pore size on in vitro degradation of three-dimensional porous poly (D, L-lactide-co-glycolide) scaffolds for tissue engineering, Journal of Biomedical Materials Research Part A 75(4) (2005) 767-777.

[57] C. Csaki, et al., Mesenchymal stem cells as a potential pool for cartilage tissue engineering, Annals of Anatomy-Anatomischer Anzeiger 190(5) (2008) 395-412.

[58] N.-C. Cheng, et al., Chondrogenic differentiation of adipose-derived adult stem cells by a porous scaffold derived from native articular cartilage extracellular matrix, Tissue Engineering Part A 15(2) (2008) 231-241.

[59] M.K. Lotz, et al., Cartilage cell clusters, Arthritis & Rheumatology 62(8) (2010) 2206-2218.

[60] V. Dexheimer, et al., Proliferation as a requirement for in vitro chondrogenesis of human mesenchymal stem cells, Stem cells and development 21(12) (2012) 2160-2169.

[61] F. Barry, et al., Chondrogenic differentiation of mesenchymal stem cells from bone marrow: differentiation-dependent gene expression of matrix components, Experimental cell research 268(2) (2001) 189-200.

[62] D.K. Temple, et al., Viscoelastic properties of human and bovine articular cartilage: a comparison of frequency-dependent trends, BMC musculoskeletal disorders 17(1) (2016) 419.

[63] B. Kundu, et al., Silk fibroin biomaterials for tissue regenerations, Advanced drug delivery reviews 65(4) (2013) 457-470.

CHAPTER 8.

Silk Fibroin-based Monolithic and Hierarchical Scaffolds for Osteochondral Regeneration

CHAPTER 8.

Silk fibroin-based monolithic and hierarchical scaffolds for osteochondral regeneration*

8.1. Abstract

Osteochondral (OC) regeneration has been facing several limitations in orthopedic surgery due to the complexity of simultaneously, repair articular cartilage and subchondral bone defects. In this study, novel biofunctional monolithic and hierarchical scaffolds composed of a horseradish peroxidase (HRP)-crosslinked silk fibroin (SF) cartilage-like layer (HSF layer) fully integrated into a HSF/ZnSr-doped β-tricalcium phosphate (β-TCP) subchondral bone-like layer (HSF-dTCP layer), were developed as a promising strategy for OC tissue regeneration. A comparative analysis was performed with a similar bilayered structure produced without ionic incorporation in β-TCP (HSF-TCP layer). A homogeneous porosity distribution was achieved throughout the scaffolds as shown by micro-computed tomography analysis. The ionic-doped bilayered scaffolds presented a wet compressive modulus (0.23 ± 0.06 MPa) and dynamic mechanical properties (ranging from 0.40 ± 0.11 to 0.59 ± 0.21 MPa) superior to that of the control scaffolds (0.19 ± 0.09 MPa and ranging from 0.26 ± 0.06 to 0.35 ± 0.09 MPa, respectively). The apatite-crystals formation, after soaking in simulated body fluid (SBF) was observed in the subchondral bone-like layers for the scaffolds incorporating TCP powders. Human osteoblasts (hOBs) and human articular chondrocytes (hACs) were co-cultured onto the bilayered structures, and monocultured in the respective cartilage and subchondral bone-half of the partitioned scaffolds. Both cell types showed good adhesion and proliferation in the respective scaffold compartments, as well as, adequate integration of the interface regions. Osteoblasts produced a mineralized extracellular matrix (ECM) and high osteopontin (OPN) expression in the subchondral bone-like layers. Chondrocytes showed GAGs deposition and aggrecan (ACAN) expression in the cartilage-like layers. Therefore, the structural adaptability and suitable mechanical properties of the biofunctional monolithic and hierarchical tissue engineered OC scaffolds, combined with the biological performance achieved using co-culturing systems, make these constructs a viable strategy for OC defects regeneration.

*This chapter is based on the following publication:

Ribeiro VP, Pina S, Costa JB, Cengiz IF, García-Fernández L, Fernández-Gutierrez M, Oliveira AL, San-Román J, Oliveira JM, Reis RL. Silk fibroin-based monolithic and hierarchical scaffolds for osteochondral regeneration. 2018, Submitted.

8.2. Introduction

Osteochondral (OC) defects are common joint injuries that affect simultaneously the articular cartilage and the underlying subchondral bone [1]. The causes associated with these deformities can be natural degradation or trauma related injuries. The natural wear of articular cartilage tissue is commonly observed in an aging population and usually leads to degenerative osteoarthritis (OA), the major cause of natural OC defects [2]. According to the literature, the prevalence of symptomatic osteoarthritis in adults ranges from about 7 to 17%, increasing at ages superior to 65 years old [3], being higher among women than men. Moreover, as stated by the United Nations, in 2050 people aged over 60 will represent more than 20% of the world population. From these 20%, it is estimated that 15% will suffer from symptomatic OA [4]. Knee (femoral-tibial joint) OC defects are very common in athletes of high competition sports involving high compressive load-bearing of the articular region [5]. The known methods used to treat OC defects include arthroscopic debridement, bone marrow stimulation techniques, and the use of OC autografts or allografts [6]. Nevertheless, these are considered palliative temporary solutions that can present limitations of immune rejection, disease transmission, and donor site morbidity [7].

Tissue engineering (TE) approaches have emerged as potential solutions for OC lesions repair and regeneration [8]. Since cartilage tissue is avascular and lacks of self-remodeling capacity, an important role is attributed to the subchondral bone in the regenerative process, which makes the reconstruction of both articular cartilage and subchondral bone as two separate areas overpassed. Still, a better knowledge of the mechanical properties, structure, and biological requirements of these two interacted tissues is required for the design of more complex scaffolding systems for OC applications.

Bilayered scaffolds emerged as potential candidates for OC TE, mainly because they can mimic the structural complexity of the natural OC tissue [9]. Different studies proposed homogeneous and heterogeneous bilayered scaffolds, using different biomaterials, scaffolding design, and fabrication methods, within *in vitro* and *in vivo* environments [10]. Bilayered scaffolds made of collagen and electrospun poly-L-lactic acid have shown to improve *in vitro* osteogenic differentiation, and *in vivo* subchondral bone and cartilage formation [11]. In another study, the fabrication of bilayered hydrogels of oligo(poly(ethylene glycol) fumarate incorporating gelatin microparticles enhanced chondrogenic and osteogenic differentiation, with great effects observed after loading microparticles with growth factors into the bilayered matrices [12]. In fact, the "hierarchical" properties of scaffolds mean that the scaffold features are comparable to that of the target tissue at molecular, microscopic, mesotrophic, and macroscopic level. For example, the nano-scale properties induced by the crosslinking process or hydroxyapatite (HAp) stoichiometry, play an important role in cell adhesion and mineralization, whereas the micrometer-scale of the scaffolds porosity, affects cell migration, ECM formation, and at some extent provides the mechanical anisotropy of scaffolds [13].

Several synthetic OC products were introduced in the market, including the Agili-C™, MaioRegen® or the TruFit® [14]. However, due to the inconsistency of results proving the full efficacy of these structures in the repair and regeneration of OC tissue, only a few are still in the market and clinically available [15, 16].

Natural polymers are considered to possess favorable biocompatibility and can easily promote cell adhesion, but have less controllable mechanical properties as compared to the synthetic ones [17]. However, silk fibroin (SF) from *Bombyx mori* has proved to exhibit tunable mechanical properties according to the final TE application, being successfully used as scaffolding material [18, 19]. In fact, silk bilayered scaffolds have shown suitable mechanical properties of both articular cartilage and subchondral bone tissues into a single and fully-integrated construct [20]. At the same time, calcium phosphates (CaPs) have shown remarkable osteoconductivity, bioactivity and biocompatibility [21], which makes the combination of SF and CaPs attractive for bone and OC regeneration scaffolding [22]. Among existing CaPs, β-tricalcium phosphate (β-TCP) has shown great osteconductivity and resorbability *in vivo* [23, 24]. Previously, our group developed bilayered SF/SF-nanoCaP scaffolds for OC TE applications showing improved mechanical properties and stability induced by the SF/nanoCaP composite layer, as well, *in vivo* biocompatibility, and new bone formation [25]. Doping β-TCP with ionic elements existing in bone, has shown enhanced mechanical properties of the scaffolds and directly affect the production and release of growth factors like bone morphogenetic protein-2 (BMP-2), and vascular endothelial growth factor (VEGF) involved on the osteogenic and angiogenic response of bone tissue [26]. Recently, it was reported that biofunctional scaffolds composed of SF and β-TCP incorporating Sr, Zn, and Mn, presented improved cell proliferation and higher osteogenic potential in comparison to SF/β-TCP scaffolds, mainly due to the ionic doping [27].

Up to date, three-dimensional (3D) networks, structural adaptability and resilient mechanical properties of hydrogels make them attractive for several TE applications [28]. However, the possibility of structuring hydrogel-based systems by combining different processing technologies allowed the creation of more robust matrices for high load-bearing applications, like bone, cartilage, and OC tissue [9, 29]. In this context, we developed hydrogen peroxide (HRP)-crosslinked SF scaffolds for articular cartilage regeneration, showing that combining this enzymatically crosslinked SF hydrogels with salt-leaching and freeze-drying technologies, the stability and stiffness of the structures can improve. In addition, the porosity required for extracellular matrix (ECM) formation and tissue ingrowth can be easily tuned. Previous studies by our group, also shown that HRP-crosslinked SF hydrogels, formed in a main amorphous conformation, presented tunable mechanical properties and gelling behavior according to the protein/crosslinker concentration [30]. Moreover, in the anti-parallel β-sheet form, these hydrogels presented higher stiffness and superior stability in response to the enzymatic degradation [31]. Based on these promising outcomes, in this study we aim to combine these multifunctional tools in order to develop 3D monolithic and hierarchical scaffolds, aiming OC repair and regeneration. We hypothesize that through these strategies we will be able to create novel bilayered structures with controlled porosity at the macro-and micro-scale and improved stability for short-to long-term OC implantation purposes. The spatially controlled incorporation of bioresorbable β-TCP should create stratified models, affecting their mineralization and mechanical response as hard templates. Thus, a HRP-mediated approach was used to crosslink SF (HSF) combined with pure and ZnSr-doped β-TCP, through salt-leaching and freeze-drying technologies. HSF was used as articular cartilage-like layer, while a 80/20 (w/w) ratio of HSF/ZnSr-doped β-TCP (HSF-dTCP) and HSF/undoped β-TCP (HSF-TCP) was used to produce the underlying subchondral bone layer. Taking into consideration the great reported results obtained from the ionic incorporation into monolayered SF-based scaffolds [26], in here we have evaluated the role of Zn+Sr doping in terms of physicochemical and biological behavior of monolithic bilayered structures. Physicochemical characterization was assessed through scanning electron microscopy (SEM), micro-computed tomography (micro-CT) and X-ray diffraction (XRD) techniques. Both static and dynamic mechanical properties were analyzed. The enzymatic degradation profile and bioactivity of the scaffolds were evaluated by soaking in protease XIV and simulated body fluid (SBF) solutions, respectively, up to 30 days. The *in vitro* cell viability, adhesion and proliferation were also evaluated by co-culturing primary human osteoblasts (hOBs) and human articular chondrocytes (hACs) into the bilayered structures up to 14 days. Monocultures of hOBs and hACs at the monolayered scaffolds were used as controls.

8.3. Materials and Methods

8.3.1. Materials and reagents

Bombyx mori cocoons were provided by the Portuguese Association of Parents and Friends of Mentally Disabled Citizens (APPACDM, Castelo Branco, Portugal). Silicone tubing was purchased from Deltalab (Barcelona, Spain). Granular sodium chloride low in endotoxins (EMPROVE®, VWR BDH Prolabo, Briare, France) was prepared in the range of 500-1000 μm using an analytic sieve shaker (AS 200 Digit, Retsch, Germany). All reagents were purchased from Sigma-Aldrich (St. Louis, MO, USA) unless otherwise stated.

8.3.2. Preparation of the bilayered scaffolds

Purified aqueous SF solution were extracted from *Bombyx mori* cocoons and obtained at high concentration (16 wt.%), following a previously reported procedure [19]. Powders of β-TCP, pure and doped with 10 mol.% of Zn and Sr, were synthesized by aqueous precipitation, and characterized as described in a previous work [27]. The cartilage-like layer of the scaffolds was produced with the HRP-crosslinked SF (HSF) solution at 1/0.26‰/1.45‰ (SF/HRP/H_2O_2), while the subchondral bone-like layer was prepared with 80/20 (w/w) ratio HSF/ZnSr-β-TCP, and HSF/β-TCP with no ionic incorporation, for comparison purposes. Firstly, the subchondral bone-like layers were produced by mixing ZnSr-β-TCP or β-TCP powders with the HSF solution and transferred into cylindrical shaped silicone molds (9 mm inner diameter), followed by adding granular sodium chloride (particle size 500-1,000 µm). After complete gelation at 37°C in the oven, the molds were immersed in fresh water and the salt was subsequently extracted (porogen) for 72 hours. Finally, the subchondral bone-like layers were removed from the molds using a biopsy punch (8 mm inner diameter; Smith & Nephew, Portugal), and cut into pieces. Secondly, the subchondral bone-like layers were placed in the bottom of new silicon molds (8 mm inner diameter) and the HSF solution was added on the top of these scaffolds in order to produce monolithic bilayered scaffolds, followed by adding granular sodium chloride particles. After complete gelation and salt-leaching process, the bilayered scaffolds were frozen at -80°C overnight, and freeze-dried (Telstar Cryodos-80, Barcelona, Spain) during 7 days. Monolayers of HSF, HSF/ZnSr-β-TCP (HSF-dTCP), and HSF/β-TCP (HSF-TCP) scaffolds, were also prepared as controls. The bilayered scaffolds are abbreviated as: BdTCP for bilayered HSF/HSF-dTCP scaffolds, and BTCP for bilayered HSF/HSF-TCP scaffolds (Figure 8-1a).

8.3.3. Physicochemical characterization

8.3.3.1. Scanning electron microscopy and energy dispersive spectroscopy analysis

The morphology of the scaffolds was analyzed by scanning electron microscopy (SEM) using a JEOL JSM-6010LV (Tokyo, Japan). Prior analysis all samples were sputter-coated with gold using a Leica EM ACE600 coater (Leica Microsystems, Wien, Austria). The elemental composition was performed by energy dispersive spectroscopy (EDS; Pegasus X4M) coupled to the SEM. Three independent areas were selected in the BdTCP and BTCP scaffolds, corresponding to the HSF layer, interface, and HSF-dTCP or HSF-TCP layer.

8.3.3.2. Micro-computed tomography

The quantitative and qualitative evaluation of the BdTCP and BTCP scaffolds microstructure was performed using a high-resolution X-ray microtomography system Skyscan 1272 (Skyscan, Kontich, Belgium). The scanning of the scaffolds was conducted using a pixel size of 3.5 μm and an X-ray source fixed at 50 keV and 200 μA. Both the diameter and height of the scaffolds were 8 mm (HSF layer: 3 mm in height; HSF-dTCP and HSF-TCP layer: 5 mm in height). The two-dimensional (2D) images in each data set (HSF layer, HSF-dTCP layer and HSF-TCP layer) were binarized automatically using the manufacturer's software (CT Analyzer v1.17, SkyScan, Kontich, Belgium), and then, the images were used for morphometric analysis by quantification of mean porosity, mean pore size, mean wall thickness and interconnectivity. The porosity and TCP content distribution profiles were also determined on the 2D images. 2D and 3D qualitative visualization of the different phases at the BdTCP and BTCP scaffolds were obtained with Data Viewer (v1.7.1.0) and CT-Vox (v3.3.0.r1412) (SkyScan, Kontich, Belgium), respectively. Three samples per scaffold were used for the qualitative and quantitative microstructure evaluation.

8.3.3.3. X-ray diffraction

The qualitative analysis of crystalline phases presented on the HSF, HSF-dTCP and HSF-TCP scaffolds was performed by X-ray diffraction (XRD) using a high-resolution Bragg–Brentano diffractometer (Bruker D8 Advance DaVinci, Karlsruhe, Germany) equipped with CuKα radiation (λ = 1.542 Å), produced at 40 kV and 40 mA. Data sets were collected in the 2θ range of 10–60° with a step size of 0.02° and 1 second for each step. The analysis of each condition was repeated three times independently.

8.3.3.4. Mechanical compressive tests

The compressive tests of the BdTCP and BTCP scaffolds were performed in wet state using a Universal Testing Machine (Instron 4505, Norwood, MA, USA). Both the diameter and height of the scaffolds were 8 mm (HSF layer: 3 mm in height; HSF-dTCP and HSF-TCP layer: 5 mm in height). Prior analysis, the samples were hydrated in phosphate-buffered saline (PBS, pH 7.4) solution until equilibrium was reached (overnight). The cross-head speed was fixed at 2 mm/min and tests were run until a 60% reduction in sample height had been achieved. The elastic modulus (*E*) was defined by the slope of the initial linear section of the stress-strain curve of each sample. The average compressive modulus and compressive strength were determined based on five samples measured for each group. HSF, HSF-dTCP and HSF-TCP scaffolds were used as controls (4 mm in height, 8 mm in diameter).

8.3.3.5. Dynamic mechanical analysis

The dynamic mechanical behavior (DMA) of the BdTCP and BTCP scaffolds was determined in a TRITEC8000B dynamic mechanical analyzer (Triton Technology, Lincolnshire, UK) at compressive mode, using the same samples sizes as the ones for the compressive tests. The measurements were carried out in hydrated state at 37°C, by immersing the samples in PBS solution. overnight, until reaching equilibrium at 37°C. The DMA spectra were obtained in a frequency scan between 0.1 and 10 Hz. A constant strain amplitude of 50 µm was maintained during the experiments. Both storage modulus (*E'*) and loss factor (*tan δ*) were obtained in the frequency range. Before the analysis, a small pre-load was applied to each sample, to ensure the contact between all the surface and the compression plates, with equivalent distance for all tested samples. Five samples of each group were tested and HSF, HSF-dTCP and HSF-TCP scaffolds were used as controls (4 mm in height, 8 mm in diameter).

8.3.4. Degradation profile

The stability of the BdTCP and BTCP scaffolds was evaluated by enzymatic degradation test. Protease XIV was derived from Streptomyces griseus (3.5 U/mg) and prepared at 2 U/mL and 0.0035 U/mL by dissolving the enzyme in PBS [32]. Samples were also incubated in PBS solution to be used as controls. The initial wet weight of each sample (n=3) was measured after hydration in PBS solution for 3 hours at 37°C, and then the scaffolds were immersed in 5 mL of protease solution or fresh PBS solution. The study was conducted at 37°C for a time period ranging from 6 hours to 30 days. The enzyme solutions were changed every 24 hours. At the end of each time point, the wet weight was measured after washing the samples with distilled water. Before weighing, samples were gently blotted with a filter paper to remove the excess liquid. The weight loss was determined following Equation 4-2:

$$\text{Weight loss (\%)} = \frac{mi-mf}{mi}\times 100$$

where m_i is the initial wet weight of the sample and m_f is the wet weight of the degraded sample, at each time point. HSF, HSF-dTCP and HSF-TCP scaffolds were used as controls.

8.3.5. *In vitro* bioactivity assay

The *in vitro* bioactivity of the BdTCP and BTCP scaffolds was evaluated by immersion in SBF solution for 15 and 30 days. Samples were immersed in SBF solution containing ionic concentrations (Na^+ 142.0, K^+ 5.0,

Ca^{2+} 2.5, Mg^{2+} 1.5, Cl^{-} 148.8, HPO_4^{-} 1.0, HCO_3^{2+} 4.2, SO_4^{2-} 0.5 mM/L, pH=7.4) similar to those of human blood plasma, at 37°C in continuous shaking (60 rpm) [33]. At the end of each time point, the samples were washed with distilled water and allowed to dry at 37°C for 3 days, followed by SEM and EDS analysis. Three samples of each group were tested and HSF, HSF-dTCP and HSF-TCP scaffolds were used as controls.

8.3.6. *In vitro* cell studies

8.3.6.1. Culture of hOBs and hACs

Primary human osteoblast (hOBs) obtained from femoral bone tissue, and human articular chondrocytes (hACs) obtained from knee articular cartilage (Innoprot, Derio, Spain), were used in this study. Cells were expanded in culture medium consisting of DMEM/F12 (Dulbecco's modified Eagle's medium/F12) GlutaMAX Supplement (Gibco®, Life Technologies, Carlsbad, CA, USA) supplemented with 10% (v/v) fetal bovine serum (FBS; Life Technologies, Carlsbad, CA, USA), 1% (v/v) antibiotic/antimycotic solution (final concentration of penicillin 100 units/mL and streptomycin 100 mg/mL, Life Technologies, Carlsbad, CA, USA), 50 mM Dexamethasone, 1% (v/v) MEM-NEAA (Gibco®, Life Technologies, Carlsbad, CA, USA) and 150 µg/mL Ascorbic acid. Cells were cultured until confluence at 37°C, 5% CO_2 incubator, changing the culture medium every 2-3 days.

8.3.6.2. Seeding and co-culture of hOBs-hACs on the bilayered scaffolds

For the co-culture system, BdTCP and BTCP scaffolds of both 8 mm in diameter and height were used (HSF layer: 3 mm in height; HSF-dTCP and HSF-TCP layer: 5mm in height) and sterilized by β-radiation (IONMED sterilization SA, Tarancón, Cuenca, Spain). Before the cell seeding, all scaffolds were hydrated in DMEM/F12, Glutamax supplemented with 1% (v/v) antibiotic/antimycotic solution, overnight in the CO_2 incubator. In the following day, the hydrated scaffolds were cut longitudinally with a blade and transferred to 24-well cell culture plates (Corning Incorporated, Life Sciences, Durham, NC, USA). Human OBs of passage 5 were detached from the flasks and seeded in a 10 µL cell suspension onto the surface of the HSF-dTCP and HSF-TCP layers, at a density of 3 x 10^5 cells/scaffold (P6). The constructs were kept in the CO_2 incubator for 3 hours and then completed with 2 mL of DMEM/F12, Glutamax supplemented with 10% (v/v) FBS, 1% (v/v) antibiotic/antimycotic solution, 50 mM Dexamethasone, 1% (v/v) MEM-NEAA and 150 µg/mL Ascorbic acid. After 24 hours, the hACs were seeded (P6) onto the surface of the HSF layers, following the same procedure described for seeding the hOBs. HSF scaffolds (8 mm in diameter and 3 mm in height), HSF-dTCP and HSF-TCP scaffolds (8 mm in diameter and 5 mm in height) were seeded with hACs and hOBs, respectively, and used as monoculture controls (Figure 8-1b). The number of cell-seeded constructs used for the different characterization techniques will be described below. Samples were harvested after culturing for 1, 7 and 14 days and the culture medium was changed every 2-3 days.

8.3.6.3. Metabolic activity of hOBs-hACs on the bilayered scaffolds

The metabolic activity of cells in the constructs was screened by the Alamar blue assay, following the manufacturer's instructions. After each culture time, the constructs were transferred to a new 24-well cell culture plate, and a 10% (v/v) AlamarBlue® (BioRad, Hercules, CA, USA) solution prepared in culture medium, was transferred to the culture plates in 1 mL/scaffold. After 3 hours in the CO_2 incubator at 37°C, 100 µL of Alamar blue solution were transferred into a 96-well cell culture plate (Greiner Bio-one, Frickenhausen, Germany) in triplicate. The fluorescence was measured in a microplate reader (Synergy HT, BioTek, Instruments, USA) at an excitation wavelength of 530/25 nm and at an emission wavelength of 590/35 nm. Three samples of each group were tested at each time-point, in three independent experiments. Scaffolds without cells were used as control.

8.3.6.4. Adhesion of hOBs-hACs on the bilayered scaffolds

Cell adhesion and distribution were observed in the constructs by SEM (Model XL 30, Philips, Eindhoven, The Netherlands). After each culture time, the constructs were rinsed in PBS solution and fixed with a 2.5% (v/v) glutaraldehyde solution for 1 hour at 4°C. Samples were dehydrated through increasing series of ethanol concentrations (30, 50, 70, 90 and 10% v/v), twice each concentration during 15 minutes, and left overnight at room temperature (RT) to dry. Prior analysis, all scaffolds were sputter-coated with gold-palladium (60:40; Polaron SC 7640, Watford, UK).

8.3.6.5. DNA quantification

The quantification of the double stranded DNA (dsDNA) was performed by using a Quant-IT PicoGreen dsDNA quantification kit (Life Technologies, Carlsbad, CA, USA), according to the manufacturer's instructions. After each culture time, samples were washed with PBS solution and kept in 1 mL of ultrapure water at -80°C until further analysis. Samples thawed at room temperature (RT) and sonicated for 1 hour to induce complete membrane lysis. The fluorescence intensities were recorded in a microplate reader at an excitation wavelength of 485/20 nm and at an emission wavelength of 528/20 nm. The quantification of DNA was calculated according to a standard curve prepared with concentrations ranging from 0 to 2 µg/mL. Three samples of each group were tested at each time-point, in three independent experiments. Scaffolds without cells were used as control.

8.3.6.6. Alkaline phosphatase activity quantification

The same lysates for DNA assay were used for alkaline phosphatase (ALP) activity quantification. The specific conversion of p-nitrophenyl phosphate (pNPP) into p-nitrophenol (pNP) was used to analyze the ALP activity of the constructs. A buffer solution containing 0.2% (w/v) pNPP was added to the supernatant in 96-well cell culture plates, in triplicate. The enzyme reaction was carried out at 37°C for 45 minutes and then a solution containing 2 M NaOH (Panreac Química SAU, Barcelona, Spain) and 0.2 mM ethylenediaminetetraacetic acid (EDTA) in distilled water was used to stop the reaction. The absorbance of the produced pNP was read at 405 nm in a microplate reader and samples concentration were determined based on a standard curve prepared with pNP values ranging from 0 to 0.2 µmol/mL. The obtained ALP concentrations were normalized against the DNA concentrations of the same samples. Three samples of each group were tested at each time-point, in three independent experiments. Scaffolds without cells were used as control.

8.3.6.7. Glycosaminoglycans quantification

The glycosaminoglycans (GAGs) quantification was performed using a dimethylmethylene blue (DMB) assay. Samples were collected after each culture time, frozen overnight and then digested in order to separate the formed ECM from the scaffolds. The digestion solution was prepared by adding to each 50 mL of digestion buffer, 25 mg of papain (Alfa Aesar, Haverhill, MA, USA) and 48 mg of n-acetyl cysteine. Digestion buffer was composed of 200 mM of phosphate buffer (sodium phosphate monobasic; Panreac Química SAU, Barcelona, Spain) containing 1 mM EDTA (pH 6.8). Samples were digested overnight at 60°C in 1 mL papain digestion solution, and centrifuged at 13,000 rpm for 10 minutes. The GAGs content was spectrophotometrically determined from the collected supernatants, using a DMB solution prepared by dissolving 16 mg DMB powder in 900 mL distilled water containing 3.04 g glycine (Honeywell Fluka, Morris Plains, NJ, USA) and 2.73 g of NaCl (Panreac Química SAU, Barcelona, Spain) (pH 3.0). The optical density (OD) was measured in a microplate reader at an absorbance of 530 nm. A chondroitin sulfate stock solution (Bioiberica, SA, Barcelona, Spain) was prepared in distilled water at 50 µg/mL in order to make a standard curve with concentrations ranging from 0 to 35 µg/mL. Three samples of each group were tested at each time-point, in three independent experiments. Scaffolds without cells were used as control.

8.3.6.8. Histology and immunofluorescence staining

Samples were collected at the end of each culture time and processed for histology. Constructs were transferred to histological cassettes and fixed with 10% (v/v) formalin solution. After paraffin-embedding, samples were serially sectioned with 20 μm thick using a microtome (Spencer 820, American Optical Company, NY, USA). Standard Hematoxylin & Eosin (Thermo Scientific, Waltham, MA, USA) staining was performed to evaluate cell distribution and ECM formation within the constructs. The presence of collagen within the ECM was determined by Sirius red/Fast green collagen staining kit (Chondrex, Redmond, WA, USA), where the Sirius red dye specifically binds to collagen and Fast green dye stains the non-collagenous proteins. Briefly, sections were stained with a mixture of 0.1% (v/v) Sirius red and 0.1% (v/v) Fast green solution saturated with picric acid. Safranin-O (0.1% v/v; Honeywell Fluka, Morris Plains, NJ, USA) staining was used to detect the distribution and content of sulfated GAGs. Sections were counterstained with Gill-2 hematoxylin (Thermo Scientific, Waltham, MA, USA) and Fast green (0.02% v/v; Honeywell Fluka, Morris Plains, NJ, USA). Staining with 2% (w/v) Alizarin Red solution (Merck, Germany) in ultrapure water, was performed to assess the matrix mineralization.

To detect protein expression, antigen retrieval was performed on the sections by incubating in 0.5% pepsin in 5 mM HCl (Fisher Scientific, Waltham, MA, USA) for 30 minutes at 37°C. The sections were permeabilized with 1% (v/v) Triton X-100/PBS for 10 minutes and blocked in 3% (w/v) BSA/PBS for 1 hour at RT. Immunolabeling was performed using as primary antibodies a rabbit anti-human polyclonal antibody against osteopontin (OPN; Abcam, Cambridge, UK; dilution 1:25) and a mouse anti-human monoclonal antibody against Aggrecan (ACAN; clone BC-3, Thermo Scientific, Waltham, MA, USA; dilution 1:5), prepared in 1% (w/v) BSA/0.2% (v/v) Triton X-100 in PBS solution and incubated overnight at 4°C. Then, the sections were incubated with the respective secondary fluorochrome-conjugated antibodies, anti-rabbit/mouse IgG (Invitrogen, Life Technologies, California, USA; dilution 1:100) for 2 hours in the dark at RT, followed by 15 minutes of incubation with 4,6-Diamidino-2-phenyindole, dilactate (DAPI; Biotium, CA, USA; dilution 1:500) for nuclei staining. Sections incubated only with the secondary fluorochrome-conjugated antibodies were used as negative controls (Supplementary Figure 8-1).

Histological and immunofluorescent sections were observed under transmitted and fluorescence microscopy (OPN in green: ex/em 488/517; ACAN in red: ex/em 594/618; DAPI in blue: ex/em 358/461), respectively, using a transmitted and reflected light microscope (Axio Imager Z1 m; Zeiss, Jena, Germany). Images were acquired using the Zen microscope processing software (Zeiss, Jena, Germany) connected to digital cameras AxioCam MRc5 and MR3 (Zeiss, Jena, Germany).

8.3.7. Statistical analysis

All the numerical results are presented as mean ± standard deviation (SD). Statistical analysis was performed using the GraphPad Prism 5.0 software (GraphPad Software, La Jolla, CA, USA). First, a Shapiro-Wilk test was used to ascertain about the data normality. For all the biological quantification assays, the differences between the experimental results were analyzed using a Kruskal-Wallis test followed by Dunn's multiple comparison test. The significance level was set to $^{*}p < 0.05$, $^{**}p < 0.01$, $^{***}p < 0.001$.

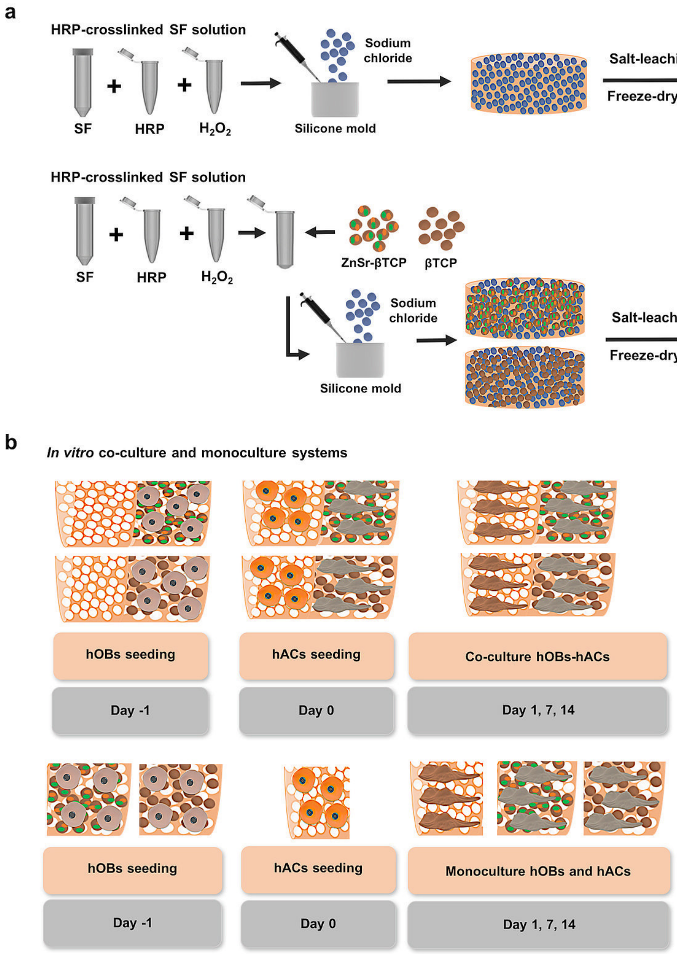
a
HRP-crosslinked SF solution
SF
HRP
H_2O_2
Sodium chloride
Silicone mold
Salt-leaching
Freeze-drying
HSF scaffold
HRP-crosslinked SF solution
SF
HRP
H_2O_2
ZnSr-βTCP
βTCP
Sodium chloride
Silicone mold
Salt-leaching
Freeze-drying
HSF-dTCP scaffold
HSF-TCP scaffold
3 mm
5 mm
8 mm
BdTCP scaffold
BTCP scaffold
b
In vitro co-culture and monoculture systems
hOBs seeding
hACs seeding
Co-culture hOBs-hACs
Day -1
Day 0
Day 1, 7, 14
hOBs seeding
hACs seeding
Monoculture hOBs and hACs
Day -1
Day 0
Day 1, 7, 14

Figure 8-1. Schematic illustration of the experimental setup adopted in this study. (a) Methodology used for preparing the BdTCP and BTCP scaffolds, creating HSF scaffolds as cartilage-like layers in combination with HSF-dTCP and HSF-TCP scaffolds in an 80/20 (w/w) ratio as subchondral bone-like layers. (b) Temporal approach followed for co-culturing hOBs and hACs on the BdTCP and BTCP scaffolds. Monoculture system of hACs on the monolayered HSF scaffolds, and hOBs on the monolayered HSF-dTCP and HSF-TCP scaffolds used as controls. Both the diameter and height of scaffolds were 8 mm (HSF layer: 3 mm in height; HSF-dTCP and HSF-TCP layers: 5 mm in height).

8.4. Results

8.4.1. Microstructure, elemental composition and TCP distribution into the bilayered scaffolds

Figure 8-2 shows the microstructure of BdTCP and BTCP scaffolds observed by SEM and the chemical elements analyzed using EDS. It can be observed that the bilayered scaffolds presented a macro- and micro-porous structure on both HSF (Figure 8-2a and d), and HSF-dTCP (Figure 8-2c) or HSF-TCP (Figure 8-2f) layers, presenting macro-pores larger than 500 µm and micro-pores that reach 10 µm. The scaffold layers were well integrated by continuous interface regions of ~500 µm thickness (Figure 8-2b and e). From EDS spectra, it was possible to detect calcium (Ca) and phosphorous (P) ions in the subchondral bone-like layers (HSF-dTCP and HSF-TCP) (Figure 8-2c, f) and interface regions (Figure 8-2b and e), as expected. The intensity of the Ca and P peaks was higher on the HSF-dTCP and HSF-TCP layers than in the interface regions, reaching Ca/P ratio values between 1.53 and 2.31 (Figure 8-2b, c, e and f). It can also be observed the presence of Zn and Sr peaks on the doped scaffolds, namely BdTCP interface (Figure 8-2b) and HSF-dTCP layer (Figure 8-2c).

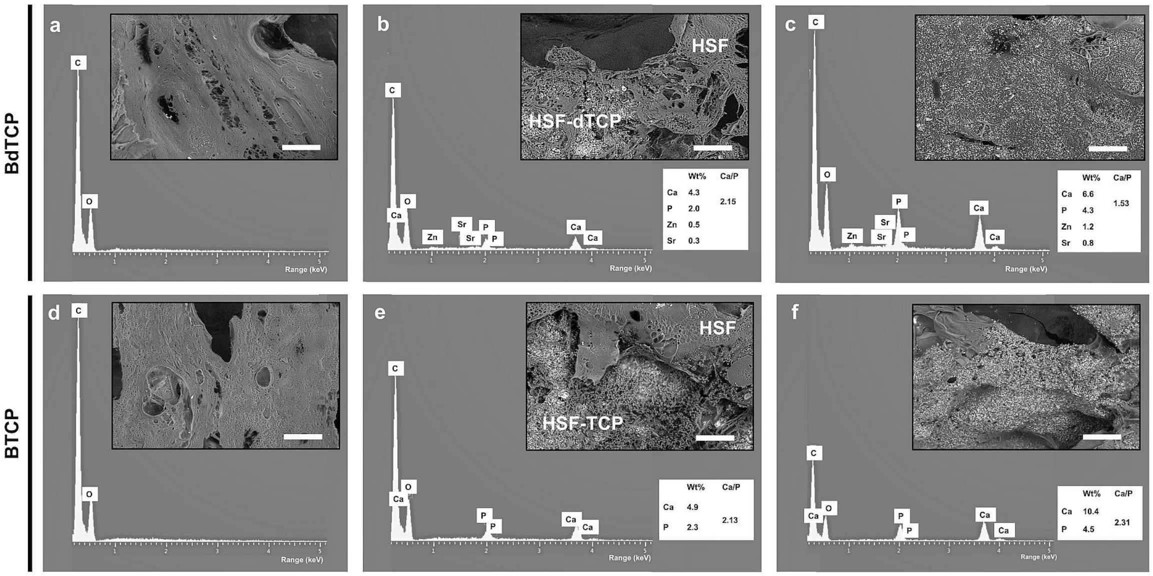

Figure 8-2. SEM micrographs (scale bar: 100 µm) and EDS elemental spectra with the ionic elements and Ca/P ratios determined at the different regions of the BdTCP and BTCP scaffolds. (a, d) HSF layers, (b, e) interface regions, (c) HSF-dTCP layer, and (f) HSF-TCP layer.

The qualitative and quantitative analysis of the BdTCP and BTCP scaffolds architecture were assessed by micro-CT. Table 8-1, shows that the bilayered scaffolds presented similar porosity and pore wall thickness, with high interconnectivity of 79.7 ± 5.9% on BdTCP scaffolds, and 75.2 ± 3.8% on BTCP scaffolds. As the bilayered scaffolds porosity decreased, from the HSF layers (89.1 ± 1.4% on BdTCP; 89.1 ± 0.6% on BTCP) to the HSF-dTCP (31.4 ± 8.4%) and HSF-TCP (21.6 ± 8.8%) layers, including the respective interfaces (76.4 ± 2.8% on BdTCP; 71.6 ± 14.6% on BTCP), the mean pore wall thickness tends to increase on both BdTCP (HSF layer: 22.6 ± 2.0 μm; Interface: 47.8 ± 5.5 μm; HSF-dTCP layer: 50.7 ± 4.4 μm) and BTCP (HSF layer: 21.5 ± 2.5 μm; Interface: 51.9 ± 2.3 μm; HSF-TCP layer: 59.2 ± 8.4 μm) scaffolds. From the 2D images, it was possible to observe the porous structure in each layer of the BdTCP (Figure 8-3a and b) and BTCP scaffolds (Figure 8-3d and e). Moreover, the TCP component (ZnSr-β-TCP and β-TCP) was retained only in the composite layers (Figure 8-3b and e), as confirmed by the blue domain present in the 3D reconstructions of the BdTCP (Figure 8-3c) and BTCP (Figure 8-3f) scaffolds. The porosity distribution profile was homogeneous in each scaffold layer (Figure 8-3g); however, a substantial increase of porosity was observed from the interface region until the HSF layers. The TCP component was evenly distributed in the HSF-dTCP and HSF-TCP layers, gradually decreasing at the interface domain and being completely absent at the HSF layers (Figure 8-3h).

Table 8-1. Microstructure of the BdTCP and BTCP scaffolds analyzed by micro-CT.

		Mean porosity (%)	**Mean wall thickness (μm)**	**Mean interconnectivity (%)**
BdTCP	**HSF**	89.1 ± 1.4	22.6 ± 2.0	79.7 ± 5.9
	Interface	76.4 ± 2.8	47.8 ± 5.5	
	HSF-dTCP	31.4 ± 8.4	50.7 ± 4.4	
BTCP	**HSF**	89.1 ± 0.6	21.5 ± 2.5	75. 2 ± 3.8
	Interface	71.7 ± 14.6	51.9 ± 2.3	
	HSF-TCP	21.6 ± 8.8	59.2 ± 8.4	

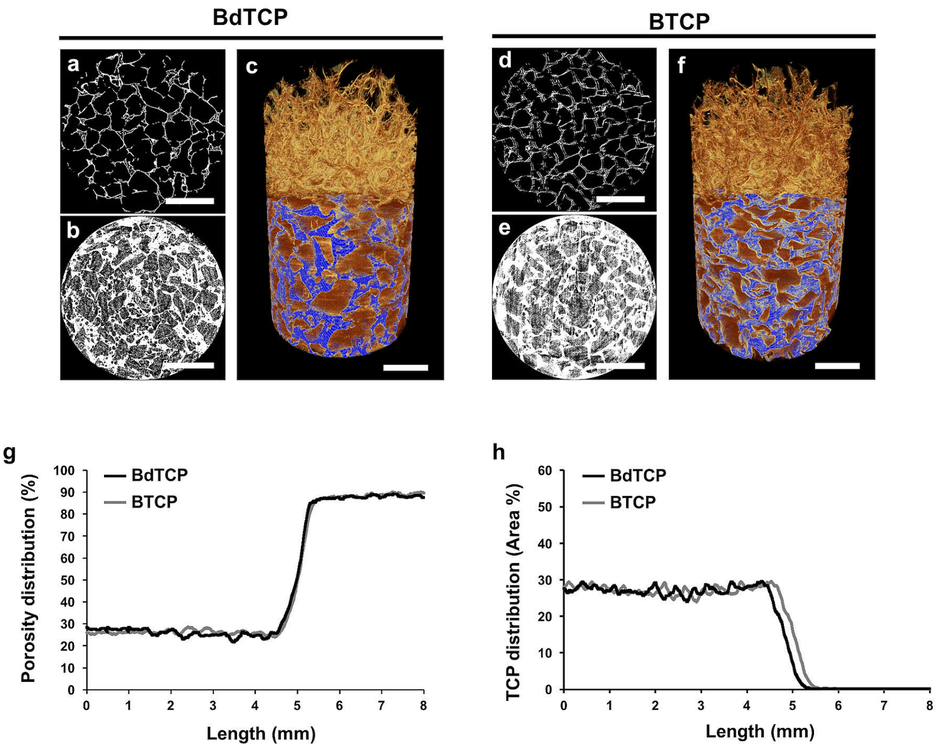

Figure 8-3. Micro-CT analysis of the BdTCP and BTCP scaffolds. 2D images of the (a, d) HSF layers, (b) HSF-dTCP layer and (e) HSF-TCP layer (scale bar: 2 mm). 3D reconstructions of the (c) BdTCP scaffolds and (f) BTCP scaffolds showing the HSF matrix in brown and the HSF-dTCP or HSF-TCP matrices in blue (scale bar: 2 mm). Change of (g) 2D porosity distribution and (h) TCP (ZnSr-β-TCP and β-TCP) component distribution from the subchondral bone-like layers (HSF-dTCP and HSF-TCP, respectively) to the cartilage-like layers (HSF).

8.4.2. Crystalline structure and mechanical properties of the scaffolds

XRD patterns of the HSF, HSF-dTCP and HSF-TCP scaffolds are displayed in Figure 8-4a. All the scaffolds showed the typical crystalline peaks of β-sheet structure (silk-II conformation), being more pronounced for HSF scaffolds with main peaks located at 20.5° and 24.3° [19, 34]. Additionally, the HSF-dTCP and HSF-TCP scaffolds showed the characteristic crystalline phases of β-TCP (standard ICDD PDF 04-014-2292) and trace amounts of β-calcium pyrophosphate (β-CPP) (standard ICDD PDF 04-009-3876). A small peak shift at 2θ ~28° toward higher 2θ, namely in the ZnSr-β-TCP powders, is also observed in these scaffolds due to the ionic presence, (zoomed area in Figure 8-4a).

As shown in Figure 8-4b, the wet compressive modulus of the BdTCP (0.23 ± 0.06 MPa) and BTCP (0.19 ± 0.09 MPa) scaffolds was higher than that obtained for the corresponding monolayered scaffolds (HSF: 0.06 ± 0.04 MPa; HSF-dTCP: 0.17 ± 0.11 MPa; HSF-TCP: 0.15 ± 0.08 MPa). The HSF scaffolds presented the lowest compressive modulus, as compared to the bilayered and monolayered composite scaffolds. A similar pattern was obtained when examined the compressive strength of HSF (0.028 ± 0.004 MPa), HSF-dTCP (0.068 ± 0.039 MPa), HSF-TCP (0.069 ± 0.036 MPa), BdTCP (0.13 ± 0.023 MPa) and BTCP (0.092 ± 0.006 MPa) scaffolds (Figure 8-4c). From the dynamic viscoelastic properties assessed by DMA (Figure 8-4d and e), it was found that the storage modulus (*E'*) of the bilayered and monolayered control scaffolds increased at lower rates, with increasing testing frequencies (from 0.1 to 10 Hz), ranging from 0.40 ± 0.11 to 0.59 ± 0.21 MPa on BdTCP scaffolds, 0.26 ± 0.06 to 0.35 ± 0.09 MPa on BTCP scaffolds, 0.18 ± 0.05 to 0.24 ± 0.09 MPa on HSF scaffolds, 0.43 ± 0.33 to 0.62 ± 0.51 MPa on HSF-dTCP scaffolds and 0.27 ± 0.09 to 0.37 ± 0.15 MPa on HSF-TCP scaffolds. In the frequency range tested, the *E'* values of BdTCP and BTCP scaffolds were similar to those of HSF-dTCP and HSF-TCP, respectively, and higher than those of HSF scaffolds, indicating that the presence of TCP instigated the reinforcement of the structure, increasing the mechanical strength. The loss factor (tan δ) obtained for the bilayered and monolayered control scaffolds were constant when the frequency increased from 0.1 to 10 Hz. All groups of scaffolds presented similar and high loss factor values for the tested frequencies.

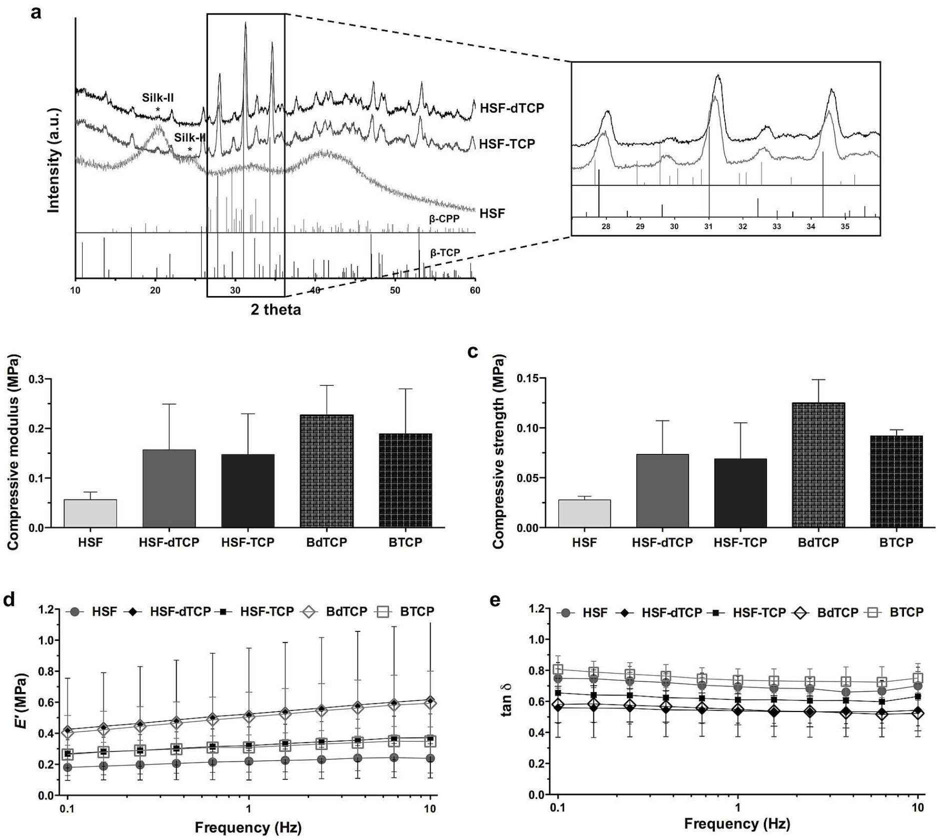

Figure 8-4. Crystalline structure and mechanical characterization of the BdTCP and BTCP scaffolds. (a) XRD patterns of the HSF, HSF-dTCP and HSF-TCP scaffolds, and zoomed area of graph in a 2θ range from 27 to 36, showing the

shift toward higher 2θ in the HSF-dTCP scaffolds. β-TCP (ICDD PDF 04-014-2292) and β-CPP (ICDD PDF 04-009-3876). (b) Compressive modulus and (c) compressive strength of the bilayered scaffolds (BdTCP and BTCP) and controls (HSF, HSF-dTCP and HSF-TCP), measured in the hydrated state. (d) Storage modulus (*E'*) and (e) loss factor (tan δ) of the bilayered scaffolds (BdTCP and BTCP) and controls (HSF, HSF-dTCP and HSF-TCP) obtained by DMA, tested at physiological conditions (pH 7.4 and 37°C).

8.4.3. Degradation properties and bioactivity evaluation of the scaffolds

The enzymatic degradation profile of the bilayered scaffolds, and the monolayered scaffolds for control, was performed using protease XIV (Figure 8-5a) [35]. As expected, the degradation rate of all tested groups was faster in the presence of protease XIV, at the highest tested concentration (2 U/mL), as compared to the protease XIV concentration of 0.0035 U/mL and to the control condition (PBS solution), as SF is prone to proteolytic degradation. HSF scaffolds presented higher weight loss than the bilayered scaffolds, and remaining monolayered control groups, in the presence of protease XIV at 2 U/mL. Nevertheless, after 3 days of testing, all the monolayered control scaffolds were completely degraded, while the BdTCP and BTCP scaffolds reached 100% weight loss after 14 and 21 days, respectively. The weight loss of samples in the presence of protease XIV at 0.0035 U/mL was stable over the first 7 days for all tested groups. However, a substantial decrease in weight loss was observed after 21 and 30 days, reaching a weight loss of ~70% on BdTCP scaffolds, ~80% on BTCP scaffolds and HSF scaffolds, ~90% on HSF-dTCP scaffolds, and 100% on HSF-TCP scaffolds. In the control conditions, all scaffolds immersed in PBS solution maintained their original weight for 30 days.

Figure 8-5b, shows the morphology of the bilayered and monolayered control scaffolds after immersion in SBF for 15 days. It was observed that the HSF-dTCP (Figure 8-5bii and vi) and HSF-TCP (Figure 8-5biv and vii) layers and scaffolds were able to induce the formation of cauliflower-like of apatite crystals, while there were no apatite crystals formed on the HSF layers (Figure 8-5bi and iii) or scaffolds (Figure 8-5v). The formation of a mineral layer at the composites surface, with similar morphology to that of HAp, was also confirmed by EDS analysis with quantified Ca/P ratio values between 1.93 and 2.43 (Figure 8-5bii, iv, vi and vii).

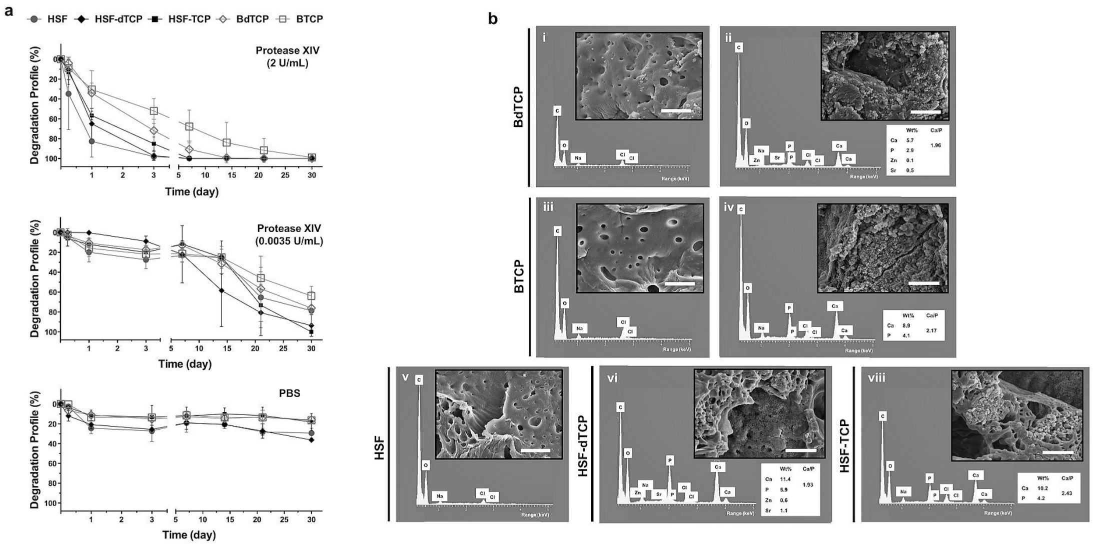

Figure 8-5. Degradation profile and *in vitro* bioactivity evaluation of the BdTCP and BTCP scaffolds. (a) Enzymatic degradation profile of the bilayered scaffolds (BdTCP and BTCP) and controls (HSF, HSF-dTCP and HSF-TCP), measured for a period of 30 days (% weight). Samples immersed in PBS were used as controls. (b) SEM micrographs (scale bar: 10 μm) and EDS spectra with the ionic elements and Ca/P ratios determined at the (i, iii) HSF layers, (ii) HSF-dTCP layer and (iv) HSF-TCP layer of the BdTCP and BTCP scaffolds, after 15 days of immersion in SBF solution. (v) HSF scaffolds, (vi) HSF-dTCP scaffolds and (vii) HSF-TCP scaffolds were also evaluated.

8.4.4. *In vitro* characterization of the bilayered scaffolds

8.4.4.1. Cell adhesion and metabolic activity

The quantitative analysis of cell viability was performed by the Alamar blue assay to evaluate the metabolic activity of cells up to 14 days in co-culture and monoculture system (Figure 8-6). It was observed that the metabolic activity of cells on both co-culture and monoculture systems, significantly increased from day 1 to day 7 (*$p < 0.05$ on HSF-TCP; **$p < 0.01$ on BdTCP; ***$p < 0.001$ on HSF and BTCP), from day 1 to day 14 (***$p < 0.001$), and from 7 to day 14 (*$p < 0.05$, except for HSF ***$p < 0.001$). The BdTCP and BTCP scaffolds co-cultured with hOBs and hACs, did not present significant differences in metabolic activity at the same culture periods. The same behavior was observed between the HSF-dTCP and HSF-TCP scaffolds monocultured with hOBs.

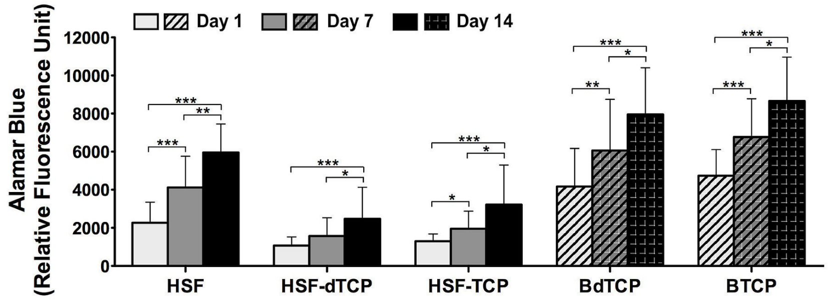

Figure 8-6. Metabolic activity of the hOBs and hACs co-cultured in the BdTCP and BTCP scaffolds for 1, 7 and 14 days as determined by Alamar blue. Monocultures of hACs in the HSF scaffolds and hOBs in the HSF-dTCP and HSF-TCP scaffolds were used as controls.

From SEM analysis (Figure 8-7), it was possible to observe that on both co-culture and monoculture systems, cells were able to adhere and spread on the surface of the bilayered and monolayered control scaffolds. After 7 and 14 days of culture, a layer of cells was formed on the co-cultured and monocultured scaffolds, showing the interface region at the BdTCP and BTCP scaffolds covered by cells. The macro-porosity also allowed cells to penetrate into the scaffolds.

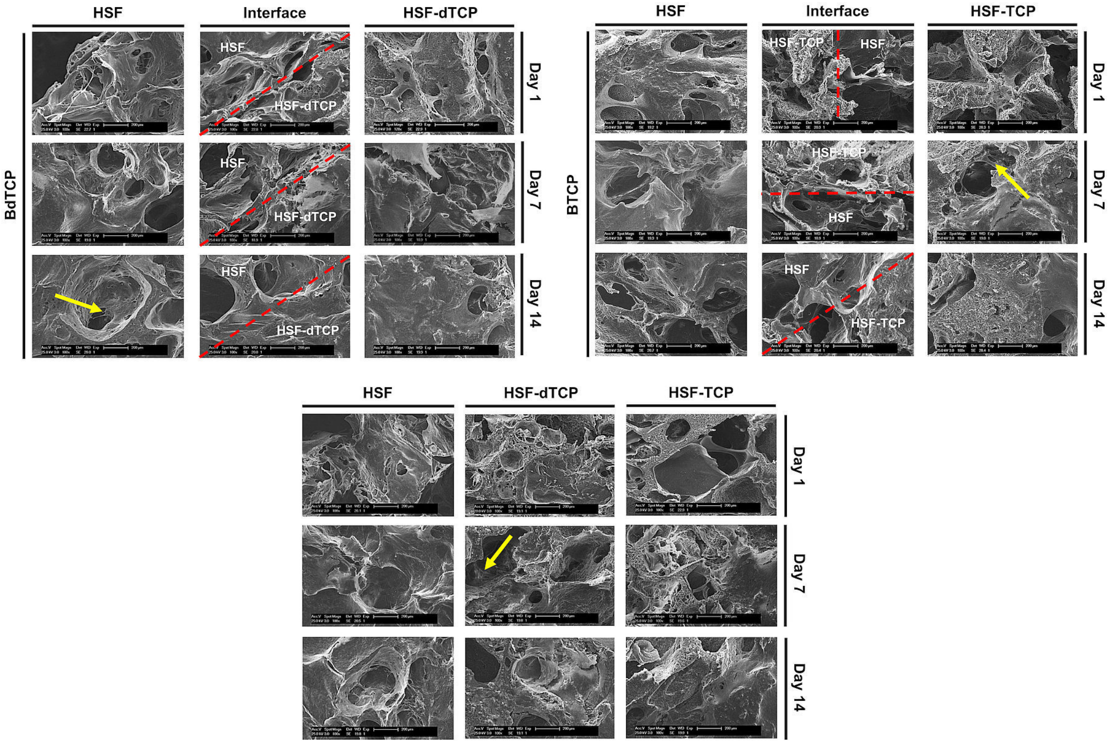
HSF
Interface
HSF-dTCP
Day 1
Day 7
Day 14
BdTCP
HSF
HSF-dTCP
HSF
Interface
HSF-TCP
BTCP
HSF-TCP
HSF
HSF
HSF-dTCP
HSF-TCP

Figure 8-7. SEM micrographs of the adhered hOBs and hACs co-cultured in the BdTCP and BTCP scaffolds, after 1, 7 and 14 days (scale bar: 200 μm). Monocultures of hACs in the HSF scaffolds and hOBs in the HSF-dTCP and

HSF-TCP scaffolds were observed as controls. The red dashed lines indicate the interface region that separates the HSF layer from the HSF-dTCP and HSF-TCP layers. The yellow arrows indicate the cells inside the macro-pores.

8.4.4.2. Evaluation of osteogenesis and chondrogenesis

Cell proliferation was quantified by DNA assay (Figure 8-8a), showing a significant increase of the DNA content on both co-culture and monoculture systems up to 14 days of culture. The bilayered scaffolds co-cultured with hOBs and hACs, presented a significant increase of the DNA content from day 1 to day 14 (**$p < 0.01$), and from day 1 to day 7 (*$p < 0.05$ on BTCP). Regarding the HSF constructs, a significant increase of the DNA content was detected from day 1 to day 14 (***$p < 0.001$) and from day 7 to day 14 (*$p < 0.05$). On the monoculture system with hOBs, a significant increase of cell proliferation was observed from day 1 to day 14 on both HSF-dTCP (***$p < 0.001$) and HSF-TCP (*$p < 0.05$) constructs, and from day 1 to day 7 on the HSF-TCP constructs (*$p < 0.05$). No significant differences were observed when compared the hOBs proliferation on the HSF-dTCP and HSF-TCP scaffolds, at the same culture periods. The co-culture groups presented the same trend.

The ALP activity of the co-cultured and monocultured cells was normalized by their respective DNA content (Figure 8-8b). In co-culture conditions, a significant increase of ALP activity was observed on both BdTCP (***$p < 0.001$ from day 1 to day 14; *$p < 0.05$ from day 7 to day 14) and BTCP (**$p < 0.01$ day 1 to day 7; ***$p < 0.001$ from day 1 to day 14; *$p < 0.05$ from day 7 to day 14) constructs. Nevertheless, no significant differences were observed when compared the ALP activity in the bilayered constructs at the same culture periods. It was observed that the ALP activity of hACs monucultured in the HSF scaffolds significantly increased from day 1 to day 14 (***$p < 0.001$). The hOBs monocultured in the HSF-dTCP and HSF-TCP scaffolds presented higher ALP activity levels, as compared to the remaining tested groups. However, the ALP activity levels in these composite scaffolds were stable until day 7 and significantly higher at day 14 on the HSF-TCP constructs (***$p < 0.001$), as compared to day 1.

The GAGs production was quantified in all types of culture (Figure 8-8c). The GAGs accumulation in the co-culture systems with hOBs and hACs, showed a non-significant increase in the BdTCP and BTCP constructs after 14 and 7 days of culture, respectively. Furthermore, no significant differences in GAGs production were found between these constructs at the same co-culture periods. In the HSF scaffolds, there was a significant increase of GAGs accumulation after 14 days of culture with hACs (**$p < 0.01$ from day 1 to day 14; ***$p < 0.001$ from day 7 to day 14). The HSF-dTCP and HSF-TCP scaffolds monocultured with hOBs followed the same trend as the HSF constructs, but did not show significant differences over time.

Nevertheless, the GAGs production on the HSF-dTCP constructs at day 7, was significantly higher (*p < 0.05) than that on the HSF-TCP constructs.

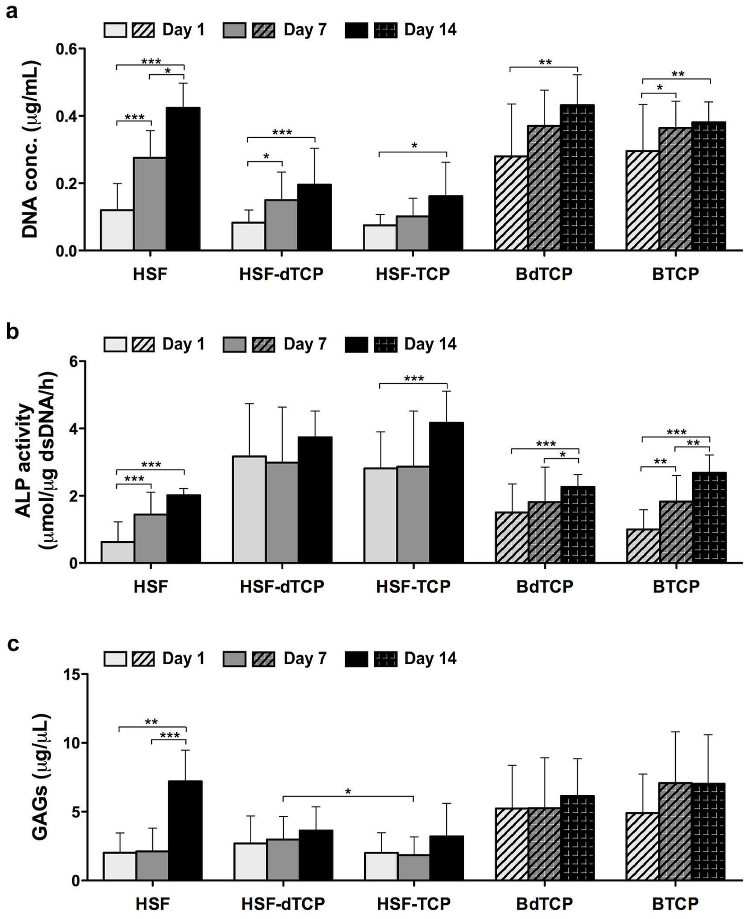

Figure 8-8. Quantification of *in vitro* osteogenesis and chondrogenesis. (a) DNA quantification, (b) normalized ALP activity against the amount of DNA, and (c) GAGs content on the BdTCP and BTCP co-cultured with hOBs and hACs for the period of 1, 7 and 14 days. Monocultures of hACs in the HSF scaffolds and hOBs in the HSF-dTCP and HSF-TCP scaffolds were used as controls.

8.4.4.3. Osteogenic and chondrogenic phenotype evaluation

Histological and immunofluorescence analysis was performed to assess the phenotypic expression and activity of the osteoblasts and chondrocytes co-cultured in the BdTCP (Figure 8-9) and BTCP (Figure 8-10) constructs. The results obtained from the H&E staining images, showed that the hOBs and hACs were able to proliferate up to 14 days of culture. At day 7 and day 14, the hACs attached to the macro-pores walls of the HSF layers formed self-aggregated clusters, whereas the hOBs spread and filled the inner porous of the

HSF-dTCP and HSF-TCP layers. The newly formed ECM was stained with Sirius red, showing after 14 days of culture a well pronounced collagen matrix deposited in the co-cultured BdTCP and BTCP scaffolds. In the HSF layers, the collagen matrix was mainly evidenced in the hACs aggregates. The GAGs deposition on the BdTCP and BTCP constructs was observed at day 14, by the positive staining for safranin-O. An increase of the ECM mineralization was observed up to 14 days of culture in the HSF-dTCP and HSF-TCP layers, as compared to the lower staining intensity observed on the HSF layers. Since the hACs tend to form thick self-aggregated clusters, the staining intensity in these clusters was considerably higher. Up to 14 days of culture, no detectable differences were observed in the type of ECM produced by the hOBs and hACs co-cultured in the BdTCP and BTCP constructs, with that produced on the corresponding monolayered control scaffolds (Figure 8-11).

The immunofluorescence images show that the hOBs cultured at the HSF-dTCP and HSF-TCP layers, and in the monolayered HSF-dTCP and HSF-TCP scaffolds, were able to express the bone-specific glycoprotein OPN over the 14 days of culture. Moreover, in the HSF cartilage-like layers and corresponding monolayered constructs a residual OPN expression was also detected. The hACs in the co-culture and monoculture systems also expressed the chondrogenic-related marker ACAN.

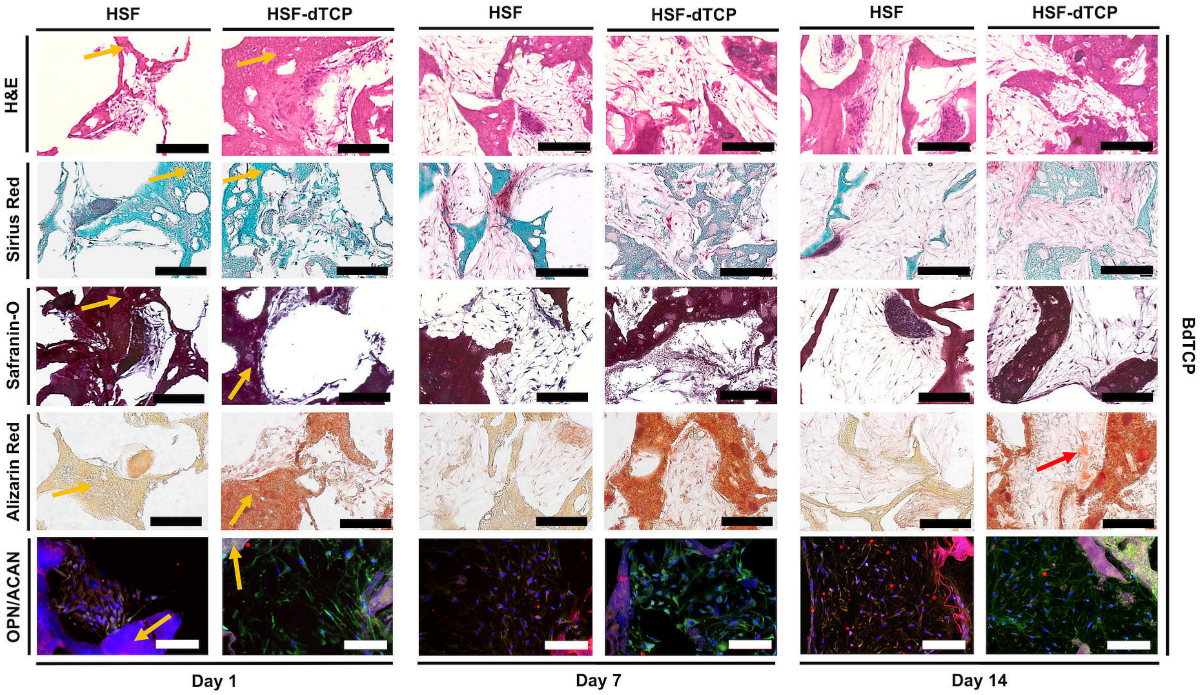

Figure 8-9. Histological and immunofluorescence analysis of the hOBs and hACs co-cultured in the BdTCP scaffolds for 1, 7 and 14 days. Standard H&E staining was used to evaluate cell distribution and ECM formation. Sirius red (red) staining was used for the visualization of collagen at the ECM, Safranin-O (red) staining was used to detect GAGs formation (scale bar: 200 µm). Representative immunofluorescence images of the osteogenic-related marker OPN

(green) and chondrogenic-related marker ACAN (red) in the co-culture system. Nuclei are stained in blue (scale bar: 100 μm). The red arrow indicates a stained area of ECM mineralization. The yellow arrows indicate the stained HSF and HSF-dTCP layers.

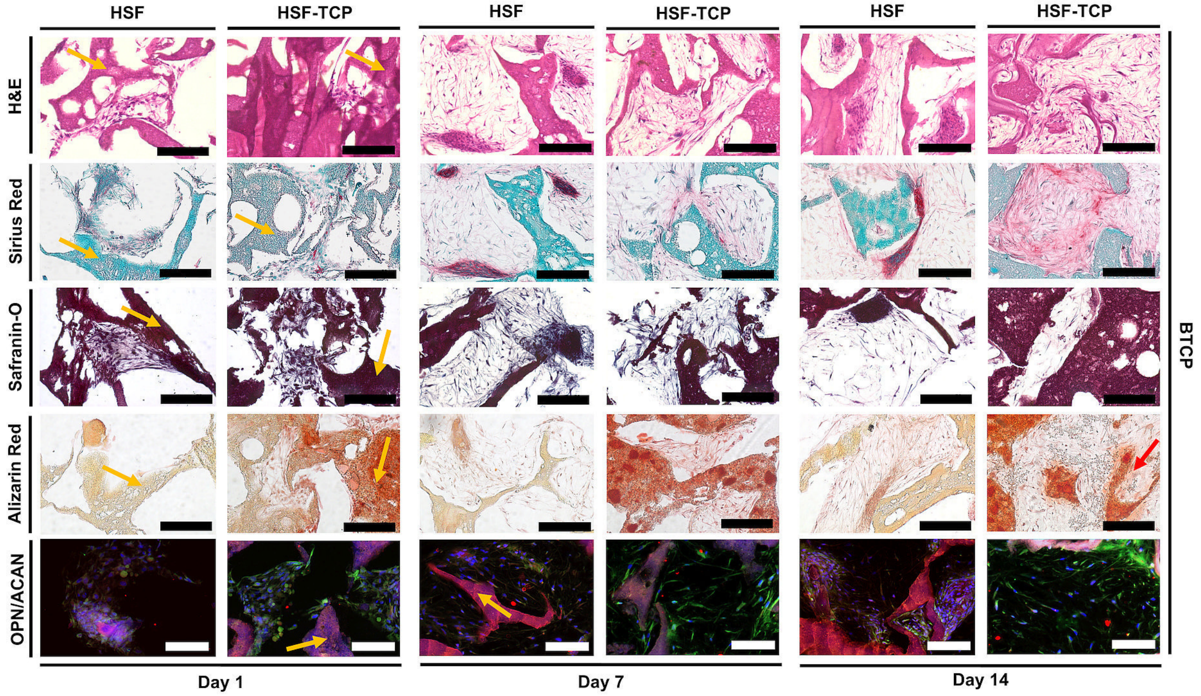

Figure 8-10. Histological and immunofluorescence analysis of the hOBs and hACs co-cultured in the BTCP scaffolds for 1, 7 and 14 days. Standard H&E staining was used to evaluate cell distribution and ECM formation. Sirius red (red) staining was used for the visualization of collagen at the ECM, Safranin-O (red) staining was used to detect GAGs formation (scale bar: 200 μm). Representative immunofluorescence images of the osteogenic-related marker OPN (green) and chondrogenic-related marker ACAN (red) in the co-culture system. Nuclei are stained in blue (scale bar: 100 μm). The red arrow indicates a stained area of ECM mineralization. The yellow arrows indicate the stained HSF and HSF-TCP layers.

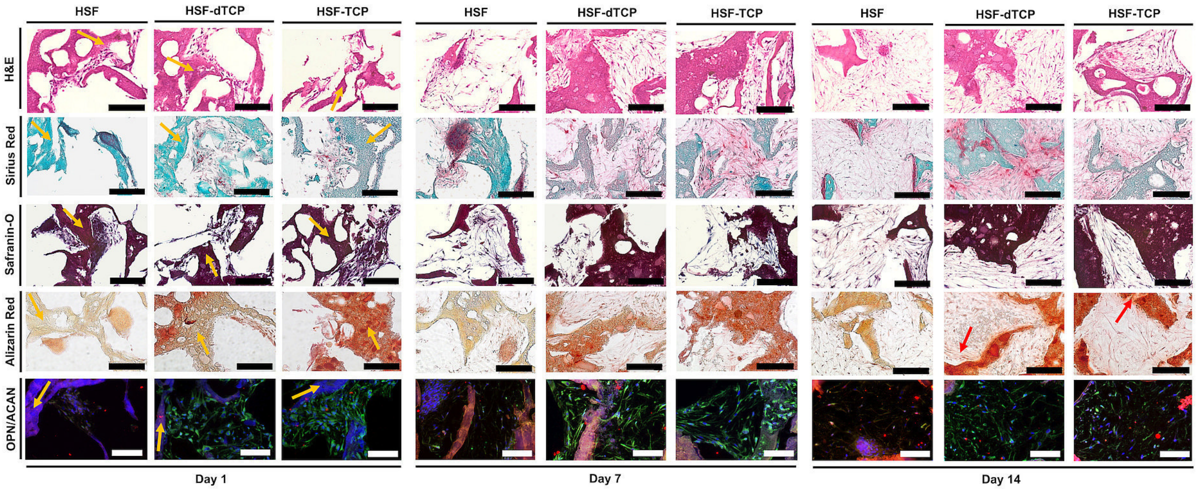

Figure 8-11. Histological and immunofluorescence analysis of the hACs monocultured in the HSF scaffolds and hOBs monocultured in the HSF-dTCP and HSF-TCP scaffolds for 1, 7 and 14 days. Standard H&E staining was used to evaluate cell distribution and ECM formation. Sirius red (red) staining was used for the visualization of collagen at the ECM, Safranin-O (red) staining was used to detect GAGs formation (scale bar: 200 μm). Representative immunofluorescence images of the osteogenic-related marker OPN (green) and chondrogenic-related marker ACAN (red) in the monoculture systems. Nuclei are stained in blue (scale bar: 100 μm). The red arrows indicate a stained areas of ECM mineralization. The yellow arrows indicate the stained HSF, HSF-dTCP and HSF-TCP scaffolds.

8.5. Discussion

The natural OC tissue consists of two distinct layers, the articular cartilage and subchondral bone, connected by a stable interface region. In general, the cartilage layer is flexible and supportive, formed by mature chondrocytes entrapped in an avascular environment composed of water, collagen type II and proteoglycans. On the other side, the subchondral bone layer is formed of several cell types, *e.g.,* osteoblasts, osteoclasts, osteocytes, and bone marrow stromal cells, involved by a vascularized environment in a bony lamella and trabeculae [36]. This complex region also contains an inorganic component of HAp and collagen type I [37]. The interface region that interconnects these two very distinct tissues is characterized by intermediate properties of both cartilage and subchondral bone tissues. Therefore, in OC TE the real challenge remains at creating monolithic and hierarchical well interconnected scaffolds that simultaneously meet the structural, mechanical, and biological requirements for chondral and subchondral bone regeneration. Different reports have proposed bilayered scaffolds for OC TE applications [9, 38, 39]. However, only few proposed a combination between high-performance SF scaffolds with nanocomposites of SF/CaP [27, 40, 41]. Yan *et al.* [25] developed porous bilayered scaffolds by fully integrating a SF layer and a SF/nanoCaP layer for OC defects regeneration, showing a spatially controllable porosity distribution through the scaffolds, and a CaP confinement to the subchondral bone-like layer. These scaffolds also supported *in vitro* cell attachment, proliferation, and rabbit bone marrow mesenchymal stromal cells (RBMSCs) osteogenic differentiation, as well as, *in vivo* cartilage regeneration in the top of SF layer, and subchondral bone ingrowth in the bottom SF/nanoCaP layer. Salt-leached SF scaffolds have shown to closely mimic the structural and mechanical complexity of tissues, such as cartilage and bone [19, 40]. Through this method, scaffolds can achieve a controlled pore size, high interconnectivity, and adjustable mechanical properties, according to the SF concentration and induced porosity. Moreover, the formation of a silk-II structure (β-sheet conformation) results in high stiffer scaffolds [34]. HRP-crosslinked SF scaffolds developed using salt-leaching and freeze-drying technologies have previously shown combined features of highly porous and mechanically stable SF scaffolds [19], with the elastic behavior of soft enzymatically crosslinked SF hydrogels [30], for cartilage regeneration purposes.

Based on our previous findings, the herein developed bilayered scaffolds resulted from interconnected HSF scaffolds and HSF-TCP composites incorporating Zn and Sr-dopants, for specific OC regeneration applications. As observed in the SEM micrographs (Figure 8-2a-f) and micro-CT analysis (Figure 8-3a-f), the BdTCP and BTCP scaffolds presented similar porous microstructure on both HSF cartilage-like layer and HSF-dTCP or HSF-TCP subchondral bone-like layers, respectively. A macro- and micro-porous structure was achieved, with interconnected structures from the top cartilage to the bottom subchondral bone-like layers. In a previous study, Li *et al.* [20] proposed a biphasic scaffold composed of SF and SF-coated Sr-hardystonite-gahnite (SHG-SF respectively for cartilage and subchondral bone-like phases, showing the formation of large pores on both cartilage (100-120 μm) and bone (400-500 μm) parts, as well as, the presence of small pores (20-40 μm) in the highly-interconnected pore walls. It is well-established that in cartilage and bone TE fields, the scaffolds should contain a wide range of pore size and interconnectivity [42]. For example, in cartilage TE, larger and interconnected pores (300-500 μm) are required to allow cell infiltration, and the formation of self-aggregated clusters and ECM, whereas smaller pores (< 50 μm) are essential to endure adequate cell adhesion and proliferation [43]. On the other side, larger pores have been reported as essential for nutrients exchange, matrix mineralization, and vascularization in bone tissue regeneration [44]. The interface region (~500 μm thick) that separates the cartilage and subchondral bone-like layers (Figure 8-2b and e) holds a significant biomechanical function in the native OC tissue by adapting to microinjuries [37]. Moreover, it creates the connection between the two OC layers, allowing that the highly-vascularized trabeculae of the subchondral bone tissue share nutrients with the adjacent articular cartilage, and at the same time anchor the collagen fibrils found in the deep zone of articular tissue [45]. EDS (Figure 8-2) and micro-CT (Figure 8-3c, f and h) analyses demonstrated the confinement of the introduced TCP powders to the interfaces on both

BdTCP and control BTCP scaffolds and respective HSF-dTCP and HSF-TCP layers. Previous studies, have shown the importance of incorporating CaPs on scaffolds performance for subchondral bone mineralization and regeneration [25, 27, 40]. Moreover, it was also reported that hydrogel-CaP composite scaffolds supported the formation of a calcified cartilage-like matrix and promoted osteointegration, as part of an OC interface TE strategy [46]. The obtained results can also be related to the substantial decrease of the scaffolds porosity (Figure 8-3g and Table 8-1), and increase of the mean wall thickness (Table 8-1) on the HSF-dTCP and HSF-TCP layers.

The mechanical properties of the scaffolds are one of the most important issues when designing scaffolds either for bone or cartilage TE purposes [42]. In case of OC TE, the mechanical properties of the reconstructive scaffolds can represent an even bigger challenge. In the native OC tissue, articular cartilage provides resistance to compressive forces at the joint, whereas the subchondral bone is responsible for withstanding most of the strength considering its larger area and lower elasticity [36]. Moreover, the mechanical properties of the articular cartilage are dependent of the zone. For example, the compressive modulus of the superficial, middle and deep zones is 0.079 MPa, 2.1 MPa and 7.75 MPa, respectively. In the case of subchondral bone, the compressive modulus is higher than that of cartilage and can reach 5.7 GPa [47]. Some studies have been producing different silk-based scaffolds with high strength and elasticity, for respectively bone and cartilage regeneration applications [19, 40]. It was shown that the wet compressive modulus of the combined bilayered structures was ~0.4 MPa, similar to that of the controls pure SF scaffolds and SF/nanoCaP scaffolds [25]. In comparison to our results, the mechanical properties of the scaffolds are enhanced due to the incorporation of the ceramic powders (ZnSr-β-TCP and β-TCP). Moreover, the compressive modulus (Figure 8-4b) and compressive strength (Figure 8-4c) of the BdTCP and BTCP scaffolds were higher than that of the corresponding monolayered control scaffolds (HSF, HSF-dTCP and HSF-TCP scaffolds), showing that the bilayered scaffolds possess stratified compressive properties due to the different mechanical properties of the cartilage and subchondral bone-like layers. These properties can closely mimic the mechanical transitions existing at the different segments of the OC tissue [1]. Interestingly, when looking at the mechanical behavior of the bilayered scaffolds, the BdTCP presented superior compressive modulus and strength than the BTCP. In fact, it have been reported that ionic-dopants (e.g., Zn and Sr) can improve the mechanical properties of the scaffolds, by means of modifying the lattice structure, microstructure, crystallinity and dissolution rate of the biomaterials [48].

Despite the mechanical properties of the bilayered scaffolds being closer to that of the native human articular cartilage tissue (1.16 MPa in the superficial articular layer) [47] and not comparable to those of the human subchondral bone (1.15 GPa) [49], different authors have demonstrated that temporary bone substitutes scaffolding should contain a compressive modulus of only few MPa [50, 51]. This should be sufficient to support the initial regenerative process, *e.g.,* withstand the hydrostatic pressures and allow cellularity for ECM ingrowth and mineralization, and not equal to the mechanical strength of the native bone tissue. It was observed that the storage modulus of the bilayered scaffolds and monolayered control scaffolds (Figure 8-4d) followed the same pattern of that determined for the static compressive modulus (Figure 8-4b). As demonstrated by Yan *et al.* [25], the BdTCP and BTCP scaffolds were able to maintain their integrity at high-frequency loading, due to the strong binding strength established between the interconnected HSF layers and HSF-dTCP or HSF-TCP layers, respectively. The high loss factor (Figure 8-4e) showed the viscoelastic nature of both BdTCP (ranging from 0.58 to 0.52) and BTCP (ranging from 0.81 to 0.75) scaffolds, confirming that the proposed scaffolds can recover from high physical loads and easily adjust to fill the OC defect site.

The degradation of the scaffolds is an important concern for all TE scenarios. Ideally, the degradation should be adjusted to follow the regenerative process of the implanted *in vivo* tissues, which forces an equilibrium between mechanical properties and degradation rate of the scaffolds [52]. When in contact to the body fluids, complex enzymatic pathways will guide the scaffolds degradation, and for that reason its *in vitro* enzymatic degradation is the best option to better predict the *in vivo* stability [53]. In this study, protease XIV degradation solutions were used based on previous studies proposing SF-based bilayered scaffolds for OC regeneration applications [25, 35]. Even though this enzyme has no activity in the human body, the response of SF to the non-specific proteolytic degradation with protease XIV will mimic the *in vivo* simultaneous activity of several ECM modulatory enzymes [35]. Our results showed that at different concentrations of protease XIV (Figure 8-5a), the BdTCP and BTCP scaffolds presented a slower degradation rate than that of the controls HSF, HSF-dTCP and HSF-TCP scaffolds. These differences can be attributed to the existence of a continuous interface region in the bilayered scaffolds, strongly integrating the two layers and hindering the proteolytic cleavage process induced by the protease XIV. Moreover, the incorporation of TCP phases into the SF polymer under enzymatic crosslinking, also made the structures less available for proteolytic degradation, especially at the highest concentration of protease XIV (2 U/mL). It is well reported in the literature that the degradation of a polymer/CaP composite depends on their physicochemical properties, such as the polymer molecular weight and level of crosslinking, CaP phase, crystallinity, and surface area, as well as, the way they were integrated into the scaffolds [54]. In a previous study by our group [25], it was observed that pure silk scaffolds presented a slightly higher weight loss profile as compared with silk-nanoCaP scaffolds, due to the dissolution of CaP. On the other hand, the combination of these two layers to form bilayered scaffolds seems to create a more complex structure with a degradation rate in between that of the controls scaffolds. The authors also observed that the bilayered silk/silk-nanoCaP scaffolds presented ~25% weight loss after 7 days in protease XIV degradation solution (0.0035 U/mL). When compared to our results, slower degradation rates were observed on the BdTCP (~10% weight loss) and BTCP (~20% weight loss) scaffolds, which can be explained by the strong covalent bonds established between the tyrosine groups in the enzymatic crosslinking process that may have hindered the β-TCP dissolution and the enzymatic degradation process [30, 31]. Moreover, the degradation profile of ~45% found on the control silk scaffolds, against the ~20% weight loss of the control HSF scaffolds also support this hypothesis.

The *in vitro* bioactivity test performed to evaluate the biomineralization of the bilayered scaffolds, showed that the HSF-dTCP (Figure 8-5bii) and HSF-TCP (Figure 8-5biv) layers were able to induce the formation of apatite-like crystals after 15 days (Figure 8-5b) and 30 days (Supplementary Figure 8-2) of soaking in a SBF solution. No influence was observed from the presence of TCP (ZnSr-β-TCP and β-TCP) powders on the HSF layers (Figure 8-5i and iii), since no crystals were formed on these layers even after 30 days of immersion. These results suggest that the proposed bilayered scaffolds can be fastly integrated into an OC defect, using the composite subchondral bone-like layers as anchor.

The importance of the bilayered 3D scaffold architectures for OC TE has been highlighted by numerous authors, stating that the interactions existing between the different cell types which compose the articular cartilage and subchondral bone tissue, can induce the diffusion of several paracrine signaling pathways that dictate the OC tissue regeneration [55]. Thus, a hOBs/hACs based co-culture method was used in this study to investigate cell behavior in the complete OC grafts, BdTCP and BTCP scaffolds. In parallel, monocultures of hACs and hOBs on the respective monolayered control scaffolds (HSF, HSF-dTCP and HSF-TCP) were used as controls (Figure 8-1b). The bilayered scaffolds showed an outstanding performance for cell seeding and proliferation, as observed from the metabolic activity (Figure 8-6) and SEM (Figure 8-7) results. On both co-culture and monoculture systems, the metabolic activity of cells increased at significant levels over the culture period, which can be explained by the chemical properties of SF, the crystalline structure of β-TCP and to the presence of ionic-dopants, as well as, by the porous structure of the scaffolds [22]. As reported somewhere, different cell behaviors can be achieved only by changing the scaffolds pore size [56, 57]. The scaffolds micro-porosity is responsible for cell attachment and spreading in the first culture periods, whereas larger pores will allow cell infiltration, proliferation and subsequent ECM formation. These reports are in good agreement with our SEM results (Figure 8-7), showing at the first culture period the hOBs and hACs adhered and spread on the scaffolds surface, and fully infiltrated the interconnected large pores at the last time-point. In addition, a significant increase of the DNA content was detected up to 14 days in both monoculture and co-culture conditions (Figure 8-8a). The obtained results also showed that the hACs monocultured on the HSF scaffolds presented similar proliferation rate, as compared to the co-cultured BdTCP and BTCP constructs. However, the monocultures of hOBs on the HSF-dTCP and HSF-TCP scaffolds showed the lowest DNA content over the culture period, suggesting that the DNA values detected on the bilayered constructs at day 14 can be attributed to the higher proliferation of the hACs in the co-culture systems. Interestingly, the ALP activity results showed an opposite behavior in all tested groups, as compared to that observed on DNA analysis (Figure 8-8b). ALP is considered an important marker of osteogenic activity being expressed by proliferating osteoblasts during *in vitro* osteogenesis [58], which is consistent to the high ALP activity levels obtained on the HSF-dTCP and HSF-TCP scaffolds monocultured with hOBs. These data can also be related to the use of the TCP (ZnSr-β-TCP and β-TCP) powders within the HSF-dTCP and HSF-TCP scaffolds, as observed on EDS (Figure 8-2c and f) and micro-CT (Figure 8-3c, f and h) analysis. Moreover, the apatite crystals formation also corroborates to this hypothesis, when these scaffolds were immersed in SBF solution (Figure 8-5bii, iv, vi and vii). The positive influence of using CaPs into silk scaffolds on the ALP activity expressed by BMSCs and human adipose-derived stem cells (hASCs) is well known [25, 27]. The amount of released GAGs by the hACs monocultured on the HSF scaffolds was significantly higher at day 14 and similar to that obtained on the co-cultured BdTCP and BTCP constructs (Figure 8-8c), following a similar tendency to that observed on DNA quantification results (Figure 8-8a).

The histological observations clearly indicated the effects of the scaffolds micro- and macro-porosity on hOBs and hACs adhesion and proliferation over the 14 days in either monoculture or co-culture systems (Figures 8-9, 8-10, and 8-11). Cells were able to attach and deeply infiltrated in the highly interconnected porous scaffolds, confirming our SEM observations (Figure 8-7). At day 1, the monocultured and co-cultured hACs were able to adhere to the pore walls, forming small aggregates. However, at day 7 and day 14 it was interesting to notice the formation of large hACs aggregates, typically formed during cartilage development [59]. An increase of the collagen deposition was also observed over the 14 days of culture in all tested groups. These results are in agreement with the literature, stating that both osteoblasts and chondrocytes cells are responsible for the collagen matrix deposition during bone and cartilage formation [60]. Consistent with the results obtained from GAGs quantification (Figure 8-8c), a positive staining for safranin-O was observed after 14 days of culturing hACs on the HSF scaffolds and layers. Moreover, the HSF-dTCP and HSF-TCP constructs and layers also showed GAGs deposition at the newly-formed matrix, which can be related to the capacity of osteoblasts for producing specific proteoglycans (decorin and biglycan) involved in the ECM formation and mineralization [61]. Jiang *et al.* [62] proposed a sequential co-culturing model using osteoblasts and chondrocytes in 3D culture showing that not only the individual chondrocytes were able to synthesize GAGs, as a GAGs matrix was formed in the co-culture system. Through the phenotypic expression of the osteogenic and chondrogenic-related markers, OPN and ACAN, it was possible to confirm that the hACs and hOBs were confined to the respective cartilage-like layer (HSF) and subchondral bone-like layers (HSF-dTCP and HSF-TCP) at the BdTCP and BTCP constructs (Figures 8-10 and 8-11). In the case of OPN, this is an important osteogenic-marker that regulates biomineralization [63]. Thus, the intense OPN expression observed on the subchondral bone-like layers of the bilayered scaffolds and corresponding monolayered composites, is in agreement with the ECM mineralization observed after 14 days of culture in the same composite structures.

Overall, the BdTCP and monolayered HSF-dTCP constructs did not show any improvements in terms of hOBs proliferation and osteogenenic activity, in comparison to the pure BTCP and monolayered HSF-TCP constructs. These results can be related to the effects of Zn and Sr ions on mesenchymal stem cells osteogenic differentiation, rather than in primary osteoblast-like cells behavior up to 14 days of culture. For example, Pina *et al.* [27] observed that the incorporation of Zn into SF/β-TCP scaffolds improved the proliferation of hASCs after 28 days of culture, while the Sr-doped scaffolds presented higher osteogenic differentiation potential, compared with the pure SF/β-TCP scaffolds. Moreover, combining Zn and Sr within the SF/β-TCP scaffolds increased osteogenic differentiation when compared to the single ionic-doped constructs.

The obtained results so far, have shown that the proposed biomaterials and combined technologies can be of great interest for producing biofunctional monolithic and hierarchical scaffolds for complex tissues regeneration, particularly for OC TE applications.

8.6. Conclusions

In this study, novel bilayered composite scaffolds made of a HRP-crosslinked SF (HSF) cartilage-like layer fully integrating HSF/ZnSr-β-TCP (HSF-dTCP) and HSF/β-TCP (HSF-TCP) subchondral bone-like layers, are proposed for OC tissue regeneration. These scaffolds presented an adequate structural integrity, as well as, controllable porosity and TCP distribution alongside the scaffolds. Superior mechanical properties were observed on the bilayered structures, with special relevance for the ionic-doped composites. The *in vitro* co-culturing of human osteoblasts (hOBs) and human articular chondrocytes (hACs), showed that cells were able to adhere, proliferate, and produce ECM in the bilayered structures. The osteogenic activity on the HSF-dTCP and HSF-TCP layers was represented by the formation of mineralized matrix, whereas the chondrogenic inducement at the HSF porous layers was characterized by GAGs deposition. The immunodetection of osteogenic and chondrogenic-related markers confirmed the confinement of the hACs and hOBs to the respective cartilage and subchondral bone-like layers of the bilayered scaffolds. Although a complementary *in vivo* evaluation is necessary to fully validate these structures, and specifically assess the welfare of the ionic presence, the physicochemical and biological properties observed suggest that these monolithic and hierarchical composite scaffolds are encouraging candidates for OC tissue repair and regeneration.

8.7. Supplementary information

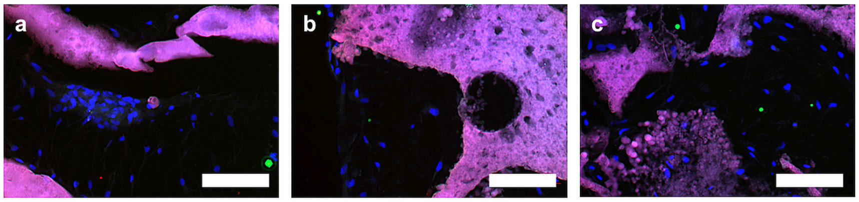

Supplementary Figure 8-1. Representative negative controls for immunofluorescence analysis of the osteogenic-related marker OPN (green) and chondrogenic-related marker ACAN (red) in the (a) HSF, (b) HSF-dTCP and (c) HSF-TCP constructs (scale bar: 100 μm).

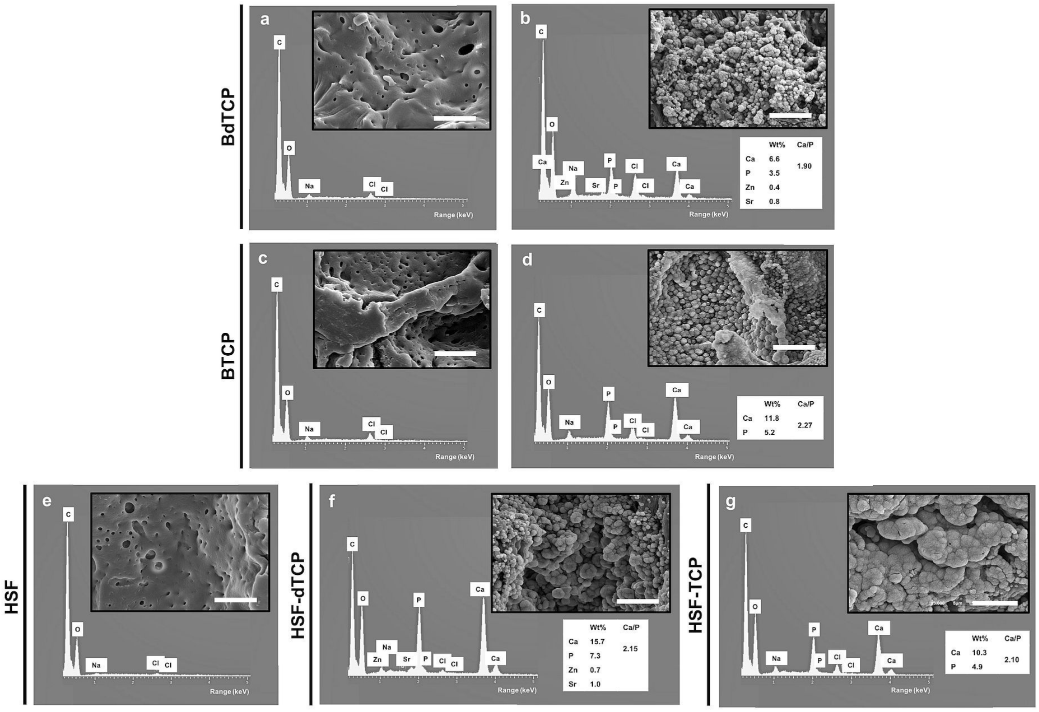

Supplementary Figure 8-2. *In vitro* bioactivity evaluation of the BdTCP and BTCP scaffolds. SEM micrographs (inset; scale bar: 10 μm) and EDS elemental spectra with the ionic elements and Ca/P ratios determined at the (a, c) HSF layers, (b) HSF-dTCP layer and (d) HSF-TCP layer of the BdTCP and BTCP scaffolds, after 30 days of immersion in SBF solution. (e) HSF scaffolds, (f) HSF-dTCP scaffolds and (g) HSF-TCP scaffolds were also evaluated.

8.8. References

[1] J. Yoo, et al., Treatment of Osteochondral Lesions of the Talus in Athletes, The Korean Journal of Sports Medicine 35(2) (2017) 77-85.

[2] C. Dall'Oca, et al., Current concepts in treatment of early knee osteoarthritis and osteochondral lesions; the role of biological augmentations, Acta Bio Medica Atenei Parmensis 88(4-S) (2017) 5-10.

[3] Z. Meng, R. Huang, Topical treatment of degenerative knee osteoarthritis, The American Journal of the Medical Sciences (2017).

[4] J. Feinglass, et al., Chronic joint symptoms and prior arthritis diagnosis in community surveys: implications for arthritis prevalence estimates, Public Health Reports (2016).

[5] W. Wei, et al., Assessing the effect of football play on knee articular cartilage using delayed gadolinium-enhanced MRI of cartilage (dGEMRIC), Magnetic resonance imaging 39 (2017) 149-156.

[6] D.L. Richter, et al., Knee articular cartilage repair and restoration techniques: a review of the literature, Sports health 8(2) (2016) 153-160.

[7] R.M. Frank, et al., Osteochondral Allograft Transplantation of the Knee: Analysis of Failures at 5 Years, The American journal of sports medicine 45(4) (2017) 864-874.

[8] F. Perdisa, et al., Cell-Free Scaffolds for the Treatment of Chondral and Osteochondral Lesions, Bio-orthopaedics, Springer2017, pp. 139-149.

[9] J.M. Oliveira, et al., Novel hydroxyapatite/chitosan bilayered scaffold for osteochondral tissue-engineering applications: Scaffold design and its performance when seeded with goat bone marrow stromal cells, Biomaterials 27(36) (2006) 6123-6137.

[10] A.M. Yousefi, et al., Current strategies in multiphasic scaffold design for osteochondral tissue engineering: a review, Journal of biomedical materials research Part A 103(7) (2015) 2460-2481.

[11] W. Zhang, et al., The promotion of osteochondral repair by combined intra-articular injection of parathyroid hormone-related protein and implantation of a bi-layer collagen-silk scaffold, Biomaterials 34(25) (2013) 6046-6057.

[12] X. Guo, et al., In vitro generation of an osteochondral construct using injectable hydrogel composites encapsulating rabbit marrow mesenchymal stem cells, Biomaterials 30(14) (2009) 2741-2752.

[13] M. Tamaddon, J. Czernuszka, The need for hierarchical scaffolds in bone tissue engineering, Hard Tissue 2 (2013) 1-8.

[14] E. Kon, et al., Acellular matrix–based cartilage regeneration techniques for osteochondral repair, Operative Techniques in Orthopaedics 24(1) (2014) 14-18.

[15] G. Filardo, et al., Treatment of knee osteochondritis dissecans with a cell-free biomimetic osteochondral scaffold: clinical and imaging evaluation at 2-year follow-up, The American journal of sports medicine 41(8) (2013) 1786-1793.

[16] J.E. Bekkers, et al., Articular cartilage evaluation after TruFit plug implantation analyzed by delayed gadolinium-enhanced MRI of cartilage (dGEMRIC), The American journal of sports medicine 41(6) (2013) 1290-1295.

[17] X. Li, et al., Biomimetic biphasic scaffolds for osteochondral defect repair, Regenerative biomaterials 2(3) (2015) 221-228.

[18] V.P. Ribeiro, et al., Silk-based anisotropical 3D biotextiles for bone regeneration, Biomaterials 123 (2017) 92-106.

[19] L.-P. Yan, et al., Macro/microporous silk fibroin scaffolds with potential for articular cartilage and meniscus tissue engineering applications, Acta biomaterialia 8(1) (2012) 289-301.

[20] J.J. Li, et al., A biphasic scaffold based on silk and bioactive ceramic with stratified properties for osteochondral tissue regeneration, Journal of Materials Chemistry B 3(26) (2015) 5361-5376.

[21] Y.N. Zhao, et al., Effects of Pore Size on the Osteoconductivity and Mechanical Properties of Calcium Phosphate Cement in a Rabbit Model, Artificial organs 41(2) (2017) 199-204.

[22] M. Farokhi, et al., Silk fibroin/hydroxyapatite composites for bone tissue engineering, Biotechnol Adv (2017).

[23] A. Ogose, et al., Histological examination of β-tricalcium phosphate graft in human femur, Journal of Biomedical Materials Research Part A 63(5) (2002) 601-604.

[24] Y. Takahashi, et al., Osteogenic differentiation of mesenchymal stem cells in biodegradable sponges composed of gelatin and β-tricalcium phosphate, Biomaterials 26(17) (2005) 3587-3596.

[25] L.-P. Yan, et al., Bilayered silk/silk-nanoCaP scaffolds for osteochondral tissue engineering: in vitro and in vivo assessment of biological performance, Acta biomaterialia 12 (2015) 227-241.

[26] L. Yanoso-Scholl, et al., Evaluation of dense polylactic acid/beta-tricalcium phosphate scaffolds for bone tissue engineering, Journal of Biomedical Materials Research Part A 95(3) (2010) 717-726.

[27] S. Pina, et al., Biofunctional Ionic-Doped Calcium Phosphates: Silk Fibroin Composites for Bone Tissue Engineering Scaffolding, Cells Tissues Organs 204 (2017).

[28] J.A. Hunt, et al., Hydrogels for tissue engineering and regenerative medicine, Journal of Materials Chemistry B 2(33) (2014) 5319-5338.

[29] J. Liao, et al., The fabrication of biomimetic biphasic CAN-PAC hydrogel with a seamless interfacial layer applied in osteochondral defect repair, Bone research 5 (2017) 17018.

[30] L.-P. Yan, et al., Tumor growth suppression induced by biomimetic silk fibroin hydrogels, Scientific reports 6 (2016) 31037.

[31] L.P. Yan, et al., Core-shell silk hydrogels with spatially tuned conformations as drug-delivery system, Journal of tissue engineering and regenerative medicine (2016).

[32] R.L. Horan, et al., In vitro degradation of silk fibroin, Biomaterials 26(17) (2005) 3385-3393.

[33] A.C. Tas, Synthesis of biomimetic Ca-hydroxyapatite powders at 37 C in synthetic body fluids, Biomaterials 21(14) (2000) 1429-1438.

[34] U.-J. Kim, et al., Three-dimensional aqueous-derived biomaterial scaffolds from silk fibroin, Biomaterials 26(15) (2005) 2775-2785.

[35] P.J. Reardon, et al., Mimicking Hierarchical Complexity of the Osteochondral Interface Using Electrospun Silk–Bioactive Glass Composites, ACS Applied Materials & Interfaces 9(9) (2017) 8000-8013.

[36] L.-P. Yan, et al., Current concepts and challenges in osteochondral tissue engineering and regenerative medicine, ACS Biomaterials Science & Engineering 1(4) (2015) 183-200.

[37] H. Madry, et al., The basic science of the subchondral bone, Knee surgery, sports traumatology, arthroscopy 18(4) (2010) 419-433.

[38] S. Zhang, et al., Bi-layer collagen/microporous electrospun nanofiber scaffold improves the osteochondral regeneration, Acta biomaterialia 9(7) (2013) 7236-7247.

[39] D.R. Pereira, et al., Gellan gum-based hydrogel bilayered scaffolds for osteochondral tissue engineering, Key Engineering Materials, Trans Tech Publ, 2014, pp. 255-260.

[40] L.-P. Yan, et al., Bioactive macro/micro porous silk fibroin/nano-sized calcium phosphate scaffolds with potential for bone-tissue-engineering applications, Nanomedicine 8(3) (2013) 359-378.

[41] A. Oliveira, et al., Controlled mineralization of nature-inspired silk fibroin/hydroxyapatite hybrid bioactive scaffolds for bone tissue engineering applications, 20th European Conference on Biomaterials. Nantes, France.

[42] D. Puppi, et al., Polymeric materials for bone and cartilage repair, Progress in Polymer Science 35(4) (2010) 403-440.

[43] D.J. Griffon, et al., Chitosan scaffolds: interconnective pore size and cartilage engineering, Acta biomaterialia 2(3) (2006) 313-320.

[44] R. Nazarov, et al., Porous 3-D scaffolds from regenerated silk fibroin, Biomacromolecules 5(3) (2004) 718-726.

[45] P.J. Yang, J.S. Temenoff, Engineering orthopedic tissue interfaces, Tissue Engineering Part B: Reviews 15(2) (2009) 127-141.

[46] N.T. Khanarian, et al., A hydrogel-mineral composite scaffold for osteochondral interface tissue engineering, Tissue Engineering Part A 18(5-6) (2011) 533-545.

[47] S. Chen, et al., Depth-dependent compressive properties of normal aged human femoral head articular cartilage: relationship to fixed charge density, Osteoarthritis and Cartilage 9(6) (2001) 561-569.

[48] S. Bose, et al., Trace element doping in calcium phosphate ceramics to Understand osteogenesis and angiogenesis, Trends in biotechnology 31(10) (2013).

[49] K. Choi, et al., The elastic moduli of human subchondral, trabecular, and cortical bone tissue and the size-dependency of cortical bone modulus, Journal of biomechanics 23(11) (1990) 1103-1113.

[50] J.J. Blaker, et al., Mechanical properties of highly porous PDLLA/Bioglass® composite foams as scaffolds for bone tissue engineering, Acta biomaterialia 1(6) (2005) 643-652.

[51] R. Zhang, P.X. Ma, Poly (α-hydroxyl acids)/hydroxyapatite porous composites for bone-tissue engineering. I. Preparation and morphology, (1999).

[52] E.A. Makris, et al., Repair and tissue engineering techniques for articular cartilage, Nature Reviews Rheumatology 11(1) (2015) 21-34.

[53] L.R. Almeida, et al., New biotextiles for tissue engineering: Development, characterization and in vitro cellular viability, Acta biomaterialia 9(9) (2013) 8167-8181.

[54] M. Abadi, et al., Synthesis of nano β-TCP and the effects on the mechanical and biological properties of β-TCP/HDPE/UHMWPE nanocomposites, Polymer Composites 31(10) (2010) 1745-1753.

[55] T.M. O'Shea, X. Miao, Bilayered scaffolds for osteochondral tissue engineering, Tissue Engineering Part B: Reviews 14(4) (2008) 447-464.

[56] C.M. Murphy, et al., The effect of mean pore size on cell attachment, proliferation and migration in collagen–glycosaminoglycan scaffolds for bone tissue engineering, Biomaterials 31(3) (2010) 461-466.

[57] S.-M. Lien, et al., Effect of pore size on ECM secretion and cell growth in gelatin scaffold for articular cartilage tissue engineering, Acta Biomaterialia 5(2) (2009) 670-679.

[58] N. Parekh, et al., In vitro study of novel microparticle based silk fibroin scaffold with osteoblast-like cells for load-bearing osteo-regenerative applications, RSC Advances 7(43) (2017) 26551-26558.

[59] C.R. Correia, et al., Chitosan scaffolds containing hyaluronic acid for cartilage tissue engineering, Tissue Engineering Part C: Methods 17(7) (2011) 717-730.

[60] P. Gómez-Picos, B.F. Eames, On the evolutionary relationship between chondrocytes and osteoblasts, Frontiers in genetics 6 (2015).

[61] R. Cancedda, Cartilage and bone extracellular matrix, Current pharmaceutical design 15(12) (2009) 1334-1348.

[62] J. Jiang, et al., Co-culture of osteoblasts and chondrocytes modulates cellular differentiation in vitro, Biochemical and biophysical research communications 338(2) (2005) 762-770.

[63] A. Martins, et al., The influence of patterned nanofiber meshes on human mesenchymal stem cell osteogenesis, Macromolecular bioscience 11(7) (2011) 978-987.

SECTION IV

EXPERIMENTAL STUDIES

CHAPTER 9.

Rapidly Responsive Silk Fibroin Hydrogels as an Artificial Matrix for the Programmed Tumor Cells Death

CHAPTER 9.

Rapidly responsive silk fibroin hydrogels as an artificial matrix for the programmed tumor cells death*

9.1. Abstract

Timely and spatially-regulated injectable hydrogels, able to suppress growing tumors in response to conformational transitions of proteins, are of great interest in cancer research and treatment. Herein, we report rapidly responsive silk fibroin (SF) hydrogels formed by a horseradish peroxidase (HRP) crosslinking reaction at physiological conditions, and demonstrate their use as an artificial biomimetic three-dimensional (3D) matrix. The proposed SF hydrogels presented a viscoelastic nature of injectable hydrogels and spontaneous conformational changes from random coil to β-sheet conformation under physiological conditions. A human neuronal glioblastoma (U251) cell line was used for screening cell encapsulation and *in vitro* evaluation within the SF hydrogels. The transparent random coil SF hydrogels promoted cell viability and proliferation up to 10 days of culturing, while the crystalline SF hydrogels converted into β-sheet structure induced the formation of TUNEL-positive apoptotic cells. Therefore, this work provides a powerful tool for the investigation of the microenvironment on the programed tumor cells death, by using rapidly responsive SF hydrogels as 3D *in vitro* tumor models.

*This chapter is based on the following publication:

Ribeiro VP, Silva-Correia J, Gonçalves G, Pina S, Radhouani H**,** Montonen T**,** Hyttinen J, Roy A, Oliveira AL, Reis RL, Oliveira JM. Rapidly responsive silk fibroin hydrogels as an artificial matrix for the programmed tumor cells death. 2018, Accepted in PLOS ONE Journal.

9.2. Introduction

Hydrogels are hydrophilic networks with high capacity to absorb and retain high quantities of water, while keeping its original structure [1]. Smart hydrogels, or stimuli-responsive hydrogels, are more appealing for cell encapsulation in a three-dimensional (3D) microenvironment, drug delivery systems and tissue engineering (TE) scaffolding. In fact, the possibility to creating such smart hydrogels capable of harboring cell ingrowth/organization and at the same time promoting the delivery of biologically active molecules due to the rapid response to environmental stimuli and high elasticity, was a great achievement in the biomedical field [2]. In the last years, several physical and chemical crosslinking methods have been developed to produce artificial hydrogel matrices temporally and spatially regulated [3]. The production of injectable hydrogels for minimally invasive clinical applications has been receiving special attention [4]. The *in situ* formation of these hydrogels is based on the aqueous mixture of polymer solutions with bioactive agents that when injected into the body will form a desired hydrogel shape into the defect site, even oddly shaped ones. The precursor hydrogel solutions can also be combined with cells, drugs and growth factors, and subsequently injected into the application site [5]. Recently, an increasing interest has been devoted to enzymatically crosslinked hydrogels to be applied as injectable matrices for the generation of functional tissue substitutes able to maintain cell phenotype of the native tissue, which is highly important for tissues like cartilage [6]. These *in situ* forming hydrogels are produced through mild reactions that in many cases are catalyzed by enzymes naturally existing in our body [7]. The specificity of these substrates avoids toxic effects that are often observed on organic solvents or photo-initiators mediated reactions [8]. Another major advantage of the enzymatic crosslinking reactions is that they can be easily applied with natural polymers that hardly support more adverse chemical or physical reactions. Moreover, the polymerization reaction can be controlled by modulating the enzyme activity, affecting the gelation rate and the hydrogels mechanical properties [8, 9].

Hydrogels derived from natural polymers have been attracting special attention since they can more closely simulate the natural extracellular matrix (ECM) environment. Some of the most studied natural hydrogels include alginate, fibrin, collagens, gelatin, chitosan and hyaluronic acid [10]. Silk fibroin (SF) derived from *Bombyx mori* silkworm is a biodegradable and biocompatible natural material that has been extensively studied for TE applications using different forms, including as membranes [11], films [12], fibers [13, 14], sponges [15] and textiles [16]. SF hydrogels have been developed by the protein conformation transition from amorphous to β-sheet induced by physical or chemical crosslinking methods involving external stimuli and long gelation times [17, 18]. In this sense, an enzyme mediated crosslinking may be the ideal method to produce fast-gelled SF-based injectable hydrogels at physiologic conditions. Our group proposed SF hydrogels preparation via a horseradish peroxidase (HRP)-mediated crosslinking in physiological conditions [19-21]. In their first systematic study, the authors observed that varied concentrations of SF and HRP/hydrogen peroxide (H_2O_2) crosslinking solutions lead to different physicochemical properties of the SF hydrogels [19]. These enzymatic crosslinking approach has shown great potential for preparing injectable hydrogels from polymers containing or functionalized with phenol group-containing molecules, including tyrosine, tyramine or aminophenol [8]. Considering that SF contains 5.3% tyrosine molecules with the required phenol groups [22], such approach was explored to produce *in situ* fast-formed hydrogels (Supplementary Figure 9-1) [23-25]. These SF hydrogels can exhibit a spontaneous conformation change under physiological conditions. Therefore, understand if and how the protein conformation changes affect cell behavior and tissue ingrowth was another major concern in applying this enzymatic crosslinking mechanism.

The 3D cell culture plays an important role in tumor biology since it enables to create an *in vivo* like microenvironment. Among the existing tools of experimental cancer research, spheroids represent an advanced *in vitro* model compared to the standard 2D cell culture, and less invasive as compared to the animal tumor models [26]. At the same time, the 3D spheroids can be expensive, time consuming and hard to obtain in more complex tumor-like model approaches [27]. Recently, cancer cell culture on 3D platforms have been attracting much attention. The use of 3D matrices has shown to closely mimic the natural tumor ECM, allowing cells to grow and show similar properties to those of cells growing under physiological conditions. In the literature, biomimetic scaffolds made of branched hollow silica microfibers were proposed to culture cancer cells in a 3D environment [28], showing that the proposed scaffolds mimic the fibrous ECM of real tumors and allowed cells to form tumor-like multicellular spheroids *in vitro* and promote tumor growth *in vivo*. Macro-porous polymeric scaffolds of nanofibrous bacterial cellulose have also been successfully proposed as *in vitro* models for the culture of breast cancer cells [29].

Among the different 3D platforms established for cancer therapy studies, hydrogels demonstrate some peculiarities in terms of response to therapeutic agents [30, 31]. For example, microfluidic 3D hydrogel models were proposed to assess anti-cancer drugs interactions for bone cancer research and therapy [32]. Previous studies, have also shown that hydrogels can be effective in studies of tumor-host interactions that regulate tumor formation and progression [33, 34]. Using a different approach, SF-based hydrogels were proposed for the controlled delivery of plasmid DNA for specific cancer gene therapy applications [35]. Another reason that promotes the use of hydrogel systems for cancer research is because they can be applied in a minimally invasive manner and over a wide range of temporal profiles. The injectable *in situ* crosslinked hydrogels ensure the localized and painless administration of cytotoxic drugs that are usually applied systemically in conventional chemotherapy, producing generalized side effects [36]. For example, in different studies anticancer-loaded injectable hydrogels have been tested as platform for the local delivering of chemotherapeutic drugs after glioblastoma resection, that is the most common, aggressive and inaccessible primary brain tumor in adults [37]. Considering the suitable properties of SF as a natural polymer platform and its applicability for producing injectable and non-toxic hydrogels, this would be an advantageous model system for cancer therapy applications.

Herein, we deeply investigate the conformational transitions of rapidly responsive SF hydrogels from random coil to β-sheet and its potential use as a biomimetic matrix for the programmed tumor cells death in 3D *in vitro* tumor models*.* An enzyme-mediated crosslinking method using HRP and H_2O_2 was used to produce in a few minutes *in situ* formed SF hydrogels at physiological conditions [20] (Supplementary Figure 9-1 and 9-2a). The spontaneous β-sheet conformation transition on the protein-based hydrogels was morphological and chemically investigated at multi-scale, and the rheological properties determined. We further explored the *in vitro* cell encapsulation within the proposed hydrogels. A human neuronal glioblastoma (U251) cell line was used to evaluate how the cells respond to the protein conformational changes, up to 14 days of culturing (Supplementary Figure 9-2b,c).

9.3. Materials and Methods

9.3.1. Materials

Silk derived from the silkworm *Bombyx mori* in the form of coccons was provided by the Portuguese Association of Parents and Friends of Mentally Disabled Citizens (APPACDM, Castelo Branco, Portugal). All reagents were purchased from Sigma-Aldrich (St. Louis, MO, USA) unless otherwise stated.

9.3.2. Preparation of silk fibroin aqueous solution and hydrogels

Purified silk fibroin (SF) was prepared by removing the glue-like protein sericine from the cocoons in a 0.02 M boiling sodium carbonate solution for 1 hour, followed by rising with distilled water in order to fully remove the degumming solution [16]. A 9.3 M lithium bromide solution was used to dissolve the purified SF for 1 hour at 70°C and dialyzed in distilled water for 48 hours using the benzoylated dialysis tubing (MWCO: 2 kDa). In the last 12 hours, SF was dialyzed in phosphate buffer saline solution (PBS, without calcium or magnesium ions) and then concentrated against a 20 wt.% poly(ethylene glycol) solution for at least 6 hours. The final concentration of SF was determined by measuring the dry weight of the SF solution placed in the oven at 70°C overnight. Meanwhile, the prepared SF solution was stored at 4°C until further use.

SF hydrogels were prepared according to the procedure described by Yan *et al.* [20]. Briefly, the stored SF solution was diluted to 16 wt.% in PBS and combined with horseradish peroxidase solution (HRP type VI, 0.84 mg/mL) and hydrogen peroxide solution (H_2O_2, 0.36 wt.%; Panreac, Barcelona, Spain), both also prepared in PBS. A mixture of 1 mL SF solution, 100 µL HRP solution and 65 µL H_2O_2 solution (1/0.52‰/1.45‰) was prepared in a 1.5 mL centrifuge tube (Eppendorf, Hamburg, Germany), and warmed in a water bath of 37°C. This formulation was chosen after some optimization process [20]. SF hydrogels were prepared by the deposition of 100 µL of mixture in tissue culture polystyrene (TCPs) coverslips (22 mm diameter, Sarstedt, Nümbrecht, Germany), unless otherwise mentioned, followed by the complete gelation in the oven at 37°C. The prepared hydrogel discs were used for further characterization tests performed after 1, 3, 7, 10 and 14 days of hydrogels formation.

9.3.3. Structural analysis of the SF hydrogels

9.3.3.1. Transmission electron microscopy

Transmission electron microscopy (TEM) was used to evaluate the natural ability of SF to form β-sheet fibrils. SF hydrogel discs were contrasted through negative staining using 2% uranyl acetate for 5 seconds. TEM images were acquired using a JEOL JEM 1400 TEM (Tokyo, Japan) and digitally recorded using a CCD digital camera Orious 1100W Tokyo, Japan.

9.3.3.2. Thioflavin T staining

The qualitative evidence of the β-sheet structure on SF hydrogels was tested using the dye thioflavin T. A 1% (w/v) thioflavin T solution was used to stain the SF hydrogels for 10 minutes followed by rinse with 70% ethanol solution and then washed with distilled water three times. Stained samples were observed under transmitted and fluorescence microscopy (ex/em 495/515 nm) using a transmitted and reflected light microscope (Axio Imager Z1m, Zeiss, Jena, Gernamy). Images were acquired using the digital cameras AxioCam MRc5 or MR3 (Zeiss, Jena, Germany), respectively, connected to the Zen microscope processing software (Zeiss, Jena, Germany).

9.3.4. Physicochemical characterization of the SF hydrogels

9.3.4.1. X-ray diffraction

The qualitative analysis of crystalline phases presented on the SF hydrogels was performed by X-ray diffraction (XRD) using a high-resolution Bragg–Brentano diffractometer (Bruker D8 Advance DaVinci, Karlsruhe, Germany) equipped with CuKα radiation (λ = 1.5418 Å), produced at 40 kV and 40 mA. SF hydrogel discs were prepared by adding 100µL of the SF/HRP/H_2O_2 mixture in polydimethylsiloxane (PDMS;

Sylgard 184 Silicone Elastomer Kit, Dow Corning, Belgium) silicone molds (8 mm diameter and 2 mm height). Data sets were collected in the 2θ range of 10–50° with a step size of 0.02° and 1s for each step. XRD measurements were repeated three times independently.

9.3.4.2. Fourier transform infrared spectroscopy

The chemical composition and structural conformation of the SF hydrogels were analyzed by Fourier transform infrared (FTIR) spectroscopy (Perkin-Elmer 1600 series equipment, CA, USA) under an attenuated total reflectance (ATR) model (IRPrestige-21, Shimadzu, Japan). SF hydrogel discs were prepared as described above. All spectra were obtained between 4600 to 800 cm^{-1} at a 4 cm^{-1} resolution with 50 scans. Each specimen was examined for at least 3 times and PBS was used as background.

9.3.4.3. Atomic force microscopy and infrared spectroscopy

The chemical characterization of the SF hydrogels was also performed combining atomic force microscopy (AFM) and IR spectroscopy at a nanoscale spatial resolution using a Resonance enhanced mode on a NanoIR-2 system by Anasys Instruments (CA, USA), equipped with a Quantum Cascade Laser (QCL) as the IR source. Samples were prepared by spin-coating (Spin Coater Model WS-650-23, Laurell Technologies, PA, USA) ZnS sampling flat substrates (Anasys Instruments, CA, USA) with the SF/HRP/H_2O_2 mixture. The spectra were acquired in a 1000-1800 cm^{-1} range with a spectral resolution of 2 cm^{-1}. Multiple spectra were acquired for each sample, averaged and smoothed using Savitzky-Golay filter.

9.3.4.4. Rheological properties

Rheological analysis was performed using a Kinexus pro+ rheometer (Malvern Instruments, UK), using the acquisition software rSpace (Malvern Instruments, UK). For the oscillatory experiments the measuring system was equipped with stainless steel (316 grade) parallel plates: an upper measurement geometry plate (8 mm diameter) and a lower pedestal (20 mm diameter) with roughened finish. Frequency sweep experiments were performed using SF hydrogel discs prepared in silicone molds (8 mm diameter and 2 mm height), as described above. The measurements were obtained by plot the frequency (Hz) as function of modulus (Pa) and with a predefined shear strain (0.53%). Temperature and time sweep experiments were performed to the SF/HRP/H_2O_2 mixture, using a large upper geometry plate (20 mm diameter) and the oscillatory experiments were performed at 1 Hz of frequency, 0.53% of shear strain and during 100 minutes (6000 seconds). The temperature sweep curve was obtained for the range of 25°C to 45°C and the time sweep curve with a fixed temperature of 37°C. For the rotational experiments the measuring system was equipped with an upper measurement geometry cone (40 mm diameter and 4° angle). Shear viscosity and shear stress were determined for the SF/HRP/H_2O_2 mixture, as a function of the shear rate (0.01 s^{-1} to 100 s^{-1}). These experiments were performed at 37°C and all plots are the average of at least 3 samples.

9.3.5. Cell culture and encapsulation in the SF hydrogels

9.3.5.1. U251 glioma cell line culture

Human neuronal glioblastoma (U251) cell line was generously donated by Prof. Joseph Costello (California University, Neurosurgery Department, San Francisco, USA) and further provided by Prof. Rui M. Reis (Life and Health Science Research Institute, University of Minho, ICVS/3B's – PT Government Associate Laboratory, Portugal). All experiments and protocols related to U251 cell line were approved by the Ethics Committee of University of Minho. U251 cell line was expanded in Dulbecco's modified Eagle's medium (DMEM) with phenol red, supplemented with 10% fetal bovine serum (FBS; Life Technologies, Carlsbad, CA, USA) and 1% antibiotic–antimycotic (Life Technologies, Carlsbad, CA, USA). Cells were cultured until confluence in a CO_2 incubator with an atmosphere of 5% CO_2 at 37°C, and the culture medium was changed every 2-3 days.

9.3.5.2. Hydrogel encapsulation of U251 cells

A mixture of 1 mL SF solution, 100 µL HRP solution and 65 µL H_2O_2 solution, was warmed in a water bath (37°C) for about 6 minutes. Then, 1 mL of the warmed mixture was homogeneously mixed with a U251 cell pellet containing 1×10^6 cells and 100 µL of cell suspension were transferred into TCPs coverslips (22 mm diameter) in a 12-well suspension cell culture plate (Corning Incorporated, Life Sciences, NC, USA), unless otherwise mentioned. The plate was then incubated for 15 minutes at 37°C in the CO_2 incubator, to complete gelation. After the gel formation, 3 mL of basal DMEM medium were added to each well and the culture medium was changed every 2 days. Samples were collected for analysis at day 1, 7, 10 and 14.

9.3.6. Cell viability and proliferation in the SF hydrogels

9.3.6.1. ATP bioluminescence assay

Cell viability was assessed using the CellTiter-Glo® Luminescent Cell Viability Assay (Promega, WI, USA). The cell-laden hydrogels were incubated in a mixture consisting of serum-free cell culture medium and CellTiter-Glo® Reagent in a 1:1 ratio, for 30 minutes at room temperature (RT). The emitted luminescence was detected in a microplate reader (Synergy HT, BioTek Instruments, Winooski, VT, USA) using a sensitivity of 120. The ATP concentration for each sample was calculated according to a standard curve prepared with concentrations ranging between 0 and 2 μmol/L, relating quantity of ATP and luminescence intensity. Hydrogels without cells were used as control.

9.3.6.2. DNA quantification

Cell proliferation was evaluated using the Quant-iT® Pico-Green dsDNA Assay Kit (Life Technologies, Carlsbad, CA, USA), according to the manufacturer's instructions. The cell-laden hydrogels were incubated at 70°C for 30 minutes and kept in 1 mL of ultrapure water at –80°C until further analysis. Before analysis, samples were thawed at RT and sonicated for 1 hour at 37°C to induce complete membrane lysis. Supernatant fluorescence was measured in a microplate reader (ex/em 485/528 nm). The DNA concentration for each hydrogel was calculated using a standard curve with concentrations ranging from 0 to 2 μg/mL, relating quantity of DNA and fluorescence intensity. Hydrogels without cells were used as control.

9.3.6.3. Live/Dead staining

A Calcein AM and propidium iodide (PI; Life Technologies, Carlsbad, CA, USA) staining was performed to confirm the viability of the encapsulated cancer cells. The cell-laden hydrogels were incubated in 1 mL PBS supplemented with 1 μg Calcein AM and 5 μg PI, for 10 minutes at 37°C in the CO_2 incubator. Samples were washed with PBS and observed under fluorescence microscopy (Calcein AM (green): ex/em 495/515 nm; PI (red): ex/em 495/635 nm) in a transmitted and reflected light microscope. Images were acquired using the digital camera MR3 connected to the respective Zen microscope software.

9.3.6.4. TUNEL assay

An *in situ* Cell Death Detection Kit, Fluorescein (Roche, Basel, Switzerland) was used in cell-laden hydrogels and sections from the cell-laden hydrogels (3.5 μm thick) to detect apoptotic cells, based on Terminal deoxynucleotidyl transferase dUTP nick end labeling (TUNEL) reaction and according to the manufacturer's instructions. Cell-laden hydrogels were fixed in 10% formalin for 1 hour at RT and permeabilized with 0.1% (v/v) of Triton X-100/0.1% (w/v) of sodium citrate (Fisher Scientific, NJ, USA). The sections from the cell-laden hydrogels were after paraffin removal, rehydrated and submitted to heat-induced antigen retrievel using 10 mM citrate buffer (pH 6; Panreac, Barcelona, Spain). After washed with PBS, the TUNEL reaction mixture (50 μL/sample) was added to the hydrogel samples and incubated for 1 hour at 37°C, in the dark. Negative control (without terminal transferase) and positive control (with DNase I recombinant 20 U/mL (Amresco) in 50 mM Tris(hydroxymethyl) aminomethane, pH 7.5, and 1 mg/mL bovine serum albumin) samples were also prepared. A counterstaining was performed using 4,6-Diamidino-2-phenyindole, dilactate (DAPI; Biotium, CA, USA). Samples were washed with PBS and observed under fluorescence microscopy (Apoptotic cells (green): ex/em 495/515 nm; DAPI (blue): ex/em 358/461 nm) as described above.

9.3.6.5. Optical projection tomography

Optical projection tomography (OPT) system was used to analyze the 3D microstructure of the SF hydrogels and to evaluate the distribution of the cell-laden SF hydrogels. SF hydrogel samples were prepared by filling fluorinated ethylene propylene (FEP) tubes with 100µL of the un-laden or cell-laden SF/HRP/H_2O_2 mixture. The specimens were immersed in an index-matching liquid (distilled water) and rotated through a series of angular positions. The center of rotation and the alignment of the samples were adjusted using a manual x-y-stage (Standa, Lithuania) in conjunction with the sample-positioning module (Standa, Lithuania) by using the 4 available axes (3 translational, 1 rotational). The acquisition consists of rotating a sample 360° in 0.9° steps and capturing an image at each rotation angle, ranging from 0° to 359.1°. A total of 400 images were acquired per sample. The OPT system was used in brightfield mode. The images were captured with an sCMOS camera (Hamamatsu, Japan) and the exposure time was adjusted from 4 ms to 20 ms depending on the transparency of the sample. Projections collected in each orientation were used to create the 3D reconstructions of each sample and the visualization of the 3D-volume was obtained using Avizo software (FEI, USA).

9.3.6.6. Selective plane illumination microscopy

Cell distribution in the SF hydrogels was also analyzed by selective plane illumination microscopy (SPIM), following the same protocol for cell-loading sample preparation described above. The samples imaged with SPIM were stained with Calcein AM (green: ex/em 494/517 nm) and Phalloidin (red: ex/em 550/575 nm). The FEP-tubes containing the samples were supported by a 4 axis-positioning device (Picard Industries, USA) and the plane of interest in each sample was found by using the 4 available axes (3 translational, 1 rotational). The fluorophore distribution in the samples was acquired my translating the sample along the detection axis while taking images at constant intervals. The images were collected with an sCMOS camera. The samples were imaged using an exposure time of 300 ms except for the day 10 and day 14 samples (exposure time of 100 ms to avoid overexposure). Images were taken in 3 µm z-steps across depth of 500 µm. Due to narrow field of view, separate stacks were acquired to cover the width of the sample. The stacks were stitched together in post processing to create a wider field of view. Finally, the stitched stacks were visualized using Avizo software.

9.3.7. Statistical analysis

All the numerical results are presented as mean ± standard deviation (SD). Statistical analysis was performed using the GraphPad Prism 5.0 Software (GraphPad Software Inc., La Jolla, CA, USA). First, a Shapiro-Wilk test was used to ascertain about the data normality. The results indicated that non-parametric tests should be used for all comparisons. The comparisons were performed using the Kruskal-Wallis test followed by Dunn's multiple comparison test. Three independent experiments were performed for all biological quantification assays, and carried out with three replicates in each culturing time. Statistical significance was set to $^{**}p < 0.01$, $^{***}p < 0.001$.

9.4. Results

9.4.1. Structure and multi-scale conformational transitions of the SF hydrogels

To clarify the relationship between hydrogels morphology and conformational changes of the SF protein, we performed a multi-scale structural characterization to evaluate the conformational distribution within the SF hydrogels over the 14 days of incubation at physiological conditions (Figure 9-1a). SF hydrogels immersed in phosphate buffer saline solution (PBS) solution at 37°C for 14 days presented a transparent morphology over the first 7 days, becoming completely opaque after 10 days of incubation (Figure 9-1b) [20]. The Transmission electron microscopy (TEM) images revealed at day 1 and day 3 the presence of a high amount of small and randomly distributed SF nanofibrils, representative of a main amorphous conformation in the hydrogels (Figure 9-1c). At day 7, the dimensions of the SF nanofibrils increased substantially, and from day 10 to day 14 the nanofibrils aggregates also increased exponentially, indicating higher order of β-sheet structures and the typical evidence of a conversion to a dominant β-sheet conformation domain [38]. Thioflavin T (ThT) staining (Figure 9-1d) came to confirm the TEM observations by the increasing evidence of SF nanofibrils and aggregates over the 14 of hydrogels incubation. The bright green fluorescence detecting protein nanofibrils in the β-sheet state was only observed from day 7, confirming the previous observations [39]. In Figure 9-1e, are represented the 3D reconstructions of the SF hydrogels obtained by Optical projection tomography (OPT) analysis. The low intensity voxels colored in blue, give a clear perception of the hydrogels microstructure and highlight their conformational changes. From day 1 to day 7, hydrogels presented a homogeneous intensities distribution characteristic of transparent hydrogels (random coil main conformation). From day 10 until day 14, an increase in entropy was observed, which is related with a random intensity distribution in high density hydrogels (β-sheet main conformation) [40, 41].

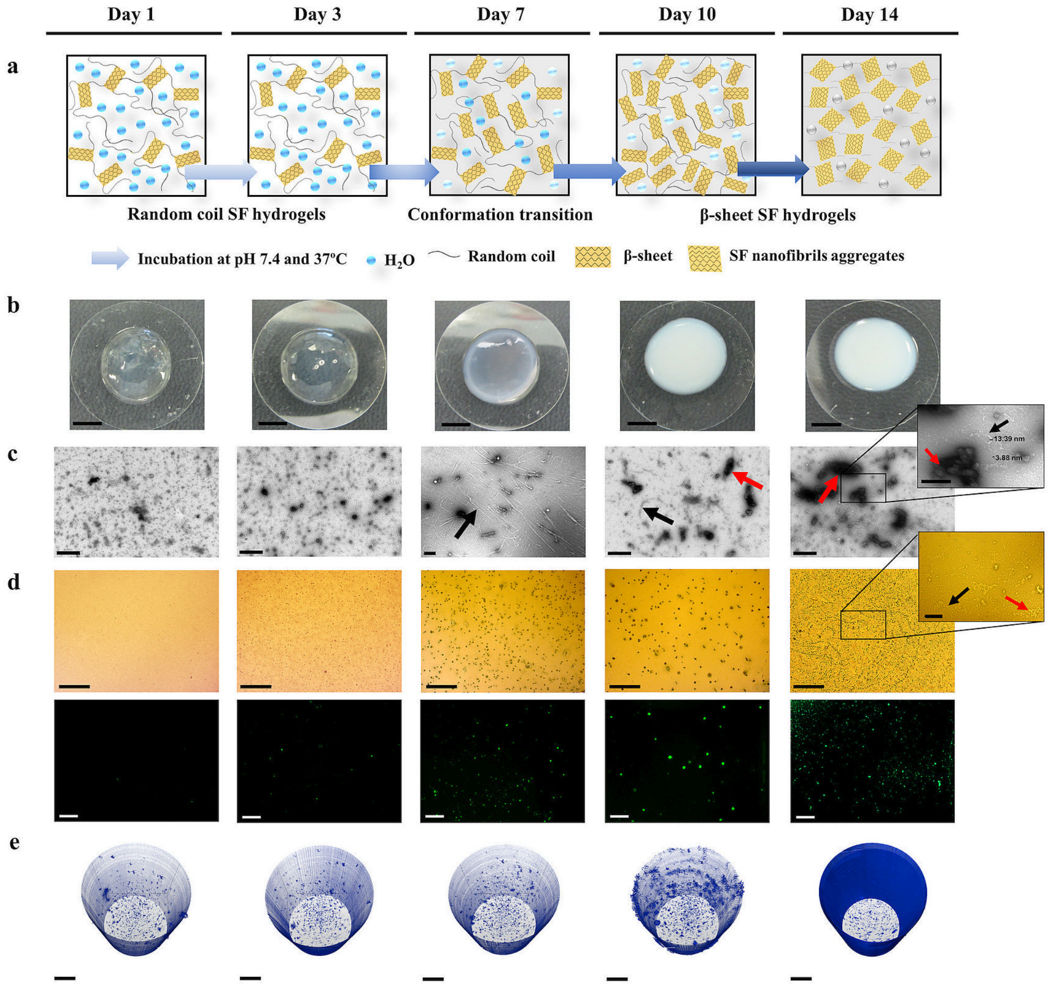
Day 1
Day 3
Day 7
Day 10
Day 14
a
Random coil SF hydrogels
Conformation transition
β-sheet SF hydrogels
Incubation at pH 7.4 and 37°C
H_2O
Random coil
β-sheet
SF nanofibrils aggregates
b
c
~13.39 nm
~3.88 nm
d
e

Figure 9-1. Structural evaluation of the SF hydrogels after incubation in PBS at 37°C for 1, 3, 7, 10 and 14 days. (a) Schematic illustration of the β-sheet structural transitions in the SF hydrogels. (b) Macroscopic images of the SF hydrogels (scale bar: 5 mm). (c) TEM micrographs of the SF hydrogels (scale bar: 500 nm for low magnification images; scale bar: 200 nm for high magnification image). (d) SF hydrogels labeled with thioflavin T (scale bar: 500 μm for low magnification images; scale bar: 100 μm for high magnification image) analyzed under the fluorescence microscope (scale bar: 200 μm). The black arrows indicate nanofibrils and the red arrows indicate aggregates. (e) OPT reconstructions of the SF hydrogels (scale bar: 500 μm).

The conformational changes of SF hydrogels were then confirmed by X-ray diffraction (XRD, Figure 9-2a) and attenuated total reflectance Fourier transform infrared spectroscopy (ATR-FTIR, Figure 9-2b). XRD analysis revealed no significant differences between the hydrogels tested with different incubation periods at 37°C (3, 7 and 14 days) in terms of peak positions, ranging from $2\theta = 28.4 - 30.8°$. The intensity of these peaks increased over time, which characterizes the typical pattern of substances undergoing an increase of crystallinity [42], represented by broad peaks at the first tested periods (3 and 7 days) converted to a crystalline diffraction pattern after 14 days of incubation. The peak identified on day 14 at $2\theta = 28.4°$ can be assigned to β-sheet crystalline domain [43] and the additional peak at $2\theta = 21°$, was only detected at day 14 and also characterizes the β-sheet structure [44]. The main absorbance peaks detected by ATR-FTIR for the SF hydrogels were on day 3 at 1643 cm^{-1} and 1545 cm^{-1} and on day 7 at 1643 cm^{-1} and 1541 cm^{-1}. These peaks are characteristic of random coil conformation and correspond to the amide I and amide II bands, respectively [45, 46]. At day 14, strong absorption peaks were detected at 1636 cm^{-1} and 1535 cm^{-1}, corresponding to the β-sheet structure on the SF hydrogels [45]. From day 3 to day 14, hydrogels presented an absorbance peak between 1250 cm^{-1} to 1252 cm^{-1}, corresponding to amide III band positions. As expected, the intensity of this peak was higher at day 14, which is an indication of the higher β-sheet crystalline domain in these hydrogels [46]. We further quantitatively and unambiguously confirmed the structural transitions between the SF hydrogels at a nanoscale by atomic force microscopy combined to IR nano-spectroscopy (AFM-IR) (Figure 9-2c). Figure 9-2d, shows the AFM nano-imaging of the SF hydrogel samples at the different tested periods, revealing that after 3 and 7 days of incubation at 37°C a series of elements were exhibited, with the presence of some globular amorphous protein aggregates with different sizes and morphologies. At day 14, a large globular protein aggregate was identified with an opaque morphology, confirming that SF hydrogels underwent conformational changes [38]. The AFM-IR spectra (Figure 9-2e) obtained for the SF hydrogels were correlated to that obtained with the conventional ATR-FTIR (Figure 9-2b). Nevertheless, through AFM-IR analysis it was possible to obtain an average structural information of samples covering larger areas of analysis, which is an important advancement considering the high structural heterogeneity of SF hydrogels at the nanoscale (Figure 9-2d) [47]. The amide band positions (I, II, II) of samples from day 3 and day 7 were quite similar and of low intensity (indistinct peaks), characteristic of a random coil main conformation (1644 cm^{-1} and 1640 cm^{-1} for amide I, 1532 cm^{-1} and 1540 cm^{-1} for amide II and 1232 cm^{-1} and 1228 cm^{-1} for amide III, respectively) [45, 46]. At day 14, all the amide signature bands shift towards higher frequency, especially those of amide I and amide II (1650 cm^{-1} for amide I, 1546 cm^{-1} for amide II and 1256 for amide III), which is a characteristic of the β-sheet structure [48, 49]. Therefore, these results suggest that the natural conformational changes of the native SF can also spontaneously occur on the SF hydrogels over time.

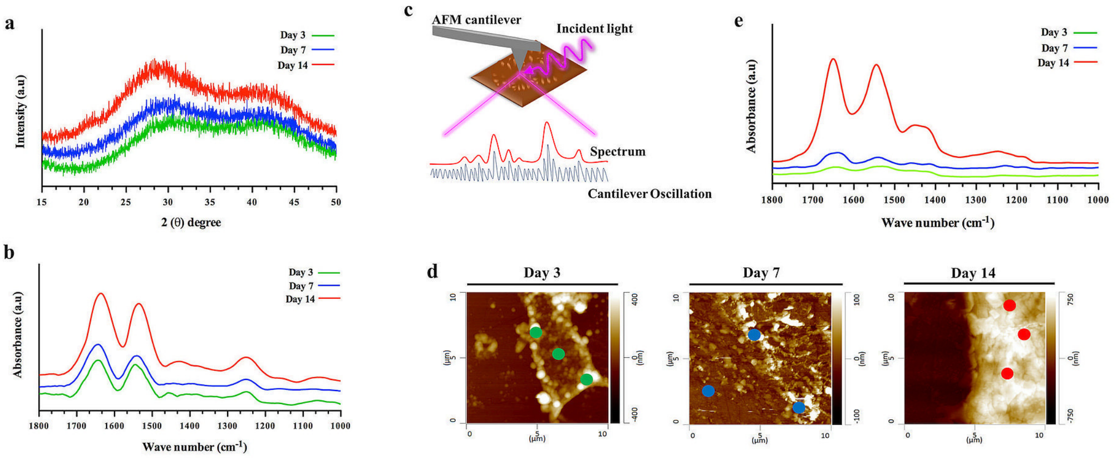

Figure 9-2. Physicochemical characterization of the SF hydrogel after incubation in PBS at 37°C for 3, 7 and 14 days. (a) XRD patterns of the SF hydrogels. (b) ATR-FTIR spectra of the SF hydrogels. (c) Schematic illustration of nanoscale IR spectroscopy using AFM-IR: IR pulses are emitted in the sample increasing the local absorption on SF nanofibrils acquired by the AFM cantilever tip, corresponding to the absorption spectroscopic peaks. (d) Tapping-mode AFM nano-images (10 μm x 10 μm), and (e) IR nano-spectra of the SF hydrogels obtained by measuring the samples at different points selected by the AFM tip, corresponding to the absorption spectroscopic signatures and indicated as green, blue and red points.

9.4.2. Viscoelastic properties and hydrogelation kinetics of the SF hydrogels

The mechanical properties of the SF hydrogels and SF/HRP/H_2O_2 mixture before gelation were analyzed by rheometer, detecting the frequency sweep as a useful tool to characterize the microstructure of a viscoelastic material. Frequency sweep curves obtained from oscillatory shear measurements performed on the SF hydrogels are shown in Figure 9-3a, revealing the dependence of storage modulus (G') (Figure 9-3ai) and loss modulus (G") (Figure 9-3aii) upon the frequency. G' measures the deformation energy stored during shear stress, i.e. the material stiffness, while G" measure the dissipated energy, i.e. the flow or liquid-like response [50]. In all tested periods, G´ was higher than the G'', showing that the produced SF hydrogels are viscoelastic solids, both in a main amorphous conformation (transparent) and in a β-sheet crystalline form (opaque) (Figure 9-3d). G' and G'' were almost independent on the oscillation frequency, but for higher values of frequency (>1 Hz) it shows a typical plastic flow behavior with G' and G'' increasing with frequency. Moreover, the G' increases substantially from day 3 to day 7, corresponding to the conformation transition period of hydrogels (Figure 9-3d). In the first 3 days is suggested a network-like structure converted in a liquid crystal-like structure from day 7 to day 14 of analysis [51]. The damping factor or loss factor (tan δ) was measured by determining the ratio G″/G′ (Table 9-1). An increase of tan δ was observed over time (from day 1 until day 14), as well as, that the damping factor was lower than 1 in all tested periods (higher storage modulus – G'), characterizing the typical behavior of elastic solids [51]. Moreover, a substantial increase of the damping factor was determined from day 3 to day 7, consistent to the G' measurements (Figure 9-3ai). SF/HRP/H_2O_2 mixture was subjected to two different oscillatory experiments, temperature (Figure 9-3bi) and time (Figure 9-3bii) sweep curves, before gelation. In both cases, a gel-like response was observed in which G' was always higher than G''. An abrupt increase of G' was observed up to 27°C and 120 seconds, indicating an increase of samples stiffness associated to the formation of a hydrogel network [18]. After a stagnation at intermediate times and on the range of temperature from 30°C to 40°C, a slight increase of G' and G'' was observed at the end of the curves (starting at 40°C and 2900 seconds), indicating that at this point the SF hydrogels were completely formed and the temperature or time did not significantly alter the final mechanical properties of the hydrogels. The prepared SF/HRP/H_2O_2 mixture was studied through rotational experiments (Figure 9-3c). Before gelation, SF/HRP/H_2O_2 mixture showed an average shear viscosity of 4.7 ± 0.37 Pa.s (Figure 9-3ci), as confirmed by the slope of the linear trend line (Figure 9-3cii). The shear viscosity values decreased with increasing shear rate (0.1 s^{-1} to 1 s^{-1}), suggesting the shear-thinning fluidic behavior of the SF/HRP/H_2O_2 mixture. At higher shear rate values (1 s^{-1} to 100 s^{-1}) a Newtonian behavior was observed represented by a constant shear viscosity [52].

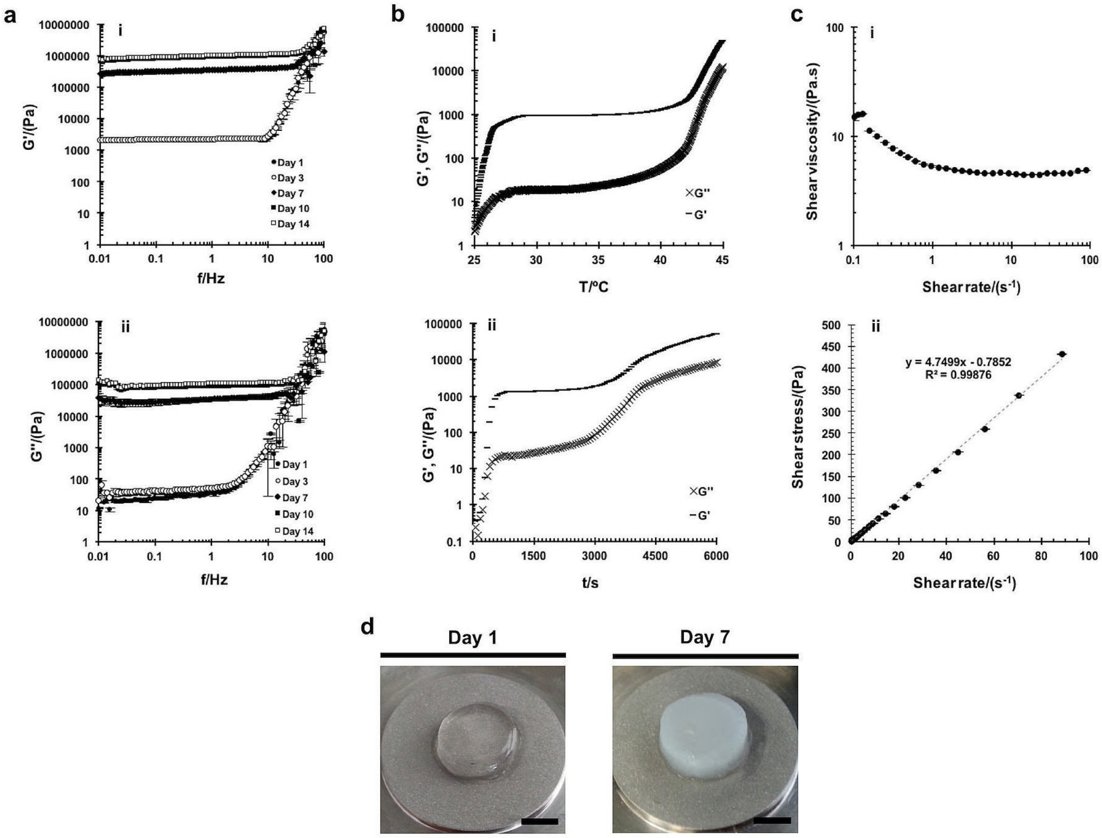

Figure 9-3. Rheological properties of the SF/HRP/H_2O_2 mixture before gelation, after SF hydrogels formation and incubation in PBS at 37°C for 1, 3, 7 and 14 days. (a) Oscillatory experiments or frequency sweep curves: (i) storage modulus as a function of frequency, and (ii) loss modulus as a function of frequency for the SF hydrogels. (b) Dynamic moduli as function of: (i) temperature, and (ii) time for the SF/HRP/H_2O_2 mixture. (c) Rotational experiments: (i) shear viscosity, and (ii) shear stress as a function of shear rate for the SF/HRP/H_2O_2 mixture. (d) Macroscopic images of SF hydrogels analyzed at day 1 and day 7 (scale bar: 4 mm).

Table 9-1. Damping factor of SF hydrogels after incubation in PBS at 37°C for 1, 3, 7, 10 and 14 days.

Time (day)	Damping factor
1	0.0121 ± 0.0004
3	0.0208 ± 0.0042
7	0.0941 ± 0.0048
10	0.1039 ± 0.0074
14	0.1078 ± 0.0017

9.4.3. Assessment of the programmed cell death in U251 cell-laden SF hydrogels and live conformational changes

Due to the conformational transitions observed on the SF hydrogels after short incubation periods, the developed hydrogels were used for U251 cell line encapsulation to evaluate the effects of the conformational changes on cell behavior. The ATP evaluation (Figure 9-4a) showed that the metabolic activity of the encapsulated cells significantly improved from day 1, as compared to the remaining culture periods (***$p < 0.001$). Nevertheless, after 10 days of culture a non-significant decrease in cellular metabolic activity was verified, as compared to day 7, corresponding to the conformation transition state of the SF hydrogels, from amorphous (transparent hydrogels) to crystalline β-sheet (opaque hydrogels) (Figure 9-4c). A non-significant increase of metabolically active cells was observed from day 10 to day 14. This cell behavior may have been induced as stress response to counter the effects of the conformational transition on SF hydrogels. Moreover, in contrast to normal differentiated cells most cancer cells respond differently to generate the energy needed for cellular processes, which affects the ATP production by cells [53]. From DNA quantification (Figure 9-4b), it was observed a significant increase of cell proliferation from day 1 to day 10 (**$p < 0.01$: from day 1 to day 7; ***$p < 0.001$: from day 1 to day 10 and from day 7 to day 10). However, at day 14 a slight decrease in cell proliferation was observed as compared to day 10, even if it has been significantly superior as compared to day 1 (***$p < 0.001$) and day 7 (**$p < 0.01$). As shown in Fig 4d, live/dead staining showed that the cell-laden SF hydrogels were capable support cell viability during the first 24 hours of culturing. At day 7 and day 10 the amount of dead cells was very similar to the living ones, and a large amount of dead cells were observed after 14 days of culturing. Cell apoptosis detected through TUNEL assay (Figure 9-4d) also revealed that no apoptosis was visualized at day 1. However, over the 14 days of culturing a substantial increase of apoptotic cells were detected at the cell-laden hydrogels, presenting at day 14 a very similar pattern to that observed on the positive control samples (Supplementary Figure 9-3a). From Figures 91-b and 9-4c it was observed that, both the un-laden and cell-laden SF hydrogels, respectively, maintained a transparent morphology until day 7, where opacity started to be noticed. After 10 days of incubation, hydrogels become completely opaque. The hydrogels TEM, ThT and OPT images (Figures 9-1c-e), showed an increase of SF nanofibrils aggregates after 7 days of incubation and the rheological analysis also showed a substantial increase of hydrogels stiffness from day 7 (Figures 9-3ai). These results indicate that the unquestionable conformational transition of SF hydrogels to a dominant β-sheet crystalline conformation affected cell proliferation and viability, increasing cell apoptosis.

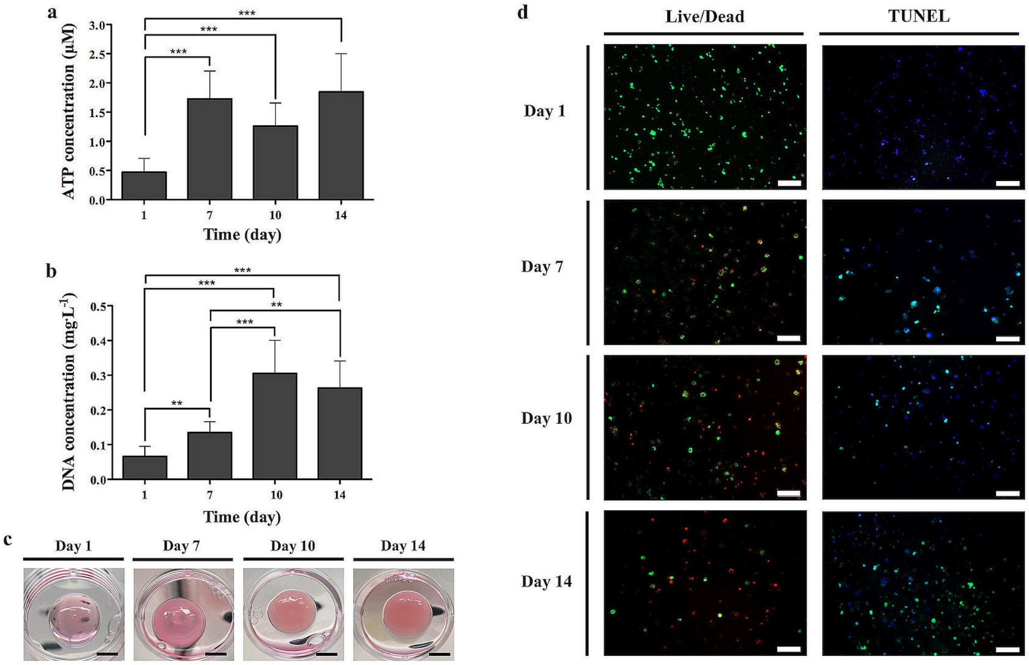

Figure 9-4. U251 cell-laden SF hydrogels cultured for 1, 7, 10 and 14 days. Cell viability and proliferation analyzed by (a) ATP assay and (b) DNA quantification, respectively. (c) Macroscopic images of the U251 cell-laden SF hydrogels (scale bar: 5 mm). (d) Live/Dead staining and fluorescence TUNEL assay of the U251 cell-laden SF hydrogels (scale bar: 200 μm). $^{**}p < 0.01$, $^{***}p < 0.001$.

The *in vitro* conformation transition behavior of the U251 cell-laden SF hydrogels was also evaluated by OPT analysis and selective plane illumination microscopy (SPIM) (Figure 9-5a). These imaging techniques allowed to create multi-scale 3D rendered images to evaluate cell distribution within the hydrogels, while being minimally invasive at the same time. OPT projections (Figure 9-5a) showed that from day 1 to day 10, U251 cells were well distributed within the hydrogels presenting a main amorphous conformation (transparent morphology) on the first 7 days of culture. At day 10 some changes were observed in the cell-laden hydrogels morphology due to the presence of some opaque depots characteristic of a β-sheet conformation transition. These opaque depots were converted in the main structure of the U251 cell-laden SF hydrogels after 14 days of culture, showing the complete transition of hydrogels conformation and confirming the previous OPT observations (Fig 1e; S1 Movie). Nevertheless, cell distribution behavior after 14 days of culture was only possible to evaluate through OPT reconstructions (Figure 9-5a), showing that cells were organized in clusters. SPIM reconstructions (Figure 9-5a), allowed not only to achieve high resolution 3D images of the cell-laden SF hydrogels using high penetration depths, as imaged and tracked the cells within the hydrogels by fluorescence labeling. At day 1 and day 7, U251 cells presented a very similar distribution within the hydrogels to that observed on OPT projections (Figure 9-5a) and reconstructions (Figure 9-5a). At day 10, cells were already organized in clusters and this effect was even more pronounced after 14 days of cell encapsulation. The sections from the U251 cell-laden hydrogels analyzed by TUNEL assay (Figure 9-5b) also showed an increase of cell clusters over the culture period accompanied by a substantial increase of apoptotic cells on day 14, suggesting that the transition from random coil (amorphous) to a β-sheet (crystalline) (Figure 9-4c) induced formation of U251 cell clusters that undergo a programmed cell death (Figure 9-5c).

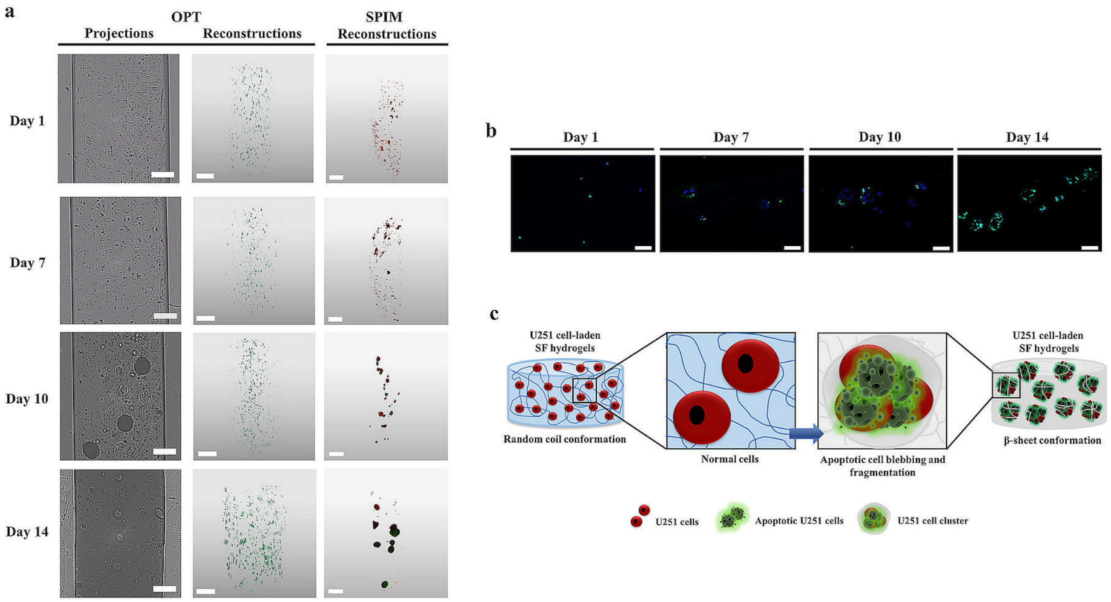
a
OPT
Projections
Reconstructions
SPIM
Reconstructions
Day 1
Day 7
Day 10
Day 14
b
Day 1
Day 7
Day 10
Day 14
c
U251 cell-laden SF hydrogels
Random coil conformation
Normal cells
Apoptotic cell blebbing and fragmentation
U251 cell-laden SF hydrogels
β-sheet conformation
U251 cells
Apoptotic U251 cells
U251 cell cluster

Figure 9-5. U251 cell-laden SF hydrogels cultured for 1, 7, 10 and 14 days. (a) OPT projections (scale bar: 400 μm), OPT reconstructions (scale bar scale bar: 500 μm) and SPIM reconstructions (scale bar: 200 μm) of the U251 cell-laden SF hydrogels. (b) Fluorescence TUNEL assay of the sections from the U251 cell-laden SF hydrogels for 1, 7, 10 and 14 days (scale bar: 50 μm). (d) Schematic illustration of the morphological changes of U251 cells during apoptosis induced by the conformational transitions of the cell-laden SF hydrogels.

9.5. Discussion

In this study, we have investigated enzymatically crosslinked SF hydrogels mediated by a HRP/H_2O_2 complex. These hydrogels were produced in a main random coil conformation, which allow them to obtain physical, mechanical and biological properties completely distinct to those reached by the SF hydrogels formed with a β-sheet conformation [17, 18], or even to those induced by electrical stimuli in main random coil conformation [54]. The high concentration of SF (16 wt.%) allowed us to obtain fast-formed hydrogels (15-20 minutes of gelling time) suitable for injectable systems [55]. The previous electrically induced SF hydrogels, were prepared from low concentrated SF, which imply longer gelation times and low mechanical properties [54]. As observed in a previous study by our group [20], the proposed SF hydrogels can be customized to yield a wide range gelling times and mechanical properties only by changing the concentration of SF and the HRP/H_2O_2 ratio, due to the tyrosine groups available in the crosslinking system [22]. The crosslinking system herein proposed, involved not only a highly-concentrated SF solution (16 wt.%), as an increased concentration of enzyme (HRP) was applied to yield faster gelation times. Moreover, the proposed highly concentrated SF hydrogels have shown high water content and swelling ability, both in the amorphous state and after β-sheet inducement, which is very important to maintain hydrogels integrity and better simulate the physiological environment [21].

The proposed rapidly responsive SF hydrogels have been previously observed to present a transparent appearance during the amorphous conformation state that gradually changes to an opaque morphology when the hydrogels are naturally converted in a β-sheet conformation [20]. This was another interesting characteristic of our hydrogels that presented significant morphological changes after 7 days of hydrogels formation, indicative of a conformational transition of SF to β-sheet crystalline form, as confirmed under TEM, ThT staining and OPT analysis (Figure 9-1c-e). These results also suggest that the applied enzymatic crosslinking on the semi-crystalline or amorphous tyrosine groups of SF may not affect the β-sheet inducement of the protein [22]. In a previous study, Ryu *et al.* [56] proposed a different approach for producing SF-PEG hybrid hydrogels, where the SF phase was naturally converted to a β-sheet conformation after 5 days of hydrogels formation. These hydrogels were formed by an initial functionalization step of SF in order to allow the photo-polymerization reaction and hydrogels formation. The post-gelation step of SF was then conducted by the natural β-sheet structural transition within the hydrogel network. Although most of the reported literature recognize that the formation of transparent SF hydrogels is associated with a random-coil conformation and opaque hydrogels present a main β-sheet conformation, it has been also reported the development of transparent SF hydrogels formed by reaction with polar reagents that resulted in an amorphous-to-crystalline conformational change [57].

The chemical characterization of the SF hydrogels (Figure 9-2a,b and e) was essential to confirm the multi-scale morphological observations and in which state of hydrogels formation the conformational transition takes place, showing that until day 7 the developed SF hydrogels presented the typical low intensity peak positions of a random coil conformation. After 14 days of hydrogels formation, high intensity absorption peaks were detected resulting from an increase of crystallinity and conversion to a dominant β-sheet conformation. Thus, understanding the structure-property relation of protein-based biomaterials can open for new possibilities of developing high-level 3D biomaterials impossible to obtain from other polymeric materials [58]. Mechanical properties constitute one of the main issues of biomaterials design for TE applications. In the specific case of hydrogels, it can be hard to produce with sufficient mechanical strength to support tissues like cartilage or subchondral bone [59]. Moreover, in most cases high elasticity is also required, which hindered its production for the desired applications. In this study, SF hydrogels presented a viscoelastic solid behavior, both in a random coil conformation or in a β-sheet opaque form [51]. Even the materials stiffness has suffered a substantial increase during the conformational transition, they still maintained the typical behavior of elastic solids, which is not the normal behavior of SF hydrogels formed in a β-sheet conformation with high stiffness but lack of elasticity [17]. The crosslinking process induced by the enzymatic complex of HRP/H_2O_2, may had a direct influence on these results [8]. As previously observed, higher contents of peroxidase and hydrogen peroxide in the crosslinking system, equivalent to those used in the present system (HRP/silk: 0.52‰; H_2O_2/silk: 1.45‰), can induce higher amount of oxidized tyrosine groups and an enhanced crosslinking degree that resulted in improved mechanical properties of the hydrogels [20]. Moreover, in both studies it was observed that regardless of the enzymatic ratio, in the amorphous state SF hydrogels presented a constant elasticity with increasing frequency and strain sweep. We were also able to distinguish the gelling point of the SF/HRP/H_2O_2 mixture by the substantial increase of samples stiffness at specific temperature and time sweep [18] and the viscoelastic behavior was also determined to evaluate the resistance to flow, which is an important concern of injectable systems [4, 51]. Polymers are known for being non-Newtonian fluid and most of them exhibit shear-thinning behavior in which the molecules are oriented along the flow direction, as observed in our results. At high shear rate, the Newtonian behavior was observed due to the molecules disorder as a result of shearing [52].

In the hydrogel-based 3D cell cultures, the seeding of cells is usually done by suspending cells in the fluidic gel precursor solution, in order to obtain the cells embedded inside the gel after gelation [60]. This is one of the major limitations of the SF hydrogels reported in the literature [17, 18]. As above mentioned, the usually applied methods for preparing SF hydrogels involve the β-sheet conformational transition of SF during the sol-gel transition, which in some cases may involve long gelation times [61]. On the other side, physical and chemical treatments proposed to shorten the SF gelation time, may also have provided useful timeframes for successful cell encapsulation [17, 18]. For example, the ultrasonication treatment of SF have shown to decrease the gelation time of SF hydrogels up to 2 hours, at the same time that a successful cell incorporation after sonication and before the rapid gelation process was observed. These hydrogels sustained cell function, proliferation and survival up to 21 days of culture [17]. The same protocol was used in a different study [62], allowing the co-encapsulation of pancreatic iselets with mesenchymal stem cells (MSCs) and ECM proteins within vortex-induced SF hydrogels. In the present study, the SF hydrogels were prepared at physiological conditions (peroxidase mediated crosslinking) and in a main random coil conformation, allowing for cell encapsulation, viability and proliferation up to 10 days of culture, corresponding to the period of SF amorphous-to-crystalline conformational transition (Figures 9-1 and 9-2). The complete transition to a dominant β-sheet conformation was verified at day 14, accompanied by a substantial increase of cell apoptosis. In previous studies [31, 63], hydrogel matrices presented superior physiological properties as *in vitro* platforms for cancer cells encapsulation and proliferation, where cells were encouraged to grow as tumor-like clusters in 3D formation. Moreover, the authors also observed that the oxygen and nutrients diffusion limitations within the hydrogel matrices resulted in cellular competition for the available nutrients, growing levels of intra-cellular hypoxia, and as consequence in the development of necrosis in the core of the *in vitro* bioengineered tumors [63]. Our suggestion is that the opacity and crystallinity induced by the β-sheet conformation may have conditioned the oxygen and nutrients diffusion within the cell-laden hydrogels, forcing the cell cluster formation. At some point, cancer cells were not able to adjust to those deficiencies ceding to a cell death by apoptosis (Figure 9-5c). It is important to reinforce that this cell behavior may be beneficial to mimic the tumor microenvironment in 3D cancer models research. The relation of a cell death induced by the β-sheet conformation of SF protein can also be raised, especially since it has been reported in the literature that fibrillar β-amyloid peptides may have cytotoxic properties [64]. Nevertheless, different SF-based structures in a β-sheet form, have proved to be able of support cell viability, proliferation and differentiation, as well as, *in vivo* biocompatibility [16]. From the OPT and SPIM reconstructions (Figure 9-5a), we were able to observe the typical behavior of cells in growing tumors, with an increase of U251 cell clusters over the culture period, especially after 14 days of culture. This cell behavior may be beneficial to mimic the tumor microenvironment in 3D cancer models research. In fact, bioengineered 3D hydrogels have already shown to induce cancer cells clusters formation in a new 3D culture concept used to assess the cell-matrix interactions implied in carcinogenesis [65]. From the cell-laden hydrogels TUNEL sections (Figure 9-5b) it was possible to closely observe that at day 14 most of these clustered cells were apoptotic, confirming that the β-sheet crystalline domain of SF hydrogels may not only affect cell distribution but also induce programmed cell death (Figure 9-5c), which reinforces the potential use of these hydrogels as biomimetic matrices for studying the programmed tumor cells death.

9.6. Conclusions

The present work demonstrates the formation of stimuli-responsive enzymatically crosslinked SF hydrogels that undergo a spontaneous conformational transition from random coil to β-sheet at physiological conditions. These hydrogels were highly resistant and presented appropriate mechanical properties to be used as injectable systems or 3D artificial matrices. They were successfully applied for cell encapsulation, showing a significant increase of U251 cells proliferation and metabolic activity in the transparent amorphous state. The spontaneous random coil-to-β-sheet conformational transition of the SF hydrogels affected the viability of cells and induced apoptosis, envisioning their use as a generic injectable system to guide cancer cells behavior and suppressing tumor progression. Furthermore, the stimuli-responsiveness and cell-loading ability of these *in situ* forming SF hydrogels, provide new insights for using these hydrogels as potential orthotopic 3D cancer models and for studying the 3D microenvironment of tumor cells.

9.7. Supplementary information

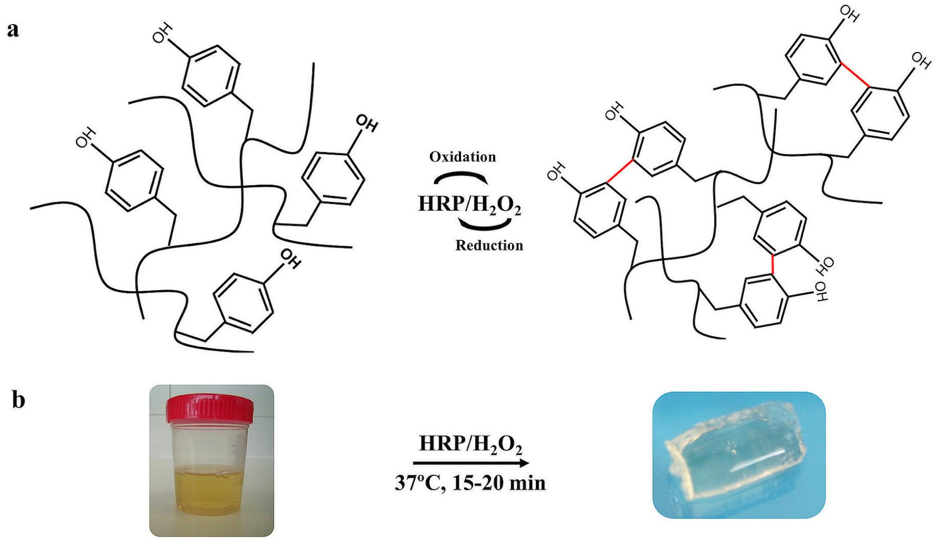

Supplementary Figure 9-1. Schematic illustration of redox-responsive enzymatically crosslinked SF hydrogels. (a) Oxidation-reduction reaction between HRP and H_2O_2 transformed the tyrosine groups of SF and induced hydrogels formation. (b) Rapidly responsive sol-gel transition combining HRP and H_2O_2 at physiological conditions (pH 7.4 and 37°C).

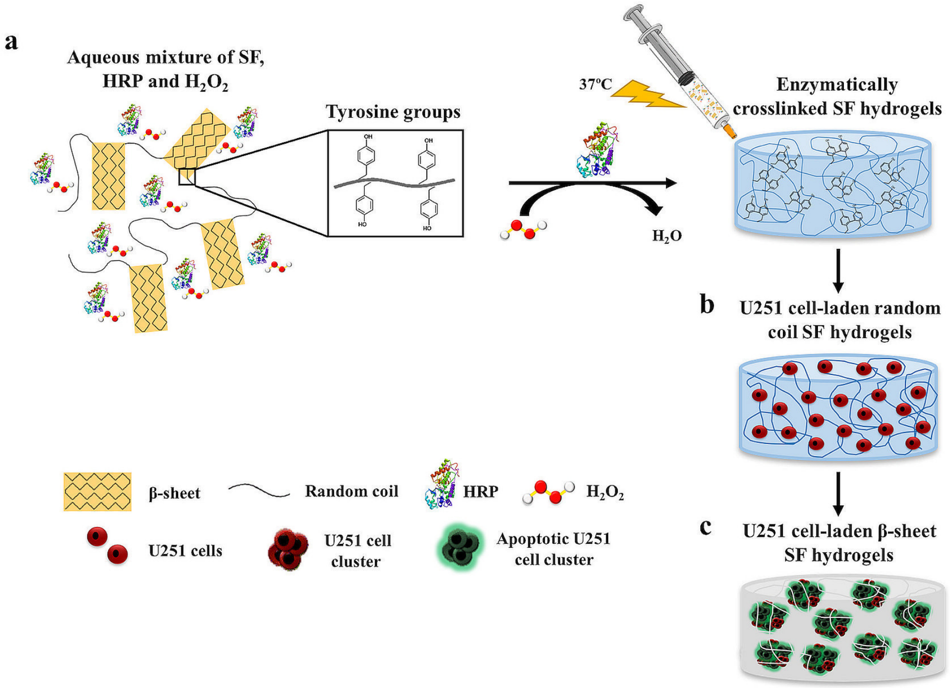
a
Aqueous mixture of SF, HRP and H_2O_2
Tyrosine groups
37°C
Enzymatically crosslinked SF hydrogels
H_2O
b
U251 cell-laden random coil SF hydrogels
c
U251 cell-laden β-sheet SF hydrogels
β-sheet
Random coil
HRP
H_2O_2
U251 cells
U251 cell cluster
Apoptotic U251 cell cluster

Supplementary Figure 9-2. Schematic illustration of *in situ* fast-formed enzymatically crosslinked SF hydrogels and *in vitro* response of U251 cell-laden SF hydrogels. (a) Peroxidase mediated crosslinking method using HRP and H_2O_2 at physiological conditions (pH 7.4 and 37°C), reacting with the tyrosine groups of the SF protein. (b) U251 cells encapsulation within the newly formed random coil SF hydrogels. (c) U251 cell-laden SF hydrogels converted into a crystalline β-sheet conformation showing U251 cell clusters organization and U251 cell death by apoptosis.

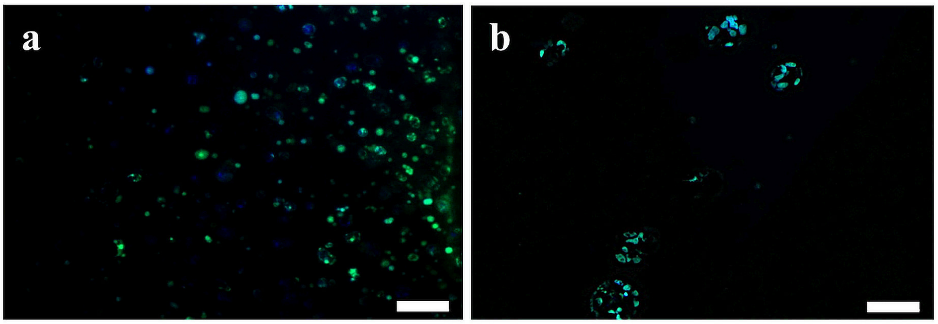

Supplementary Figure 9-3. Positive control for fluorescence TUNEL assay. (a) U251 cell-laden SF hydrogels (scale bar: 200 μm) and (b) sections from the U251 cell-laden SF hydrogels (scale bar: 50 μm).

9.8. References

[1] J. Elisseeff, Hydrogels: structure starts to gel, Nature materials 7(4) (2008) 271-273.

[2] L.-W. Xia, et al., Nano-structured smart hydrogels with rapid response and high elasticity, Nature communications 4 (2013).

[3] W. Hennink, C.F. Van Nostrum, Novel crosslinking methods to design hydrogels, Advanced drug delivery reviews 64 (2012) 223-236.

[4] L. Yu, J. Ding, Injectable hydrogels as unique biomedical materials, Chemical Society Reviews 37(8) (2008) 1473-1481.

[5] S. Sakai, et al., An injectable, in situ enzymatically gellable, gelatin derivative for drug delivery and tissue engineering, Biomaterials 30(20) (2009) 3371-3377.

[6] L. Liu, et al., In situ forming hydrogels based on chitosan for drug delivery and tissue regeneration, asian journal of pharmaceutical sciences 11(6) (2016) 673-683.

[7] S. Sakai, et al., Enzymatically crosslinked carboxymethylcellulose–tyramine conjugate hydrogel: cellular adhesiveness and feasibility for cell sheet technology, Acta biomaterialia 5(2) (2009) 554-559.

[8] L.S.M. Teixeira, et al., Enzyme-catalyzed crosslinkable hydrogels: emerging strategies for tissue engineering, Biomaterials 33(5) (2012) 1281-1290.

[9] R. Jin, et al., Enzymatically-crosslinked injectable hydrogels based on biomimetic dextran–hyaluronic acid conjugates for cartilage tissue engineering, Biomaterials 31(11) (2010) 3103-3113.

[10] J.L. Drury, D.J. Mooney, Hydrogels for tissue engineering: scaffold design variables and applications, Biomaterials 24(24) (2003) 4337-4351.

[11] Y. Cai, et al., Silk fibroin membrane used for guided bone tissue regeneration, Materials Science and Engineering: C 70 (2017) 148-154.

[12] M. Yang, et al., Ice-Templated Protein Nanoridges Induce Bone Tissue Formation, Advanced Functional Materials (2017).

[13] C.-X. Sun, et al., Bone Morphogenic Protein-2 (rhBMP2)-Loaded Silk Fibroin Scaffolds to Enhance the Osteoinductivity in Bone Tissue Engineering, Nanoscale Research Letters 12(1) (2017) 573.

[14] E. Yu, et al., Fabrication and Characterization of Electrospun Thermoplastic Polyurethane/Fibroin Small-Diameter Vascular Grafts for Vascular Tissue Engineering, International Polymer Processing 31(5) (2016) 638-646.

[15] S. Font Tellado, et al., Fabrication and characterization of biphasic silk fibroin scaffolds for tendon/ligament-to-bone tissue engineering, Tissue Engineering Part A 23(15-16) (2017) 859-872.

[16] V.P. Ribeiro, et al., Silk-based anisotropical 3D biotextiles for bone regeneration, Biomaterials 123 (2017) 92-106.

[17] X. Wang, et al., Sonication-induced gelation of silk fibroin for cell encapsulation, Biomaterials 29(8) (2008) 1054-1064.

[18] T. Yucel, et al., Vortex-induced injectable silk fibroin hydrogels, Biophysical journal 97(7) (2009) 2044-2050.

[19] R.L. Reis, et al., Hydrogels derived from silk fibroin: Methods and uses thereof, A4TEC Association, Portugal, 2014.

[20] L.P. Yan, et al., Tumor Growth Suppression Induced by Biomimetic Silk Fibroin Hydrogels, Scientific Reports 6 (2016) 31037.

[21] L.P. Yan, et al., Core-shell silk hydrogels with spatially tuned conformations as drug-delivery system, Journal of Tissue Engineering and Regenerative Medicine 11(11) (2016) 3168-3177.

[22] C.Z. Zhou, et al., Silk fibroin: structural implications of a remarkable amino acid sequence, Proteins: Structure, Function, and Bioinformatics 44(2) (2001) 119-122.

[23] A. Sundarakrishnan, et al., Phenol red-silk tyrosine cross-linked hydrogels, Acta biomaterialia 42 (2016) 102-113.

[24] M. McGill, et al., Molecular and macro-scale analysis of enzyme-crosslinked silk hydrogels for rational biomaterial design, Acta biomaterialia 63 (2017) 76-84.

[25] B.P. Partlow, et al., Highly tunable elastomeric silk biomaterials, Advanced functional materials 24(29) (2014) 4615-4624.

[26] M.V. Shirmanova, et al., Live Cell Imaging of Viscosity in 3D Tumour Cell Models, Multi-Parametric Live Cell Microscopy of 3D Tissue Models, Springer2017, pp. 143-153.

[27] M.E. Katt, et al., In vitro tumor models: advantages, disadvantages, variables, and selecting the right platform, Frontiers in bioengineering and biotechnology 4 (2016) 12.

[28] P. Qiu, et al., Silica-Based Branched Hollow Microfibers as a Biomimetic Extracellular Matrix for Promoting Tumor Cell Growth In Vitro and In Vivo, Advanced Materials 25(17) (2013) 2492-2496.

[29] G. Xiong, et al., A novel in vitro three-dimensional macroporous scaffolds from bacterial cellulose for culture of breast cancer cells, Journal of Biomaterials and Nanobiotechnology 4(04) (2013) 316.

[30] C. Fischbach, D.J. Mooney, Polymers for pro-and anti-angiogenic therapy, Biomaterials 28(12) (2007) 2069-2076.

[31] H. Huang, et al., Peptide hydrogelation and cell encapsulation for 3D culture of MCF-7 breast cancer cells, PloS one 8(3) (2013) e59482.

[32] S. Bersini, et al., A microfluidic 3D in vitro model for specificity of breast cancer metastasis to bone, Biomaterials 35(8) (2014) 2454-2461.

[33] D.W. Hutmacher, et al., Translating tissue engineering technology platforms into cancer research, Journal of cellular and molecular medicine 13(8a) (2009) 1417-1427.

[34] F.P. Seib, et al., Tissue engineering a surrogate niche for metastatic cancer cells, Biomaterials 51 (2015) 313-319.

[35] K. Greish, et al., Silk-elastinlike protein polymers improve the efficacy of adenovirus thymidine kinase enzyme prodrug therapy of head and neck tumors, The journal of gene medicine 12(7) (2010) 572-579.

[36] H.T. Ta, et al., Injectable chitosan hydrogels for localised cancer therapy, Journal of Controlled Release 126(3) (2008) 205-216.

[37] C. Bastiancich, et al., Anticancer drug-loaded hydrogels as drug delivery systems for the local treatment of glioblastoma, Journal of Controlled Release 243 (2016) 29-42.

[38] S. Bai, et al., Controllable transition of silk fibroin nanostructures: an insight into in vitro silk self-assembly process, Acta biomaterialia 9(8) (2013) 7806-7813.

[39] R. Zheng, et al., Proteins can convert to β-sheet in single crystals, Protein science 13(5) (2004) 1288-1294.

[40] E. Figueiras, et al., Optical projection tomography as a tool for 3D imaging of hydrogels, Biomedical optics express 5(10) (2014) 3443-3449.

[41] A.M. Soto, et al., Optical projection tomography technique for image texture and mass transport studies in hydrogels based on gellan gum, Langmuir 32(20) (2016) 5173-5182.

[42] M.A.d. Moraes, et al., Preparation and characterization of insoluble silk fibroin/chitosan blend films, Polymers 2(4) (2010) 719-727.

[43] M. Sah, K. Pramanik, Preparation, characterization and in vitro study of biocompatible fibroin hydrogel, African Journal of Biotechnology 10(40) (2011) 7878-7892.

[44] G.M. Nogueira, et al., Hydrogels from silk fibroin metastable solution: Formation and characterization from a biomaterial perspective, Materials Science and Engineering: C 31(5) (2011) 997-1001.

[45] D. Wilson, et al., Conformational transitions in model silk peptides, Biophysical journal 78(5) (2000) 2690-2701.

[46] S. Ghosh, et al., Direct-Write Assembly of Microperiodic Silk Fibroin Scaffolds for Tissue Engineering Applications, Advanced Functional Materials 18(13) (2008) 1883-1889.

[47] C. Marcott, et al., Applications of AFM-IR—Diverse Chemical Composition Analyses at Nanoscale Spatial Resolution, Microscopy Today 20(6) (2012) 16-21.

[48] N. Qin, et al., Nanoscale probing of electron-regulated structural transitions in silk proteins by near-field IR imaging and nano-spectroscopy, Nature communications 7 (2016).

[49] S.Y. Cho, et al., Carbonization of a stable β-sheet-rich silk protein into a pseudographitic pyroprotein, Nature communications 6 (2015).

[50] C. Yan, D.J. Pochan, Rheological properties of peptide-based hydrogels for biomedical and other applications, Chemical Society Reviews 39(9) (2010) 3528-3540.

[51] T.T. Le, et al., The behavior of aged regenerated Bombyx mori silk fibroin solutions studied by 1 H NMR and rheology, Biomaterials 29(32) (2008) 4268-4274.

[52] J. Aho, et al., Rheology as a tool for evaluation of melt processability of innovative dosage forms, International journal of pharmaceutics 494(2) (2015) 623-642.

[53] M.G. Vander Heiden, et al., Understanding the Warburg effect: the metabolic requirements of cell proliferation, science 324(5930) (2009) 1029-1033.

[54] G.G. Leisk, et al., Electrogelation for protein adhesives, Advanced materials 22(6) (2010) 711-715.

[55] A. Gutowska, et al., Injectable gels for tissue engineering, The Anatomical Record 263(4) (2001) 342-349.

[56] S. Ryu, et al., Dual mode gelation behavior of silk fibroin microgel embedded poly (ethylene glycol) hydrogels, Journal of Materials Chemistry B 4(26) (2016) 4574-4584.

[57] A.N. Mitropoulos, et al., Transparent, Nanostructured Silk Fibroin Hydrogels with Tunable Mechanical Properties, ACS Biomaterials Science & Engineering 1(10) (2015) 964-970.

[58] X. Chen, et al., Conformation transition kinetics of Bombyx mori silk protein, Proteins: Structure, Function, and Bioinformatics 68(1) (2007) 223-231.

[59] K.M. Park, et al., Thermosensitive chitosan–Pluronic hydrogel as an injectable cell delivery carrier for cartilage regeneration, Acta biomaterialia 5(6) (2009) 1956-1965.

[60] G.Y. Lee, et al., Three-dimensional culture models of normal and malignant breast epithelial cells, Nature methods 4(4) (2007) 359-365.

[61] U.-J. Kim, et al., Structure and properties of silk hydrogels, Biomacromolecules 5(3) (2004) 786-792.

[62] N.E. Davis, et al., Enhanced function of pancreatic islets co-encapsulated with ECM proteins and mesenchymal stromal cells in a silk hydrogel, Biomaterials 33(28) (2012) 6691-6697.

[63] C.S. Szot, et al., 3D in vitro bioengineered tumors based on collagen I hydrogels, Biomaterials 32(31) (2011) 7905-7912.

[64] H. Kadowaki, et al., Amyloid β induces neuronal cell death through ROS-mediated ASK1 activation, Cell Death & Differentiation 12(1) (2005) 19-24.

[65] D. Loessner, et al., Bioengineered 3D platform to explore cell–ECM interactions and drug resistance of epithelial ovarian cancer cells, Biomaterials 31(32) (2010) 8494-8506.

SECTION V

GENERAL CONCLUSIONS

CHAPTER 10.

General Conclusions and Final Remarks

CHAPTER 10.

General conclusions and final remarks

10.1. General conclusions

In tissue engineering and regenerative medicine field, biomaterials occupy a place of relevance. Different biomaterials have been proposed for this purpose, being silk fibroin (SF) of particular interest as biomaterial since it can be processed into different forms, acquiring different properties. Moreover, this protein has shown to exhibit tunable properties according to the molecular conformation.

SF has been structured as three-dimensional (3D) matrix for cell adhesion and proliferation, in the form of membranes, films, scaffolds or hydrogels. Depending on the target tissue of implantation, different structuring approaches can be applied in order to achieve adequate mechanical support and biological cues in the defect site. SF-based scaffolds and hydrogels have been proposed for bone and cartilage tissue engineering applications. However, an improvement of the mechanical properties and structural integration of the SF-based materials is crucial for the successful regeneration of the tissues. Based on this, different studies were conducted in this thesis in order to create SF-based scaffolds with unique advanced properties to better fulfill the requirements of bone, cartilage and OC tissue engineering and regenerative medicine. Moreover, an additional source of application was envisioned for enzymatically crosslinked SF hydrogels with adequate properties to be used as injectable systems and 3D platforms for cancer research. Several studies have been proposing SF-based scaffolds for different tissue engineering applications. The application of fiber-based technologies or the incorporation of inorganic particles reinforcement, arose as a possible solution to improve the mechanical properties of scaffolds.

A weft-knitted textile technology was used in this thesis as a strategy to create highly-reproducible SF scaffolds with improved mechanical properties and structural stability. Moreover, the possibility of modify the surface properties of such structures and access their influence over biological behavior was also tested. The SF textile scaffolds three-dimensionality was also adjusted by processing the weft-knitted SF fabrics spaced by a monofilament of polyethylene terephthalate (PET). A similar 3D structure entirely made of PET was established for comparative purposes. Using this fully automated processing rote, novel 3D biotextile architectures were developed for bone regeneration applications.

An enzymatic-mediated method was used to crosslink SF, and in combination with salt-leaching/freeze-drying technologies proposed to produce macro-/micro-porous SF scaffolds. Herein, a revolutionary gelation method consisting of horseradish peroxidase (HRP) and hydrogen peroxide (H_2O_2), allowed for producing rapidly-formed SF scaffolds with suitable mechanical performance and structural stability for cartilage tissue engineering applications. In order to endow the developed HRP-crosslinked SF scaffolds with osteoconductive properties aiming at bone regeneration, ionic-doped (zinc and strontium) β-tricalcium phosphate (β-TCP) particles and pure β-TCP particles were introduced into the HRP-crosslinked SF solution prior gelation, followed by salt-leaching and freeze-drying methodologies. The composite scaffolds were layered together with the HRP-crosslinked SF scaffolds to generate monolithic bilayered scaffolds for osteochondral (OC) tissue regeneration.

Besides the development of the SF-based scaffolds, the peroxidase-induced crosslinking method was also applied in this thesis for hydrogels preparation. In the literature, several SF hydrogels have been proposed using different gelation methods. However, most of them are not suitable to be used as injectable systems involving long gelation times and harsh preparation conditions. The proposed HRP-crosslinked SF hydrogels are formed in a few minutes at physiological conditions, being ideal for injectable purposes. Furthermore, SF hydrogels with spatially controlled properties were produced in a main amorphous molecular conformation, suitable for cell encapsulation studies.

In the following Sections are presented the general conclusions of the experimental work described in Chapters 5 to 9.

10.1.1. Surface modification treatments on SF biotextiles for tissue engineering applications

SF scaffolds have been prepared through different processing methodologies for engineering tissues like bone, cartilage, meniscus, ligament or tendon. However, mimicking the mechanical properties of such tissues can be a big challenge for scaffolds' processing and for a successful tissue regeneration. Chapter 5, described a weft-knitted textile technology for producing SF scaffolds with improved mechanical properties and structural stability. Moreover, the possibility of tuning the surface properties of such materials with chemical and physical treatments (NaOH solution, UV/O_3 exposure, and air plasma treatment followed by AAc, VPA and VSA grafting) was also evaluated. The novelty of this work relied on the fact that it was possible to modulate SF biotextiles with different properties for tissue engineering applications. The physical characterization of the presented SF scaffolds indicated that the proposed treatments had a positive effect on the fibers mechanical strength and ductility. The morphological study revealed that the textile scaffolds presented a highly porous structure at surface level, and the chemical analysis confirmed the successful modifications of the surfaces with different effects over the scaffolds' topography and wettability. The *in vitro* biological characterization of the fiber-based scaffolds positively influenced the adhesion and spreading of L929 fibroblasts cells, in comparison to the round morphology of cells seeded in SF membranes used as control. Therefore, the developed SF textile scaffolds were found to be excellent candidates for tissue engineering scaffolding, showing tunable properties according to the target application. This study also opened a new window to the fabrication of load-bearing and anisotropical SF-based textile scaffolds for specific bone tissue engineering applications.

10.1.2. SF-based 3D biotextiles for bone regeneration

Textile-based scaffolds have been developed and applied for bone tissue engineering. However, non-of these scaffolds were made of SF or processed with different textile technologies to increase their three-dimensionality and anisotropic properties. Chapter 6, reported the production of two weft-knitted SF fabrics spaced by a PET monofilament. A different knitting technology was used to fabricate spacer scaffolds entirely made of PET for comparative analysis. This study presented a good example of how textile technologies can be used for different scaffolding approaches. In this particular case, it was possible to increase the scaffolds' three-dimensionality and internal porosity to obtain an accurate matrix formation in the bone remodeling process. Moreover, suitable load-bearing and anisotropic properties were presented by the spacer fabrics, indicative of their structural similarities to the flat bone and making them desirable for specific cranio-maxillofacial bone tissue applications. Both knitted spacer fabrics promoted the attachment, viability, proliferation and migration of human adipose-derived stem cells (hASCs). The SF-PET scaffolds promoted the typical pattern of alkaline phosphatase (ALP) activity on cells under osteogenic differentiation, accompanied by extracellular matrix (ECM) mineralization. Moreover, the osteogenic differentiation inducement within the knitted spacer scaffolds was also confirmed by the genotypic and phenotypic expression of bone-related markers. The *in vivo* chick chorioallantoic membrane (CAM) assay revealed higher angiogenic response on the SF-PET scaffolds, but both spacer fabrics allowed tissue ingrowth and blood vessels infiltration after subcutaneous implantation in mice. These promising results demonstrated that the developed 3D biotextiles present suitable architecture and structural stability, suitable for osteogenic differentiation and bone tissue regeneration. Moreover, the precise control of the processing and the reproducibility of the textile technologies make them desired for different scaffolding strategies.

10.1.3. Enzymatically crosslinked SF scaffolds with potential for cartilage tissue engineering

Different approaches have been proposed for producing SF matrices for specific cartilage tissue engineering applications. Hydrogels, amongst all matrices, are those that present more similarities to the native cartilage tissue. However, the mechanical properties of hydrogels are in most cases inferior to that of human cartilage. At the same time, porous scaffolds can achieve better mechanical strength but also lose resilience and hydration properties. Thus, the improvement of the mechanical properties of the SF hydrogels, maintaining an elastic behavior and swelling capacity, is critical for the successful cartilage tissue regeneration. Chapter 7, described novel SF scaffolds with adequate mechanical properties and structural behavior, derived from the enzymatic crosslinking of high-concentrated aqueous SF solution (16 wt.%). A HRP-mediated method was used to crosslink SF in the presence of H_2O_2, with formulation of 1/0.26‰/1.45‰ (SF/HRP/ H_2O_2). The novelty of this work consisted in the application of salt-leaching and freeze-drying methodologies to process the SF crosslinking solution and form high performance HRP-crosslinked SF scaffolds. In this study, the initial physicochemical characterization indicated that the developed scaffolds presented β-sheet conformation. The morphological analysis revealed a macro-/micro-porous structure, and micro-CT results further demonstrated a high porosity and interconnectivity in the scaffolds. The compressive tests showed that mechanical properties of the HRP-crosslinked SF scaffolds were significantly higher in the dry state. The scaffolds also presented large swelling capability, maintaining their structural integrity up to 30 days at physiological conditions. During long-term degradation, an adequate biostability was also observed. Human ASCs showed good adhesion and proliferation within the scaffolds, favored by their macro-/micro-porous structure. Chondrogenic induction was pronounced by the higher glycosaminoglycans (GAGs) content detected in constructs cultured in chondrogenic differentiation medium. Chondrogenic differentiation of hASCs was also assessed by the genotypic and phenotypic expression of chondrogenic-related markers, and deposition of cartilage-specific ECM. The DMA analysis showed that the mechanical properties of scaffolds improved after 28 days of culture under chondrogenic conditions. Furthermore, these scaffolds allowed deeply tissue ingrowth when subcutaneously implanted in mice. Therefore, the developed HRP-crosslinked SF scaffolds were good candidates to be used in cartilage tissue engineering scaffolding. With this study, further options were taken in consideration to prepare bioactive and load-bearing multifunctional scaffolds for other tissue engineering applications, including for bone tissue and OC tissue.

10.1.4. Enzymatically crosslinked bilayered SF/SF-β-TCP scaffolds with potential for osteochondral tissue engineering

Chapter 8 proposed novel bilayered scaffolds for OC defects regeneration. The proposed HRP-crosslinked SF scaffolds were of improved structural and mechanical properties for cartilage tissue engineering. However, these scaffolds were not osteoconductive and their mechanical properties did not fill the requirements of human bone tissue. Therefore, the enhancement of the mechanical properties and bioactivity of the HRP-crosslinked SF scaffolds was proposed by the incorporation of ZnSr doped-β-TCP in the solution phase. The salt-leaching technique was further used to create porous-like structures. To produce macro-/micro-porous bilayered scaffolds a HRP-crosslinked SF layer and a HRP-crosslinked SF/ZnSr-TCP layer were fully integrated. Pure HRP-crosslinked SF/SF-β-TCP scaffolds were used for comparative purposes. The bilayered scaffolds presented a suitable stability due to the β-sheet conformation inducement and enzymatic crosslinking process of SF. Superior mechanical properties were achieved due to the TCP incorporation. Spatially controllable porosity and TCP distribution/confinement were also obtained with the bilayered scaffolds. After immersion in simulated body fluid (SBF) apatite formation was observed, but restricted to the composite layers. These layers promoted higher ALP activity when seeded with human osteoblasts (hOBs) and co-cultured with human articular chondrocytes (hACs), seeded in the HRP-crosslinked SF layer. The formation of a mineralized matrix was also observed in the composite layers, whereas the chondrogenic inducement was represented by the GAGs deposition at the HRP-crosslinked SF porous layer. The bilayered scaffolds supported cells attachment, viability, and proliferation in the respective scaffold compartments, as well as, good integration at the cartilage and bone tissues interface regions. These promising results demonstrated that the proposed bilayered scaffolds are promising candidates for OC tissue engineering applications.

10.1.5. Enzymatically crosslinked SF hydrogels as 3D matrices for cell encapsulation studies

In Chapter 9, it is demonstrated that injectable SF hydrogels can also be produced by the proposed HRP-crosslinking system. These hydrogels were formed in a few minutes and under physiological conditions, which is advantageous when compared to the SF hydrogels prepared elsewhere which may include longer gelation times and more aggressive preparation conditions, limiting their properties as injectable systems. Furthermore, the peroxidase-induced SF hydrogels were formed in a main amorphous conformation, with completely distinct properties as compared to the SF hydrogels of β-sheet conformation reported in previous studies. They presented a transparent appearance and viscoelastic properties of injectable hydrogels, suitable for cell encapsulation, viability and proliferation. Furthermore, a spontaneous molecular conformation transition from random coil to β-sheet was confirmed after 7 to 10 days of hydrogels formation, affecting cell viability and inducing apoptosis. These versatile SF hydrogels not only bring new insights on the use of SF as a biomaterial, but their versatility makes them possible candidates for several biomedical applications, ranging from tissue engineering and regenerative medicine to cancer therapy studies.

10.2. Final remarks

In this thesis, several approaches were proposed to manipulate SF as biomaterial for different tissue engineering and biomedical applications. Scaffolds and hydrogels were produced, tuned and functionalized to better fulfil the several applications requirements. In the case of SF scaffolds, they were proposed as textile materials for tissue engineering and bone regeneration. Moreover, an enzymatic approach was proposed to crosslink SF and produce scaffolds and hydrogels suitable for different applications. Regarding the SF scaffolds, they have shown potential for cartilage tissue engineering applications and tunable properties for bone and OC scaffolding strategies. The pore size of the textile-based SF scaffolds is around several hundred micrometres which is adequate for bone tissue engineering. The HRP-crosslinked SF scaffolds also presented a mean pore size suitable for cartilage matrix formation and infiltration. These hypotheses have been confirmed by *in vitro* osteogenic and chondrogenic differentiation studies, and *in vivo* acellular experiments to screen tissue ingrowth. However, future works involving the use of differentiating stem cells integrated in the scaffolds and combined with a specific bioreactor, can increase the cell seeding efficiency and better mimic the proliferation and differentiation process, providing additional clues to the present studies. The hydrostatic pressure of bioreactors can be adjusted towards enhancing the chondrogenic differentiation of the cells. Long-term *in vivo* studies using big animal models and cell-loaded scaffolds implanted in bone and cartilage defects, need to be considered for the respective textiles and peroxidase-mediated SF scaffolds. Moreover, the biomechanical properties and degradation profile of the explants should also be monitored. Biological factors, such us growth factors or hormones, can be directly incorporated into the scaffolds or using nanoparticles, cyclodextrins or even liposomes as carriers of specific drugs (bisphosphonates or glycosamine sulphate), to stimulate bone and cartilage tissues repair and regeneration. In the specific case of bone tissue engineering, the vascularization in the scaffolds is extremely important. The angiogenic effect of the textile-based scaffolds was analysed by means of performing the CAM assay. Nevertheless, the co-culture of endothelial cells and osteoblasts into these scaffolds is worthy of study.

Concerning the bilayered scaffolds, further *in vitro* biological evaluation should be performed. The double chamber bioreactors could be specifically used for performing long-term *in vitro* studies, by seeding and culturing different cells in the chondral and subchondral bone-like layers. For example, chondrogenic and osteogenic differentiation studies can be performed in the chondral and subchondral bone-like layers, respectively. Moreover, the evaluation of the newly formed chondral and bony tissues in the respective layers should be addressed. This includes the evaluation of specific osteo- and chondro-genic related markers, such us Collagen I, Collagen IIa, COMP, Aggrecan, Sox-9, Osteocalcin, Osteopontin, ALP. The engineered OC interface should also be addressed, not only in terms of integrated mechanical properties but also for the formation of calcified cartilage tissue and associated specific genes expression, like Collagen X, MMPs, PTHrP and Runx2. *In vivo*, long-term implantation studies should be performed using cell-free or cell-based approaches. Herein, the OC scaffolds can be first engineered *in vitro* for the incorporation of growth factors like BMPs, FGFs, TGF-β1, IGF-I or PDGF into the chondral and subchondral bone-like layers, to induce neocartilage tissue and bone formation. Previous to implantation, OC tissue obtained from a healthy human knee can be used to mechanically test the fixation and stability of the OC scaffolds to the implantation sites. Moreover, when performing *in vivo* implantation into OC defects, external mechanical stimulus on the implanted site may also be employed, such us continuous passive motion, early weight bearing or continuous active motion. The use of traditional therapeutic approaches of electrotherapy may also be considered.

The peroxidase-mediated crosslinked SF hydrogels have shown to be promising for a wide range of applications. Contrary to most of the reviewed SF hydrogels, these are formed in a main amorphous conformation compatible with cell encapsulation. Moreover, they are formed at physiological conditions and using an enzymatic crosslinking system suitable with the human body. Thus, they can be evaluated as injectable matrices for filling tissues and delivery specific drugs and growth factors as short-term release systems. Since these hydrogels become crystalline over time, which affects cell viability, they were envisioned as 3D platforms for cancer therapy studies. Moreover, considering that the tyrosine groups reacting in the SF enzymatic crosslinking process are common in host tissues, these SF hydrogels could covalently bind to the host tissue during the enzymatic crosslinking and embrace the tumor, enhancing material/tissue affinity. The hydrogels allowed for the typical behavior of tumor-like cells, with the formation of clusters especially after β-sheet conformation transition. Further studies investigating the hypothesis that β-sheet conformation transition induces hypoxia within the hydrogel structure which favors the formation of clustered cells, will be of great interest to understand the effect of this biomaterial in the tumor microenvironment. The further incorporation of anti-cancer drugs within the cell-encapsulated SF hydrogels or even previous encapsulation, may also be considered for testing new cancer therapies.

After concluding this thesis, some interesting ideas can still be explored not only to fully validate the proposed work, but also to cover new fields of investigation. Some of them are currently being pursued by our research group, in particular:

1. Evaluation of the regenerative potential of the proposed bilayered scaffolds on rabbit models of OC defects;
2. Development of HRP-crosslinked SF/Elastin bioinks for treatment of degenerated intervertebral disc;
3. Development of 3D bioprinted HRP-crosslinked SF scaffolds for fibrocartilage regeneration;
4. Production of nerve guidance conduits from HRP-crosslinked SF hydrogels;
5. Generation of a 3D bone cancer model based on SF hydrogels crosslinked by HRP/calcium peroxide (CaO_2) system.